Dissertation

Search for the Standard Model Higgs Boson and Test of CP Invariance in Vector-Boson Fusion Production of the Higgs Boson in the Fully Leptonic $H \to \tau^+\tau^- \to \ell^+\ell^- 4\nu$ Final State in Proton-Proton Collisions with the ATLAS Detector at the LHC

Christian Schillo

Fakultät für Mathematik und Physik
Albert-Ludwigs-Universität Freiburg

Search for the Standard Model Higgs Boson and Test of CP Invariance in Vector-Boson Fusion Production of the Higgs Boson in the Fully Leptonic $H \to \tau^+\tau^- \to \ell^+\ell^- 4\nu$ Final State in Proton-Proton Collisions with the ATLAS Detector at the LHC

Dissertation

zur Erlangung des Doktorgrades der
Fakultät für Mathematik und Physik der

Albert-Ludwigs-Universität
Freiburg im Breisgau

vorgelegt von
Christian Schillo

Mai 2016

Dekan:	Prof. Dr. Kröner
Betreuer der Arbeit:	Prof. Dr. Markus Schumacher
Prüfer:	Prof. Dr. Gregor Herten
	JProf. Dr. Harald Ita
	Prof. Dr. Markus Schumacher

Datum der mündlichen Prüfung:
27. Oktober 2016

Contents

1 Introduction

The Standard Model of particle physics (SM) describes the physics of elementary particles, leptons and quarks, and their interactions. It provides insight into the matter of our universe, its constituents and also its properties. There are four different forces through which elementary particles interact: the electromagnetic, weak, strong and gravitational interaction. In 1960, Glashow, Weinberg and Salam established an electroweak theory, that unifies the electromagnetic and weak interaction. The electroweak and strong interaction form the SM, whereas gravitation is presently not included in a unified and consistent quantum field theory with the other interactions. SM interactions of elementary particles are mediated via gauge bosons and a large number of SM predictions have been precisely confirmed by current measurements at LEP[1], Tevatron or the LHC[2]. The predictive power of the SM has recently been demonstrated by the discovery of the Higgs boson at CMS and ATLAS[3] based on 2011 and 2012 data [1, 2]. The Higgs boson was predicted by Englert, Brout and Higgs already in 1964 [3–5]. The corresponding analyses exploit various Higgs boson production modes and its decay modes into gauge bosons.

The Higgs boson is an important part of the SM and is the result of a mechanism called electroweak symmetry breaking. The SM is based on the concept of local gauge invariance, which initially requires that the gauge bosons mediating the interactions are massless. However, electroweak gauge bosons are observed to be massive. By breaking the electroweak symmetry, masses of the gauge bosons and also of the fermions are generated. The resulting Higgs boson couples to all massive fermions and gauge bosons with a coupling strength proportional to the corresponding particle masses. The mass of the Higgs boson itself is not predicted by the SM and needs to be determined experimentally. The measured mass value of the Higgs boson is about 125 GeV based on combined analyses by CMS and ATLAS [6]. So far, all measurements of the Higgs boson properties such as cross sections, couplings and quantum numbers are consistent with the SM prediction.

The first part of the thesis presents the search for the SM Higgs boson in the fully leptonic decay mode $H \to \tau^+\tau^- \to \ell^+\ell^- 4\nu$, where both τ leptons are required to decay into electrons or muons, based on the $\sqrt{s} = 8$ TeV dataset with an amount of $\int \mathcal{L}dt = 20.3$ fb^{-1}. Such di-lepton signal events can be reconstructed very precisely in the detector due to the characteristic lepton isolation. The corresponding lepton neutrinos are detected indirectly in terms of missing energy in the detector. The

[1] **L**arge **E**lectron-**P**ositron **C**ollider
[2] **L**arge **H**adron **C**ollider
[3] **C**ompact **M**uon **S**olenoid and **A** **T**oroidal **L**HC **A**pparatu**S**.

confirmation of fermionic Higgs boson couplings beside of the already observed couplings to vector bosons would further complete the picture of the SM Higgs sector. The analysis is based on multivariate analysis techniques and provides a measurement of the Higgs boson signal strength normalised to the SM prediction. In the second part of the thesis, a study of the charge-parity (CP) structure of Higgs boson couplings to vector bosons is presented. This test of CP invariance in vector-boson fusion production of the Higgs boson is also based on the 8 TeV dataset and the decay channel $H \to \tau^+\tau^- \to \ell^+\ell^- 4\nu$, using CP-odd observables such as the Optimal Observable method. The CP analysis provides central confidence intervals for the CP-mixing parameter $\tilde{d}$, which enables CP-odd contributions to the CP-even coupling structure of the Standard Model HVV interaction within the framework of an effective field theory. In the SM, Higgs boson couplings to vector bosons are thus expected to be CP conserving. If CP violating anomalous coupling structures were observed, this could give explanation to currently unsolved questions of physics such as the origin of the imbalance of matter and anti-matter (baryon asymmetry) in the observable universe.

The thesis will proceed as follows. Chapter 2 gives an introduction to the theory of the SM, its limitations and anomalous Higgs boson couplings. Chapters 3 and 4 provide an overview of the experimental setup of the ATLAS experiment at the LHC and the reconstruction and identification of physics objects at ATLAS. The analysis of the search for the SM Higgs boson in the decay channel $H \to \tau^+\tau^- \to \ell^+\ell^- 4\nu$ is presented in chapter 5. Based on the same decay channel, chapter 6 presents a test of CP invariance in vector-boson fusion production of the Higgs boson. In the chapters 7 and 8, the estimation of background processes at the LHC, in particular the estimation of $Z/\gamma^* \to \tau^+\tau^-$ via the Embedding method [7], and systematic uncertainties are discussed. The statistical methods that are applied to extract the Higgs boson signal, are explained in chapter 9. Chapter 10 provides the final results of both analysis, the search and the CP analysis. Finally, chapter 11 summarizes the results of the ATLAS analyses, that combine the decay mode $H \to \tau_{\text{lep}}\tau_{\text{lep}}$, presented in this thesis, with the modes $H \to \tau_{\text{lep}}\tau_{\text{had}}$ and $H \to \tau_{\text{had}}\tau_{\text{had}}$ for 7 TeV and 8 TeV data in case of the search analysis [8] and with the mode $H \to \tau_{\text{lep}}\tau_{\text{had}}$ for 8 TeV data in case of the CP analysis [9]. The search for $H \to \tau^+\tau^- \to \ell^+\ell^- 4\nu$ and the test of CP invariance in vector-boson fusion Higgs boson production as well as the studies on the Embedding method presented in the context of this thesis have been published in Ref. [8], [9] and [7].

2 Theory

This chapter provides an overview of the Standard Model of particle physics. The SM describes the physics of elementary particles and their fundamental interactions. In section 2.1, the particle content as well as basic information about quantum electrodynamics, the electroweak theory and quantum chromodynamics is presented. Furthermore, the breaking of the electroweak symmetry is explained, a phenomena that is responsible for generated masses of the electroweak gauge bosons by introducing a new scalar field called Higgs field. Although the SM is confirmed by a large set of measurements, open questions are specified that cannot be explained by the SM. Section 2.2 provides information about the production mechanism, the decay modes and the properties of the SM Higgs boson. Recent theoretical and experimental constraints on Higgs boson properties are also mentioned. In addition, non-SM couplings of the Higgs boson are also discussed in section 2.3, that violate the CP invariance of the SM. Such CP violating Higgs boson couplings might contribute to the baryon asymmetry of the observable universe, that cannot be explained by the SM.

2.1. Standard Model of Particle Physics

The SM is a relativistic quantum field theory, based on the principle of local gauge invariance. Predictions by the SM are confirmed very precisely by a large set of experiments.

2.1.1. Elementary Particles

Elementary particles are grouped into fermions and bosons. Fermions of the SM follow the Fermi-Dirac statistics with spin 1/2. There are leptons and quarks, which are divided into three generations with different flavour. Leptons are electrons, muons and τ leptons (e, μ and τ) each with a negative charge of -1[1] and the corresponding electrically neutral neutrinos (ν_e, ν_μ and ν_τ). Quarks are divided into up, charm and top quarks (u, c and t) each with the charge of $+2/3$ and down, strange and bottom quarks (d, s and b) with the charge of $-1/3$. For every lepton and quark, there is a corresponding anti-particle with the complementary charge. The division into three generations of leptons and quarks stems from the

[1] The charge of particles is given in units of the elementary charge $q_e = 1.602177 \cdot 10^{-19}$ C.

difference in the particle masses[2]. Matter consists of electrons and quarks of the first generation.

The fundamental interactions between elementary particles are based on the exchange of gauge bosons. These gauge bosons are vector bosons with spin 1. Three of the four known fundamental interactions are described by the SM: the *electromagnetic*, the *weak* and the *strong* interaction. Gravitation as a fourth interaction is negligible for small distance interactions, when compared to the three SM interactions, and is neglected in the SM.

The electromagnetic force acts on charged particles by exchanging photons γ. Since photons are massless, the electromagnetic interaction has infinite range. The weak force acts on all fermions via the exchange of W and Z bosons. These gauge bosons are heavy, which manifests in the short distance of the weak interaction. The strong force acts on quarks by exchanging gluons. Gluons couple to the color charge of quarks[3]. Quarks do not occur as free particles since final state particles have to be colorless. With increasing distance, quarks are combined into multi-quark bound states called hadrons (confinement). Such hadrons consist either of a quark anti-quark pair (meson) or of three quarks (baryon). Mesons and baryons are color neutral and can be directly measured in the detector in contrast to single quarks. However, quarks behave like quasi free particles at short distances (asymptotic freedom) as assumed in proton proton collisions at the LHC. Tables 2.1 and 2.2 summarize the properties of the fundamental elementary particles and the gauge bosons of the SM.

2.1.2. Quantum Electrodynamics

The theory of quantum electrodynamics (QED) is an example of local gauge symmetry [14, 15]. It assumes invariance of the Lagrange density $\mathcal{L}$ under local phase transformations of the field $\psi(x)$

$$\psi \quad \rightarrow \quad e^{i\alpha(x)}\psi. \tag{2.1}$$

The Lagrange density of a free fermion field ψ is given by

$$\mathcal{L} \quad = \quad \overline{\psi}(x)(i\gamma^{\mu}\partial_{\mu} - m_f)\psi(x) \ , \tag{2.2}$$

where m_f is the fermion mass. Based on Hamilton's principle, the Euler-Lagrange equations of motion (Dirac equation) for free fermion fields can be deduced from equation 2.2

$$(i\gamma^{\mu}\partial_{\mu} - m_f)\psi(x) = 0 \ . \tag{2.3}$$

[2]Fermions of the first generation include the lightest leptons or up- and down-type quarks whereas third generation fermions are rather heavy. In the SM, neutrinos are assumed to be massless. However, the observation of neutrino oscillation hints to small non-zero masses [10–12].

[3]The color charge of quarks can be red, blue or green.

Leptons (Spin 1/2)				
Generation	Flavour		Charge [q_e]	Mass [MeV]
First	$\mathbf{e}$	Electron	-1	0.511
	$\boldsymbol{\nu_e}$	Electron neutrino	0	$< 2 \cdot 10^{-6}$
Second	$\boldsymbol{\mu}$	Muon	-1	105.7
	$\boldsymbol{\nu_\mu}$	Muon neutrino	0	< 0.2
Third	$\boldsymbol{\tau}$	τ lepton	-1	1777.0
	$\boldsymbol{\nu_\tau}$	τ lepton neutrino	0	< 18.2
Quarks (Spin 1/2)				
Generation	Flavour		Charge [q_e]	Mass [MeV]
First	$\boldsymbol{u}$	Up	2/3	1.7-3.1
	$\boldsymbol{d}$	Down	-1/3	4.1-5.7
Second	$\boldsymbol{c}$	Charm	2/3	1290
	$\boldsymbol{s}$	Strange	-1/3	80-130
Third	$\boldsymbol{t}$	Top	2/3	172900
	$\boldsymbol{b}$	Bottom	-1/3	4190

Table 2.1. *Elementary particles of the SM: leptons and quarks [13].*

Gauge bosons (Spin 1)					
Interaction	Vector boson		Charge [q_e]	Mass [MeV]	Distance [m]
Electromagnetic	$\boldsymbol{\gamma}$	Photon	0	0	∞
Weak	$\mathbf{W}^{\pm}$	Charged boson	± 1	80.4	$< 10^{-15}$
	$\mathbf{Z}$	Neutral boson	0	91.2	
Strong	$\boldsymbol{g}$	8 gluons	0	0	$\approx 10^{-15}$

Table 2.2. *Elementary particles of the SM: gauge bosons of the fundamental interactions [13].*

However, the Dirac equation is not invariant under local gauge transformations. Local phase transformations in QED are defined by

$$\psi \quad \rightarrow \quad e^{iQ\chi(x)}\psi \tag{2.4}$$

according to transformations of the unitary group $U(1)$. Here, Q is the charge operator and $\chi = \chi(x)$ a gauge phase. To assure local gauge invariance of the Dirac equation, the *covariant derivative* $\mathcal{D}_\mu = \partial_\mu + iQA_\mu$ and a vector field $A_\mu = A_\mu(x)$ are introduced. The vector field must transform according to

$$A_\mu \quad \rightarrow \quad A_\mu - \partial_\mu\chi. \tag{2.5}$$

to preserve the local gauge symmetry. Replacing the derivative in equation 2.2 by the covariant derivative and choosing a vector field, that fulfills equation 2.5, results in the QED Lagrange density

$$\mathcal{L}_{QED} = \overline{\psi}(x)(i\gamma^\mu\mathcal{D}_\mu - m_f)\psi(x) - \frac{1}{4}F_{\mu\nu}F^{\mu\nu}, \tag{2.6}$$

which is invariant under local gauge transformations. The field tensor $F_{\mu\nu}$ is defined by $F_{\mu\nu} = \partial_\mu A_\nu - \partial_\nu A_\mu$.

In summary, the invariance of the QED Lagrange density can be restored by introducing the photon field $A_\mu(x)$ in terms of a covariant derivative $\mathcal{D}_\mu$ and corresponding additional kinematic terms $\frac{1}{4}F_{\mu\nu}F^{\mu\nu}$ of the photon. The fermions couple to the photon via the electrical charge Q, which also determines the strength of the coupling. The photon must be massless ($m_\gamma = 0$) since a mass term, typically in terms of $\frac{1}{2}m_\gamma^2 A_\mu A^\mu$ for massive vector fields, would spoil the invariance under local gauge transformations. The equation of motion for free fermions in QED is then given by

$$(i\gamma^\mu\partial_\mu - m_f)\psi(x) = q\gamma^\mu A_\mu\psi(x)\ . \tag{2.7}$$

QED is a renormalisable theory, that is able to make high precision predictions of the electromagnetic processes of elementary particles [16].

2.1.3. Electroweak Theory

In 1967, Glashow, Weinberg and Salam presented a unified electroweak gauge theory, which combines the QED and the weak interaction [17–19]. The electroweak theory divides the fermions into left- and right-chiral fields

$$\psi = \psi_L + \psi_R = \frac{1}{2}(1-\gamma^5)\psi + \frac{1}{2}(1+\gamma^5)\psi\ . \tag{2.8}$$

The fermion fields in the electroweak theory are summarized in multiplets according to the weak isospin quantum number I_3 as shown in table 2.3. Left-chiral fermions are ordered in isospin doublets ψ_L and couple to neutral and charged currents by exchanging $W^\pm$ and Z bosons or photons. Neutrinos occur only in the left-chiral

Fermions			Q	Y	I_3
$\begin{pmatrix}\nu_e\\ e\end{pmatrix}_L$	$\begin{pmatrix}\nu_\mu\\ \mu\end{pmatrix}_L$	$\begin{pmatrix}\nu_\tau\\ \tau\end{pmatrix}_L$	0 -1	-1 -1	$+1/2$ $-1/2$
$\begin{pmatrix}u\\ d\end{pmatrix}_L$	$\begin{pmatrix}c\\ s\end{pmatrix}_L$	$\begin{pmatrix}t\\ b\end{pmatrix}_L$	$+2/3$ $-1/3$	$+1/3$ $+1/3$	$+1/2$ $-1/2$
e_R	μ_R	τ_R	-1	-2	0
u_R	c_R	t_R	$+2/3$	$+4/3$	0
d_R	s_R	b_R	$-1/3$	$-2/3$	0

Table 2.3. *Left- and right-chiral fermion fields and the corresponding quantum numbers: Q is the electrical charge, Y the hypercharge and I_3 the configuration of the weak isospin [14]. Quarks with isospin $I_3 = -1/2$ are not the quark mass eigenstates. They correspond to the electroweak mixed eigenstates, which can be extracted using the CKM matrix according to the Cabbibo-GIM scheme [15, 20, 21].*

state, due to their vanishing mass. Right-chiral fermions form isospin singlets ψ_R and couple to neutral currents.

The electroweak theory is based on the symmetry groups $SU(2)_L \times U(1)_Y$. The group $U(1)_Y$ contains all unitary transformations of dimension one analogous to the QED theory. The hypercharge Y is the quantum number of the group. It is defined by the Gell-Mann-Nishijima relation

$$Q = I_3 + Y/2 \,. \tag{2.9}$$

The local phase transformation of $U(1)_Y$ for the left-chiral doublets ψ_L and the right-chiral singlets ψ_R is

$$\psi_L \;\rightarrow\; e^{i\frac{g'}{2}Y\chi(x)}\psi_L \,, \tag{2.10}$$

$$\psi_R \;\rightarrow\; e^{i\frac{g'}{2}Y\chi(x)}\psi_R \,. \tag{2.11}$$

The local gauge transformation of $SU(2)_L$ acts on left-chiral doublets and is defined by

$$\psi_L \;\rightarrow\; e^{i\frac{g}{2}\boldsymbol{\tau}\boldsymbol{\beta}(x)}\psi_L \,. \tag{2.12}$$

The vector $\boldsymbol{\tau}$ consists of the Pauli matrices while $\boldsymbol{\beta}(x)$ represents the three rotation angles. The factors g and g' are the coupling constants of the gauge groups $U(1)_Y$ and $SU(2)_L$. As explained in case of the QED theory, gauge invariance under local phase transformations cause the existence of additional gauge fields. The gauge fields of the electroweak theory are B_μ and $\mathbf{W}_\mu = \left(W^1_\mu, W^2_\mu, W^3_\mu\right)$. The covariant derivative in case of the electroweak theory is then defined by

$$\mathcal{D}_\mu = \partial_\mu + ig\frac{\boldsymbol{\tau}}{2}\mathbf{W}_\mu + ig'\frac{Y}{2}B_\mu. \tag{2.13}$$

Replacing the derivative in equation 2.2 by the covariant derivative of equation 2.13 yields the electroweak Lagrange density

$$\begin{aligned}\mathcal{L}_{EW} &= \bar{\psi}_L \gamma^\mu \left(i\partial_\mu - g\frac{\boldsymbol{\tau}}{2} \cdot \mathbf{W}_\mu - g'\frac{Y}{2}B_\mu \right) \psi_L \\ &\quad + \bar{\psi}_R \gamma^\mu \left(i\partial_\mu - g'\frac{Y}{2}B_\mu \right) \psi_R \\ &\quad - \frac{1}{4}\mathbf{W}_{\mu\nu} \cdot \mathbf{W}^{\mu\nu} - \frac{1}{4}B_{\mu\nu}B^{\mu\nu}, \end{aligned} \tag{2.14}$$

that includes couplings of the left and right-handed fermion fields $\psi_{L/R}$ to the gauge fields. Kinematic terms of the gauge fields needs to be added to ensure the invariance of the Lagrange density under local gauge transformations. These kinematic terms $\mathcal{L}_{kin} = -\frac{1}{4}\mathbf{W}_{\mu\nu}\mathbf{W}^{\mu\nu} - \frac{1}{4}B_{\mu\nu}B^{\mu\nu}$ contain the tensors $\mathbf{W}_{\mu\nu} = \partial_\mu \mathbf{W}_\nu - \partial_\nu \mathbf{W}_\mu + ig\mathbf{W}_\mu \times \mathbf{W}_\nu$ and $B_{\mu\nu} = \partial_\mu B_\nu - \partial_\nu B_\mu$. The tensor $\mathbf{W}_{\mu\nu}$ for $SU(2)$ is more complex than than B_μ for $U(1)$ due to the non-Abelian structure of the interaction.

To identify the well-known charged W-bosons, the gauge fields need to be rewritten in terms of eigenstates of the charge operator

$$W_\mu^\pm = \frac{1}{\sqrt{2}}(W_\mu^1 \mp iW_\mu^2) \,. \tag{2.15}$$

The charged vector bosons act only on left-handed fermions. The Z boson couples also to right-chiral fermion fields and can therefore not identified with W_μ^3, since it only couples to left-chiral fields. In addition, the gauge field B_μ can not be identified with the photon, because photons do not couple to neutrinos due to their chargeless nature. By mixing both fields W_μ^3 and B_μ

$$\begin{pmatrix} A_\mu \\ Z_\mu \end{pmatrix} = \begin{pmatrix} \cos\theta_w & \sin\theta_w \\ -\sin\theta_w & \cos\theta_w \end{pmatrix} \begin{pmatrix} B_\mu \\ W_\mu^3 \end{pmatrix}, \tag{2.16}$$

the known physical fields can be constructed. The Z-boson corresponds to the vector field Z_μ and the photon to A_μ. The coupling constants can then be expressed as $g = e/\sin\theta_w$ and $g' = e/\cos\theta_w$ with θ_w being the weak mixing angle.

To guarantee gauge invariance and renormalisation of the electroweak $SU(2)_L \times U(1)_Y$ theory, no mass terms can be included in $\mathcal{L}_{EW}$ for the fermion and gauge boson fields[4]. However, experiments show that fermions and gauge bosons do have mass. Electroweak symmetry breaking provides a solution in terms of the Englert-Brout-Higgs-Guralnik-Hagen-Kibble mechanism (hereafter called the Higgs mechanism) [3–5, 22, 23]. This mechanism generates mass terms of the electroweak gauge boson while assuring gauge invariance and renormalisation. It is explained in section 2.1.4.

[4] As an example, the cross section of vector boson scattering $WW \to WW$ diverges in case of massive gauge bosons due to additional longitudinal components of the vector fields, which would violate unitarity.

2.1.4. Electroweak Symmetry Breaking

The Higgs mechanism has already been proposed by Englert, Brout, Higgs, Guralnik, Hagen and Kibble in 1964 [3–5, 22, 23] and introduces a new isospin doublet of the charged scalar field Φ^+ and the neutral complex scalar field Φ^0 with a hypercharge quantum number of $Y = 1$

$$\Phi = \begin{pmatrix} \Phi^+ \\ \Phi^0 \end{pmatrix} \qquad (Y = 1). \tag{2.17}$$

The Lagrange density of the Higgs doublet is defined by

$$\mathcal{L}_{Higgs} = (\partial_\mu \Phi)^\dagger (\partial^\mu \Phi) - V_{Higgs}(\Phi^\dagger, \Phi) \tag{2.18}$$

with $V_H(\Phi^\dagger, \Phi) = -\mu^2 \Phi^\dagger \Phi + \lambda^2 (\Phi^\dagger \Phi)^2$ being the Higgs potential. The $SU(2)_L \times U(1)_Y$ gauge invariant Lagrange density for the Higgs fields and the kinematic terms of the electroweak gauge bosons is then defined by

$$\begin{aligned} \mathcal{L}_{EW'} &= \mathcal{L}_{Higgs} + \mathcal{L}_{kin} \\ &= (\mathcal{D}^\mu \Phi)^\dagger (\mathcal{D}^\mu \Phi) + \mu^2 \Phi^\dagger \Phi - \lambda^2 (\Phi^\dagger \Phi)^2 \\ &\quad -\frac{1}{4} \mathbf{W}_{\mu\nu} \mathbf{W}^{\mu\nu} - \frac{1}{4} B_{\mu\nu} B^{\mu\nu}. \end{aligned} \tag{2.19}$$

The vacuum expectation value Φ_{min} of the Higgs doublet (minimum of the Higgs potential) is non-zero under the assumption $\mu^2 > 0$. Since this ground state is degenerate, it can be chosen as

$$\Phi_{min} = \frac{1}{\sqrt{2}} \begin{pmatrix} 0 \\ v \end{pmatrix} . \tag{2.20}$$

This specific choice breaks the electroweak symmetry spontaneously from $SU(2)_L \times U(1)_Y$ into $U(1)_Q$ [24]. The charged complex Higgs field, which would add mass to photons, and the imaginary part of the scalar field vanish. Thus, the four degrees of freedom of the initial complex Higgs isospin doublet are reduce to one non-vanishing degree of freedom, a real scalar Higgs field. Spontaneous symmetry breaking of the electroweak theory is illustrated in figure 2.1 for a complex Higgs field. The fluctuations $H(x)$ around the ground state Φ_{min}

$$\Phi(x) = \frac{1}{\sqrt{2}} \begin{pmatrix} 0 \\ v + H(x) \end{pmatrix} \tag{2.21}$$

are then interpreted as Higgs boson. Massless scalar fields that result from electroweak symmetry breaking from the Nambu-Goldstone theorem are absorbed into the longitudinal degrees of freedom of the $W^\pm$ and Z gauge bosons via unitary transformations. Equations 2.19 and 2.21 lead to the Lagrange density

$$\begin{aligned} \mathcal{L}_{EW''} &= \frac{1}{2} \partial^\mu H \partial_\mu H - \mu^2 H^2 - \frac{1}{4} \mathbf{W}_{\mu\nu} \mathbf{W}^{\mu\nu} - \frac{1}{4} B_{\mu\nu} B^{\mu\nu} \\ &\quad + \frac{g^2 v^2}{4} \left(|W_\mu^+|^2 + |W_\mu^-|^2 \right) + \frac{g^2}{8} W_\mu^+ W^{-\mu} (2vH + H^2) \\ &\quad + \frac{1}{8} \frac{g^2}{\cos^2 \theta_w} Z_\mu Z^\mu (v^2 + 2vH + H^2). \end{aligned} \tag{2.22}$$

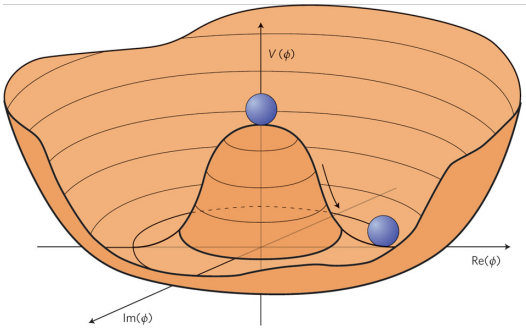

Figure 2.1. *Potential of a complex Higgs ϕ field with a degenerate ground state. The symmetry is broken by choosing the specific ground state $Im(\phi) = 0$ [25].*

The electroweak Lagrange density after symmetry breaking includes interaction terms of the Higgs boson with gauge bosons, Higgs self-coupling terms and mass terms of the vector bosons and the Higgs boson itself. The mass of the Higgs boson and the vector bosons are given by

$$m_H = \sqrt{2}\mu = v\sqrt{2\lambda}\,, \tag{2.23}$$

$$M_W = \frac{gv}{2}\,, \tag{2.24}$$

$$M_Z = \frac{M_W}{\cos\theta_w}\,. \tag{2.25}$$

The photon remains massless. The Higgs vacuum expectation value is

$$G_F = \frac{\sqrt{2}}{8}\left(\frac{g}{M_W}\right) = (\sqrt{2}v^2)^{-1} \tag{2.26}$$

with G_F the Fermi constant of electroweak interactions. Measurements of G_F yield a vacuum expectation value of $v \approx 246$ GeV.

Spontaneous symmetry breaking of the electroweak theory generates mass terms of the gauge bosons. However, it cannot explain the observed fermion masses. To achieve such mass terms for fermions, ad-hoc contributions for the couplings of the Higgs boson to fermions need to be added to the SM Lagrange density. These contributions to the Lagrange density are called Yukawa couplings $\mathcal{L}_{Yukawa}$. The Yukawa terms for the first generation of leptons ($\psi_L = L_L$ and $\psi_R = e_R$) and quarks ($\psi_L = Q_L$ and $\psi_R = u_R, d_R$) are defined by

$$\mathcal{L}_{Yukawa} = g_e\overline{L}_L\Phi e_R + g_d\overline{Q}_L\Phi d_R + g_u\overline{Q}_L\tilde{\Phi}u_R + h.c.\,, \tag{2.27}$$

where g_f are the coupling strength parameters between the Higgs boson and fermions and $\tilde{\Phi} = i\sigma_2\Phi^*$ the charge conjugate Higgs field. Analogous to the first generation, there are Yukawa couplings for generating mass terms for all generations of the fermions. The coupling parameters g_f are proportional to the masses of the fermions

$$g_f = m_f\frac{\sqrt{2}}{v}\,. \tag{2.28}$$

That is, the coupling strength of the Higgs boson to heavy leptons and quarks is enhanced compared to lighter ones.

Thus, the electroweak symmetry breaking is based on the presence of an additional scalar Higgs field in terms of a complex isospin doublet. The Higgs potential has a non-zero vacuum expectation value. By breaking the symmetry spontaneously, mass terms are generated for the $W^{\pm}$ and Z gauge bosons by absorbing three of the four degrees of freedom of the Higgs field into the longitudinal components of these vector bosons. The remaining degree of freedom can be interpreted as Higgs boson. The mass of the Higgs boson is an unknown parameter and can only be determined by measurements. In addition, ad-hoc Yukawa couplings of the fermions to the Higgs boson are introduced to generate mass terms also for the fermions.

2.1.5. Quantum Chromodynamics

The strong interaction between quarks is based on quantum chromodynamics (QCD) [26, 27] and acts on the color charge, a special property of quarks. There are three different color charges (red, green and blue), which are described by the vectors

$$\chi_r = \begin{pmatrix} 1 \\ 0 \\ 0 \end{pmatrix}, \qquad \chi_g = \begin{pmatrix} 0 \\ 1 \\ 0 \end{pmatrix}, \qquad \chi_b = \begin{pmatrix} 0 \\ 0 \\ 1 \end{pmatrix}. \tag{2.29}$$

The quark wave function Ψ is then defined by $\Psi = \psi \cdot \chi_{r,g,b}$ where ψ denotes the wave function with respect to space, spin and flavour. Local phase transformations in QCD are based on the $SU(3)$ symmetry group and are given by

$$\Psi \rightarrow e^{i\frac{g_s}{2}\sum_{i=1}^{8}\lambda_i\beta_i(x)}\Psi. \tag{2.30}$$

These transformations act on the color charge of the quarks[5]. The $SU(3)$ transformation generators can be represented by the eight *Gell-Mann matrices* λ_i. To guarantee gauge invariance in QCD, the gauge field G_i^{μ} is introduced via the covariant derivative

$$\mathcal{D}^{\mu} = \partial^{\mu} + i\frac{g_s}{2}\sum_{i=1}^{8}\lambda_i G_i^{\mu}. \tag{2.31}$$

The QCD Lagrange density for a specific quark flavour is then defined by

$$\mathcal{L}_{QCD} = \overline{\Psi}(i\gamma_{\mu}\mathcal{D}^{\mu} - m)\Psi - \frac{1}{4}\sum_{i=1}^{8} G_{i,\mu\nu}G_i^{\mu\nu}\ . \tag{2.32}$$

The kinematic terms of the gauge fields contain the tensor $G_i^{\mu\nu} = \partial^{\mu}G_i^{\nu} - \partial^{\nu}G_i^{\mu} - g_s f_{jkl}G_k^{\mu}G_l^{\nu}$, where f_{jkl} are the anti-symmetric structure constants of the $SU(3)_C$ group. $SU(3)_C$ is non-Abelian, which leads to couplings of different quarks to gauge

[5] The color charge is indicated by the labeling $SU(3)_C$.

fields with the same coupling strength g_s[6]. Similar to the lepton flavour changing $W^{\pm}$ bosons of the electroweak theory, different linear combinations of the QCD gauge fields leads to the actual gauge bosons, the gluons. There are eight gluons: six of them carry color charge, which change the color of the interacting quarks, and two of them are neutral in color, leading to color charge conserving currents. Due to the color charge of the gluons, they are self-interacting in terms of three or four gluon vertices. The coupling constant of the strong interaction is referred to as $\alpha_s = g_s^2/4\pi$.

2.1.6. Standard Model Lagrange Density

In summary, the SM is described by the gauge groups $SU(3)_C \times SU(2)_L \times U(1)_Y$, corresponding to the strong and the electroweak interaction. Complex scalar Higgs fields generate the masses of the electroweak gauge bosons via spontaneous symmetry breaking. The breaking of the symmetry leads to the existence of the scalar Higgs boson. Fermion masses are generated by specific Yukawa couplings to the Higgs boson. The SM includes nineteen free parameters: nine fermion masses (e, μ, τ-leptons and six quarks), three mixing angles and a CP-violating phase of the quark mixing matrix (CKM-Matrix), the coupling constants of the QED and QCD (α_{QED} and α_s), the Fermi constant G_F, a CP-violating phase of the QCD[7], the mass of the Z boson and the mass of the Higgs boson. The overall Lagrange density of the SM consists of the individual contributions

$$\mathcal{L}_{SM} = \mathcal{L}_{EW''} + \mathcal{L}_{Yukawa} + \mathcal{L}_{QCD} \tag{2.33}$$

2.1.7. Limitations of the Standard Model

Although high precision measurements agree well with the SM predictions, there are fundamental questions that cannot be answered by the SM. Moreover, the SM is expected to be an effective theory at the current scales of accessible energies. Open questions are:

- **Unification of Gauge Couplings**
  The choice of SM symmetry groups $SU(3)_C \times SU(2)_L \times U(1)_Y$ seem to be rather unnatural. A more fundamental underlying symmetry is expected, called *Grand Unified Theory* (GUT) [28]. However, extrapolating the coupling strength parameters of the SM gauge groups towards higher energies does not result in a single crossing point as GUT would predict.

- **Dark Matter**
  Approximately 25% of the energy of the universe consists of non-baryonic

[6] This is analogous to the electroweak theory, where the $SU(2)_L$ group is also non-Abelian and the coupling strength g between fermions and $W^{\pm}$ bosons is identical.

[7] This phase tends to be small since no CP-violation has been observed in QCD so far.

matter. This component is referred to as dark matter, which shows non-relativistic behavior [29]. Potential dark matter candidates are for example weakly interacting massive particles (WIMPs), which do not take part in the electromagnetic interaction. The SM does not contain candidates for dark matter.

- **Hierarchy Problem and Fine Tuning**
  The mass of the Higgs boson is subject to large quantum corrections that are quadratically divergent. If the SM is required to be valid up to high energies, these corrections are magnitudes of order larger than the energy scale of the electroweak theory. To keep the Higgs boson mass at a reasonable energy level of 100 GeV, the parameters of the theory needs to be fine-tuned. However, such adjustments are rather unnatural, which is usually referred to as the *fine tuning problem* [30–32]. Furthermore, the vacuum expectation value of the Higgs field (~ 246 GeV) is many orders of magnitude lower than the energy scale of GUTs (10^{15-16} GeV), called the *hierarchy problem*.

The theory of supersymmetry (SUSY) provides a possible solution to these open questions. SUSY predicts a large set of new elementary particles, that differ in spin by 1/2 compared to the SM particles. Thus there exists a SUSY boson or fermion for every SM fermion or boson particle [33, 34]. The evolution of the coupling strength parameters in a SUSY theory to higher energies results in a single point of interaction for the three couplings of the electromagnetic, weak and strong interaction at $\sim 10^{16}$ GeV. The introduction of a discrete symmetry called R-parity ensures the conservation of the baryon and fermion numbers. Due to R-parity, the lightest SUSY particle is a stable, electrically neutral, massive and weakly interacting particle. Thus, the neutralino is a dark matter candidate. Furthermore, divergencies in the Higgs boson mass due to higher order corrections cancel due to counter terms of the SUSY particles. SUSY theories could also include gravitation, which is not considered in the SM theory. So far, no SUSY particles have been observed and large regions of parameter space are meanwhile excluded. SUSY particles are expected to have large masses based on symmetry breaking. With the upcoming LHC operation at its design luminosity, SUSY at higher energy scales might become accessible.

- **Baryon Asymmetry**
  Baryonic and anti-baryonic matter in the observable universe is not balanced. There is no reason for preferring a specific charge over the other and equal amounts of matter of both types should have been produced in the big bang as expected in the SM. A possible source of baryon asymmetry is the violation of charge (C) and charge-parity (CP) conservation. The SM quark-mixing (CKM) matrix, which describes the transformation of a quark into a quark with different flavour by exchanging a W boson, includes a complex phase that causes CP-violation. However, the effect of the CP-violating complex phase in SM is found to be too small for explaining the baryon asymmetry in the early universe. A potential additional source of CP-violation is discussed

in section 2.3, which deals with anomalous non-SM CP-violating couplings of the Higgs boson to gauge bosons.

2.2. Higgs Boson of the Standard Model

2.2.1. Production and Decay at the LHC

The mass of the Higgs boson is not predicted by the SM and needs therefore to be determined by measurements. Once the Higgs boson mass is known, the production cross sections and the branching ratios of the Higgs boson decay modes can be extracted. At the LHC, SM Higgs bosons are produced mainly via gluon fusion (GGF), vector-boson fusion (VBF) and vector boson (VH) or top quark (ttH) associated production modes, as illustrated in figure 2.2. The cross sections of the different Higgs boson production modes as function of its mass at $\sqrt{s} = 8$ TeV are shown in figure 2.3 (a). Gluon fusion is the dominant process amongst all production modes followed by vector-boson fusion. The branching ratios of the various decay modes as function of the mass are shown in figure 2.3 (b). For small Higgs boson mass values, the dominant decay modes are $H \to b\bar{b}$ and $H \to \tau\tau$ while for high masses the Higgs boson decays predominantly into vector bosons $H \to WW/ZZ$.

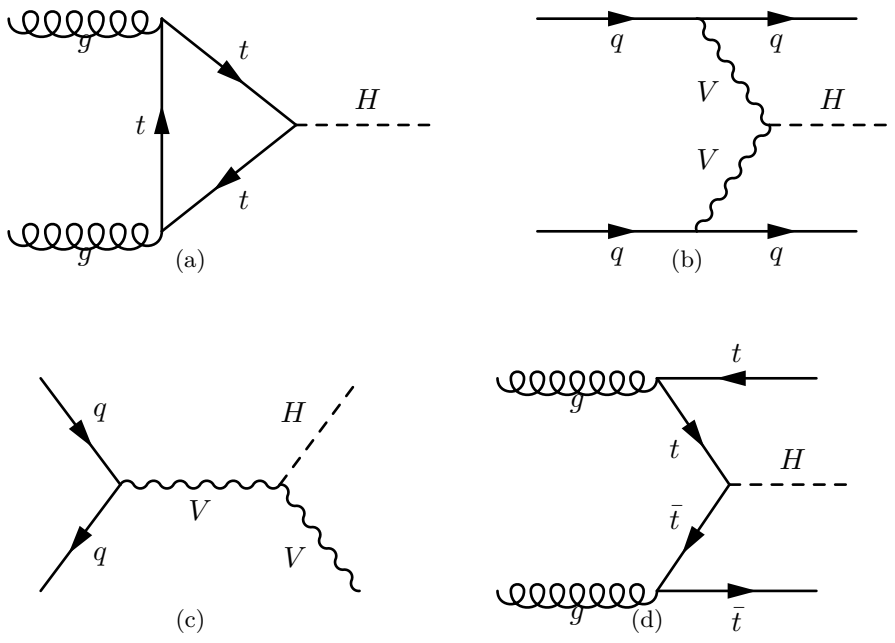

Figure 2.2. *Examples of tree-level diagrams for the production of a Higgs boson: gluon fusion (a), vector-boson fusion (b), vector boson associated (c) and top quark associated (d) Higgs boson production.*

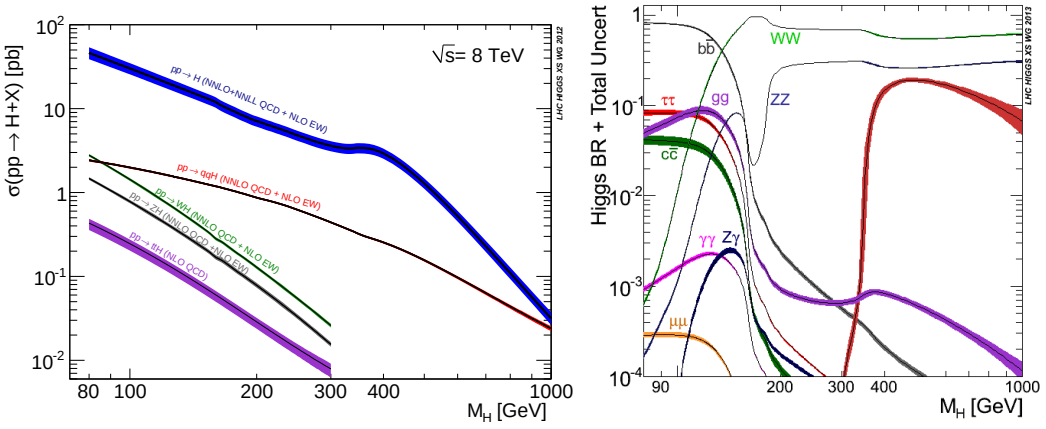

(a) (b)

Figure 2.3. *Standard Model Higgs boson production cross sections at* $\sqrt{s} = 8$ TeV *(a) and decay branching ratios (b) as function of the Higgs boson mass [35].*

2.2.2. Theoretical and Experimental Constraints

The mass of the Higgs boson is a free parameter in the SM. However, it is constrained by certain theoretical arguments.

The electroweak symmetry breaking introduces a mass term for the W gauge boson. Such longitudinal degrees of freedom for massive vector bosons cause divergencies in the cross section of vector boson scattering processes ($WW \to WW$), that depend on the mass of the Higgs boson. That is, the corresponding cross section increases with the center of mass energy, leading to violation of unitarity for high mass values. Since unitarity must not be violated, bounds on the Higgs boson mass can be derived. The mass of the SM Higgs boson is predicted to be approximately less than 1 TeV [36].

The requirement of vacuum stability leads to further theoretical constraints on the Higgs boson mass. In the limit of high energy scales up to the Planck scale, the quartic Higgs coupling λ[8], which depends strongly on the mass of the SM Higgs boson and the top quark, tend to become negative. This would lead to instabilities of the electroweak vacuum. Lower limits on the Higgs boson mass can then be determined by requiring the vacuum to remain stable in the regime of high energies. Using a measured top quark mass of 173.1 ± 0.7 GeV(average of measurements from Tevatron, CMS and ATLAS), Higgs mass values below 126 GeV are excluded at 98% confidence level based on next-to-next-to leading

[8]The quartic Higgs coupling at tree level is $\lambda = m_H^2/2v^2$, where v is the vacuum expectation value and m_H the mass of the Higgs boson.

order calculations in QCD [37]. Current LHC measurements of the Higgs boson mass hints at a meta-stable electroweak vacuum state as shown in figure 2.4.

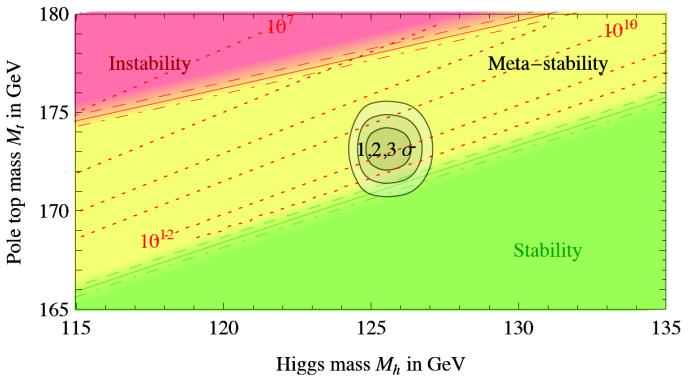

(a)

Figure 2.4. *Regions of stability and instability of the SM vacuum in the (m_H,m_t) plane. The experimentally preferred region in terms of 1,2 and 3 σ contours is indicated by the gray areas [37].*

Higher order corrections of electroweak observables (such as masses or decay widths of the electroweak vector bosons, the top quark mass or weak mixing angle) depend on the mass of the Higgs boson due to corresponding loop diagrams. The Higgs boson mass can therefore be estimated indirectly by performing a combined fit to precision data of these electroweak observables. The observables were mainly obtained from measurements at LEP and Tevatron [38, 39]. Figure 2.5 shows the χ^2 of the combined electroweak fit of the observables as a function of the m_H. The best-fit Higgs boson mass value is found to be 94^{+29}_{-24} GeV with an upper limit of $m_H < 152$ GeV at 95% one-sided confidence level [40].

While the Higgs mechanism was suggested by Higgs, Englert, Brout, Guralnik and Kibble already in 1962, it took 50 years until experimentalists were able to claim the discovery of the Higgs boson in direct searches at the LHC. The discovery was achieved by measurements from CMS [1] and ATLAS [2] using $\sqrt{s} = 7$ TeV and $\sqrt{s} = 8$ TeV data recorded until July 2012. Figure 2.6 shows the local p-value as function of the mass of the Higgs boson measured with the ATLAS experiment. At a mass of approximately 125 GeV, an excess is observed with the significance of 5.9 σ. Since then, both experiments provide evidence for the Higgs boson in the decay channels $\gamma\gamma$, WW, ZZ and $\tau\tau$ and further search analysis for the decay into $b\bar{b}$, $\mu\mu$ and $Z\gamma$ [41]. The ATLAS measurement of the overall Higgs boson signal strength[9] results in $\mu = 1.18^{+0.15}_{-0.14}$, using the full 2011 and 2012 dataset with an integrated luminosity of 4.7 fb^{-1} and 20.3 fb^{-1} respectively. This is fully consistent with the SM prediction ($\mu = 1$) [41]. The combined and individual signal strength values are shown in figure 2.7. The measured mass of the Higgs boson is found to

[9]Signal strength μ is defined as the obtained cross section divided by the expected SM cross section including a SM Higgs boson. If the measured cross section is consistent with the SM, $\mu = 1$ is expected.

be 125.09 ± 0.24 GeV based on the combination of results from ATLAS and CMS in the decay channels $H \to \gamma\gamma$ and $H \to ZZ$ [6] and is thus consistent with the electroweak fit in the SM.

After the discovery of the Higgs bosons, the properties of the Higgs boson have also been investigated, such as the spin and parity quantum numbers as well as the structure of the tensor coupling. Based on ATLAS and CMS measurements in the decay channels $H \to ZZ$, $H \to WW$ and $H \to \gamma\gamma$, alternative non-SM Higgs boson hypotheses with respect to the corresponding parity and spin quantum numbers such as spin 2 models have been excluded at the confidence level of more than 99.9% [42, 43]. Furthermore, the tensor structure of the Higgs boson to vector bosons has been studied in the decay channels $H \to ZZ$ and $H \to WW$. The results are compatible with SM expectation and constraints on non-SM tensor couplings have been derived. In summary, no deviations of the phenomenology of the Higgs boson from the SM prediction have been observed so far.

2.3. CP-Violating Higgs Boson Couplings

Baryon asymmetry (see section 2.1.7), the imbalance of baryonic matter and anti-matter in the early universe, cannot be explained by the SM, where neutrinos are assumed to be massless. Based on the Sakharov conditions [44–46], the violation of the C- and CP-invariance is needed to cause baryon asymmetry. In the SM, the

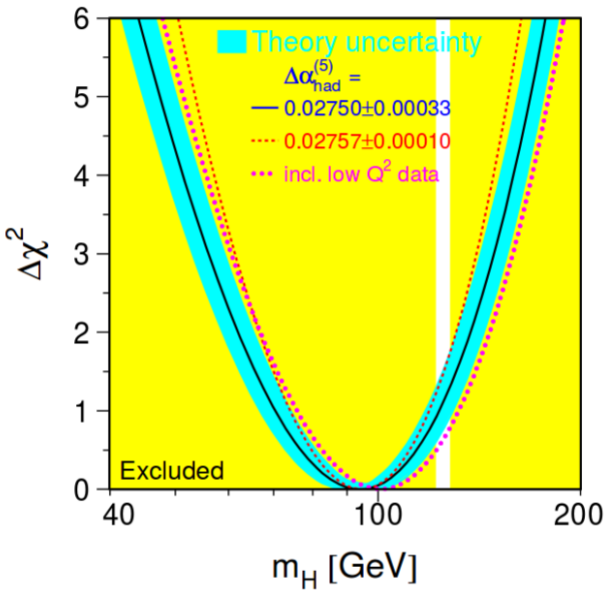

(a)

Figure 2.5. $\Delta\chi^2$ *as a function of* m_H *performing a global fit of the SM to electroweak precision data (black solid line). The blue band represents the theoretical uncertainty due to missing higher order corrections [40].*

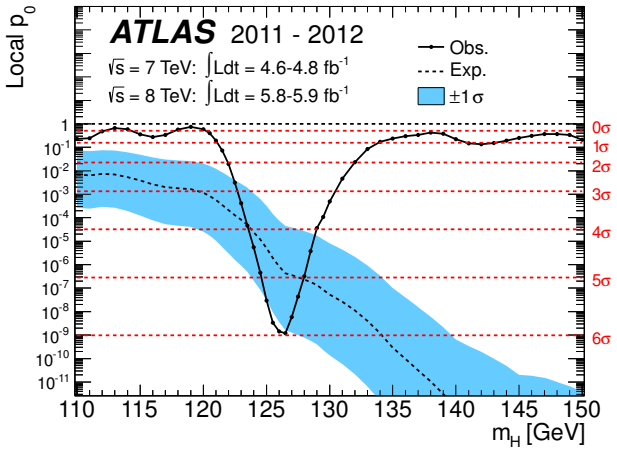

Figure 2.6. *The observed (solid line) and expected (dashed line) local p_0 value as a function of m_H. The expected local p_0 is derived using the corresponding SM Higgs boson mass hypothesis. The blue band represents the uncertainties on the expected p_0 [2].*

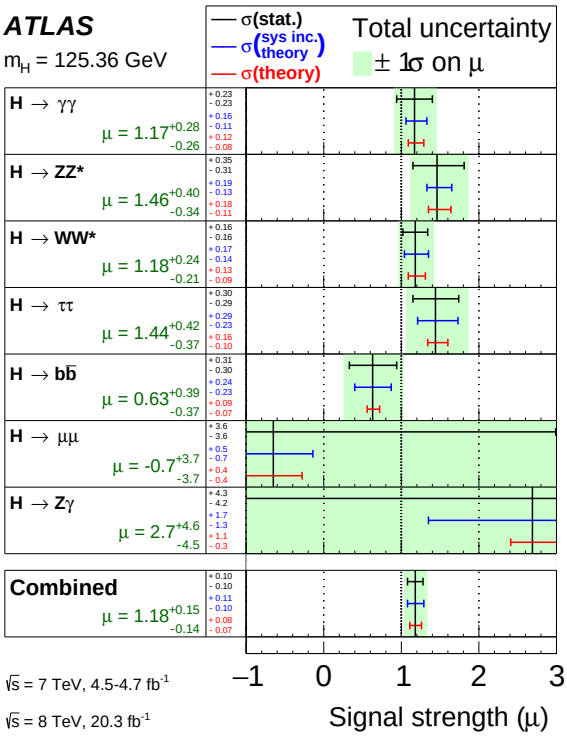

Figure 2.7. *Observed signal strengths values and uncertainties for different Higgs boson decay channels and the overall combination at ATLAS [41].*

only source of CP-violation stems from a complex phase of the CKM-matrix [20, 21]. However, the measured size of this complex phase in the SM [47, 48] is too small to explain the baryon asymmetry in the observable universe [49]. Since CP-violation is not expected in the SM Higgs sector, any CP-violating mechanism in the production or decay of the Higgs boson is a strong hint of new physics that could explain the imbalance of matter and anti-matter. Such sources of CP-violation might for example stem from small CP-odd contributions to the SM Higgs boson coupling structure (CP mixed scenarios), which is one of the topics of this thesis.

Current ATLAS and CMS measurements of Higgs boson production cross sections, branching ratios as well as its spin and CP quantum numbers and the HVV tensor structure in bosonic decay modes do not show any deviations from SM couplings [42, 43]. Figure 2.8 shows corresponding distributions of the test statistic $\tilde{q}$[10] for various non-SM Higgs boson spin and parity scenarios in comparison to the SM scenario. The measured value of the test statistic is consistent with the SM expectation in each of the comparisons and the alternative hypotheses are excluded at 99.9% confidence level. In addition, specific measurements of Higgs boson CP properties in the decay mode $H \to \gamma\gamma$ performed at the ATLAS experiment provide limits on CP-violating couplings to massive vector bosons in the VBF Higgs boson production mode, based on an effective field theory approach [50]. Absolute event rates are used in the corresponding analysis as well as CP-even observables, that are not directly sensitive to CP mixed coupling structures. No significant deviations of the investigated tensor structure of Higgs boson interactions from the Standard Model predictions are observed in this case. In the present thesis, the CP-invariance of Higgs boson couplings to vector bosons is studied based on CP-odd observables. These observables are directly sensitive to the CP coupling structure of the Higgs boson to vector bosons. More about CP sensitive observables can be found in section 6.1.1.

The following sections discuss anomalous CP mixed Higgs boson couplings to vector bosons in the framework of an effective field theory. The effective Lagrange density for anomalous HVV couplings can be constructed in a model independent way by adding higher dimensional operators to the dimension-four SM Lagrange density, that preserve the $SU(2)_L \times U(1)_Y$ gauge symmetry [51, 52]. The effective Lagrange density is expanded in powers of $1/\Lambda$ with Λ being the scale of new physics.

$$\mathcal{L}_{eff} = \mathcal{L}_{SM} + \frac{1}{\Lambda}\mathcal{L}_1 + \frac{1}{\Lambda^2}\mathcal{L}_2 + ... \tag{2.34}$$

While there is only one dimension-five operator in $\mathcal{L}_1$ that violates lepton number conservation, a large set of dimension-six operators in $\mathcal{L}_2$ can be constructed, based on scalar, vector and fermion fields. The dimension-five operator would lead to massive neutrinos and neutrino mixing, which can be neglected in the present use case of physics at the electroweak scale. Thus, only dimension-six operators are considered, that give rise to small deviations from the SM CP-conserving Higgs

[10] The test statistic $\tilde{q}$ is based on a maximum likelihood approach as explained in chapter 9.

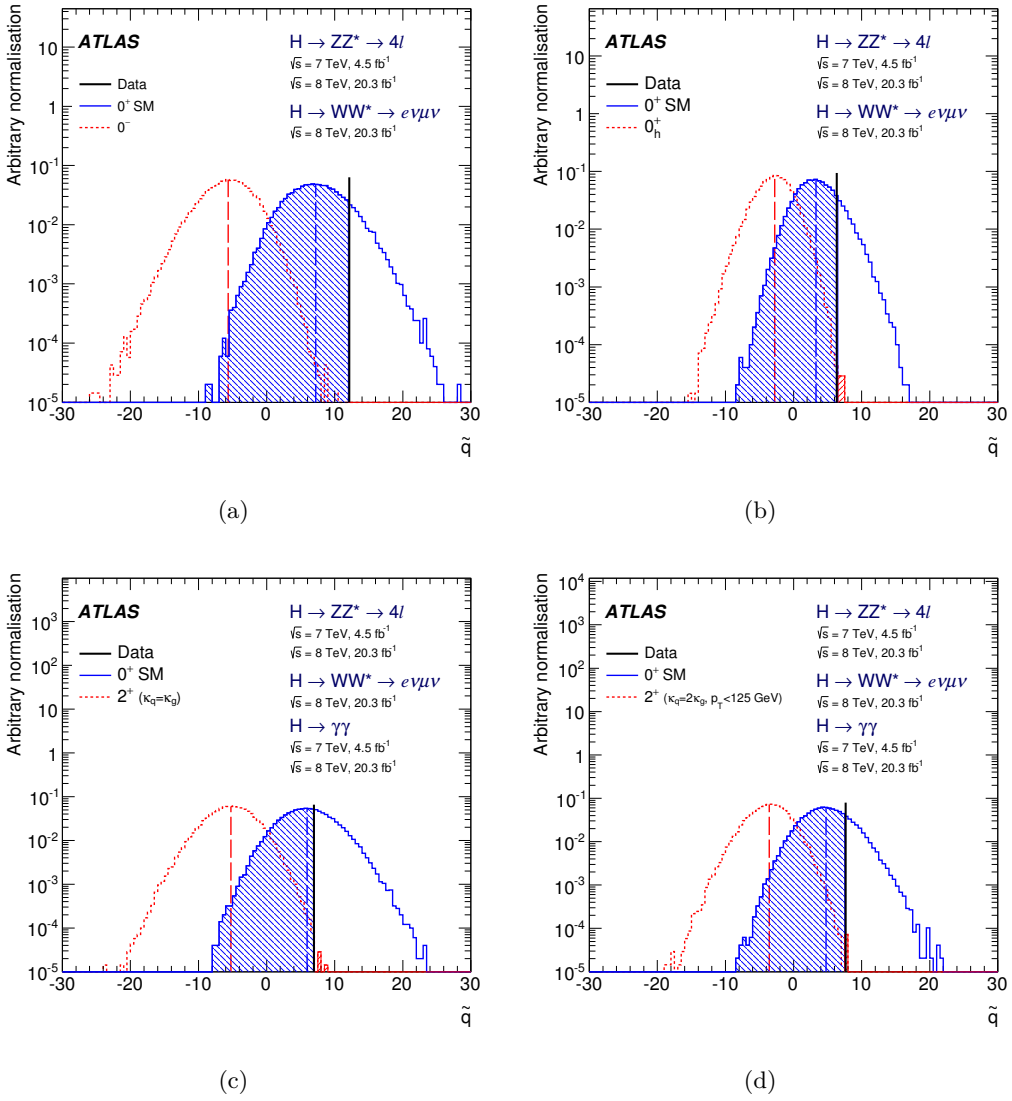

Figure 2.8. *Test statistic distributions for different spin and parity J^P Higgs boson hypothesis (red dashed line) compared to the SM 0^+ signal hypothesis (blue solid line): SM vs. non-SM spin-0 CP-odd (a), SM vs. non-SM spin-0 CP-even (b), SM vs. non-SM spin-2 with universal couplings (c), SM vs. non-SM spin-2 with non-universal couplings (d). The observed value of the test statistic is consistent with the SM prediction (black line). The corresponding p-values are indicated by the blue shaded area. The alternative hypotheses are rejected at more than 99.9% confidence level [42].*

boson couplings to vector bosons [53]. The effective Lagrange density is therefore defined by

$$\begin{aligned} \mathcal{L}_{eff} &= \mathcal{L}_{SM} + \frac{1}{\Lambda^2}\mathcal{L}_2 \\ \mathcal{L}_2 &= f_{\tilde{B}B}\mathcal{O}_{\tilde{B}B} + f_{\tilde{W}W}\mathcal{O}_{\tilde{W}W} + f_{\tilde{B}}\mathcal{O}_{\tilde{B}}, \end{aligned} \tag{2.35}$$

where $f_{\tilde{B}B}$, $f_{\tilde{W}W}$ and $f_{\tilde{B}}$ are dimensionless Wilson coefficients. The relevant dimension-six operators include the Higgs doublet Φ and the electroweak gauge fields B^μ and $W^{i,\mu}$ (i = 1,2,3). Only CP-odd operators are considered in $\mathcal{L}_2$ in this case, that do not preserve the CP invariance of the SM Higgs boson couplings to vector bosons

$$\mathcal{O}_{\tilde{B}B} = \Phi^+ \hat{\tilde{B}}_{\mu\nu}\hat{B}^{\mu\nu}\Phi, \tag{2.36}$$

$$\mathcal{O}_{\tilde{W}W} = \Phi^+ \hat{\tilde{W}}_{\mu\nu}\hat{W}^{\mu\nu}\Phi, \tag{2.37}$$

$$\mathcal{O}_{\tilde{B}} = (D_\mu\Phi)^+ \hat{\tilde{B}}^{\mu\nu}D_\nu\Phi. \tag{2.38}$$

$\hat{V}_{\mu\nu}$ denotes the field-strength tensor and $\tilde{V}_{\mu\nu} = \frac{1}{2}\epsilon_{\mu\nu\rho\sigma}V^{\rho\sigma}$ the dual field strength tensors with $\hat{B}_{\mu\nu} + \hat{W}_{\mu\nu} = i\frac{g'}{2}B_{\mu\nu} + i\frac{g}{2}\sigma_a W^a_{\mu\nu}$. The covariant derivative is given by $D_\mu = \partial_\mu + \frac{i}{2}g'B_\mu + ig\frac{\sigma_a}{2}W^a_\mu\sigma_a$.

$\mathcal{O}_{\tilde{B}}$ contributes to the CP-violating charged triple gauge boson couplings $\tilde{\kappa}_\gamma$ and $\tilde{\kappa}_Z$. These couplings are related by $\tilde{\kappa}_\gamma = -\cot^2\theta_W\tilde{\kappa}_Z = \frac{m_W^2}{2\Lambda^2}f_{\tilde{B}}$ and are highly constrained by LEP measurements [54–56]. Thus, the contribution from operator $\mathcal{O}_{\tilde{B}}$ is not further considered here. The effective Lagrange density can then be re-written in terms of mass eigenstates of the Higgs boson H, the weak gauge bosons Z and $W^\pm$ and the photon A after breaking the electroweak symmetry [57]

$$\begin{aligned} \mathcal{L}_{eff} &= \mathcal{L}_{SM} + \tilde{g}_{HAA}H\tilde{A}_{\mu\nu}A^{\mu\nu} + \tilde{g}_{HAZ}H\tilde{A}_{\mu\nu}Z^{\mu\nu} \\ &\quad + \tilde{g}_{HZZ}H\tilde{Z}_{\mu\nu}Z^{\mu\nu} + \tilde{g}_{HWW}H\tilde{W}^+_{\mu\nu}W^{\mu\nu}_-. \end{aligned} \tag{2.39}$$

The different couplings HWW, HZZ, $HZ\gamma$ and $H\gamma\gamma$ contribute to the VBF Higgs boson production mode. Requiring invariance of the Lagrange density under $SU(2)_L \times U(1)_Y$ transformations involves constraints on these couplings. Therefore, only two of the couplings are independent with the relations

$$\tilde{g}_{HAA} = \frac{g}{2m_W}(\tilde{d}\sin^2\theta_W + \tilde{d}_B\cos^2\theta_W) \tag{2.40}$$

$$\tilde{g}_{HAZ} = \frac{g}{2m_W}\sin 2\theta_W(\tilde{d} - \tilde{d}_B) \tag{2.41}$$

$$\tilde{g}_{HZZ} = \frac{g}{2m_W}(\tilde{d}\cos^2\theta_W + \tilde{d}_B\sin^2\theta_W) \tag{2.42}$$

$$\tilde{g}_{HWW} = \frac{g}{m_W}\tilde{d}\,, \tag{2.43}$$

where both dimensionless parameters $\tilde{d}$ and $\tilde{d}_B$ are defined by

$$\tilde{d} = -\frac{m_W^2}{\Lambda^2}f_{\tilde{W}W} \tag{2.44}$$

$$\tilde{d}_B = -\frac{m_W^2}{\Lambda^2}\tan^2\theta_W f_{\tilde{B}B}. \tag{2.45}$$

Since the couplings of the Higgs boson to the different vector bosons cannot be distinguished in the experiment, the CP analysis of this thesis is based on the assumption $\tilde{d} = \tilde{d}_B$. The parameter $\tilde{d}_B$ is related to the couplings parameter $\tilde{\kappa}_{HWW}$ via $\tilde{d}_B = -\tilde{\kappa}_{HWW}/\kappa_{SM} \tan\alpha$, which has been used in the CP analysis performed by ATLAS in the decay channels $H \to WW$ and $H \to ZZ$ [42]. The specific choice of $\tilde{d}_B$ in the context of this thesis can be translated into the relation $\tilde{\kappa}_{HWW} = \tilde{\kappa}_{HZZ}$ as assumed in the CP analysis by ATLAS. That is, the results of both analysis, the one presented in this thesis and the one by ATLAS, are fully comparable.

The choice $\tilde{d} = \tilde{d}_B$ results in the following relations for the $\tilde{g}_{HVV}$ couplings from equation 2.39

$$\tilde{g}_{HAA} = \tilde{g}_{HZZ} = \frac{1}{2}\tilde{g}_{HWW} = \frac{g}{2m_W}\tilde{d} \qquad \text{and} \qquad \tilde{g}_{HAZ} = 0. \tag{2.46}$$

The tensor structure for Higgs boson couplings to two identical or charge conjugated gauge bosons in the effective Lagrange density is then given by

$$T^{\mu\nu}(p_1, p_2) = \sum_V \frac{2m_V^2}{v} g^{\mu\nu} + \sum_V \frac{2g}{m_W} \tilde{d}\, \varepsilon^{\mu\nu\rho\sigma} p_{1\rho} p_{2\sigma}, \tag{2.47}$$

where p_1 and p_2 are the four momenta of the vector bosons $V = W,\ Z,\ \gamma$. The first term includes CP-even contributions of the SM and the second term CP-odd contributions due to the dimension-six operators and the assumption $\tilde{d} = \tilde{d}_B$. Thus, the matrix element for VBF Higgs boson production

$$\mathcal{M}_{\tilde{d}} = \mathcal{M}_{\text{SM}} + \tilde{d} \cdot \mathcal{M}_{\text{CP-odd}} \tag{2.48}$$

is the sum of the CP-even SM contribution $\mathcal{M}_{\text{SM}}$ and the CP-odd part $\mathcal{M}_{\text{CP-odd}}$ and therefore causes CP-violation in the couplings of the Higgs boson to gauge bosons. The CP-violating contribution is linear in the parameter $\tilde{d}_B$. The differential cross section is given by the squared matrix element

$$|\mathcal{M}_{\tilde{d}}|^2 = |\mathcal{M}_{\text{SM}}|^2 + \tilde{d} \cdot 2\,\text{Re}(\mathcal{M}_{\text{SM}}^* \mathcal{M}_{\text{CP-odd}}) + \tilde{d}^2 \cdot |\mathcal{M}_{\text{CP-odd}}|^2 \tag{2.49}$$

$$d\sigma_{\tilde{d}} = d\sigma_{\text{SM}} + \tilde{d} \cdot d\sigma_{\text{CP-odd}} + \tilde{d}^2 \cdot d\sigma_{\text{CP-even}}. \tag{2.50}$$

$|\mathcal{M}_{\text{SM}}|^2$ and $\tilde{d}^2 \cdot |\mathcal{M}_{\text{CP-odd}}|^2$ are CP-even contributions to the differential cross section and do not cause any CP violation. CP violating Higgs boson couplings are solely based on the CP-odd interference term $\text{Re}(\mathcal{M}_{\text{SM}}^* \mathcal{M}_{\text{CP-odd}})$, which contributes linearly in $\tilde{d}_B$ to the differential cross section $d\sigma_{\tilde{d}}$. In contrast to the differential cross section, the total cross section $\sigma_{\tilde{d}}$ does not depend on the interference term, since integrating over a CP-even phase space erases CP-odd contributions. Moreover, it is the squared CP-odd matrix element contribution, that leads to an increase in the predicted event yield. The corresponding dependence on this term is quadratic in $\tilde{d}$.

3 Experimental Setup

3.1. The Large Hadron Collider

The *Large Hadron Collider* (LHC) [58] is the most powerful particle collider at present and aims to explore physics at the TeV scale. It was built by the *European Organization for Nuclear Research* (CERN), starting in 1998, and is located near Geneva in Switzerland.

The LHC is a synchrotron accelerator, that enables proton-proton or heavy ion collisions at high energies. On 10 September 2008, CERN successfully managed to force protons to travel the full length of the LHC for the first time. The collider is placed in the former tunnel of the *Large Electron-Positron Collider* (LEP) [59] 50 to 175 meters underground with a circumference of 27 kilometers. 1232 dipole magnets, each with 15 meters in length, bend the beams on its circular path and 392 quadrupole magnets, each with 5 to 7 meters, focus the beam. In total, about 9600 magnets are installed in the LHC machine with more than 1600 of them being superconducting electromagnets. The peak magnetic dipole field reaches a value of 8.33 T. There are two separate beam pipes, each hosting one of the two particle beams, which travel in opposite directions. The beam lines intersect at four interaction points, where the main LHC experiments are located. Additional magnets squeeze the beams at these interaction points with intent to increase the instantaneous luminosity. The LHC is designed to collide protons at beam energies up to 7 TeV with an instantaneous peak luminosity of $\mathcal{L} = 10^{34}$ cm^{2}s^{-1}. Such high beam intensities exclude the use of anti-proton beams, which have for example been used in the proton-anti-proton collider *Tevatron* [60]. Within the beam, protons are accumulated in proton *bunches*, containing about 1.1×10^{11} protons per bunch. There can be up to 2808 proton *bunches* in the accelerator simultaneously, separated with a nominal bunch spacing of 25 ns, which corresponds to roughly 7 meters. First collisions in all four experiments took place in November 2009 with a center-of-mass energy of 900 GeV. The high energy physics program of the LHC started on 30 March 2010 in the proton-proton mode with a center-of-mass energy of 7 TeV.

The CERN accelerator complex [61] is shown in figure 3.1 and consists of several accelerator systems, which increase the energy of protons or ions successively before they are injected into the LHC main ring. The proton source is a bottle of hydrogen at one end of the linear particle accelerator *Linear Accelerator 2* (LINAC2) [62, 63]. Electric fields ionize the hydrogen atoms before they enter LINAC2, which accelerates the protons to the energy of 50 MeV. The protons then enter the *Proton Synchrotron*

Booster (PSB) [62, 63], which consists of four superimposed synchrotron rings and increases the energy to 1.4 GeV. LINAC3 [64] is the first step in the accelerator chain for heavy ion collisions and provides accelerated lead nuclei for LHC and fixed target experiments. Before the lead nuclei from LINAC3 are fed into the LHC main ring, they have to be further accelerated by *The Low Energy Ion Ring* (LEIR) [65]. Protons from PSB and heavy ions from LEIR are injected into the *Proton Synchrotron* (PS) [62, 63]. The PS produces bunch trains and increases the energy up to 25 GeV before the injection into the *Super Proton Synchrotron* (SPS) [66]. The SPS is the second largest machine in the LHC accelerator complex with 7 kilometers in circumference and provides a further gain in energy of up to 450 GeV. Bunches from SPS can then be transferred to the LHC and other experiments. Within the LHC, proton bunches can be accumulated and accelerated to a maximum energy of 7 TeV, which lasts approximately 20 minutes, and can circulate for several hours under normal operating conditions.

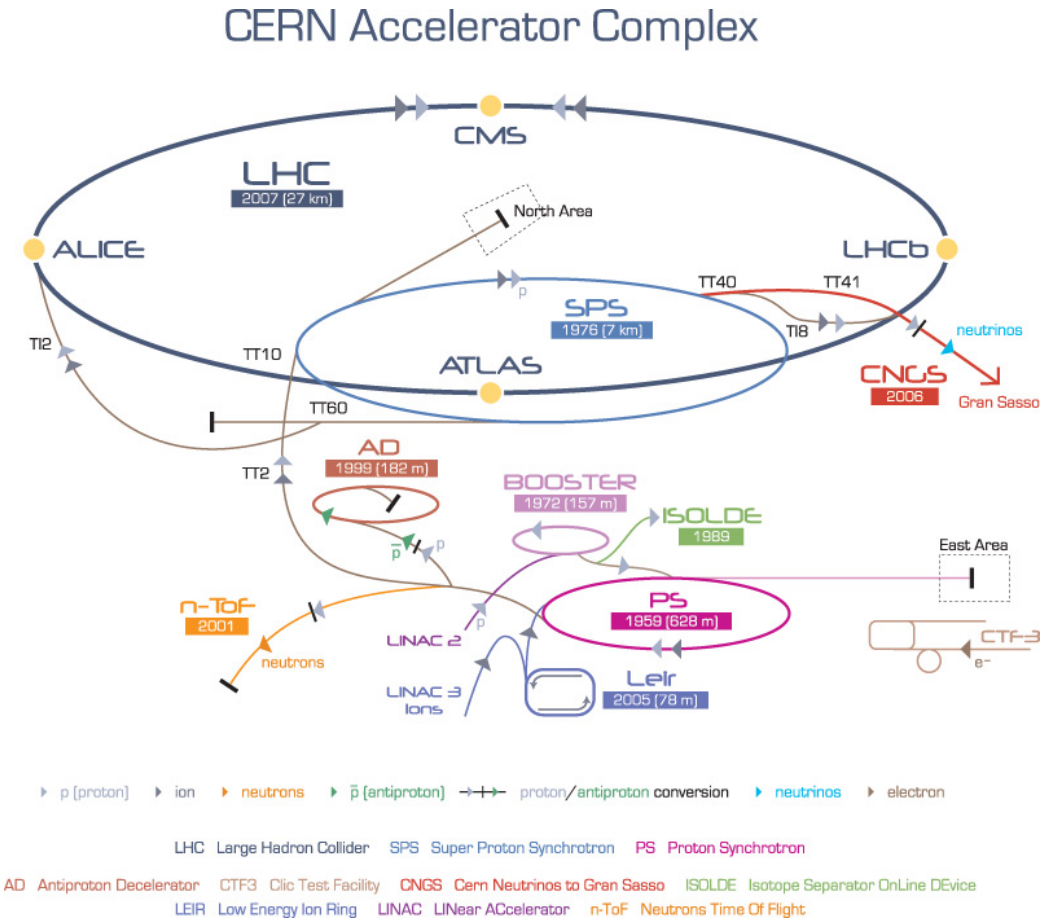

Figure 3.1. *CERN accelerator complex. Various pre-accelerators are needed to achieve the design center-of-mass energy of 14 TeV in LHC proton-proton collisions. The four main LHC experiments are marked with yellow points [67].*

There is one experiment located at each of the four LHC interaction points: ATLAS [68], CMS [69], ALICE [70] and LHCb [71].

ATLAS (A Toroidal LHC ApparatuS) and CMS (Compact Muon Solenoid) are general-purpose detectors, targeting precision measurements of Standard Model processes, which include QCD, electroweak and flavor physics and measurements in the Higgs sector. Furthermore, their aim is to discover new physics such as supersymmetry or models, including spatial dimensions. The ATLAS detector is currently the largest-volume detector at a collider. The analysis in this thesis uses data, obtained with the ATLAS experiment, which is discussed in detail in the sections below. CMS is based on a different design than ATLAS. In comparison to ATLAS, which uses two magnet systems (one solenoid, surrounding the inner detector, and one toroidal field in the outer muon spectrometer), CMS is constructed around a large superconducting solenoid, which achieves magnetic field strengths of up to 4 T, allowing the precise measurement of muon trajectories. In contrast to those general-purpose detectors, ALICE (A Large Ion Collider Experiment) is constructed for analyzing lead-ion collisions and for studying the quark-gluon plasma, whose properties are important for understanding QCD. LHCb (Large Hadron Collider beauty) specializes in b physics and constructed as a forward spectrometer. It addresses fundamental questions of the matter-antimatter asymmetry of the universe by measuring CP violation in b hadron interactions. Further smaller LHC experiments are MoEDAL [72], which searches for exotic states such as magnetic monopoles, LHCf [73], which detects particles very close to the beam axis, and finally TOTEM [74], measuring the effective size of the proton at the LHC.

3.2. The ATLAS Detector

The ATLAS detector, shown in figure 3.2, is the largest-volume detector at a collider at present. It is forward-backward symmetric with respect to the interaction point, 46 meters long, 25 meters high and 25 meter wide with a total weight of 7000 tonnes. It is located at LHC *Point 1* about 100 meters underground. ATLAS is a general-purpose detector, which aims to perform precision measurements of the Standard Model and to search for new physics phenomena. On 4 July 2012, the ATLAS collaboration announced the discovery of a new elementary particle, being consistent with the hypothetical Higgs boson at that time. The discovery of a Higgs boson within relatively short time of early data taking demonstrates the extraordinary performance of the experiment including grid computing and its potential to extend frontiers of high energy physics in the upcoming years of operation. The high LHC instantaneous luminosity, which results in many additional inelastic scattering events per bunch crossing, and the dominant QCD jet production cross section at the hadron collider make high demands on the ATLAS detector in order to reach its physics goals. Fast and radiation-hard electronics and high detector granularity are needed to resolve overlapping events and physics objects such as reconstructed particles. Furthermore, a large acceptance in pseudorapidity and the azimuthal angle is required for a high geometrical coverage, which is for

example crucial for the reconstruction of missing transverse momentum. Important requirements are also excellent momentum resolution, pattern recognition and high reconstruction and identification efficiencies of particles to measure their properties precisely. Additionally, a sophisticated trigger system, which is the first step in the chain of selecting events, is necessary to reduce the rates of events collected to a reasonable level. The innermost part of ATLAS hosts the Inner Detector (ID) within a radius of 1.15 m, which consists of semi-conductor pixel (Pixel), strip (SCT) and transition radiation (TRT) detectors for momentum and vertex measurements. The ID is embedded into a magnetic field of 2 T, generated by a superconducting solenoid. The calorimetry is placed within an outer radius of 4.25 m and provides energy and position measurements of particle showers, based on liquid-argon technology for the electromagnetic (ECal) and parts of the hadronic (HCal) calorimeters and scintillator-tile technology for the bulk of the hadronic calorimeter. The muon spectrometer (MS) is located in the outermost part of the ATLAS detector in an air-core toroid system with a radius of 12.5 m and contains three layers of tracking and additional muon trigger chambers. This section describes each individual component of the ATLAS detector [68]. The design resolution of each sub-detector part is given in table 3.1.

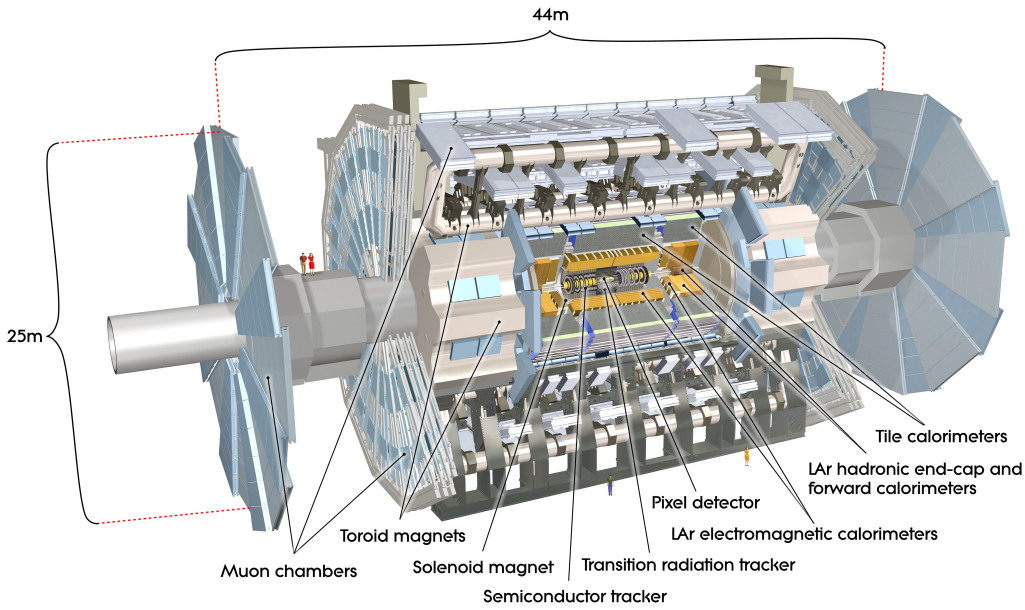

Figure 3.2. *Cut-away view of the ATLAS detector [68].*

3.2.1. Nomenclature

In this section, the ATLAS coordinate system is defined and important variables, typically used in data analysis, are introduced. The z-axis lies in beam direction, whereas the x-axis, which points to the center of the LHC ring, and the y-axis span the transverse plane. The coordinate system is right-handed and the y-axis points

Detector component	Target resolution	Coverage
Inner Detector (ID)	$\sigma_{p_T}/p_T = 0.05\% \oplus 1\%$	$\lvert\eta\rvert < 2.5$
Electromag. Calorimeter (ECal)	$\sigma_E/E = 10\%/\sqrt{E} \oplus 0.7\%$	$\lvert\eta\rvert < 3.2$
Hadr. Calorimeter (HCal)		
Barrel & Hadr. End-Cap (HEC)	$\sigma_E/E = 50\%/\sqrt{E} \oplus 3\%$	$\lvert\eta\rvert < 3.2$
Forward Calorimeter (FCal)	$\sigma_E/E = 100\%/\sqrt{E} \oplus 10\%$	$3.1 < \lvert\eta\rvert < 4.9$
Muon Spectrometer (MS)	$\sigma_{p_T}/p_T = 10\%$ at $p_T = 1$ TeV	$\lvert\eta\rvert < 2.7$

Table 3.1. *Target resolution and measurement coverage region in η of the ATLAS detector for each component individually [68]*

upwards. The point of origin is equal to the interaction point, where both beams intersect. The polar angle θ and the azimuthal angle ϕ are measured relative to the z-axis and around the beam direction respectively. The scalar quantities of energy and momentum and the vector quantity of missing energy in the transverse plane are denoted as E_T, p_{T} and $\mathbf{E}_T^{\mathrm{miss}}$. They are typical variables at hadron colliders, since they do not depend on the boost of the hard scattering rest-frame in beam direction. The rapidity is defined as $y = \frac{1}{2}\ln(\frac{E+p_L}{E-p_L})$, where p_L is the longitudinal momentum component of the corresponding particle in beam direction. For relativistic or massless particles the rapidity coincide with the pseudorapidity $\eta = -\ln(\tan\frac{\theta}{2})$, which only depends on θ and not on the individual particle energy. Rapidity and pseudorapidity differences Δy and $\Delta\eta$ are Lorentz invariant (in the limit $E >> m$) and do therefore not depend on any frame choice unlike $\Delta\theta$. For this reason they are preferred variables to describe the direction of particle trajectories with respect to the beamline. The transverse and longitudinal impact parameters d_0 and z_0 are specified as the transverse distance to the beam axis and the z-position at the point of closest approach of particle trajectories with respect to a specific interaction vertex.

3.2.2. Inner Detector

The ATLAS Inner Detector (ID) is responsible of measuring charged tracks above a nominal threshold of $p_T > 0.5$ GeV within $\eta < 2.5$. It achieves an excellent pattern recognition, momentum resolution and the measurement of primary and secondary vertices from heavy flavor or τ lepton decays. Furthermore, it provides electron identification within $\eta < 2.0$ over a wide range of electron energies. The ID has an approximate length of 6.2 m and consists of three sub-detectors, which are arranged cylindrically around the beam axis inside the radius of 1.15 m: the pixel detector (Pixel), semi-conductor tracker (SCT) and transition radiation detector (TRT). Figure 3.3(a) illustrates the ID setup and 3.3(b) gives a detailed side view, including proportions of the individual components. The ID is located in a 2 T magnetic solenoid field for momentum and charge measurements.

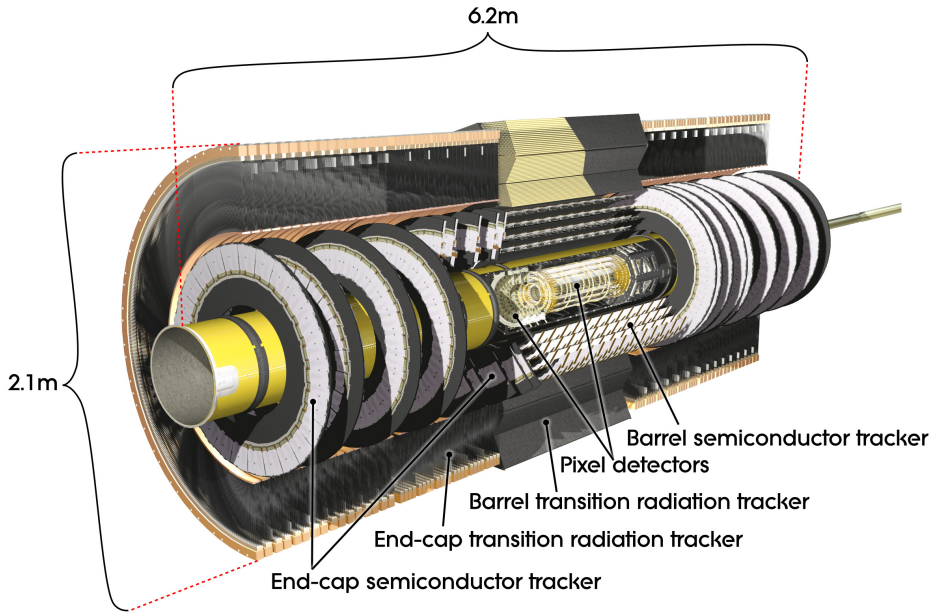

(a)

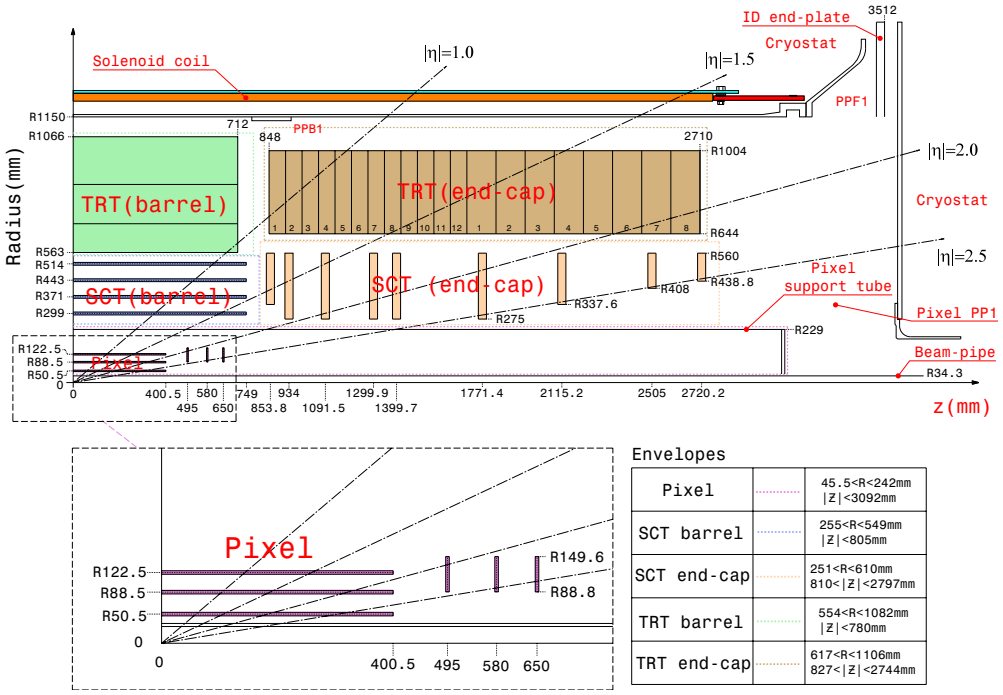

(b)

Figure 3.3. *Cut-away view of the ATLAS ID, including overall dimensions (a) and the different sub-components for tracks with various η values (b) [68].*

Pixel Detector

The detector part with the highest granularity, achieving an excellent vertex resolution, is the silicon pixel detector, which is located in the innermost part of ATLAS. The pixel detector covers the region $|\eta| < 2.5$ and is composed of three layers of identical pixel sensors. It is divided into a barrel and two end-cap regions with a minimum pixel size of $R - \phi \times z = 50 \times 400\ \mu\text{m}^2$. Secondary vertex measurements are also performed, where the layer closest to the beam called *b-layer* plays an important role. In the barrel part, the layers are arranged cylindrically around the beam axis, whereas they are installed perpendicular to the beam axis in terms of end-caps in the forward regions. The intrinsic accuracies in the barrel and the end-caps are 10 μm $(R - \phi)$ and 115 μm (z) or (R) respectively. In total, the pixel detector has approximately 80.4 million readout channels. For adequate noise suppression, the silicon sensors operate at low temperatures of approximately -5 to -10°C.

Semi-Conductor Tracker

Subsequent to the pixel detector, there is the SCT with a coverage of $|\eta| < 2.5$. It consists of four double silicon micro-strip layers for space point measurements in the barrel region. Within each double layer, one set of strips is aligned axially with respect to the beam axis and one set slightly aligned with a small stereo angle of 40 mrad to enable measurements of z-coordinates of the track. The strip modules in each layer are made of two 6.4 cm long daisy-chained sensors with a strip pitch of 80 μm. In forward direction, nine additional double end-cap layers on each side with strip modules radially to the beam and a stereo angle of 40 mrad are installed. The intrinsic accuracies per module are 17 μm $(R - \phi)$ and 580 μm (z) in the barrel and 17 μm $(R - \phi)$ and 580 μm (R) in the end-caps. The SCT has approximately 6.3 million readout channels.

Transition Radiation Tracker

The TRT forms the outer part of the ID and reconstructs tracks within $\eta < 2.0$. It is a combination of a straw and a transition radiation tracker and consists of straw tubes with a diameter of 4 mm and a length of 144 cm parallel to the beam axis in the barrel region and 37 cm long radially arranged straws in the end-cap wheels. Only $R - \phi$ position information is provided by the TRT. Charged particles, crossing the straws, ionize a gas mixture of $Xe/CO_2/O_2$ and generate a current in the tungsten wire in the middle of each straw. Transition radiation of minimum ionizing particles can enhance the signal amplitudes significantly, which improves the electron identification capabilities. The intrinsic accuracy is 130 μm $(R - \phi)$ per straw. Despite the lower precision of straw tubes compared to silicon sensors, the TRT contributes substantially to the combined measurement of the ID, because of its high number of measurement points per track (typically 36 hits per track)

and the longer track length. The TRT operates at room temperature and has a total number of about 351.000 readout channels.

3.2.3. Calorimetry

The calorimeters are designed to perform precise energy and position measurements of physics objects such as electrons, photons and hadrons. A full azimuthal coverage in ϕ around the beam axis and coverage up to $\eta < 4.9$ in pseudorapidity is provided. The calorimeters have a sampling structure with alternating thin layers of absorbing and active material, which accurately measures the evolution of electromagnetic or hadronic showers. The sampling calorimeters in ATLAS are based on various technologies and are capable of measuring the full variety of physics objects, produced at the LHC. An important feature of the calorimetry in ATLAS is the prevention of a punch-through into the muon system. Therefore the thickness of the calorimeter has to be sufficiently large to confine the deposited energy of showers within the calorimeter volume, which is also crucial for an adequate measurement of missing transverse energy. The ATLAS calorimeter system is shown in figure 3.4 and consists of an inner part, the electromagnetic calorimeter (ECal), an outer part, the hadronic calorimeter (HCal), and forward calorimeters (FCal).

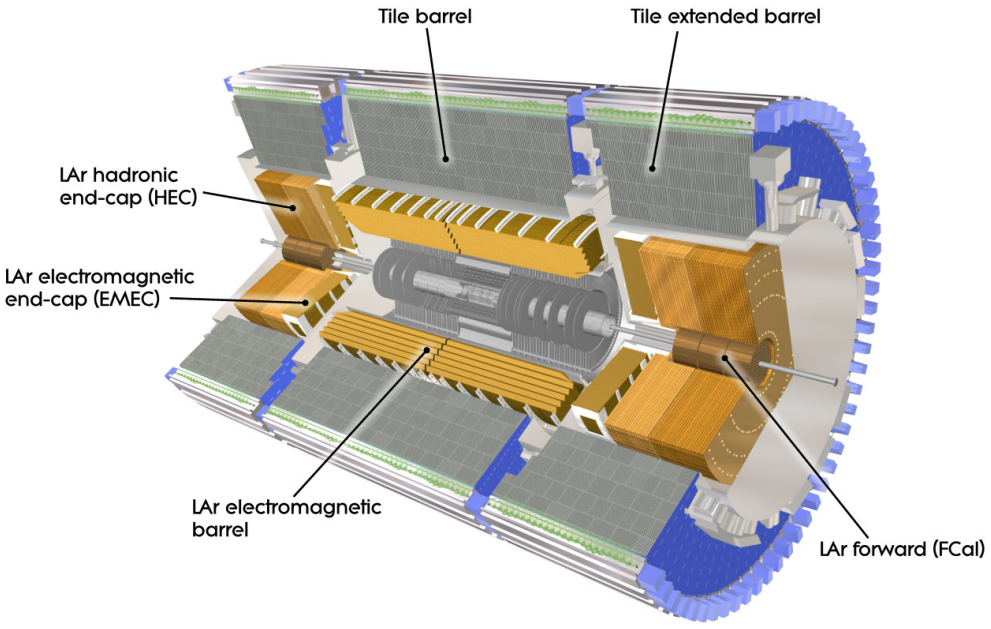

Figure 3.4. *Cut-away view of the ATLAS calorimetry system [68].*

Electromagnetic Calorimeter

The ECal is composed of a barrel part within $|\eta| < 1.475$ and a forward part in the region of $1.375 < |\eta| < 3.2$, which is divided into two end-cap wheels perpendicular to the beam axis on each side. Liquid Argon (LAr) is used as active detector sampling material and the absorbing plates are made of lead and stainless steel. An accordion structure of the calorimeter modules is chosen, illustrated in figure 3.5 for barrel modules, to avoid gaps and to ensure therefore full ϕ symmetry of the detector response. Each barrel module consists of three layers of different thickness and segmentation. The first layer is relatively thin but segmented very finely along the η direction, whereas the middle layer is much thicker with a coarser segmentation and collects the largest energy fraction. The third layer is segmented quite coarsely, because it only collects tails of the electromagnetic showers. The end-cap sampling modules are constructed similar to the barrel ones, using three layers in the region of $1.5 < |\eta| < 2.5$ and two layers elsewhere. An extra thin sampling layer of LAr is installed in front of the first layer in the region $|\eta| < 1.8$, which provides shower sampling measurements to correct for energy loss due to the material budget of the ID and the solenoid. Overall, the ECal has a particularly high granularity, especially in the acceptance region of the ID to increase for example the precision of measuring electrons and photons[1], with a minimum calorimeter cell size of 2.5×2.5 cm^2 $(\eta - \phi)$. The number of readout channels is approximately 170.000.

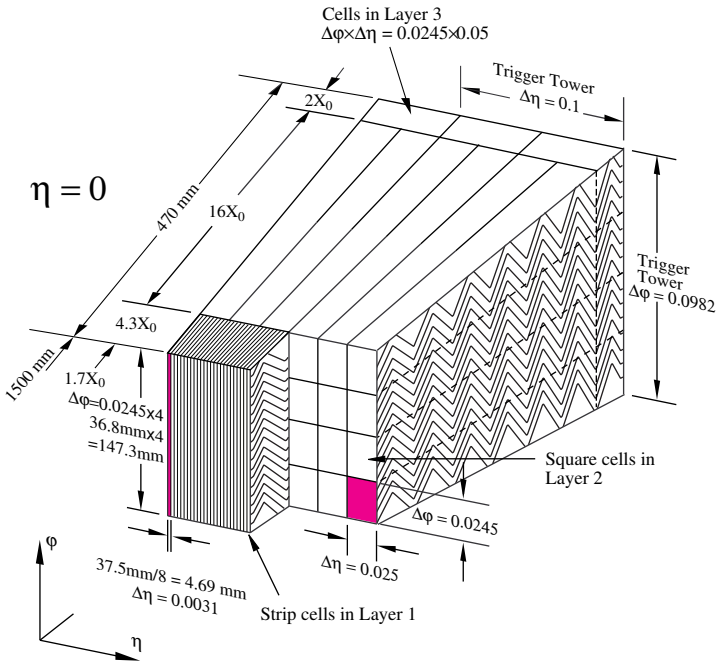

Figure 3.5. *ECal Barrel module with its three layers in ϕ direction and the corresponding granularity in $(\eta - \phi)$ [68].*

[1]Electrons and photons are fully absorbed by the ECal.

Hadronic Calorimeter

The HCal system consists of the tile calorimeter (Tile), the LAr hadronic end-caps (HEC) and the LAr forward calorimeter (FCal).

The Tile is a sampling calorimeter in "sandwich" design, which uses scintillator tiles as active material and steel plates as absorber. It forms the central part of the HCal within the region $|\eta| < 1.7$ outside the ECal and has a cylindrical setup with the inner radius of 2.28 m and an outer radius of 4.25 m. Its structure is divided into an inner barrel ($|\eta| < 1.0$) with the length of 5.8 m and two extended barrels ($0.8 < |\eta| < 1.7$) with the length of 2.6 m. Each barrel module contains 64 wedge-shaped modules with an azimuthal size of $\Delta\phi \approx 0.1$. There are three radial layers of different interaction lengths in the Tile with calorimeter cells of the size $\Delta\eta \times \Delta\phi = 0.1 \times 0.1$ in the first two layers and a cell size of $\Delta\eta \times \Delta\phi = 0.2 \times 0.1$ in the third layer. The profile of the Tile including the different layers in η direction is shown in figure 3.6. In comparison to the ECal, it is feasible for the HCal to have a lower granularity, because of a wider spread of hadronic showers. The Tile calorimeter has approximately 10.000 readout channels.

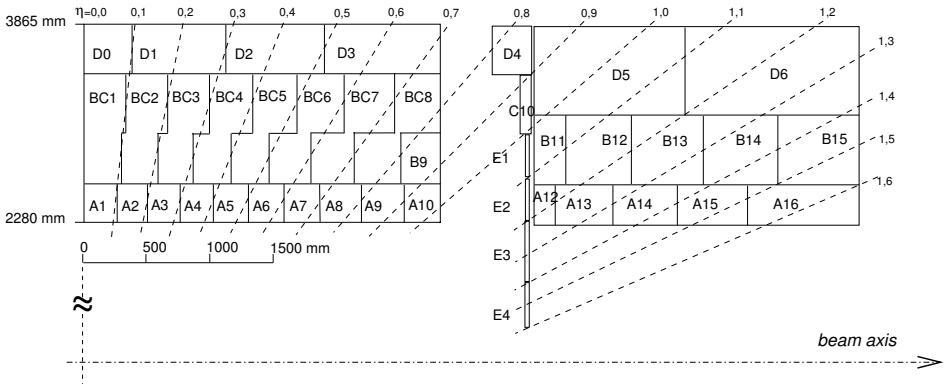

Figure 3.6. *Segmentation in depth and eta of the tile calorimeter modules in the central (left) and extended (right) barrels [68].*

The hadronic end-cap calorimeters (HEC) consist of two independent wheels on each side, covering the region of $1.5 < |\eta| < 3.2$. They are placed behind the ECal end-caps, with whom they share common LAr cryostats. The HEC uses copper as absorber and LAr as the active material. Each wheel is made of 32 wedge-shaped modules perpendicular to the beam axis with an inner radius of 0.474 m and an outer radius of 2.03 m. The wheels contain two layers in depth with calorimeter readout cells of the size $\Delta\eta \times \Delta\phi = 0.1 \times 0.1$ in the region $|\eta| < 2.5$ and $\Delta\eta \times \Delta\phi = 0.2 \times 0.2$ for larger η values.

The forward calorimeters (FCal) cover a range of $3.1 < |\eta| < 4.9$. The FCal is based on LAr as active material and is composed of three modules in each end-cap. The first module uses copper as absorber and measures electromagnetic showers. The second and third are made of tungsten as the absorbing material and are

hadronic calorimeters. The FCal is located in the cryostats of the HEC, keeping the calorimeter system compact, while reducing potential crack regions and radiation background sources, which might reach the muon spectrometer.

3.2.4. Muon Spectrometer

The muon spectrometer (MS) is designed to detect charged particles passing the calorimeters, which are mainly muons. It is located in the outermost part of the ATLAS detector within large superconducting air-core toroid magnets and measures muon momenta, based on the bending of trajectories. Figure 3.7 shows the layout of the spectrometer. The momenta can be determined standalone by the MS over a wide range, from a few GeV up to a few TeV with reasonable resolution. The MS covers an acceptance region of $|\eta| < 2.7$ for momentum measurements and of $|\eta| < 2.4$ for triggering on muons. The number of readout channels is approximately 800.000.

The magnet system is divided into a barrel, eight air-core toroids in the region $|\eta| < 1.4$, and two smaller end-cap toroids in the region $1.6 < |\eta| < 2.7$, which are inserted in the barrel toroid and fall into line with the solenoid. In the transition region, the deflection is provided by a combination of both fields. The overall magnetic field, which is continuously monitored by 1800 Hall sensors, is about 4 T and mostly orthogonal to the trajectories of the muons. The light structure of the magnet system minimizes multiple scattering effects and therefore avoids degradation of momentum resolution.

The layout of the precision muon chambers follow the symmetry of eight octants of the toroids. In the barrel region, three cylindrical layers of chambers are installed at radii of approximately 5 m, 7.5 m and 10 m. Four wheels perpendicular to the beam axis form both end-caps respectively and are located at distances of about 7.4 m, 10.8 m, 15 m and 21.5 m from the interaction point in front of and behind the small toroid magnets. At $\eta \approx 0$, a gap in the coverage of the chambers exists, because of services to the ID, the solenoid and the calorimeters. There are also crack regions due to detector support structures in the region of $\eta \approx 1.2$ and additionally at $\phi = 240\circ$ and $\phi = 300\circ$ due to the feet which support the barrel part of the detector.

Precision momentum measurements are performed by *Monitored Drift Tube chambers* (MDTs), which cover the full acceptance range of $|\eta| < 2.7$. These drift tubes operate with Ar/CO_2 gas at a pressure of 3 bar and provide a resolution of 35 μm per chamber. Within the forward region of $2.0 < |\eta| < 2.7$, the innermost MS tracking layer contains *Cathode-Strip Chambers* (CSCs) instead of MDTs, which are multi-wire proportional chambers with cathodes segmented into strips. In contrast to MDTs, the CSCs have a high-rate capability and a low neutron sensitivity, which is necessary especially in forward directions. The CSCs provide a resolution of 40 μm in the bending plane and about 5 mm in the transverse plane per chamber. To achieve these resolutions, an excellent knowledge about the alignment of the

chambers within the MS is required (typically at the level of 30 μm), which is accomplished by an optical alignment system, monitoring all chamber positions.

In addition to the tracking chambers, fast trigger chambers are installed, which provide information about tracks within a few tens of nanoseconds and which are able to identify bunch-crossings. In the barrel region ($|\eta| < 1.05$), *Resistive Plate Chambers* (RPC) are chosen, which are gaseous parallel electrode-plate detectors, having a good spatial resolution and moderate-rate capability. In forward region within $1.05 < |\eta| < 2.4$, *Thin Gap Chambers* (TGCs) are mounted for triggering, which are multi-wire proportional chambers, providing a higher-rate capability. Beside of trigger information, the RPCs and TGCs complete the measurements of the precision tracking chambers by adding a second orthogonal coordinate to each hit of the trajectory.

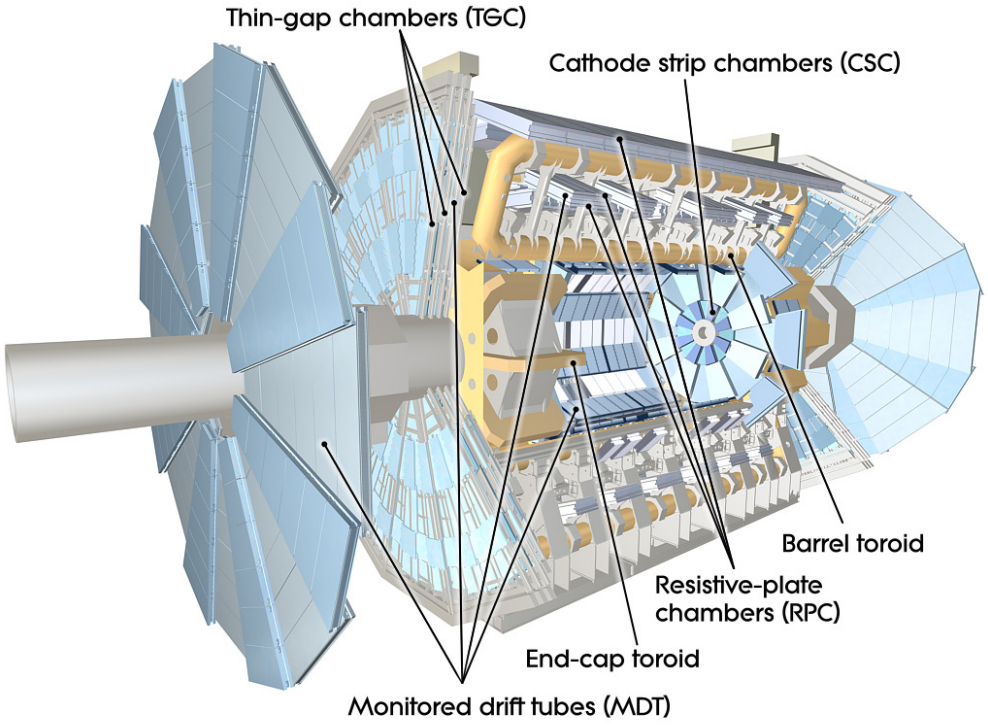

Figure 3.7. *Cut-away view of the ATLAS muon system [68].*

3.2.5. Forward Detectors

Three smaller detectors are installed in the forward region of the ATLAS detector. The first two detectors provide a measurement of luminosity, which is delivered to ATLAS. LUCID (Luminosity measurement using Cerenkov Integrating Detector) is placed at a distance of $\pm$17 m from the interaction point and measures inelastic proton-proton scattering. ALFA (Absolute Luminosity For ATLAS) is located at a distance of $\pm$240 m from the interaction point very close to the beam (down to

approximately 1 mm) and is made of Roman pots, which contains a scintillating fiber tracker. The third detector is the Zero-Degree Calorimeter (ZDC) at ±140 m from the interaction point. Its function is the determination of the centrality of heavy-ion collisions.

3.2.6. Trigger and Data Acquisition

The trigger system provides a first threshold of background suppression and reduces the rate of the incoming data record to a feasible amount. The system consists of three trigger levels: Level 1 (L1), Level 2 (L2) and the event filter (EF). L1 is hardware based while L2 and EF are performed offline using computing farms.

L1 uses a limited amount of detector information to trigger events within a very short time. It reduces the rate to approximately 75 kHz. Figure 3.8 illustrates the L1 work-flow. The L1 selection searches for high-E_T calorimeter objects like electrons, photons, jets, τ leptons, missing transverse energy or the scalar sum of transverse energy and for high-p_T muons, triggered in the MS. The *Central Trigger Processor* (CTP) decides if an event is accepted, based on the multiplicity of trigger objects, passing certain energy and momentum thresholds. The identification of events to pass one to higher trigger levels is a fundamental but challenging task at the nominal bunch spacing of 25 ns, and the L1 trigger must arrive at a decision within 2.5 μs. In addition, the detector information has to be kept additionally in memory for further processing, since the typical time-of-flight for muons to reach the MS exceeds the time interval between bunch-crossings.

Subsequently, the L1 output serves as seed for L2 with so-called *Regions-of-Interest* (ROIs), depending on η and ϕ, employing the full detector granularity and precision of the ID, MS and calorimeters to provide a further rate reduction down to 3.5 kHz with an average processing time per event of 40 ms.

For events passing L2, the full detector information is assembled in an *event-building* procedure and is sent to the EF. The EF is based on offline techniques, using fully built events and thus extends the object and event selection. It further reduces the rate finally to approximately 200 Hz, which is a manageable rate size to record permanently at the CERN Tier 0 computing center for offline analysis. The average event processing time of the EF is about four seconds.

The data acquisition (DAQ) system manages the movement of data between the various trigger levels. The DAQ stores for example data from L1 in local buffers and sends event information, associated to ROIs, to the L2. Additionally, it manages configuration, control and monitoring tasks of software and hardware components.

3.3. Data Conditions

LHC *Run1* data taking can be divided into datasets for the year 2011 and 2012. While in 2011, the center-of-mass energy was 7 TeV, the LHC was operating at

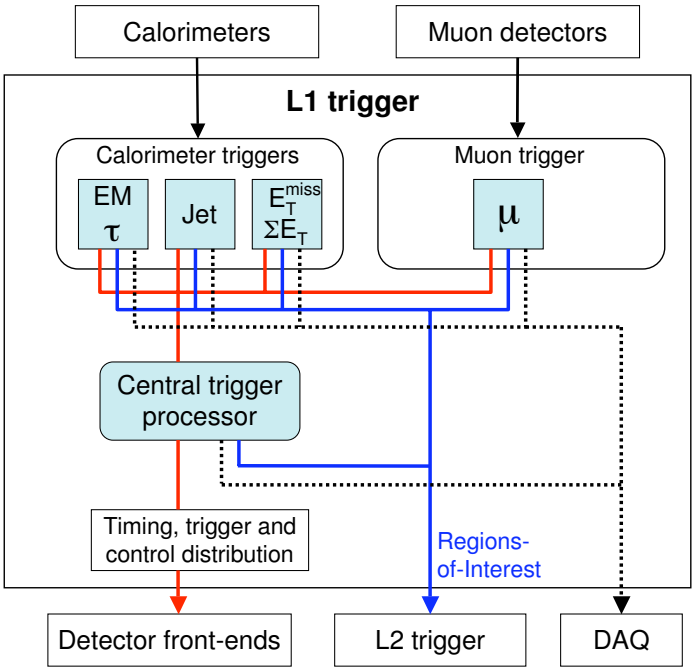

Figure 3.8. *Work-flow of the Level 1 trigger system [68].*

8 TeV in 2012. Data taking in 2011 started in March and ended in October, corresponding to an integrated luminosity of $\int \mathcal{L}dt = 5.08$ fb^{-1}, which has been recorded with the ATLAS detector. From this, 4.57 fb-1 have been assessed with good data quality and can be used for physics analysis. From April to December 2012, data at the center-of-mass energy of 8 TeV were collected. An integrated luminosity of 21.3 fb^{-1} has been recorded, providing an amount of 20.3 fb^{-1} suitable for physics analysis. This high data taking efficiency for good quality data emphasizes the outstanding performance of the ATLAS experiment. The total integrated luminosity versus time is illustrated in figure 3.9. The official luminosity uncertainty is ±1.8% for 2011 and ±2.8% for 2012 data and is derived, following the methodology in [75, 76]. The bunch spacing was adjusted to $\Delta t = 50$ ns in both years. In August 2012, the instantaneous peak luminosity reached a maximum of 7.562 10^{33} cm^{-2}s^{-1}. Table 3.2 provides an overview of the relevant conditions of data taking during 2011 and 2012.

Due to the high instantaneous luminosity and high event rates in 2012, the rate of events recorded by the trigger system exceed the nominal rate of 400 Hz at the EF level [78]. With increasing rates, the number of inelastic proton-proton interactions per bunch crossing μ is enhanced, which leads to additional tracks and calorimeter energy deposits in the hard scattering events of interest. This source of background is often referred to as *pile-up* (PU) and can have a significant impact on object reconstruction, as explained in chapter 4. It is common to differentiate between *in-time* and *out-of-time* PU. The first type contains PU within the same bunch crossing, whereas the latter one addresses PU contributions from neighboring

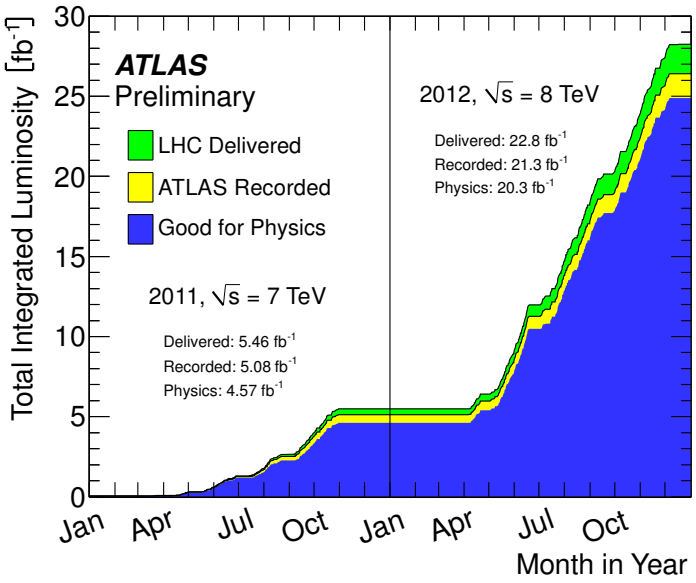

Figure 3.9. *Cumulative luminosity versus time delivered by the LHC (green), recorded by ATLAS (yellow), and certified to be good quality data (blue) during stable beams and for pp collisions at 7 and 8 TeV center-of-mass energy in 2011 and 2012 [77].*

bunch crossings. Figure 3.10 shows a comparison of PU conditions in 7 TeV and 8 TeV data. The high luminosity in 2012 leads to a mean value of PU interactions of $\langle\mu\rangle = 20.7$ per bunch crossing.

The analysis, presented in this thesis, uses the full 8 TeV dataset, which has been recorded in 2012 with an integrated luminosity of $\int \mathcal{L}dt = 20.3$ fb^{-1}. The amount of 7 TeV data, recorded in 2011, is not included in the main analysis here due to its marginal impact on the final results. Chapter 11 will additionally summarize the results of the combined analysis, using both 7 TeV and 8 TeV datasets.

Year	2011	2012
Center-of-mass energy	7 TeV	8 TeV
Integrated luminosity (good quality data)	4.57 fb^{-1}	20.3 fb^{-1}
Instantaneous peak luminosity	3.848 10^{33} cm^{-2}s^{-1}	7.562 10^{33} cm^{-2}s^{-1}
Bunch spacing	50 ns	50 ns
Luminosity uncertainty	1.8%	2.8%

Table 3.2. *Summary of Run1 data taking conditions in 2011 and 2012.*

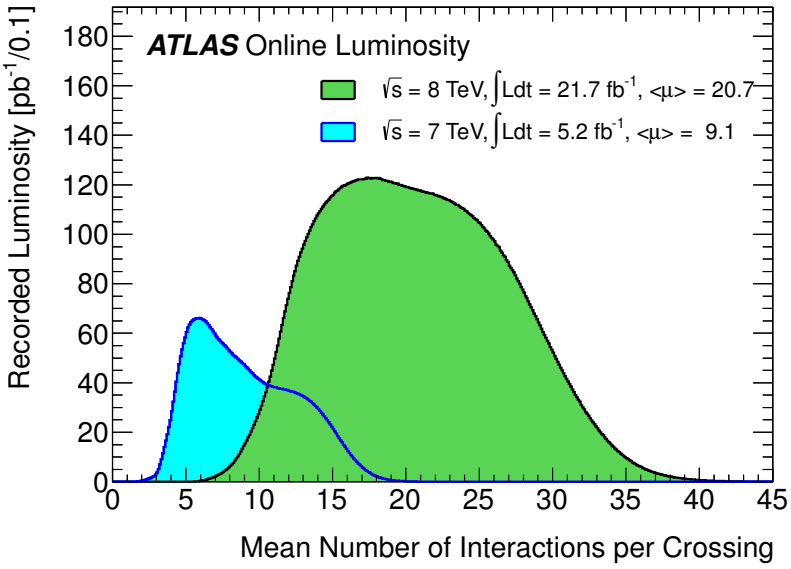

Figure 3.10. *Luminosity-weighted distribution of the mean number of interactions per bunch crossing for the 2011 and 2012 data. The mean number of interactions per crossing corresponds the mean of the Poisson distribution on the number of interactions per crossing calculated for each bunch. It is calculated from the instantaneous per bunch luminosity as* $\mu = L_{bunch} \times \sigma_{inel}/(f_r n_{bunch})$ *where* L_{bunch} *is the per bunch instantaneous luminosity,* σ_{inel} *is the inelastic cross section, which we take to be 71.5 mb for 7TeV collisions and 73.0 mb for 8 TeV collisions,* n_{bunch} *is the number of colliding bunches and* f_r *is the LHC revolution frequency [77].*

3.4. Event Simulation

Apart from observed events of real particle collisions in a detector, one also relies on simulated events, which represent the knowledge of the underlying physics. Event simulation is fundamental for making predictions in high energy physics. Therefore, the simulated events should contain as accurate and detailed physics information as possible. The ingredients of generating complete simulated events with high final state particle multiplicities, which are comparable to the observed data at the LHC, are explained in this section. Since full event simulation is complex, its evolution is factorized into several sub-tasks. At first, there is the description of the hard scattering process. In addition, initial (ISR) and final state radiation (FSR) has to be considered, causing multiple particle event topologies. An important task is the simulation of multiple parton soft interactions and beam remnants, called *underlying event* (UE). Furthermore the hadronization of final state quarks and gluons, based on QCD fragmentation and confinement, is described by phenomenological models. All these steps are implemented in software programs called *event generators*, which produce simulated high energy physics events, using Monte Carlo techniques. Figure 3.11 illustrates the full complexity of the event description by an event generator. Once events are produced at generator level, a simulation of the detector has to be

applied to simulate the response of the detector such as efficiencies, misidentification or momentum and energy resolution. In the following sections, the theoretical background and the evolution of the generation of simulated events is presented [79–81].

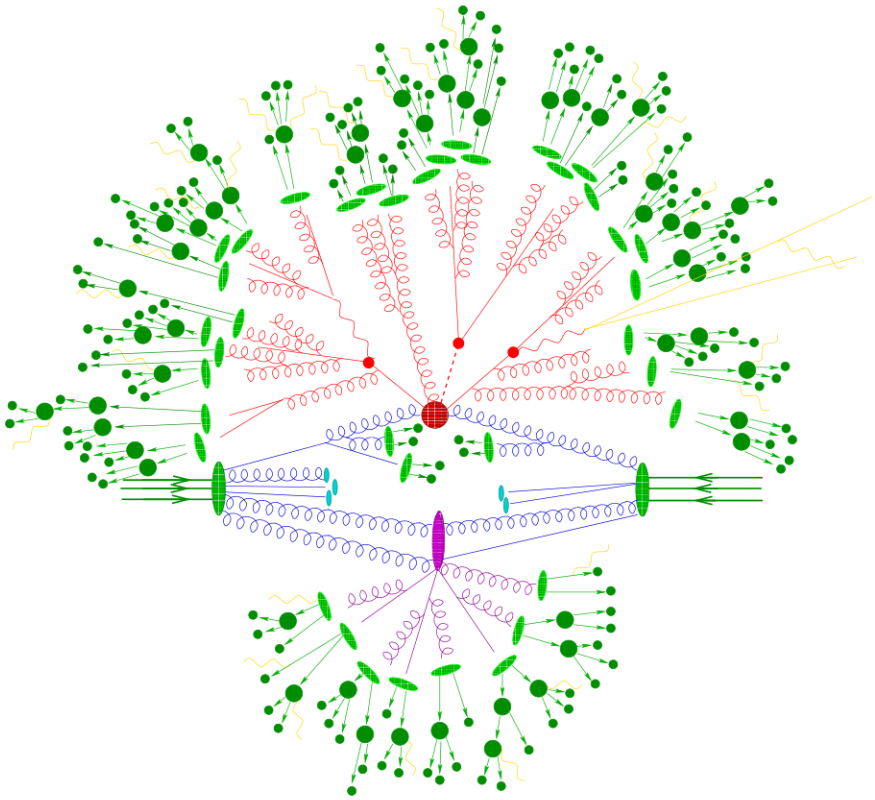

Figure 3.11. *Illustration of top quark associated Higgs boson production in the SHERPA [82] event generator. Initial partons (blue) take part in the hard interaction (big red blob), which results in two top quarks and the Higgs boson (solid and dashed red lines) and their subsequent decays (small red blobs). Further hard QCD radiation takes place in the event (red). Beam remnants are left over (light blue blobs) and an underlying event is produced (purple blob). Partons in the final state hadronize (light green blobs) and can decay (dark green blobs). QED photon radiation is included in addition (yellow) [83].*

3.4.1. Hard Scattering and PDFs

Scattering at the LHC can be divided into hard and soft processes, both based on the theory of QCD. Hard processes, such as the Higgs boson production or more generally events with high p_T objects, can be described using perturbation theory. However, soft processes are dominated by non-perturbative effects of QCD. The hadronic cross section σ_{AB} of proton A colliding with proton B can be formulated

as

$$\sigma_{AB\to X} = \int dx_a dx_b f_a(x_a, \mu_F) f_b(x_b, \mu_F) \sigma_{ab\to X}(x_a x_b \sqrt{s}, \mu_R), \tag{3.1}$$

where $\sigma_{ab\to X}(x_a x_b \sqrt{s}, \mu_R) = \sigma_0 + \alpha_s(\mu_R)\sigma_1 + \alpha_s^2(\mu_R)\sigma_2 + ...$ is the partonic cross section of the parton-parton interaction $ab \to X$, which can be calculated as a perturbation series in α_s (here next-to-next-to-leading order), using matrix elements at a given center-of-mass energy $\sqrt{s}$. The renormalisation scale μ_R has to be introduced in the renormalisation step e.g. via dimensional regularization to solve problems with divergent integrals, so-called ultra violet divergencies (UV), when calculating Feynman graphs, which include loop contributions such as the gluon self energy. These UV divergences can be absorbed in terms of the running coupling $\alpha_s(\mu_R)$, whose scale dependence can be determined by renormalisation group equations (RGEs). x_i is the momentum fraction of the corresponding parton a and b with respect to the proton. $f_i(x_i, \mu_F)$ is called *parton distribution function* (PDF) of the proton, describing the non-perturbative structure of the hadron. Problems arise in the calculation of the hard scattering partonic cross section, when perturbative corrections of collinear emitted partons are taken into account. Such corrections cause infra-red divergencies (IR), which can be regularized, introducing the factorization scale μ_F. The IR divergent parts in the cross sections can then be written in an universal form of splitting functions, which gives the probabilities of radiating additional partons, connected to the vertices ggg and qqg, and can be re-summed to all orders. These splitting functions are part of the DGLAP [84–86] equations

$$\frac{df_i(x, \mu_F)}{d \log \mu_F^2} = \frac{\alpha_s}{2\pi} \sum_{jk} \int_x^1 \frac{dx'}{x'} P_{i\to jk}(x/x') f_j(x_j, \mu_F), \tag{3.2}$$

where $P_{i\to jk}(z)$ are splitting functions for the process $i \to jk$, being $q \to qg$, $\bar{q} \to g\bar{q}$, $g \to q\bar{q}$ or $g \to gg$, with the momentum fraction z of particle j with respect to particle i. DGLAP is a set of integro-differential equations, whose solutions are the PDFs $f_i(x_i, \mu_F)$ as function of μ_F, which can then be used in the partonic cross section to absorb IR divergencies. The PDF dependence on x_i is taken from fits to observed data such as data from deep inelastic and hard scattering. That is, the PDF is finally measured at a given energy scale while its evolution is predicted by theory. There are several sets of PDFs available, provided from different collaborations (NNPDF [87], CTEQ [88], MSTW [89]) and depending on various input data. An example of a PDF at different scales from the MSTW collaboration is shown in figure 3.12, which can be interpreted as the probability density for a certain parton within the proton to have a longitudinal momentum fraction x at a specific scale Q. The uncertainties on PDFs mainly arise from uncertainties on the input data, the functional form of the PDF parametrization and uncertainties on α_s.

In this way the UV and IR divergencies are absorbed by the running coupling α_S and the PDFs respectively and the problem of combining hard and soft scale

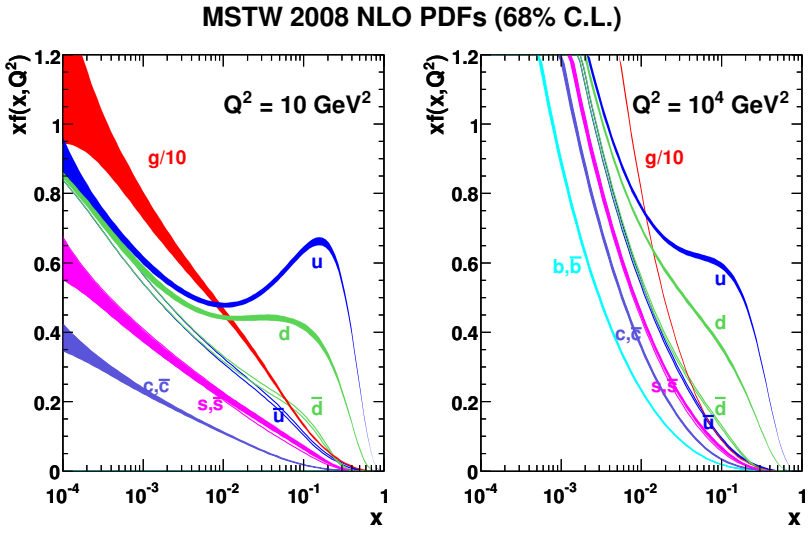

Figure 3.12. *MSTW 2008 NLO PDFs at $Q^2 = 10$ GeV^2 and $Q^2 = 10^4$ GeV^2 [89]*

processes in the calculation of the hadronic cross section can be fully factorized. This is a general feature of hard scattering processes in this context, which is often referred to as *factorization theorem* [90]. Formally, the hadronic cross section does not depend on both scales to all orders of perturbation theory. In practice, the more orders are included in the calculations, the smaller is the scale dependence of the cross section prediction. A usual choice of the scales is $\mu_R = \mu_F = Q^2$ and the theoretical uncertainties on cross section calculations are estimated from corresponding scale variations.

3.4.2. Parton Shower

Parton showers are an alternative approach to describe collisions in high energy physics based on perturbative QCD calculations. It is an "all order" approach in contrast to the order-by-order calculation of matrix elements. Parton showers relate partons taking part in the hard scattering to additional partons radiated at lower p_T scales down to the QCD cutoff scale Λ_{QCD}, which is typically chosen at ≈ 1 GeV. They describe collinear and soft parton radiation to all orders of QCD. Below the cutoff scale, physics has to be described by non-perturbative processes such as hadronization (see section 3.4.3). The method of parton showers is based on the DGLAP [84–86] formalism and uses splitting functions, which were introduced in the previous section. The splitting functions $P_{i\to jk}(z)$ can be re-written in terms of a Sudakov form factor

$$\Delta(Q, Q_0) = \frac{\alpha_s}{2\pi} \int_{Q_0}^{Q} dQ \sum_{jk} \int_{x_{\min}}^{x_{\max}} dx P_{i\to jk}(x), \tag{3.3}$$

[2] Q is the hard scale, which characterizes the parton parton interaction.

where the integration over momentum fraction x has to be restricted to an allowed range to avoid singularities, corresponding to very soft gluon production. This factor describes the probability of the evolution of a quark or a gluon from a higher scale Q_0 to a lower scale Q without radiating a parton. Equation 3.3 describes the no-branching probability for final state partons. The Sudakov form factors for initial state radiation can be constructed in a similar way but includes an additional dependence on the parton density in terms of a PDF weighted sum. Due to its probabilistic nature, it is convenient to realize parton showers by Monte Carlo simulation (see section 3.4.5).

3.4.3. Hadronization

QCD effects cannot be calculated perturbatively at long distances. Therefore, the process of hadronization, which describes the transformation of colored partons into colorless hadrons due to an increase in strong interaction with distance (confinement), is based on phenomenological models. One example of such a model, called *string fragmentation*, is implemented in PYTHIA [81], where a string, reflecting a *color flux tube*, connects two quarks. The potential energy, stored in the string, is assumed to depend linearly on the distance of the quarks. Once a string breaks down with increasing distance, new color singlet quark pairs are produced. The remaining partons are combined into mesons and baryons within the scope of allowed possibilities. In this model, the hadronization process stops when only on-shell hadrons are left. Since many of the produced hadrons are unstable, the masses and decay properties of these particles, such as decay modes and corresponding branching ratios, have to be included properly.

3.4.4. Multiple Interactions

Due to the composite structure of the proton, there can be additional softer parton interactions in a proton-proton collision on top of the hard scattering process, which is referred to as *underlying event* (UE). The understanding of such effects is crucial especially for precision measurements of hard interactions, where such underlying soft processes are non-negligible. In addition to the UE, proton remnants are left, which are color connected to the partons, taking part in the hard scattering, and which are part of the overall fragmenting system. The modeling of these multiple interaction effects is typically based on non-perturbative or semi-perturbative phenomenological models. There are also approaches to describe multiple interactions using real data such as the *Perugia Tunes* [91].

Furthermore, contributions from pile-up effects have to be considered as well due to parton interactions in the same or neighboring bunch crossing, as explained in section 3.3.

3.4.5. Event Generation

Simulations are needed to compare theory predictions to measured data. In high energy physics, one is interested in simulated events, which have the same structure as the actual measured data in real collisions. Such simulated events are produced with *event generators*, software libraries containing the implementation of theory, in a standardized format.

The challenge of these programs is the combination of hard and soft scale physics, as discussed in the previous sections. An event generator typically combines the best of the two worlds, namely matrix element calculations for the hard scattering process with parton showers, which describe the soft regime of parton emission and the subsequent hadronization. Nevertheless, the naive combination may lead to double-counting of cross section contributions in regions, which overlap kinematically. There are different techniques that can be implemented to avoid double-counting, such as the CKKW [92] or MLM [93] matching procedure, which are based on a phase space division into regions of small angle and low energy emissions for parton showers and large angle and high energy kinematics for matrix elements calculations. Furthermore, the parton shower is an important ingredient for hadron collider events, because of large final state multiplicities, which are observed in real events. For example in PYTHIA [81], parton showers are realized, using forward evolution in time for the FSR description, and backward evolution in the case of ISR. The evolution is applied subsequently until a certain cutoff scale of the branching is reached.

The event generators employ Monte Carlo (MC) techniques for hard scattering, parton showers and hadronization, based on random number generation and acceptance-rejection methods to calculate cross sections or differential distributions and to generate simulated events. Some examples of event generators, which are used in this analysis, are the multi-purpose leading order generators PYTHIA [81] and HERWIG [94] and the multi-leg leading order generators with leading order matrix element and parton shower matching SHERPA [82] and ALPGEN [95]. The packages PYTHIA, HERWIG and SHERPA include implementations of parton shower, hadronization and UE in addition and can be interfaced with other programs. The program ACER [96] specializes in the production of W and Z bosons in association with several jets, including jets from b-quarks. POWHEG [97] and MC@NLO [98] are examples of generators for next-to-leading order calculations with next-to-leading order matrix element and parton shower matching. Examples of further interfaces are PHOTOS [99] for QED radiative corrections in decays of resonances and TAUOLA [100] for simulating decays of τ leptons, including spin correlations.

3.4.6. Detector Simulation

The simulated events, using MC event generators, are produced at particle level. A sophisticated detector simulation is needed on top to transform the generated events

into a format, which is comparable to real data, obtained with the ATLAS detector. The simulation is based on GEANT4 [101], which describes the different detector components and its complex geometry and response precisely. First, the simulation program transforms the output of the event generators in terms of four-vectors of particles into trigger information, simulated hits in the tracking system or the muon spectrometer and energy deposits in the calorimeters. In a second digitization step, the detector response is simulated to what is expected from the output of readout electronics of the ATLAS detector in real collision events. This includes an estimation of noise and of pile-up and detector conditions, corresponding to real data taking periods. Since the detector simulation output is standardized, it can be fed into the ATLAS reconstruction procedure, which is explained in the next chapter 4. The full ATLAS simulation software and infrastructure, which allows for applying each of the above steps subsequently, is described in detail in [80, 102].

The samples for simulated events, which are used in the analysis, are summarized in section 5.1 and 5.2. They are produced with various event generators and passed through the full detector simulation.

4 Object Selection

A good performance of the reconstruction and identification of physics objects such as leptons, jets[1] or missing transverse energy is essential to investigate many of the interesting physics processes at the LHC. Starting from raw data or simulated events, passing the detector simulation, information at the level of hits in the tracking system and energy deposits in the calorimeters needs to be converted into physics objects suitable for analysis. The reconstruction of physics objects consists of various algorithms, which are implemented in the ATLAS reconstruction software [102]. Many of these algorithms use high-level detector information from the ATLAS Inner Detector (ID) 3.2.2, the calorimeters (ECal and HCal) 3.2.3 and the muon spectrometer (MS) 3.2.4, such as reconstructed tracks and clusters of calorimeter cells instead of single hits in the tracking system and energy deposits in individual cells. Several identification criteria, based on track and hit information, exist for reconstructed objects, resulting in various working points with respect to different selection efficiencies and background rejection. Differences in energy scales, momentum resolution and identification efficiencies between reconstructed objects in data and simulated events have to be corrected in each analysis (see chapters 5 and 6). More information about corrections and the corresponding systematic uncertainties can be found in 8.

In the search for $H \rightarrow \tau^+\tau^- \rightarrow l^+l^-4\nu$, electrons and muons as well as jets need to be considered. Due to the four neutrinos in the final state, which cannot be detected directly in the experiment, the reconstruction of missing transverse energy $\mathbf{E}_T^{\text{miss}}$ plays an important role. This chapter will provide an overview of the algorithms and techniques concerning reconstruction, identification and also calibration of the relevant physics objects.

4.1. Tracking

The reconstruction of tracks of charged particles takes place in the ID, using a sequence of algorithms [103]. Tracks are a fundamental ingredient for the reconstruction of many other physics objects, which are discussed in sections below. In a first step, three-dimensional representations of the silicon detector (Pixel and SCT) measurements serve as seeds for track reconstruction. This so-called *inside-out* algorithm adds hits successively, using a combinatorial Kalman filter, moving

[1] Jets are bundles of hadrons as explained in section 4.5.

outwards from the interaction point. Ambiguities in track candidates are removed, based on the presence and number of hits of the tracks in the detector layers, and the remaining tracks are extended into the TRT. The inside-out algorithm requires reconstructed track transverse momenta higher than $p_T > 400$ MeV. If no seed has been found to initialize the inside-out algorithm, the consecutive *outside-in* algorithm starts from TRT track segments, which are extrapolated to the ID by adding silicon hits. While the inside-out approach specializes to find primary particles, which are directly produced in the hard scattering, the outside-in approach targets mainly secondary particles, which originate from the decay of primary particles and which might therefore lead to missing silicon hits. Tracks are then refitted in both algorithms. At least 9 silicon hits are required to minimize the impact of fake tracks due to high pile-up conditions [104]. Furthermore, regions of inactive modules must be avoided. The track reconstruction efficiency ranges from approximately 70 % for low track p_T and high η to 90 % for higher p_T in the central part of the detector. The dependence of the efficiency on the pile-up conditions is less than 1% [105].

4.2. Vertexing

The vertex reconstruction employs an *iterative vertex finding* algorithm [106]. A vertex seed is based on the z-position of closest approach to the beam spot center of reconstructed tracks, which have to fulfill certain track quality criteria to ensure their compatibility with the interaction point. Such seeds and additional nearby tracks are used in an iterative χ^2 fit, called *adaptive vertex fitting* algorithm, to determine the vertex position. Each associated track carries a weight depending on the fitted χ^2, which reflects the level compatibility with the corresponding vertex. If the track is displaced by more than 7 σ with respect to its χ^2 probability, it serves as seed for a new vertex fitting procedure. Reconstructed vertices must contain at least two tracks. If several vertices are found in an event, the one with the highest $\sum p_{T,\text{track}}^2$ is denoted as primary vertex. The vertex reconstruction efficiency for a single reconstructable[2] interaction is approximately 90 %. With increasing number μ of interactions per event the efficiency decreases to approximately 50 % for $\mu = 41$ [105].

4.3. Electrons

The selection of isolated prompt electrons suffers from significant background contamination due to misidentified hadrons, leptons from heavy-flavour decays and electrons from photon conversions. For this reason, it is important to efficiently reconstruct and identify isolated electrons within the full detector acceptance, while at the same time ensuring high background rejection. The measurement of

[2] In a reconstructable event, at least two charged particles with $\eta < 2.5$ and $p_T > 400$ MeV are required.

reconstruction and identification efficiencies is based on *tag-and-probe* methods, using electrons from the decays $Z \to e^+e^-$, $J/\Psi \to e^+e^-$and $W \to e\nu_e$ [107, 108].

4.3.1. Trigger

This section provides an overview of the trigger strategy for electrons. The general ATLAS trigger system is introduced in section 3.2.6. At L1, the transverse energy E_T of electromagnetic showers is computed within windows of $\Delta\eta \times \Delta\phi \approx 0.1 \times 0.1$ in the calorimeters. If a certain E_T threshold is exceeded, these energy deposits serve as seeds for the simplified L2 reconstruction, which combines information from calorimeters and the tracking system. In the next step, triggered objects are passed to the EF, which uses offline software to continue reconstruction. L2 and EF form the so-called High-Level Triggers (HLT). In the analysis, presented in this thesis, a combination of single lepton and combined lepton triggers is used.

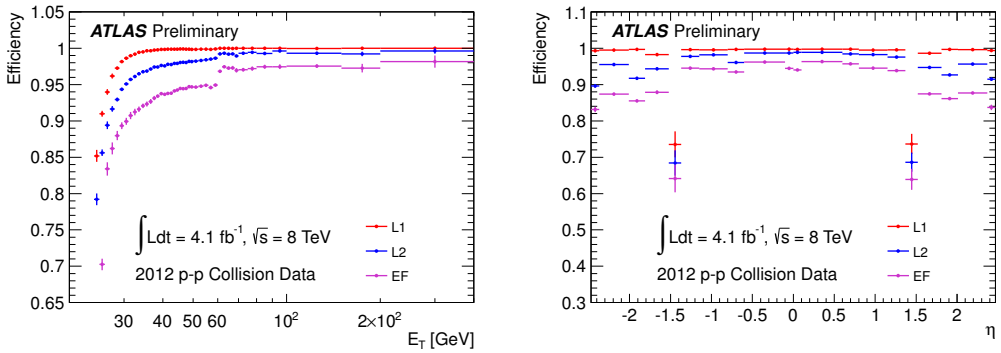

(a) (b)

Figure 4.1. *L1, L2 and EF Trigger efficiencies as a function of E_T and η of reconstructed electrons for the trigger combination of e24vhi_medium1 and e60_medium1 in 2012 [109].*

To select electrons with medium or high E_T, a trigger combination of *e24vhi_medium1* and *e60_medium1* is chosen[3]. An electron transverse energy threshold of 24 GeV and 60 GeV at EF level is required respectively. The overall trigger efficiency in this case reaches a plateau of 97% at $E_T = 60$ GeV. Figure 4.1 shows the efficiency dependence of the trigger combination on E_T and η. Concerning the trigger nomenclature, v indicates an η dependence of the E_T threshold at L1 level, h a requirement on hadronic leakage at L1 level and i a relative track isolation at EF level. Furthermore, both triggers require *medium* identification criteria at HLT level. In the analysis, these triggers are combined with the di-electron trigger *2e12Tvh_loose1* and the combined electron-muon trigger *e12Tvh_medium1_mu8* with an E_T threshold for electrons of 12 GeV at EF level, to exploit also the low E_T region. Both triggers

[3]The trigger *e60_medium1* recovers an efficiency loss of *e24vhi_medium1* in regions of high electron energies.

increase the efficiency for di-lepton final state events, that is important for the analyses presented in the thesis. T denotes a separation of L1 and HLT thresholds to ensure that the HLT is in the turn-on efficiency region of L1. The triggers hold the lowest possible thresholds without trigger pre-scaling within the period of 2012 data taking.

4.3.2. Reconstruction

The acceptance region for reconstructed electrons in the analysis lies within $\eta < 2.47$, where combined measurements of the ID (Section 3.2.2) and the ECal (Section 3.2.3) allow for track-to-cluster association, excluding the crack region $1.37 < |\eta| < 1.52$ between the ECal barrel and end-caps. The electron reconstruction in ATLAS has been evaluated, using proton-proton collision data, which has been recorded in 2011 and 2012 [107, 108].

In a first step, electromagnetic clusters in the ECal are defined, which are seeded from energy deposits with $E_T >$ 2.5 GeV, applying a *sliding-window* algorithm in (η-ϕ) space. The electron track-fitting procedure then uses information about hits in the tracking system and the distance in (η-ϕ) between ID track extrapolations and regions-of-interest (RoIs), based on properties of the ECal clusters. After a first candidate is found, the track parameters are re-fitted using a Gaussian Sum Filter [110], which accounts for bremsstrahlung effects and improves the performance of reconstruction. If at least one track with more than three silicon hits matches a cluster in the middle layer of the ECal within $|\Delta\eta| < 0.05$ and $|\Delta\phi| < 0.05$ or 0.1 [4] an electron candidate is formed. For TRT-only tracks with less than 4 silicon hits, the $|\Delta\eta|$ and $|\Delta\phi|$ thresholds are slightly adjusted. If more than one track is matched successfully, tracks with hits in the pixel detector and a minimal ΔR distance between the extrapolated track and the cluster's barycenter are preferred. To differentiate between prompt electrons and electrons from photon conversions, information about close-by tracks and displaced vertices are considered.

The estimation of the total electron candidate's energy consists of several contributions: the estimated energy in front of the ECal, within the ECal cluster, outside the cluster and beyond the ECal. The energy loss of the electrons due to material in front of the calorimeter, sampling material or leakage is mainly estimated from simulation.

The measurement of the electron reconstruction efficiencies in (E_T-η) bins is based on a tag-and-probe method using $Z \to e^+e^-$ events. The efficiency is about 97% for electrons with $E_T = 15$ GeV and increases to 99% for $E_T = 50$ GeV, averaged over η. For electrons averaged over the range $E_T > 15$ GeV, the efficiency increases from 95% at low $\eta$to 99% at high η. The corresponding uncertainties vary from 0.5% to 2% for low E_T and decrease below 0.5% for high E_T. The differences in efficiencies between data and simulation are smaller than 2% and need to be corrected for.

[4] The different values of $|\Delta\phi|$ depends on the side of track bending with respect to the cluster to take bremsstrahlung losses in azimuthal distance into account

4.3.3. Identification

The electron identification efficiency measurements are based on proton-proton collision data, collected in 2012 [108]. There are different identification working points of sequential cuts, called *loose*, *medium*, *tight* and *multi-lepton*.

In this analysis, the *medium* identification criterion is chosen. Typical variables, which are used in this cut-based approach, depend on electromagnetic and hadronic calorimeter quantities (e.g. fractions of energy deposits in different calorimeter layers or the width of electromagnetic shower shapes) or track quality and track-cluster-matching criteria (e.g. number of ID hits, impact parameters or distances between clusters and their associated tracks in (η-ϕ) space). Such shower shape and track variables of reconstructed electrons allow for high background rejection.

Averaged over η, the identification efficiencies for *medium* ranges from 80% at $E_T = 15$ GeV to more than 90% for $E_T \geq 50$ GeV, while its uncertainty is approximately 5-6% below $E_T = 25$ GeVand 1-2% above this threshold. The pile-up dependency of the efficiencies is smaller than 4% in the range of 1 to 30 reconstructed primary vertices.

To further reduce background due to misidentified hadrons or non-isolated electrons from heavy-flavour decays, isolation criteria can be applied. The calorimeter-based isolation $E_T^{\text{cone}\Delta R}$ is defined as sum of transverse energy in calorimeter cells within a cone of size ΔR around the electron cluster's barycenter, while the track-based isolation $p_T^{\text{cone}\Delta R}$ is the sum of transverse momentum of tracks within a cone around the electron's track. All tracks have to be associated to the primary vertex, from which the electron originates. The working points of relative isolation, which are used in the analysis, are summarized in table 4.1. In case of calorimeter based isolation, corrections are applied, which account for electron energy leakage outside the cone and pile-up effects, depending on the number of primary vertices.

In summary, the combined reconstruction and *medium* identification efficiencies vary from approximately 78% at low $E_T = 15$ GeV to more than 90% for $E_T > 50$ GeV, as can be seen in figure 4.2. Differences between efficiencies in data and simulated events are corrected in the analysis to achieve a reasonable modeling of the simulation. The correction factors (ratio of measured combined efficiencies for data divided by simulation) are close to unity over a wide range in η and E_T with a certain deviation of a few percent in very high η or low E_T regions.

Object	Isolation
electron	$E_T^{\text{cone}\Delta R}/E_T^e < 9\%$, $\Delta R = 0.2$
	$p_T^{\text{cone}\Delta R}/p_T^e < 17\%$, $\Delta R = 0.4$
muon	$E_T^{\text{cone}\Delta R}/E_T^\mu < 9\%$, $\Delta R = 0.2$
	$p_T^{\text{cone}\Delta R}/p_T^\mu < 18\%$, $\Delta R = 0.4$

Table 4.1. *Summary of the relative lepton isolation working points, which are used in the analysis.*

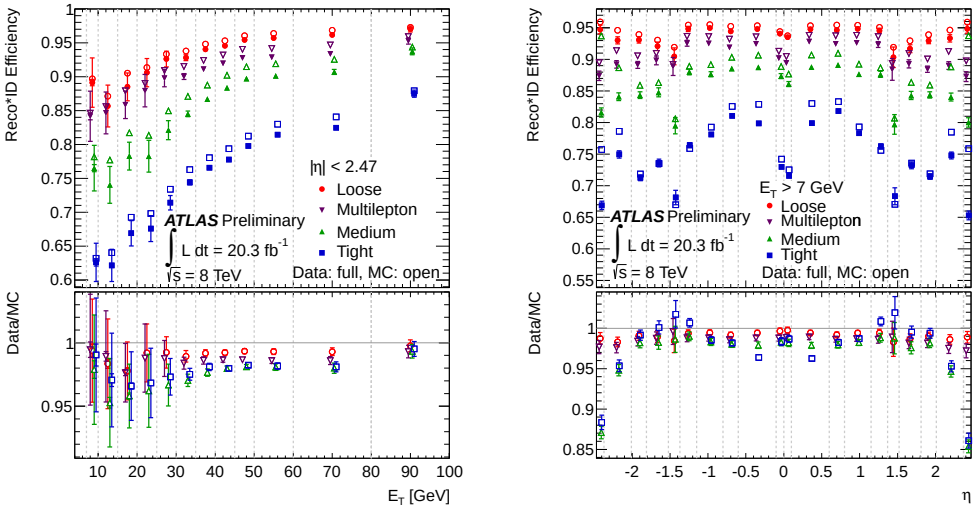

(a) (b)

Figure 4.2. *Combined reconstruction and identification efficiency as a function of E_T (a) and η (b) for cut-based identification loose, medium, tight and multi-lepton, measured in data in comparison to simulation for electrons from $Z \to e^+e^-$ events. The uncertainties are statistical (inner error bars) and statistical+systematic (outer error bars) [108].*

4.3.4. Energy Calibration

The ECal has been initially calibrated via test beam measurements. To further improve the calibration and reduce its uncertainties, the known mass of the Z boson resonance is used to adjust the energy scale in a data-driven way, using $Z \to e^+e^-$ decays, which has been additionally cross-checked with $J/\Psi \to ee$ events as well [111]. An alternative strategy of studying the ratio E/p of the ECal energy E divided by the ID track momentum p confirms the measurement of the energy scale, assuming the ID momentum scale and alignment is well known.

The parametrization of a residual miscalibration is chosen as $E_{true} = E_{meas}(1 + \alpha_i)$ for a specific detector region i. E_{meas} is the measured energy in the calorimeter at cluster level. The derived energy calibration correction factors α are shown in figure 4.3 for different calorimeter regions. The corrections have been determined in a fit of the measured di-electron mass in data to the Z lineshape, minimizing a negative unbinned log-likelihood after a simulation based energy correction due to leakage outside the cluster and absorption in the passive calorimeter material. The correction factors α_i are within 2% in the barrel and 5% in forward regions. The electron energy scale uncertainty ranges from 0.3% to 1.6% for central electrons

within $\eta < 2.47$, depending on E_T and η. Sources of uncertainties arise for example from the imperfect knowledge about material in front of the calorimeter, the presampler detector energy scale, non-linearities in readout electronics or background and pile-up contribution, as well as the fit procedure in the α determination.

The electron energy resolution is determined from the $Z \to e^+e^-$ and $J/\Psi \to e^+e^-$ line shape. The resolution in data is found to be slightly worse than in simulation. Therefore, an additional electron energy smearing correction is applied to simulated events.

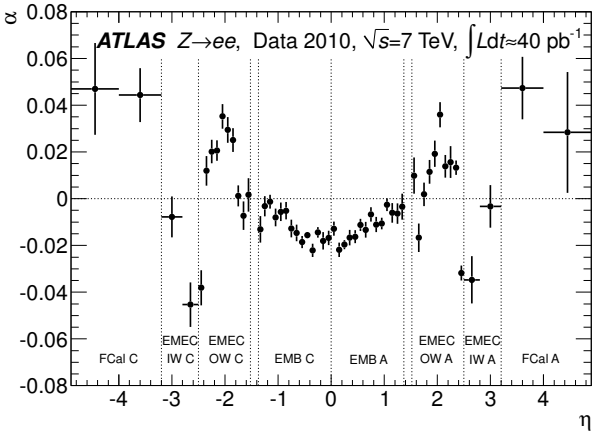

(a)

Figure 4.3. *Energy scale correction factors α depending on η of the electron cluster. The correction factors are derived in a fitting procedure using $Z \to e^+e^-$ events from data [111].*

4.4. Muons

For the detection of muons, information from the ID, the calorimeters and the MS is used. Muons are minimum ionizing particles and interact minimally with the calorimeter material, meaning they leave only a small fraction of energy in the calorimeters in contrast to electrons, photons or hadrons. Therefore, muons measured in the MS suffer only from a very low background contamination. The MS provides momentum measurements with a relative resolution below 3% in the region low and intermediate muon p_T up to a few hundred GeV and of approximately 10% at $p_T \approx 1$ TeV. The overall performance of the ATLAS MS is discussed in section 3.2.4. In the analysis, reconstructed muons within $|\eta| < 2.5$ are used, covering the acceptance region of the ID and the MS, to allow for muon track measurements in both detectors independently and for a subsequent track-matching procedure.

4.4.1. Trigger

The muon trigger system consists of the L1, L2 and EF muon trigger. The L1 is formed by three layers of RPCs in the barrel region $|\eta| < 1.05$ and three layers of TGCs in the end-cap regions $1.05 < |\eta| < 2.4$ as described in section 3.2.4. L1 muons need a coincidence of hits in two or three layers of RPCs or TGCs, depending on the corresponding trigger threshold. L1 covers 99% of the detector acceptance in the end-cap regions and about 80% in the barrel region, which is mainly due to limited geometric coverage because of services and support structures at $\eta \approx 0$. Regions-of-interest (RoIs) with typical dimensions of 0.1×0.1 (0.03×0.03) in $\Delta\eta \times \Delta\phi$ within the RPCs (TGCs) are sent to L2, if L1 is passed.

At L2, information from the MDTs and CSCs in forward regions is consulted to construct a *stand-alone* (SA) muon in the MS, which is then combined with an ID track. The muon momentum is derived from the weighted average of the L2 SA muon and the ID track.

In the EF step, two different approaches exist. The first one uses RoIs, passing L1 and L2 requirements, and combines SA muons with ID tracks. If no *combined* muon is found, ID tracks are extrapolated to the MS with an attempt to match track segments. However if no muons are found by this RoI-based approach, a second *full-scan* (FS) procedure is applied. It searches for reconstructed tracks in the full ID and MS respectively without restrictions to RoIs, trying to form FS muons by combining tracks from both detector parts.

In the analysis, an asymmetric di-muon trigger *mu18_tight_mu8_EFFS* is used for the corresponding di-lepton final states. This trigger requires two FS muons at EF level with $p_T > 18$ GeV and $p_T > 8$ GeV respectively, after a combined EF muon with $p_T > 18$ GeV and passing a *tight* quality criterion with respect to the number of hits in the RPCs and TGCs is found. Furthermore the electron-muon-trigger *e12Tvh_medium1_mu8* is added to the selection, using a single muon trigger *mu8* with $p_T > 8$ GeV for combined muons together with a single electron trigger.

The trigger efficiencies are measured from $Z \to \mu^+\mu^-$ and $J/\Psi \to \mu^+\mu^-$ decays, using tag-and-probe techniques to cover the medium and low p_{T} range of $p_T \lesssim 100$ GeV and $p_T \lesssim 10$ GeV, respectively [112]. For efficiency measurements in the high p_{T} region, data samples with events from top quark and W+jet production are used, where a muon originates from the decay of a W boson. These events are selected by applying triggers, based on calorimeter properties such as the missing transverse momentum $\mathbf{E}_T^{\mathrm{miss}}$. Figure 4.4 shows the efficiencies of the various analysis muon triggers as a function of p_{T} in the barrel and end-cap regions. The *mu18* trigger reaches a plateau efficiency in data of about 70% (86%) in the barrel (end-cap) region and the FS *mu8* an efficiency of about 99% (98%). The *mu8* trigger, which is used in the combined electron-muon trigger, provides an efficiency of nearly 80% (85%) in the barrel (end-cap) region. Systematic uncertainties on the trigger efficiencies arise mainly from the tag-and-probe or the trigger based methodology and pile-up or muon p_{T} dependencies. The overall uncertainties on

the efficiencies for medium p_{T} muons are below 1%. Differences between efficiencies from data and simulation are corrected in the analysis, depending on η and ϕ of the corresponding muons.

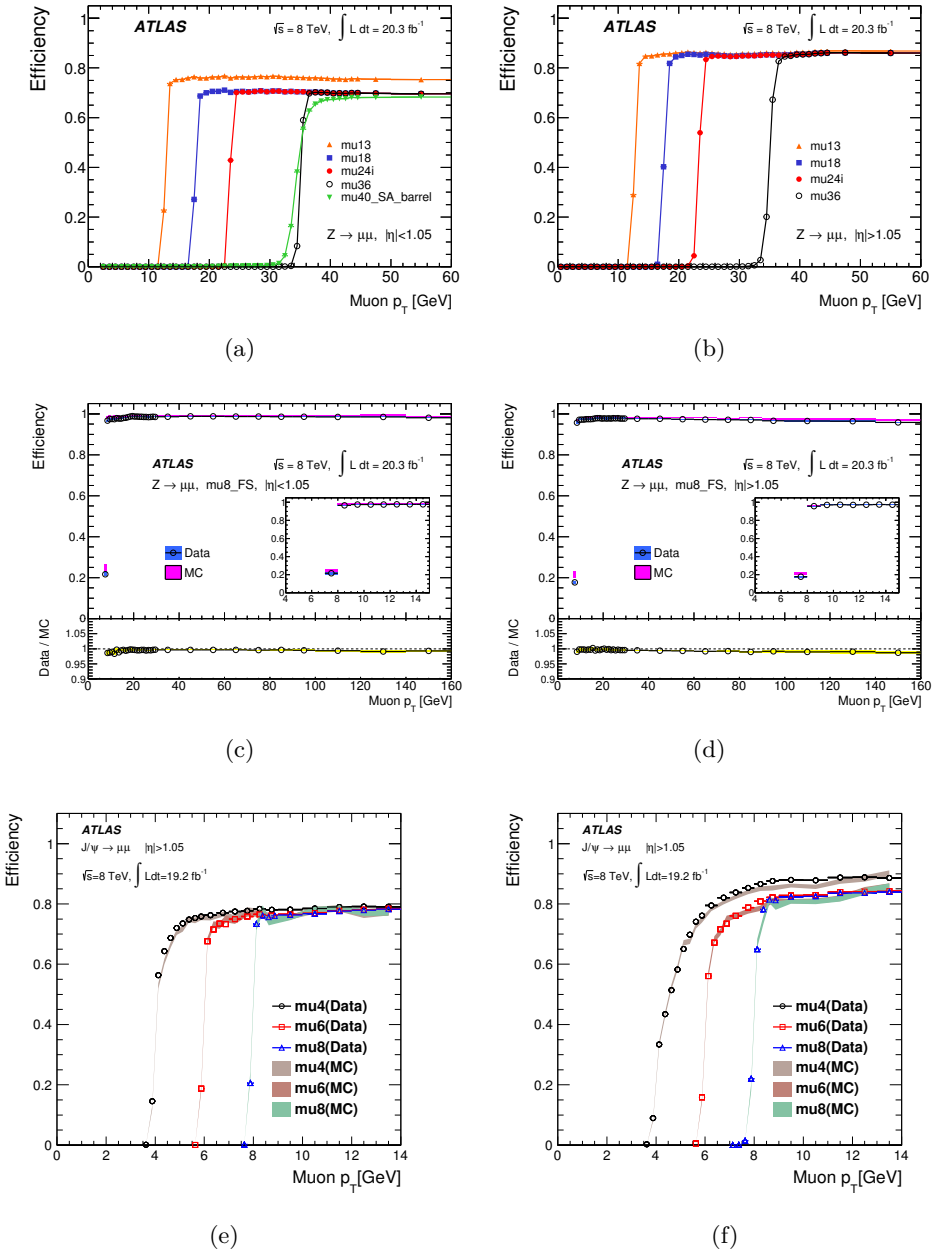

Figure 4.4. *Efficiencies measured in data for mu18 trigger (blue) in barrel (a) and end-cap (b) region as a function of p_{T}. Efficiencies measured in data in comparison to simulation for the FS mu8 trigger in barrel (c) and end-cap (d) region as a function of p_{T}. Data efficiencies for low p_{T} mu8 trigger (blue) compared to efficiencies from simulation (green) in barrel (e) and end-cap (f) region as a function of p_{T} [112].*

4.4.2. Reconstruction and Identification

Several types of reconstructed muons exist, according to the combination of the available information from the ID, the calorimeters and the MS [113]. Muons, based on reconstructed MS-only trajectories, are labeled as *stand-alone* (SA), where at least two layers of MS chambers have to be traversed by the muon candidate. The SA muon track is then extrapolated to the point of closest approach with the beam line. An estimate of the energy loss within the calorimeters due to minimum ionization is taken into account. The starting point of a *segment-tagged* (ST) muon is an ID track, which has to match with at least one track segment in the MDT or CSC chambers in the MS. *Combined* (CB) muons are formed by combining independently reconstructed tracks in the ID and the MS. For the combination of ID and SA tracks, a statistical procedure is used, based on various track parameters and the corresponding covariance matrix. While there are different combination strategies provided by ATLAS, the statistical combination is often referred to as *Chain1*. For completeness, there is also the strategy *Chain2*, which performs a global refit, using ID and MS hits. In the analysis, Chain1 CB muons with *tight* selection criteria [114] are chosen. Additional identification quality criteria with respect to ID tracks are applied, accounting for Inner Detector conditions: at least 1 Pixel hit, at least 5 SCT hits, not more than 2 Pixel or SCT sensors traversed by a muon track without hits and at least 6 TRT hits for muons within the TRT acceptance region $0.1 < |\eta| < 1.9$ of which less than 10% must be outliers[5]. The muon reconstruction efficiencies are measured via a tag-and-probe method in $Z \to \mu^+\mu^-$, $J/\Psi \to \mu^+\mu^-$ and $\Upsilon \to \mu^+\mu^-$ events and are shown in figure 4.5. For CB muons, the reconstruction efficiency is mostly above 96% as function of η and p_{T}, except for a significant efficiency loss in a few regions. For example at $\eta \approx 0$, the MS is only partially equipped because of services for the ID and the calorimeters. Furthermore, merely one layer of MS chambers has been installed in the region of $1.1 < |\eta| < 1.3$ at the time of Run1 data taking. Additionally, there is a decrease in efficiency for very low p_{T} muons, which tend to be absorbed in the calorimeters or to be bent back before reaching the MS. Systematic uncertainties on the CB muon efficiencies are well below 1% and stem mainly from the tag-and-probe methodology (eg. dependence of the tag-and-probe efficiency on the muon isolation criteria). Differences between the efficiencies from data and simulation are within 2% and are corrected in the analysis.

As in the case of electrons, muons are required to be isolated to reduce background contamination from for example non-isolated muons from heavy-flavour decays. The calorimeter- and track-based isolation cuts are summarized in table 4.1. $E_T^{\mathrm{cone}\Delta R}$ corrections are applied in the analysis to recover efficiency losses due to high pile-up conditions.

[5] An outlier is a single measurement that is not consistent with the final fitted track and therefore not user in the fit.

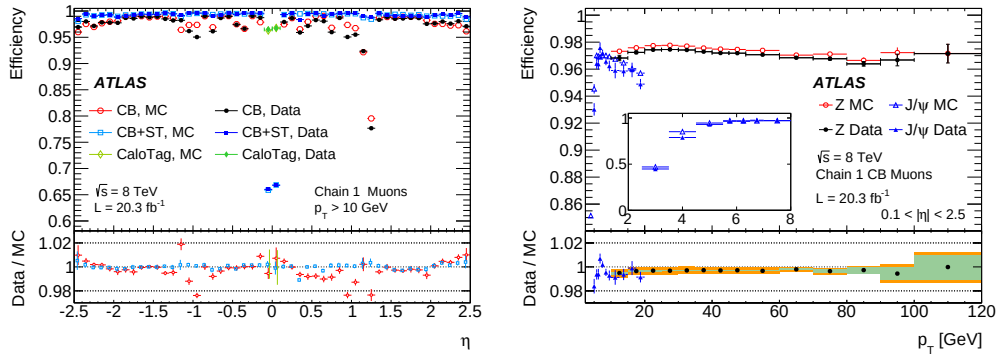

(a) (b)

Figure 4.5. *Muon reconstruction efficiencies as function of η (a) for different muon types of Chain1. The efficiencies for CB muons are shown in red for simulated events and in black for data. The lower panel shows the ratio between efficiencies measured in data and simulation, including statistical and systematic uncertainties in the error bar, which are used as correction factors to simulation in the analysis. In (b) the reconstruction efficiency, depending on p_{T} and integrated over $0.1 < |\eta| < 2.5$, is illustrated for CB muons of Chain1 for different validation samples. The errors of the ratio of data divided by simulation includes statistical only (green) and statistical+systematic uncertainties (yellow) [113].*

4.4.3. Momentum Scale and Resolution

Since the estimated detector geometries and the material distributions, which are used in the detector simulation (Section 3.4.6), are not perfectly aligned, corrections of the momentum scale and resolution as function of p_{T}, η and ϕ are applied to further improve the modeling of simulated events. The determination and validation of the momentum scale and resolution corrections, including its uncertainties, is based on binned likelihood fits to di-muon invariant mass distributions in $Z \to \mu^+\mu^-$, $J/\Psi \to \mu^+\mu^-$ and $\Upsilon \to \mu^+\mu^-$ events [113]. The ID scale correction is less than 0.1% with an uncertainty of 0.02% in the central region and 0.2% for more forward regions. Concerning the MS momentum scale, the correction is below 0.1% over a wide range in η and increases to approximately 1% for low p_{T} muons. The momentum resolution needs to be smeared by a factor of 10% and 15% for simulated ID and MS tracks. Figure 4.6 shows the significant improvement of the resonance line shapes of simulated events for the different validation samples, after correcting the momentum scale and resolution.

4.5. Jets

Single final state partons, quarks and gluons, cannot be observed directly. Colorless hadrons are formed instead, due to long distance parton showering (see section 3.4.2) and subsequent hadronization (see section 3.4.3). With increasing momentum of the

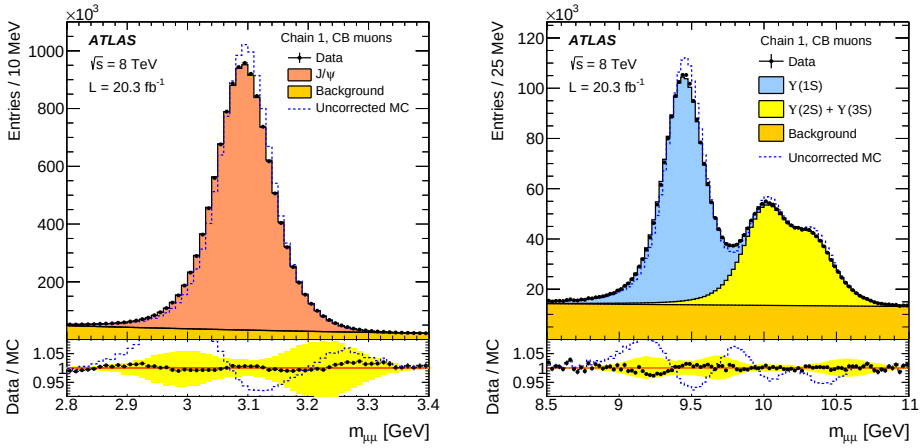

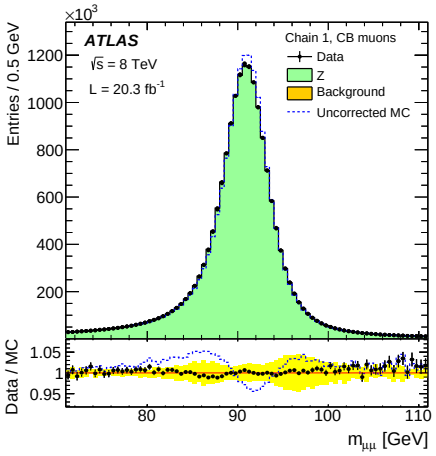

Figure 4.6. *Di-muon invariant mass in $J/\Psi \to \mu^+\mu^-$ (a), $\Upsilon \to \mu^+\mu^-$ (b) and $Z \to \mu^+\mu^-$ (c) events, selecting combined muons. The black points represent data and the colored histograms the expected signal and background contribution from simulation. The dashed line indicates simulated events without applying the momentum scale and resolution corrections. The lower panel shows the ratio of data divided by simulation. The yellow band reflects the systematic uncertainties on the corrections [113].*

primary quark or gluon, the outgoing hadrons are more and more colimated within a certain cone, which can be detected in terms of energy clusters in the ATLAS calorimeters. Such bundles of hadrons are referred to as *jets* and provide information about the underlying short distance physics. It is important to define these jet observables in a such a way, that predicted theoretical cross sections at parton level can still be measured precisely and that the non-perturbative effects of long distance physics are minimized. Therefore sophisticated jet reconstruction algorithms have been developed, which have to satisfy certain requirements. First, the algorithm needs to be infrared and collinear safe (ICR), meaning that the reconstruction of a

jet must not depend on soft or collinear gluon radiation. The jet energy for example must not change, if the primary quark radiates collinear or soft gluons. An ICR safe algorithm should rather absorb such gluons within the reconstructed jet. Second, the reconstruction algorithm has to be invariant under a boost along the beam axis in case of hadron-hadron collisions. Therefore the transverse momentum p_T, the azimuthal angle ϕ or the pseudo-rapidity η have to be used as ingredients of the algorithm. And third, effects from the underlying event (UE) 3.4.4 should not influence the jet reconstruction. In hadron-hadron collisions, only a small fraction of the incoming partons take part in the hard scattering, which is typically related to jets with high momenta. Most of the partons interact softly and form jets, which are close to the beam axis. This geometrical characteristic can be used to minimize UE effects. In the following sections, the jet reconstruction algorithm and the corresponding jet energy calibration, which are actually used in the analysis, are presented. Jet related quantities are very important observables for the analysis, because jets are part of the final state topology of signal events, especially with respect to the Higgs boson production in VBF mode (see section 2.2.1).

4.5.1. Topological Clusters

The jet reconstruction starts from *topological clusters* (topo-clusters), which are reconstructed in the calorimeters [115, 116]. The topological clustering makes use of the fine segmentation of the calorimeters and is able to dissolve the shower topology by adding neighboring cells subsequently, starting from a single cell as seed. The seed cell is required to exceed a certain absolute energy signal with a signal-over-noise threshold of $S/N = 4$. Neighboring cells are iteratively added to the seed to form a cluster, if they reach a signal-over-noise threshold of at least $S/N = 2$. In a final step, all cells in the neighborhood of the growing cluster are included in addition. The total noise in the cells consists of electronic noise and a contribution due to pile-up effects, which is estimated from simulation. Figure 4.7 shows a significant impact of the average number of pile-up interactions μ on the calorimeter noise per cell as a function of $|\eta|$. The topo-cluster algorithm achieves an efficient calorimeter noise suppression, which is crucial for data taking in 2012 with $\langle\mu\rangle = 20.7$. Furthermore, it includes a splitting step, which attempts to separate showers of close-by particles by searching for local energy maxima in cells above a threshold of 500 MeV. Its energy is defined as the sum of energy deposits in all cells within the cluster and the direction as the energy weighted average of the cell corresponding azimuthal angles and pseudorapidities. Each topo-cluster is assigned a four-momentum based on its energy and direction measurement, assuming zero mass.

4.5.2. Energy Calibration

Topo-clusters can be calibrated on the electromagnetic (EM) scale or via the *local cell signal weighting* (LCW) method [116]. The EM scale [117–125] provides an energy

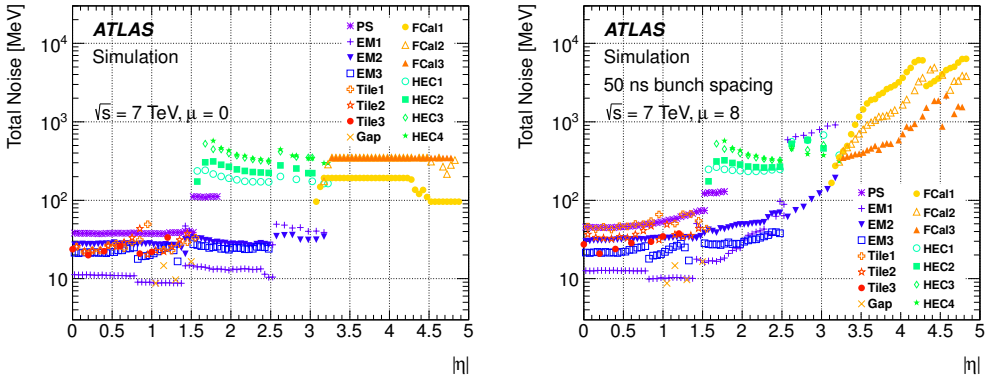

(a) (b)

Figure 4.7. *Cell noise on the EM scale as a function of $|\eta|$ for data conditions in 2010 and 2011 with an average number of pile-up interactions of $\mu = 0$ and $\mu = 8$ respectively. The colors indicate the different parts of the ATLAS calorimeters [116].*

measurement in the calorimeters, assuming that the shower is of electromagnetic origin, whereas the LCW scale considers also hadronic contributions. The LCW scale provides an appropriate cluster-by-cluster energy calibration and improves the cluster resolution, by adding information about the cluster structure. The LCW scale is the preferred calibration in the analysis. In the LCW calibration procedure, topo-clusters are classified as originating from either electromagnetic or hadronic showers, based on the energy density and longitudinal shower depths of the clusters. This procedure takes the non-compensation of the calorimeters into account [6]. In addition, corrections are applied, which account for the energy loss in inactive detector regions and for the loss of signal below certain noise thresholds during the clustering [126]. The LCW calibration and correction factors depend on the cell location and cluster properties and are determined via simulation of neutral and charged pions.

4.5.3. Reconstruction

Jets are reconstructed with topo-clusters as input, using the *anti-k_t* algorithm [127], which is implemented within the FASTJET software package [128, 129]. The following distances, used by the algorithm, need to be defined: the distance d_{ij} between clusters i and j and the distance d_{iB} between cluster i and the beam B with

$$d_{iB} = k_{ti}^{2p}, \tag{4.1}$$

$$d_{ij} = min(k_{ti}^{2p}, k_{tj}^{2p}) \frac{\Delta_{ij}^2}{R^2} \tag{4.2}$$

[6] All ATLAS Calorimeters are non-compensating, which means that electromagnetic interacting particles e and hadronic particles h with the same kinematic energy deposit a different amount of energy in the calorimeters such that the response ratio is $\frac{h}{e} < 1$.

where $\Delta_{ij}^2 = (y_i - y_j)^2 + (\phi_i - \phi_j)^2$ and k_{ti} is the transverse momentum, y_i the rapidity and ϕ_i the azimuthal angle of cluster i. R is called *distance parameter* and p regulates the relative power of the energy versus geometrical scales. The jet reconstruction is based on the identification of the smallest distance d_{ij} or d_{iB}. If $d_{ij} < d_{iB}$, then two clusters i and j are combined by adding the individual cluster momenta. This iterative process stops, if the requirement $d_{iB} < d_{ij}$ is fulfilled. Then, i is called jet and removed from the list of all jet reconstruction input clusters. For the anti-k_t algorithm, p is set to -1, which means that clusters from soft particles tend to be combined with clusters from harder ones. This approach provides circular jet shapes with radius R in the case of hard jets and more complex shapes for softer jets. In the analysis, a distance parameter of $R = 0.4$ is chosen. This jet reconstruction algorithm can be applied to simulated particles (truth jets), to ID tracks (track jets) and to energy deposits in the calorimeter (calorimeter jets), which are used in the present analyses.

Besides the energy calibration at cluster level (EM or LCW), further calibration corrections are applied to calorimeter jets to ensure that reconstructed energies correspond to that of the stable parton energy [116]. The corrections account for pile-up effects by subtracting an energy offset, depending on the number of reconstructed primary vertices N_{PV} and the expected number of pile-up interactions μ in bins of p_T and η. Figure 4.8 (a) shows the pile-up dependence of the calorimeter jet p_T as function of the number of vertices for various track jet $p_T^{\text{track jet}}$ working points. Furthermore, differences in the energy and pseudorapidity of calorimeter jets in comparison to truth jets are taken into account. Figure 4.8 (b) and (c) shows the average energy response $R^{\mathrm{EM/LCW}} = E_{\mathrm{jet}}^{\mathrm{EM/LCW}} / E_{\mathrm{jet}}^{\mathrm{truth}}$ for different jet energies as function of $|\eta_{\mathrm{jet}}|$ at EM and LCW scale. The energy corrections are smaller for high jet energies and depend strongly on the detector region. In addition, the direction of each calorimeter jet is adjusted in a way, that it points back to the reconstructed primary vertex instead of the detector origin.

The overall performance of the jet response can be improved significantly by using the LCW instead of EM scale. The corresponding corrections are determined mainly from simulation. Differences between reconstructed jets in data and simulated events are estimated from in situ transverse momentum balance techniques between the jets and corresponding reference objects, such as Z-bosons, photons or multiple jet systems (see [116]). The combined data-simulation correction factors are shown in figure 4.8 (d). The jet energy resolution (JER), which is measured directly from data, is comparable to the resolution in simulated events. Residual effects are well below 10% and therefore introduced as systematic uncertainty in terms of a smearing factor, depending on the p_T of the jet.

The total jet energy scale uncertainty as function of p_T is illustrated in figure 4.9. It is composed of uncertainties, stemming from the in situ and pile-up corrections, close-by jets and the jet response dependencies on flavour compositions. The uncertainties are about 2% in the barrel region and increase to 6% in the end-cap region for low p_T jets. They are smaller for jets with higher p_T.

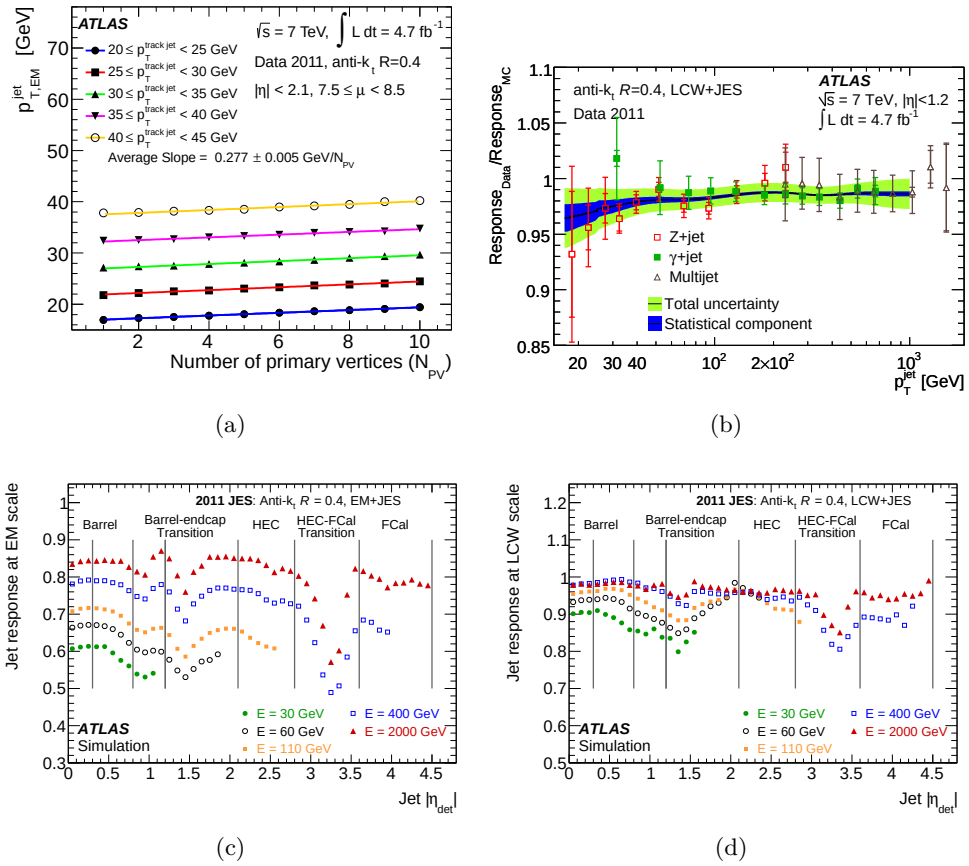

Figure 4.8. *Transverse momentum of anti-k_t calorimeter jets with $R = 0.4$, measured in data in bins of track-jet p_T as a function of the number of primary vertices (a). Ratio of average jet response, measured in data and simulation, for jets within $\eta < 1.2$ as a function of p_T for the different in situ techniques for anti-k_t jets with $R = 0.4$ (b). Average response of reconstructed jets from simulation for EM (c) and LCW (d) calibration, including corrections, as function of η for different jet energies [116].*

In the region of $|\eta| < 2.4$, ID tracks can be associated to calorimeter jets. The pile-up discriminating variable *Jet-Vertex Fraction* (JVF) [130] is introduced as

$$\mathrm{JVF}(\mathrm{jet}_i, \mathrm{vtx}_j) = \frac{\sum_m p_T^{\mathrm{trk},m}(\mathrm{jet}_i, \mathrm{vtx}_j)}{\sum_k \sum_l p_T^{\mathrm{trk},l}(\mathrm{jet}_i, \mathrm{vtx}_k)}, \tag{4.3}$$

giving the fraction of the scalar sum of transverse momenta p_T^{trk} of tracks, matched to jet i and to the primary vertex (vtx) j, divided by the total scalar sum of p_T^{trk} of tracks, matched to jet i and originating from all reconstructed vertices. Pile-up tracks do typically not originate from the primary vertex and therefore JVF reflects the probability of pile-up like contributions to the calorimeter jets. A cut on JVF< 0.5 is used in the analysis for low p_T jets with $p_T < 50$ GeVand $|\eta| < 2.4$ to suppress jets stemming from pile-up.

To differentiate between jets from the hard scattering process and those from beam-

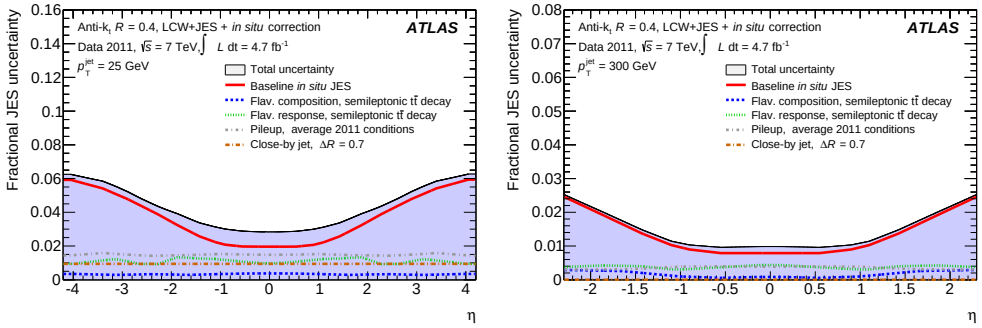

(a) (b)

Figure 4.9. *Fractional jet energy scale uncertainties for anti-k_t jets with $R = 0.4$ and LCW scale, including corrections, as function of η for low p_T (a) and high p_T (b) jets. Several uncertainties are sample dependent and are included for semi-leptonic top quark decays, using pile-up conditions from 2011 [116].*

induced backgrounds (beam-gas or beam-halo), cosmic muons or calorimeter noise, different jet quality selection criteria are provided [131], which result in various levels of jet selection efficiencies and rejection efficiencies of misidentified jets, so called fake jets such as reconstructed jets from underlying photons. These selection criteria are mainly based on variables, which depend on energy fractions in different calorimeter parts. In the analysis, the *Looser* criteria are used. Figure 4.10 shows the efficiencies for several criteria in specific detector regions. The efficiencies are measured in di-jet events, using a tag-and-probe method [126]. For the very loose selection criterion, the jet selection efficiency is above 99.8% in all η and p_T ranges for jet $p_T > 20$ GeV. Differences between data and simulation are well within 1%.

4.5.4. b-Tagging

In the analysis, the signal process from VBF Higgs production mode is not expected to produce jets, originating from b quarks (b jets). Processes including b jets typically include top quarks, which decay in almost all cases into bottom quarks due to the CKM matrix element $V_{tb} \approx 1$. Therefore background processes such as top quark production, which include b jets in the final state, can be reduced by vetoing events with b jets. In this section, the b-tagging algorithm MV1 [132] is introduced, which allows for the discrimination between b jets and light flavoured jets. The MV1 algorithm is chosen in the analysis.

The MV1 b-tagging algorithm combines three independent algorithms IP3D, SV1 and JetFitter [133], using an artificial neural network, which is trained with b jets as signal and light flavour jets as background. IP3D uses information from track impact parameters. The lifetime of hadrons containing b quarks is sufficiently large, so that they can travel a certain distance, before they decay inside the detector. Therefore a displaced secondary vertex can be observed and the impact parameters

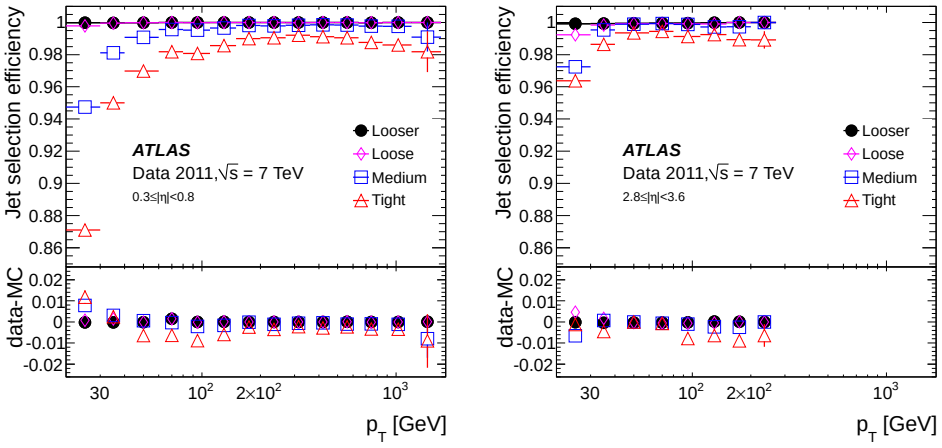

(a) (b)

Figure 4.10. *Jet quality selection efficiencies for anti-k_t jets with $R = 0.4$ as function of p_T in a central region $0.3 \leq |\eta| < 0.8$ (a) and a more forward region $2.8 \leq |\eta| < 3.6$ (b) for the different selection criteria [116]. The black points correspond to the very loose criterion, which is chosen in the analysis.*

of the corresponding b jets are expected to be larger, compared to light quark jets, which originate directly from the primary vertex. The IP3D algorithm uses a likelihood ratio approach, comparing two-dimensional input histograms of signed transverse and longitudinal impact parameter significances d_0/σ_{d_0} and z_0/σ_{z_0} with pre-defined distributions of b quark and light quark hypotheses. Also SV1 employs a likelihood ratio technique. However, it uses secondary vertex properties such as the number of two-track vertices associated to the jet, the invariant mass of the secondary vertex and the ratio of the sum of energies of jet tracks associated to the secondary vertex and all tracks of the jet. JetFitter tries to resolve a flight path of the b hadron and is capable to dissolve b and c hadron vertices. This approach is based on a likelihood approach as well and uses similar input variables than SV1 plus additional variables, such as the flight length significances.

Combining all three algorithms, MV1 provides a powerful discriminator in terms of a tag weight for each jet, which reflects the probability of b or light quarks as jet origin. An operating point, which corresponds to an overall b jet efficiency ϵ_b of 70%, is chosen. Figure 4.11 displays the MV1 b jet efficiencies as function of jet p_T, measured in semi-leptonic top quarkevents [134], and the corresponding correction factors, accounting for residual data-simulation differences. The corrections factors range from 0.965 to 1.008, depending on jet p_T, with a total uncertainty between 1.8% and 8.4%. The main systematic uncertainties stem from the modeling in simulation such as the hadronization model, the underlying PDFs or parton showering, which is introduced in section 3.4. The misidentification rate, to tag light quark jets as b jets, is measured in an inclusive jet sample and ranges from 0.5% to 2.5% depending on jet p_T and η for the chosen working point of $\epsilon_b = 70\%$ [132]. Its correction factors vary from 1.12 to 1.53 with total uncertainties between 15% and 43%.

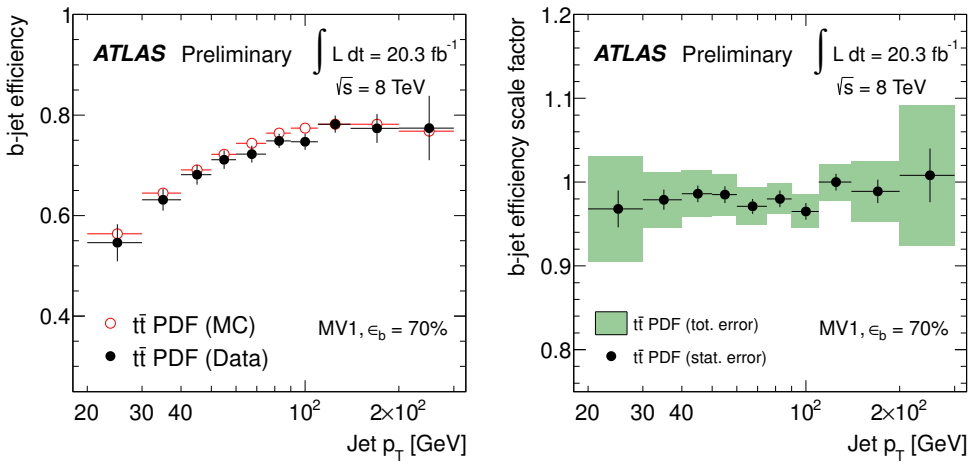

(a) (b)

Figure 4.11. *The b-tag efficiencies (a) and the corresponding corrections scale factors (b) as function of jet p_T for anti-k_t jets with $R = 0.4$ at EM scale, measured in semi-leptonic top quarkevents for an MV1 operating point of 70% b-tag efficiency [134].*

4.6. Tau Leptons

τ leptons can either decay hadronically or leptonically into an electron or muon and corresponding neutrinos. The branching ratio of the τ lepton decay into lighter leptons is approximately 35%. Due to the mass of 1.777 GeV and a proper decay length of 87 μm, τ leptons decay before reaching active detector material. Hadronic decay modes have a branching ratio of 65%, in which 72% (22%) of all cases contain one (three) charged pions, called *one (three) prong* decays. In most remaining cases, the decay products consist of charged Kaons. 78% of these hadronic decay modes include up to one neutral pion in addition.

Such hadronically decaying τ leptons are reconstructed as jets in the calorimeters. The anti-k_t algorithm with $R = 0.4$ at LCW scale provides seeds for candidates in the τ reconstruction algorithm. Background contributions, which can be misidentified as hadronically decaying τ leptons, stem from quark or gluon jets. Electrons can also appear in one prong decays as they are typically reconstructed with one track. The τ identification makes therefore use of shower shapes, charged particle track information and displaced vertex properties. Several variables are combined in terms of Boosted Decision Trees, which are also used in the analysis and introduced in section 5.6, as identification algorithm to reject jets and other charged leptons. It is important to achieve a reasonably good energy resolution and small energy scale uncertainties in case of resonance measurements such as $Z/\gamma^* \to \tau^+\tau^-$. Also a precise measurement of the hadronically decaying τ lepton identification efficiencies is of much interest in case of searches such as the $H \to \tau^+\tau^-$ analysis. Since the hadronic decay channels $H \to \tau_{\text{lep}}\tau_{\text{had}}$ and $H \to \tau_{\text{had}}\tau_{\text{had}}$ are not the main subject of this thesis, the reader is referred to the description of the τ reconstruction and

identification in [135]. The fully leptonic decay channel $H \to \tau^+\tau^- \to \ell^+\ell^- 4\nu$ vetoes hadronic τ lepton decays based on the *medium* working point for identification efficiency.

4.7. Missing Transverse Momentum

Non-interacting particles such as neutrinos (true missing energy) or particles, that are not detected due low reconstruction efficiencies, underestimated energy scales or PU and UE effects (fake missing energy), contribute to the total missing energy in events. In proton-proton collisions, the exact momentum of the incoming partons within the protons is unknown and the full missing energy four-vector cannot be reconstructed. Hence, the missing transverse momentum four-vector $\mathbf{E}_T^{\text{miss}}$ is defined as the negative transverse four-vector sum of all detected objects, which reflects the momentum imbalance in the event and which is invariant under boost along the beam axis. The scalar energy component is denoted as $E_T^{\text{miss}} = \sqrt{(p_x^{\text{miss}})^2 + (p_y^{\text{miss}})^2}$. In the leptonic decay $H \to \tau^+\tau^- \to l^+l^- 4\nu$, four final state neutrinos are expected, that leads to a significant amount of $\mathbf{E}_T^{\text{miss}}$. In this section, the reconstruction of $\mathbf{E}_T^{\text{miss}}$ and corresponding pile-up suppression methods are explained, which is particularly important for the high pile-up conditions in 2012.

4.7.1. Reconstruction

All reconstructed and calibrated physics objects contribute in the $\mathbf{E}_T^{\text{miss}}$ calculation [136]

$$\mathbf{E}_T^{\text{miss}} = \mathbf{E}_T^{\text{miss},e} + \mathbf{E}_T^{\text{miss},\gamma} + \mathbf{E}_T^{\text{miss},\tau} + \mathbf{E}_T^{\text{miss,jet}} + \mathbf{E}_T^{\text{miss,soft}} + \mathbf{E}_T^{\text{miss},\mu}, \tag{4.4}$$

where $\mathbf{E}_T^{\text{miss,type}} = -\sum \mathbf{p}_T^{\text{type}}$ for a given object type (electrons e, photons γ, τ leptons, jets, soft objects and muons μ).

$\mathbf{E}_T^{\text{miss},e}$, $\mathbf{E}_T^{\text{miss},\gamma}$, $\mathbf{E}_T^{\text{miss},\tau}$ are calculated from calorimeter clusters, associated to calibrated electrons (Section 4.3), photons at the EM scale and τ jets at LCW scale (Section 4.6). The $\mathbf{E}_T^{\text{miss,jet}}$ term includes pile-up corrected anti-k_t LCW jets with $R = 0.4$ and $p_T > 20$ GeV(Section 4.5). The soft $\mathbf{E}_T^{\text{miss,soft}}$ term contains tracks and noise suppressed topo-clusters (Section 4.5.1), which are not associated to any of the high-p_T objects from above. The overlap of topo-cluster and track contributions is removed. In addition, the parametrized energy loss in the calorimeters of combined muons is subtracted from the soft term, to avoid a double counting of the muon energy. $\mathbf{E}_T^{\text{miss},\mu}$ contains energy contributions from combined and ST muons (Section 4.4).

4.7.2. Pile-Up Suppression

Pile-up effects have a significant impact on $\mathbf{E}_T^{\text{miss}}$. Therefore pile-up suppression requirements are applied to restore the $\mathbf{E}_T^{\text{miss}}$ response and resolution to values similar to conditions obtained in the absence of pile-up [137]. The jet and soft term contribution are particularly affected by pile-up, since they mainly stem from hadronic energy deposits. Reconstructed jets with $p_T > 20$ GeV have already been pile-up corrected during calibration.

Two pile-up suppression methods are provided to correct the soft term $\mathbf{E}_T^{\text{miss,soft}}$. The first approach is based on the event transverse momentum density and the corresponding jet area, which is similar to pile-up corrections during jet reconstruction. In this analysis, a second approach is employed, which is based on the *soft term vertex fraction* (STVF). It is defined as the fraction of tracks matched to the soft term contribution and associated to the primary vertex compared to all tracks matched to the soft term

$$\text{STVF} = \sum_{i}^{N_{\text{trk soft}}^{\text{PV}}} p_{T,i}^{\text{trk soft,PV}} \Big/ \sum_{k}^{N_{\text{vtx}}} \sum_{j}^{N_{\text{trk soft}}^{\text{k}}} p_{T,j}^{\text{trk soft,k}}, \tag{4.5}$$

where PV denotes the primary vertex, N_{vtx} the number of vertices, $p_T^{\text{trk soft, vertex}}$ the transverse momentum of a soft term track and $N_{\text{trk soft}}^{\text{vertex}}$ the number of soft term tracks, associated to a specific vertex. The soft term $\mathbf{E}_T^{\text{miss,soft}}$ is finally scaled by this STVF correction factor, which reflects the degree of pile-up in each event. Figure 4.12 shows the $\mathbf{E}_T^{\text{miss}}$ resolution as a function of the total sum of transverse energy $\sum E_T$ per event, measured in simulated $H \to \tau^+\tau^-$ events. An improvement of the resolution is observed by applying STVF pile-up suppression. Compared to simulated events from the $Z/\gamma^* \to \ell^+\ell^-$ decay, the improvement in $H \to \tau^+\tau^-$ events is smaller because of a higher jet multiplicity, where the jet term dominates the soft term. In figure 4.13, the STVF $\mathbf{E}_T^{\text{miss}}$ linearity, defined as the mean value of $(E_T^{\text{miss}} - E_T^{\text{miss,truth}})/E_T^{\text{miss,truth}}$, shows a positive bias for small values of E_T^{miss}, due to limitations in the resolution measurements, and a negative bias of about 5% at higher E_T^{miss} values. In case of signal events from VBF Higgs boson production, the linearity is even improved.

Uncertainties, related to the $\mathbf{E}_T^{\text{miss}}$ reconstruction, depend on the various physics objects, which are used to build the final $\mathbf{E}_T^{\text{miss}}$ term. For this reason, all individual systematic variations are propagated and combined in the $\mathbf{E}_T^{\text{miss}}$ calculation. In addition, systematic uncertainties on the resolution and the scale of the soft term $\mathbf{E}_T^{\text{miss,soft}}$ are evaluated, which stem from the modeling of simulated event and pile-up effects. The uncertainties are derived from data and simulation comparisons, using $Z \to \mu^+\mu^-$ events without final state jets. The scale and resolution uncertainty of $\mathbf{E}_T^{\text{miss,soft}}$ are measured to be 7.9% and 4.8% respectively in the STVF approach [136].

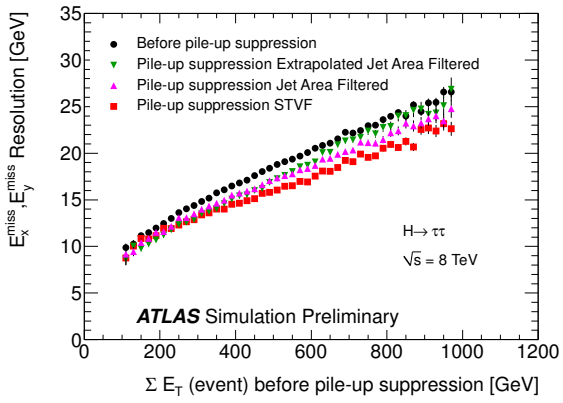

(a)

Figure 4.12. $\mathbf{E}_T^{miss}$ *resolution as function of total transverse energy in the event (summing* p_T *of muons and total transverse energy in the calorimeter), determined in simulated* $H \to \tau^+\tau^-$ *events. The resolution is shown before and after pile-up suppression for jet area and STVF based methods [136].*

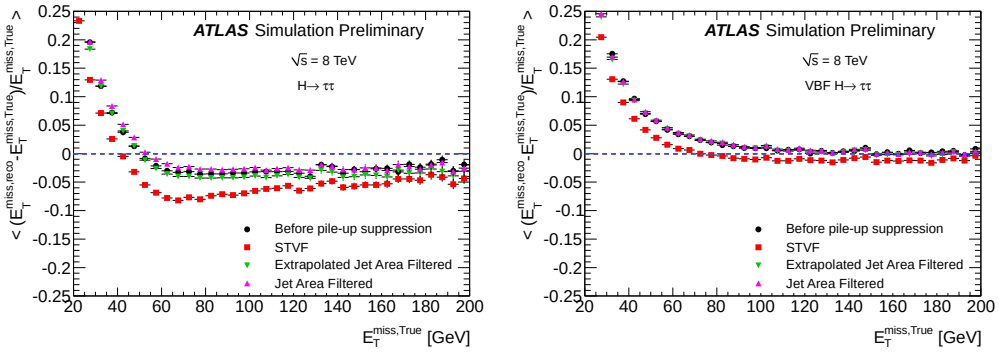

(a) (b)

Figure 4.13. $\mathbf{E}_T^{\text{miss}}$ *linearity as function of the true missing transverse momentum* $E_T^{miss,truth}$ *measured in* $H \to \tau^+\tau^-$ *events (a) including all Higgs boson production modes and* $H \to \tau^+\tau^-$ *events from VBF Higgs boson production mode only(b) [136].*

5 Search for the Higgs Boson in $H \to \tau^+\tau^- \to \ell^+\ell^- 4\nu$ Decays

The discovery of the Higgs boson by the ATLAS and CMS collaborations in 2012 has proven that the new particle with the mass of approximately 125 GeV couples to vector bosons. The Standard Model additionally predicts Higgs boson couplings also to fermions. The search for the Higgs boson in the decay mode $H \to \tau^+\tau^-$ is a key analysis for confirming these fermion couplings due to the corresponding large branching ratio predicted by the Standard Model. This chapter describes the analysis of the search for the Standard Model Higgs boson in the fully leptonic final state $H \to \tau^+\tau^- \to \ell^+\ell^- 4\nu$. This specific final state provides a clean signature in the detector. The signal topology is characterized by two reconstructed leptons, electrons or muons, with opposite charge, jets and a significant amount of transverse missing energy due to the four final state neutrinos, which appear in the τ lepton decays. The reconstruction and identification algorithms to select such objects are discussed in detail in chapter 4. The analysis is based on basic event selection and signal topology specific categorization criteria and applies multivariate data analysis techniques. The full 8 TeV dataset with an amount of $\int \mathcal{L}dt = 20.3$ fb^{-1} is used, which has been recorded in 2012 with the ATLAS detector. The first two sections 5.1 and 5.2 provide an overview of the relevant signal and background processes in the analysis. Section 5.3 presents the event selection in order to enhance the signal-to-background ratio and to suppress background events, which mimic the signal final state topology. In section 5.4, the analysis categories (VBF and Boosted category) are defined, which are applied in addition to the event selection to separate signal events from different Higgs boson production processes and to enhance the sensitivity. Section 5.5 deals with methods to reconstruct the invariant mass of the Higgs boson, using information from its decay products. The reconstructed mass of the Higgs boson candidate is an important variable to separate the different signal and background components. Section 5.6 is dedicated to Boosted Decision Trees (BDTs), which are used in the analysis to combine several background discriminating variables into a single one-dimensional variable. The BDT classifier achieves a powerful separation between signal and background events. The results of the analysis are presented in section 10.1.

5.1. Signal Processes

The different Higgs boson production modes in the Standard Model have been introduced in section 2.2. In figure 5.1(a-c), examples of leading-order diagrams of the different productions modes are illustrated: gluon fusion (GGF), vector-boson fusion (VBF) and vector boson associated[1] (VH) production. The subsequent decay of the Higgs boson into τ leptons is also shown. The Standard Model branching ratio $\mathcal{B}$ of the Higgs boson decay into two τ leptons is 6.32 % with a relative uncertainty of $+5.71\%/-5.67\%$, assuming a Higgs boson mass of 125 GeV [138]. Figure 5.1(d) shows the Born level diagram of a leptonic τ lepton decay into an electron or a muon, and neutrinos. The branching ratio for this is 35.24% [13]. Thus, the branching ratio of the fully leptonic di-τ decay is 12.42%. Higgs boson decays into vector bosons are treated as background as mentioned in section 5.2.1. Table 5.1 summarizes the event generators and the predictions of the cross section times branching ratio ($\sigma \times \mathcal{B}$) at 8 TeV, which have been used for simulating and normalising the signal samples. All cross sections are quoted for $\sqrt{s} = 8$ TeV conditions at the LHC. In the present analysis, a Higgs boson mass of 125 GeV is assumed. Theoretical uncertainties on cross sections and differential distributions are discussed in chapter 8.

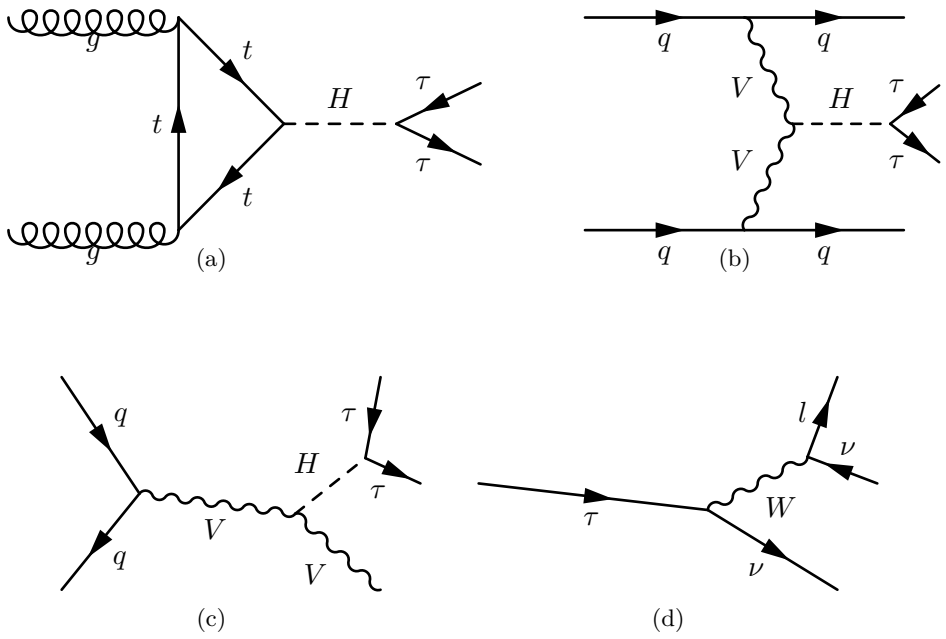

Figure 5.1. *Examples of tree-level diagrams for the relevant signal processes in the analysis of the search for $H \to \tau^+\tau^- \to \ell^+\ell^- 4\nu$: Gluon fusion (a), vector-boson fusion (b) and vector boson associated (c) Higgs boson production, including the subsequent decay into τ leptons. The leptonic decay of the τ lepton at tree-level is shown in (d), where $l = e, \mu$.*

[1]The vector boson associated Higgs boson production is usually referred to as *Higgs Strahlung*.

Signal $m_H = 125$ GeV	$\sigma \times \mathcal{B}$ [pb] at $\sqrt{s} = 8$ TeV			Event Generator
GGF $H \to \tau^+\tau^-$	1.22	NNLO+NNLL	[138–147]	Powheg [97] + Pythia8 [81, 148]
VBF $H \to \tau^+\tau^-$	0.10	(N)NLO	[138, 149–151]	Powheg + Pythia8
W $H \to \tau^+\tau^-$	0.0445	NNLO	[138, 152, 153]	Pythia8
Z $H \to \tau^+\tau^-$	0.0262	NNLO	[138, 152, 153]	Pythia8
Background				
$Z/\gamma^* \to \tau^+\tau^-$	5500	NNLO	[154, 155]	Alpgen [95] + Pythia8/Herwig [94]
$Z/\gamma^* \to e^+e^-$	5500	NNLO	[154, 155]	Alpgen + Pythia8/Herwig
$Z/\gamma^* \to \mu^+\mu^-$	5500	NNLO	[154, 155]	Alpgen + Pythia8/Herwig
VBF $Z/\gamma^* \to \ell^+\ell^-$	1.1	LO	[82]	Sherpa [82]
$q\bar{q} \to WW$	54	NLO	[156]	Alpgen + Herwig
$gg \to WW$	1.4	NLO	[157]	GG2WW [157] + Herwig
$WZ/\gamma*$, $Z/\gamma * Z/\gamma*$	30	NLO	[156]	Herwig
$H \to W^+W^-$	4.7	equivalent to $H \to \tau^+\tau^-$		equivalent to $H \to \tau^+\tau^-$
$t\bar{t}$	253	NNLO+NNLL	[158–163]	Powheg + Pythia8
Single top (s-channel)	5.6	NNLO	[164]	Powheg + Pythia8
Single top (t-channel)	87.8	NNLO	[165]	AcerMC [96] + Pythia6 [81]
Single top (Wt)	22	NNLO	[166]	Powheg + Pythia8
$W \to \ell\nu$ ($\ell = e, \mu, \tau$)	36900	NNLO	[154, 155]	Alpgen + Pythia8

Table 5.1. *Signal and background processes, which are considered in the analysis. Cross section predictions are quoted for $\sqrt{s} = 8$ TeV, including the order of perturbative QCD calculation. In addition, the event generators are specified, which have been used for simulating events. For the signal processes, Standard Model Higgs boson production is assumed. The kinematics of $Z/\gamma^* \to \tau^+\tau^-$ are estimated in a data-driven way, however the normalisation is taken from simulation. Background sources, including misidentified leptons (e.g. events from single top quark production, $W \to \ell\nu$ and QCD multi-jet), are based on data-driven methods too and the corresponding simulated events are used for cross checks at best. QCD multi-jet events are not simulated and information about the corresponding production and its measurement at the LHC can be found in [167, 168].*

5.1.1. Gluon Fusion Higgs Boson Production

The GGF Higgs boson production cross section is already proportional to α_s^2 at leading-order (LO) due to the heavy quark loop. QCD radiative corrections increase the GGF cross section significantly and are therefore essential for Higgs boson searches at the LHC. The state of the art cross section prediction for GGF has been calculated at fixed next-to-next-to-leading order (NNLO) plus next-to-next-to-leading logarithmic (NNLL) accuracy for soft-gluon contributions [139–145]. Next-to-leading order (NLO) electroweak (EW) corrections are included as well [146, 147]. The total GGF Higgs production cross section calculation results in 19.27 pb with relative uncertainties of $+7.2\%/-7.8$ % due to renormalisation and factorization scale variations [138]. Parton distribution function (PDF) and α_s uncertainties are about $+7.5\%/-6.9\%$. In addition, the p_T spectrum of the Higgs boson, produced in the GGF mode, is corrected by re-weighting the simulated events [8], based on NNLO and NNLL calculations by HRES2.1 [169]. The GGF mode is the dominant Higgs boson production process at the LHC. GGF Higgs boson events are simulated with Powheg [97] at NLO QCD, which is interfaced to Pythia8 [81, 148] for subsequent parton shower, hadronization and underlying event effects as explained in section 3.4.5. The CT10 [88] set is chosen as the PDF for the Powheg generator.

5.1.2. Vector-boson fusion Higgs Boson Production

Although its production cross section is more than one order of magnitude smaller than in the GGF mode, Higgs boson production via VBF plays an important role at the LHC, since the topology of VBF-like processes is quite unique. Due to the EW coupling of the incoming quarks to the vector bosons, there is no color exchange between the partons, which results in two well separated jets with high transverse momenta in forward direction and low hadronic activity in the central part of the detector. Such characteristics can be utilized to tag VBF-like events and thus enhance signal by applying a specific set of VBF cuts, which will be explained in section 5.3. The VBF cross section is calculated at the level of full NLO QCD and EW corrections [149–151]. An additional correction is applied, which accounts for NNLO QCD effects [170]. The total cross section for the production of a Higgs boson is 1.578 pb with relative uncertainties of $+0.2\%/-0.2$ % due to scale variations and $+2.6\%/-2.8$ %, reflecting PDF and α_s uncertainties. VBF Higgs boson events are simulated at NLO QCD with Powheg and Pythia8 using CT10 PDFs in an analogous manner as for GGF events. Since NLO EW corrections affect also the transverse momentum of the Higgs boson p_T^H, VBF signal events generated with Powheg plus Pythia are re-weighted accordingly based on comparisons of p_T^H with Hawk [171, 172], which takes EW corrections into account.

5.1.3. Vector Boson Associated Higgs Boson Production

The cross section for the VH production mode is calculated with NNLO accuracy in QCD [152], including NLO EW corrections [153]. Concerning W boson associated production, the total cross section amounts to 0.7046 pb with relative QCD scale and PDF plus α_s uncertainties of $\pm 1.0\%$ and $\pm 2.3\%$ respectively [138]. The cross section for the Z boson associated production mode is 0.4153 pb with relative uncertainties of $\pm 3.1\%$ for scale variations and $\pm 2.5\%$ due to PDF and α_s uncertainties [138]. VH processes are simulated at LO with Pythia8, using CTEQ6L1 [173] PDF sets. VH processes play a minor role in the analysis because of their relatively small production cross sections.

5.1.4. Top Quark Associated Higgs Boson Production

The top quark associated Higgs boson production (ttH) is neglected in the analysis due to the very small production cross section of 0.1293 pb with relative uncertainties of $+3.8\%/-9.3\,\%$ due to scale and $+8.1\%/-8.1\,\%$ due to PDF and α_s variations [138]. Furthermore, specific VBF selection criteria are applied in the analysis, which suppress events from the ttH mode per definition, as explained in section 5.3 and 5.4.

5.2. Background Processes

The relevant background processes with two final state leptons are the production of Z bosons with the subsequent decay into electrons, muons or τ leptons and di-boson processes, which include two vector bosons WW, WZ/γ^* or $Z/\gamma^*Z/\gamma^*$. In addition, the production of top quark pairs has to be considered. Events with at least one mis-identified (*fake*) lepton appear typically in QCD multi-jet, single top quark or W boson plus jets processes. Information about the corresponding cross section predictions and the event generation of background processes is summarized in table 5.1.

5.2.1. Z Boson and Di-Boson Production

The dominant background source includes events from the production of a Z/γ^* boson in association with jets, which decays into a pair of leptonically decaying τ leptons $Z/\gamma^* \to \tau^+\tau^- \to \ell^+\ell^- 4\nu$. An example of the production of a Z/γ^* boson in association with one additional jet is illustrated in figure 5.2(a). The decay $Z/\gamma^* \to \tau^+\tau^-$ is an irreducible background process because its final state topology is similar to the signal process. In the analysis, $Z/\gamma^* \to \tau^+\tau^-$ events are estimated in a data-driven way to reduce the dependency on simulation. The estimation procedure is referred to as the *Embedding* method and is based on the kinematic properties of the Z/γ^* boson in $Z/\gamma^* \to \mu^+\mu^-$ data events. $Z/\gamma^* \to \mu^+\mu^-$ events from data are

modified in a way, that the original muons are replaced by τ leptons, whose decay is simulated, using the Tauola [100] program. Tracks and calorimeter deposits of the muons are then removed from the original data event. The information about Z/γ^* boson kinematics, jets, pile-up, underlying event and detector noise in the final hybrid event is thus directly taken from data. The Embedding technique is justified by lepton universality and explained in section 7.1.

Further important background sources are $Z/\gamma^* \to e^+e^-$ and $Z/\gamma^* \to \mu^+\mu^-$. Two prompt isolated leptons with opposite electric charge mimic the same flavour decay modes of the fully leptonic $H \to \tau^+\tau^- \to \ell^+\ell^- 4\nu$ signal process. Nevertheless, these prompt decays are easier to suppress compared to $Z/\gamma^* \to \tau^+\tau^-$, as no neutrinos appear in the final state. The various $Z/\gamma^* \to \ell^+\ell^-$ samples have been simulated with Alpgen [95], including $Z/\gamma^* \to \tau^+\tau^-$ for cross-checking the Embedding approach (see section 7.1). The Alpgen program has been interfaced to Herwig [94] for parton shower, hadronization and underlying event in a low invariant di-lepton mass region ($10\ \text{GeV} < m_{\ell\ell} < 60\ \text{GeV}$) and to Pythia8 [148] in a high one ($60\ \text{GeV} < m_{\ell\ell} < 2\ \text{TeV}$). LO matrix elements for up to five partons and the MLM matching scheme [93] for matrix element and parton shower matching are used for generating events. CTEQ6L1 [173] is chosen as PDF parametrization. The inclusive cross section for the production and decay of $Z/\gamma^* \to \ell^+\ell^-$ (ℓ is e, μ or τ) in the range of $10\ \text{GeV} < m_{\ell\ell} < 2\ \text{TeV}$ is 5.50 nb, calculated at NNLO QCD level, with relative uncertainties of $\pm 1\%$ for QCD scales and $\pm 4\%$ for PDF and α_s uncertainties [154, 155, 174]. The cross section is used for normalising the individual simulated final state samples. No EW corrections are taken into account in the corresponding cross sections and the generated events for the background processes. However, since the VBF Higgs production mode is of particular importance for this analysis, additional Z/γ^* samples are used that include vector-boson fusion diagrams, as this processes represent an important background production mechanism that is not included in the standard Pythia8 background samples. These events are simulated with Sherpa [82] and the CT10 [88] PDF parametrization. The sample is normalised to the LO cross section of 1.1 pb [82].

A typical di-boson Feynman diagram is shown in figure 5.2 (b). Two prompt leptons in the final state from the leptonic decay of a Z/γ^* boson or two leptonically decaying W bosons in association with additional jets imitate the signal process ($WW \to \ell\nu\ell\nu$, $WZ/\gamma^* \to q\nu\ell\ell$ or $Z/\gamma^*Z/\gamma^* \to \ell\ell\ell qq$). The production of WZ/γ^* and $Z/\gamma^*Z/\gamma^*$ is simulated with Herwig and the corresponding samples are normalised to an inclusive NLO production cross section of 30 pb [156]. The quark induced production of $q\bar{q} \to WW$ is simulated with Alpgen and Herwig generating the parton shower. The sample is normalised to the NLO production cross section of 54 pb [156]. The cross section for the gluon induced production $gg \to WW$ is 1.4 pb at LO [157] and the events are generated with GG2WW [157] and Herwig at LO. In case of Herwig or Alpgen, the CTEQ6L1 [173] PDF parametrization is chosen, while CT10 is used for GG2W. The PDF plus α_s and QCD scale uncertainties for WZ/γ^*, $Z/\gamma * Z/\gamma^*$ and $q\bar{q} \to WW$ are estimated to be about $\pm 4\%$ and $\pm 5\%$ respectively, while the corresponding uncertainty for $gg \to WW$ is about $\pm 30\%$ [174].

The Higgs boson decay into two W bosons $H \to W^+W^- \to \ell^+\nu\ell^-\nu$ is considered as background in the analysis of the search for the Higgs boson. The same event generators are used as for the $H \to \tau^+\tau^-$ signal. The inclusive $H \to W^+W^-$ production cross section is 4.7 pb [138].

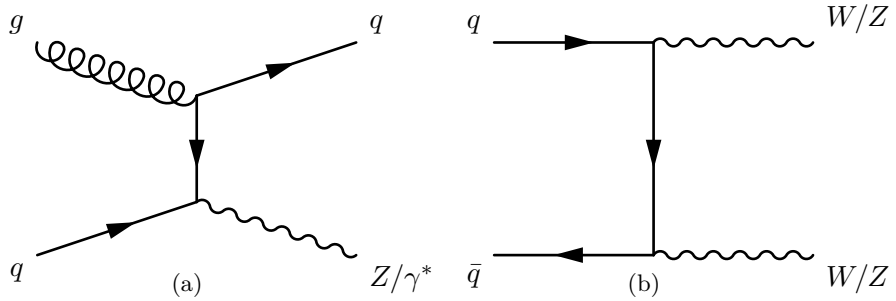

Figure 5.2. *Examples of diagrams for the production of a Z boson in association with a jet (a) and di-boson production (b).*

5.2.2. Top Quark Pair and Single Top Quark Production

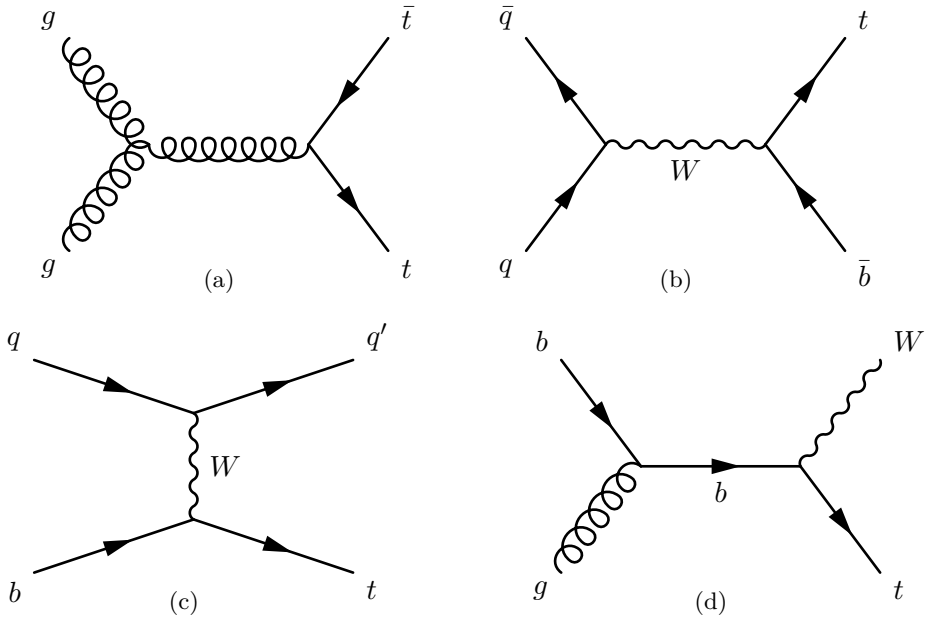

Figure 5.3. *Example diagrams of top quark pair production (a), the s-channel (b), t-channel (c) and W boson associated (d) production of a single top quark.*

Processes with top quarks are typically characterized by a larger number of jets in the final state. Due to the CKM matrix element $V_{tb} \approx 1$, top quarks decay preferably into bottom quarks, which implies the presence of b jets in top quark events. Figure 5.3 (a) shows an example diagram of top quark pair production. Both top quarks decay into a b quark and a W boson respectively, which can decay into a prompt lepton and neutrino ($t\bar{t} \to \ell\nu b\ell\nu b$). Such final state topologies of

top quark pair production contain two prompt leptons and a certain amount of $\mathbf{E}_T^{\text{miss}}$, which can mimic the signal process. In addition, semi-leptonic decays of b hadrons might contribute to the number of leptons in the final state. Top quark pair processes are simulated at NLO with Powheg [97], which has been interfaced to Pythia8 to model the parton shower, hadronization and underlying event. The PDFs are parametrized by CT10. The cross section of top quark pair production at the LHC is 253 pb and has been calculated at the level of NNLO and with NNLL accuracy for soft emissions [158–163]. The relative uncertainty due to QCD scale variations is ±6%. PDF and α_s uncertainties are ±8% [174].

Concerning single top quark production modes, the cross sections are 5.6 pb for the s-channel [164], 87.8 pb for the t-channel [165] and 22 pb for the production of a top quark in association with a W boson [166] at the level of NNLO. Figures 5.3 (b), (c) and (d) show examples of the different single top quark production modes. Events have been generated using Powheg plus Pythia8 for the s-channel and W associated single top quark pair production. The t-channel single top quark sample has been simulated with AcerMC [96] plus Pythia6 [81]. CTEQ6L1 is used for the PDF parametrization in case of AcerMC and CT10 in case of Powheg samples. Single top quark events can contain two prompt leptons such as the W boson associated process ($Wt \to l\nu bl\nu$).

5.2.3. Fake Leptons

Reconstructed jets might be misidentified as prompt final state (fake) leptons. The background category of fake leptons summarizes several processes, characterized by a larger jet multiplicity and at most one prompt true final state lepton, which mimic the signal topology. Such processes often have a relatively high cross section and are therefore not negligible in the analysis. Typical processes are the production of single top quarks, which contains one prompt and one fake final state lepton, and QCD multi-jet events with quarks or gluons, faking both leptons. Furthermore, events with top quark pairs, which result in less than two real leptons and additional jets ($t\bar{t} \to \ell\nu bqqb$), can contribute to the fake lepton background as well. The production of a leptonically decaying W boson in association with light quark jets are also a potential source of fake di-lepton events. Examples of QCD multi-jet and W boson plus jet processes are shown in figure 5.4(a) and (b).

Although the background of fake leptons is not negligible in the analysis of the fully leptonic decay channel $H \to \tau^+\tau^- \to \ell^+\ell^- 4\nu$, it is relatively small compared to other background sources due to the ability of the lepton identification algorithms and additional isolation requirements to effectively select true leptons with minimal contamination. Fake leptons due to misidentified jets tend to have a higher activity nearby the reconstructed track or calorimeter cluster and are suppressed significantly by applying isolation criteria. The dominant fraction of fake leptons arise from QCD multi-jet processes, since the corresponding cross section at the LHC exceeds those of other background sources by many orders of magnitude. The measured inclusive jet cross section and the cross section for di-jet events at the LHC are

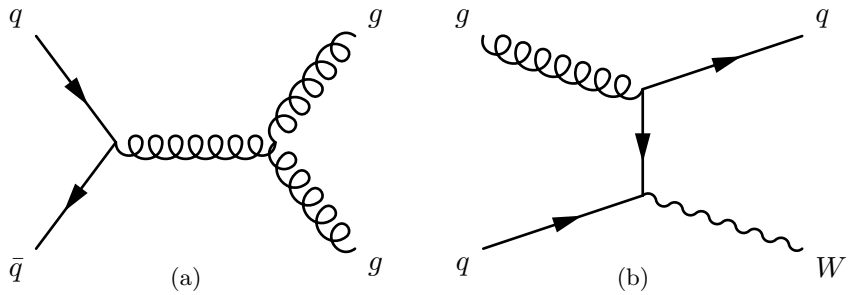

Figure 5.4. *Examples of diagrams of a QCD multi-jet process (a). W boson production in association with one additional jet is shown in (b).*

presented in [167, 168]. The production cross section of W bosons, including the decay $W \to \ell\nu$ ($\ell = e, \mu$, or tau), is 36800 pb at NNLO [154, 155]. The W boson production samples have been simulated with Alpgen and Pythia8 using CTEQ6L1 for parametrizing the PDFs. Most of the single top quark processes, where a hadronically decaying W boson is produced, contribute also to the fake lepton background. The different single top quark production modes have been introduced in the previous section 5.2.2. In the analysis, the simulated samples for the contribution from fake leptons are only used for cross-checks since this background is estimated in a data-driven way, which is based on a template method and described in section 7.5. In case of the event generators Powheg and Herwig, the decay of τ leptons is simulated separately with Tauola [100]. Bremsstrahlung effects are simulated with Photos [99] for all samples. The simulated signal and background events undergo a full simulation of the ATLAS detector response, using GEANT4 [101] as explained in section 3.4.6. For the estimation of additional pile-up effects, minimum-bias interactions simulated with Pythia are overlaid with the nominal simulated events, using the AU2 [175] tune. The simulation of in-time and out-of time pile-up effects is adapted to the luminosity profile of the corresponding data and the data taking periods.

The background modeling and estimation, based on simulation or data-driven methods, are discussed in detail in section 7.

5.3. Event Selection

The detector signature of the decay $H \to \tau^+\tau^- \to \ell^+\ell^- 4\nu$ is characterized by exactly two oppositely charged leptons and a certain amount of $\mathbf{E}_T^{\text{miss}}$ due to neutrinos. The possible combinations of final state lepton flavours in the fully leptonic decay channel are two electrons (e^+e^-), two muons ($\mu^+\mu^-$) and one electron and one muon ($e^+\mu^-$ or $e^-\mu^+$). The different decay channels are denoted as ee and $\mu\mu$ for same flavour (SF) and $e\mu$ ($p_T^e > p_T^\mu$) or μe ($p_T^\mu > p_T^e$) for different flavour (DF) final states. The event display in figure 5.5 shows an event candidate in the $e\mu$ channel, which is consistent with the VBF topology. Two additional forward jets are present in the event, which indicate the production of the Higgs boson in the

VBF mode. The following sections describe the selection of $H \to \tau^+\tau^-$ events in the fully leptonic channel.

5.3.1. Event Cleaning

Before requiring on signal specific kinematic properties, the collected data is cleaned and only events from a *Good Runs List* (GRL) are considered in the analysis, corresponding to the luminosity of $\int \mathcal{L}dt = 20.3$ fb^{-1} for 8 TeV. The GRL excludes events that were recorded during periods, where the detector was not in full operational mode or in unusual configurations. To reject events from cosmic rays and beam-halo effects, each event is required to have at least one reconstructed vertex consistent with the intersection of both beams with more than three associated tracks. Further selection criteria of the object reconstruction algorithms ensure, that the relevant objects are related to the primary vertex as described in section 4. Events are also removed if any reconstructed jet is found likely to have originated from beam-gas effects or calorimeter noise. The corresponding loose selection

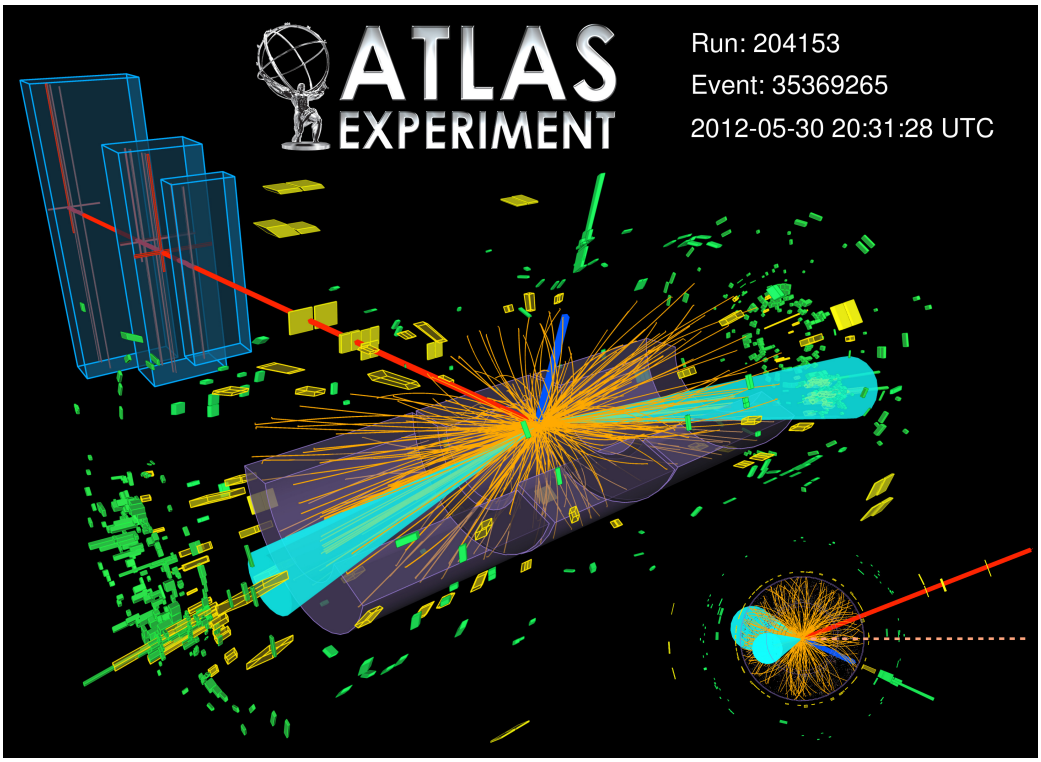

Figure 5.5. *Data event display of a Higgs boson candidate in the decay channel $H \to \tau^+\tau^- \to e^{\pm}\,\mu^{\mp} 4\nu$. The electron track is marked in blue and the muon track in red. The dashed orange line illustrates the $\mathbf{E}_T^{\text{miss}}$ vector, which is assumed to reflect reflect the four neutrinos. Two forward jets are present in the event (cyan cones), which indicates the production of the Higgs boson via vector-boson fusion [8].*

for such jet quality criteria depends mostly on the energy fraction in the EM calorimeter [116]. In addition, events are removed within particular data taking periods, if reconstructed jets are pointing to specific regions in the ATLAS tile calorimeter, where problems occurred during that time of data-taking. Events, including noise bursts in the liquid argon detectors, are also vetoed. The procedure of event cleaning ensures good data quality and reduces non-physical and technical detector effects or physical non-collision background processes.

5.3.2. Trigger

A combination of various lepton triggers is used in the analysis in order to enable the selection of all combinations of final state leptons in the decay mode $H \to \tau^+\tau^- \to \ell^+\ell^- 4\nu$. The specific trigger items are introduced in sections 4.3.1 and 4.4.1 for electrons and muons respectively. Events with two electrons (ee channel) are selected if either the single electron trigger *e24vhi_medium1* or *e60_medium1* is fired or if it is triggered by the di-electron item *2e12Tvh_loose1*. The di-muon final state ($\mu\mu$ channel) is triggered via the di-muon item *mu18_tight_mu8_EFFS*, which requires two muons with asymmetric trigger thresholds. Events including one electron and one muon ($e\mu$ channel) are selected, using either the combination of single electron triggers *e24vhi_medium1* or *e60_medium1* or the combined lepton trigger *e12Tvh_medium1_mu8*. For each channel, additional lepton transverse momenta thresholds are required in the offline selection for the leading and sub-leading lepton, which are typically $2 - 3$ GeV above the individual trigger thresholds to ensure that trigger efficiencies are in the plateau region. The channel specific trigger requirements and offline p_{T} thresholds are summarized in table 5.2. In case of the ee and $e\mu$ channel, the single electron trigger is prioritized, meaning that the event is rejected if an electron with relatively high transverse momentum $p_T^e > 26$ GeV is not selected by the single electron trigger. On top of the trigger requirements per event, each lepton has to be matched to the corresponding event trigger[2]. Differences between the efficiencies of data and simulated events are considered by applying p_{T}, η and ϕ dependent correction factors to the simulated leptons [109, 112].

Channel	Trigger	Threshold
ee	*e24vhi_medium1* || *e60_medium1*	$p_T^{e,1} > 26$ GeV
	2e12Tvh_loose1	$p_T^{e,1} > 15$ GeV, $p_T^{e,2} > 15$ GeV
$\mu\mu$	*mu18_tight_mu8_EFFS*	$p_T^{\mu,1} > 20$ GeV, $p_T^{\mu,2} > 10$ GeV
$e\mu$	*e24vhi_medium1* || *e60_medium1*	$p_T^{e} > 26$ GeV
	e12Tvh_medium1_mu8	$p_T^{e} > 15$ GeV, $p_T^{\mu} > 10$ GeV

Table 5.2. *Trigger items and transverse momentum thresholds for each analysis final state channel.*

[2]Trigger matching is a geometric mapping of the offline lepton candidate, which might have triggered the event, to the fired detector trigger chamber.

5.3.3. Preselection

Besides the event cleaning and trigger requirements, a sequence of cuts on topological and kinematic properties of the reconstructed objects in each event is applied to enhance the signal-to-background ratio.

Event candidates are required to contain exactly two leptons with opposite charge. Both final state leptons are required to be isolated. There are track-based and calorimeter-based isolation criteria for electrons and muons, which are sensitive to additional activity within a specific region around the lepton tracks or the calorimeter barycenter of the lepton candidate. The lepton isolation is explained in the sections 4.3.3 and 4.4.2 and summarized in table 4.1. Since fake leptons mainly arise from mis-identified jets, which tend to have multiple tracks nearby the reconstructed lepton track and typically exhibit enhanced activity in the calorimeters, the isolation requirements reduce the probability to identify a jet as a lepton (fake leptons) significantly. They are indispensable at the LHC to suppress the overwhelming background contribution from QCD multi-jet processes due to the large corresponding cross section. The isolation cuts also reduce the number of events with true leptons from semi-leptonic decays of bottom or charm hadrons within jets originating for example from events with top quarks.

The reconstructed leptons have to fulfill the basic transverse momentum thresholds of $p_T^e > 15$ GeV and $p_T^\mu > 10$ GeV and trigger requirements to reduce fake leptons from QCD multi-jet processes. To guarantee statistical independence between the different $H \to \tau^+\tau^-$ final state decay channels $\tau_{\text{lep}}\tau_{\text{lep}}$, $\tau_{\text{lep}}\tau_{\text{had}}$ and $\tau_{\text{had}}\tau_{\text{had}}$ with respect to the combined analysis described in section 11, fully leptonic final state events must not include additional reconstructed hadronic τ leptons. The reconstruction of hadronic τ leptons is discussed in section 4.6. A working point of 85% for the τ identification efficiency is chosen to reduce the mis-identification probability of electrons as hadronic τ leptons. The τ candidates are required to exceed a visible transverse energy of $E_T^\tau > 20$ GeV. Furthermore, reconstructed jets have to fulfill the transverse momentum threshold of $p_T^j > 20$ GeV. The jet reconstruction is explained in section 4.5. Objects are removed from an event, if they overlap each other within a cone of $\Delta R = \sqrt{\Delta\phi^2 + \Delta\eta^2} < 0.2$: all muons are kept, then electrons are removed, then τ leptons and in a final step jets. This procedure avoid the double-counting of reconstructed objects. For example, an electron can be reconstructed and identified as both an electron candidate as well as a jet.

A sequence of cuts on kinematic variables of the selected objects is applied to reduce specific background components and enhance the relative signal contribution. The various background processes, which have been introduced in section 5.2, differ in their kinematic properties and can therefore be separated from the signal. Figure 5.6 shows basic example distributions of the invariant di-lepton mass $m_{\ell\ell}$, the missing transverse energy E_T^{miss} and the transverse momenta of the leading and sub-leading lepton ${p_T^\ell}^{1,2}$ after applying the previously introduced cleaning and basic two leptons selection criteria. Differences between the various signal and background processes in these distributions mainly arise from resonances decaying to di-lepton final states,

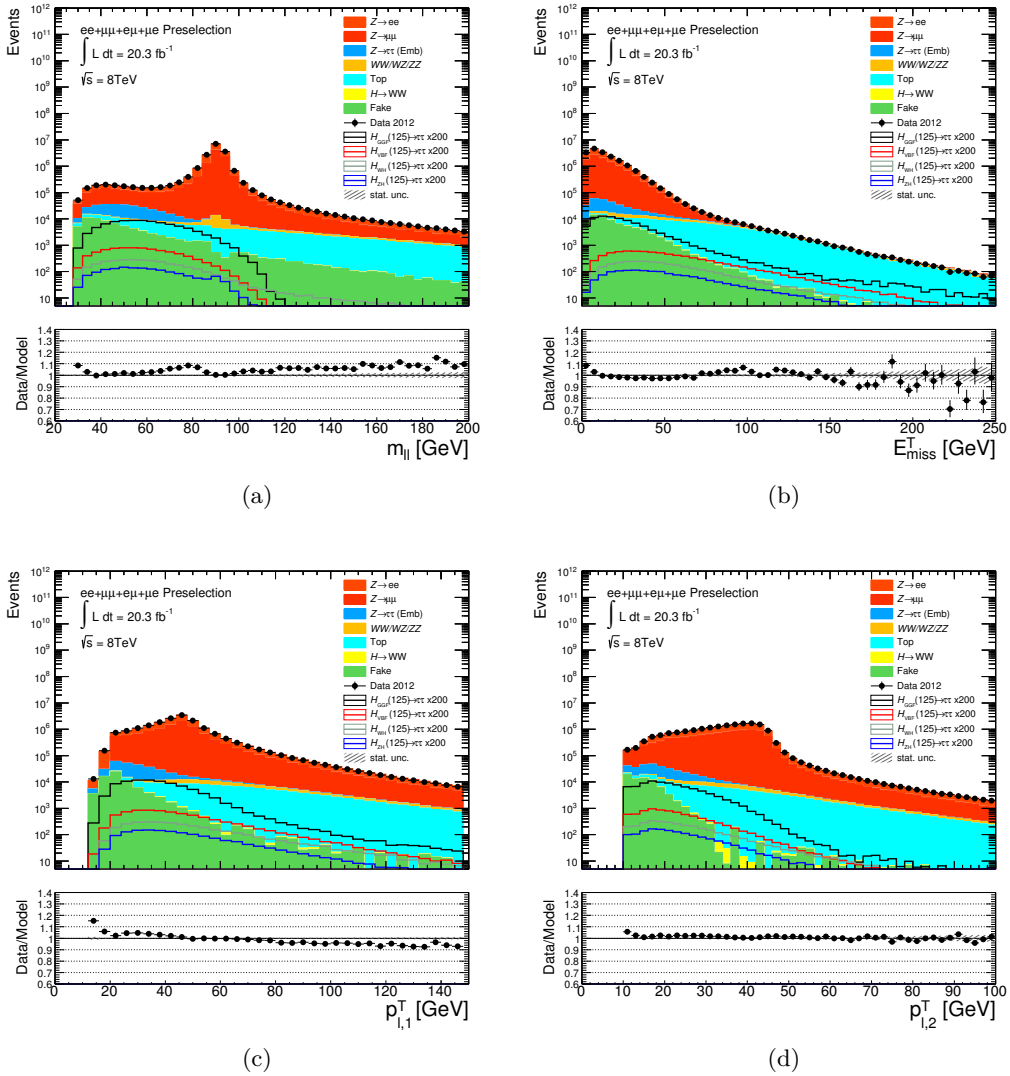

Figure 5.6. *Distributions of the invariant di-lepton mass $m_{\ell\ell}$, E_T^{miss} and the transverse momenta of leading and sub-leading lepton $p_T^{\ell\ 1,2}$ after selection of exactly two isolated leptons, including event cleaning requirements, τ lepton veto and overlap removal cuts of the specific objects in the event. The error band includes statistical uncertainties only. Background modeling is explained in section 7.*

the number of neutrinos in the event and different masses of the decaying particles. Residual deviations of the background model from data are expected to be covered by systematic uncertainties, which are not evaluated at this stage of preselection. However, a large number of systematic uncertainties is considered after the full event selection, which is discussed extensively in chapter 8. The set of sequential cuts is summarized in table 5.3 and its motivation is given below.

The decay of the Z boson resonance into pairs of electrons or muons has an

Category	Selection Cuts
Preselection	Exactly two isolated oppositely charged leptons $p_T^e > 15$ GeV and $p_T^\mu > 10$ GeV Events with τ_{had} candidates are rejected 30 GeV $< m_{\ell\ell} < 100$ (75) GeV for DF (SF) events $\Delta\phi(\ell_1, \ell_2) < 2.5$ $E_{\text{T}}^{\text{miss}} > 20$ (40) GeV for DF (SF) events $E_{\text{T}}^{\text{miss,HPTO}} > 40$ GeV for SF events $p_{\text{T}}^{\ell_1} + p_{\text{T}}^{\ell_2} > 35$ GeV Events with a b-tagged jet with $p_{\text{T}} > 25$ GeV are rejected $0.1 < x_{\tau_1}, x_{\tau_2} < 1$ $m_{\tau\tau}^{\text{coll}} > m_Z - 25$ GeV At least one jet with $p_{\text{T}} > 40$ GeV
VBF	Preselection A second jet with $p_{\text{T}}^{j_2} > 30$ GeV $\Delta\eta(j_1, j_2) > 2.2$
Boost	Preselection Failing the VBF selection $p_{\text{T}}^H > 100$ GeV

Table 5.3. *Summary of the event selection for the $\tau_{\text{lep}}\tau_{\text{lep}}$ channel. The preselection is always applied before applying criteria defining the analysis categories VBF and Boosted. The labels (1) and (2) refer to the leading (highest p_T) and sub-leading final-state objects (leptons, jets). The variables are defined in the text.*

extraordinarily high cross section, compared to other background and signal sources in this region, and is therefore suppressed in the selection of signal events with same flavour (SF) leptons by applying the cut $m_{ee/\mu\mu} < 75$ GeV. Further reduction of such processes can be achieved by requiring $\Delta\phi(\ell_1, \ell_2) < 2.5$, since most of the Z bosons are produced with low transverse momenta at the LHC, which results in a back-to-back event topology of the leptonic decay products. $Z/\gamma^* \to e^+e^-/\mu^+\mu^-$ decays do not contain any final state neutrinos, unlike the signal process, which leads typically to low missing transverse momentum in the corresponding events. A cut on $E_{\text{T}}^{\text{miss}} > 40$ GeV is therefore required. Residual (fake) $E_{\text{T}}^{\text{miss}}$ in $Z/\gamma^* \to e^+e^-/\mu^+\mu^-$ events originate mostly from resolution effects, undetected hadronic particles, imperfect object reconstruction, pile-up and underlying event effects or detector noise. The $E_{\text{T}}^{\text{miss}}$ requirement can be improved by introducing the variable $E_{\text{T}}^{\text{miss,HPTO}}$, which is calculated from objects with high transverse momentum in the event (final state leptons and jets with $p_T > 25$ GeV) and does therefore not take soft terms into account unlike the default $E_{\text{T}}^{\text{miss}}$calculation, as discussed in section 4.7.1. Both missing transverse momentum variables are highly correlated for processes with neutrinos but less correlated for processes without neutrinos. For this reason, a cut on $E_{\text{T}}^{\text{miss,HPTO}} > 40$ GeV is added in case of SF final state events. The decay of the Z boson into a pair of τ leptons is an irreducible background and its final state topology mimics the signal process. Further suppression of the $Z/\gamma^* \to \tau^+\tau^-$ background can be achieved by exploiting the invariant mass of the

di-τ system. Since final state neutrinos are present in this process as well as in the signal process, special algorithms are necessary to reconstruct the invariant mass of the system, discussed in section 5.5. Low mass resonances from the decay of charmonium and bottonium are rejected by requiring $m_{\ell\ell} > 30$ GeV with $\ell = e, \mu$ for all final state channels.

Events with top quark pairs are non-resonant processes with respect to the reconstructed final state di-lepton system. The decay of heavy top quarks results in long tails at higher values in the distributions of lepton transverse momenta and the invariant di-lepton mass. Thus, the cut on $m_{ee/\mu\mu}$ in SF events to reduce the number of resonant Z boson decays is complemented by a cut on $m_{e\mu/\mu e} < 100$ GeV in different flavour events (DF) to suppress events from top quark pair production with one final state electron and one muon. If at least one b-tagged jet with $p_T^j > 25$ GeV is found, the event is discarded since jets in signal processes typically originate from light quarks. The MV1 b-tagging algorithm with a b jet selection efficiency of 70% is used for this purpose as explained in section 4.5.4. The basic lepton isolation requirements further increase the rejection of top quark pair events. Furthermore, the τ lepton decay products in signal processes (i.e. two leptons and four neutrinos) are collimated in case of boosted high-p_T Higgs bosons. Thus, the direction of the missing transverse momentum vector tends to lie between those of the two leptons. The relation can be addressed in terms of cutting on the fraction x_1 and x_2 of the τ lepton momentum, carried by the final state leptons, with $0.1 < x_1, x_2 < 1$. Due to the non-resonant structure of the di-lepton system in events from top quark pair production, the missing transverse momentum vector does not necessarily lie in between the lepton vectors. Therefore, a large fraction of such events have negative values of x_1 and x_2. The calculation of x_1 and x_2 is explained in section 5.5, where the collinear approximation is introduced.

The properties of the di-lepton system in di-bosonic events with Z/γ^* bosons ($WZ\gamma^*$ and $Z\gamma^*Z\gamma^*$ events) are similar to $Z/\gamma^* \to ee, \mu\mu$ decays. For this reason, the same set of cuts reduces also the background contribution from di-boson processes to some degree. Two real leptons can also stem from WW events, in which both W bosons decay leptonically. In general, di-bosonic events are expected to contain less neutrinos than the signal topology. Therefore, a cut on $E_{\mathrm{T}}^{\mathrm{miss}} > 20$ GeV in DF events is added to the corresponding SF requirement. Neutrinos, which arise from the leptonic decay of W bosons, do not necessarily fly collinear to prompt leptons in di-bosonic events and the requirement $0.1 < x_1, x_2 < 1$ reduces the background contamination of di-boson processes significantly. To avoid overlapping the analysis of the search for $H \to WW^* \to \ell\nu\ell\nu$ [176], the mass of the di-τ system in the collinear approximation is required to satisfy $m_{\tau\tau}^{\mathrm{coll}} > m_Z - 25$ GeV.

Fake leptons from QCD multi-jet, single top and W boson production processes are mainly reduced by lepton isolation requirements. The $E_{\mathrm{T}}^{\mathrm{miss}}$ cut provides further suppression, because no neutrinos are expected to be present in QCD multi-jet events, which is the dominant source of fake leptons at the LHC in the analysis. The scalar sum of the lepton transverse momenta is required to satisfy $p_{\mathrm{T}}^{\ell_1} + p_{\mathrm{T}}^{\ell_2} > 35$ GeV, since QCD multi-jet events are typically low in p_T. The cuts on x_1 and x_2 provide

additional separation due to the non-resonant structure of the di-lepton system in the background processes of fake leptons.

All event candidates need to contain at least one jet, which satisfies a p_T threshold of $p_T^j > 40$ GeV, to increase the ability of distinguishing signal events from different Higgs boson production modes. The VBF topology contains two high p_{T} jets per definition and can easily be tagged by requiring a basic set of VBF specific cuts. Events with boosted Higgs bosons in association with at least one jet are dominated by the GGF mode and can also be reasonably well separated from background events. In addition to increased background rejection, the high p_T jet requirement improves the modeling of missing transverse momentum since in boosted Higgs boson topologies, soft term contributions in the $E_{\mathrm{T}}^{\mathrm{miss}}$ reconstruction play a minor role, as explained in section 4.7.1.

The separation power of all variables, which are used in the preselection to suppress background processes, is illustrated in appendix A.1 in various shape comparisons between signal and background components. The category definitions for investigating both production modes, VBF and GGH, are given in section 5.4.

5.4. Categorization

In addition to the preselection, two exclusive sets of selection criteria are applied to exploit event topologies from different Higgs boson production modes. The following analysis categories are defined:

5.4.1. VBF category

The production of Higgs bosons in the vector-boson fusion mode is characterized by two forward jets with high transverse momentum as shown in section 5.1. Thus, a second jet is required with $p_{\mathrm{T}}^{j_2} > 30$ GeV. Both jets are expected to be well separated in pseudorapidity due to the t-channel diagram of VBF Higgs boson production shown in figure 5.1 (b) and a cut of $\Delta\eta(j_1, j_2) > 2.2$ is applied. The largest fraction of signal events in the VBF category stems from the VBF production mode (56% for $m_H = 125$ GeV), but also the GGF mode contributes significantly (43.5% for $m_H = 125$ GeV).

5.4.2. Boosted category

At tree-level, the gluon fusion Higgs boson production does not involve outgoing partons as can be seen in figure 5.1. Additional QCD radiation leads to a non-zero transverse momentum of the Higgs boson. The topology of such boosted Higgs boson events differs clearly from background processes, which can be used to suppress the irreducible $Z/\gamma^* \to \tau^+\tau^-$ background. The selection of boosted Higgs boson candidates is defined by requiring a large transverse momenta of the Higgs boson

decay system $p_{\mathrm{T}}^{H} > 100$ GeV, which is calculated from the vector sum of both final state leptons and the missing transverse momentum. Selected events for the VBF category are excluded in the Boosted category to ensure orthogonality. The dominant fraction of signal in the Boosted category stems from the GGF production mode (64% for $m_H = 125$ GeV), while the contribution from the VBF mode is much smaller (18% for $m_H = 125$ GeV).

The definitions of the VBF and Boosted categories are summarized in table 5.3. Distributions of the number of jets N_{jet}, the distance in pseudorapidity $\Delta\eta(j_1, j_2)$ between the leading jets in two jet events, the transverse momentum of the subleading jet p_T^j and the Higgs boson p_T^H after preselection are shown in figure 5.7 and highlight clearly the topological differences of signal and background processes, which are utilized to define the categories. The model is in good agreement with the observed data at preselection level. The cut values of $\Delta\eta(j_1, j_2)$, p_T^j and p_T^H are chosen to be rather loose, as a Boosted Decision Tree will be applied to each category to further distinguish signal from background. In the training of Boosted Decision Trees, an adequate amount of sample statistics for the various background components is needed. Boosted Decision Trees combine several variables into a final one-dimensional classifier with optimal separation power between signal and backgrounds events. The method of Boosted Decision Trees is explained in section 5.6.

The selection efficiencies of signal events for the different production modes and mass hypothesis after applying the full selection are listed in table 5.4. At higher Higgs boson masses, the selection efficiencies increase mainly due to higher momenta of the final state leptons. Although the signal efficiencies seem small, the tight phase space cuts are necessary to reasonably suppress background processes and to increase the final sensitivity. The number of expected and observed events in the VBF and the Boosted category are quoted in table 5.5. The signal over background ratio in the VBF category ($s/b \leq 1/60$ for $m_H = 125$ GeV) exceeds the one of the Boosted category ($s/b \leq 1/140$ for $m_H = 125$ GeV). The background composition in the individual categories is further explained in chapter 7.

Signal Process	Selection Efficiencies [%]					
	VBF			Boosted		
	m_H [GeV]			m_H [GeV]		
	110	125	150	110	125	150
$(VBF)H \to \tau^+\tau^-$	3.26	4.04	4.32	1.36	1.67	1.82
$(GGF)H \to \tau^+\tau^-$	0.20	0.26	0.34	0.53	0.67	0.91
$(W)H \to \tau^+\tau^-$	0.14	0.16	0.16	1.87	2.41	3.27
$(Z)H \to \tau^+\tau^-$	0.13	0.15	0.18	1.47	2.08	2.66

Table 5.4. *Selection efficiencies [%] of signal events for different production modes and various Higgs boson mass hypothesis in the VBF and Boosted category.*

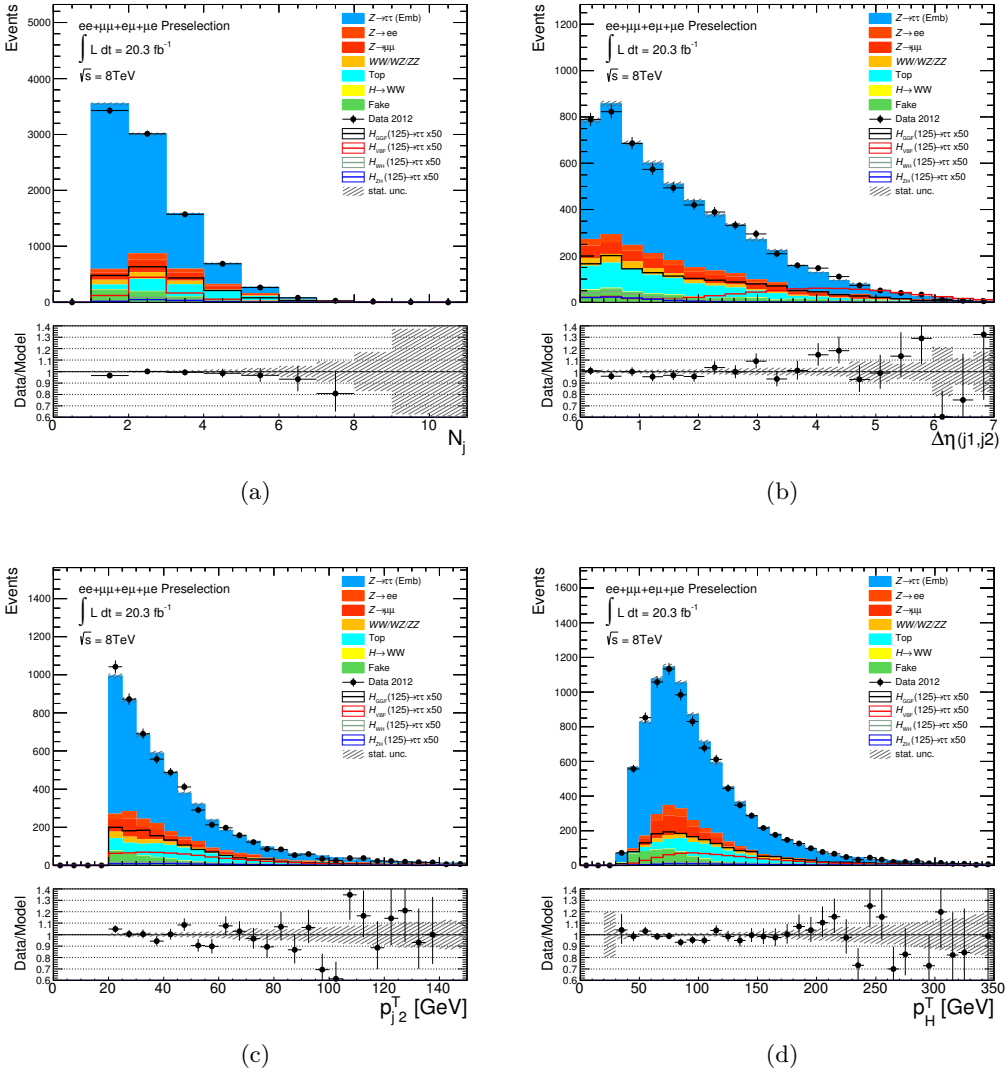

Figure 5.7. *Distributions of the number of jets N_{jet}, the distance in pseudorapidity $\Delta\eta(j_1, j_2)$, the transverse momentum of the sub-leading jet p_T^j and the Higgs boson p_T^H after preselection. The variables are used to define the VBF and Boosted categories. The error band includes statistical uncertainties only.*

Process	Expected Number of Events	
	VBF	Boosted
$m_H = 110$ GeV		
$(VBF)H \to \tau^+\tau^-$	11.24 ± 0.08	4.74 ± 0.05
$(GGF)H \to \tau^+\tau^-$	8.70 ± 0.30	17.80 ± 0.40
$(W)H \to \tau^+\tau^-$	0.27 ± 0.04	3.70 ± 0.10
$(Z)H \to \tau^+\tau^-$	0.15 ± 0.02	1.84 ± 0.06
$m_H = 125$ GeV		
$(VBF)H \to \tau^+\tau^-$	9.44 ± 0.05	3.90 ± 0.03
$(GGF)H \to \tau^+\tau^-$	7.30 ± 0.20	14.20 ± 0.20
$(W)H \to \tau^+\tau^-$	0.175 ± 0.007	2.69 ± 0.03
$(Z)H \to \tau^+\tau^-$	0.095 ± 0.004	1.36 ± 0.02
$m_H = 150$ GeV		
$(VBF)H \to \tau^+\tau^-$	2.39 ± 0.02	0.97 ± 0.01
$(GGF)H \to \tau^+\tau^-$	1.84 ± 0.04	3.67 ± 0.06
$(W)H \to \tau^+\tau^-$	0.027 ± 0.005	0.55 ± 0.02
$(Z)H \to \tau^+\tau^-$	0.017 ± 0.003	0.28 ± 0.01
$Z/\gamma^* \to \tau^+\tau^-$	601.2 ± 7.9	2221.5 ± 16.5
$t\bar{t}$	142.7 ± 6.4	410.0 ± 11.4
$Z/\gamma^* \to e^+e^-$	51.5 ± 3.6	86.9 ± 5.8
$Z/\gamma^* \to \mu^+\mu^-$	117.0 ± 8.8	137.3 ± 7.2
Di-boson	30.9 ± 3.0	165.7 ± 7.1
Fake leptons	60.8 ± 4.1	98.0 ± 5.5
$(VBF)H \to W^+W^-$	3.37 ± 0.1	1.6 ± 0.1
$(GGF)H \to W^+W^-$	3.1 ± 0.2	7.2 ± 0.3
$(W)H \to W^+W^-$	0.10 ± 0.05	1.00 ± 0.10
$(Z)H \to W^+W^-$	0.01 ± 0.01	0.56 ± 0.09
Total Signal ($m_H = 110$ GeV)	20.4 ± 0.3	28.1 ± 0.4
Total Signal ($m_H = 125$ GeV)	17.0 ± 0.2	22.2 ± 0.2
Total Signal ($m_H = 150$ GeV)	4.27 ± 0.1	5.5 ± 0.1
Total Background	1010.6 ± 14.8	3129.7 ± 23.8
Data	1014 ± 31.8	3095 ± 55.6

Table 5.5. *Expected event yields in the VBF and Boosted category. The numbers are quoted for all signal samples of different Higgs boson mass hypothesis and background samples. The samples have been generated and normalised with the event generators and cross section from the sections 5.1 and 5.2. A Higgs boson mass of $m_H = 125$ GeV is assumed for $H \to W^+W^-$ processes. Uncertainties are statistical only.*

5.5. Mass Reconstruction

In the search for $H \to \tau^+\tau^-$, the invariant mass reconstruction of the di-τ system provides an important and powerful variable, which allows for good separation between signal and background. However, the presence of neutrinos in the signal topology requires specific algorithms to determine the reconstructed mass of the Higgs boson candidate. There are two mass reconstruction techniques, which are used in the analysis:

5.5.1. Collinear Approximation

The reconstructed invariant Higgs boson mass in the collinear approximation m_{coll} is based on two assumptions [177]. First, E_T^{miss} is assumed to stem only from neutrinos of the $H \to \tau^+\tau^-$ decay and second, the τ lepton and its decay products e, μ and ν are collinear ($\phi^{\text{vis}} = \phi^{\nu}$ and $\theta^{\text{vis}} = \theta^{\nu}$ for the polar and azimuthal angle of the decay products). In the case of $H \to \tau^+\tau^- \to \ell^+\ell^- 4\nu$, the decay products are two final state electrons or muons and four neutrinos, which cannot be detected directly but are inferred through the presence of missing transverse momentum. The momentum $p_{1,2}^{\text{miss}}$ of the neutrino system from each of the two decaying τ leptons can be calculated in the collinear approximation by solving the equations

$$\begin{aligned} E_T^{x,\text{miss}} &= p_1^{\text{miss}} \sin\theta_1^{\text{vis}} \cos\phi_1^{\text{vis}} + p_2^{\text{miss}} \sin\theta_2^{\text{vis}} \cos\phi_2^{\text{vis}} \\ E_T^{y,\text{miss}} &= p_1^{\text{miss}} \sin\theta_1^{\text{vis}} \sin\phi_1^{\text{vis}} + p_2^{\text{miss}} \sin\theta_2^{\text{vis}} \sin\phi_2^{\text{vis}}. \end{aligned} \tag{5.1}$$

Furthermore, the fraction of τ lepton momenta x_1 and x_2 carried by the final state leptons in the collinear approximation is introduced [178]

$$x_{1,2} = \frac{p_{T1,2}^{\ell}}{p_{T1,2}^{\ell} + p_{T1,2}^{\text{miss}}} = \frac{p_{1,2}^{\ell}}{p_{1,2}^{\tau}}. \tag{5.2}$$

Assuming massless leptons, equations 5.1 and 5.2 lead to the reconstructed invariant di-τ mass

$$m_{\text{coll}}^2 = \frac{m_{\ell\ell}^2}{x_1 x_2}. \tag{5.3}$$

The collinear approximation works well for boosted Higgs bosons with high p_T^H, where the decay products are collimated. However, the equation system 5.1 becomes degenerate in topologies, where the Higgs boson decay products emerge back-to-back due to a vanishing p_T^H. In the analysis, back-to-back topologies are excluded by applying a cut on $\Delta\phi(\ell_1, \ell_2)$. In addition, both categories utilize boosted Higgs boson events per definition by requiring at least one high p_T jet. The collinear approximation is quite sensitive to the resolution of the missing transverse momentum, which could lead to an overestimation of the invariant mass of the Higgs boson.

5.5.2. Missing Mass Calculator

Without assuming collinearity of the decay products of each τ lepton, there is no unique solution for the reconstruction of the invariant mass of the di-τ system, since the corresponding set of equations is under-constrained. The set of equations consists of the on-mass-shell requirement of the τ leptons and the measurable quantities such as the transverse E_T^{miss} components ($E_T^{x,\text{miss}}$ and $E_T^{y,\text{miss}}$) assuming $E_T^{\text{miss}} = \sum_{\text{neutrinos}} p_T^{\nu}$ and the momenta and invariant masses ($p_{1/2}^{\text{vis}}$ and $m_{\text{vis1/2}}$) of the visible τ decay products:

$$\begin{aligned}
E_T^{x,\text{miss}} &= p_1^{\text{miss}} \sin\theta_1^{\text{miss}} \cos\phi_1^{\text{miss}} + p_2^{\text{miss}} \sin\theta_2^{\text{miss}} \cos\phi_2^{\text{miss}} \\
E_T^{y,\text{miss}} &= p_1^{\text{miss}} \sin\theta_1^{\text{miss}} \sin\phi_1^{\text{miss}} + p_2^{\text{miss}} \sin\theta_2^{\text{miss}} \sin\phi_2^{\text{miss}} \\
m_{\tau 1}^2 &= m_{\text{miss1}}^2 + m_{\text{vis1}}^2 + 2\sqrt{p_1^{\text{vis}} + m_{\text{vis1}}^2}\sqrt{p_1^{\text{miss}} + m_{\text{miss1}}^2} \\
&\quad -2p_1^{\text{vis}} p_1^{\text{miss}} \cos\Delta\theta_1 \\
m_{\tau 2}^2 &= m_{\text{miss2}}^2 + m_{\text{vis2}}^2 + 2\sqrt{p_2^{\text{vis}} + m_{\text{vis2}}^2}\sqrt{p_2^{\text{miss}} + m_{\text{miss2}}^2} \\
&\quad -2p_2^{\text{vis}} p_2^{\text{miss}} \cos\Delta\theta_2.
\end{aligned} \tag{5.4}$$

The unknown variables are the momenta $p_{1/2}^{\text{miss}}$, the invariant masses $m_{\text{miss1/2}}^2$ and the angles $\theta_{1/2}^{\text{miss}}$ and $\phi_{1/2}^{\text{miss}}$ of both neutrino systems, which each contains two neutrinos in the fully leptonic decay channel. The Missing Mass Calculator algorithm (MMC) [179] provides a single value for the reconstructed invariant mass m_{MMC} of the di-τ system. This is accomplished by scanning over the unknown variables of the neutrinos and solving the equation system 5.4 for each scan point. The m_{MMC} solution at each scan point is then weighted based on the matrix element of the corresponding τ lepton decay. The most probable value for the reconstructed invariant mass among all solutions of the scan[3] is returned as final m_{MMC} value. The scan is performed in the unknown variables $\theta_{1/2}^*$, the angle between the final state lepton in the τ lepton rest frame and the boost direction of the τ lepton in the lab frame, and the invariant mass of the neutrino system $m_{\text{vis1/2}}^2$. The choice of the τ lepton rest frame in case of the scan in $\theta_{1/2}^*$ simplifies the calculation of the matrix element based weight significantly. In addition to the four unknown variables, a scan in E_x^{miss} and E_y^{miss} is performed. Since the m_{MMC} solution is affected significantly by the E_T^{miss} resolution, each of these scan points is weighted by a Gaussian probability function, that depends on the scalar sum $\sum_i E_T^i$ of all transverse energy deposits i in the calorimeter, in addition to the τ lepton decay matrix element weight. This additional scan reduces the potential bias due to E_T^{miss} resolution effects. The six-dimensional scan is then used for retrieving corrected values of $E_{x/y}^{\text{miss}}$, which then enters again the four dimensional only scan in $\theta_{1/2}^*$ and $m_{\text{vis1/2}}^2$. The MMC provides a solution for the reconstructed invariant mass m_{MMC} of the di-τ system for 99% of all events in the $H \to \tau^+\tau^-$ and $Z/\gamma^* \to \tau^+\tau^-$ samples. The residual

[3] The reconstructed mass value, at which the distribution of m_{MMC} evaluated for each scan point has its maximum, is chosen as most probable value and returned by the MMC algorithm [179].

failure rate, where no solution in each of the scan points is found, can be mainly explained by outliers of the $E_{\mathrm{T}}^{\mathrm{miss}}$ measurement.

A comparison of both invariant mass reconstruction algorithms m_{coll} and m_{MMC} is shown in figure 5.8 for the VBF and Boosted categories respectively. Both approaches are able to reconstruct the invariant mass of $H \to \tau^+\tau^-$ and $Z/\gamma^* \to \tau^+\tau^-$, which are fundamental variables for the separation of signal and irreducible backgrounds events. The width of the m_{MMC} distribution is 20 GeV(20 GeV) for the signal in the VBF (Boosted) category and therefore smaller than the one for the collinear approximation with a width of 24 GeV(24 GeV). In case of $Z \to \tau^+\tau^-$ processes a similar behaviour is expected. The sophisticated MMC approach is chosen as default option for reconstructing the invariant mass of the Higgs boson due to its improved resolution compared to the collinear approach.

5.6. Boosted Decision Trees

Boosted Decision Trees (BDTs) are a multivariate analysis technique (MVA), which is used in the analysis to separate Higgs boson signal events from background processes. MVA techniques typically improve the signal versus background separation significantly compared to a pure cut-based selection approach.

The basic concept of a Decision Tree is illustrated in figure 5.9. Decision Trees classify events into signal-like or background-like categories. It is based on a binary tree, which consists of multiple sets of sequential cuts on specific input variables and results in different *leaf nodes* for signal and background events [180]. In contrast to a simple cut-based selection, a Decision Tree divides the phase space into several hypercubes instead of a single one, improving the separation power between signal and background. A single Decision Tree is prone to statistical fluctuations in the training samples, which might bias the cut sequences artificially (over-training). For this reason, a *boosting* procedure is applied, which typically repeats the application of the Decision Tree several times [181]. The same training samples are used for each individual Decision Tree but the single events within the samples are re-weighted according to the mis-classification rate of the predecessor Decision Tree. The BDTs finally provide a single classifier by calculating a weighted average of the output from the individual Decision Trees, where the weights depend on the underlying boosting algorithm. The final one dimensional classifier is transformed such that it takes continuous values in the range from -1 for very background-like to +1 for signal-like events. BDTs are less prone to over-training effects compared to single Decision Trees.

In the following sections, the settings (section 5.6.1), the training (section 5.6.2) and the optimization (section 5.6.3) of the BDTs for both categories are discussed. The performance of the chosen BDTs is outlined in section 5.6.4.

5.6.1. Settings

The cut sequences of a single Decision Tree are determined in the training step, based on the *Gini Index* separation (*gini*). The *gini* criterion is defined as $gini = p(1-p)$ with p being the fraction of signal events in the training sample. It reaches its maximum for a fully mixed sample with $p = 0.5$. For each tree in the forest of the BDT, the variables and the corresponding cut values are chosen such that the increase in the *gini* separation between a parent node and the sum of the

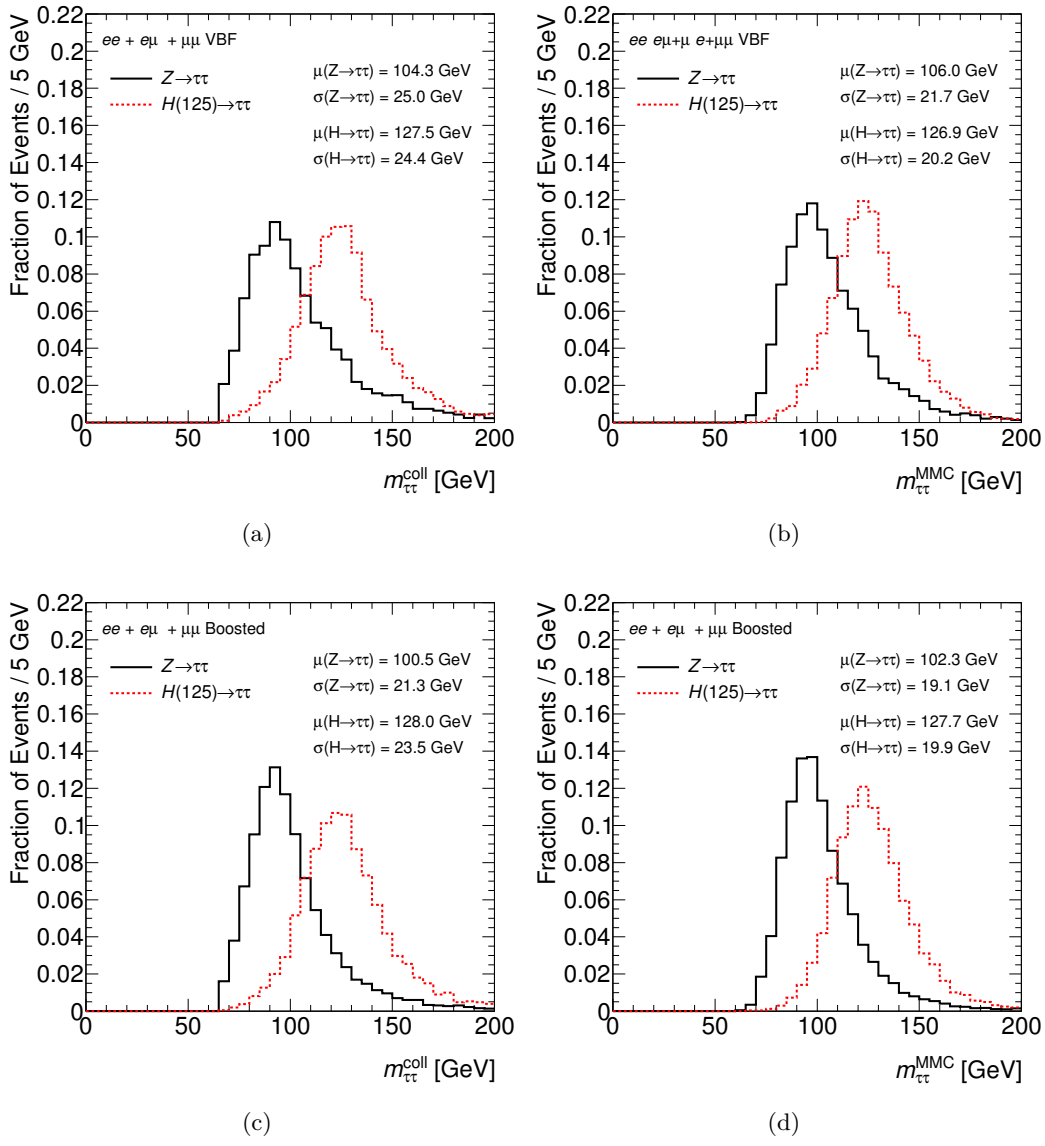

Figure 5.8. *Distributions of both di-τ invariant mass reconstruction algorithms m_{coll} (left column) and m_{MMC} (right column) for the VBF (top row a and b) and Boosted category (bottom row c and d).*

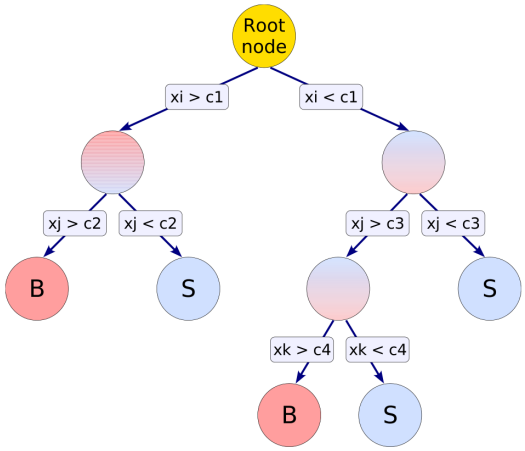

Figure 5.9. *Schematic view of a Decision Tree [180]. Multiple binary decisions form sequences of kinematic cuts, which categorize events into signal-like or background-like leaf nodes.*

indices of the two daughter nodes, weighted by their relative fraction of events, is maximized.

The boosting algorithm is chosen to be *Gradient Boosting* (*GradBoost*) [180]. It combines several single Decisions Trees i, so-called weak learners $f_i(x)$, into one BDT response function $F(x)$ in terms of a weighted sum $F(x) = \sum \alpha_i f_i(x)$, where x denotes the events in the training sample. The weights α_i are adjusted such that a specific loss function $L(F, y)$ is minimized, which reflects the deviation of the model $F(x)$ from the underlying true value y with $y = +1$ for signal and $y = -1$ for background events. In case of the *GradBoost* algorithm, the loss function is a binomial log-likelihood function

$$L(F, y) = \ln\left(1 + e^{-2F(x)y}\right). \tag{5.5}$$

The minimization for determining the coefficients α_i is done iteratively using a steepest-descent approach. The *GradBoost* algorithm is relatively robust in presence of data fluctuations and outliers.

BDT settings	VBF	Boosted
Separation type	*gini*	*gini*
Boosting type	*GradBoost*	*GradBoost*
N_{Tree}	250	1000
β	0.05	1.0
$n_{\text{size}}^{\text{min}}$	1.3%	1.0%
d_{max}	4	3

Table 5.6. *Optimized BDT settings, which are used for the BDTs in VBF and Boosted category.*

Further BDT parameters are the number of Decision Trees in the BDT forest N_{Tree}, the shrinkage parameter β, which controls the learning rate of each subsequent Decision Tree, the minimum percentage of training events in the leaf nodes $n_{\text{size}}^{\text{min}}$ and the depth of the Decision Trees d_{max}, which defines the maximum number of cuts in the sequences before a result is obtained. More details about the BDT parameters and their optimization is discussed in section 5.6.3. Table 5.6 summarizes the optimized BDT settings, that are finally used in the analysis.

5.6.2. Training

The BDT training defines the individual weak learners and the overall response function depending on the BDT parameter settings, the signal and background samples and the pool of input variables, which can be accessed by the individual Decision Trees.

The BDTs have been trained with signal samples for the Higgs boson mass of $m_H = 125$ GeV in the VBF and Boosted category. In case of the VBF category, the signal training sample includes only Higgs boson events from the VBF production mode to optimize the BDT with respect to this particular mode. Events from non-VBF production modes behave more background-like compared to the VBF production mode and would therefore decrease the sensitivity if used in the training. In the Boosted category, which excludes the VBF-like phase space, the kinematic differences between the Higgs boson production modes (VBF, GGF and VH) are smaller compared to the VBF category. In addition, the sensitivity is expected to be smaller due to a larger background contamination. Therefore, all Higgs boson production modes have been used to train the BDT in the Boosted category.

To guarantee an unbiased evaluation of the MVA, the signal and background training samples must be statistically independent from the testing samples, which are finally used in the analysis. To avoid limitations of the sample statistics, a cross-evaluation procedure is applied for the training and testing. Each sample is divided into two sub-samples according to even and odd numbering of the individual events: one BDT is trained, using a sub-sample with even only events, and one, using odd events. Each BDT is then tested on the contrary sub-sample: odd events are tested using the BDT from the training with even events and vice versa. In summary, two BDTs are used in each category respectively, which have been extracted from statistically independent sets of training samples without halving the the total number of events for testing. The overall BDT distribution is then the combination of the BDT distributions for each test samples. Data events are also numbered consecutively and the same recipe is applied to divide the dataset into two sub-samples for testing.

The BDTs combine various discriminating variables into one single one-dimensional classifier, which is continuously distributed in the range from -1 (background-like) to +1 (signal-like). Numerous variables have been tested in the BDT training and only the ones are added to the final set of input variables, which contribute significantly to the BDT separation between signal and background components. The following

sets of input variables are chosen for training the BDTs in the VBF and Boosted category, respectively:

VBF	Boosted
m_{MMC}	m_{MMC}
$\Delta R(\ell_1, \ell_2)$	$p_{\mathrm{T}}^{j_1}$
$m_{j_1 j_2}$	m_{τ,τ,j_1}
$\Delta\eta(j_1, j_2)$	$C_\phi(\ell\ell, E_{\mathrm{T}}^{\mathrm{miss}})$
$\min[\Delta\eta(\ell\ell, j)]$	$m_{\ell\ell}$
$C_\eta(jj, \ell_1) \cdot C_\eta(jj, \ell_2)$	$p_T^{\ell_1}$
$C_\eta(jj, j_3)$	$\Delta\phi(\ell_1, \ell_2)$
	Sphericity
	$E_{\mathrm{T}}^{\mathrm{miss}}/p_{\mathrm{T}}^{\ell_2}$

Table 5.7. *Discriminating variables, which are used in the training of the BDT in the VBF and the Boosted category.*

VBF category specific input variables

- $\mathbf{\Delta R(\ell_1, \ell_2)}$
  The distance $\Delta R = \sqrt{\Delta\phi^2 + \Delta\eta^2}$ between both final state leptons separates Higgs boson events from all non-$Z/\gamma^* \to \tau^+\tau^-$ background components. The variable tends to be distributed at higher values for such background processes compared to the signal (figure 5.11(a) and A.17).

- $\mathbf{m_{j_1 j_2}}$
  The invariant mass of the two leading jets is sensitive to the VBF signal event topology. The values are typically higher for VBF signal than for background events due to the relatively high p_T and the separation of the forward jets, which are produced in the VBF mode (figure 5.11(b) and A.18).

- $\mathbf{\Delta\eta(j_1, j_2)}$
  The distance $\Delta\eta$ between both leading jets is the most prominent variable with a strong separation between background processes and the signal component from the VBF production mode. A loose cut on this variable is already used in the preselection to define the VBF category. The distinct large η separation of the leading forward jets in VBF signal events stems from the t-channel contribution in the VBF Higgs boson production (figure 5.11(c) and A.19).

- $\mathbf{\min[\Delta\eta(\ell\ell, j)]}$
  The variable provides the minimum $\Delta\eta$ distance between the vector of the two lepton system and one of the jets. The Higgs boson decay products in VBF signal events emerge typically between both leading forward jets within the central detector region. Since there is low hadronic activity between both forward jets in these signal events due to the missing color exchange of the incoming quarks, the minimum distance between the lepton system and the

jets tend to be larger for VBF signal than for background processes (figure 5.11(d) and A.20).

- $\mathbf{C}_\eta(\mathbf{jj}, \ell_\mathbf{1}) \cdot \mathbf{C}_\eta(\mathbf{jj}, \ell_\mathbf{2})$
  The η centrality quantifies the η position of an object k with respect to the two leading jets in an event. Its definition is

$$C_\eta(jj, k) = \exp\left[\frac{-4}{(\eta_{j_1} - \eta_{j_2})^2}\left(\eta_k - \frac{\eta_{j_1} + \eta_{j_2}}{2}\right)^2\right], \tag{5.6}$$

  where η_{j_1} and η_{j_2} are the pseudorapidities of the two leading jets and η_k the one of the probed object k. The η centrality is a continuous variable, which reaches a value of 1 when the object is in the middle of both leading jets with respect to η, 1/e when the object is collinear with one of both jets and $< 1/\mathrm{e}$ when the object is outside the opening angle of the jets in η.

  In this case, the BDT input variable is defined as the product of η centralities for both final state leptons ℓ_1 and ℓ_2. As already mentioned, the Higgs boson decay products tend to emerge in the central region of the detector, resulting in higher values of the centrality product in VBF signal events compared to background events (figure 5.11(e) and A.21).

- $\mathbf{C}_\eta(\mathbf{jj}, \mathbf{j_3})$
  The η centrality can also be evaluated for a third jet in the event. If only two jets are present in the event, a default value of -0.5 is assigned to the variable. Due to the low hadronic activity between the two forward jets in VBF signal events because of the absence of color exchange of the incoming quarks, the variable tends to adopt smaller values and more often the default value for VBF signal than for background processes (figure 5.11(f) and A.22).

Boosted category specific input variables

- $\mathbf{p}_\mathrm{T}^{\mathbf{j_1}}$
  At leading order, Higgs bosons produced via GGF mode are not expected to have any transverse momentum since no initial state radiation occurs. Any initial state radiation leads to a boost of the Higgs boson. Therefore, the transverse momentum $p_\mathrm{T}^{j_1}$ of the leading jet is connected with the p_T of the Higgs boson. In GGF signal events, the $p_\mathrm{T}^{j_1}$ distribution has a longer tail at high values compared to background events. In addition, also VBF signal events tends to be distributed at higher $p_\mathrm{T}^{j_1}$ values because of the characteristic high p_T forward jets (figure 5.12(a) and A.24).

- $\mathbf{m}_{\tau\tau\mathbf{j_1}}$
  The invariant mass of the di-τ system in the collinear approximation and the leading jet tends to be higher for signal compared to background events due to the large Higgs boson mass of 125 GeV and a relatively high jet p_T in boosted signal events. The effect is more pronounced for signal events from VBF production mode since the leading jets are expected to have larger transverse momenta than in the GGF mode. The variable separates signal

especially from the resonant $Z/\gamma^* \to \ell^+\ell^-$ background contribution because of a smaller mass and p_{T} of the Z boson compared to the Higgs boson (figure 5.12(b) and A.25).

- $\mathbf{C}_\phi(\ell\ell, \mathbf{E}_{\mathrm{T}}^{\mathrm{miss}})$
  The ϕ centrality is a variable that quantifies the relative angular position of an object k with respect to both final state leptons in the transverse plane. The transverse plane is transformed such, that the direction of the leptons are orthogonal and that the smaller ϕ angle between the leptons defines the positive quadrant of the transformed plane. The ϕ centrality is defined as the sum of the x- and y-components of the unit vector of the object k in this transformed plane:

$$C_\phi^A(\ell\ell, k) = \sin(\phi_k - \phi_{l_1}) / \sin(\phi_{l_2} - \phi_{l_1}) \tag{5.7}$$

$$C_\phi^B(\ell\ell, k) = \sin(\phi_{l_2} - \phi_k) / \sin(\phi_{l_2} - \phi_{l_1}) \tag{5.8}$$

$$C_\phi(\ell\ell, k) = \frac{C_\phi^A(\ell\ell, k) + C_\phi^B(\ell\ell, k)}{\sqrt{C_\phi^A(\ell\ell, k)^2 + C_\phi^B(\ell\ell, k)^2}}. \tag{5.9}$$

  The variable is evaluated for the missing transverse momentum vector $\mathbf{E}_T^{\mathrm{miss}}$ and tends to be larger for non-$Z/\gamma^* \to \tau^+\tau^-$ background components in comparison to the signal. Neutrinos, originating from the τ lepton decay products in case of $H \to \tau^+\tau^-$ or $Z/\gamma^* \to \tau^+\tau^-$, typically move in similar directions than the corresponding leptons due to the large boost of the Higgs or Z boson in the Boosted category. This effect causes the $\mathbf{E}_T^{\mathrm{miss}}$ vector to be in between both leptonic decay products, which is not necessarily the case for non-resonant processes or background events with fake missing transverse momentum such as $Z/\gamma^* \to e^+e^-/\mu^+\mu^-$ decays (figure 5.12(c) and A.26).

- $\mathbf{m}_{\ell\ell}$
  The visible invariant mass of the lepton system discriminates mainly between signal and $Z/\gamma^* \to \ell^+\ell^-$ events. Background events, including top quark pair and di-bosonic processes, are also reasonably well separated from the signal (figure 5.12(d) and A.27).

- $\mathbf{p}_{\mathbf{T}}^{\ell_1}$
  The transverse momentum of the leading lepton discriminates between signal and $Z/\gamma^* \to e^+e^-/\mu^+\mu^-$ events, which typically provide larger values for $p_T^{\ell_1}$ due to prompt leptonic decays, and events with fake leptons with a much a softer lepton p_T spectrum (figure 5.12(e) and A.28).

- $\boldsymbol{\Delta\phi}(\ell_\mathbf{1}, \ell_\mathbf{2})$
  At preselection level, the distance $\Delta\phi$ between the two leptons separates signal mostly from $Z/\gamma^* \to \ell^+\ell^-$ processes, where the Z boson has very low p_{T} and the leptonic decay products have a back-to-back topology. However in a boosted phase space, leptonic decays of Higgs or Z bosons with high

p_{T} result in small $\Delta\phi$ values since the final state leptons are collimated. Due to the smaller Z boson mass compared to the Higgs boson mass, the $Z/\gamma^* \to \tau^+\tau^-$ events are accumulated at even lower values of $\Delta\phi$. This is not necessarily the case for non-resonant di-lepton final states such as top quark pair production processes, which tend to occur at much higher $\Delta\phi$ (figure 5.12(f) and A.29).

- **Sphericity**
  The variable describes the isotropy of the energy flow in the event [182]. It is based on the momentum tensor

$$S^{\alpha\beta} = \frac{\sum_i p_i^\alpha p_i^\beta}{\sum_i |\vec{p_i}^2|}, \tag{5.10}$$

  where α and β are tensor indices. The summation is performed over the momenta of the selected leptons and jets in the event. The sphericity S of the event is then defined in terms of the two smallest eigenvalues λ_2 and λ_3 of this tensor,

$$S = \frac{3}{2}(\lambda_2 + \lambda_3). \tag{5.11}$$

  The sphericity has good separation power between signal and all background components. The energy flow of background events tends to be more isotropic and is shifted to higher sphericity values than for boosted signal events (figure 5.13(a) and A.30).

- $\mathbf{E_{\mathrm{T}}^{\mathrm{miss}}/p_{\mathrm{T}}^{\ell_2}}$
  The ratio of the missing transverse momentum and the sub-leading lepton p_T separates especially $Z/\gamma^* \to e^+e^-/\mu^+\mu^-$ processes from the signal. Such background processes contain only a small amount of fake $E_{\mathrm{T}}^{\mathrm{miss}}$ compared to real $E_{\mathrm{T}}^{\mathrm{miss}}$ due to neutrinos in signal processes with larger lepton transverse momenta because of prompt leptonic Z boson decays (figure 5.13(b) and A.31).

Common input variable

- $\mathbf{m_{\mathrm{MMC}}}$
  The invariant mass of the di-τ system, which is based on the Missing Mass Calculator algorithm as described in section 5.5, discriminates well between signal and the dominant $Z/\gamma^* \to \tau^+\tau^-$ background due to the lower mass of the Z boson compared to the assumed Higgs boson mass. This variable is used in both the VBF and the Boosted category. It is one of the most important discriminating variables as shown below (figure 5.10, A.16 and A.23).

The BDT input variables in the VBF and Boosted category are summarized in table 5.7 and shown in the figures 5.10, 5.11, 5.12 and 5.13. Overall, the background prediction is in good agreement with the data and only in case of the m_{MMC} distribution in the VBF category, a potential upwards fluctuation in the region of $m_{\mathrm{MMC}} = 125$ GeV is visible. The significance of this excess, which is determined with respect to the final BDT classifier distribution, is discussed in section 10.1.

Appendix A.2 shows a full set of comparisons of the input variables for the individual signal and background components in both categories, to highlight their separation power.

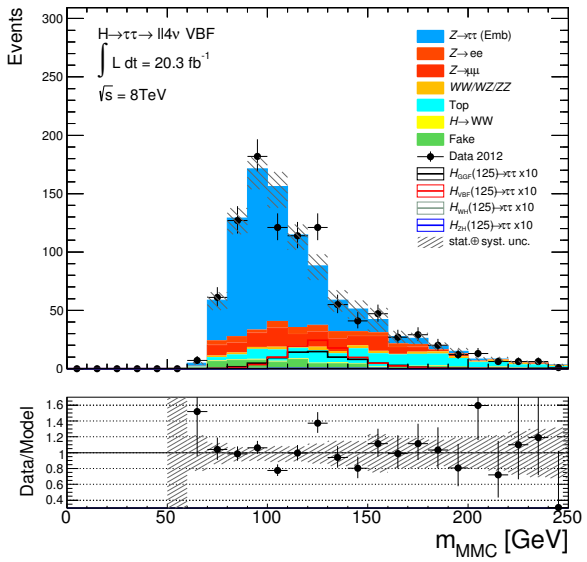

(a)

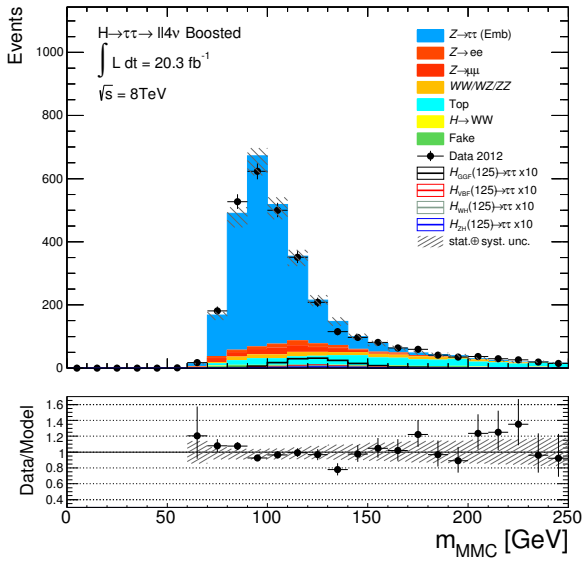

(b)

Figure 5.10. *Distributions of the invariant di-τ mass, using the Missing Mass Calculator algorithm, in the VBF and Boosted category. The invariant m_{MMC} mass is used as BDT input variable in both categories. The error band includes statistical and systematic normalisation uncertainties.*

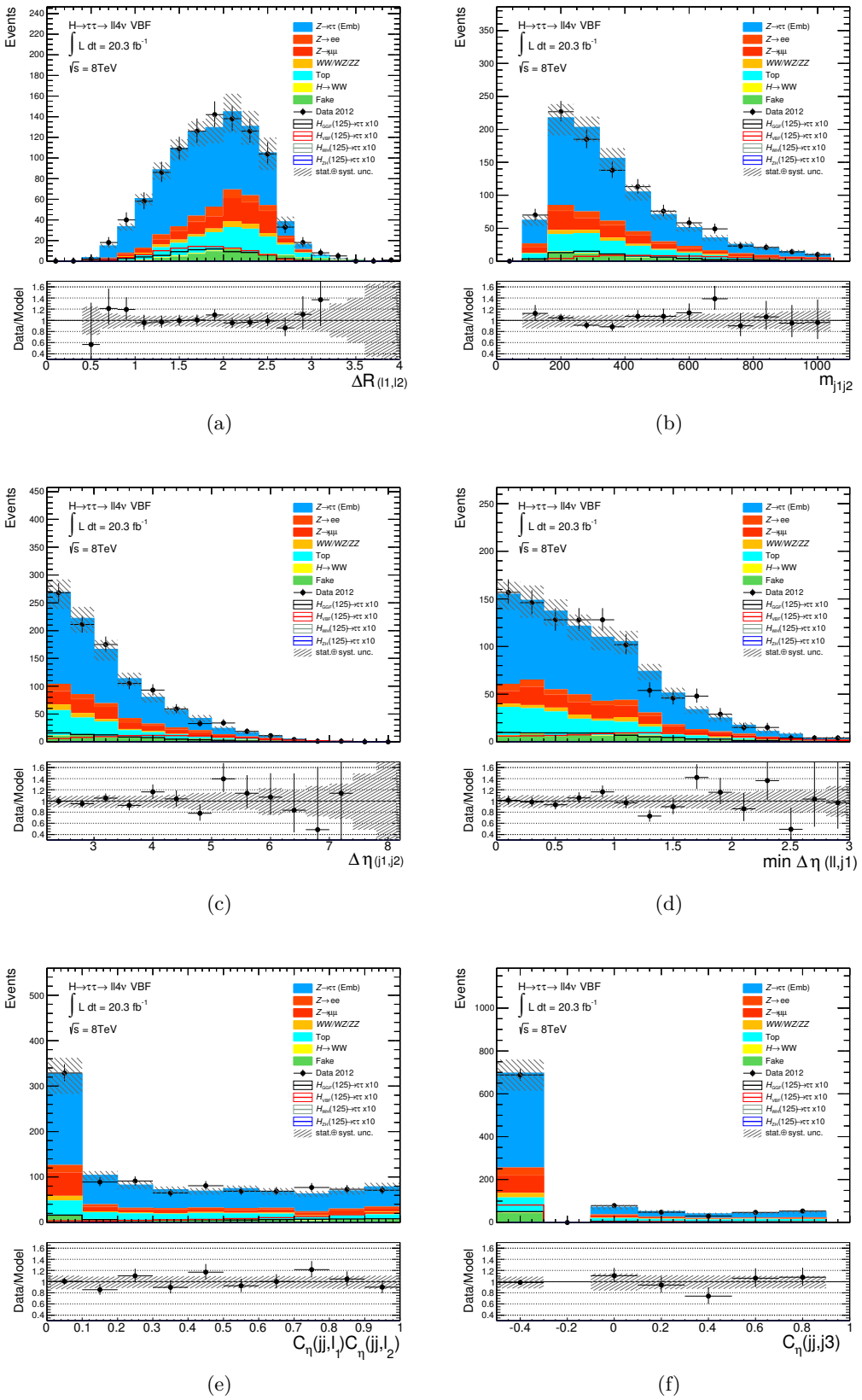

(a) (b) (c) (d) (e) (f)

Figure 5.11. *Distributions of the BDT input variables in the VBF category:* $\mathbf{\Delta R(\ell_1,\ell_2)}$ *(a),* $\mathbf{m_{j_1 j_2}}$ *(b),* $\mathbf{\Delta\eta(j_1,j_2)}$ *(c),* $\mathbf{min[\Delta\eta(\ell\ell,j)]}$ *(d),* $\mathbf{C_\eta(jj,\ell_1)\cdot C_\eta(jj,\ell_2)}$ *(e) and* $\mathbf{C_\eta(jj,j_3)}$ *(f). The error band includes statistical and systematic normalisation uncertainties.*

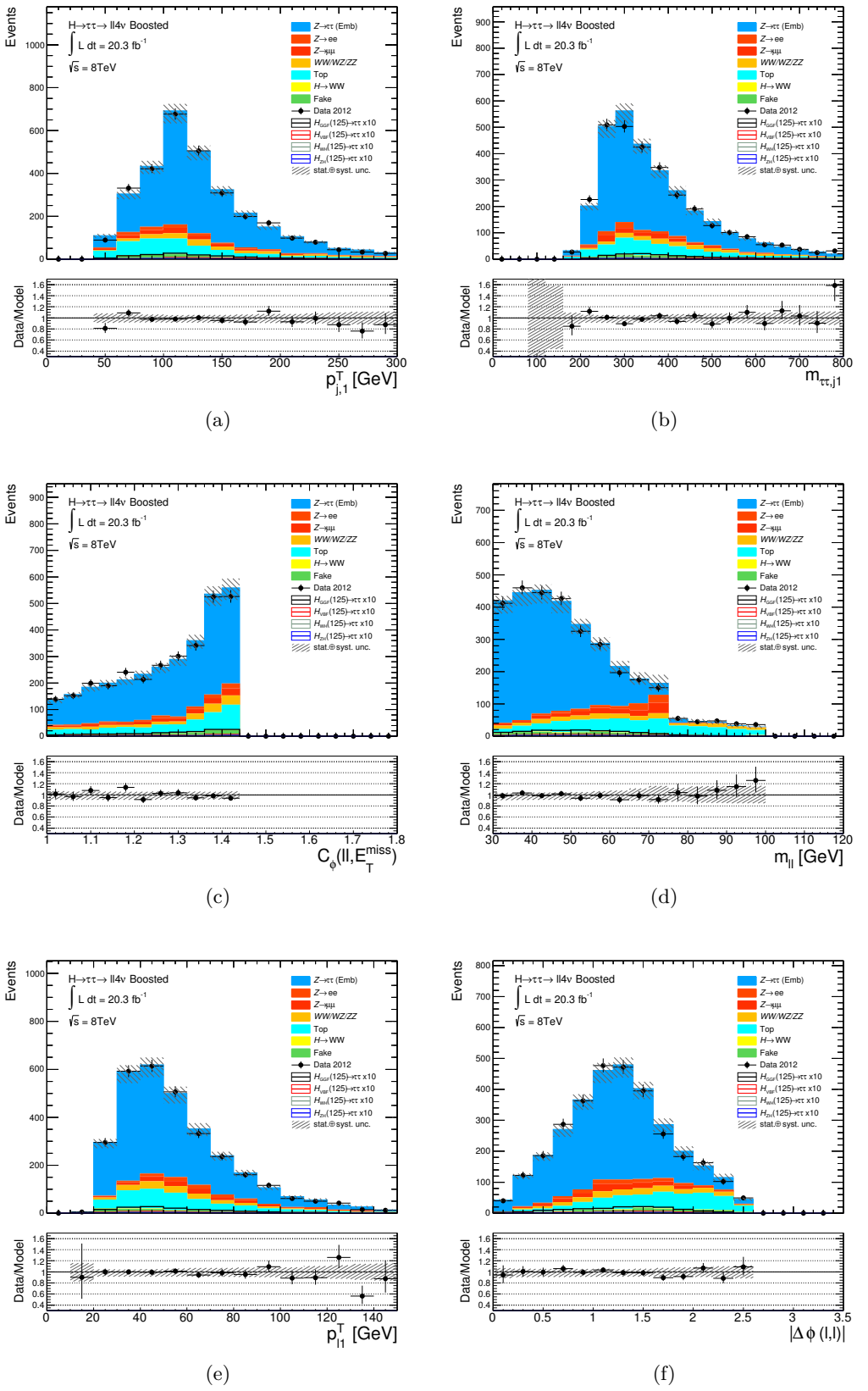

Figure 5.12. *Distributions of the BDT input variables in the Boosted category:* $\mathbf{p_T^{j_1}}$ *(a),* $\mathbf{m_{\tau\tau j_1}}$ *(b),* $\mathbf{C}_\phi(\ell\ell, \mathbf{E}_\mathrm{T}^\mathrm{miss})$ *(c),* $\mathbf{m}_{\ell\ell}$ *(d),* $\mathbf{p_T^{\ell_1}}$ *(e) and* $\mathbf{\Delta}\phi(\ell_\mathbf{1}, \ell_\mathbf{2})$ *(f). The error band includes statistical and systematic normalisation uncertainties.*

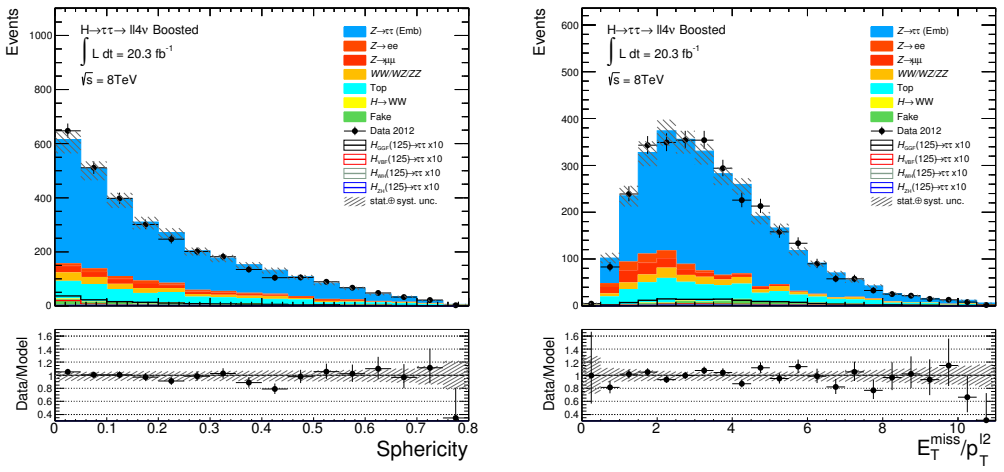

(a) (b)

Figure 5.13. *Distributions of the BDT input variables in the Boosted category:* ***Sphericity*** *(a) and* $\mathbf{E}_{\mathrm{T}}^{\mathrm{miss}}/\mathbf{p}_{\mathrm{T}}^{\ell_2}$ *(b). The error band includes statistical and systematic normalisation uncertainties.*

BDT input variable ranking			
VBF		Boosted	
Variable	Importance	Variable	Importance
m_{MMC}	0.243	m_{MMC}	0.135
$C_\eta(jj,\ell_1)\cdot C_\eta(jj,\ell_2)$	0.212	$m_{\ell\ell}$	0.127
$m_{j_1j_2}$	0.158	$\Delta\phi(\ell_1,\ell_2)$	0.124
$C_\eta(jj,j_3)$	0.122	$C_\phi(\ell\ell,E_{\mathrm{T}}^{\mathrm{miss}})$	0.120
$\Delta\eta(j_1,j_2)$	0.112	Sphericity	0.117
$\Delta R(\ell_1,\ell_2)$	0.089	$p_{\mathrm{T}}^{j_1}$	0.100
$\min[\Delta\eta(\ell\ell,j)]$	0.065	$E_{\mathrm{T}}^{\mathrm{miss}}/p_{\mathrm{T}}^{\ell_2}$	0.098
		$p_T^{\ell_1}$	0.093
		m_{τ,τ,j_1}	0.087

Table 5.8. *The importance of all BDT input variables in both categories. The quoted value is the mean value of both cross-evaluation training cases. The higher the importance value is, the more contributes the specific variable to the separation between signal and background.*

To quantify the importance of each BDT input variable, a ranking procedure is defined. The ranking is based on the number of occurrences of the variable in leaf nodes of all Decision Trees within the BDTs. Each occurrence is additionally weighted by the number of events in the leaf node and the squared *gini* separation gain. Table 5.8 shows the BDT input variables ranking and lists the average value of the corresponding importance with respect to both cross-evaluation training samples for the VBF and Boosted category. The highest ranked input variable in both categories is found to be m_{MMC}.

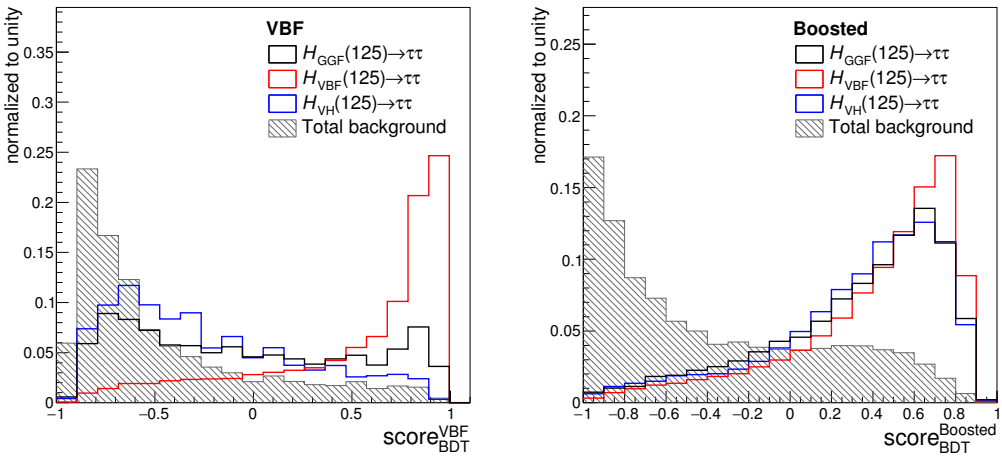

(a) (b)

Figure 5.14. *Distribution of the final BDT classifier for the individual signal components compared to the total background model in the VBF and Boosted category.*

Figure 5.14 shows the final BDT classifiers for both categories. Events, trained as signal, peak near a value of +1 and events, trained as background, are accumulated in the region of -1. All background processes considered in the analysis are used in the background training sample (see chapter 7). A good separation in case of the VBF category is observed due to the unique kinematic properties of the VBF signal process, which has been used as the exclusive signal component in the training. Signal processes from GGF and VH production have not been considered in the training, for which reason such events are accumulated at more background-like values of the BDT classifier. In case of the Boosted category, all signal processes have been used in the BDT training. They are well separated from background events although there are indications for a lower sensitivity compared to the VBF category due to broader classifier distributions.

5.6.3. Optimization

The optimization of the BDT parameter settings is based on the separation power S_{BDT}, which is defined as

$$S_{BDT} = \frac{\hat{s} - \hat{b}}{\sqrt{\sigma_s^2 + \sigma_b^2}}, \tag{5.12}$$

with $\hat{s}$ and $\hat{b}$ being the mean values of the BDT classifier distributions for the signal and background samples. σ_s and σ_b are the corresponding RMS values of the distributions.

Since a four dimensional scan in the relevant BDT parameters is very costly in terms of time, a two-dimensional scan in N_{Tree} and d_{max} has been performed calculating S_{BDT} at each scan point. Figure 5.15 shows the regions of optimal separation S_{BDT} in this two dimensional plane in both categories. Concerning the remaining parameters β and $n_{\text{size}}^{\text{min}}$, only a one dimensional scan has been performed respectively, using the optimized values for N_{Tree} and d_{max}, as shown in figure 5.16. The final working points for these parameters are chosen to be within regions that maximize S_{BDT} as indicated in the corresponding figures by markers. The absolute values of S_{BDT} for the VBF exceeds the one for the Boosted category, which indicates a higher sensitivity of the analysis in the VBF compared to the Boosted category. While the BDT is relatively sensitive to N_{Tree}, d_{max} and β, the minimal node size $n_{\text{size}}^{\text{min}}$ hardly effects its ability to separate signal from background events. The final optimized BDT settings, which are used in the analysis, are summarized in table 5.6.

5.6.4. Performance

A useful measure to estimate the quality of a MVA is the *Receiver Operating Characteristic* (ROC). The ROC curve displays the background rejection r_{bkg}, which is defined as one minus the background selection efficiency ($r_{\text{bkg}} = 1 - \varepsilon_{\text{bkg}}$), as function of the signal selection efficiency ε_{sig} with respect to cutting on the MVA classifier distribution. Figure 5.17 shows the ROC curve for the BDTs in both categories. The sample labels A and B denote the two cross-evaluation sub-samples for the BDT training and testing[4]. A diagonal straight ROC curve from ($r_{\text{bkg}} = 1, \varepsilon_{\text{sig}} = 0$) to ($r_{\text{bkg}} = 0, \varepsilon_{\text{sig}} = 1$) represents uniformly distributed classifiers for signal and background. The more the ROC curve tends to the upper right edge ($r_{\text{bkg}} = 1, \varepsilon_{\text{sig}} = 1$), the better performs the BDT in terms of signal versus background separation. The ROC curve of the BDT for the VBF category shows a better performance than the BDT for the Boosted category. No significant disagreements in the ROC curves of both cross-evaluation sub-samples A and B are

[4]Each event is labeled with a unique number consecutively. The samples for cross-evaluation are denoted as A (training with even events and testing with odd events) and B (training with odd events and testing with even events). Thus, independent samples for training and testing are defined and cross-evaluated in the analysis to avoid a loss of sample statistics as explained in section 5.6.2.

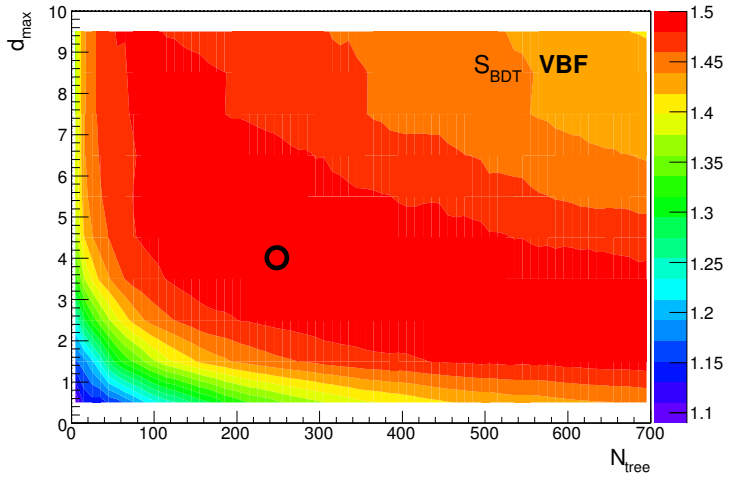

(a)

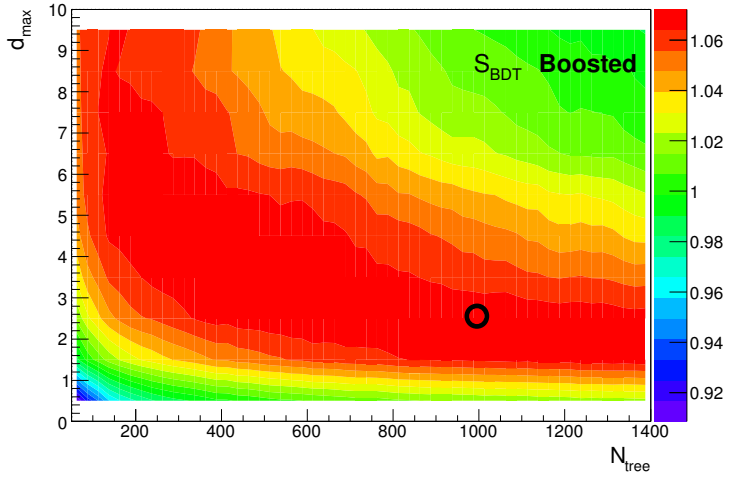

(b)

Figure 5.15. *Separation S_{BDT} of the BDT classifier between signal and background as function of N_{tree} and d_{max} for the VBF (a) and Boosted category (b). The circle indicates the chosen working points in the analysis. Optimal regions are colored red.*

observed, which demonstrates the stability with respect to statistical fluctuations in one of the sub-samples.

A comparison of the training and testing samples in each of the sub-samples A and B is shown in figure 5.18 for signal and background events. The VBF BDT classifier distributions for testing and training are in good agreement, which is also reflected by its corresponding high χ^2 probability. Concerning the Boosted category, training and testing distributions also agree reasonably well and only minimal over-training is observed despite a much smaller χ^2 probability. The agreement

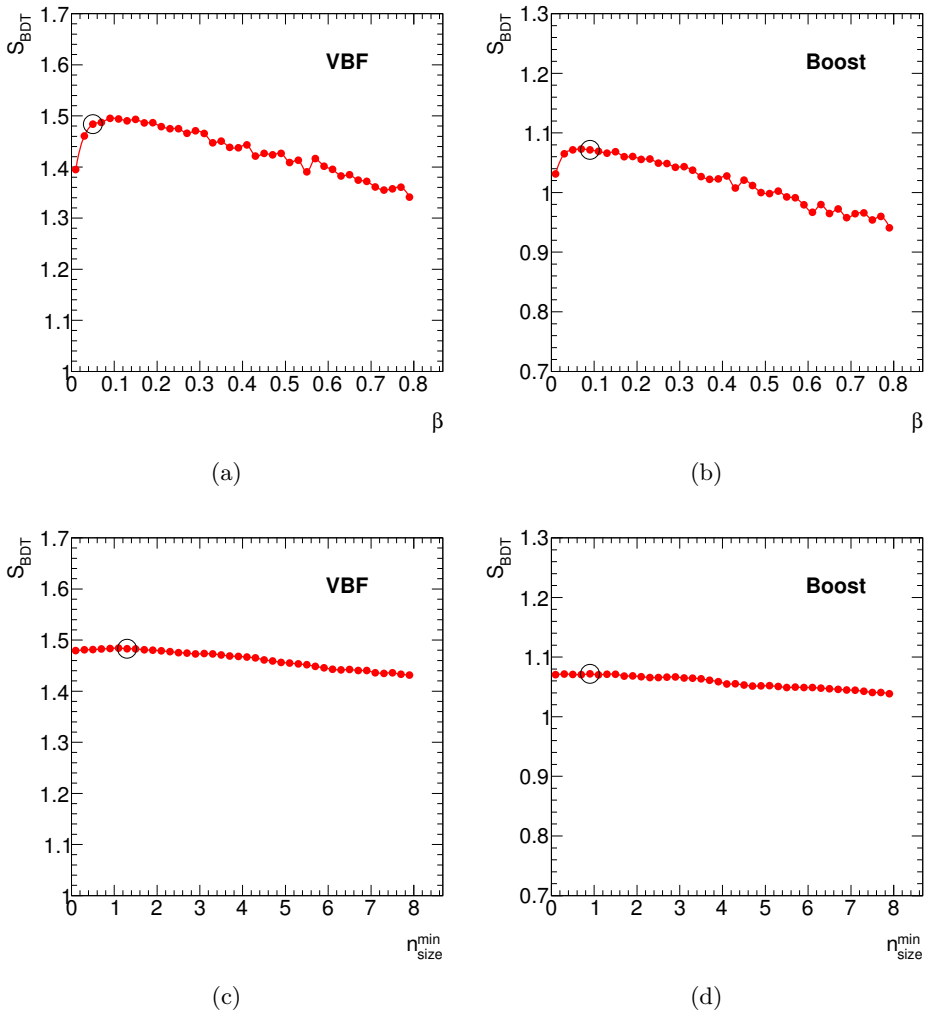

Figure 5.16. *Separation S_{BDT} of the BDT classifier between signal and background as function of β (a and b) and n_{size}^{min} (c and d) for the VBF and Boosted category respectively. The circle indicates the chosen working points in the analysis.*

in these comparisons emphasizes the low sensitivity to over-training effects of the BDTs, which are used in the present analysis.

Figure 5.19 shows the final BDT classifier distribution of the prediction for signal and background in comparison to the observed data in both categories. As for the various BDT input variables, which have been discussed in section 5.6.2, the background model is in good agreement with the measurement within regions, that are dominated by background-like events. In the very signal-like bins of the distribution, upwards fluctuations in both categories are noticeable. For the VBF category, such upwards fluctuations have already been indicated in the m_{MMC} distribution (see figure 5.10). The significance of this observation and the compatibility of the data excess with a Standard Model Higgs boson signal is discussed in detail in section 10.1.

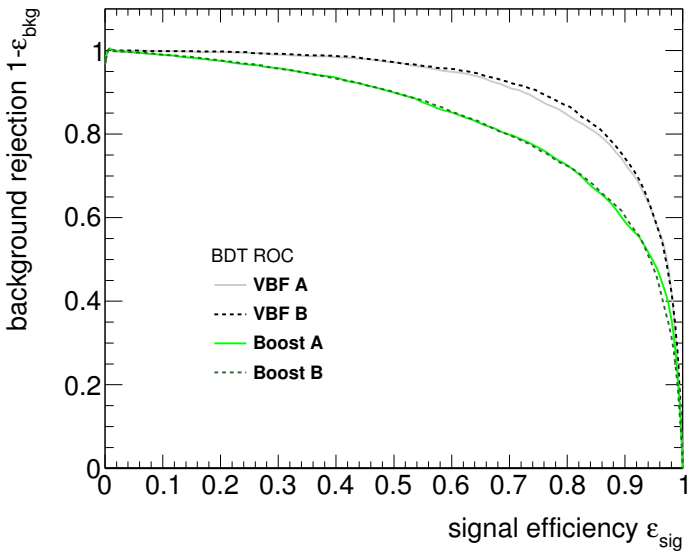

Figure 5.17. *ROC curve of the BDTs for both cross-evaluation samples A and B in the VBF and Boosted category.*

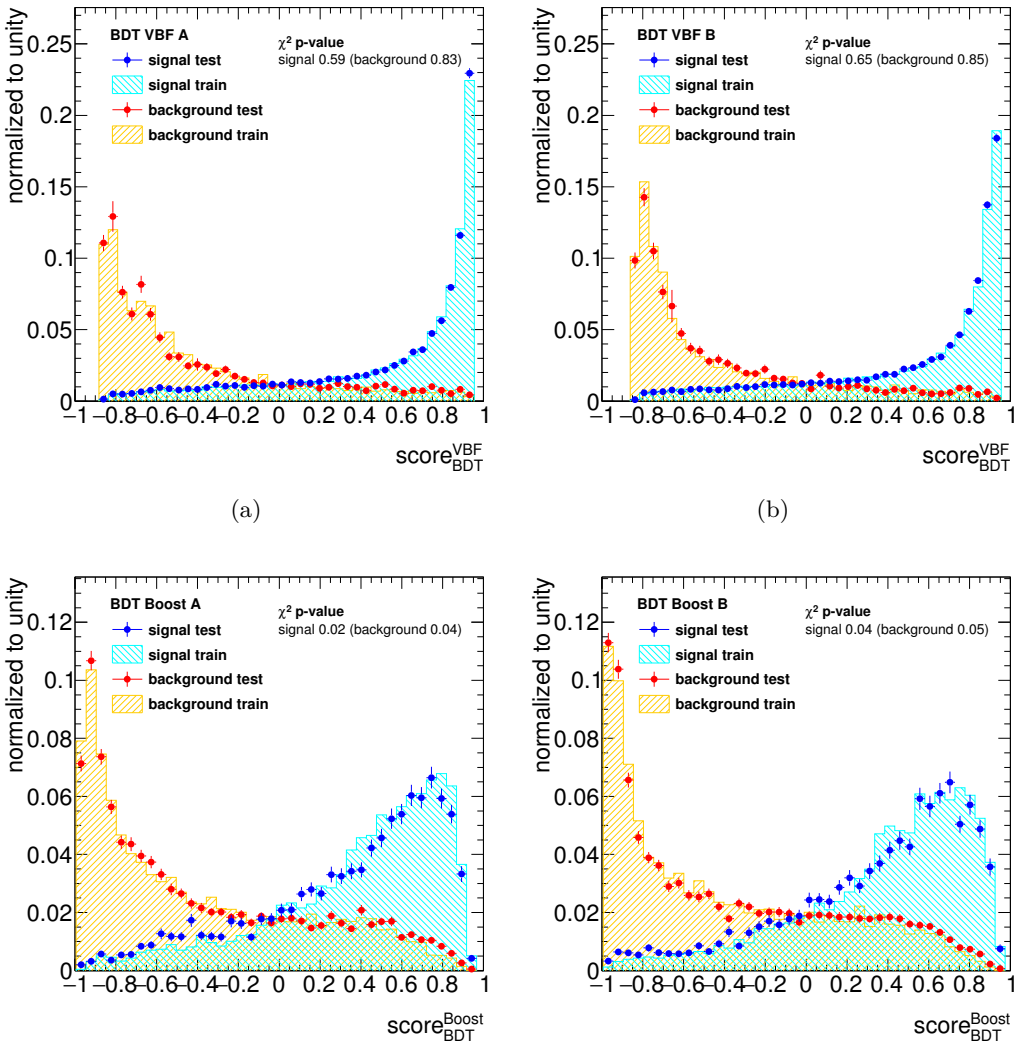

Figure 5.18. *Comparison of training and testing signal (light and dark blue) and background (light and dark red) samples with respect to the corresponding BDT classifier distributions for both cross-evaluation cases A and B in VBF and Boosted category.*

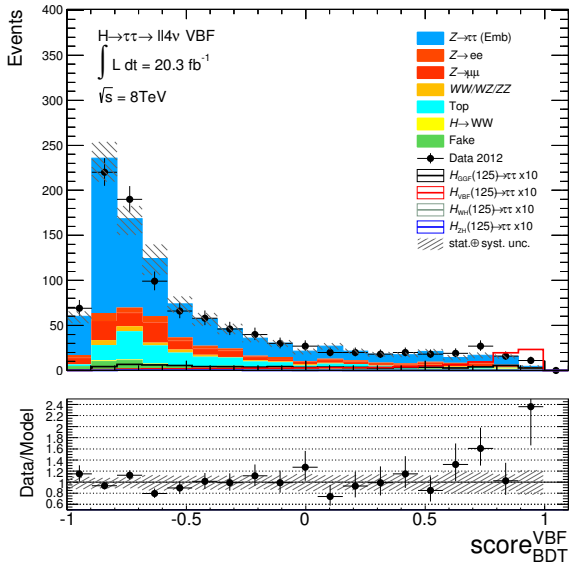

(a)

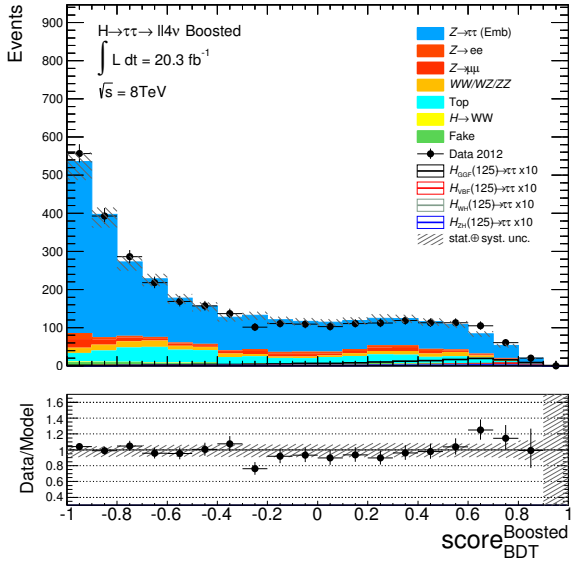

(b)

Figure 5.19. *Final BDT classifier distribution of the background model compared to the observed data in the VBF category (a) and the Boosted category (b). The top quark and $Z/\gamma^* \to e^+e^-/\mu^+\mu^-$ background is normalised to data, based on information from dedicated control regions. Di-boson and $H \to WW$ background processes are normalised to the corresponding theoretical cross-section. $Z/\gamma^* \to \tau^+\tau^-$ and fake lepton background processes are estimated in a data-driven way. Background estimation is explained in detail in chapter 7.*

6 Test of CP Invariance in VBF Higgs Boson Production in $H \to \tau^+\tau^- \to \ell^+\ell^- 4\nu$ Decays

The analysis presents a test of the CP-invariance in the Higgs boson production via vector-boson fusion in the fully leptonic decay $H \to \tau^+\tau^- \to \ell^+\ell^- 4\nu$ [9]. It is based on the method of the Optimal Observable and uses the full 8 TeV dataset with an amount of $\int \mathcal{L}dt = 20.3$ fb^{-1}, which has been recorded in 2012 with the ATLAS detector. CP-violating contributions to the SM coupling of the Higgs boson to the electroweak gauge bosons are parametrized by a single parameter $\tilde{d}$ within the framework of an effective field theory (see section 2.3). In the first part, the signal processes are discussed (see section 6.1). A re-weighting method is used for generating CP-mixed signal samples. In addition, the method of the Optimal Observable is explained, which is used as final discriminant in the fitting procedure to determine central confidence intervals on the CP-mixed parameter $\tilde{d}$. The second part provides an overview of the background estimation (see section 6.2). Third, the analysis strategy and the event selection are presented (see section 6.3. The results of the measurement are shown in section 10.2.

6.1. Signal processes

The analysis focuses on testing the CP-invariance of the HVV vertex. Therefore, Higgs boson events from the VBF mode with $m_H = 125$ GeV are considered as the signal process of interest. In the SM, the HVV couplings are predicted to be CP-conserving. Any observation of CP-violation would point to physics beyond the SM. The anomalous couplings are described in the framework of an effective field theory as explained in section 2.3. Each CP-mixed scenario is parametrized by a single parameter $\tilde{d}$, which controls the size of the CP-odd admixture to the SM CP-even HVV couplings. Both Higgs boson decay channels into τ leptons ($H \to \tau^+\tau^-$) and vector bosons ($H \to W^+W^-$) are utilized to select signal events. Only anomalous Higgs boson couplings to vector bosons are considered as signal in this analysis, while couplings to fermions such as the $H\tau\tau$ decay vertex and the GGF Higgs boson production vertex are assumed to be SM-like.

To measure potential CP-mixed signal scenarios, observables are defined, which are sensitive to CP-violation. Section 6.1.1 presents examples of such CP-odd

observables, which are used as the final discriminant in the present analysis to separate CP-mixed scenarios from the pure SM one. In section 6.1.2, the reweighting method for generating the CP-mixed signal samples is explained. Since anomalous HVV couplings contribute also to the vertex of the $H \to W^+W^-$ decay, section 6.1.3 discusses the impact of these contributions on the measurement.

6.1.1. CP-odd Observables

The test of CP-invariance in this analysis is based on CP-odd observables, which are sensitive to CP-violation. In case of pure SM processes, these observables have a mean value of zero while for CP-violating processes it does not vanish. This approach is a model independent way of testing the CP-invariance. Two such observables are presented and explained in this section. The first one is called *Optimal Observable OO* and is chosen as default final discriminant in the present analysis. It combines information of a high-dimensional phase space into a one-dimensional variable and has therefore a rather high discriminating power between pure SM signal samples and signal including anomalous couplings. An alternative approach uses a much simpler observable called signed $\Delta\phi(j_1, j_2)$, which is based on the difference in the azimuthal angle between the two leading jets.

- **Optimal Observable**

  The Optimal Observable provides a powerful tool to measure coupling parameters in differential cross sections. The coupling parameter of interest in the present analysis is $\tilde{d}$ and the method of the Optimal Observable is applied to test the CP-invariance of the HVV couplings. The concept is based on using full information of the entire kinematic phase space. In VBF-like phase space regions, the final state consists of two tagging jets and the Higgs boson. It is therefore characterized by seven variables with the assumption that the system of identified Higgs boson decay products has a mass of 125 GeV, while jet masses are neglected. Momentum conservation in the transverse plane is also assumed. The Optimal Observable combines these phase space variables into a single observable. This observable is optimal in the sense that the statistical uncertainties on the measured parameter of interest are the smallest possible ones that can be determined by any method. This holds if the cross section dependence on the parameter of interest is linear, i.e. assuming small $\tilde{d}$ values and neglecting quadratic $\tilde{d}^2$ contributions in the matrix element. Thus, the method of the Optimal Observable provides the highest sensitivity compared to all other methods. It was first introduced in Ref. [183] for estimating a single parameter of interest based on the mean value of the Optimal Observable. It was proven that a likelihood fit to the differential distribution of the Optimal Observable corresponds to a likelihood fit to the manifold differential cross section [184]. The Optimal Observable approach can be extended to the estimation of multiple coupling parameters, which can also include non-linear quadratic terms in the matrix element [185–187].

The Optimal Observable, which is used to measure $\tilde{d}$ in the present analysis, is defined as the interference term in the squared matrix element of equation 2.49 divided by the squared SM matrix element

$$OO = \frac{2Re(\mathcal{M}^{*}_{\text{SM}}\mathcal{M}_{\text{CP-odd}})}{|\mathcal{M}_{\text{SM}}|^2}. \tag{6.1}$$

The distribution of the Optimal Observable for various CP-mixed scenarios of VBF $H \rightarrow \tau^+\tau^-$ events is shown in figure 6.1. The pure SM scenario is defined by $\tilde{d}$=0 and the corresponding distribution is symmetric with the mean value $< OO >= 0$. In case of CP-mixed scenarios, the distribution is skewed to negative (positive) values of the Optimal Observable with $< OO >\neq 0$ according to negative (positive) $\tilde{d}$ values. The following considerations help to understand the behavior of the shape of CP-odd observable distributions for different CP-mixed signal samples. Based on equation 2.50, the expectation value of the normalised Optimal Observable distribution is defined by

$$\begin{aligned} < OO > &= \frac{1}{\int d\sigma} \int OO \; d\sigma, \\ &= \frac{\int OO \; (d\sigma_{\text{SM}} + \tilde{d} \; d\sigma_{\text{CP-odd}} + \tilde{d}^2 \; d\sigma_{\text{CP-even}})}{\int (d\sigma_{\text{SM}} + \tilde{d} \; d\sigma_{\text{CP-odd}} + \tilde{d}^2 \; d\sigma_{\text{CP-even}})}, \\ &= \frac{\tilde{d} \int OO \; d\sigma_{\text{CP-odd}}}{\int d\sigma_{\text{SM}} + \tilde{d}^2 \int d\sigma_{\text{CP-even}}} \end{aligned} \tag{6.2}$$

exploiting the fact that the expectation value of the CP-odd Optimal Observable is zero for CP-even differential cross section terms and that the integral over CP-odd cross section terms vanishes. Equation 6.2 shows that the expectation value of OO is linear in $\tilde{d}$ for small $\tilde{d}$ values, while it approximates zero for larger values due to the quadratic term in $\tilde{d}$ in the denominator. That is, the pure CP-odd signal scenario results in a mean value $< OO >= 0$ as well as the pure SM case. This indicates that the corresponding mean value of the CP-odd observables presented in this analysis is especially sensitive to CP-violation for small $\tilde{d}$ admixtures.

The matrix elements, which are needed for calculating the Optimal Observable, are extracted from Hawk [171, 172] at LO accuracy. The input variables to the corresponding matrix element calculation are the four-momenta of both tagging jets and the Higgs boson and the Bjorken momentum fractions $x^{\text{Bjorken}}_{1/2}$ of both initial partons. These Bjorken values are calculated according to

$$x^{\text{Bjorken}}_{1/2} = \frac{M_{Hjj}}{\sqrt{s}} e^{\pm y_{Hjj}}, \tag{6.3}$$

under the assumption of energy and momentum conservation, where x^{Bjorken}_1 denotes the value for the incoming parton in the positive and x^{Bjorken}_2 in the negative z-direction. M_{Hjj} and y_{Hjj} are the invariant mass and the rapidity of the vectorial sum of the tagging jets and the Higgs boson four momenta. The Optimal Observable can then be calculated event-by-event at reconstruction

level. Since the flavour of the incoming and outgoing partons is unknown, the numerator and denominator in equation 6.1 is defined by the sum of matrix elements

$$\begin{aligned} 2Re(\mathcal{M}^*_{\text{SM}}\mathcal{M}_{\text{CP-odd}}) &= \sum_{ijkl} f_i(x_1)f_j(x_2)2Re\left(\mathcal{M}^{*ij\to klH}_{\text{SM}}\mathcal{M}^{ij\to klH}_{\text{CP-odd}}\right) \\ |\mathcal{M}_{\text{SM}}|^2 &= \sum_{ijkl} f_i(x_1)f_j(x_2)|\mathcal{M}^{ij\to klH}_{\text{SM}}|^2 \end{aligned} \quad (6.4)$$

over all parton flavour configurations $ij \to klH$, where each individual matrix element is weighted according to the PDF value f_i of the corresponding incoming parton i. The CT10 [88] PDF parametrization has been chosen for calculating the weighted sum.

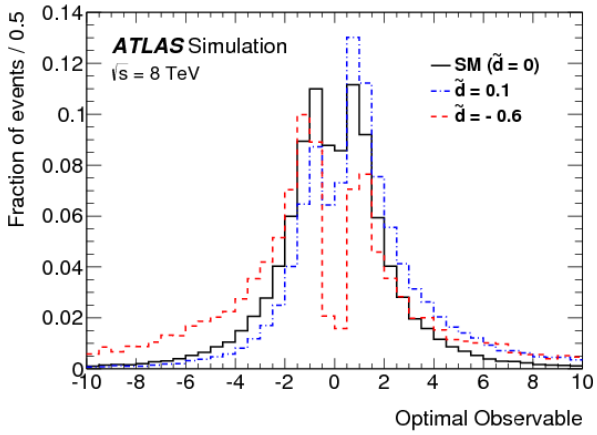

Figure 6.1. *Distribution of the Optimal Observable for VBF Higgs boson signal events for $\tilde{d} = -0.6, 0.0, 0.1$ at parton level. The SM signal sample was generated with the* MG5_aMC@NLO *[188] with LO accuracy. It is then re-weighted to the different CP-mixed scenarios. Following selection cuts at parton level are applied: at least two outgoing partons with $p^T_{p_1/p_2} > 25$ GeV within the detector acceptance of $|\eta_{p_1/p_2}| < 4.5$, invariant mass of $m_{p_1p_2} > 500$ GeV and a pseudo-rapidity gap $\Delta\eta(p_1, p_2) > 2.8$ [9].*

- **Signed $\Delta\Phi(j_1, j_2)$**

  The signed $\Delta\phi(j_1, j_2)$ variable is a simple CP-odd observable, which can be used to probe the HVV vertex structure in the VBF Higgs boson production mode as suggested in Ref. [189]. It is defined by

$$\epsilon_{ijkl} b^i_+ p^j_+ b^k_- p^l_- = 2p^T_+ p^T_- \sin\Delta(\phi_+ - \phi_-) = 2p^T_+ p^T_- \sin\Delta\phi(j_1, j_2). \quad (6.5)$$

  The indices $+/-$ denote the detector hemispheres in positive/negative direction of the beam axis. The variables $b^i_{+/-}$ indicate the four-momenta of the proton beams and $p^i_{+/-}$ the ones of the two tagging jets. $\phi_{x/-}$ are the azimuthal angles of the jets. The reconstructed jets point into different hemispheres,

i.e. events with two tagging jets measured in the same hemisphere are not considered in the analysis. The $\Delta\phi(j_1, j_2)$ variable is signed depending on the configuration of the outgoing jets (positive sign if the leading jet points into the hemisphere of the positive beam axis direction and vice versa) and is therefore a parity odd observable. Figure 6.2 illustrates the behavior of this variable at parton level.

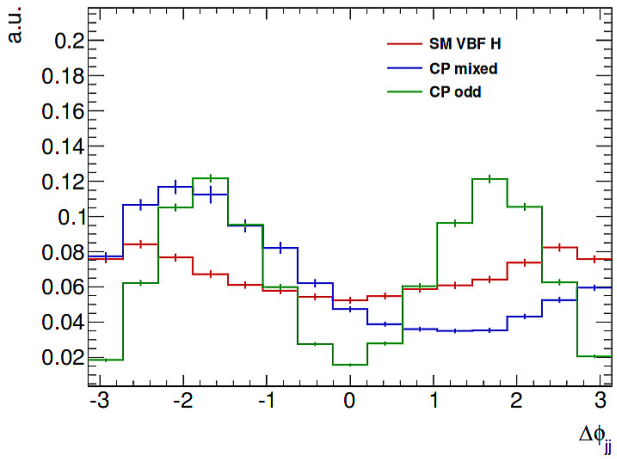

Figure 6.2. *Distribution of signed $\Delta\phi(j_1, j_2)$ for the SM, pure CP-odd and an arbitrary CP-mixed scenario. The distributions of the pure SM and the CP-odd scenario are symmetric while having different shapes. The shape of the CP-mixed scenario is shifted with a non-vanishing mean value.*

Similar to the Optimal Observable, the mean value of the distribution of the signed $\Delta\phi(j_1, j_2)$ vanishes in case of CP-even or CP-odd signal events and is non-zero for CP-mixed scenarios.

Testing CP-invariance can be achieved by measuring the mean value of the CP-odd observables and comparing the results to the prediction for different CP-mixed $\tilde{d}$ scenarios. In addition, a full likelihood fit to the differential distributions of the observables can be performed to determine central confidence intervals on $\tilde{d}$.

6.1.2. Modelling of the CP-violating Signal

The SM VBF Higgs boson samples are generated with Powheg+Pythia8 [81, 97] at NLO accuracy assuming a Higgs boson mass of $m_H = 125$ GeV as summarized in table 5.1.

The non-SM signal processes of the analysis include CP-odd admixtures to the tensor structure of the SM HVV vertex. Such anomalous couplings are described by the $\tilde{d}$ parameter. The corresponding samples are generated by re-weighting the SM signal sample, since a full simulation at various $\tilde{d}$ scan points would be too time and CPU consuming. The event weights w are based on the ratio of the

squared matrix element value for a CP-mixed scenario of the VBF Higgs boson signal (defined by a specific $\tilde{d}$ value) to the SM matrix element $w = |\mathcal{M}_{\tilde{d}}|^2/|\mathcal{M}_{\mathrm{SM}}|^2$. The Hawk [171, 172] program is used for calculating the LO SM and non-SM matrix elements. The input parameters of the matrix element calculation are the flavours of the initial partons, the flavour and four-momenta of the outgoing partons and the four-momentum of the Higgs boson. The Bjorken values $x_{1/2}^{\mathrm{Bjorken}}$, which describe the kinematics of the incoming partons, are then determined based on energy and momentum conservation (see equation 6.3). The simulated NLO events are categorized into $2 \to 2 + H$ and $2 \to 3 + H$ processes depending the number of outgoing partons and the LO matrix element is calculated accordingly.

The method of generating CP-mixed signal via re-weighting SM Higgs boson events is validated by comparing them with directly generated non-SM signal events. These samples are produced using the MG5_aMC@NLO [188] program, which is able to generate signal events from VBF Higgs boson production with anomalous couplings at NLO accuracy. Figure 6.3 shows a comparison of the Optimal Observable and signed $\Delta\phi(j_1, j_2)$ distributions using re-weighted and directly generated signal events. The re-weighting method proves to be a good approximation to a full NLO description of the non-SM processes with anomalous couplings. Remaining differences in the shape are taken into account as systematic uncertainties, as explained in section 8.3.1.

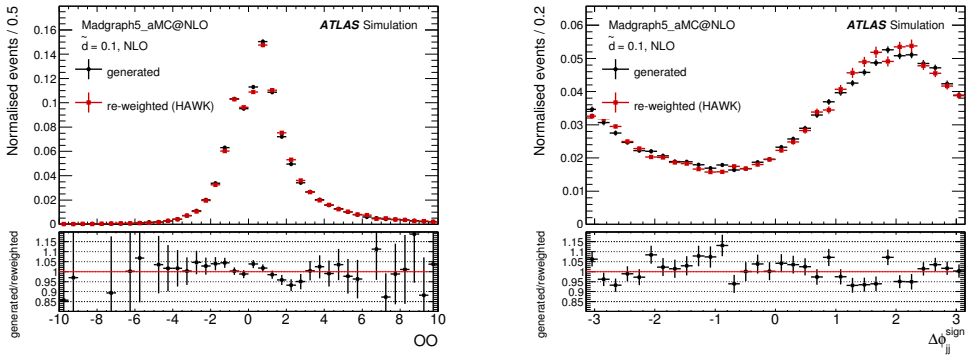

Figure 6.3. *Distribution of OO (a) and signed $\Delta\phi(j_1, j_2)$ (b) for $\tilde{d}$=0.1 at parton level. The CP-mixed sample in red is produced by re-weighing a SM sample and is compared to a directly generated sample for anomalous couplings. The SM and non-SM sample are both generated using* MG5_aMC@NLO *at NLO accuracy.*

6.1.3. Anomalous Couplings in the Decay

When testing CP-invariance in the HVV vertex, contributions of anomalous couplings do not only contribute to the production of the Higgs boson but also to the decay $H \to W^+W^-$. The effect of such contributions to the decay vertex on the

CP-odd observable is discussed in this section. Furthermore, it is assumed that the coupling of the Higgs boson to leptons and thus the $H \to \tau^+\tau^-$ vertex structure are SM-like.

In the present analysis, the relative contribution of signal events from VBF $H \to W^+W^-$ processes is approximately 20% compared to VBF $H \to \tau^+\tau^-$ and is therefore rather significant. A specific re-weighting has been applied to generate $H \to W^+W^-$ samples including anomalous couplings also in the decay. This re-weighting is used to study the impact of anomalous couplings on the distribution of the CP-odd observables. It is based on MG5 [190] matrix elements at LO accuracy and has been validated by using GGF instead of VBF $H \to W^+W^-$ processes assuming SM-like couplings in the GGF Higgs boson production vertex. Thus, the effect of anomalous couplings in the decay can be easily separated from the production part of the Higgs boson process. The validation of the re-weighting is then performed by comparing the re-weighted SM GGF $H \to W^+W^-$ events to non-SM events directly generated with MG5. Figure 6.4 shows the distribution of $\Delta\phi$ between the two final state leptons, which is sensitive to anomalous couplings in the decay $H \to W^+W^- \to \ell\nu\ell\nu$. In the comparison of both samples, a relatively large $\tilde{d}$ value of 1 has been chosen to validate the re-weighting for better illustration. The re-weighted sample is found to match the directly generated one and can therefore also be applied to the VBF Higgs boson signal sample as discussed below.

The impact of anomalous couplings in the decay on the Optimal Observable is estimated by comparing SM VBF $H \to W^+W^-$ signal events with the same sample but re-weighted to a relatively extreme scenario of $\tilde{d}$=0.5 for the decay. Since the CP-mixed weights for the production and the decay factorizes, the re-weighted test sample takes only anomalous couplings in the decay into account while keeping the production vertex SM-like. The observed differences shown in figure 6.5 are an estimate for the impact of anomalous couplings in the decay on the Optimal Observable. Since the differences are small and within statistical uncertainties, the specific additional re-weighting of the decay vertex in $H \to W^+W^-$ events can be neglected in the present analysis.

6.2. Background processes

SM Higgs boson samples for the VH and GGF mode are treated as background components. GGF H+1jet events have been generated with Powheg at NLO accuracy with the scale evolved according to the MINLO procedure Minlo [191, 192]. Furthermore, Pythia8 was used for parton shower and the PDF is parametrized according to CT10 [88]. This differs from the GGF Higgs boson sample used in the search for $H \to \tau^+\tau^- \to \ell^+\ell^-4\nu$ since the Minlo sample is expected to provide a better modeling for GGF events in the VBF-like phase space region.

The estimation of further background processes is fully consistent with the one from the analysis of the search for $H \to \tau^+\tau^- \to \ell^+\ell^-4\nu$. Top quark, $Z \to e^+e^-/\mu^+\mu^-$ and di-boson processes are taken from simulation with the normalisation

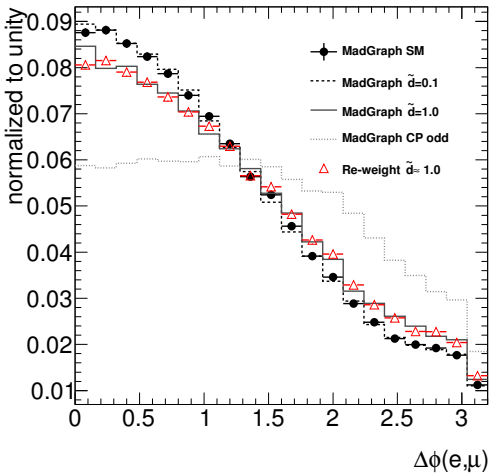

Figure 6.4. *Comparison of the $\Delta\phi(e,\mu)$ distribution in the fully leptonic GGF $H \to W^+W^-$ decay channel for various $\tilde{d}$ CP-mixed scenarios. The samples in black are directly generated with* MG5 *for $\tilde{d}$=0.1,1.0, pure SM ($\tilde{d}$=0) and CP-odd ($\tilde{d}$=∞) scenarios. The sample in red is the re-weighted SM sample for $\tilde{d}$=1.0.*

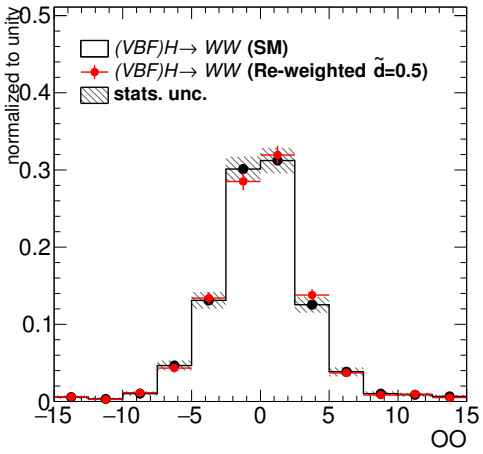

Figure 6.5. *Comparison of the Optimal Observable in the fully leptonic VBF $H \to W^+W^-$ decay channel. Pure SM events are shown in black and re-weighted SM events for $\tilde{d}$=0.5 in red, which include anomalous couplings in the decay only while keeping the production vertex SM-like.*

of the corresponding background samples being estimated using data control regions. $Z \to \tau^+\tau^-$ and fake lepton processes are estimated in a data-driven way. Information about event generators and cross section predictions is summarized in table 5.1. Details about the validation of the different background estimation approaches can be found in chapter 7.

Category	Selection Cuts
CP	Preselection A second jet with $p_{\mathrm{T}}^{j_2} > 30$ GeV $\Delta\eta(j_1, j_2) > 2.2$ $\mathrm{score}_{\mathrm{BDT}}^{\mathrm{VBF}} > 0.68$ $\lvert OO\rvert < 15$

Table 6.1. *Summary of the event selection of the CP analysis. The selection follows closely the VBF category of the analysis of the search for $H \to \tau^+\tau^- \to \ell^+\ell^- 4\nu$ (see chapter 5).*

6.3. Event Selection

The present analysis exploits the VBF category of the analysis of the search for $H \to \tau^+\tau^- \to \ell^+\ell^- 4\nu$ to test the CP-invariance in the HVV couplings. The event selection of the CP analysis consists of the same lepton and trigger selection criteria as well as the preselection and the VBF categorization as quoted in chapter 5. At least two tagging jets are required with $p_T^{j_{1/2}} > 40/30$ GeV with a pseudo-rapidity gap of $\Delta\eta(j_1, j_2) > 2.2$. In the VBF category, BDTs were trained to separate VBF Higgs boson signal from background processes. An additional cut on this BDT classifier is introduced to enhance the number of signal events from VBF Higgs boson processes. The signal region of the CP analysis is defined as the three most signal-like bins of the BDT classifier in the VBF category according to the binning that was chosen for the fit in the search for $H \to \tau^+\tau^- \to \ell^+\ell^- 4\nu$ analysis. This corresponds to a cut value of $\mathrm{score}_{\mathrm{BDT}}^{\mathrm{VBF}} > 0.68$. The aim of the analysis is the determination of a central confidence interval of the $\tilde{d}$ CP-mixed parameter, based on maximum likelihood fits to the Optimal Observable or alternatively the signed $\Delta\phi(j_1, j_2)$ distribution in this region. Since the relative statistical uncertainties on background event yields for high absolute values of the Optimal Observable become very large, an additional cut of $|OO| \leq 15$ is applied. The definition of the signal region is quoted in table 6.1.

The expected number of background events in the signal region is 37.3 ± 2.4 including also non-VBF SM Higgs boson events, where $Z/\gamma^* \to \tau^+\tau^-$ is the dominant background contribution. The number of expected SM signal VBF Higgs boson events is 6.3 ± 0.1. Statistical uncertainties are quoted here. In total, 54 data events are observed, which indicates an excess with respect to the background only hypothesis as expected from the search for the $H \to \tau^+\tau^-$ analysis. The expected event yields for the SM signal of VBF $H \to \tau^+\tau^-/W^+W^-$ processes and all background contributions in the signal region of the CP analysis are given in table 6.2. In case of using signed $\Delta\phi(j_1, j_2)$ as final discriminant, events are rejected where both jets emerge in the same hemisphere as discussed in section 6.1.1. The fraction of events in the signal region, which are rejected due to the usage of signed $\Delta\phi(j_1, j_2)$, is approximately 1% for signal and 10% for background processes and the number of expected event in table 6.2 decreases accordingly.

Process	Expected Number of Events
$(VBF)H \to \tau^+\tau^-$ (SM)	5.21 ± 0.04
$(VBF)H \to W^+W^-$ (SM)	1.04 ± 0.04
$Z/\gamma^* \to \tau^+\tau^-$	19.5 ± 1.5
$t\bar{t}$	3.5 ± 0.8
$Z/\gamma^* \to e^+e^-$	3.7 ± 1.0
$Z/\gamma^* \to \mu^+\mu^-$	4.3 ± 0.8
Di-boson	2.5 ± 0.9
Fake leptons	2.2 ± 0.7
(non-VBF)$H \to \tau^+\tau^-/W^+W^-$	1.6 ± 0.1
Total Signal (SM)	6.25 ± 0.06
Total Background	37.3 ± 2.4
Data	54

Table 6.2. *Expected event yields in the signal region of the CP analysis. The signal event yields are quoted for SM prediction. The samples have been generated and normalised with the event generators and cross section according to table 5.1. A Higgs boson mass of* $m_H = 125$ GeV *is assumed for all signal processes.* $Z \to \tau^+\tau^-$ *and fake lepton background contributions are estimated data-driven. Uncertainties are statistical only.*

The cut on the VBF BDT classifier of $\text{score}_{\text{BDT}}^{\text{VBF}} > 0.68$ was chosen such that the simple statistical counting significance (see section 9.2) is optimized while keeping a reasonable amount of statistics according to at least one expected event in the sample for each background contribution. The cut values were chosen to agree with the bin edges of on the binning used in the fit to the BDT classifier distribution in the search for $H \to \tau^+\tau^- \to \ell^+\ell^- 4\nu$. The statistical significance $\mathcal{Z}_0$ as function of the cut on the BDT classifier is shown in figure 6.6. The decrease in significance by choosing three instead of less bins of the signal-like BDT classifier values is moderate.

The relative selection efficiencies for signal events in the VBF category to appear in the signal region of the CP analysis, due to the cut on the BDT classifier, are listed in table 6.3. The change in the efficiency is moderate and ranges from approximately 48% for the SM signal scenarios to 44% for more extreme CP-mixed scenarios with $\tilde{d}$=-0.6. By applying the BDT cut, the total background yield is reduced to approximately 4% of the expected background in the search analysis. The shape of the BDT classifier distribution is not significantly affected by the various scenarios. Furthermore, the observed event yield is not used in the fit to constrain $\tilde{d}$.

Since fits to the CP-odd observables are performed for various $\tilde{d}$ scenarios, it must be ensured that the cut on the BDT classifier does not bias the shape of the observables. Figure 6.7 shows the dependency of the Optimal Observable as a function of the BDT classifier range. The mean value of the Optimal Observable fluctuates around zero within $| < OO > | < 0.2$, which is in reasonable agreement with statistical

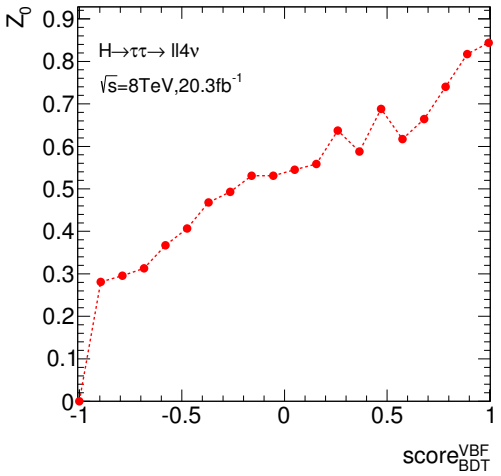

Figure 6.6. *Statistical counting significance as function of the cut on the BDT classifier in the VBF category.*

uncertainties, for the pure SM VBF Higgs boson signal and the total background expectation. In addition, the RMS of the distribution of the Optimal Observable for signal events can be approximated by a constant mean value of 3.4. This behavior indicates, that the Optimal Observable properties do not depend significantly on the BDT classifier. Therefore, the chosen cut on the classifier is a valid approach to define a signal-enhanced region to test the CP-invariance using the Optimal Observable. Similar behavior is observed for the alternative CP-odd variable signed $\Delta\phi(j_1, j_2)$.

Figure 6.8 shows the distributions observed and predicted for both CP-odd observables, the Optimal Observable and signed $\Delta\phi(j_1, j_2)$, in the signal region of the CP analysis. As expected from the analysis of the search for $H \to \tau^+\tau^-$, an excess is observed in data compared to the full background model. The number of bins and the bin width are found to be optimal in terms of maximal sensitivity and stable fit results. The final fit to the observables and the measured central confidence interval with respect to the $\tilde{d}$ parameter are presented in section 10.2.

The fit model includes additional control regions according to the analysis of the search for $H \to \tau^+\tau^- \to \ell^+\ell^- 4\nu$. The dedicated top quark and $Z \to e^+e^-/\mu^+\mu^-$ enriched regions of the VBF category control the normalisation of the corresponding

Signal Scenario	Rel. Selection Eff. [%]
$\tilde{d}$=0.0 (SM)	48.4 ± 0.5
$\tilde{d}$=0.1	47.6 ± 0.5
$\tilde{d}$=-0.6	44.0 ± 0.5

Table 6.3. *Relative selection efficiencies of the BDT classifier cut for the sum of expected $H \to \tau^+\tau^-/W^+W^-$ events for different CP-mixed scenarios.*

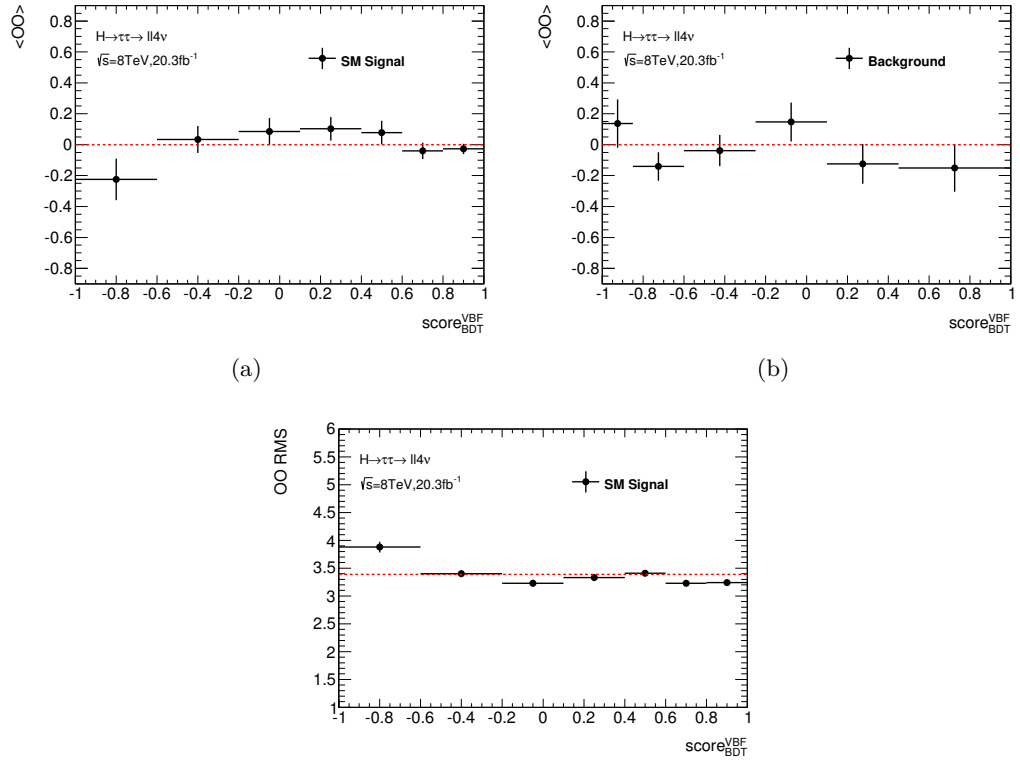

Figure 6.7. *Mean value of the Optimal Observable distribution in the signal region of the CP analysis for signal (a) and background (b) events and the RMS of the Optimal Observable distribution for signal events (c). The uncertainties include the statistical error on the mean and the RMS value in each case.*

samples. The definitions are summarized in table 7.2. Furthermore, the distribution of the VBF BDT classifier in an orthogonal background-like region defined by $\text{score}_{\text{BDT}}^{\text{VBF}} < 0.05$ orthogonal to the signal region is included. This control region is added to constrain the dominant $Z/\gamma^* \to \tau^+\tau^-$ background contribution. In case of the search analysis, this is mainly achieved by performing the fit also in the Boosted category, which includes a much larger amount of statistics and is not included in the CP analysis. The distribution in this region corresponds to the 10 most background-like bins of the BDT classifier distribution, which was used in the fit for the VBF category of the search analysis. To reduce the impact of statistical fluctuations, the classifier distribution in this low BDT control region is re-binned by a factor of two. This results in 5 equidistant bins, which are used in the final fit of the CP analysis in addition to the signal and the control regions for top and $Z \to e^+e^-/\mu^+\mu^-$ background, that consider only event yields but not the Optimal Observable distribution. Each control region contains a cut on $|OO| < 15$ to take the efficiency of the corresponding cut in the signal region into account. The modeling of the Optimal Observable and the signed $\Delta\phi(j_1, j_2)$ distributions in the

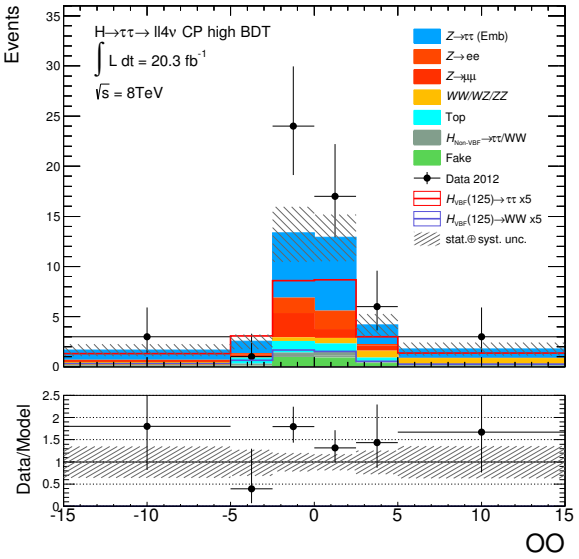

(a)

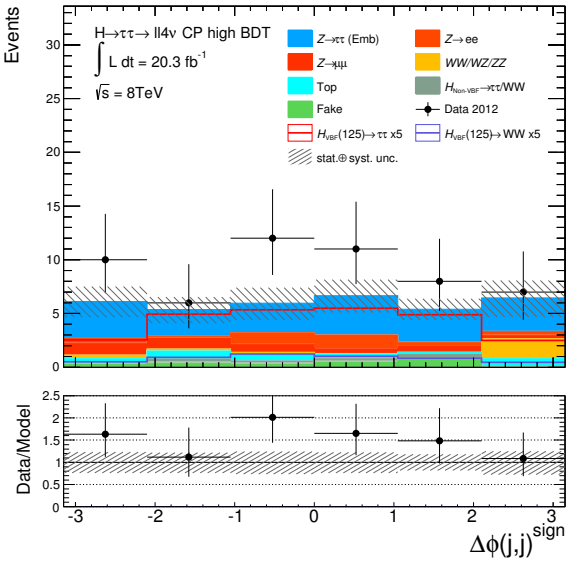

(b)

Figure 6.8. *Optimal Observable (a) and signed $\Delta\phi(j_1, j_2)$ distribution (b) of the background model in the signal region of the CP analysis compared to the observed data. The error bar contains statistical and systematic normalisation uncertainties.*

various control regions is in good agreement with the observed data as shown in section 7. The description of systematic uncertainties follows the search analysis except for some additional nuisance parameters, which are discussed in chapter 8.

7 Background Modeling

The chapter addresses the background model in the analysis of the search for the Higgs boson in the decay $H \to \tau^+\tau^- \to \ell^+\ell^- 4\nu$ and the measurement of its CP properties. The estimation of background processes follows the same methodology in both analyses. Figure 7.1 displays the composition of the backgrounds in terms of relative fractions for each background component in the VBF and Boosted category and the CP analysis.

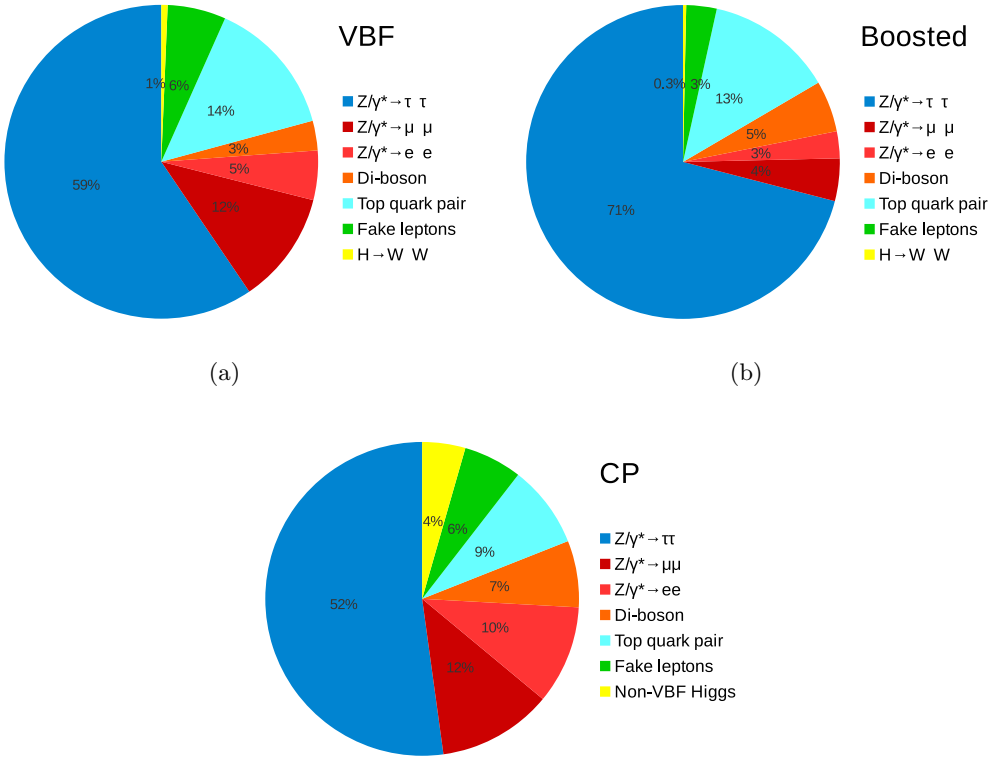

Figure 7.1. *Background composition in the VBF and Boosted category and in the signal region of the CP analysis. In case of the CP analysis, the non-VBF Higgs background component contains contributions from* $(GGF/V)H \to \tau^+\tau^-/W^+W^-$.

The irreducible $Z/\gamma^* \to \tau^+\tau^-$ background is the dominant component in all signal

regions and is estimated in a data-driven way, using the *Embedding* method (see section 7.1). Furthermore, single Z boson production processes or di-boson events, including prompt leptonic vector boson decays, contribute significantly to the overall background composition (see section 7.2 and 7.3) as well as top quark pair production processes (see section 7.4). The corresponding background events are simulated while the sample normalisation is estimated using control regions in data. A further non-negligible background component at the LHC covers events with *fake* leptons, which are mainly due to the mis-identification of jets. Typical sources of fake leptons are QCD multi-jet, top quark and W boson production processes with less than two prompt real leptons in the final state (see section 7.5). The fake lepton background estimation is based on data. In addition, there is also a smaller contribution from fully leptonic $H \to W^+W^-$ decays, which mimic events from the $H \to \tau^+\tau^-$ signal process (see section 7.6).

7.1. $Z/\gamma^* \to \tau^+\tau^-$

The decay of the Z boson into two τ leptons is an irreducible background in the present analyses. The relative contribution to the overall background yield is about 59% in the VBF category, 71% in the Boosted category and about 52% in the signal region of the CP analysis. Thus, $Z/\gamma^* \to \tau^+\tau^-$ is the largest background component in all categories and a reliable model of these processes is of utmost importance. The corresponding background estimation is therefore based on a data-driven technique called the Embedding method [7].

The basic idea of the Embedding method consists of the selection of $Z/\gamma^* \to \mu^+\mu^-$ events from data and the replacement of both reconstructed muons in these events with τ leptons, whose decay into electrons or muons is then simulated. The resulting events with this replacement can be used to represent the $Z/\gamma^* \to \tau^+\tau^-$ background. The method is justified by lepton universality and approximately identical Z boson, jet and lepton kinematics. The benefit of the Embedding method is the extraction of essential event properties from data rather than from simulation because the corresponding $Z/\gamma^* \to \mu^+\mu^-$ data control region is basically free of signal[1]. These properties include Z boson and jet kinematics, pile-up and underlying event effects. This improves the estimation of selection efficiencies and the description of the BDT input variables especially in boosted or VBF-like phase space regions, where a robust modeling of jets is required. Furthermore, the usage of data-driven background estimation techniques reduces the number of systematic uncertainties that need to be considered, whether they be experimental (e.g. energy scale or resolution of simulated jets) or theoretical (e.g. the modeling of the Z boson p_{T} spectrum in simulated events). Since $Z/\gamma^* \to \tau^+\tau^-$ is an irreducible background component, it is very difficult to define dedicated control regions where signal-contributions are negligible, in order to validate or correct the modeling from MC samples.

[1] The branching ratio of $H \to \mu^+\mu^-$ is about 10^{-5} and therefore negligible in the analysis.

In summary, the Embedding method provides a minimally biased sample of $Z/\gamma^* \to \tau^+\tau^-$events based on a very pure $Z/\gamma^* \to \mu^+\mu^-$ control region. The basic selection of $Z/\gamma^* \to \mu^+\mu^-$ events as well as further event modifications within the Embedding method cause a loss of information about the absolute normalisation of the Embedding sample. Therefore, it is normalised to the simulated $Z/\gamma^* \to \tau^+\tau^-$ ALPGEN sample after basic event cleaning, di-lepton and the analysis trigger requirements for each final state individually[2]. However, the normalisation for this background estimate is entirely unconstrained in the final fit.

7.1.1. Embedding Method

The Embedding method is divided into several technical steps: the $Z/\gamma^* \to \mu^+\mu^-$ selection in data, the replacement of muons with τ leptons and the simulation of the subsequent decay, the removal of the original muon track and calorimeter information from the data event, the merging of the original data and the Z decay into τ leptons and the re-reconstruction of the final hybrid event. The sequence of the Embedding method consists of five steps, which are illustrated in the flow chart in figure 7.2.

1. *Selection of $Z/\gamma^* \to \mu^+\mu^-$ data events*

   As input for the Embedding method, $Z/\gamma^* \to \mu^+\mu^-$ events from collision data are used according to the selection summarized in table 7.1. Events are selected by a di-muon trigger with the threshold of 18 GeV for the leading and 8 GeV for the sub-leading muon or a single-muon trigger with the threshold of 24 GeV. Two reconstructed muons with opposite charge, exceeding the p_T thresholds of 20 GeV for the leading and 15 GeV for the sub-leading muon, are required. The muon reconstruction is explained in detail in section 4.4. Both muons must satisfy the relative track isolation criterion $p_T^{\mathrm{cone}\Delta R}/p_T^{\mu} < 20\%$ with $\Delta R = 0.4$. The invariant mass of the muon pair must exceed at least 40 GeV. If there are three or more muons in the event, the two muons with a common vertex, whose invariant mass is closest to the mass of the Z boson, are chosen as seed for the Embedding method.

2. *Z boson decay into τ leptons*

   Firstly, the four-momentum of each of the reconstructed muons is extracted from the data event.

   The muons are then transformed in a second sub-step into τ leptons by rescaling the muon momenta according to $p_\tau = \sqrt{E_\mu^2 - m_\tau^2}$. Here, the energy E_μ of the τ leptons is kept unchanged while the mass is changed appropriate to the value m_τ, with the transverse momentum scaled accordingly. The production vertex of the τ leptons is set equal to the one of the original muons.

[2] Same flavour final states contain two electrons ee or muons $\mu\mu$ while the different flavour final states contain one electron and one muon $e\mu$ or μe, where the first lepton denotes the one with the higher transverse momentum.

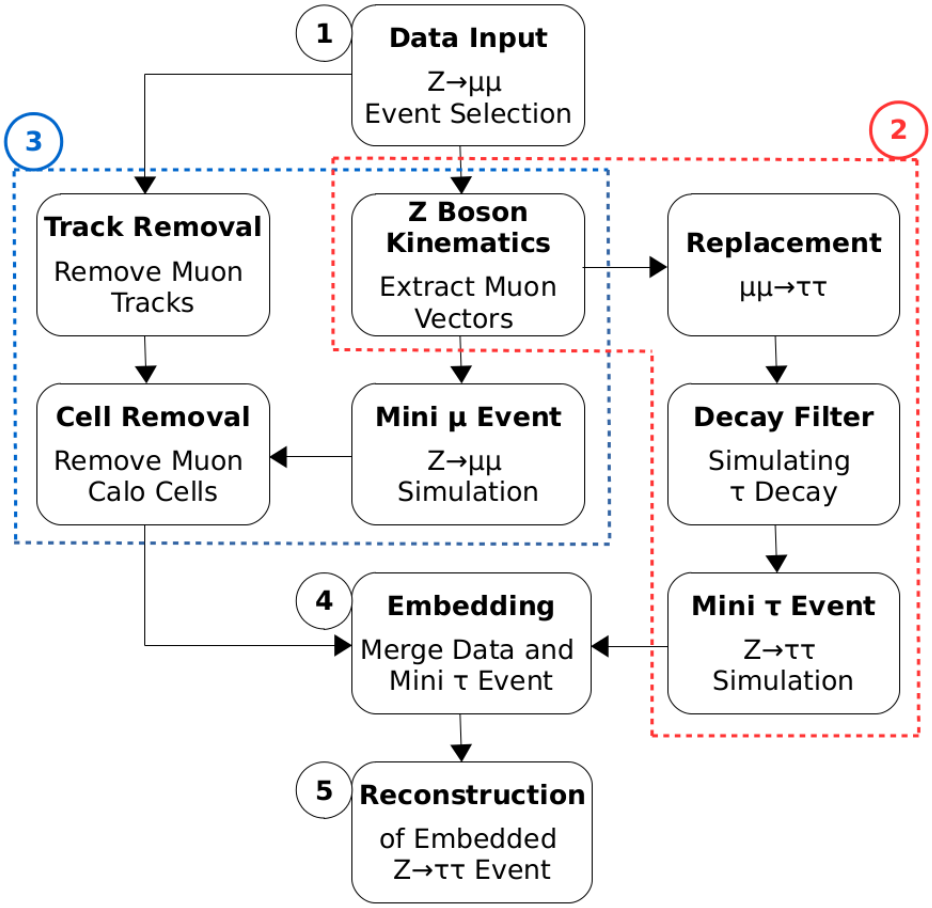

Figure 7.2. *Flowchart of the Embedding method.*

Thus, the decay of the Z boson into a pair of muons has been transformed into a Z boson decay into τ leptons.

Third, the decay of each of the τ leptons into an electron or a muon is simulated with the Tauola [100] program, which takes spin correlations and polarization effects of the τ leptons into account. The polarization of the Z boson is chosen to be randomly distributed by Tauola according to an average polarization of zero, since the parton configuration in the initial state cannot be accessed directly here. Event-based correction weights are applied using the TauSpinner program [193, 194], which accounts for the actual non-zero average Z boson polarization. TauSpinner determines the most probable initial state parton configuration based on the kinematics of the Z boson decay products. Furthermore, the Photos [99] program simulates QED photon radiative corrections in the τ lepton decay.

A large number of final state electrons and muons, which are generated in the simulated decay of the τ leptons by Tauola, fall below the analysis

Selection	Definition
$Z/\gamma^* \to \mu^+\mu^-$ Embedding input	Trigger *mu18_tight_mu8_EFFS* or *EF_mu24i_tight*, at least two muons with opposite charge, $p_T^{\mu,1/2} > 20/15$ GeV, isolated muons using $p_T^{\text{cone}\Delta R}/p_T^{\mu} < 20\%$ with $\Delta R = 0.4$, $m_{\mu\mu} > 40$ GeV
High Statistics $Z/\gamma^* \to \tau^+\tau^-$ control region	Analysis triggers, at least two leptons with opposite charge, different flavour final states only, $p_T^{\ell,1/2} > 25/20$ GeV, $40 \text{ GeV} < m_{\ell\ell} < 85$ GeV $p_T^{\ell,1} + p_T^{\ell,2} + E_T^{\text{miss}} + \sum_i p_T^{j,i} < 150$ GeV $\cos\Delta\phi(\mathbf{E}_T^{\text{miss}}, \mathbf{p}_T^{\ell,1}) + \cos\Delta\phi(\mathbf{E}_T^{\text{miss}}, \mathbf{p}_T^{\ell,2}) > -0.7$, Events with a b-tagged jet with $p_{\text{T}} > 25$ GeV are rejected
Dedicated VBF/Boosted control regions	Preselection, VBF or Boosted category requirements, $m_{\ell\ell}^{\text{HPTO}} < 100$ GeV

Table 7.1. *Selection criteria used in the Embedding method for selecting $Z/\gamma^* \to \mu^+\mu^-$ data events as input and further control region definitions for validating the Embedding sample. Event cleaning cuts are required in all cases.*

offline p_T thresholds. That is, a substantial amount of events in the original $Z/\gamma^* \to \mu^+\mu^-$ dataset would be lost. Therefore, a decay filter is implemented in a fourth sub-step, forcing the final state electrons to be above a p_T threshold of 12 GeV and muons above 8 GeV. 1000 decay configurations of the di-τ system are simulated by TAUOLA in each event. The first decay configuration passing the offline thresholds is then chosen as final state for further processing. In addition, the decay filter efficiency is determined by dividing the number of configurations passing the offline thresholds by the number of total simulated decay configurations. This filter efficiency is then applied as an event weight to correct the bias from the TAUOLA p_T filter.

Finally, the $Z/\gamma^* \to \tau^+\tau^-$ mini-event, which does not contain pile-up and underlying-event effects or additional physics objects apart from the τ lepton decay products, is then processed with the full ATLAS detector simulation and reconstruction. During detector simulation, the calorimeter noise is turned off because it is already included in the original data event, which is merged with the mini-event later on.

3. *Removal of muon tracks and calo cells*

Before merging the $Z/\gamma^* \to \tau^+\tau^-$ mini-event and the original $Z/\gamma^* \to$

$\mu^+\mu^-$ data event, the data event must have the original muons from the Z boson decay removed. Corresponding muon tracks are thus removed from the event. Then, energy deposits in the calorimeter associated to muons are also removed from the event. For this purpose, a $Z/\gamma^* \to \mu^+\mu^-$ mini-event is simulated based on the same kinematics of the Z boson decay into muons from the original event to estimate the corresponding energy deposits in the calorimeter cells. Calorimeter noise is turned off in this case. These cell energies in the mini-event are then subtracted from the original data event. Thus, the remaining data event contains pile-up and underlying-event effects as well as all physics objects except for those from the original Z boson decay products.

4. *Embedding*

   In this step, the $Z/\gamma^* \to \tau^+\tau^-$ mini-event is embedded into the cleaned data event. Therefore, all tracks in the mini-event are copied to the data event. The cell energies in the mini-event are added to the cell energies of the data event. The result of this merging step is a hybrid event, which contains a simulated $Z/\gamma^* \to \tau^+\tau^-$ process within the real data environment.

5. *Reconstruction of the hybrid event*

   The Embedding hybrid event is passed again to the reconstruction algorithm, that is a re-reconstruction of the $Z/\gamma^* \to \tau^+\tau^-$ process is performed. This is necessary because additional energy deposits in the calorimeter due to pile-up or underlying-event effects from the cleaned data event might influence the value of $\mathbf{E}_T^{\text{miss}}$ from the mini-event, which is only based on the neutrinos from the τ decay. In this final event re-reconstruction step, all physics objects are recreated except for charged particle tracks since the effect here is assumed to be negligible in the present analyses. The basic steps of the Embedding method is illustrated in a sequence of event displays in figure 7.3.

Potential caveats of the Embedding method are discussed in more detail in the next section 7.1.2.

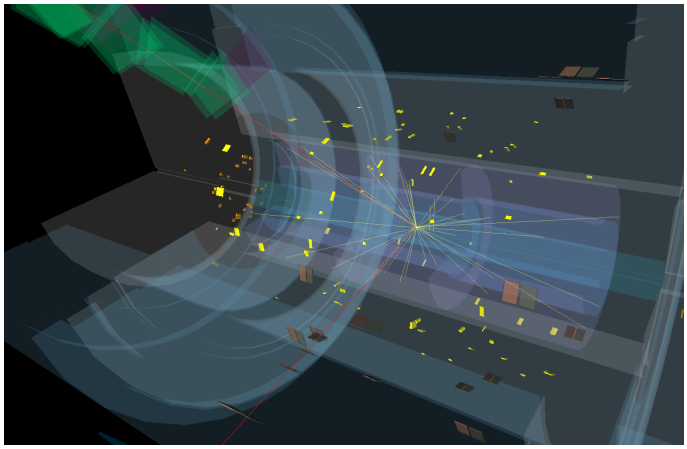

(a)

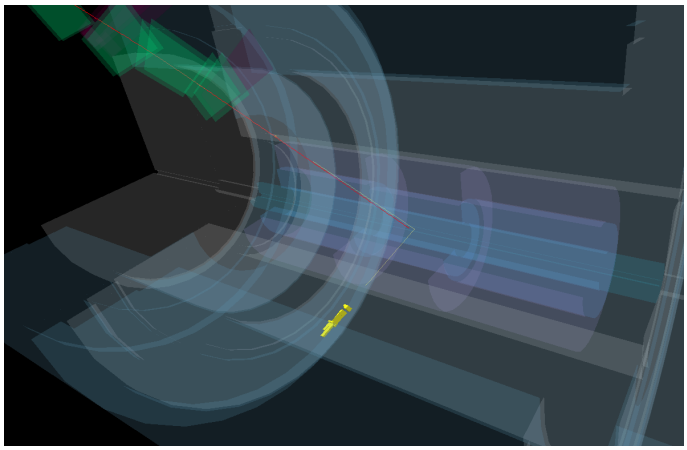

(b)

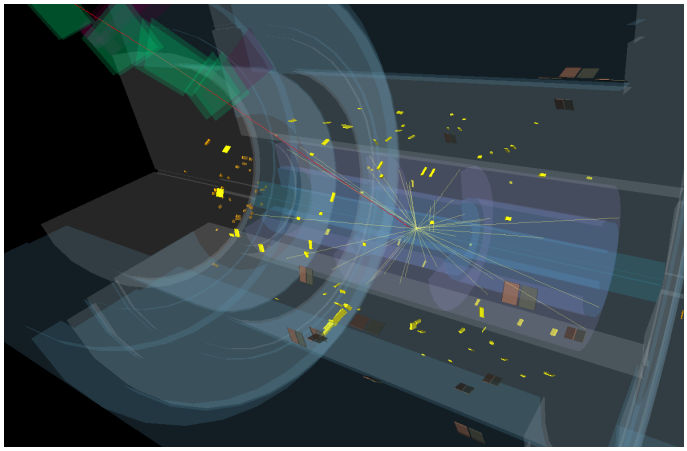

(c)

Figure 7.3. *Event displays for basic steps in the Embedding method: the original $Z/\gamma^* \to \mu^+\mu^-$ data event (a), the $Z/\gamma^* \to \tau^+\tau^-$ mini-event with the upper τ lepton decaying into a muon and the lower one into an electron indicated by the yellow cluster (b) and the final Embedding hybrid event $Z/\gamma^* \to \tau^+\tau^- \to e^+\mu^-$ (c). Inner detector tracks in light yellow, muon tracks in red, ECAL clusters in yellow, Tile cell deposits in brown, traversed muon spectrometer segments in green.*

7.1.2. Corrections

The $Z/\gamma^* \to \tau^+\tau^-$ Embedding sample is based on the full 8 TeV dataset. It is treated as collision data with additional corrections, that are needed to compensate potential caveats of the Embedding method. These corrections are summarized in the following section.

- *τ Decay Filter*

  As already explained in section 7.1.1, the τ decay products in the $Z/\gamma^* \to \tau^+\tau^-$ mini-event simulated with Tauola are forced to exceed certain p_T thresholds to avoid a decrease in statistics. The resulting bias in the kinematics of the decay products is corrected by applying the Tauola filter efficiency as an event weight. This efficiency is calculated in each event on-the-fly by simulating 1000 decays of the corresponding di-τ lepton configuration while counting the number of decays, in which the decay products exceed the p_T thresholds. Figure 7.4 shows the sum of transverse momenta of the neutrinos in the event for the unfiltered and filtered samples before and after applying the correction. In case of the filtered sample without correction, the distribution is shifted to smaller values of $\sum p_T^{\nu}$ because the leptons from the τ decay are forced to have larger transverse momenta, which decreases the neutrino momenta by trend. The corrected filtered sample is then again in good agreement with the unfiltered one, which validates the filter correction that is finally applied in the analysis.

- *Z Boson Polarization*

  The polarization of the Z boson is not taken into account correctly in the simulation of the τ lepton decay, because the initial parton configuration for the production of the Z boson is unknown at this stage in the Embedding method (see section 7.1.1). The Tauola program initially assumes an average polarization of zero, which is corrected by applying event weights accounting for the actual non-zero average polarization. These event weights are based on TauSpinner, which determines the most probable initial state configuration depending on the kinematics of the τ lepton decay products. The effect of the Z boson polarization is shown in figure 7.5. The distribution of $m_{\ell\ell}$ at parton level for an unpolarized $Z/\gamma^* \to \tau^+\tau^-$ sample before and after applying the correction is compared to a sample including polarization effects. A clear improvement is visible when applying the polarization correction.

- *Resolution and FSR Effects*

  An intrinsic feature of the Embedding method is the impact of detector resolution effects of the original reconstructed muons on the Z boson kinematics in the Embedding events. Final state radiation from the original muons might bias the kinematics of the Z boson as well.

  To study the resolution and FSR effects, alternative Embedding samples have been generated [7]. Figure 7.6(a) compares the visible di-muon mass

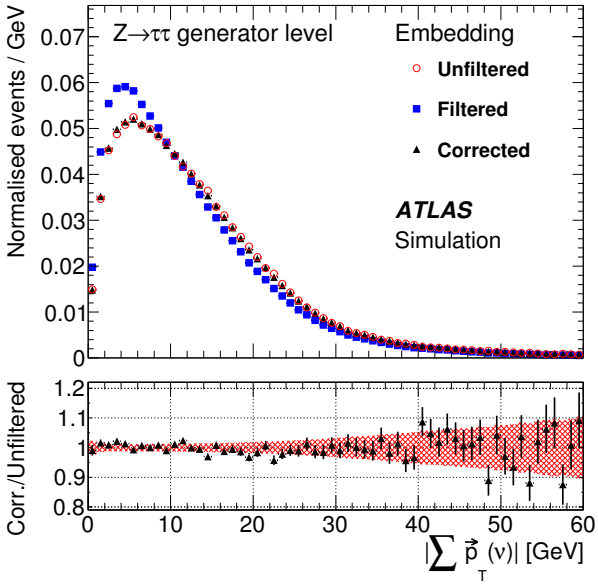

(a)

Figure 7.4. *Distribution of the summed transverse momenta of all neutrinos for Embedding events at generator level without the* TAUOLA *filter (red), applying the filter (blue) and correcting the filtered sample with the corresponding filter efficiencies per event (black) [7].*

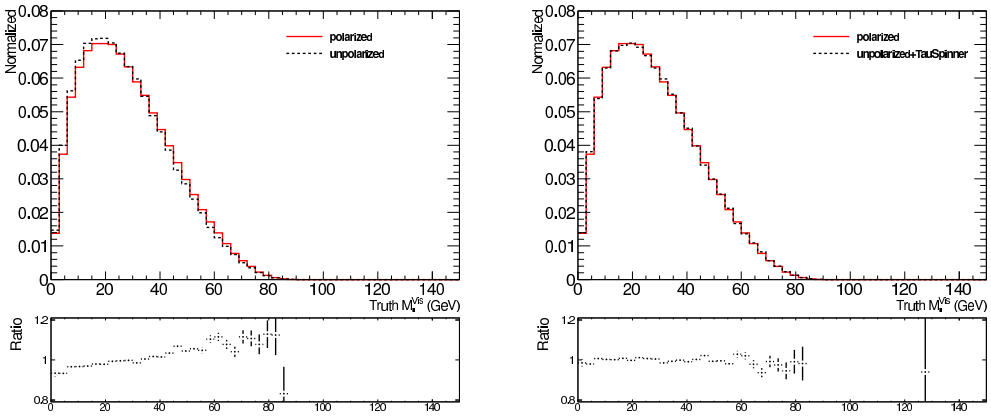

(a) (b)

Figure 7.5. *Comparison of the visible mass of the leptonic τ lepton decay products for unpolarized and polarized $Z/\gamma^* \to \tau^+\tau^-$ events (a). Performance of the* TAUSPINNER *corrections(b).*

of $Z/\gamma^* \to \mu^+\mu^-$ events from data with an Embedding sample, where the original data muons are replaced with simulated muons in contrast to τ leptons such as in the default Embedding method ($\mu \to \mu$ Embedding). A significantly

broader distribution in case of the Embedding sample is observed due to the doubling of the muon reconstruction resolution and FSR.

To prove this assumption, figure 7.6(b) shows the same comparison using a sample, where the $\mu \to \mu$ Embedding is performed on a simulated $Z/\gamma^* \to \mu^+\mu^-$ Alpgen sample instead of real data. Simulated samples allow access to information at the generator level, where there is an absence of detector resolution effects. Here, generated muons are used in the Embedding method before reconstruction and FSR. No discrepancies are observed when comparing the visible di-muon mass of these generator seeded $\mu \to \mu$ Embedding events with the fully simulated $Z/\gamma^* \to \mu^+\mu^-$ Alpgen sample.

Nevertheless, figure 7.6(c) indicates that the impact of such effects on the present analyses is negligible due to the much larger di-τ mass resolution: a $\mu \to \tau$ Embedding sample, based on simulated $Z/\gamma^* \to \mu^+\mu^-$ input events at generator level, is compared to the corresponding Embedding sample using reconstructed muons as seeds. Both distributions agree well within uncertainties and thus no muon resolution nor FSR corrections are needed in the analyses.

- *Background Contamination*

  The input data sample used in the Embedding method contains two reconstructed muons is basically free of signal. The fraction of $H \to \tau^+\tau^-/W^+W^-$ events in the corresponding control region is at the sub-permille level as can be seen in figure 7.7. However, the sample does not purely consist of $Z/\gamma^* \to \mu^+\mu^-$ processes. There is a residual contamination from top quark events and di-boson production with two reconstructed final state muons. Such events might be double counted in the present analyses after replacing the muons with τ leptons once in the Embedding sample and additionally in the specific top quark and di-boson background sample.

  To estimate the impact of such double counted di-τ events in the analysis, the expected number of top quark and di-boson events containing at least two τ leptons at generator level, fulfilling the Embedding input selection cuts $p_T^{\mu,1/2} > 20/15$ GeV, $|\eta^{\mu,1/2}| < 2.5$ and $m_{\mu\mu} > 40$ GeV(if more than two τ leptons are present in the event, the di-τ combination with an invariant mass closest to the Z boson mass is chosen), has been evaluated in the VBF and Boosted category. The fraction of potentially double counted events in the di-boson sample is about 10% (15%) and in the top quark sample about 3% (2%) in the VBF (Boosted) category. Figure 7.8 shows the BDT score distribution of these events. While the fraction of di-τ events is negligible in case of the top quark sample, a much larger fraction is present in the di-boson sample. However, the total yield of di-boson events is relatively small in the present analyses and the subset of di-τ events is still in the order of the statistical uncertainty of the total di-boson prediction per bin. Therefore, the effect is deemed to be negligible, and no additional correction is applied. The impact on the signal region of the CP analysis is even smaller, since the di-τ

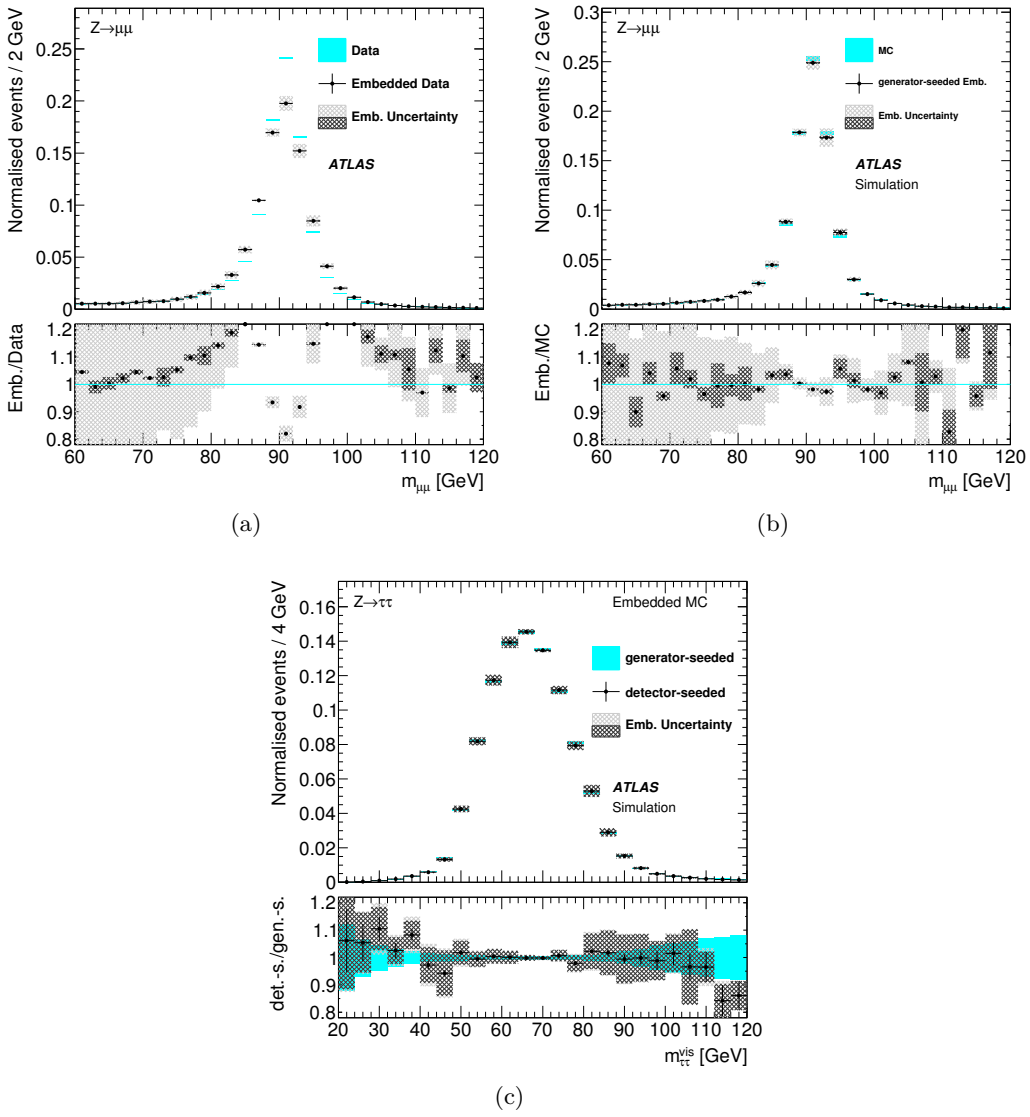

Figure 7.6. *The visible di-muon mass distribution of the $Z/\gamma^* \to \mu^+\mu^-$ Embedding input sample from data compared to the corresponding $\mu \to \mu$ Embedding events (a). A much broader distribution is observed for Embedding events due to muon resolution and FSR effects. No such deviations are observed in simulated $\mu \to \mu$ Embedding events, where muons at generator level and therefore before reconstruction and FSR are used as seed, compared to a fully simulated $Z/\gamma^* \to \mu^+\mu^-$ sample (b). The visible di-τ mass for simulated $\mu \to \tau$ Embedding samples using reconstructed muons and generator level muons as seed (c). No differences are observed due to the much larger di-τ mass reconstruction resolution compared to muon resolution and FSR effects [7].*

events for these processes are mainly distributed in the background-like region of the BDT score.

A final source of contamination that has been considered is from $Z/\gamma^* \to$

$\tau^+\tau^- \to \mu^+\mu^-$. Such processes cause unwanted seeds in the Embedding method, resulting in fake $Z/\gamma^* \to \tau^+\tau^-$ events with very low final state lepton p_T. The relative fraction of such processes in the di-muon input sample is less than 1%. Due to the low transverse momenta of the leptonic decay products in this case, the corresponding events are expected to be further suppressed by the analysis specific trigger thresholds. Therefore, the effect is also considered to be negligible.

- *Muon Trigger and Reconstruction Efficiencies*

  Since the Embedding method is based on $Z/\gamma^* \to \mu^+\mu^-$ collision data, the final Embedding sample is affected by muon trigger and reconstruction efficiencies due to the initial di-muon selection. These effects are corrected using (η,ϕ) and (η, p_T) dependent trigger and reconstruction efficiencies according to Ref. [112] and [113].

  The efficiencies for the di-muon trigger *mu18_tight_mu8_EFFS* and single-muon trigger *EF_mu24i_tight* are shown in figure 4.4. In case of the di-muon trigger, the overall efficiency is calculated by combining the single trigger leg efficiencies $\epsilon_{\mu_1}^{\text{leg}_1}\epsilon_{\mu_2}^{\text{leg}_2} + \epsilon_{\mu_1}^{\text{leg}_2}\epsilon_{\mu_2}^{\text{leg}_1} - \epsilon_{\mu_1}^{\text{both legs}}\epsilon_{\mu_2}^{\text{both legs}}$. The muon reconstruction efficiencies are shown in figure 4.5.

  The final correction factor is applied in terms of an event weight and is defined as the reciprocal of the product of trigger and reconstruction efficiencies for

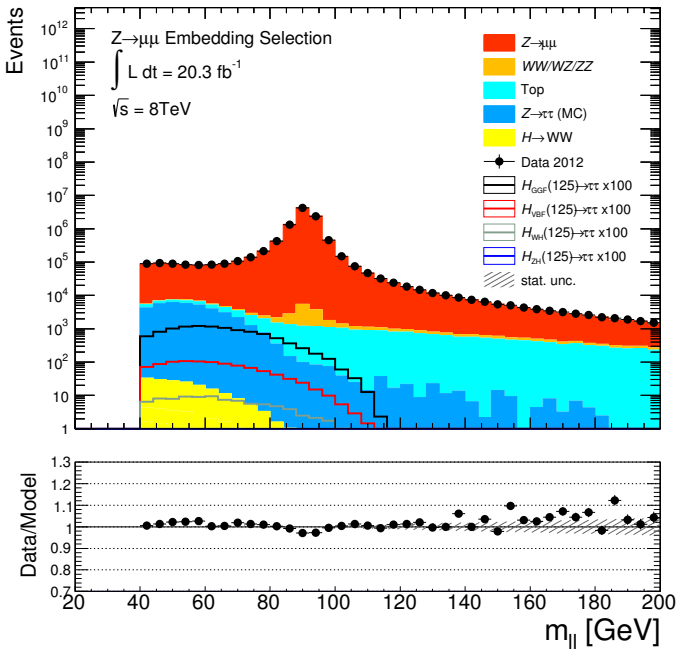

Figure 7.7. *Visible di-muon mass distribution after the $Z/\gamma^* \to \mu^+\mu^-$ Embedding input selection defined in table 7.1.*

both selected muons. Furthermore, it has been ensured that the muon p_T thresholds and the cut on the invariant di-muon mass in the Embedding input selection is chosen loose enough to not bias the final Embedding $Z/\gamma^* \to \tau^+\tau^-$ sample with respect to analysis specific selection criteria.

- *Analysis Trigger Efficiencies*

  Overall, the Embedding method processes reconstructed objects only. However, the storage of proper trigger information in the event reconstruction would require the Embedding procedure to be at hit level. Therefore, no trigger

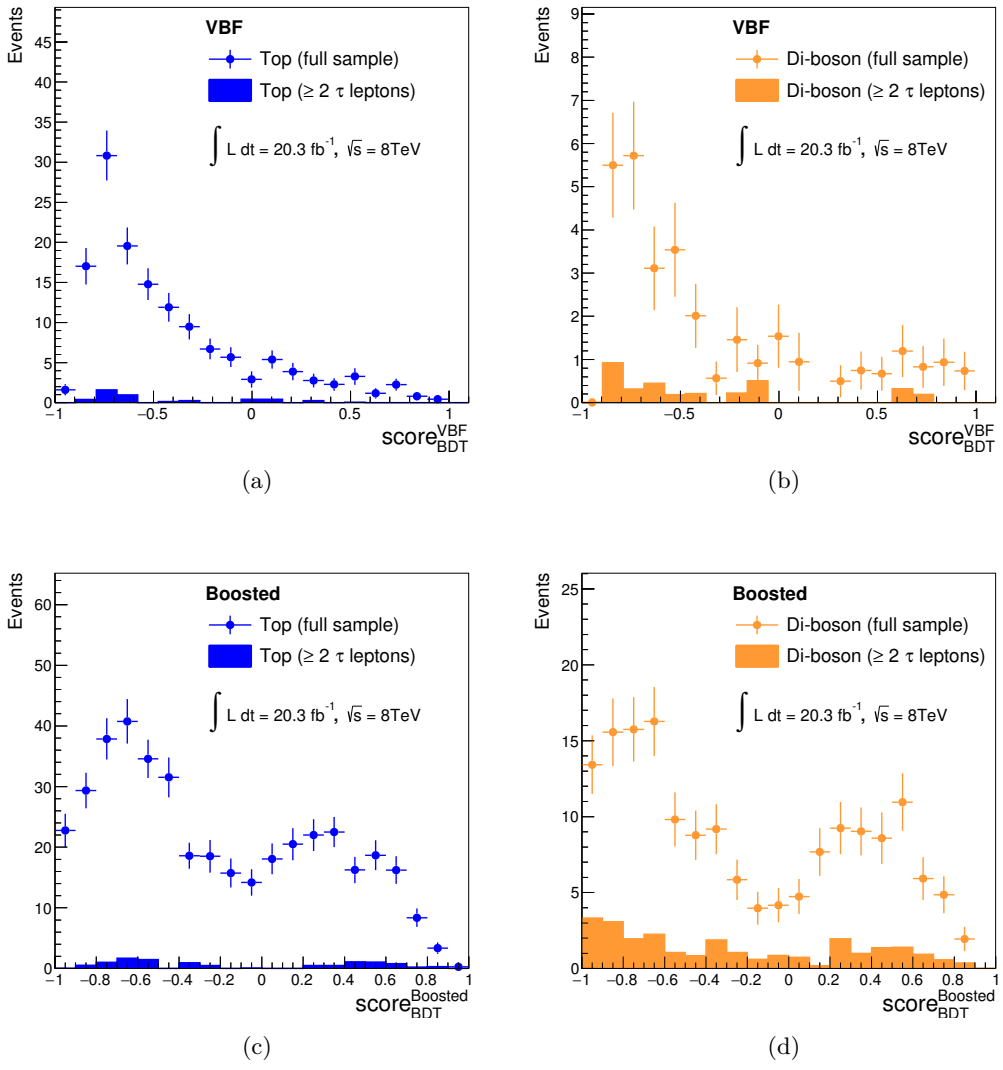

Figure 7.8. *BDT score distributions in the VBF and Boosted category for top quark and di-boson processes including the corresponding distributions for events with at least two τ leptons at generator level.*

information with respect to the τ lepton decay products is available in the final Embedding sample.

In the present analyses, the specific muon and electron triggers are emulated by applying the trigger p_T thresholds summarized in table 5.2. In addition, corrections are applied in terms of event weights based on the corresponding trigger efficiencies according to section 4.4.1 and 4.3.1 for muons and electrons. The formula for calculating di-lepton efficiencies from the individual trigger legs was described in the previous section.

These corrections have been validated using the simulated $Z/\gamma^* \to \tau^+\tau^-$ Alpgen sample. The $p_T^{\ell_1/\ell_2}$ distributions after requiring the trigger p_T thresholds including the nominal trigger selection are compared to the distributions after requiring the offline thresholds without the nominal triggers but including the efficiency corrections, which corresponds to the default treatment of the Embedding sample. Residual differences, that are observed in this comparison, are additionally corrected in the present analyses. The corresponding additional correction factors depend on $(p_T^{\ell_1}, p_T^{\ell_2})$ as shown in figure 7.9 for each final state and trigger selection case.

The Embedding method related systematic uncertainties mainly stem from the isolation of the original reconstructed muons, the subtraction of simulated calorimeter cell energies due to the muons and detector related uncertainties with respect to the simulated final state leptons from the τ lepton decay. The systematic uncertainties are discussed in detail in section 8.3. The performance of the various corrections, which are applied to the Embedding sample, is discussed in the next section 7.1.3.

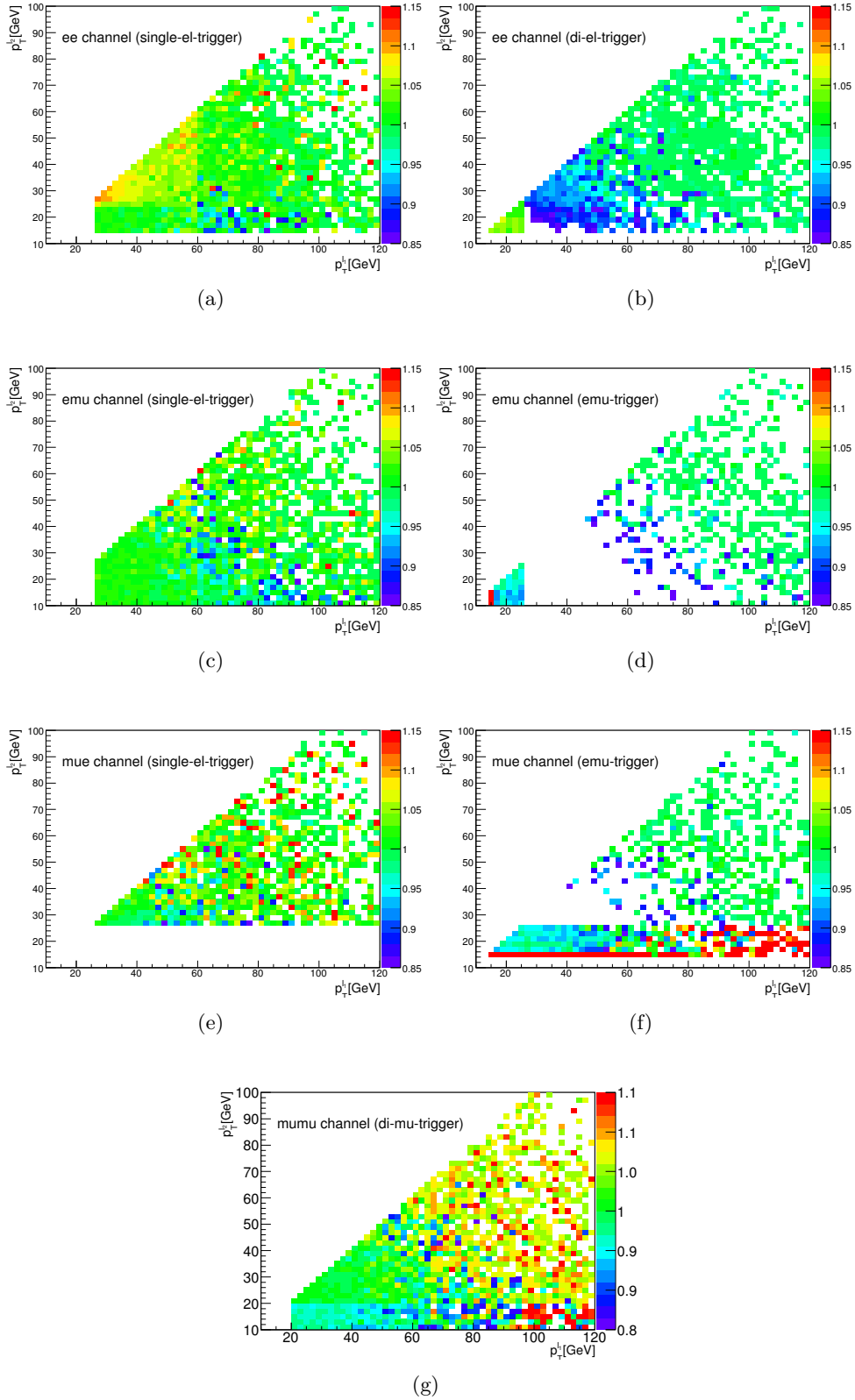

(a) (b) (c) (d) (e) (f) (g)

Figure 7.9. *Additional correction factors accounting for differences in the default analysis trigger selection including lepton p_T thresholds and the trigger treatment applied to the Embedding sample, which consists of the trigger specific p_T thresholds and event weights based on the corresponding trigger efficiencies. The correction factors depend on the transverse momenta of the leading and sub-leading final state lepton. Trigger selection cases in the ee (a,b), eμ (c,d), μe (e,f) and μμ (g) final state channel of the analyses according to table 5.2. In case of 2D histogram bins with small statistics, the correction factor is set to unity.*

7.1.3. Validation

The section addresses the performance of the Embedding method and the modeling of the Embedding sample. First, a fully simulated $Z/\gamma^* \to \tau^+\tau^-$ Alpgen sample is compared to a $\mu \to \tau$ Embedding sample, which is seeded by simulated $Z/\gamma^* \to \mu^+\mu^-$ events from Alpgen. Secondly, the Embedding sample from collision data, which is the default sample in the present analyses, is compared to data in dedicated control regions.

Embedding of Simulated $Z/\gamma^* \to \mu^+\mu^-$ Events

The comparison of the fully simulated $Z/\gamma^* \to \tau^+\tau^-$ Alpgen sample with $\mu \to \tau$ Embedding events, seeded by simulated $Z/\gamma^* \to \mu^+\mu^-$ Alpgen events, provides a basic performance test of the Embedding method. Unlike $Z/\gamma^* \to \tau^+\tau^-$ enriched reference samples from data, the fully simulated sample is absolutely pure and is furthermore expected to be well reproduced by the Embedding sample that is based on simulated events as well.

The figures 7.10 and 7.11 show the impact of the individual Embedding corrections on basic distributions for p_T, η and ϕ of the leptons from the τ decay. The improvement in the transverse momentum distributions mainly stems from the corrections due to the analysis specific trigger requirements and the Z boson polarization. Especially in the lower p_T range below 40 GeV, where most of the events are expected, the Embedding sample approximates the simulated $Z/\gamma^* \to \tau^+\tau^-$ sample better after applying these corrections. The shape of the pseudorapidity and azimuthal angle of the leptons is improved by the muon reconstruction and trigger efficiency corrections. These corrections restore efficiency gaps in regions, where the MS is only partially equipped because of services for the ID and the calorimeters.

Further kinematic distributions for $m_{\ell\ell}$, m_{MMC}, $p_{j_1}^T$ and $E_{\mathrm{T}}^{\mathrm{miss}}$ are shown in figure 7.12. Relative differences for all distributions are below 5% in regions where most of the events are accumulated, but tend to be larger for higher values of these variables. These differences are mainly due to the isolation of the original muon seeds, the subtraction of calorimeter cell energies from the muons and the re-reconstruction of the hybrid event. However, the Embedding sample is still in reasonable agreement with the fully simulated $Z/\gamma^* \to \tau^+\tau^-$ sample in each of the distributions considering the corresponding statistical and Embedding specific systematic uncertainties.

Data Control Regions

The $\mu \to \tau$ Embedding sample, which is used in the present analyses, is seeded by $Z/\gamma^* \to \mu^+\mu^-$ collision data events. The modeling of the Embedding sample has been validated in dedicated $Z/\gamma^* \to \tau^+\tau^-$-enriched control regions. In these

control regions, all non-$Z/\gamma^* \to \tau^+\tau^-$ background processes are estimated by the corresponding background specific methods, which are also explained in this chapter.

The definition of one of the $Z/\gamma^* \to \tau^+\tau^-$ regions, called "high statistics" control region, is summarized in table 7.1. It contains a large number of events with typically low jet multiplicity. It is defined by cutting on the scalar sum of the transverse momenta of the leptons and jets and the missing transverse energy, which mainly reduces the top quark background. Furthermore, a cut on the sum of the cosine of $\Delta\phi(\mathbf{E}_T^{\text{miss}}, \mathbf{p}_T^{\ell,1/2})$ for both final state leptons is applied, which forces the $\mathbf{E}_T^{\text{miss}}$ vector to be mostly within the opening angle of the lepton momentum vectors as expected in case of $Z/\gamma^* \to \tau^+\tau^-$ decays. The relative fraction of the $Z/\gamma^* \to \tau^+\tau^-$ component with respect to the total expected background prediction is approximately 90%, while the residual background component stems mainly from $Z/\gamma^* \to e^+e^-/\mu^+\mu^-$ and di-boson processes. The $H \to \tau^+\tau^-$ signal contribution is below 0.3% and therefore considered to be negligible. Figures 7.13 and 7.14 show distributions of basic kinematic variables. The observed data is well described by

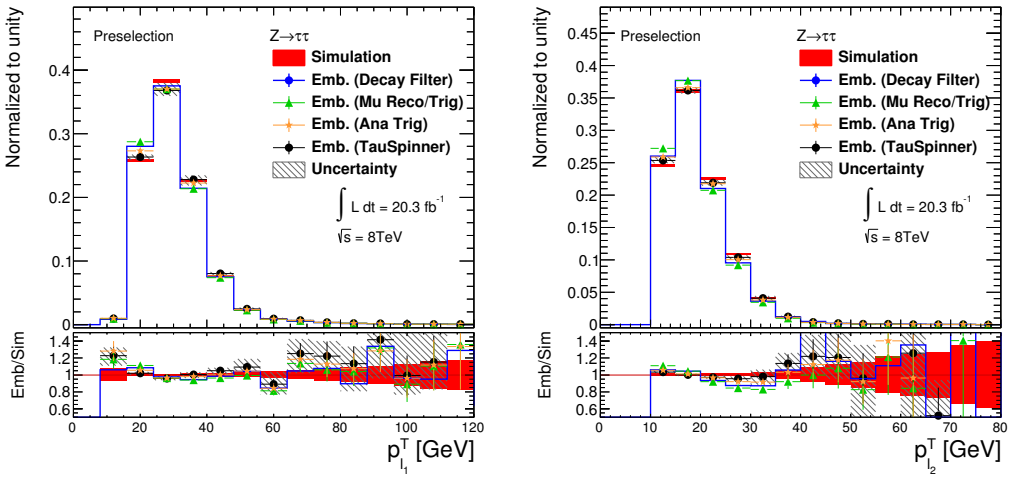

(a) (b)

Figure 7.10. *Comparison of $p_{l_{1/2}}^T$ of the simulated $Z/\gamma^* \to \tau^+\tau^-$* ALPGEN *sample (red) with the Embedding sample, seeded by simulated $Z/\gamma^* \to \mu^+\mu^-$* ALPGEN *events. The Embedding sample with* TAUOLA *decay filter event weights applied (blue) is compared to the same sample including additional muon reconstruction and trigger efficiency corrections (green), analysis specific trigger corrections (orange) and Z boson polarization corrections, which corresponds to the full set of corrections (black). The corrections are applied successively. The selection is defined by a basic set of event cleaning cuts and the di-lepton requirements including analysis triggers. The individual error bars contain statistical uncertainties only. The grey error band contains the statistical uncertainties of the Embedding sample including all corrections and the embedding specific systematic uncertainties (see section 8.3.2). The red error band reflects the statistical uncertainties of the simulated $Z/\gamma^* \to \tau^+\tau^-$ sample.*

the background prediction and differences are covered by systematic uncertainties.

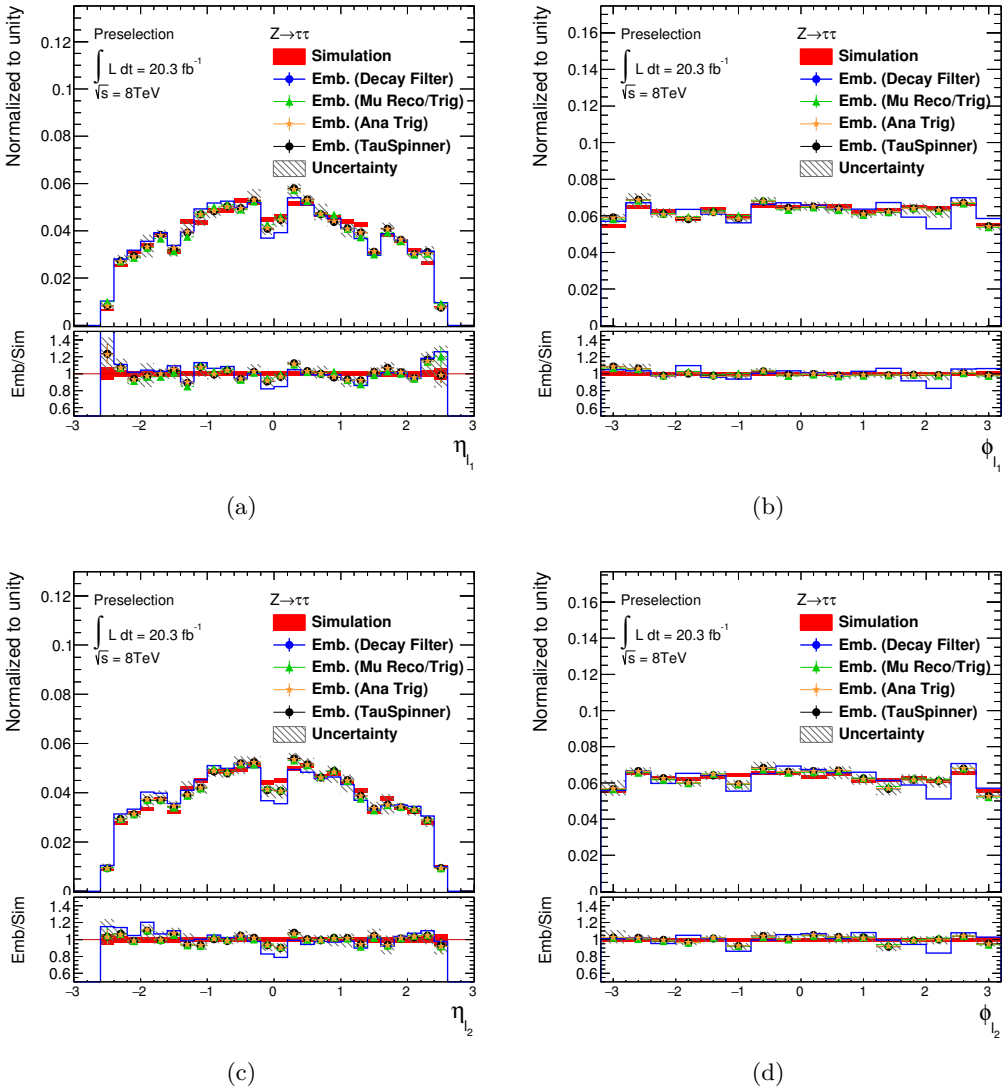

Figure 7.11. *Comparison of $\eta_{\ell_{1/2}}$ and $\phi_{\ell_{1/2}}$ of the simulated $Z/\gamma^* \to \tau^+\tau^-$* Alpgen *sample (red) with the Embedding sample, seeded by simulated $Z/\gamma^* \to \mu^+\mu^-$* Alpgen *events. The Embedding sample with* Tauola *decay filter event weights applied (blue) is compared to the same sample including additional muon reconstruction and trigger efficiency corrections (green), analysis specific trigger corrections (orange) and Z boson polarization corrections, which corresponds to the full set of corrections (black). The corrections are applied successively. The selection is defined by a basic set of event cleaning cuts and the di-lepton requirements including analysis triggers. The individual error bars contain statistical uncertainties only. The error band contains the statistical uncertainties of the Embedding sample including all corrections and the embedding specific systematic uncertainties (see section 8.3.2). The red error band reflects the statistical uncertainties of the simulated $Z/\gamma^* \to \tau^+\tau^-$ sample.*

To achieve good background modeling, the full set of Embedding specific corrections has to be applied.

Dedicated control regions for the VBF and Boosted category are defined by applying an additional cut on $m_{\ell\ell}^{\mathrm{HPTO}} < 100$ GeV in addition to the categorization require-

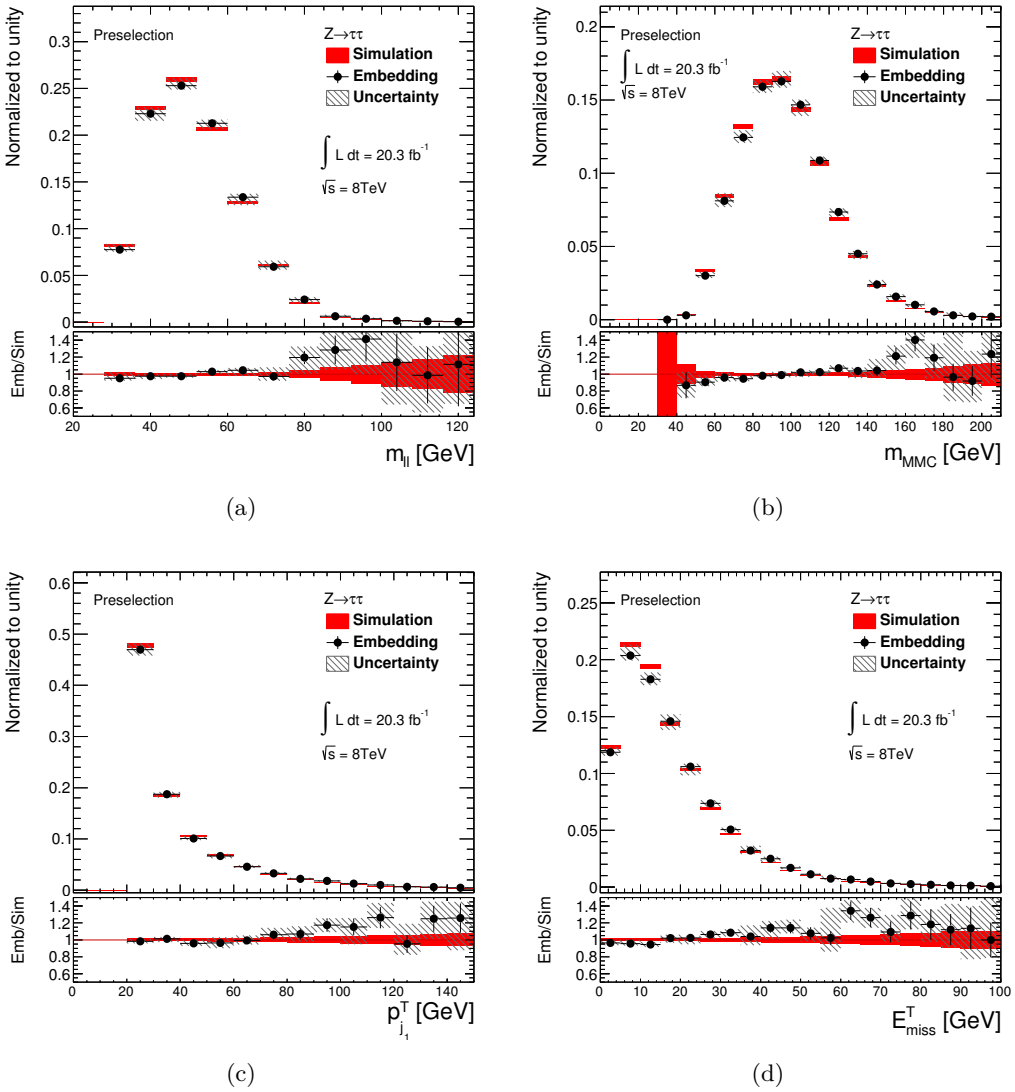

Figure 7.12. *Comparisons of distributions for $m_{\ell\ell}$, m_{MMC}, $p_{j_1}^T$ of the simulated $Z/\gamma^* \to \tau^+\tau^-$ ALPGEN sample (red) with the Embedding sample, seeded by simulated $Z/\gamma^* \to \mu^+\mu^-$ ALPGEN events (black). The Embedding sample includes the full set of Embedding specific corrections. The selection is defined by a basic set of event cleaning cuts and the di-lepton requirements including the analysis triggers. The error band contains the statistical uncertainties of the Embedding sample including all corrections and the embedding specific systematic uncertainties (see section 8.3.2). The red error band reflects the statistical uncertainties of the simulated $Z/\gamma^* \to \tau^+\tau^-$ sample.*

ments, as summarized in table 5.5.1. The high-p_T object mass $m_{\ell\ell}^{\mathrm{HPTO}}$ is based on the collinear approximation (see 5.5.1) using $E_{\mathrm{T}}^{\mathrm{miss,HPTO}}$ instead of the default reconstructed missing transverse energy. Using this alternative invariant mass approximation avoids cutting directly on the default m_{MMC} mass reconstruction although both variables are correlated for processes with real missing transverse energy. Contributions from Higgs boson signal processes are reduced significantly in this control region while the relative $Z/\gamma^* \to \tau^+\tau^-$ contribution is enhanced. The distributions of the reconstructed invariant mass m_{MMC} in the dedicated control region for both categories are shown in figure 7.15. Due to the irreducibility of $Z/\gamma^* \to \tau^+\tau^-$ and a higher jet multiplicity, these control regions are not as pure as the high statistics control region and also top quark and fake lepton processes contribute to the non-$Z/\gamma^* \to \tau^+\tau^-$ background beside of $Z/\gamma^* \to e^+e^-/\mu^+\mu^-$ processes. However, the category specific control regions are much closer to the signal region. The purity of these control regions with respect to $Z/\gamma^* \to \tau^+\tau^-$ is approximately 75% in the VBF and 86% in the Boosted category. Further BDT input variables are shown in 7.16 for the VBF category and in figure 7.17 and 7.18 for the Boosted category. The background prediction is in good agreement with the observed data for all variables within systematic uncertainties on the background normalisation.

The CP analysis is based on the VBF category as explained in chapter 6. The signal region is defined by adding a cut on the BDT classifier $\mathrm{score}_{\mathrm{BDT}}^{\mathrm{VBF}} > 0.68$ and a cut the Optimal Observable of $|OO| < 15$. In case of signed $\Delta\phi(j_1, j_2)$as final discriminant, both leading jets are required to be in different hemispheres. The BDT classifier distribution of background-like events is included in the fit in a control region, which is defined by reverting the cut on the BDT classifier $\mathrm{score}_{\mathrm{BDT}}^{\mathrm{VBF}} < 0.05$. Figure 7.19 shows the CP-odd observables, the Optimal Observable and signed $\Delta\phi(j_1, j_2)$, in this dedicated low BDT control region, which is dominated by $Z/\gamma^* \to \tau^+\tau^-$ background events.

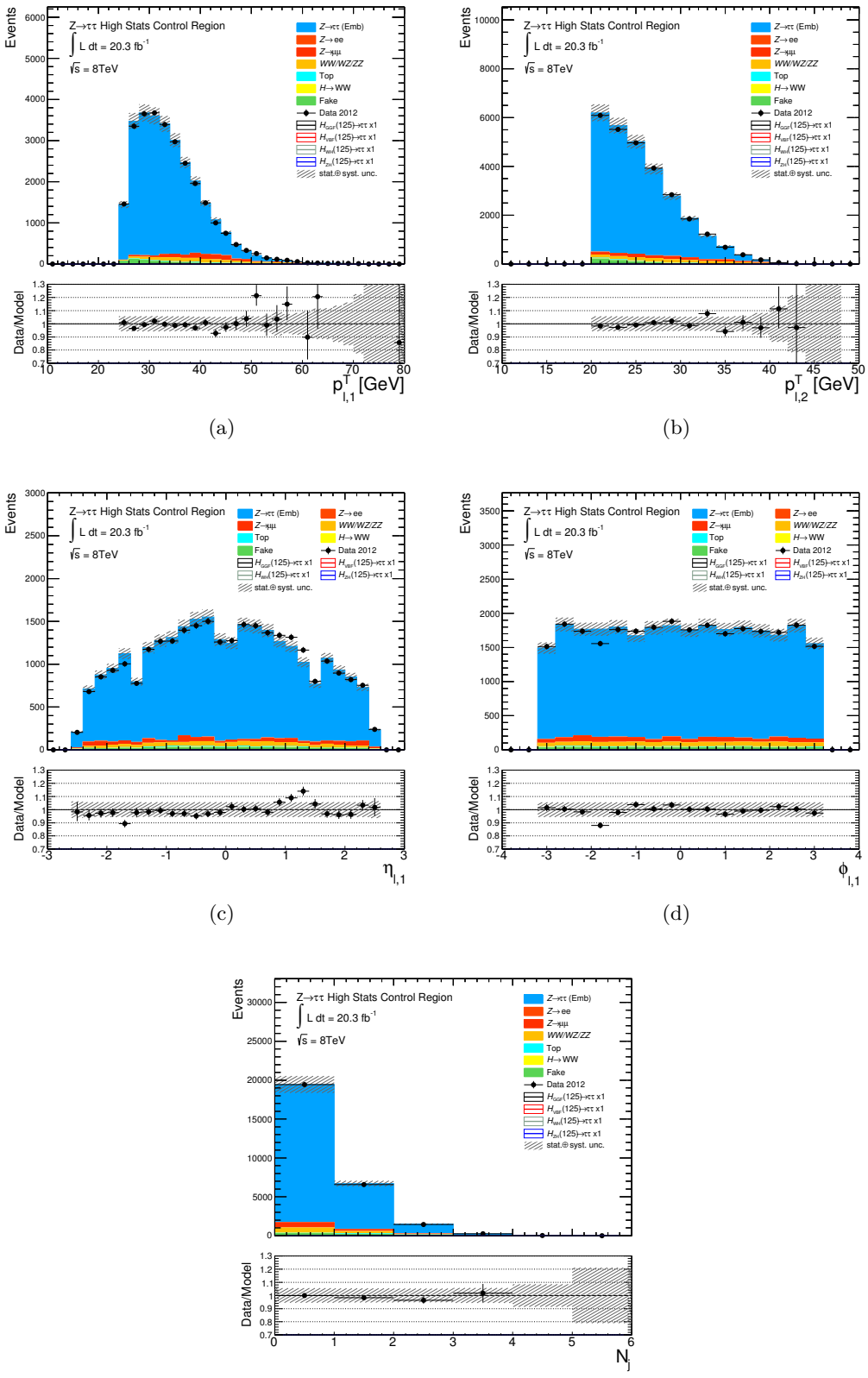

(a) (b) (c) (d) (e)

Figure 7.13. *Distributions of basic kinematic variables in the high statistics $Z/\gamma^* \to \tau^+\tau^-$ control region. The full set of Embedding specific corrections is applied. The error band contains statistical and systematic uncertainties on the normalisation of the Embedding sample.*

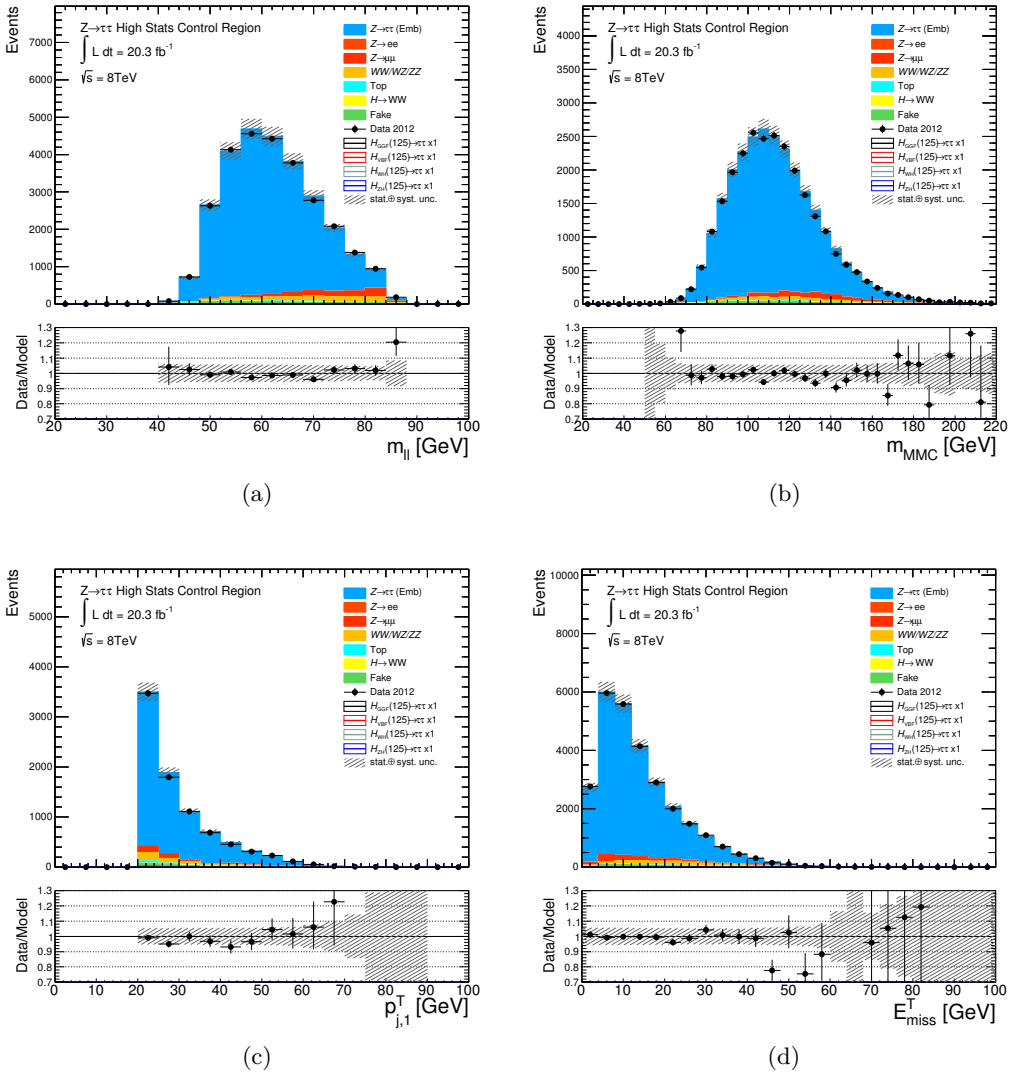

Figure 7.14. *Distributions of basic kinematic variables in the high statistics $Z/\gamma^* \to \tau^+\tau^-$ control region. The full set of Embedding specific corrections is applied. The error band contains statistical and systematic uncertainties on the normalisation of the Embedding sample.*

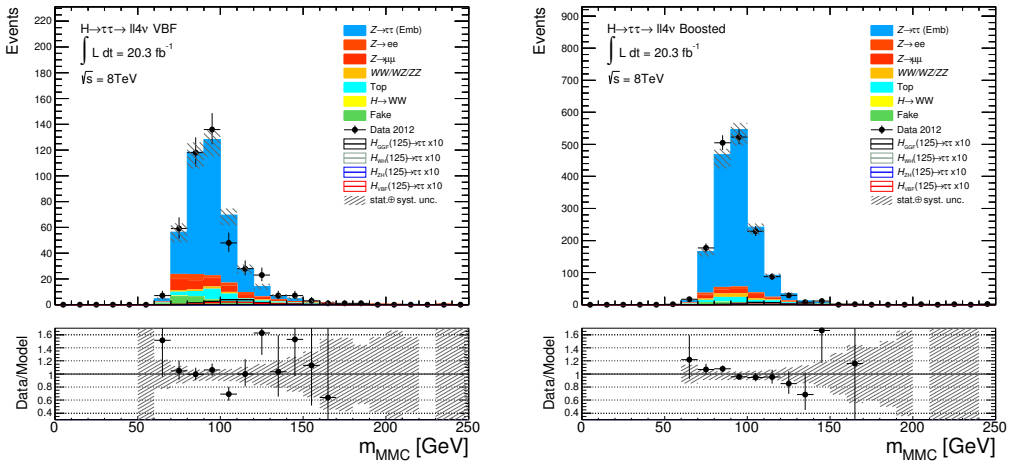

(a) (b)

Figure 7.15. *Distributions of the invariant di-τ mass, using the Missing Mass Calculator algorithm, in the dedicated $Z/\gamma^* \to \tau^+\tau^-$ control region of the VBF and Boosted category. The invariant m_{MMC} mass is used as BDT input variable in both categories. The full set of Embedding specific corrections is applied. The error band contains statistical and systematic uncertainties on the normalisation of the Embedding sample.*

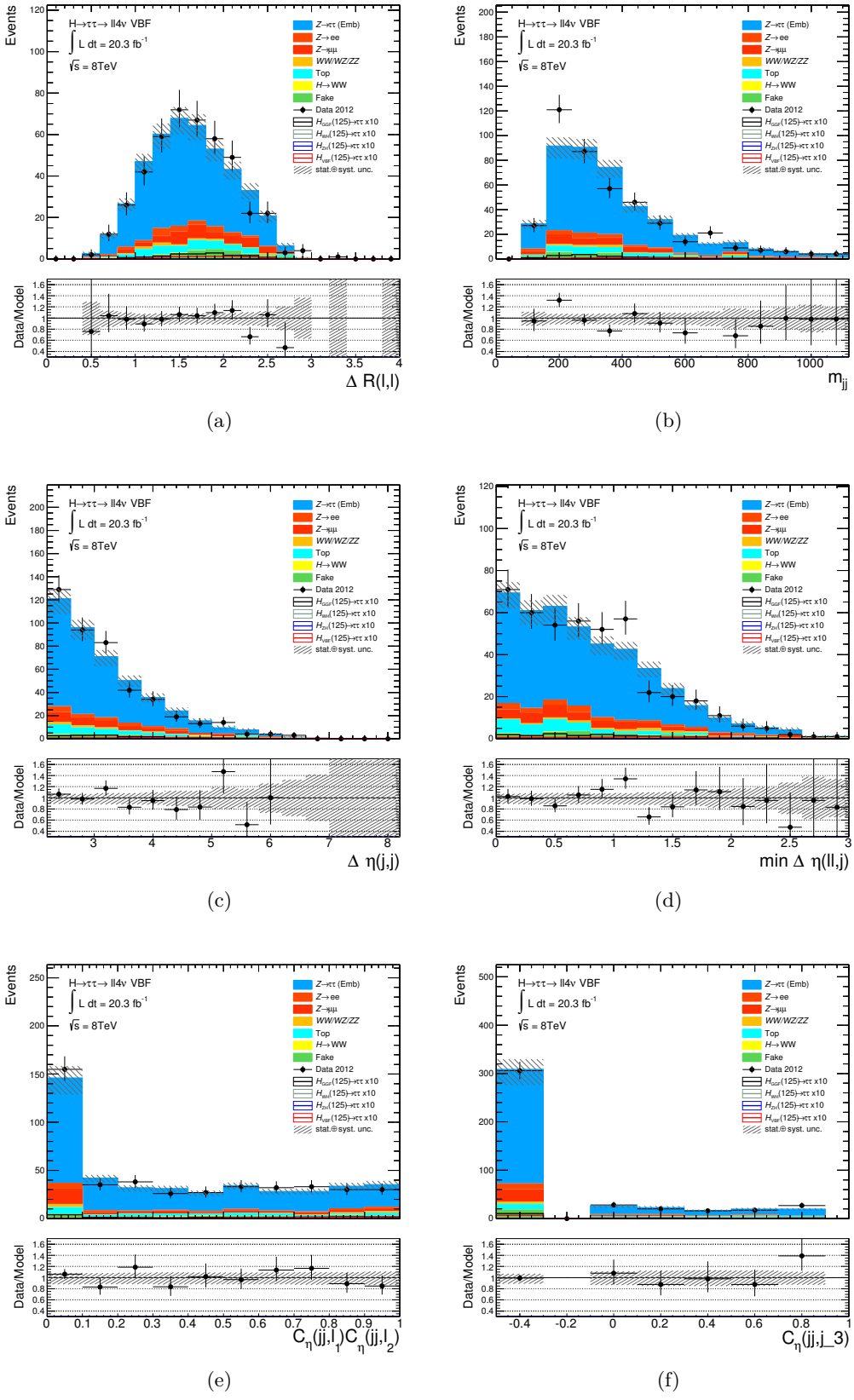

Figure 7.16. *Distributions of the BDT input variables in the dedicated $Z/\gamma^* \to \tau^+\tau^-$ control region of the VBF category. The full set of Embedding specific corrections is applied. The error band contains statistical and systematic uncertainties on the normalisation of the Embedding sample.*

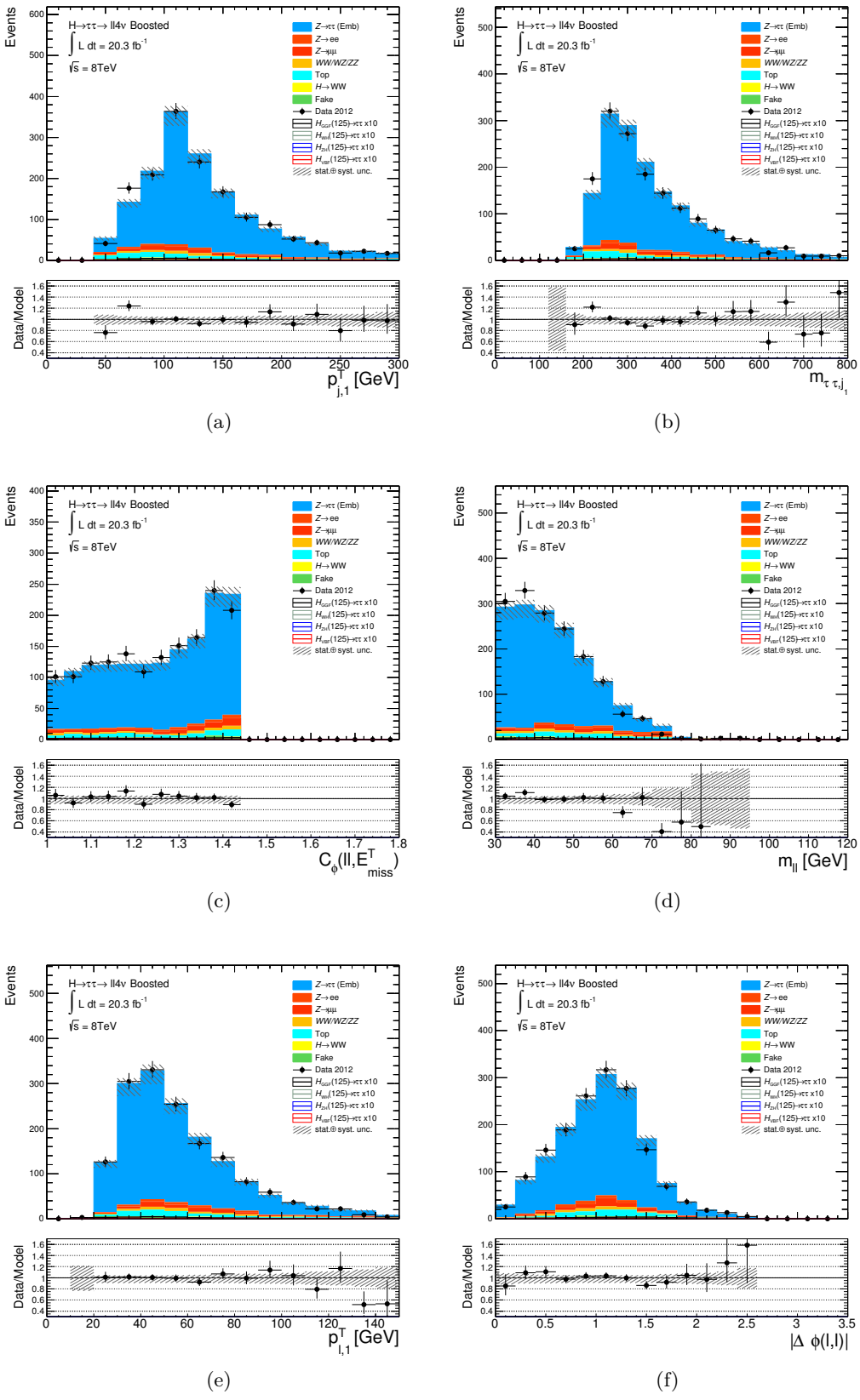

Figure 7.17. *Distributions of the BDT input variables in the dedicated $Z/\gamma^* \to \tau^+\tau^-$ control region of the Boosted category. The full set of Embedding specific corrections is applied. The error band contains statistical and systematic uncertainties on the normalisation of the Embedding sample.*

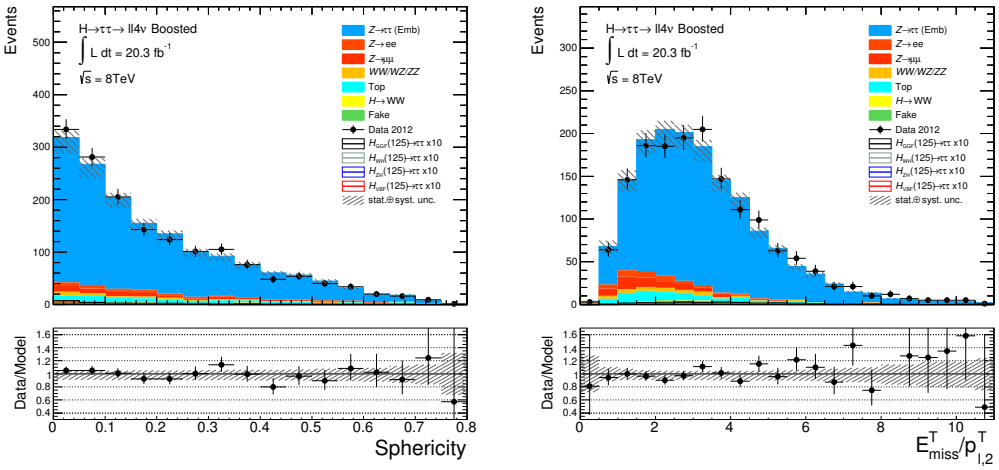

(a) (b)

Figure 7.18. *Distributions of the BDT input variables in the dedicated $Z/\gamma^* \rightarrow \tau^+\tau^-$ control region of the Boosted category. The full set of Embedding specific corrections is applied. The error band contains statistical and systematic uncertainties on the normalisation of the Embedding sample.*

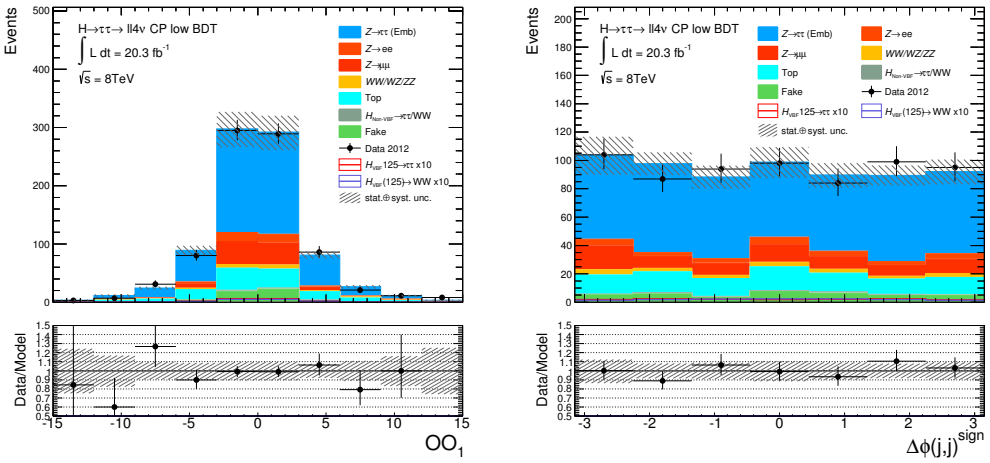

(a) (b)

Figure 7.19. *Distributions of the Optimal Observable and signed $\Delta\phi(j_1, j_2)$ in the low BDT control region of the CP analysis. The full set of Embedding specific corrections is applied. The error band contains statistical and systematic uncertainties on the normalisation of the Embedding sample.*

7.2. $Z/\gamma^* \to e^+e^-/\mu^+\mu^-$

Background events from $Z/\gamma^* \to e^+e^-/\mu^+\mu^-$ processes contribute 17% and 7% to the overall background in the VBF and Boosted category. The relative contribution increases to 22% in the signal region of the CP analysis.

The nominal samples for $Z/\gamma^* \to e^+e^-/\mu^+\mu^-$ processes are simulated with Alpgen [95], based on LO matrix elements for up to five partons (see section 5.2.1). However, these samples do not take electroweak Z boson production modes into account such as VBF processes, which have to be considered as background in the search for a VBF Higgs boson signal. Therefore, electroweak Z boson samples generated with Sherpa [82] are also considered as mentioned in section 5.2.1. Since $Z/\gamma^* \to e^+e^-/\mu^+\mu^-$ is an important background in the same flavour final states of the search for $H \to \tau^+\tau^- \to \ell^+\ell^- 4\nu$ and because the VBF specific phase space cuts limit statistics in these samples significantly, further VBF-filtered Alpgen samples are included to increase the number of generated events. These samples are divided into a loose and a tight VBF-filtered subset, which are characterized by the generator level phase space cuts $\Delta\eta(j,j) > 2.0$ / $m_{jj} > 200$ GeV and $\Delta\eta(j,j) > 4.0$ / $m_{jj} > 400$ GeV with respect to the two leading jets in each event. To avoid double-counting, events in overlapping phase space regions at generator level of different sub-samples are used only from one of the samples. Figure 7.20 illustrates the composition of the full background model in the same flavour final state after basic preselection cuts, where $Z/\gamma^* \to e^+e^-/\mu^+\mu^-$ events dominate. The VBF-filtered sub-samples contribute mainly in the VBF-like phase space at high $\Delta\eta(j,j)$ values. The relative contribution of electroweak Z boson production events is overall small but increases towards higher values of $\Delta\eta(j,j)$.

A systematic deviation of the background model from data of up to 20% is observed in the region of $\Delta\eta(j,j) \gtrsim 3$ as indicated in figure 7.21. Since the analyses rely on a good modeling of $\Delta\eta(j,j)$ especially in the VBF category, the differences are corrected by re-weighting the simulated $Z/\gamma^* \to e^+e^-/\mu^+\mu^-$ events to the distribution in data. Further information about the $\Delta\eta(j,j)$-dependent event weights can be found in section 8.3.4.

The overall modeling of the $Z/\gamma^* \to e^+e^-/\mu^+\mu^-$ background is shown in figure 7.22 in terms of basic distributions of lepton kinematics, the missing transverse energy and the transverse momentum of the leading jet after the full preselection (see table 5.3) in a dedicated control region, which includes same flavour final state events only requiring 80 GeV $< m_{ee/\mu\mu} <$ 100 GeV. All control region definitions are summarized in table 7.2. The model is in reasonable agreement with the data in terms of its normalisation and the shape of each distribution. Residual differences are expected to be covered by systematic uncertainties, which have not been evaluated at preselection level.

Figures 7.23, 7.24 and 7.25, 7.26, 7.27 show the full set of BDT input variables in dedicated control regions of the VBF and the Boosted category, which are defined by selecting same flavour final state events only with a modified visible mass cut

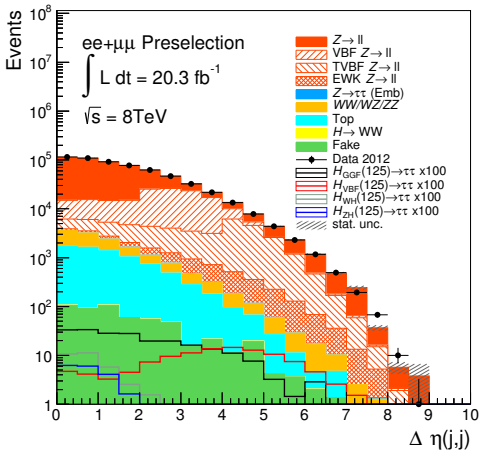

Figure 7.20. *Distribution of $\Delta\eta(j,j)$ after basic cleaning cuts (see section 5.3), requiring two oppositely charged same flavour leptons and a cut on the visible mass $80\,GeV < m_{ee/\mu\mu} < 100\,GeV$. The $Z/\gamma^* \to e^+e^-/\mu^+\mu^-$ sample is split into the nominal, loose VBF-filtered (VBF), tight VBF-filtered (TVBF)* Alpgen *[95] and the electroweak VBF* Sherpa *[82] (EWK) sub-samples. The error band includes statistical uncertainties only.*

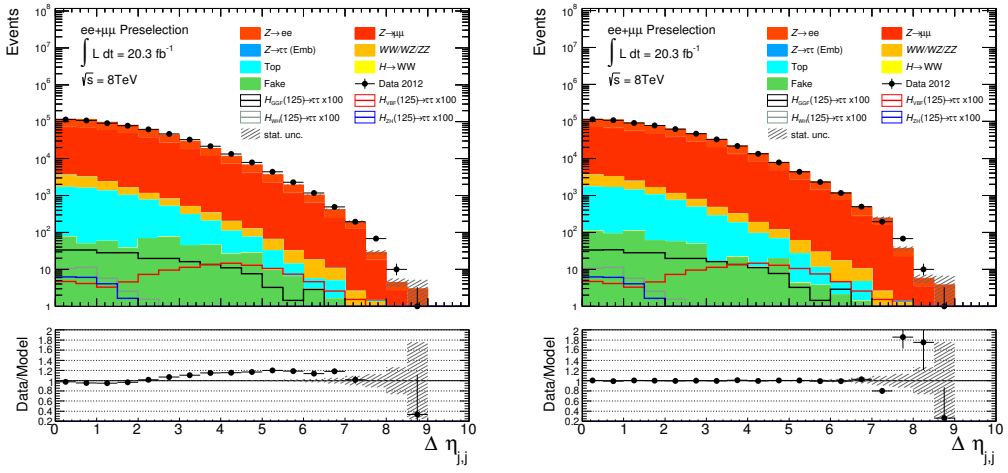

Figure 7.21. *Distribution of $\Delta\eta(j,j)$ after basic cleaning cuts (see section 5.3), requiring two oppositely charged same flavour leptons and a cut on the visible mass of 80 GeV $< m_{ee/\mu\mu} <$ 100 GeV: (a) default $Z/\gamma^* \to e^+e^-/\mu^+\mu^-$ sample and (b) re-weighted $Z/\gamma^* \to e^+e^-/\mu^+\mu^-$ sample. Figure (b) is a consistency check and matches per definition since the re-weighting is based on the same distribution. The weights have been determined before cutting on the visible mass. The error band includes statistical uncertainties only.*

Control region	Definition
$Z \to e^+e^-/\mu^+\mu^-$-enriched	Preselection / VBF / Boosted, 80 GeV $< m_{ee/\mu\mu} <$ 100 GeV, same flavour only
$t\bar{t}$-enriched	Preselection / VBF / Boosted, b jet tag
Di-boson-enriched	$p_T^{\ell_2} > 30$ GeV, different flavour only, $p_{\mathrm{T}}^{\ell_1} + p_{\mathrm{T}}^{\ell_2} > 60$ GeV, 20 GeV $< E_{\mathrm{T}}^{\mathrm{miss}} <$ 60 GeV, $\Delta\phi(\ell_1, \ell_2) < 2.3$, $x_{\tau_1} > 0.8$, $x_{\tau_2} > 0.7$, 2 jets at most, Events with a b-tagged jet with $p_{\mathrm{T}} > 25$ GeV are rejected, $p_T^{j1} <$ 50 GeV in events with at least one jet
Fake lepton-enriched	$p_T^{\mathrm{cone}\Delta R}$ isolation inverted, $E_T^{\mathrm{cone}\Delta R}$ isolation disposed
Fake lepton template normalisation	Two leptons with opposite charge, 30 GeV $< m_{ee/\mu\mu} <$ 75 GeV (same flavour events), 30 GeV $< m_{e\mu} <$ 100 GeV (different flavour events), at least one jet, $p_T^{j1} > 40$ GeV, Events with a b-tagged jet with $p_{\mathrm{T}} > 25$ GeV are rejected

Table 7.2. *Definitions of dedicated control regions, used for validating the background model. Cleaning and basic preselection cuts such as trigger requirements are included in all cases. In case of the preselection, VBF or Boosted category as selection criteria, only the explicitly quoted cut is modified in the nominal selection. Concerning fake lepton control regions, the lepton isolation criteria are summarized in table 4.1.*

80 $GeV < m_{ee/\mu\mu} <$ 100 GeV. No significant deviations from data are observed. Furthermore, the BDT classifier distributions measured in data are well reproduced by the model in the control regions as shown in figure 7.28. While the separation power of the BDT classifier between signal and the $Z/\gamma^* \to e^+e^-/\mu^+\mu^-$ background is excellent in the VBF category, a second peak appears at higher values of the classifier in the Boosted category stemming from events with boosted Z boson topologies. The different sources of uncertainties, which are related to the estimation of the $Z/\gamma^* \to e^+e^-/\mu^+\mu^-$ background, are explained in section 8.3.4. Uncertainties on the normalisation of the simulated $Z/\gamma^* \to e^+e^-/\mu^+\mu^-$ samples are on the scale of 50% in both categories. The relatively large uncertainty stems from detector

related uncertainties on the jet energy scale and the jet energy resolution. Since the spectrum of the leading jet transverse momentum in $Z/\gamma^* \to e^+e^-/\mu^+\mu^-$ events tends to be soft, as shown in figure A.11, with a steeply falling flank at the threshold $p_T^{j1} > 40$ GeV applied in the analysis, variations in the jet energy can have a large impact on the expected number of events in the signal regions.

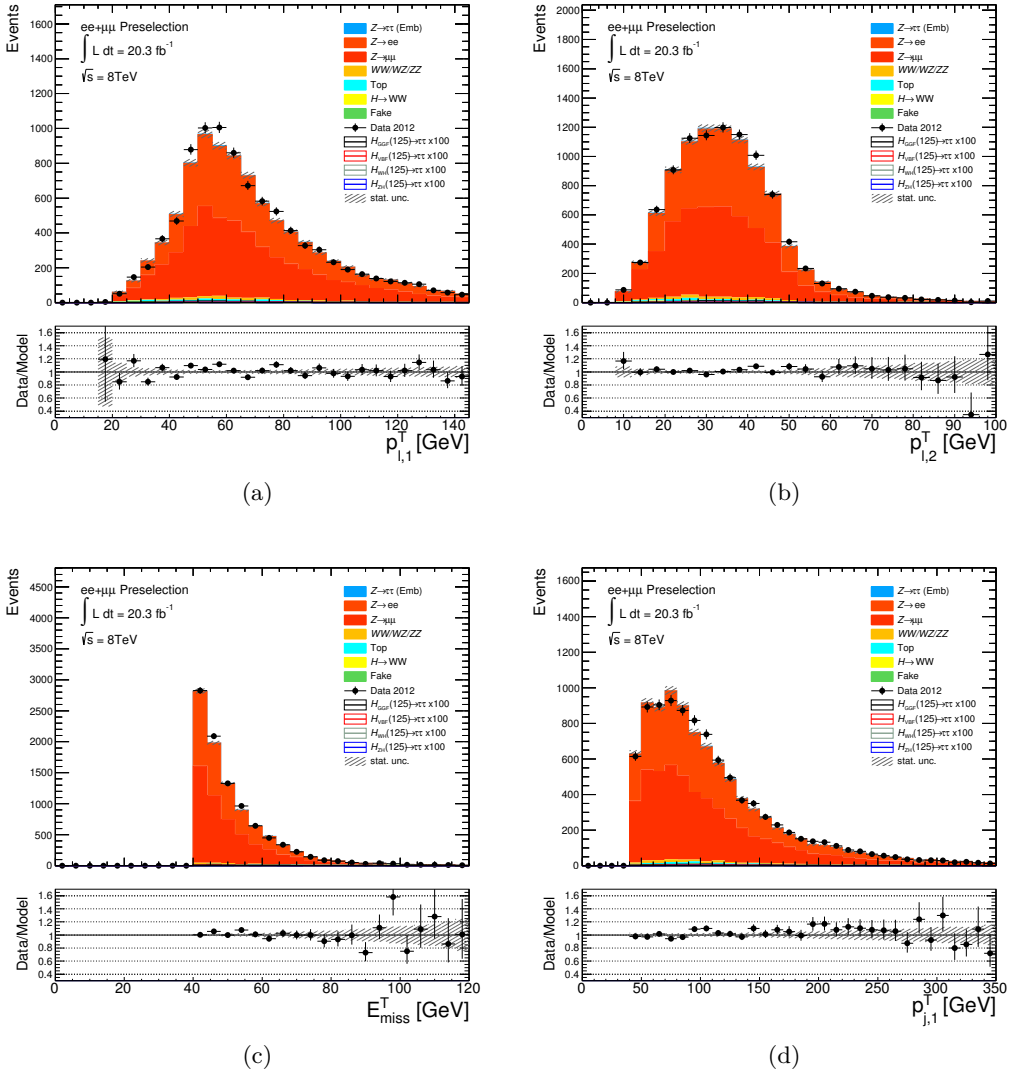

(a) (b)

(c) (d)

Figure 7.22. *Basic distributions of p_T^{l1}, p_T^{l2}, $E_{\mathrm{T}}^{\mathrm{miss}}$ and p_T^{j1} after preselection and before categorization (see section 5.3) selecting same flavour events only with a cut on 80 GeV $< m_{ee/\mu\mu} <$ 100 GeV. The error band includes statistical uncertainties only.*

Event yield information from the dedicated $Z/\gamma^* \to e^+e^-/\mu^+\mu^-$ control regions of the VBF and Boosted category is included in the fit of the search for $H \to \tau^+\tau^- \to \ell^+\ell^-4\nu$ in terms of counting experiments to constrain the corresponding background normalisation. The normalisation fit parameters for the complete

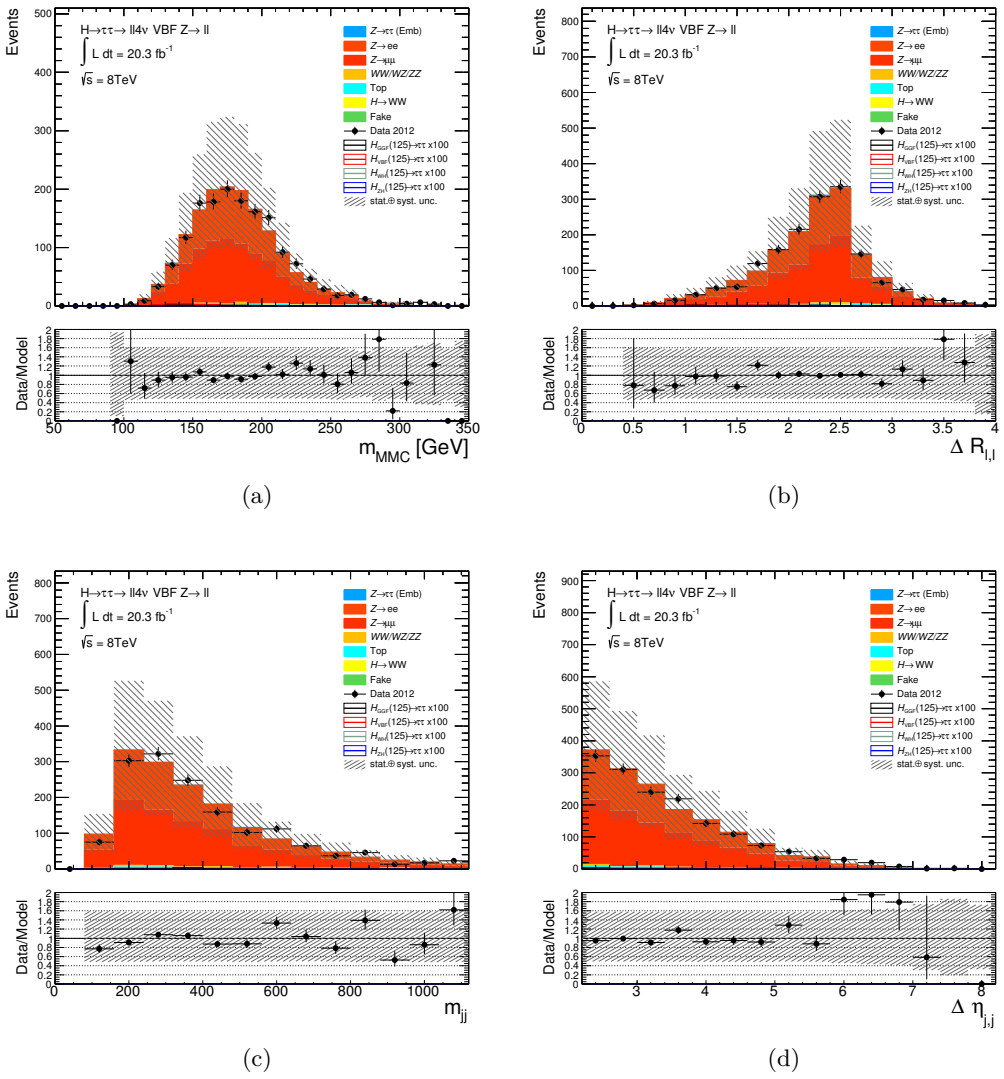

(a) (b)

(c) (d)

Figure 7.23. *BDT input variables in the dedicated $Z \to e^+e^-/\mu^+\mu^-$ control region of the VBF category. The error band includes statistical and systematic normalisation uncertainties.*

$Z/\gamma^* \to e^+e^-/\mu^+\mu^-$ sample are correlated across the signal and control regions but treated as uncorrelated across both categories to account for differences in the modeling of the VBF-like and boosted phase space. Normalisation parameters are not constrained prior to the fit and are then constrained primarily through the presence of these control region event yields in the VBF and Boosted categories, respectively. That is, the shape of the final discriminant is taken from simulation while the background sample is normalised to data. The initial prefit normalisation in each category is corrected such that normalisation differences with respect to data are compensated in the control regions of the VBF and Boosted category. The prefit scale factors are determined by dividing the measured number of data

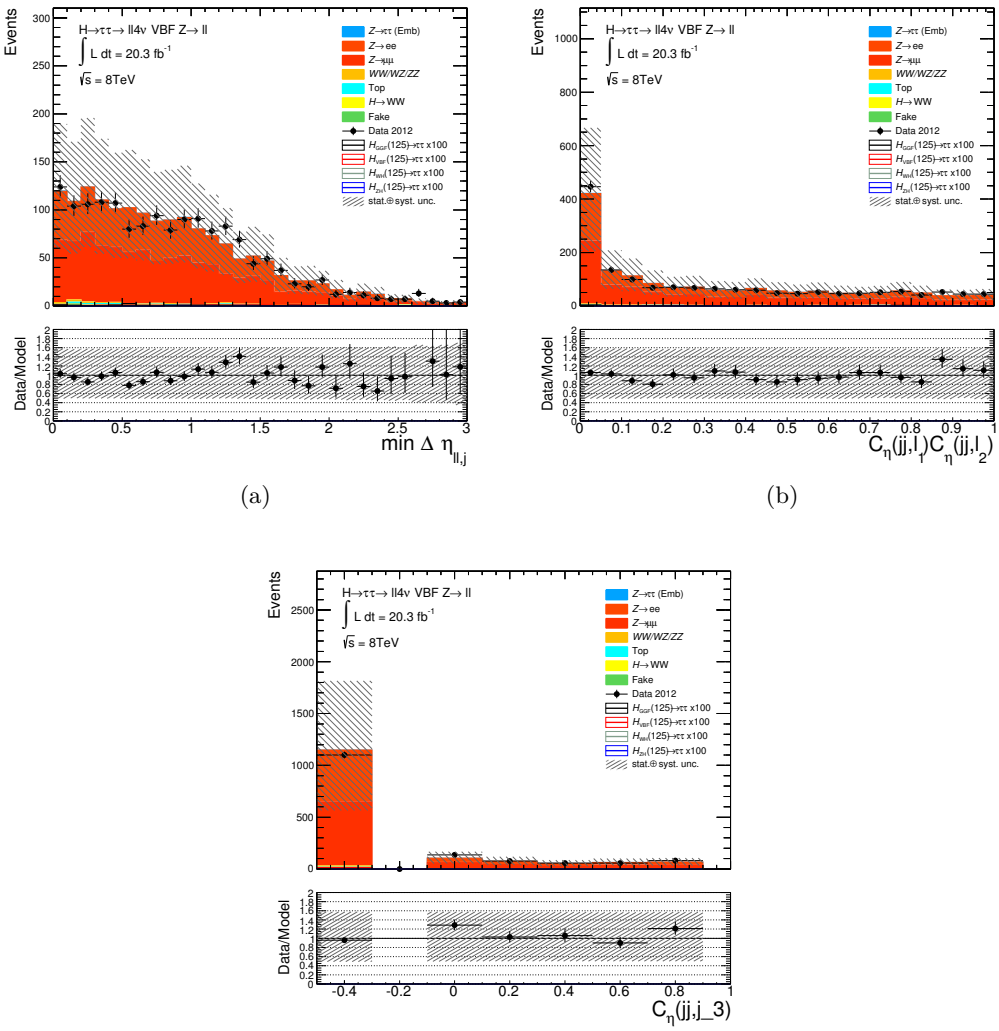

(a) (b) (c)

Figure 7.24. *BDT input variables in the dedicated $Z \to e^+e^-/\mu^+\mu^-$ control region of the VBF category. The error band includes statistical and systematic normalisation uncertainties.*

events subtracting the number of expected non-$Z/\gamma^* \to e^+e^-/\mu^+\mu^-$ events by the expected number of $Z/\gamma^* \to e^+e^-/\mu^+\mu^-$ events in the corresponding control region. These factors are given in table 7.3 for the $Z/\gamma^* \to \mu^+\mu^-$ and $Z/\gamma^* \to e^+e^-$ sample in the VBF and Boosted category respectively. They are close to unity, which demonstrates a reasonable modeling already at prefit level.

The three most signal-like bins of the BDT classifier in the VBF (Boosted) category are expected to contain 3.7 ± 1.0 (3.6 ± 1.0) $Z/\gamma^* \to e^+e^-$ and 4.3 ± 0.8 (5.7 ± 1.7) $Z/\gamma^* \to \mu^+\mu^-$ events at prefit level. This corresponds to a relative fraction of 22% (6%) for $Z/\gamma^* \to e^+e^-/\mu^+\mu^-$ background compared to the total background in these

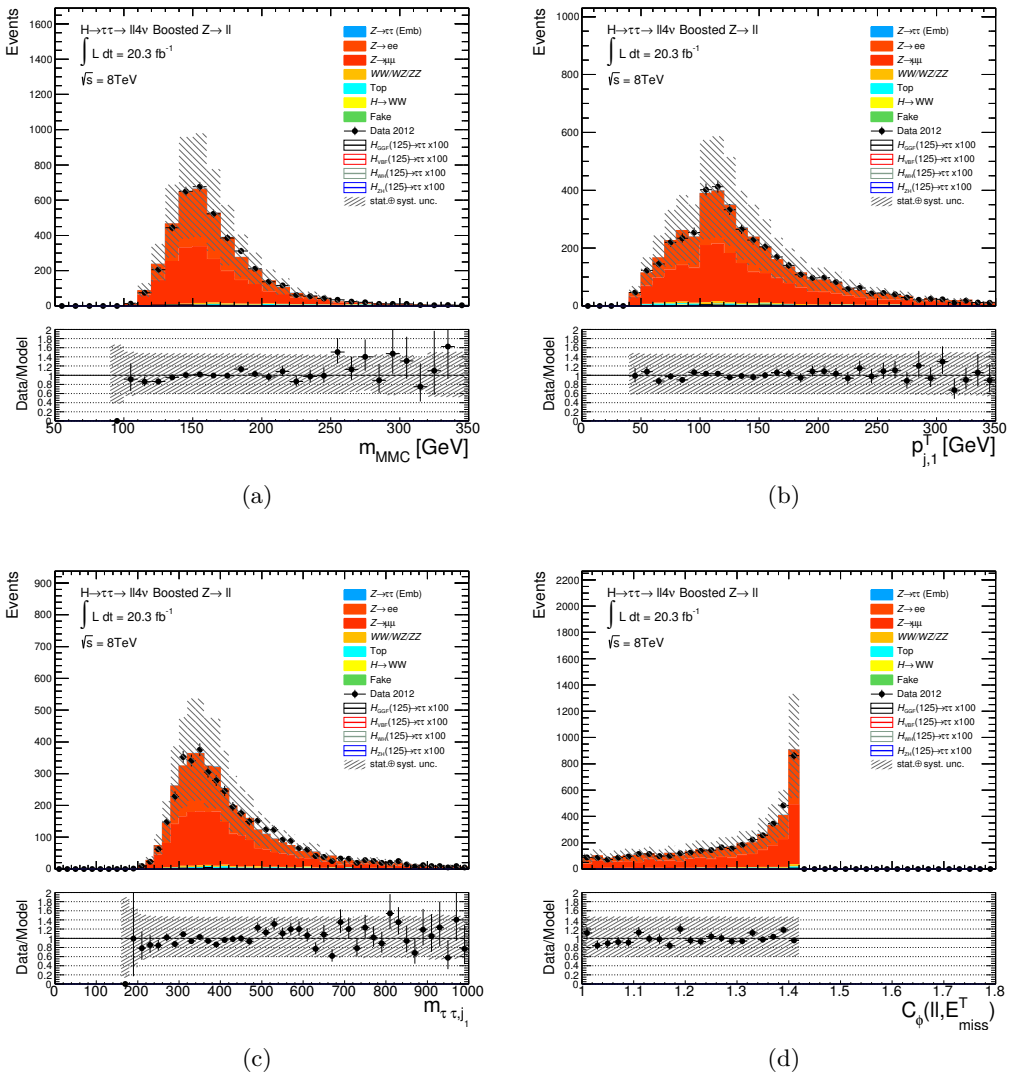

Figure 7.25. *BDT input variables in the dedicated $Z \to e^+e^-/\mu^+\mu^-$ control region of the Boosted category. The error band includes statistical and systematic normalisation uncertainties.*

bins. The shape of the BDT classifier distribution for $Z/\gamma^* \to e^+e^-/\mu^+\mu^-$ events compared to signal is shown in figure A.32 and A.33.

Concerning the CP analysis, the $Z/\gamma^* \to e^+e^-/\mu^+\mu^-$ control region of the VBF category is also included in the fit in terms of a counting experiment to constrain the normalisation of the $Z/\gamma^* \to e^+e^-/\mu^+\mu^-$ sample. The control region is defined as in the VBF category adding the cut $|OO| < 15$, which is applied in the signal region as well.The prefit scale factors are determined by dividing the measured number of data events subtracting the number of expected non-$Z/\gamma^* \to e^+e^-/\mu^+\mu^-$ events by the expected number of $Z/\gamma^* \to e^+e^-/\mu^+\mu^-$ events in the corresponding control region.

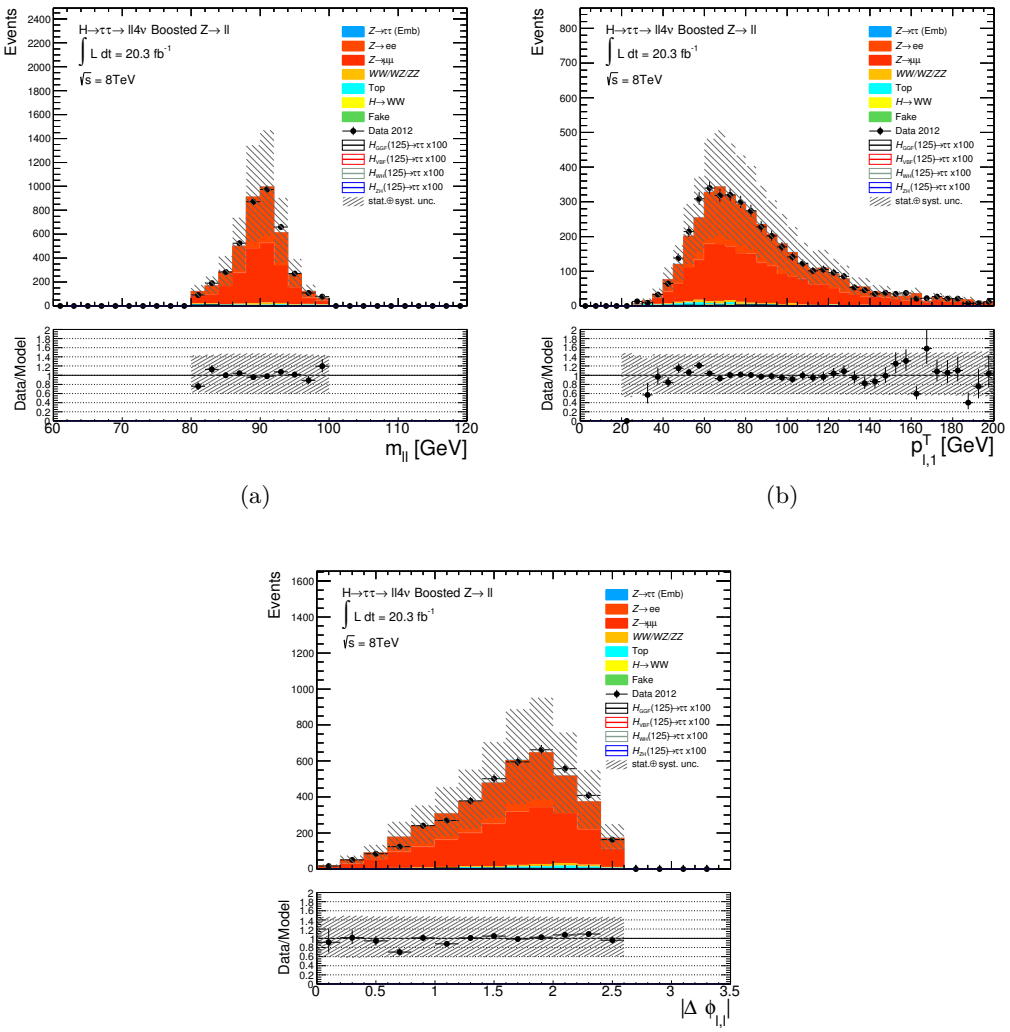

(a) (b)

(c)

Figure 7.26. *BDT input variables in the dedicated $Z \to e^+e^-/\mu^+\mu^-$ control region of the Boosted category. The error band includes statistical and systematic normalisation uncertainties.*

In case of signed $\Delta\phi(j_1, j_2)$ as final discriminant, both leading jets are required to emerge in different hemispheres. Figure 7.29 shows the Optimal Observable and signed $\Delta\phi(j_1, j_2)$ distributions in this control region. The data is well described by the model and distributed symmetrically around a value of zero as expected for purely CP-even Standard Model processes. A comparison of the Optimal Observable shape in the high BDT signal region and the low BDT control region to the $H \to \tau^+\tau^- \to \ell^+\ell^- 4\nu$ and $H \to W^+W^-$ signal samples from the VBF production mode is shown in figures A.34 and A.35.

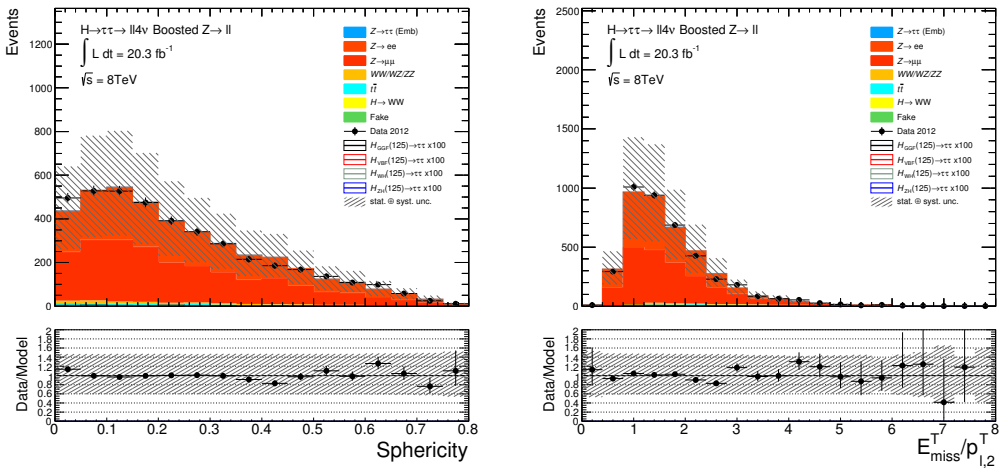

(a) (b)

Figure 7.27. *BDT input variables in the dedicated $Z \to e^+e^-/\mu^+\mu^-$ control region of the Boosted category. The error band includes statistical and systematic normalisation uncertainties.*

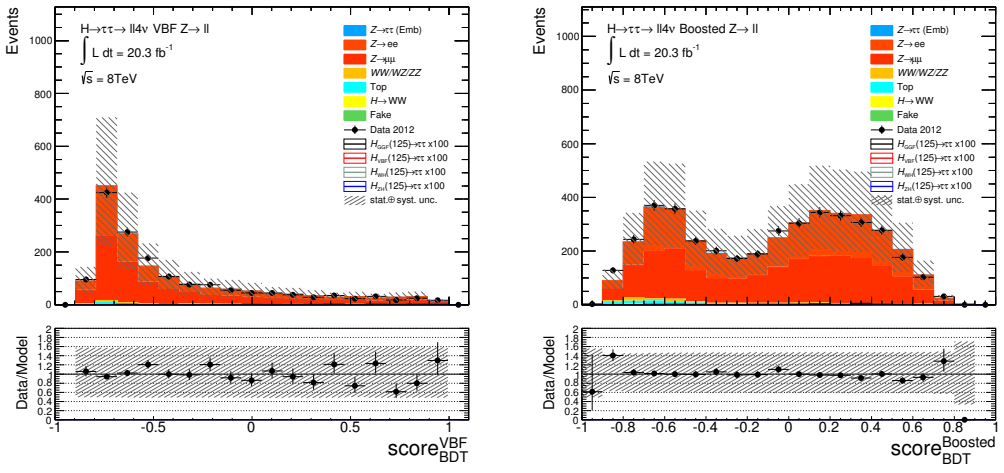

(a) (b)

Figure 7.28. *BDT classifier distributions in the dedicated $Z \to e^+e^-/\mu^+\mu^-$ control regions of the VBF and Boosted category. The error band includes statistical and systematic normalisation uncertainties.*

Process	Normalisation Factors	
	VBF	Boost
$Z \to e^+e^-$	0.98 ± 0.04	1.03 ± 0.03
$Z \to \mu^+\mu^-$	1.03 ± 0.04	1.01 ± 0.03
$t\bar{t}$	1.00 ± 0.05	1.02 ± 0.03

Table 7.3. *Prefit normalisation factors in the VBF and Boosted category, that compensate differences between a specific background model and data. The scale factors are determined in the control regions and applied also in the signal regions. The uncertainties include statistical information only.*

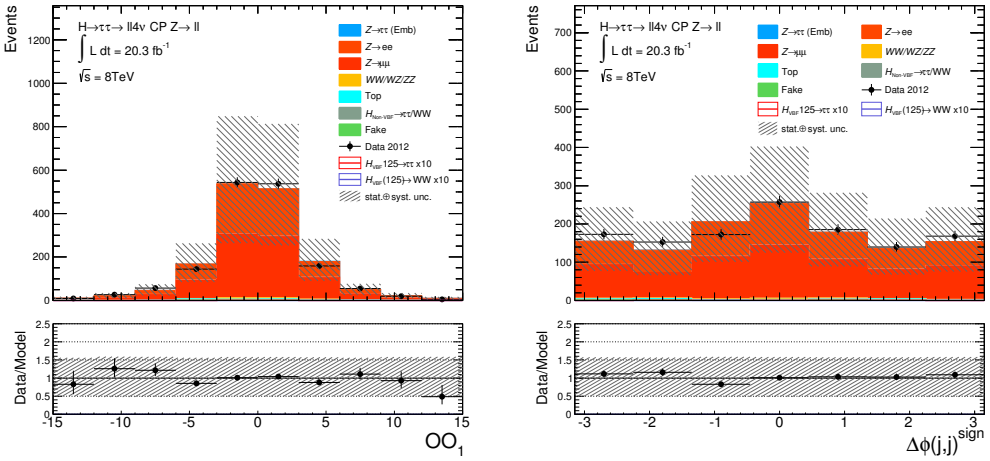

Figure 7.29. *Optimal Observable distribution (a) and signed $\Delta\phi(j_1, j_2)$ (b) in the dedicated $Z \to e^+e^-/\mu^+\mu^-$ control region of the CP analysis. An additional cut on $|OO| < 15$ is included to model the corresponding efficiency of the signal region. In case of signed $\Delta\phi(j_1, j_2)$ as final discriminant, both leading jets are required to emerge in different hemispheres. The error band includes statistical and systematic normalisation uncertainties.*

7.3. Di-Boson

The fraction of di-boson processes is about 3% in the VBF and 5% in the Boosted category with respect to the total background. In the CP analysis, the relative contribution is about 7%. The estimation of di-boson processes is based on simulation (see section 5.2.1). The selected di-boson sample is composed of $WZ/\gamma*$, $Z\gamma * Z\gamma*$ and WW sub-samples with a relative contribution of 10%, 7% and 83% in the VBF and 12%, 6% and 82% in the Boosted category respectively. Processes including two leptonically decaying W bosons are therefore the dominating component.

A dedicated control region is defined to enhance events from di-boson processes by modifying a large number of preselection cuts, based on the distributions shown in appendix A.1. The control region definition is listed in table 7.2. Harsher p_T^ℓ cuts allow suppression of fake lepton events, while the different flavour requirement and the lower cuts on $m_{\ell\ell}$ and $E_{\mathrm{T}}^{\mathrm{miss}}$ reject events from $Z/\gamma^* \to e^+e^-/\mu^+\mu^-$. The cut on $\Delta\phi(\ell_1, \ell_2)$ decreases considerably the number of resonant decays from Z boson events. The upper limit on the number of reconstructed jets and the upper cut on p_T^{j1} reduces $t\bar{t}$ events. The bulk of di-boson events is typically located above a threshold of $x_{\tau_1} > 0.8$ and $x_{\tau_2} > 0.7$. Figure 7.30 shows as an example the distribution of p_T^ℓ in the di-boson control region. A certain amount of $t\bar{t}$ events is indeed present, which are however shifted to higher p_T^ℓ values compared to di-boson events. Although some upwards fluctuations in single bins are observed, the overall modeling of the di-boson distribution is considered to be tolerably reasonable.

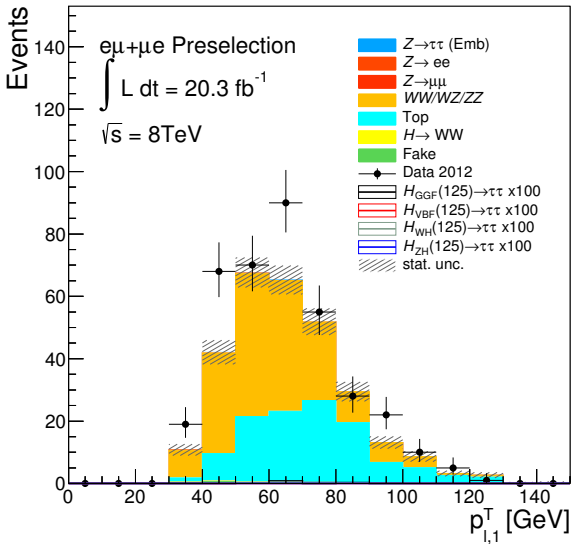

Figure 7.30. *Distribution of the leading lepton transverse momentum in the dedicated di-boson-enriched control region. The definition of the control region is described in table 7.2. The error band contains statistical uncertainties.*

To simplify the final fit model of the search for $H \to \tau^+\tau^- \to \ell^+\ell^- 4\nu$ and the CP

analysis and to reduce the vulnerability to statistical fluctuations, the relatively small di-boson background is merged with the $Z/\gamma^* \to e^+e^-/\mu^+\mu^-$ background component. Figure 7.31 compares the shape of the BDT classifier for the di-boson, the $Z/\gamma^* \to e^+e^-/\mu^+\mu^-$ and the combined signal samples. A good separation between signal and background is observed. In the VBF category, di-boson events exhibit the same shape as events from $Z/\gamma^* \to e^+e^-/\mu^+\mu^-$ in the full range of the classifier. A consistent behavior of both samples is also observed in the region of signal-like classifier values in the Boosted category, where a second peak structure appears. The similarity of the BDT classifier distributions of both background components, particularly in the signal-like region, justifies the merging of the corresponding samples. The unconstrained normalisation factor introduced in section 7.2 for the $Z/\gamma^* \to e^+e^-/\mu^+\mu^-$ background, is finally used for the merged sample. Therefore, deviations in the normalisation of the di-boson sample from data are taken into account in the fit as well. The merged sample consists of 31 ± 3 and 166 ± 7 expected di-boson and 169 ± 10 and 224 ± 9 $Z/\gamma^* \to e^+e^-/\mu^+\mu^-$ events in the VBF and Boosted category, respectively. In the three most signal-like bins of the BDT classifier, 2.5 ± 0.9 (12.7 ± 2.0) di-boson events are expected in the VBF (Boosted) category, which corresponds to a fraction of 7% (8%) with respect to the total background prediction. The shape of the BDT classifier distribution for di-boson compared to signal events in the VBF and Boosted category is shown in figures A.32 and A.33.

Concerning the CP analysis, the shape of the Optimal Observable distribution for di-boson compared to the VBF $H \to \tau^+\tau^- \to \ell^+\ell^- 4\nu$ and $H \to W^+W^-$ signal in the signal region and the low BDT control region is shown in figures A.34 and A.35. The Optimal Observable distribution is symmetric around zero as expected for SM processes but slightly broader compared to other background sources. The di-boson sample statistics are however limited in the signal region of the CP analysis.

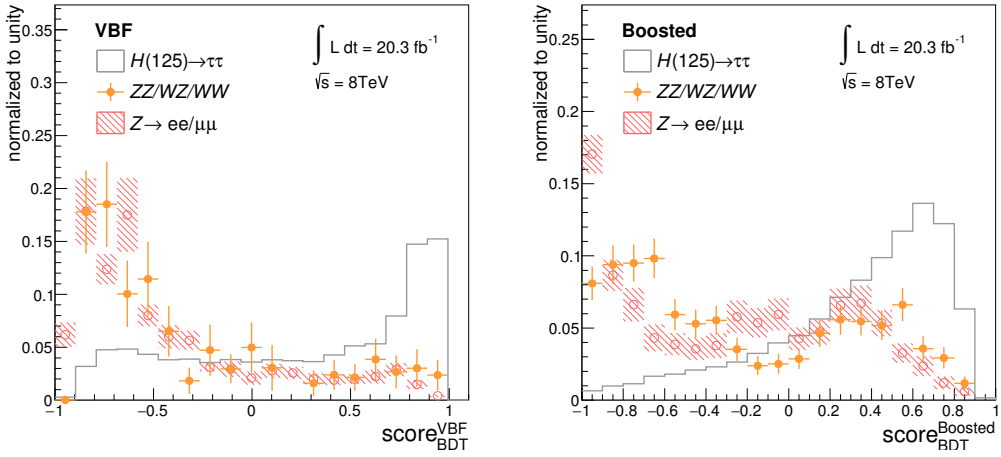

(a) (b)

Figure 7.31. *Distribution of the BDT classifier for di-boson, $Z/\gamma^* \to e^+e^-/\mu^+\mu^-$ and signal events in the VBF (a) and the Boosted (b) category.*

7.4. Top Quark Pair and Single Top Quark Production

The contribution of top quark processes ($t\bar{t}$ and single top quark production) to the overall background model is about 14% and 13% in the VBF and Boosted category and about 9% in the signal region of the CP analysis.

Top quark processes are estimated using simulation (see section 5.2.2). To validate the top quark background estimation and determine the corresponding sample normalisation, dedicated control regions are defined by inverting the nominal b jet veto selection criterion. A b jet tag provides a pure control sample for the top quark background, since b jets mainly originate from events with top quarks. The purity of the top quark-enriched control region is about 85% in the VBF and Boosted category. Figure 7.32 includes basic variables of lepton kinematics, the transverse missing energy and the transverse momentum of the leading jet after preselection including a b tag. The background model is in reasonable agreement with the data already at preselection level although slightly more data events ($\leq 4\%$) are observed than expected. The systematic normalisation uncertainties are typically at the level of 8% in both categories and stem from uncertainties on the b tag efficiency and the background estimation procedure itself, based on comparisons of top quark samples from different event generators. Therefore, residual differences in the normalisation and the shape of the distributions between data and the background model are expected to be covered by systematic uncertainties, which are not evaluated at preselection level. The sources of systematic uncertainties with respect to the top quark background estimation are discussed in section 8.3.4.

Figures 7.33, 7.34 and 7.35, 7.36, 7.37 show the distributions of the BDT input variables in dedicated category specific control regions of the VBF and Boosted category, which are again characterized by a b jet tag requirement in addition to the usual categorization cuts. All control region definitions are summarized in table 7.2. The modeling of the top quark background is in reasonable agreement with the observed data within systematic uncertainties. The distribution of the BDT classifier is shown in figure 7.38. The data is well reproduced by the simulated top quark sample. Similar to the $Z/\gamma^* \to e^+e^-/\mu^+\mu^-$ background distribution, a second peak at more signal-like classifier values is observed for top quark events in case of the Boosted category.

In addition to the dedicated $Z/\gamma^* \to e^+e^-/\mu^+\mu^-$ control regions in the VBF and Boosted categories, the event yields for the top quark control regions are also added to the fit model to constrain the background normalisation for $t\bar{t}$. The normalisation factors are correlated across the signal and control regions but uncorrelated across both categories to take differences in the modeling of both phase space regions into account. The initial prefit normalisation of the top quark sample is corrected such that differences between prediction and data are compensated in the control regions. The prefit scale factors of the VBF and Boosted category are listed in table 7.3 and are consistent with unity, which denotes a good modeling of the simulated top

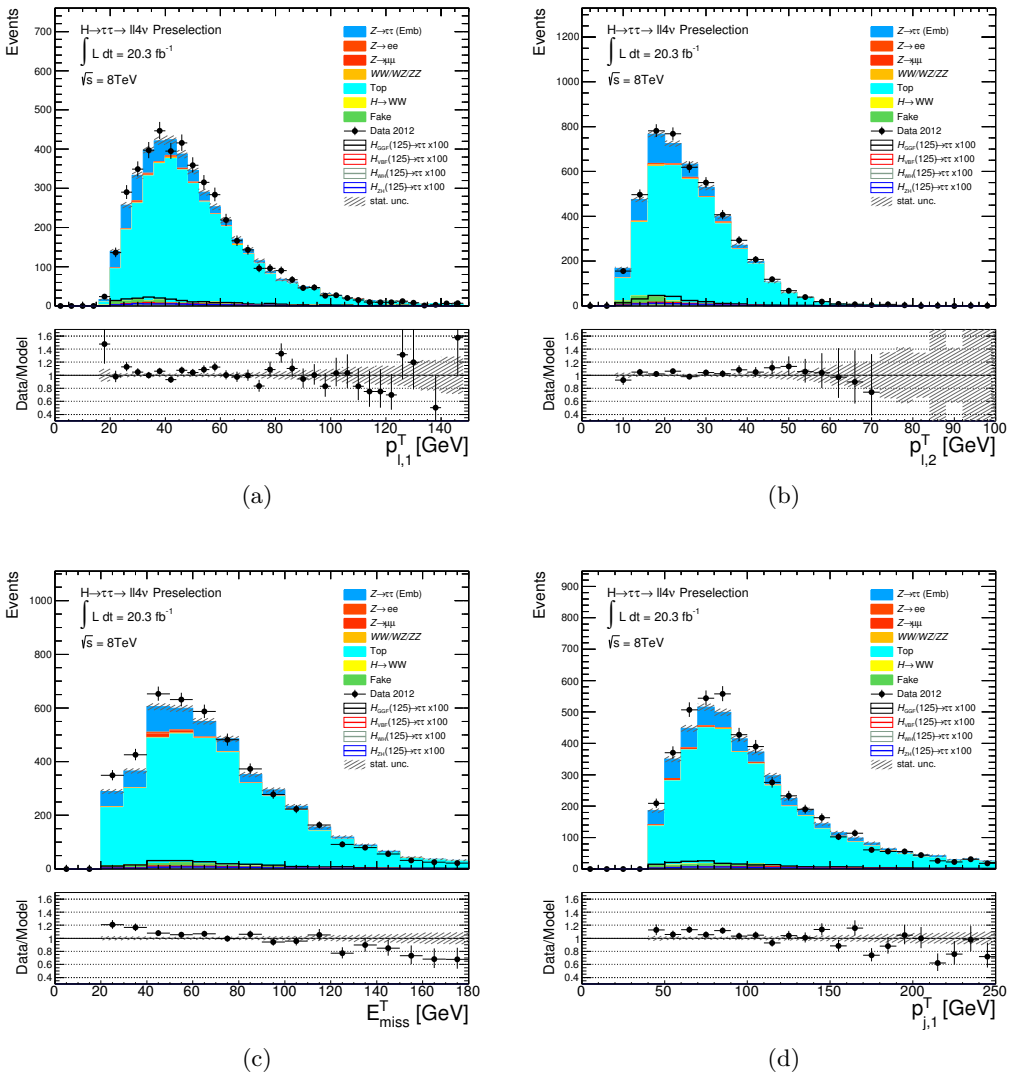

Figure 7.32. *Basic distributions of p_T^{l1}, p_T^{l2}, $E_{\mathrm{T}}^{\mathrm{miss}}$ and p_T^{j1} after preselection and before categorization (see section 5.3), including a b jet tag. The error band includes statistical uncertainties only.*

quark sample. Nonetheless, the top quark normalisation is free to float in the final fit.

The three most signal-like bins of the BDT classifier distributions contain 3.5 ± 0.9 and 28.2 ± 2.9 expected events in the VBF and Boosted category at prefit level, which corresponds to a relative fraction of 9% and 18% with respect to the total background prediction. A comparison of the BDT classifier shape for top quark events with signal is shown in figures A.32 and A.33 for the VBF and Boosted categories.

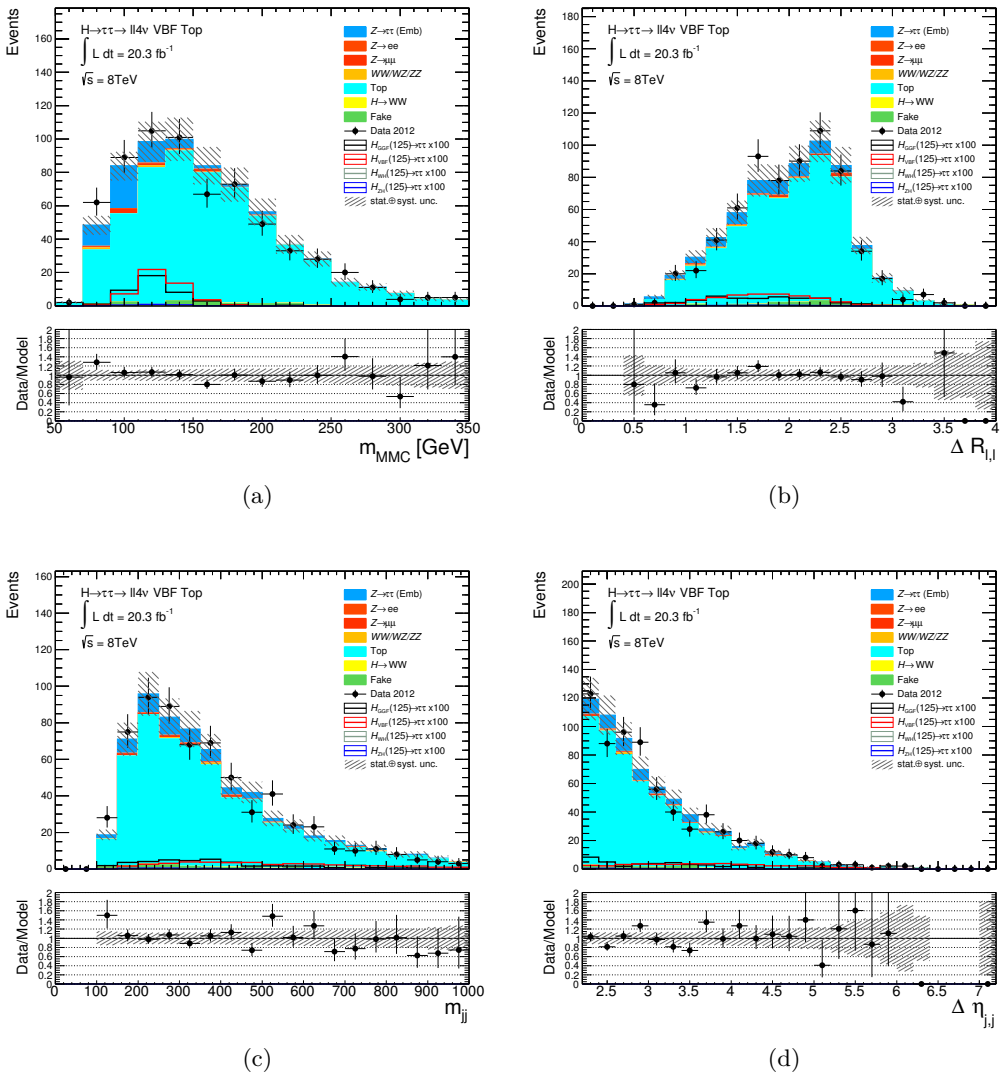

(a) (b)

(c) (d)

Figure 7.33. *BDT input variables in the dedicated top quark control region of the VBF category. The error band includes statistical and systematic normalisation uncertainties.*

Information from the VBF top quark control region is also included in the fit of the CP analysis to constrain the top quark normalisation. The same definition is chosen as in the VBF category with the additional cut $|OO < 15|$ to be consistent with the signal region. The control region is again implemented in terms of a counting experiment and only the event yields are used in the fit. Figure 7.39 shows the modeling of the Optimal Observable and signed $\Delta\phi(j_1, j_2)$ in this region. The data is well described by the prediction. Shape comparisons of the top quark background with the signal can be found in figures A.34 and A.35 for the signal and low BDT control region of the CP analysis. Events from Standard Model top quark processes are found to be distributed symmetrically around an Optimal Observable value of

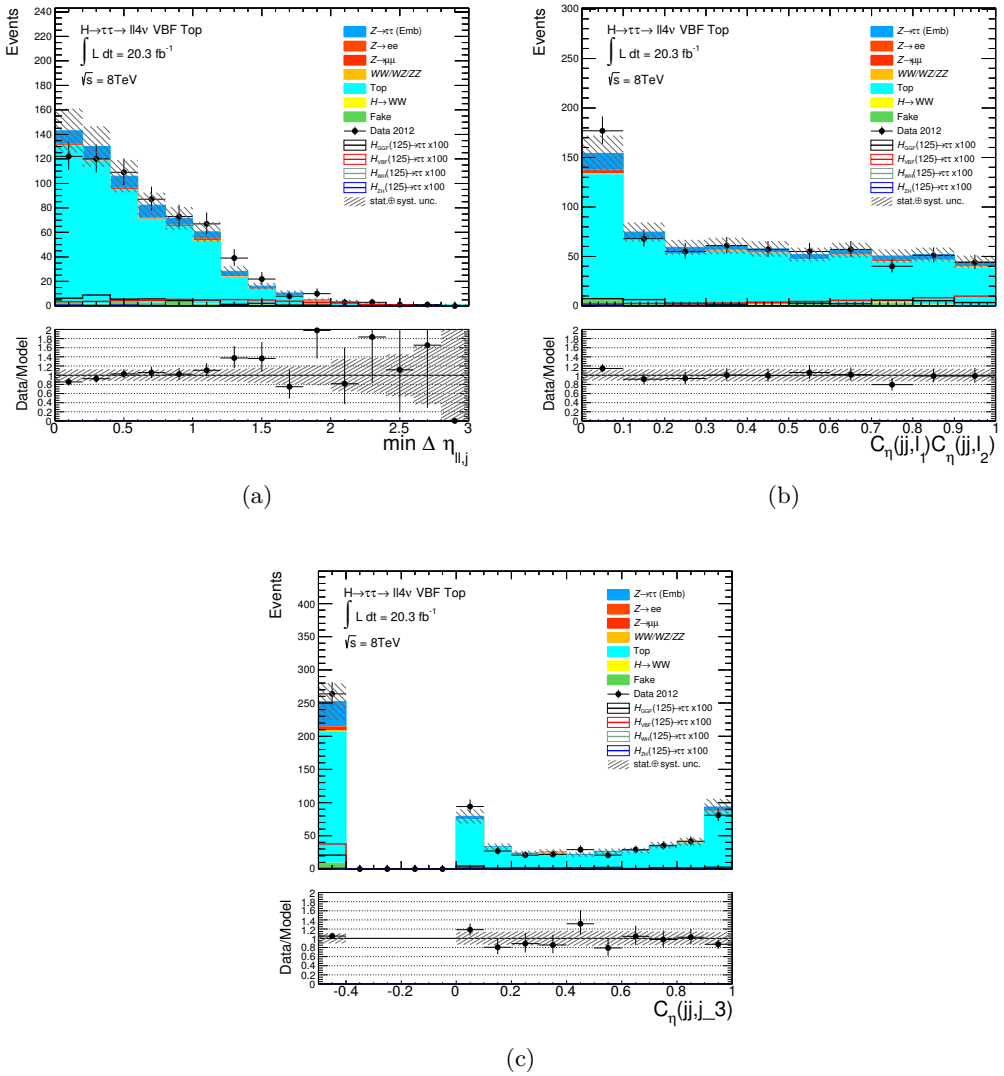

(a) (b)

(c)

Figure 7.34. *BDT input variables in the dedicated top quark control region of the VBF category. The error band includes statistical and systematic normalisation uncertainties.*

zero within statistics.

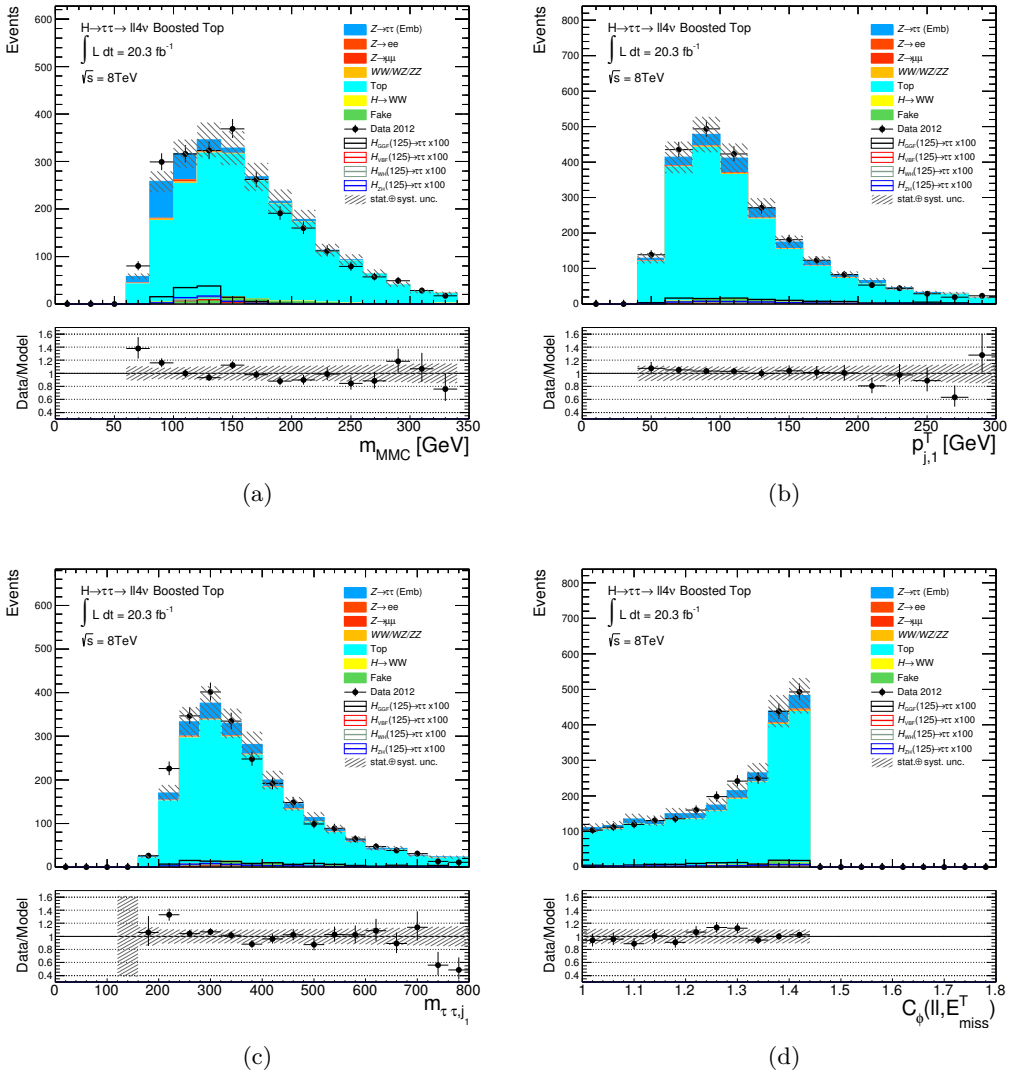

Figure 7.35. *BDT input variables in the dedicated top quark control region of the Boosted category. The error band includes statistical and systematic normalisation uncertainties.*

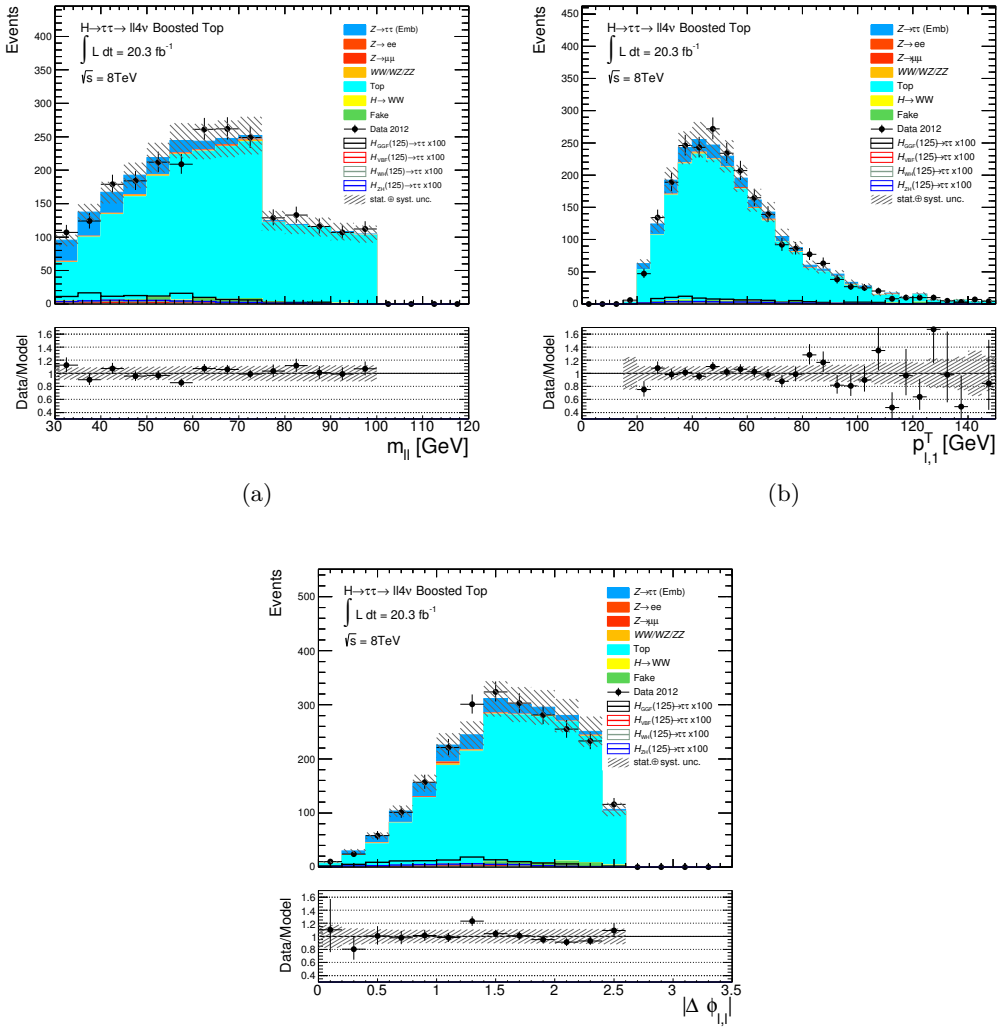

(a) (b)

(c)

Figure 7.36. *BDT input variables in the dedicated top quark control region of the Boosted category. The error band includes statistical and systematic normalisation uncertainties.*

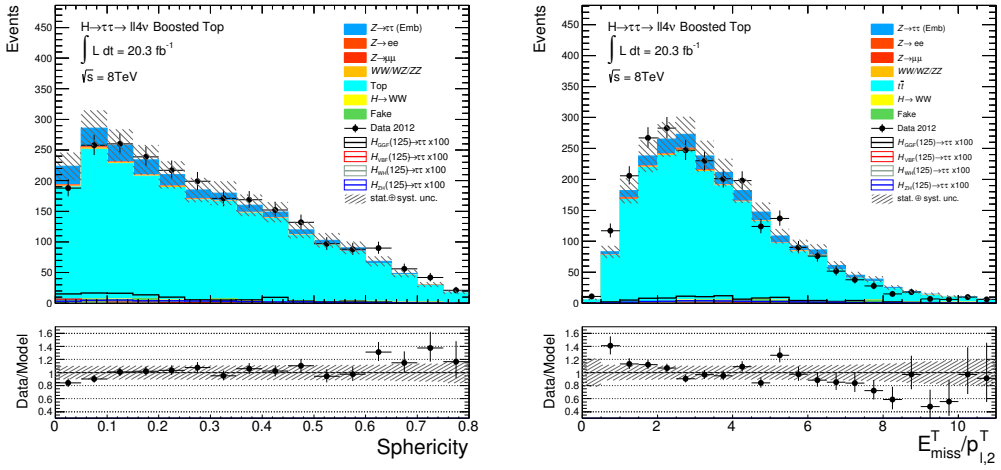

(a) (b)

Figure 7.37. *BDT input variables in the dedicated top quark control region of the Boosted category. The error band includes statistical and systematic normalisation uncertainties.*

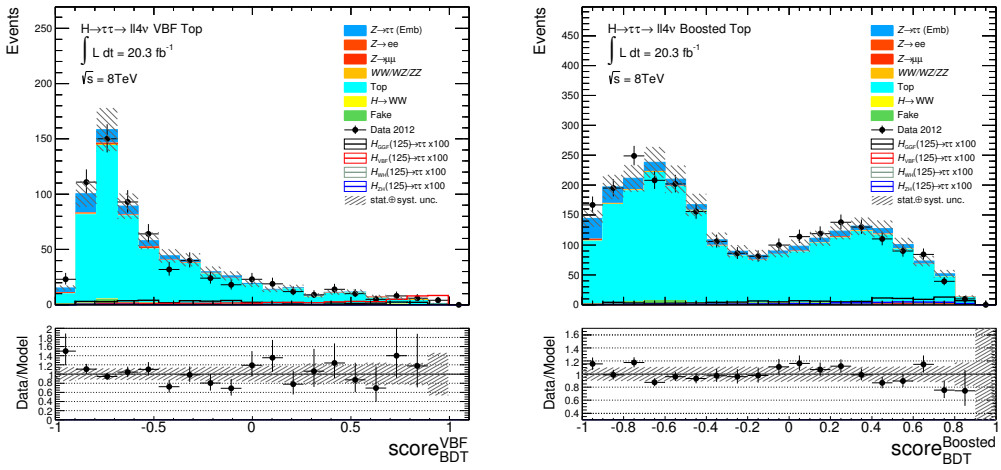

(a) (b)

Figure 7.38. *BDT classifier distributions in the dedicated top quark control regions of the VBF (a) and Boosted (b) category. The error band includes statistical and systematic normalisation uncertainties.*

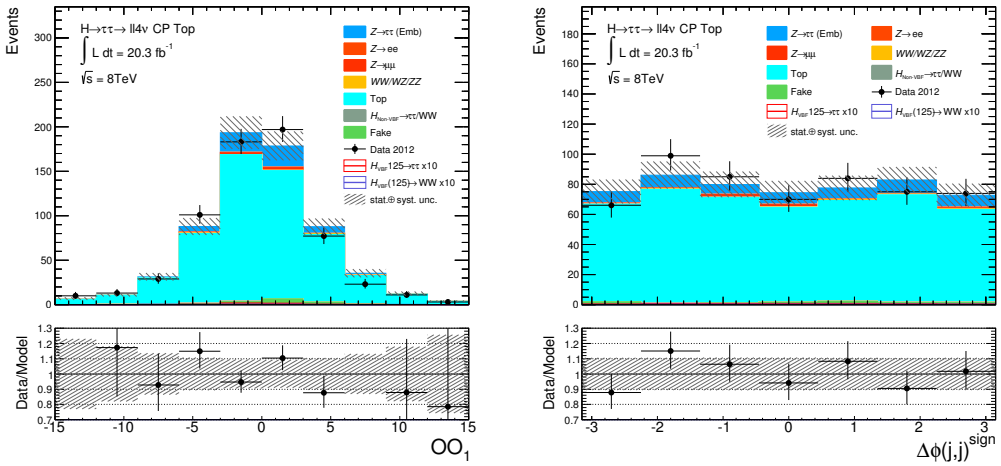

(a) (b)

Figure 7.39. *Optimal Observable (a) and signed $\Delta\phi(j_1, j_2)$ (b) distribution in the dedicated top quark control region of the CP analysis. An additional cut on $|OO| < 15$ is included to model the corresponding efficiency of the signal region. In case of signed $\Delta\phi(j_1, j_2)$ as final discriminant, both leading jets are required to emerge in different hemispheres. The error band includes statistical and systematic normalisation uncertainties.*

7.5. Fake Leptons

Background events with fake leptons originate from processes with at least one reconstructed object, which is mis-identified as a lepton such as jets or photons faking an electron. Typical processes, including fake leptons, are single top quark events and the production of top quark pairs, where one of the top quarks decays into a bottom quark and a hadronically decaying W boson. Other important sources of fake leptons in the analyses are QCD multi-jet events and the production of a W boson in association with jets. The relative fraction of background from fake leptons compared to the total background is about 6% in the VBF category and in the signal region of the CP analysis and approximately 3% in the Boosted category. Although the cross section of such processes is rather large at the LHC, they are strongly suppressed in the present analyses due to the lepton isolation criteria, which are summarized in table 4.1.

The generation of a QCD multi-jet sample with sufficiently large statistics is very time and CPU consuming because of the small selection efficiency of the present analyses. Furthermore, higher order QCD corrections, which are important in case of pure QCD multi-jet processes, are typically missing in simulated events. Therefore, the estimation of fake leptons is based on a data-driven template method instead, using dedicated fake lepton control regions. In this section, the template method and its assumptions is discussed. A template, which describes the shape of a particular observable for events with fake leptons, is extracted from a dedicated fake lepton control region by subtracting all non-fake background components from the observed data. This template is then used in the signal region for estimating the fake lepton background distribution. The normalisation of the template is determined in a fit to data after a basic set of preselection cuts, where the signal is still negligible and the amount of fake lepton events is large enough to provide stable fit results. The non-fake background components are expected to be well modeled at this stage of the selection by the corresponding specific background estimation methods. The fitting procedure is based on a minimum χ^2 estimation of the background model with respect to data with the fake lepton template normalisation being the only unconstrained parameter. The template method assumes equivalent shapes of the fake lepton distributions for each variable in the fake control and the signal region. Furthermore, the normalisation factors of the templates are assumed to be independent from the various signal region cuts, since they are determined at preselection but applied in the VBF and Boosted category and the signal region of the CP analysis in the end.

In the analyses, the fake lepton control region of a given signal selection (VBF or Boosted category or signal region of the CP analysis) is defined by the same selection cuts but inverting the lepton track isolation $p_T^{\mathrm{cone}\Delta R}$ and removing the requirement on calorimeter isolation $E_T^{\mathrm{cone}\Delta R}$. Since fake leptons, mainly mis-identified jets, tend to be unisolated, inverting or loosening lepton isolation cuts results in high purity control regions. The template normalisation is determined after basic preselection cuts with regular lepton isolation requirements listed in table 7.2 by fitting the

fake lepton template of the sub-leading lepton transverse momentum distribution p_T^{l2}. The variable p_T^{l2} provides a good separation between the non-fake lepton background and much softer fake lepton events, which improves the ability of the χ^2 minimization to constrain the template normalisation. Normalisation factors are determined in all four final state channels of the analyses since the corresponding event selection efficiencies differ, which is mainly due to the different electron and muon p_{T} thresholds. The template method is illustrated in figure 7.40.

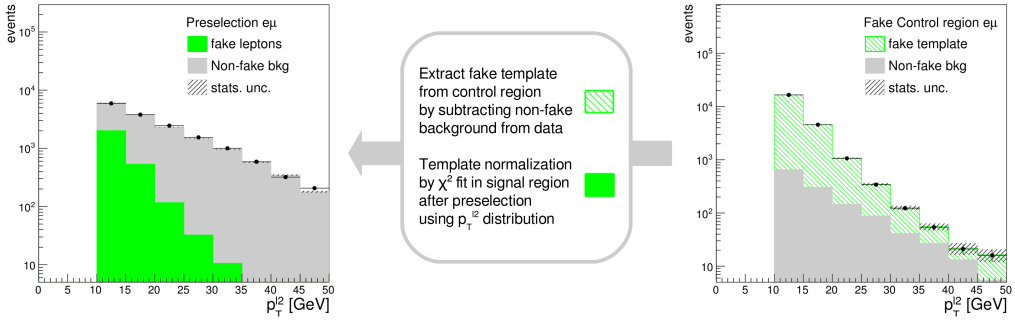

Figure 7.40. *Sketch of the data-driven template method, which is used in the analyses to estimate the fake lepton background. The template for a specific variable is extracted from a fake control region by modifying the lepton isolation criteria. The template normalisation is determined for each final state (here eμ example) by fitting the transverse momentum template of the sub-leading lepton at preselection level using regular lepton isolation based on a minimum χ^2 estimation. The normalisation factors are then used for all templates in the final signal region.*

Figure 7.41 shows the distributions of p_T^{l2} for each final state in the fake lepton control region after basic preselection cuts, where the template normalisation is determined. The control regions are dominated by fake lepton events with more than 70% of the contribution attributed to QCD multi-jet events in each of the final states. The residual fake lepton contribution consists of events from top quark and W boson production processes in approximately equal parts, based on studies using the corresponding simulated samples from table 5.1. The best fit fake template normalisation factors are summarized in table 7.4. Figure 7.42 shows the background model after preselection, where the template fit has been performed. The distributions are in reasonable agreement with the data for each final state. At this preselection level, the normalisation of the $Z/\gamma^* \to e^+e^-$ and $Z/\gamma^* \to \mu^+\mu^-$ background samples has been corrected by the scale factors 0.985 and 0.944 according to differences in the normalisation with respect to data in dedicated same flavour final state control regions, which are defined by changing the visible di-lepton mass cut into 80GeV$< m_{ee/\mu\mu} <$ 100GeV.

To verify the underlying assumption of the template method concerning cut-independent normalisation factors, the fit is performed after adding further cuts of the actual signal selection to the basic preselection, which is used for determining the default template normalisation factors. The additional selection criteria are $\Delta\phi(\ell_1, \ell_2) < 2.5$ and $0.1 < x_{\tau_1}, x_{\tau_2} < 1$, while the condition 115 GeV $< m_{\mathrm{coll}} <$

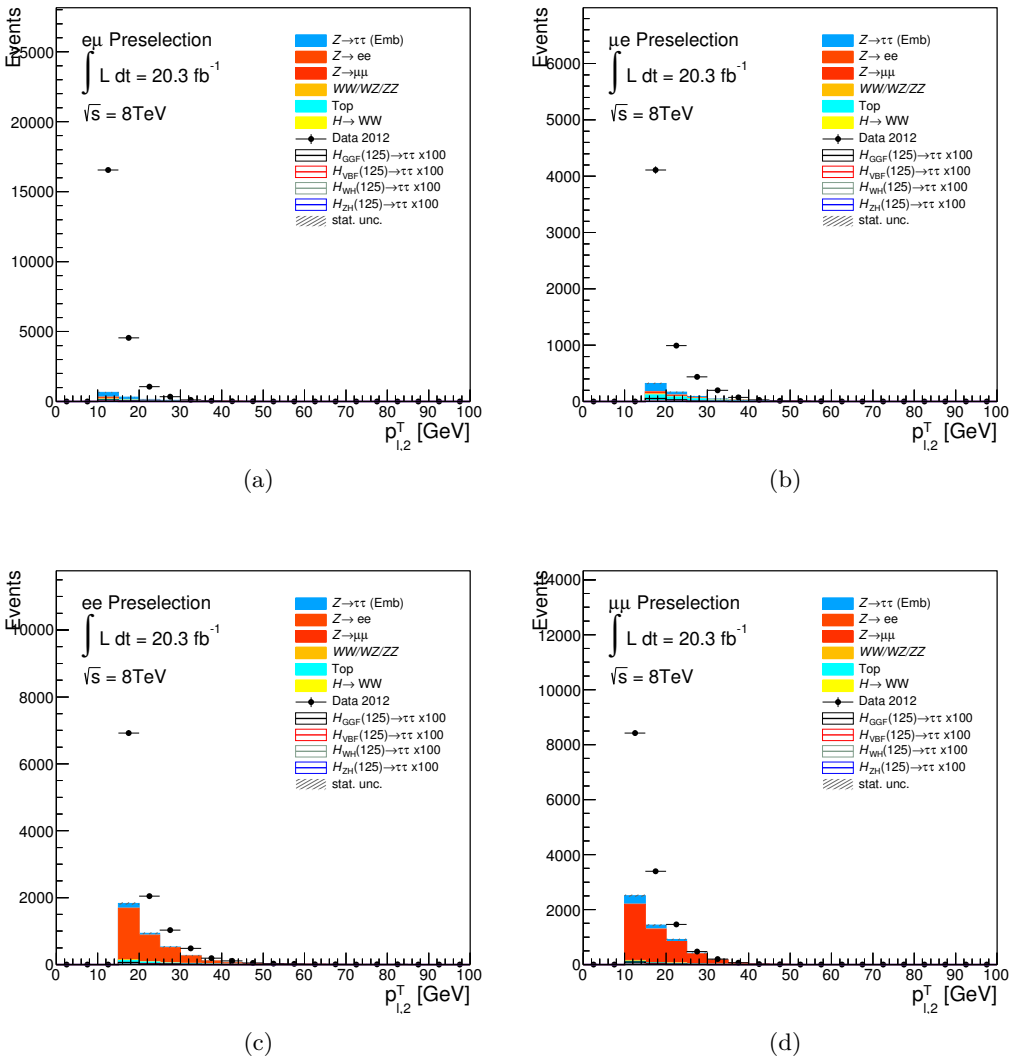

Figure 7.41. *Distributions of the transverse momentum of the sub-leading lepton in the fake lepton control region for each final state after basic preselection cuts, where the normalisation of the fake lepton templates is determined. The excess in data is expected to stem from fake lepton events. The selection, which is used for normalising the templates, and the corresponding fake control region are defined in table 7.2.*

135 GeV is imposed as well, to reduce the signal contribution. The alternative normalisation factors are listed in table 7.4 and have been extracted after correcting the normalisation of the $Z/\gamma^* \to e^+e^-$ and $Z/\gamma^* \to \mu^+\mu^-$ background by a factor of 0.95 and 0.91. The factors are in reasonable agreement with the default normalisation factors and the p_T^{l2} spectra are well modeled compared to data as shown in figure 7.43.

The fake lepton template normalisation taken from the fit is anti-correlated with the

Final state	Nominal Fake SF	Alternative Fake SF
eμ	0.126 ± 0.005	0.111 ± 0.010
μe	0.102 ± 0.014	0.106 ± 0.032
ee	0.234 ± 0.034	0.227 ± 0.065
$\mu\mu$	0.297 ± 0.033	0.293 ± 0.043

Table 7.4. *Fake lepton template normalisation factors (Fake SF) for each final state, determined by minimizing χ^2 of the expected background with respect to data after basic preselection cuts (default), which are listed in table 7.2, and the additional signal selection cuts $\Delta\phi(\ell_1, \ell_2) < 2.5$, $0.1 < x_{\tau_1}, x_{\tau_2} < 1$ and $m_{coll} < 115$ GeV, $m_{coll} > 135$ GeV for suppressing signal events (alternative).*

normalisation of the non-fake lepton background. Since a large set of uncertainties is included for all non-fake lepton samples and the fake lepton contribution is relatively small, no template fit specific normalisation uncertainties are considered for this background. However, an uncertainty due to the transfer of the template from the fake control region with anti-isolated leptons to the signal region with isolated leptons is assigned on the normalisation of this background. The systematic uncertainties are discussed in section 8.3.3.

It has also been assumed that the shape of the fake lepton distribution in the signal region is well described by the template, which is taken from the fake lepton control region. To verify this assumption, figure 7.44 shows the fake lepton template for the BDT classifier in the VBF and Boosted category requiring two leptons with the same charge instead of the opposite charge. The templates are then compared to corresponding templates from the same charge fake control region. These modified categories, which include events with two isolated leptons of the same charge instead of oppositely charged leptons, are signal free and can therefore be used to test the template shape for differences stemming from any bias due to the transfer from control regions with anti-isolated leptons to the signal regions with isolated leptons. The templates from both regions are in reasonable agreement within statistical uncertainties in each category. Since data statistics in the same charge regions are relatively low, shape uncertainties based on such differences are determined after loosening some of the signal selection cuts as explained in section 8.3.3.

The total expected fake lepton contribution in the VBF (Boosted) category at prefit level is approximately 61 ± 4.1 (98 ± 5.5) events, which corresponds to a fraction of 6% (3%) of the total background prediction. In the three most signal-like bins of the BDT classifier distribution 2.1 ± 0.7 (7.4 ± 1.5) events are expected, which corresponds to 6% (5%) of the total background in these bins. The separation between fake lepton and signal events with respect to the BDT classifier is illustrated in figure A.32 and A.33 for the VBF and Boosted category.

In the CP analysis, the fake lepton background is also estimated by the template method in the same way. The Optimal Observable distribution of fake lepton events is shown in figures A.34 and A.35 compared to Higgs boson events from the VBF

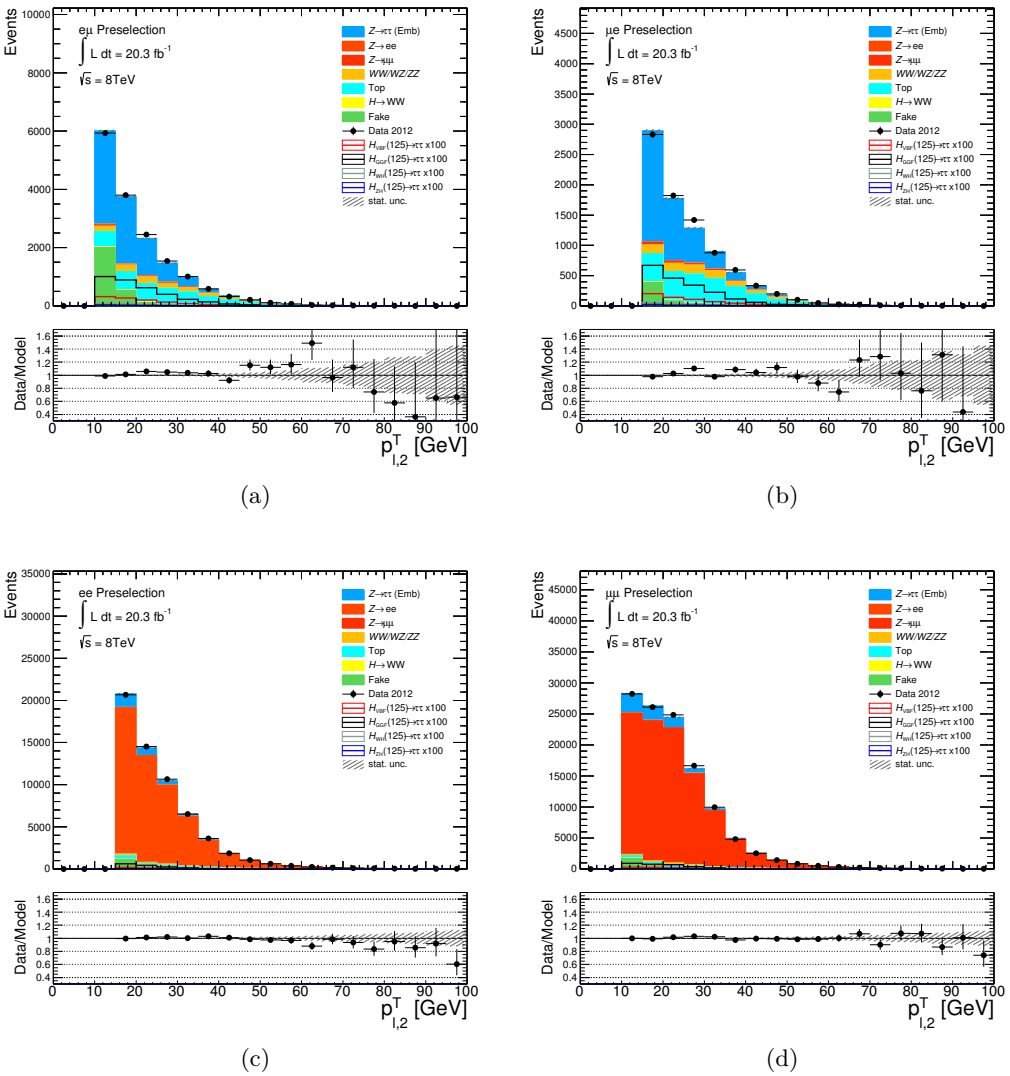

Figure 7.42. *Distributions of the transverse momentum of the sub-leading lepton for each final state including two isolated leptons after basic preselection cuts, where the normalisation of the fake lepton templates is determined. The selection, which is used for normalising the templates, is defined in table 7.2. The fake lepton templates are normalised using the factors from table 7.4.*

production mode in the high BDT signal and the low BDT control region.

7.6. $H \to W^+W-$

Higgs boson decays $H \to W^+W^- \to \ell^+\nu\ell^-\nu$ are treated as background in the analysis of the search for $H \to \tau^+\tau^- \to \ell^+\ell^-4\nu$. The estimation of this background

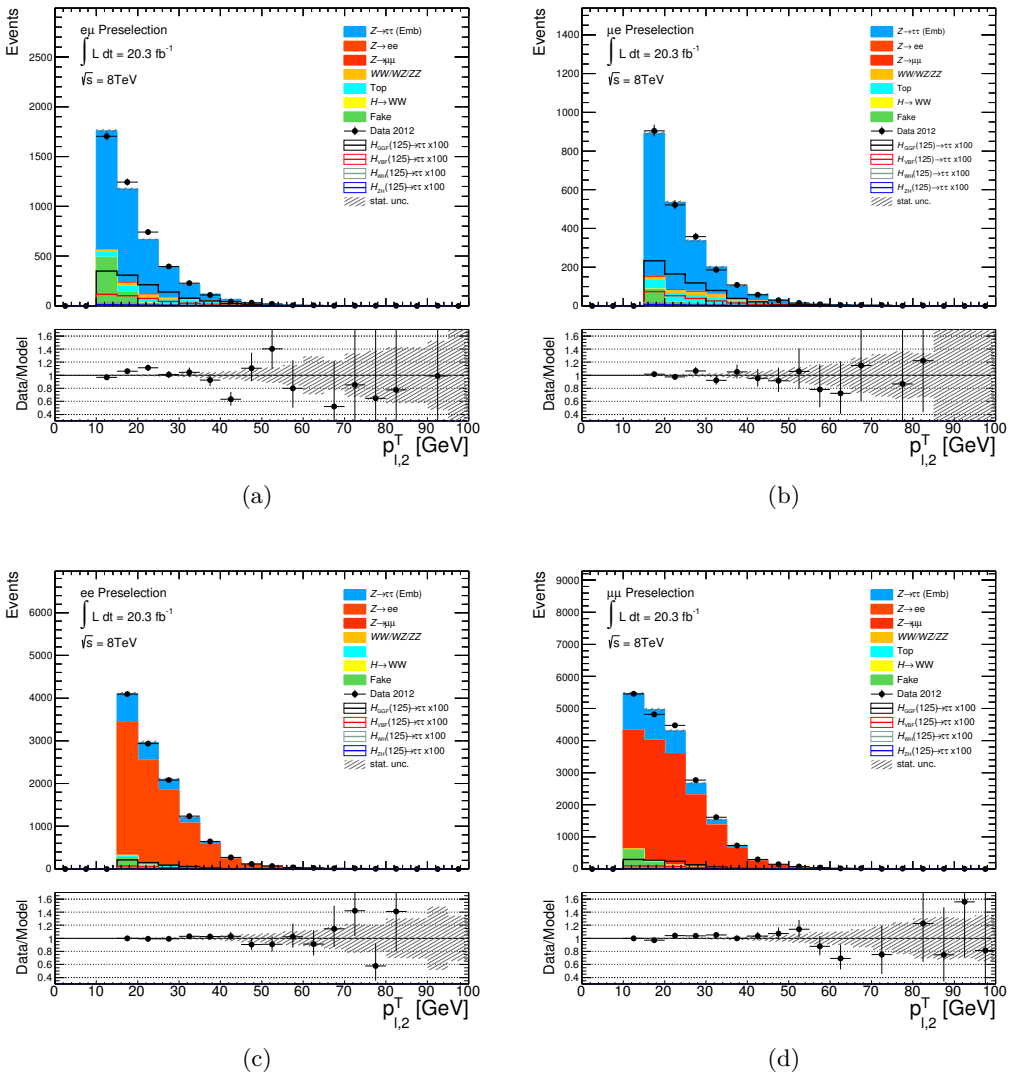

Figure 7.43. *Distributions of the transverse momentum of the sub-leading lepton for each final state including two isolated leptons after basic preselection cuts, where the normalisation of the fake lepton templates is determined, including the additional cuts* $\Delta\phi(\ell_1, \ell_2) < 2.5$ *and* $0.1 < x_{\tau_1}, x_{\tau_2} < 1$ *and the signal suppressing cut on* $m_{coll} <$ 115 GeV, $m_{coll} > 135$ GeV. *The selection used for normalising the templates is defined in table 7.2. The fake lepton templates are normalised with the alternative scale factors from table 7.4.*

contribution is performed using Monte Carlo samples normalised according to table 5.1. These samples for GGF and VBF production modes are generated with POWHEG while PYTHIA is used in case of VH modes. Figure 7.45 shows the BDT classifier distribution of the individual production modes in both categories. As expected, events from the VBF mode are accumulated at signal-like classifier values in the VBF category, while the BDT in the Boosted category provides a slightly

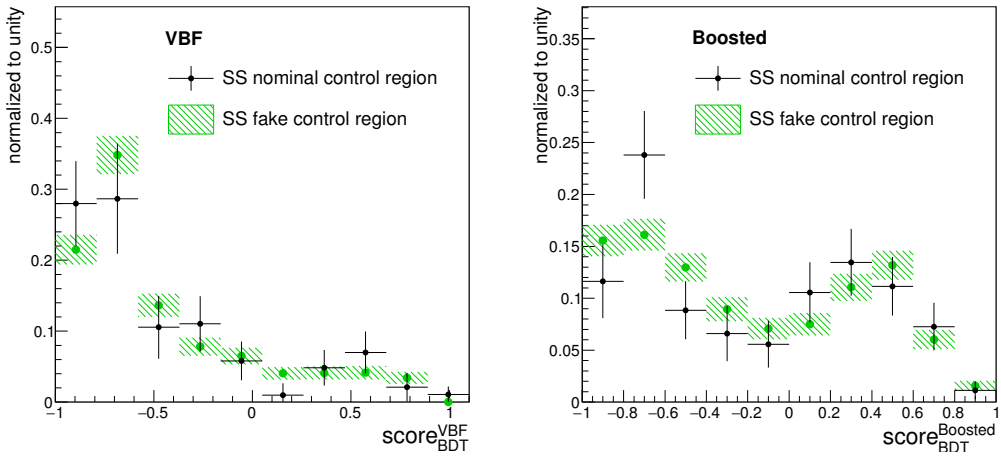

(a) (b)

Figure 7.44. *Comparison of the BDT classifier template taken from a same charge control region in the VBF and Boosted category, where both leptons are isolated and have the same charge, and the corresponding same charge fake control region.*

better separation from the signal.

The expected number of events in the three highest bins of the BDT classifier is 1.4 ± 0.1 (1.5 ± 0.1) compared to 6.5 ± 0.1 (7.2 ± 0.1) for the $H \to \tau^+\tau^- \to \ell^+\ell^- 4\nu$ signal in the VBF (Boosted) category. The event yields for $H \to W^+W^- \to \ell^+\nu\ell^-\nu$ correspond to a relative background contribution of approximately 4% (1%) in these bins. Hence, the $H \to W^+W-$ background component plays a minor role in the search for $H \to \tau^+\tau^- \to \ell^+\ell^- 4\nu$, which is mainly due to the preselection cut $m_{\tau\tau}^{\text{coll}} > m_Z - 25$ GeV in order to avoid an overlap with the analysis of the search for $H \to WW^* \to \ell\nu\ell\nu$ [176]. In the final fit of the analysis, the normalisation of $H \to W^+W^-$ is fixed to the Standard Model cross section.

In the CP analysis, the VBF mode of $H \to W^+W^- \to \ell^+\nu\ell^-\nu$ is treated as signal along with the corresponding di-τ Higgs boson decays since their Optimal Observable and signed $\Delta\phi(j_1, j_2)$ distributions are sensitive to CP-violation. Therefore, only the non-VBF mode Higgs boson decays into two W boson contribute to the background. The relative fraction of these events is about 1% with respect to the total background in the signal region of the CP analysis.

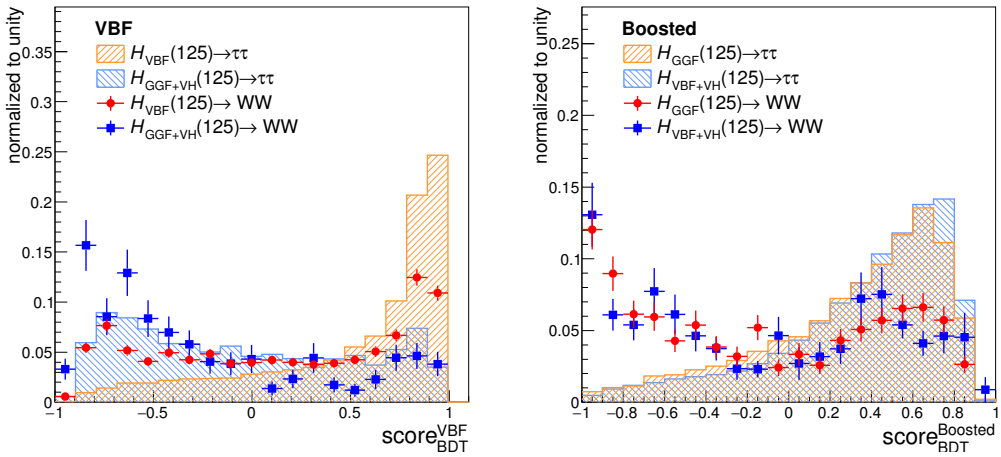

(a) (b)

Figure 7.45. *BDT classifier distribution the individual production modes of the Higgs boson including the subsequent decay into two τ leptons and two W bosons in VBF (a) and Boosted (b) category.*

8 Systematic Uncertainties

Systematic uncertainties in the analysis of the search for $H \to \tau^+\tau^- \to \ell^+\ell^- 4\nu$ and the CP analysis stem from various sources. Firstly (see section 8.1), there are experimental uncertainties due to the luminosity measurement and limitations in the determination of trigger, reconstruction and identification efficiencies of physics objects, which need to be accounted for in the event simulation. Imperfections in the calibration of energy scales and the momentum resolution of leptons, jets or the missing transverse energy contribute as well. These uncertainties are propagated to the full analyses by varying specific parameters of all simulated samples during the event reconstruction. Secondly (see section 8.2), theory related uncertainties need to be considered, when generating events. There are uncertainties due to the choice of parton density distributions, the QCD scale and the modeling of the underlying event and parton shower as well as missing higher orders in calculations of cross section or branching ratio predictions and approximative higher order corrections. Thirdly (see section 8.3), uncertainties due to data-driven background estimation techniques are included. There are also CP analysis specific uncertainties due to the usage of re-weighting the Standard Model signal sample to represent non-SM signals. The various uncertainties are propagated to the analyses and affect both the estimated event yields as well as the shapes of differential distributions. While the normalisation effect of variations within the uncertainties is quoted in each of the sections mentioned so far, the shape variations are presented in section 8.4. Additional pruning criteria are explained, which are used to determine which sources of systematic uncertainties can be neglected, either on the final event yields or on differential distributions. Further smoothing and symmetrization algorithms reduce the impact of statistical fluctuations on systematic variations. The impact of the relevant uncertainties, which are discussed in this section, on the final results of the search and the CP analysis is summarized in section 10.

The extraction of the best-fit signal strength $\hat{\mu}$ is based on a profile likelihood approach. Uncertainties, which are quoted in the following sections, and normalisation factors are included in the likelihood function in terms of additional degrees of freedom, so called *nuisance parameters*. A detailed description of the fitting procedure and the likelihood function of the analyses is given in chapter 9. An overview and additional information about the the fit model of the analysis of the search for $H \to \tau^+\tau^- \to \ell^+\ell^- 4\nu$ and the CP analysis, such as the importance[1]

[1] Importance in this context means the impact of the nuisance parameters on the final results of the different analyses in terms of nuisance parameter rankings as explained in more detail in section 10.

of all nuisance parameters, can be found in appendix B. In this appendix, also a summary and short description of all nuisance parameters acronyms can be found, that are used in the following sections.

8.1. Experiment Uncertainties

8.1.1. Luminosity

The integrated luminosity is used to normalise the signal samples. The uncertainty on the measured luminosity in 2012 data is $\pm 2.8\%$. Information about the data conditions in 2012 and the derivation of the luminosity can be found in section 3.3. The normalisation of each background sample is extracted from data in dedicated control regions. Therefore, no luminosity uncertainty needs to be considered for these background processes.

8.1.2. Trigger & Reconstruction Efficiencies

The normalisation effect of systematic uncertainties of lepton trigger efficiencies is at the order of 1-2% in the VBF and Boosted category and the CP analysis. The trigger selection, summarized in section 4.3.1, combines single- and di-lepton triggers. Uncertainties on reconstruction and identification efficiencies are approximately 1% for muons and $< 1\%$ for electrons in both analyses. The reconstruction and identification algorithms of leptons are discussed in sections 4.3.2, 4.3.3 and 4.4.2. The measurement of trigger and reconstruction efficiencies and their corresponding uncertainties is mainly based on the tag-and-probe method [107–109, 112, 113].

Since events with at least one b-tag jet are vetoed in the signal region selections and a b-tag jet is required in the top quark enriched control regions, uncertainties on b-tagging efficiencies need to be considered (b-tagging has been discussed in section 4.5.4). There are 26 different uncertainties related to b-tagging, which are determined by diagonalizing the corresponding covariance matrix [132–134]. These components are divided into groups of uncertainties for tagging b, c and light flavour quarks as well as τ leptons. The resulting uncertainties on the final expected event yields are 7-12% at most for top quark processes in the signal regions and $< 1\%$ for all non top quark processes. In the top quark enriched control regions, the uncertainties on the event yields from top quark processes are 2-3%.

The uncertainty on the jet efficiency due to Jet-Vertex-Fraction (JVF) criteria (see section 4.5.3) is estimated to be $< 1\%$ for all processes in the various regions and categories of the analyses [130]. In addition, specific modules of the tile calorimeter were accidentally either temporarily or permanently masked throughout all data taking periods, which leads to a bias in the jet reconstruction. The estimated effect on the expected event yields when rejecting such affected events is at most 1% in case of the VBF category and the CP signal region and about 2% in the Boosted

category. This uncertainty is applied to all processes of the corresponding analysis and referred to as BCH.

Table 8.1 summarizes the effect of the systematic uncertainty on the above mentioned efficiencies on the final event yields in the signal regions of the VBF and Boosted category and the CP analysis. The uncertainties are applied to all simulated samples. They have been determined by propagating official ATLAS results to the full analyses. Uncertainties on the shape of the BDT classifier, the Optimal Observable and signed $\Delta\phi(j_1, j_2)$ distributions are discussed and summarized in section 8.4.

8.1.3. Energy Scales & Momentum Resolution

The calibration of the electron energy or muon momentum scale as well as the resolution measurements are based on Z boson, J/Ψ and Υ decays with electrons or muons in the final state (see sections 4.3.4 and 4.4.3). To estimate the corresponding uncertainties with respect to the present analyses, the energy and momentum scales are varied by $\pm 1\sigma$ in the event reconstruction. Additional smearing factors are applied per event in case of the energy and momentum resolution. The 1σ deviations and smearing factors are taken from the official ATLAS measurements [111, 113]. The muon momentum resolution uncertainty is decomposed into components for the ID and the MS, which are treated as uncorrelated. Since the measurements of the electron and muon scales and resolutions are very precise, the propagated uncertainties are $< 1\%$ in all regions and categories.

The jet energy calibration and the modeling of jet momentum is described in sections 4.5.2 and 4.5.3. As for electrons and muons, the jet energy resolution uncertainty is estimated by smearing the nominal jet energy. This results in a one-sided uncertainty of $\leq 6\%$ for all processes except for the $Z/\gamma^* \to e^+e^-/\mu^+\mu^-$ background, where it is one of the dominating uncertainties of 14-25% depending on the analysis and the category. The typically low jet multiplicity for such processes and the special VBF-like and boosted phase space requirements cause a large dependence of the final event yield on the jet energy resolution (see section 7.2). The one-sided jet energy resolution uncertainty is symmetrized (see section 8.4). The uncertainties on the jet energy scale, which are propagated to the analyses, are divided into several groups [116]

- **In-situ analysis uncertainties** determined from the Z+jet, γ+jet and multi-jet balance methods. These uncertainties are subdivided into groups of statistical, detector, modeling and mixed components.
- **Intercalibration uncertainties** in different detector η regions. This uncertainty is subdivided into a statistical and a modeling component.
- **Flavour composition and response uncertainties** due to the limited knowledge about the quark/gluon jet composition and a difference in the calorimeter response of quark or gluon initiated jets. In the present analyses,

VBF			
Efficiency	VBF$H \to \tau^+\tau^-$	GGF$H \to \tau^+\tau^-$	V$H \to \tau^+\tau^-$
Trigger	$\pm 1\%$	$\pm 1\%$	$\pm 1\%$
Electrons	$\pm 1\%$	$\pm 1\%$	$\pm 1\%$
Muons	$\pm 1\%$	$\pm 1\%$	$\pm 1\%$
b-jets	$< 1\%$	$< 1\%$	$< 1\%$
JVF	$< 1\%$	$< 1\%$	$\pm 1\%$
BCH	$\pm 1\%$	$\pm 1\%$	$\pm 1\%$
Efficiency	top quark	$Z \to ee/\mu\mu$ & di-boson	$H \to W^+W^-$
Trigger	$\pm 1\%$	$\pm 2\%$	$\pm 1\%$
Electrons	$\pm 1\%$	$< 1\%$	$\pm 1\%$
Muons	$\pm 1\%$	$\pm 1\%$	$\pm 1\%$
b-jets	$\pm 10\%$	$< 1\%$	$< 1\%$
JVF	$< 1\%$	$\pm 2\%$	$\pm 1\%$
BCH	$\pm 1\%$	$\pm 1\%$	$\pm 1\%$
Boosted			
Efficiency	VBF$H \to \tau^+\tau^-$	GGF$H \to \tau^+\tau^-$	V$H \to \tau^+\tau^-$
Trigger	$\pm 1\%$	$\pm 1\%$	$\pm 1\%$
Electrons	$\pm 1\%$	$\pm 1\%$	$\pm 1\%$
Muons	$\pm 1\%$	$\pm 1\%$	$\pm 1\%$
b-jets	$< 1\%$	$< 1\%$	$< 1\%$
JVF	$< 1\%$	$< 1\%$	$< 1\%$
BCH	$\pm 2\%$	$\pm 2\%$	$\pm 2\%$
Efficiency	top quark	$Z \to ee/\mu\mu$ & di-boson	$H \to W^+W^-$
Trigger	$\pm 1\%$	$\pm 1\%$	$\pm 1\%$
Electrons	$\pm 1\%$	$< 1\%$	$\pm 1\%$
Muons	$\pm 1\%$	$\pm 1\%$	$\pm 1\%$
b-jets	$+12\%/-11\%$	$< 1\%$	$< 1\%$
JVF	$< 1\%$	$+5\%/-1\%$	$< 1\%$
BCH	$\pm 2\%$	$\pm 2\%$	$\pm 2\%$
CP			
Efficiency	VBF$H \to \tau^+\tau^-$	VBF$H \to W^+W^-$	non VBF Higgs
Trigger	$\pm 1\%$	$\pm 1\%$	$\pm 1\%$
Electrons	$\pm 1\%$	$< 1\%$	$< 1\%$
Muons	$\pm 1\%$	$\pm 1\%$	$\pm 1\%$
b-jets	$< 1\%$	$< 1\%$	$< 1\%$
JVF	$< 1\%$	$< 1\%$	$< 1\%$
BCH	$\pm 1\%$	$\pm 1\%$	$\pm 1\%$
Efficiency	top quark	$Z \to ee/\mu\mu$ & di-boson	
Trigger	$\pm 1\%$	$\pm 1\%$	
Electrons	$\pm 1\%$	$\pm 1\%$	
Muons	$\pm 1\%$	$\pm 1\%$	
b-jets	$+8\%/-7\%$	$< 1\%$	
JVF	$+8\%/-1\%$	$+1\%/-2\%$	
BCH	$\pm 1\%$	$\pm 1\%$	

Table 8.1. *Relative uncertainties on the expected event yields (up/down in [%]) in the signal region of the VBF and Boosted categories and the CP analysis due to selection, trigger and reconstruction efficiency uncertainties. In case of the CP analysis, the uncertainties are quoted for pure SM signal.*

the calorimeter response uncertainty is treated as uncorrelated between samples, where the reconstructed jets are assumed to originate from gluons or quarks.

- **b jet uncertainty** as exclusive composition and response uncertainty for this specific quark type.
- **Pile-up uncertainty** due to in-time and out-of-time pileup. The separate components for this are dependent on the number of primary vertices, average interactions per bunch-crossing, transverse momentum and jet topology. The topology dependent uncertainty components are treated as uncorrelated between processes, where gluons or quarks are expected to take part in the hard scattering interaction.

Energy scale uncertainties are one of the main sources of uncertainties for all simulated processes, especially in case of $Z/\gamma^* \to e^+e^-/\mu^+\mu^-$ and top quark background contributions. The uncertainties for these specific processes are typically more pronounced in the signal-like BDT classifier region, which is equivalent to the signal region of the CP analysis.

Systematic variations of the energy and the momentum components of the leptons and jets are propagated to the missing transverse energy. This also affects the final expected event yields since the event selection includes a cut on $E_{\mathrm{T}}^{\mathrm{miss}}$. Furthermore, the uncertainty on the energy scale and resolution of the soft $E_{x/y}^{\mathrm{miss,soft}}$ term is taken into account. The soft term reconstruction is explained in section 4.7.1 and the effect of its uncertainty is typically small, since the analysis exploits boosted phase space regions and event topologies with real $E_{\mathrm{T}}^{\mathrm{miss}}$ from neutrinos, where soft terms have only a minor impact.

The normalisation uncertainties due to energy and momentum scales and their resolution are summarized in tables 8.2, 8.3 and 8.4 for the signal regions of the search for $H \to \tau^+\tau^- \to \ell^+\ell^- 4\nu$ and the CP analysis. Information about corresponding shape uncertainties are given in section 8.4.

8.2. Theoretical Uncertainties

Various theory related uncertainties are considered for simulated processes and samples normalised to theoretical cross sections. These uncertainties originate from missing higher order corrections, the precision of parton density functions, the choice of Monte Carlo event generators and the modeling of parton shower and the underlying event.

8.2.1. Missing Higher Order Corrections

The accuracy of cross section predictions and the different event generator software used for simulating signal and background samples are quoted in table 5.1.

VBF			
	VBF$H \to \tau^+\tau^-$	GGF$H \to \tau^+\tau^-$	V$H \to \tau^+\tau^-$
E/p_T Resolution			
Electrons	$< 1\%$	$< 1\%$	$< 1\%$
Muons	$< 1\%$	$< 1\%$	$< 1\%$
Jets	$\pm 1\%$	$\pm 1\%$	$\pm 6\%$
E_T^{miss} soft term	$< 1\%$	$< 1\%$	$< 1\%$
E/p_T Scale			
Electrons	$< 1\%$	$< 1\%$	$< 1\%$
Muons	$< 1\%$	$< 1\%$	$< 1\%$
Jets in-situ	$\pm 3\%$	$\pm 5\%$	$+7\%/-6\%$
Jets intercalib	$\pm 5\%$	$+8\%/-7\%$	$+8\%/-6\%$
Jets flavour	$+4\%/-3\%$	$+5\%/-6\%$	$+9\%/-6\%$
Jets b jet	$< 1\%$	$< 1\%$	$< 1\%$
Jets pile-up	$\pm 2\%$	$+1\%/-2\%$	$+5\%/-3\%$
E_T^{miss} soft term	$< 1\%$	$< 1\%$	$< 1\%$
	top quark	$Z \to ee/\mu\mu$ & di-boson	$H \to W^+W^-$
E/p_T Resolution			
Electrons	$< 1\%$	$< 1\%$	$< 1\%$
Muons	$< 1\%$	$< 1\%$	$< 1\%$
Jets	$\pm 3\%$	$\pm 25\%$	$\pm 6\%$
E_T^{miss} soft term	$< 1\%$	$< 1\%$	$< 1\%$
E/p_T Scale			
Electrons	$< 1\%$	$\pm 2\%$	$< 1\%$
Muons	$< 1\%$	$< 1\%$	$< 1\%$
Jets in-situ	$\pm 3\%$	$+14\%/-18\%$	$+4\%/-6\%$
Jets intercalib	$+5\%/-4\%$	$+21\%/-22\%$	$+7\%/-9\%$
Jets flavour	$+3\%/-4\%$	$+17\%/-22\%$	$+5\%/-6\%$
Jets b jet	$< 1\%$	$< 1\%$	$< 1\%$
Jets pile-up	$\pm 1\%$	$+7\%/-8\%$	$+2\%/-3\%$
E_T^{miss} soft term	$< 1\%$	$\pm 1\%$	$< 1\%$

Table 8.2. *Relative uncertainties on the expected event yields in the signal region of the VBF category due to energy and momentum resolution and scale uncertainties.*

Boosted			
	VBF$H \to \tau^+\tau^-$	GGF$H \to \tau^+\tau^-$	V$H \to \tau^+\tau^-$
E/p_T Resolution			
Electrons	$< 1\%$	$< 1\%$	$< 1\%$
Muons	$< 1\%$	$< 1\%$	$< 1\%$
Jets	$< 1\%$	$\pm 1\%$	$+2\%/-3\%$
E_T^{miss} soft term	$< 1\%$	$< 1\%$	$< 1\%$
E/p_T Scale			
Electrons	$< 1\%$	$< 1\%$	$< 1\%$
Muons	$< 1\%$	$< 1\%$	$< 1\%$
Jets in-situ	$\pm 1\%$	$+3\%/-4\%$	$\pm 3\%$
Jets intercalib	$< 1\%$	$\pm 2\%$	$\pm 2\%$
Jets flavour	$\pm 2\%$	$\pm 5\%$	$\pm 4\%$
Jets b jet	$< 1\%$	$< 1\%$	$< 1\%$
Jets pile-up	$< 1\%$	$\pm 1\%$	$\pm 1\%$
E_T^{miss} soft term	$< 1\%$	$< 1\%$	$< 1\%$
	top quark	$Z \to ee/\mu\mu$ & di-boson	$H \to W^+W^-$
E/p_T Resolution			
Electrons	$< 1\%$	$< 1\%$	$< 1\%$
Muons	$< 1\%$	$< 1\%$	$< 1\%$
Jets	$< 1\%$	$\pm 14\%$	$\pm 2\%$
E_T^{miss} soft term	$< 1\%$	$\pm 1\%$	$< 1\%$
E/p_T Scale			
Electrons	$\pm 1\%$	$+5\%/-3\%$	$< 1\%$
Muons	$< 1\%$	$< 1\%$	$< 1\%$
Jets in-situ	$+4\%/-3\%$	$+14\%/-10\%$	$\pm 4\%$
Jets intercalib	$+1\%/-2\%$	$+12\%/-9\%$	$+2\%/-3\%$
Jets flavour	$\pm 2\%$	$+19\%/-14\%$	$+4\%/-3\%$
Jets b jet	$+2\%/-1\%$	$< 1\%$	$< 1\%$
Jets pile-up	$\pm 1\%$	$+6\%/-4\%$	$+2\%/-1\%$
E_T^{miss} soft term	$< 1\%$	$+2\%/-1\%$	$< 1\%$

Table 8.3. *Relative uncertainties on the expected event yields in the signal region of the Boosted category due to energy and momentum resolution and scale uncertainties.*

CP			
	VBF$H \to \tau^+\tau^-$	VBF$H \to W^+W^-$	non VBF Higgs
E/p_T Resolution			
Electrons	$< 1\%$	$\pm 1\%$	$\pm 1\%$
Muons	$< 1\%$	$+1\%/-3\%$	$< 1\%$
Jets	$\pm 3\%$	$\pm 3\%$	$< 1\%$
E_T^{miss} soft term	$< 1\%$	$\pm 1\%$	$\pm 1\%$
E/p_T Scale			
Electrons	$< 1\%$	$< 1\%$	-2.6/2.2
Muons	$< 1\%$	$< 1\%$	$< 1\%$
Jets in-situ	$+4\%/-5\%$	$+3\%/-6\%$	$+4\%/-9\%$
Jets intercalib	$+7\%/-8\%$	$+6\%/-10\%$	$+10\%/-12\%$
Jets flavour	$+4\%/-5\%$	$+2\%/-6\%$	$+4\%/-8\%$
Jets b jet	$< 1\%$	$< 1\%$	$< 1\%$
Jets pile-up	$+1\%/-2\%$	$+3\%/-5\%$	$+1\%/-5\%$
E_T^{miss} soft term	$< 1\%$	$< 1\%$	$< 1\%$
	top quark	$Z \to ee/\mu\mu$ & di-boson	
E/p_T Resolution			
Electrons	$+1\%/-11\%$	$< 1\%$	
Muons	$+10\%/-7\%$	$+2\%/-3\%$	
Jets	$\pm 3\%$	$\pm 22\%$	
E_T^{miss} soft term	$+6\%/-7\%$	$+4\%/-10\%$	
E/p_T Scale			
Electrons	$+4\%/-9\%$	$+1\%/-3\%$	
Muons	$+30\%/-6\%$	$+7\%/-3\%$	
Jets in-situ	$+30\%/-46\%$	$+14\%/-19\%$	
Jets intercalib	$+8\%/-26\%$	$+30\%/-21\%$	
Jets flavour	$+2\%/-17\%$	$+12\%/-29\%$	
Jets b jet	$+8\%/-20\%$	$< 1\%$	
Jets pile-up	$+21\%/-15\%$	$+3\%/-12\%$	
E_T^{miss} soft term	$+19\%/-1\%$	$+1\%/-4\%$	

Table 8.4. *Relative uncertainties on the expected event yields in the signal region of the CP analysis due to energy and momentum resolution and scale uncertainties. A SM signal is assumed.*

For estimating uncertainties due to missing higher order QCD corrections, the renormalisation and factorization scales μ_R and μ_F are varied by a factor of two around the nominal QCD scale value [35]. Samples, including these scale variations, are then processed through the nominal selection for the analysis emulated at parton level. This leads to process, analysis and category dependent QCD scale uncertainties.

In case of the VBF and VH Higgs boson signal samples, the nominal QCD scales are set to $\mu_{\mathrm{F}} = \mu_{\mathrm{R}} = {m_W}^2$ and the uncertainties on the cross sections are estimated to be 1-4% depending on the analysis, the corresponding category and the process. In addition, an overall 2% uncertainty due to higher order electroweak corrections is applied [8, 35]. Concerning the VBF Higgs boson signal in the CP analysis, the same set of scale uncertainties is applied as in the VBF category. No noticeable effect has been observed when re-evaluating the uncertainties for the change in the selection efficiency due to the cut on the BDT classifier.

The estimation of QCD scale uncertainties on the GGF Higgs boson process is also determined at parton level by scale variations of a factor of two around the nominal value $\mu_{\mathrm{F}} = \mu_{\mathrm{R}} = \sqrt{m_H^2 + p_T^2}$. The uncertainty is significant and at the order of $+26\%/-21\%$ in the VBF category, where the GGF contribution is non-negligible. In the nominal Boosted category, the GGF QCD scale uncertainty is implemented by two uncorrelated uncertainties, one for the inclusive Boosted category[3] and one for the phase space overlap of the inclusive Boosted with the VBF category following the recipe of Ref. [195]. The second uncertainty of the overlapping phase space region is treated as anti-correlated to the GGF QCD scale uncertainty in the VBF category. In total, the scale uncertainty on the GGF Higgs boson production cross section in the Boosted category dominates at $+31\%/-24\%$.

The QCD scale uncertainties of the GGF Higgs boson sample in the CP analysis are assumed to be the same as in the VBF category. The additional effect of the change in the selection efficiency due to the cut on the BDT classifier is found to be negligible. This has been studied in comparing the relative selection efficiencies from the VBF category into the CP signal region of the nominal GGF H+1jet and an alternative H+2jets Minlo [191, 192] sample. The differences between both Minlo samples correspond to on-top uncertainties on the LO description of the second jet in the default sample. However, uncertainties on the shape of the Optimal Observable or rather signed $\Delta\phi(j_1, j_2)$ are included based on the comparison of both samples.

QCD scale variations for the background cross sections are determined in a similar way and found to be $\pm 6\%$ for top quark, $\pm 1\%$ for $Z/\gamma^* \to e^+e^-/\mu^+\mu^-$ and $\pm 5\%/\pm 30\%$ for quark/gluon induced di-boson processes [196, 197]. Since the normalisation of these background samples is free to float in the fit and mainly

[2] The mass of the electroweak W gauge boson is denoted by m_W.

[3] The inclusive Boosted category is defined by selecting all events within the nominal Boosted category without rejecting events falling into the VBF category.

$\mathcal{BR}$ uncertainty	
$H \to \tau^+\tau^-$	$\pm 6\%$
$H \to W^+W^-$	$\pm 4\%$

Table 8.5. *Uncertainties on the Higgs boson branching ratios of interest for $m_H =$ 125 GeV.*

constrained by dedicated data control regions, the cross section uncertainties are not applied.

The VBF Higgs boson signal topology is characterized by a low third jet activity due to missing color-flow between the incoming quarks. The BDT classifier of the VBF category is therefore trained to suppress events with a third jet by using an effective third jet veto via the variable $C_\eta(jj, j_3)$. That is, the classifier mimics a third jet veto although it is not required explicitly in the event selection of the VBF category. Since the cross section of GGF Higgs boson events produced with a third jet is only known with leading order accuracy, a large uncertainty of at most 20% is introduced for VBF-like GGF Higgs boson events at high classifier values. The uncertainty is considered as shape variation as shown in section 8.4.

Missing higher order corrections cause uncertainties not only for the production of Higgs boson events but also for the decay [35]. The uncertainties on the $H \to \tau^+\tau^-$ branching ratio ranges from 3-7% depending on the hypothetical Higgs boson masses varying from 150 GeV to 100 GeV. In case of the decay $H \to W^+W^-$ into vector bosons, the corresponding uncertainty is 2-6%. Table 8.5 lists the branching ratio uncertainties assuming a Higgs boson mass of 125 GeV.

8.2.2. Parton Density Functions

The choice of PDF introduces an uncertainty of the acceptance of different production processes. They are estimated by varying the default PDF parametrization of the samples within its uncertainties and by changing the underlying PDF sets in addition. The CT10 [88] parametrization is used for the nominal GGF and VBF Higgs boson sample. Differences are observed after re-weighting the events to MSTW2008NLO [89], NNPDF [87] and the CT10 eigen-tune parametrization. The largest variation in the expected event yield is then used as normalisation uncertainty for the corresponding Higgs boson sample. It is $\pm 6\%$ and $\pm 5\%$ for the GGF Higgs boson process in the VBF and Boosted category and about $\pm 1\%$ for VBF and VH processes in both categories. PDF acceptance uncertainties on the shape of the BDT classifiers are included as well (see section 8.4). The normalisation uncertainties of the VBF category are also included in the CP analysis while uncertainties on the Optimal Observable and signed $\Delta\phi(j_1, j_2)$ shape are found to be negligible.

There are also PDF uncertainties on the cross section prediction of processes. The uncertainties on the Higgs boson production cross sections are $\pm 3\%$ for VBF and

	VBF/CP			Boosted		
	GGF	VBF	VH	GGF	VBF	VH
QCD scale	$+26\%/-21\%$	$\pm3\%$	$\pm1\%$	$+31\%-27\%$	$\pm3\%$	$\pm4\%$
EW scale	-	$\pm2\%$	-	-	$\pm2\%$	-
PDF	$\pm10\%$	$\pm3\%$	$\pm3\%$	$\pm9\%$	$\pm3\%$	$\pm3\%$
PS & UE	$\pm4\%$	$\pm1\%$	$\pm1\%$	$\pm9\%$	$\pm7\%$	$\pm7\%$
EvGen	-	$\pm4\%$	-	$\pm2\%$	-	-

Table 8.6. *Theory related systematic uncertainties in the different analyses for the signal samples. In case of the CP analysis, the uncertainties are quoted for a SM signal.*

VH processes and ±8% for GGF processes. The PDF uncertainties on cross sections of background processes are estimated to be ±8% for top quark processes and ±4% for $Z/\gamma^* \to e^+e^-/\mu^+\mu^-$ and di-boson processes. Since the normalisation of these background components is unconstrained in the fit, no uncertainties are applied.

8.2.3. Parton Shower, Underlying Event & Event Generators

The estimation of uncertainties on the GGF and VBF Higgs boson production mode due to the parton shower and underlying event model is based on differences in the event yields from samples generated with Powheg+Pythia [81, 97] and Powheg+Herwig [94]. The uncertainties are found to be ±4% or ±9% for the GGF and ±1% or ±7% for the the VBF Higgs boson production mode in the VBF or Boosted category. The same uncertainties as in the VBF category are used in the CP analysis. Shape uncertainties on the discriminating variables are also applied as shown in section 8.4.

For estimating the uncertainty due to the choice of the default event generator for Higgs boson processes, Powheg events are compared to events generated with Mc@NLO [98] for the GGF mode and to MG5_aMC@NLO [188] for the VBF mode. The samples use Herwig for the parton shower modeling. The uncertainty on the acceptance due to the event generator choice is ±2% for the GGF mode in the Boosted category and ±4% for the VBF mode in the VBF category. No shape uncertainty needs to be applied since the effect is found to be small for both.

The full set of theory related systematic uncertainties on the signal samples is summarized in table 8.6.

8.3. Signal & Background Estimation

8.3.1. CP-mixed Signal Re-weighting

In the CP analysis, the CP-mixed signal samples are generated by a matrix element based re-weighting of the pure Standard Model Higgs boson signal. A shape

uncertainty is assigned to this re-weighting method due to differences obtained in comparing directly generated CP-mixed signal events with re-weighted SM events. The samples compared have been generated with aMC@NLO [188] at NLO accuracy. Figure 6.1 shows the distribution of the Optimal Observable for both samples at parton level. The uncertainty is then estimated by applying the differences between these distributions as Optimal Observable dependent weights in the event reconstruction of the signal process. Residual differences at reconstruction level between the nominal signal sample from the default matrix element based re-weighting and the same signal sample modified with the additional event weights are used to estimate the final uncertainty. The same approach is used for the signed $\Delta\phi(j_1, j_2)$ distribution. The event weights derived at parton level for $\tilde{d} = 0.1$ are shown in figure 8.1. For reasons of simplifications, these event weights are applied to all $\tilde{d}$ signal samples and the one-sided uncertainties are then symmetrized at the reconstruction level.

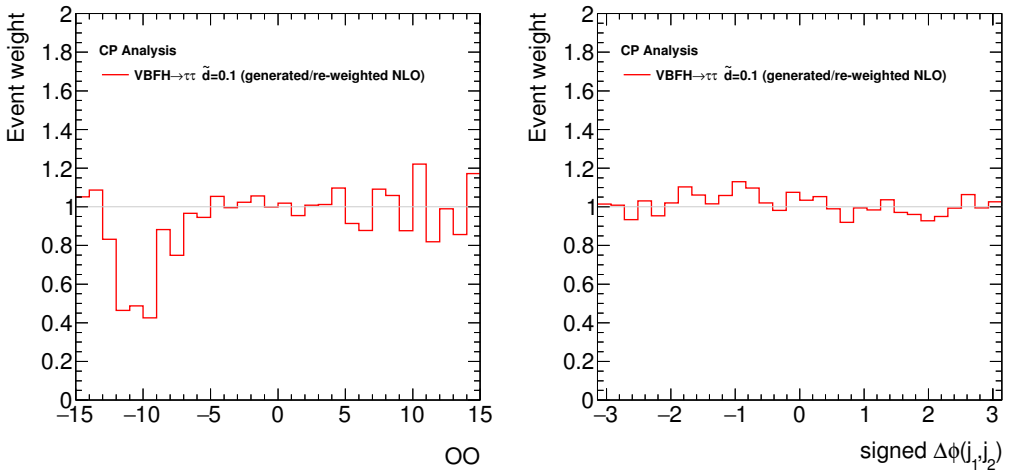

Figure 8.1. *Event weights derived by dividing the Optimal Observable and signed $\Delta\phi(j_1, j_2)$ distributions of directly generated signal events by SM but re-weighted signal events for $\tilde{d} = 0.1$ at parton level. The samples have been generated with* aMC@NLO *at the level of NLO.*

8.3.2. $Z \to \tau^+\tau^-$ Embedding

$Z/\gamma^* \to \tau^+\tau^-$ processes are estimated in a mostly data-driven way using the Embedding method (see section 7.1). However, the decay of the τ leptons into electrons or muons is still taken from simulation. For this reason, corresponding experimental uncertainties need to be considered in the analyses. These concerns uncertainties on the lepton trigger, identification and reconstruction efficiencies as well as the energy scale and resolution of reconstructed leptons. Table 8.7 summarizes the normalisation uncertainties from these sources for the VBF and Boosted categories, as well as for the signal region of the CP analysis. Since the final reconstruction of the Embedding hybrid event is not entirely comparable to a

VBF				
	$Z \to \tau_e\tau_e$	$Z \to \tau_\mu\tau_\mu$	$Z \to \tau_e\tau_\mu$	$Z \to \tau_\mu\tau_e$
Electrons				
Efficiency	$\pm 1\%$	$< 1\%$	$\pm 1\%$	$\pm 1\%$
Resolution e	$< 1\%$	$< 1\%$	$< 1\%$	$< 1\%$
Scale e	$+1\%/-2\%$	$< 1\%$	$\pm 1\%$	$< 1\%$
Muons				
Efficiency	$< 1\%$	$\pm 2\%$	$\pm 1\%$	$\pm 1\%$
Resolution	$< 1\%$	$< 1\%$	$< 1\%$	$< 1\%$
Scale	$< 1\%$	$< 1\%$	$< 1\%$	$< 1\%$
Boosted				
	$Z \to \tau_e\tau_e$	$Z \to \tau_\mu\tau_\mu$	$Z \to \tau_e\tau_\mu$	$Z \to \tau_\mu\tau_e$
Electrons				
Efficiency	$\pm 1\%$	$< 1\%$	$< 1\%$	$\pm 1\%$
Resolution e	$< 1\%$	$< 1\%$	$< 1\%$	$< 1\%$
Scale e	$\pm 1\%$	$< 1\%$	$\pm 1\%$	$< 1\%$
Muons				
Efficiency	$< 1\%$	$\pm 2\%$	$< 1\%$	$\pm 1\%$
Resolution	$< 1\%$	$< 1\%$	$< 1\%$	$< 1\%$
Scale	$< 1\%$	$< 1\%$	$< 1\%$	$< 1\%$
CP				
	$Z \to \tau_e\tau_e$	$Z \to \tau_\mu\tau_\mu$	$Z \to \tau_e\tau_\mu$	$Z \to \tau_\mu\tau_e$
Electrons				
Efficiency	$\pm 2\%$	$< 1\%$	$< 1\%$	$\pm 1\%$
Resolution e	$\pm 5\%$	$< 1\%$	$+3\%/-2\%$	$+2\%/-1\%$
Scale e	$+8\%/-3\%$	$< 1\%$	$+2\%/-1\%$	$\pm 1\%$
Muons				
Efficiency	$< 1\%$	$\pm 2\%$	$< 1\%$	$\pm 1\%$
Resolution	$< 1\%$	$+6\%/-1\%$	$+3\%/-2\%$	$+9\%/-3\%$
Scale	$< 1\%$	$+5\%/-1\%$	$+2\%/-1\%$	$+6\%/-5\%$

Table 8.7. *Relative uncertainties on the expected event yield for the Embedding sample in the VBF and Boosted category and the CP analysis due to lepton efficiency, resolution and scale uncertainties.*

purely simulated event, the efficiency uncertainties are treated as uncorrelated to the ones from the fully simulated background samples.

Furthermore, there are sources of uncertainties originating from the implementation of the Embedding technique itself [7]:

- **Muon Isolation**
  The default isolation criterion for reconstructed muons in the Embedding input events taken from collision data is $p_T^{\text{cone}\Delta R}/p_T^{\mu} < 20\%$ with $\Delta R = 0.4$. This ensures a high purity of the $Z/\gamma^* \to \mu^+\mu^-$ input dataset. However, the isolation of the initial muons affects the environment of the embedded τ lepton and its decay products, which might bias the properties of the final hybrid event. To estimate the impact of the initial muon isolation on the

$Z/\gamma^* \to \tau^+\tau^-$ background in the analyses, the ad-hoc choice of the default isolation is changed into an upwards variation[4] by tightening the isolation into $p_T^{\text{cone}\Delta R}/p_T^{\mu} < 6\%$ with $\Delta R = 0.4$ and $E_T^{\text{cone}\Delta R}/E_T^{\mu} < 4\%$ with $\Delta R = 0.2$. The downwards variation is defined by not applying any isolation criteria. Such variations also account for effects from background contamination, particularly from non-prompt or fake muons from top quark processes.

- **Muon Cell Energy**
  The energy deposits of the initial muons in the calorimeter cells are estimated by simulating a stand-alone $Z/\gamma^* \to \mu^+\mu^-$ event on-the-fly within the Embedding method. The simulated cell energies are then subtracted from the original data event. To estimate the impact of corresponding simulation uncertainties on the Embedding event, the cell energy deposits are varied by $\pm 20\%$ before subtracting and further processing. The size of the variations is motivated by comparisons of the Embedding events from collision data or simulation with fully simulated $Z/\gamma^* \to \tau^+\tau^-$ events.

Figure 8.2 shows the effect of the muon isolation and cell energy variations at preselection level on the m_{MMC}, $m_{\ell\ell}$ and p_T^{j1} distributions before applying categorization cuts. The differences between the nominal and the varied distributions of these basic kinematic variables are at the order of 5% at most. Shape uncertainties on the final discriminating variables in the various signal regions are discussed in section 8.4.

Detector resolution or final state radiation effects of the initial muons are expected to be negligible as shown in section 7.1.2. Therefore, such effects are not considered in terms of systematic uncertainties in the analyses.

The $Z/\gamma^* \to \tau^+\tau^-$ leptonic final states ee, $\mu\mu$, $e\mu$ and μe are treated as separate background samples in the fit to account for the different trigger paths of these sub-channels of the analyses. However, the samples are correlated by a common unconstrained normalisation factor. When studying the effect of introducing two alternative uncorrelated normalisation factors, one for the different and one for the same flavour final states, a difference of 15% in comparing both postfit normalisation parameter values was observed. This tension is assumed to be related to a potential mismodeling of the Embedding specific trigger emulation, which needs to be applied to the Embedding sample since no trigger information is available here due to technical reasons. It is therefore applied to the same flavour final state channels as additional normalisation uncertainty. This allows for a certain compensation of the above described tension between same and different flavour final states, which is observed when decorrelating the normalisation into two independent factors.

[4] In the following sections, uncertainties are quoted in terms of upwards and downwards uncertainty components depending on the direction of the variation of the corresponding uncertainty parameter value.

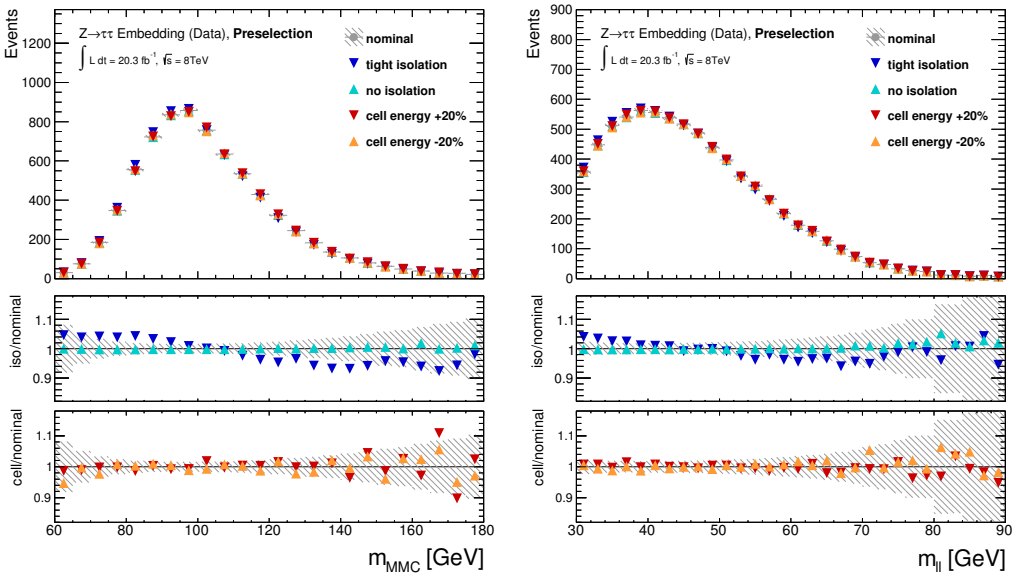

(a) (b)

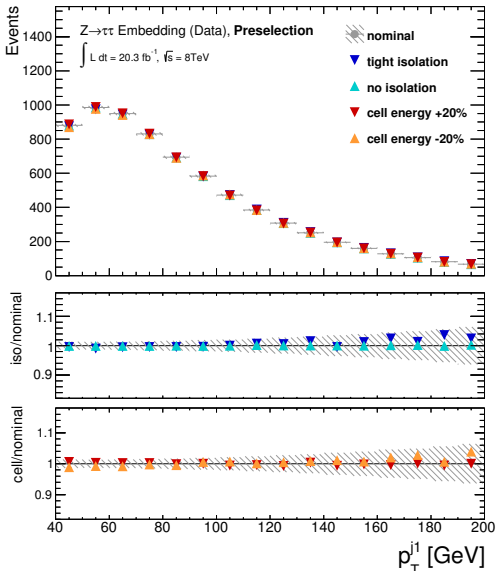

(c)

Figure 8.2. *Comparison of distributions of the Embedding sample for different shape uncertainty variations due to the isolation and the calorimeter energy estimation of the initial muons in the Embedding method. Basic variables (m_{MMC}, $m_{\ell\ell}$ and p_T^{j1}) are shown at preselection level before dividing the analysis into categories. The error bars include statistical uncertainties.*

8.3.3. Fake Lepton Template

The estimation of background contributions from fake leptons is based on a template method as discussed in section 7.5. An uncertainty is assigned for the extrapolation of the background estimate from the fake control region, defined by lepton anti-isolation criteria, to the signal region. The uncertainty is estimated by comparing the fake templates from alternative signal-free same sign control regions according to the nominal signal and fake control regions. The same sign regions are defined by requiring two leptons with the charges of the same electrical sign instead of opposite sign. The approach is based on the assumption, that the charge and the isolation of the leptons are uncorrelated. A comparison of both same sign templates for the BDT classifier distributions is shown in figure 7.44 and the observed differences are applied as an uncertainty on the shape. That is, the final systematic upwards variation is extracted by applying the ratio of the shapes from the same sign control regions in terms of a re-weighting to the nominal fake template. The downwards fluctuation is extracted by symmetrizing the upwards variation. These shape uncertainties are derived for the BDT classifier distribution of the VBF and Boosted category and the Optimal Observable and signed $\Delta\phi(j_1, j_2)$ distribution of the CP analysis.

Uncertainties on the normalisation of the template due to the χ^2 fit are relatively small and about 1-3%. However, larger differences in the leading lepton distributions of the same sign templates are observed, especially in the Boosted category, as shown in figure 8.3. Event weights are derived to correct for these differences, which are then applied when re-evaluating the nominal BDT classifier template. Residual differences in the normalisation between the nominal and the re-evaluated BDT classifier template are applied as an additional uncertainty of 20% in the VBF category and the CP analysis and 30% in the Boosted category. Fake leptons are a minor background contribution in the signal regions of the analysis. Therefore, the relatively large uncertainties are not expected to affect the results significantly.

8.3.4. Top Quark & $Z \to e^+e^-/\mu^+\mu^-$

The estimation of observable distributions of top quark and $Z/\gamma^* \to e^+e^-/\mu^+\mu^-$ processes is based on simulation and has been validated in sections 7.2 and 7.4. However, the normalisation of both background samples is taken from data via free-floating normalisation factors in the fit, that are constrained by dedicated data control regions. This results in a decrease of theory uncertainties on cross section predictions. Nevertheless, uncertainties on the extrapolation from the control region into the signal region must be taken into account.

- *Top Quark Background*
  Extrapolation uncertainties are estimated by comparing the performance of top quark samples simulated with the default event generator Powheg+Pythia and the alternative generator MC@NLO+Herwig in the top quark control regions. Both samples are normalised to match the observed event yields in data. Differences in the normalisation correction factors of 6% for the VBF

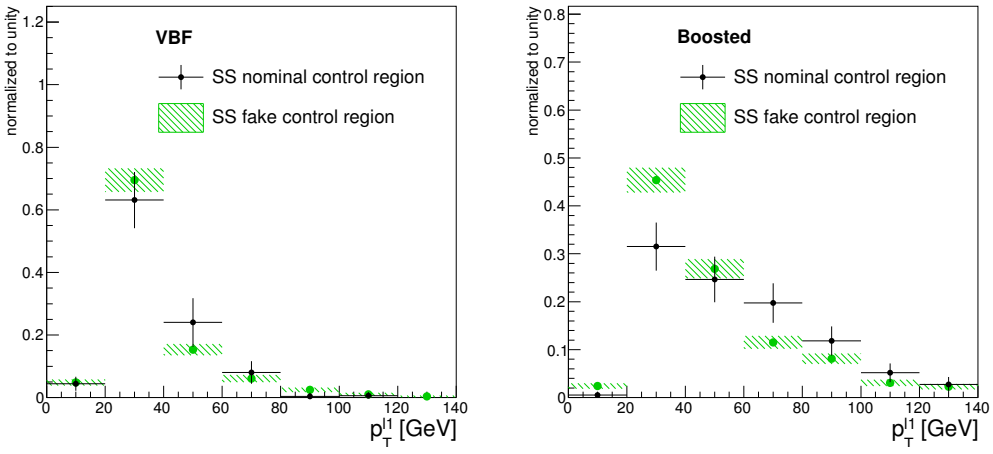

(a) (b)

Figure 8.3. *Leading lepton distribution of the fake template in the same sign control regions of the VBF and Boosted category. The error bars include statistical uncertainties.*

category and the CP analysis and 3% for the Boosted category are observed and considered as extrapolation uncertainties on the normalisation. The differential distributions of the final discriminating variables for both event generators match within statistical uncertainties. Nevertheless, the transfer of the normalisation from the control region to the signal region might be biased by requiring at least one b jet instead of a b jet veto. However, no dependency of the correction factors on the transverse momentum of the leading b jet is observed in the control regions, which indicates the robustness of extrapolating background estimates from the top quark control regions to the signal regions.

- *$Z/\gamma^* \to e^+e^-/\mu^+\mu^-$ Background*
  Extrapolation uncertainties on the transfer from the dedicated control regions, defined by applying a Z boson mass window cut, into the signal region is estimated by varying the size of this window. The tested cut values are 80 GeV $< m_{\ell\ell} <$ 89 GeV, 89 GeV $< m_{\ell\ell} <$ 92 GeV, 92 GeV $< m_{\ell\ell} <$ 100 GeV and 80 GeV $< m_{\ell\ell} <$ 100 GeV with the latter window being the default choice for determining the normalisation correction factors. The largest difference between the correction factors is found to be ±6% and is applied as extrapolation uncertainty on the normalisation of $Z/\gamma^* \to e^+e^-/\mu^+\mu^-$ in all categories.

  Furthermore, a $\Delta\eta(j,j)$ dependent re-weighting in the VBF category is applied to the simulated $Z/\gamma^* \to e^+e^-/\mu^+\mu^-$ events to improve the background modeling as explained in section 7.2. A larger dependency of the correction factors on $E_{\mathrm{T}}^{\mathrm{miss}}$ has been observed. Since the nominal event selection includes a cut on $E_{\mathrm{T}}^{\mathrm{miss}}$, an additional uncertainty on the re-weighting is considered in the analyses. Figure 8.4 shows the event weights as function of $\Delta\eta(j,j)$

determined at preselection level before and after cutting on $E_{\mathrm{T}}^{\mathrm{miss}}$ with the latter one being used as default correction. The alternative weights before cutting on $E_{\mathrm{T}}^{\mathrm{miss}}$ are then applied to each event in the event reconstruction, which results in an estimate for the corresponding systematic uncertainty after processing the full analysis. This one-sided uncertainty is then symmetrized in the analyses. Its impact on the expected event yield of $Z/\gamma^* \to e^+e^-/\mu^+\mu^-$ is about 5% in the VBF category and 8% in the CP analysis, while the effect in the Boosted category is negligible.

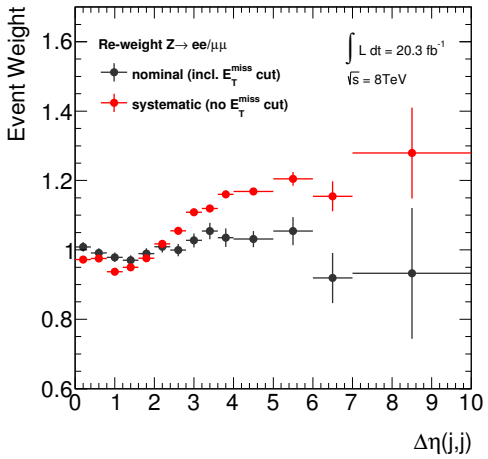

Figure 8.4. *Event weights as function of $\Delta\eta(j,j)$, which are used to correct the modeling of simulated $Z/\gamma^* \to e^+e^-/\mu^+\mu^-$ events.*

8.4. Shape Uncertainties

The sources of uncertainties presented in this chapter enter the final fit in terms nuisance parameters. Each uncertainty is implemented by normalisation and shape nuisance parameters with respect to the BDT classifier, the Optimal Observable or signed $\Delta\phi(j_1, j_2)$ distributions according to section 9. Distributions of shape variations are therefore normalised to the nominal distribution. Since many of the systematic uncertainties are relatively small, insignificant nuisance parameters are removed by applying certain pruning criteria. Furthermore, the statistics of specific background samples is rather low because of the particular phase space regions under consideration. To reduce the impact of the statistical noise and to stabilize the final fit, the remaining shape uncertainties are smoothed and symmetrized. The shape uncertainties used in the present analyses for the BDT classifier, the Optimal Observable and the signed $\Delta\phi(j_1, j_2)$ distributions are summarized in this section. The impact of the relevant shape uncertainties on the final results of the search and the CP analysis is shown in section 10.

8.4.1. Pruning

An upwards or downwards variation corresponds to the $\pm 1\sigma$ estimation of a specific source of uncertainty. In case of normalisation uncertainties, only nuisance parameters are taken into account in the fit with at least one of the relative up and down variations being greater than 0.5% with respect to the nominal value. The pruning criteria for shape uncertainties requires a χ^2-test[5] of both variations with the nominal distribution. Only the largest statistical uncertainty of the varied and the nominal distributions is considered in the χ^2-calculation, since its correlation is unknown. If the corresponding p-value for both variations $\chi^2_{\text{up/down}}$ is below the value 0.95, the shape uncertainty is considered to be significant and the nuisance parameter is kept in the final fit.

A second additional criterion is applied according to a bin-by-bin significance for all background samples. The significance is defined by the deviation of the varied from the nominal event yield per bin divided by the total statistical uncertainty of the background prediction in this bin[6]. If none of the bin-by-bin significances is above 10%, the shape uncertainty is considered to be insignificant and therefore rejected.

The different ad-hoc pruning thresholds have been studied in detail and the current values are found to be reasonable working points that ensure stable fit results.

8.4.2. Smoothing & Symmetrizing

To reduce the impact of statistical fluctuations, a smoothing algorithm is applied to the ratio of the upwards or downwards shape variations with the nominal distribution. The smoothed ratio is then multiplied with the nominal distribution again to reproduce the variation. Processing ratios instead of distributions avoids an over-smoothing of the varied distributions. The corresponding algorithm is implemented in Root [198] in the TH1::Smooth(1) function. Statistical fluctuations might additionally cause shifts in the same direction for both upwards and downwards variations. Such scenarios can lead to ambiguities and problems in the minimization of the fitting procedure such as multiple local minima. To avoid problems, the smaller variation is mirrored[7] while the larger uncertainty is kept unchanged. This symmetrization approach is used for single bins of shape uncertainties and in case of normalisation uncertainties.

[5] The χ^2-test value is defined by the sum $\chi^2 = \sum_{i \in \text{Bins}} (n_i^{\text{nom}} - n_i^{\text{up/down}})^2 / \max\{\sigma_i^{\text{nom}}, \sigma_i^{\text{up/down}}\}$ over bins of a distribution, where $n_i^{\text{nom/up/down}}$ are the nominal, upwards or downwards varied event yields per bin. The p-value (see section 9.2) of the χ^2-value, assuming a χ^2-probability density with degrees of freedom equal to the number of bins, provides a measure for the compatibility of the distributions.

[6] The bin-by-bin significance is defined by $S_i = |n_i^{\text{nom}} - n_i^{\text{up/down}}| / \sigma_i^{\text{tot}}$, where σ_i^{tot} is the statistical uncertainty of the total background expectation

[7] That is, an upwards/downwards fluctuation in a bin is converted into a downwards/upwards variation with the same size.

8.4.3. Final Discriminants

The uncertainties, presented in this chapter, are propagated to the signal regions of the analyses. Tables 8.8, 8.9, 8.10 and 8.12 summarize the full set of shape uncertainties, which are not rejected by the pruning criteria, for the VBF and Boosted category and the signal region of the CP analysis. Shape uncertainties in the control regions are not quoted here, since the top quark and $Z/\gamma^* \rightarrow e^+e^-/\mu^+\mu^-$ enriched regions do not use any shape information and the low BDT classifier value region of the CP analysis is consistent with the VBF category. The most significant shape variations according to the lowest χ^2 p-values are shown in figures 8.5 and 8.6 for the VBF category, figures 8.7 and 8.8 for the Boosted category and figure 8.9 and 8.10 for the signal region of the CP analysis.

VBF				
	$H \to \tau^+\tau^-$			
	VBF	GGF	WH	ZH
JER	×		×	×
JES_Detector1	×	×	×	×
JES_Modelling1	×	×	×	×
JES_Detector3	×			
JES_Eta_StatMethod	×		×	
JES_PilePt	×			
JES_PileRho_TAU_QQ			×	
JES_Statistical2	×			
JES_Eta_Modelling_LL	×	×	×	×
JES_FlavComp_TAU_G		×		
JES_FlavComp_TAU_Q	×		×	×
JES_FlavResp	×		×	×
JES_Mu	×			
JES_NPV	×		×	×
QCDscale_ggH_m23		×		
	$Z \to \tau_e\tau_e$	$Z \to \tau_\mu\tau_\mu$	$Z \to \tau_e\tau_\mu$	$Z \to \tau_\mu\tau_e$
ANA_EMB_MFS	×	×	×	×
EL_SCALE	×		×	
MET_RESOSOFT		×	×	×
MET_SCALESOFT	×		×	
	top quark	$Z \to ee/\mu\mu$ & di-boson	Fake Leptons	
ANA_LL12_Fake_bv_SH			×	
JER	×	×		
JES_Modelling1	×	×		
JES_Eta_Modelling_LL	×	×		
JES_FlavComp_TAU_G	×	×		
JES_FlavResp	×			
	$H \to W^+W^-$			
	VBF	GGF	WH	ZH
JER	×	×		
JES_Modelling1	×	×		
JES_Eta_StatMethod	×			
JES_PilePt	×			
JES_Statistical1		×		
JES_Eta_Modelling_LL	×	×		
JES_FlavComp_TAU_G		×		
JES_FlavComp_TAU_Q	×			
JES_NPV		×		

Table 8.8. *Shape uncertainties on the BDT classifier used in the fit for the VBF category of the $H \to \tau^+\tau^- \to \ell^+\ell^- 4\nu$ analysis. A short description of the nuisance parameter acronyms can be found in appendix B.*

Boosted				
	$H \to \tau^+\tau^-$			
	VBF	GGF	WH	ZH
EL_SCALE	×	×		×
JER	×	×	×	×
JES_Detector1	×	×	×	×
JES_Modelling1	×	×	×	×
JES_Detector2				×
JES_Detector3				×
JES_Mixed1				×
JES_Mixed2		×		
JES_Modelling2			×	
JES_Modelling3				×
JES_PilePt				×
JES_PileRho_TAU_GG		×		
JES_PileRho_TAU_QQ	×		×	×
JES_Statistical1		×		×
JES_Statistical2				×
JES_Eta_Modelling_LL	×	×	×	×
JES_FlavComp_TAU_G		×		
JES_FlavComp_TAU_Q	×		×	×
JES_FlavResp	×	×	×	×
JES_NPV		×	×	×
MET_RESOSOFT		×	×	×
MET_SCALESOFT	×		×	×
MUMS_RES				×
MU_SCALE	×	×		×
	$Z \to \tau_e\tau_e$	$Z \to \tau_\mu\tau_\mu$	$Z \to \tau_e\tau_\mu$	$Z \to \tau_\mu\tau_e$
ANA_EMB_ISOL			×	
ANA_EMB_MFS	×		×	×
EL_RES	×		×	×
EL_SCALE	×		×	×
MET_RESOSOFT			×	×
MET_SCALESOFT	×			×
MUID_RES		×		
MUMS_RES		×		
MU_SCALE		×		×

Table 8.9. *Shape uncertainties on the BDT classifier used in the fit for the Boosted category of the $H \to \tau^+\tau^- \to \ell^+\ell^- 4\nu$ analysis. A short description of the nuisance parameter acronyms can be found in appendix B.*

Boosted				
	top quark	$Z \to ee/\mu\mu$ & di-boson	Fake Leptons	
JER	×	×		
JES_Detector1		×		
JES_Modelling1	×	×		
JES_Eta_StatMethod	×	×		
JES_Modelling2		×		
JES_PilePt		×		
JES_Eta_Modelling_LL	×	×		
JES_FlavComp_TAU_G	×	×		
JES_FlavResp		×		
		$H \to W^+W^-$		
	VBF	GGF	WH	ZH
EL_SCALE	×			
JER	×	×		
JES_Detector1	×	×		
JES_Modelling1	×	×		
JES_Detector2	×	×		
JES_Detector3	×	×		
JES_Eta_StatMethod	×	×		
JES_Modelling2	×	×		
JES_Modelling3	×	×		
JES_Modelling4		×		
JES_PilePt	×	×		
JES_PileRho_TAU_GG		×		
JES_PileRho_TAU_QQ	×			
JES_Statistical1	×	×		
JES_Statistical3	×	×		
JES_Eta_Modelling_LL	×	×		
JES_FlavComp_TAU_G		×		
JES_FlavComp_TAU_Q	×			
JES_FlavResp	×	×		
JES_Mu	×	×		
JES_NPV	×	×		
MET_RESOSOFT	×	×		
MET_SCALESOFT	×	×		
MU_SCALE		×		

Table 8.10. *Shape uncertainties on the BDT classifier used in the fit for the Boosted category of the $H \to \tau^+\tau^- \to \ell^+\ell^- 4\nu$ analysis. A short description of the nuisance parameter acronyms can be found in appendix B.*

CP (Optimal Observable)				
	$H \to \tau^+\tau^-$			
	VBF	GGF	WH	ZH
JER	×	×	×	×
JES_1112_Detector1	×			
JES_Eta_Modelling_LL	×	×	×	×
JES_FlavComp_TAU_Q	×			
JES_FlavResp	×			
UE_gg_BDT		×		
UE_qq_BDT	×			
QCDscale_ggH_BDT		×		
REWEIGHT	×			
	$H \to W^+W^-$			
	VBF	GGF	WH	ZH
JER	×			
JES_Modelling1	×			
UE_gg_BDT		×		
UE_qq_BDT	×			
REWEIGHT	×			
	$Z \to \tau_e\tau_e$	$Z \to \tau_\mu\tau_\mu$	$Z \to \tau_e\tau_\mu$	$Z \to \tau_\mu\tau_e$
ANA_EMB_ISOL				×
	top quark	$Z \to ee/\mu\mu$ & di-boson	Fake Leptons	
JER		×		
JES_Modelling1		×		
JES_Eta_Modelling_LL		×		
JES_FlavComp_TAU_G		×		
JES_FlavResp		×		
JES_NPV		×		

Table 8.11. *Shape uncertainties on the Optimal Observable used in the fit for the signal region of the CP analysis. The same maximum set of shape uncertainties is applied to all $\tilde{d}$ signal samples. A short description of the nuisance parameter acronyms can be found in appendix B.*

CP (signed $\Delta\phi(j_1, j_2)$)				
		$H \to \tau^+\tau^-$		
	VBF	GGF	WH	ZH
JER		×	×	
JES_1112_Detector1			×	
JES_1112_Modelling1		×		
JES_Eta_Modelling_LL		×	×	×
JES_FlavComp_TAU_G		×		
JES_FlavComp_TAU_Q			×	
UE_gg_BDT		×		
UE_qq_BDT	×			
QCDscale_ggH_BDT		×		
REWEIGHT	×			
		$H \to W^+W^-$		
	VBF	GGF	WH	ZH
JER	×			
JES_Eta_Modelling_LL		×		
UE_gg_BDT		×		
UE_qq_BDT	×			
QCDscale_ggH_BDT		×		
REWEIGHT	×			
	$Z \to \tau_e\tau_e$	$Z \to \tau_\mu\tau_\mu$	$Z \to \tau_e\tau_\mu$	$Z \to \tau_\mu\tau_e$
ANA_EMB_ISOL_2012				×
ANA_EMB_MFS_2012				×
	top quark	$Z \to ee/\mu\mu$ & di-boson	Fake Leptons	
JER	×	×		
JES_1112_Detector1	×			
JES_1112_Modelling1		×		
JES_2012_Modelling4	×			
JES_2012_PileRho_TAU_QG	×			
JES_2012_Statistical2	×			
JES_2012_Statistical3	×			
JES_Eta_Modelling_LL	×	×		
JES_FlavComp_TAU_G	×	×		
JES_FlavResp	×	×		
JES_NPV		×		

Table 8.12. *Shape uncertainties on signed $\Delta\phi(j_1, j_2)$ used in the fit for the signal region of the CP analysis. The same maximum set of shape uncertainties is applied to all $\tilde{d}$ signal samples. A short description of the nuisance parameter acronyms can be found in appendix B.*

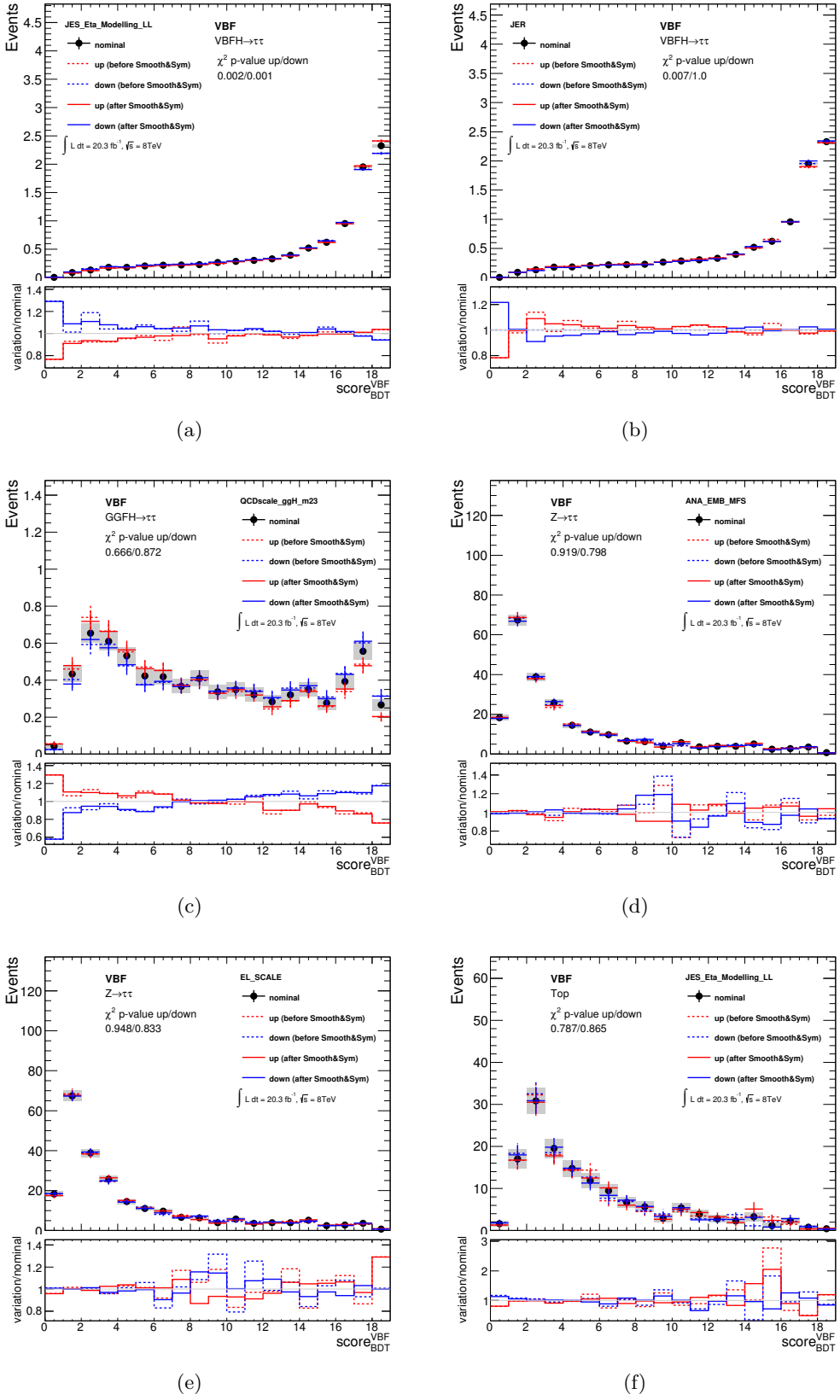

Figure 8.5. *Most significant shape uncertainties on signal and background samples in the VBF category. Comparison of the nominal distribution with the variations before and after smoothing and symmetrization. The original binning has been re-mapped into equidistant bins from one to the maximal number of bins of the BDT classifier distribution used in the fit. A short description of the nuisance parameter acronyms can be found in appendix B.*

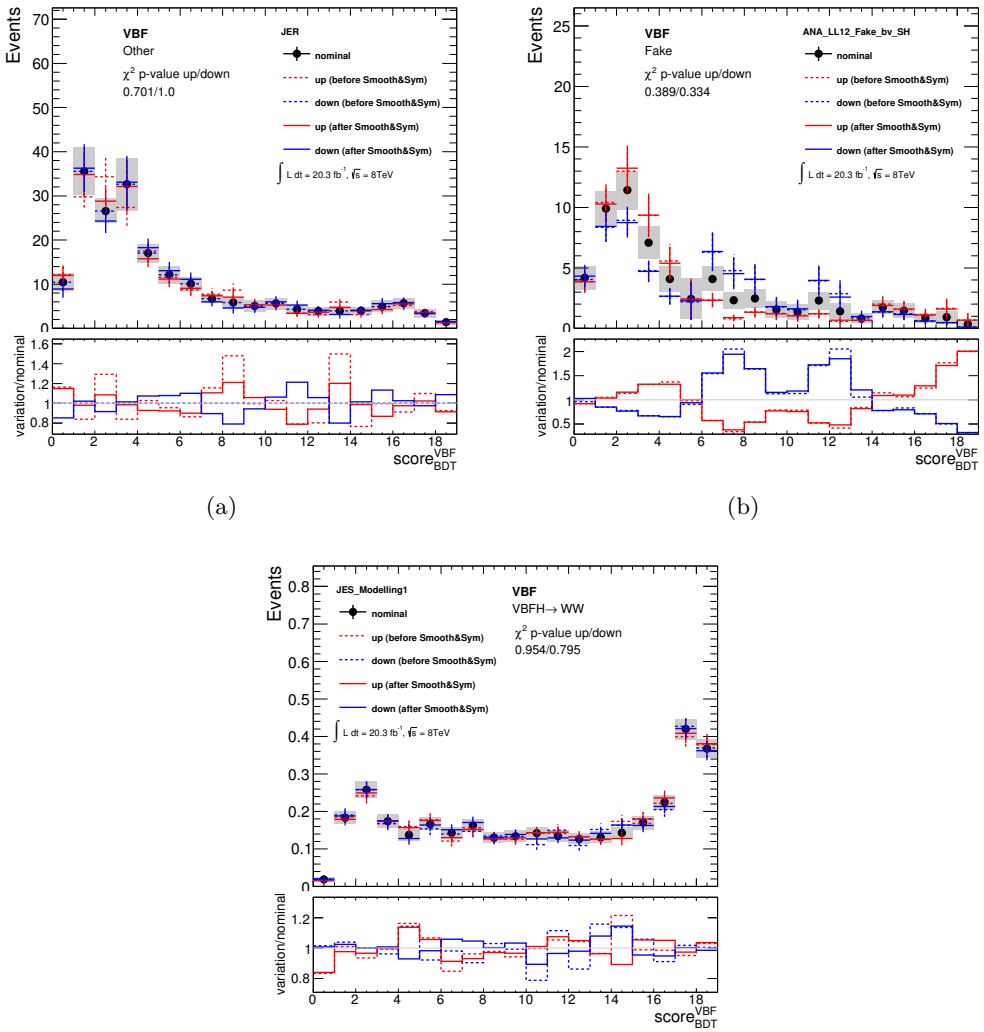

Figure 8.6. *Most significant shape uncertainties on signal and background samples in the VBF category. Comparison of the nominal distribution with the variations before and after smoothing and symmetrization. The original binning has been re-mapped into equidistant bins from one to the maximal number of bins of the BDT classifier distribution used in the fit. A short description of the nuisance parameter acronyms can be found in appendix B.*

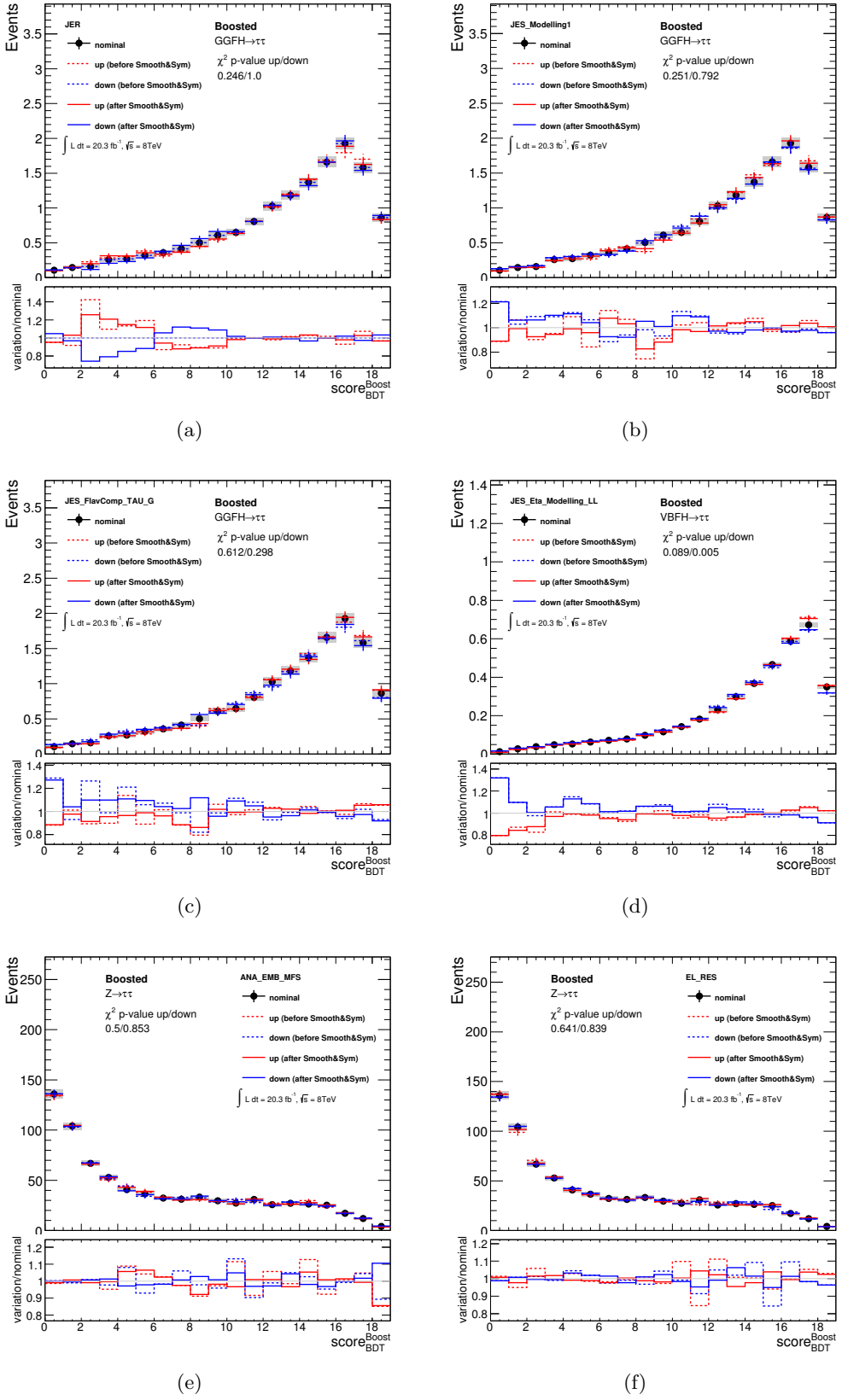

Figure 8.7. *Most significant shape uncertainties on signal and background samples in the Boosted category. Comparison of the nominal distribution with the variations before and after smoothing and symmetrization. The original binning has been re-mapped into equidistant bins from one to the maximal number of bins of the BDT classifier distribution used in the fit. A short description of the nuisance parameter acronyms can be found in appendix B.*

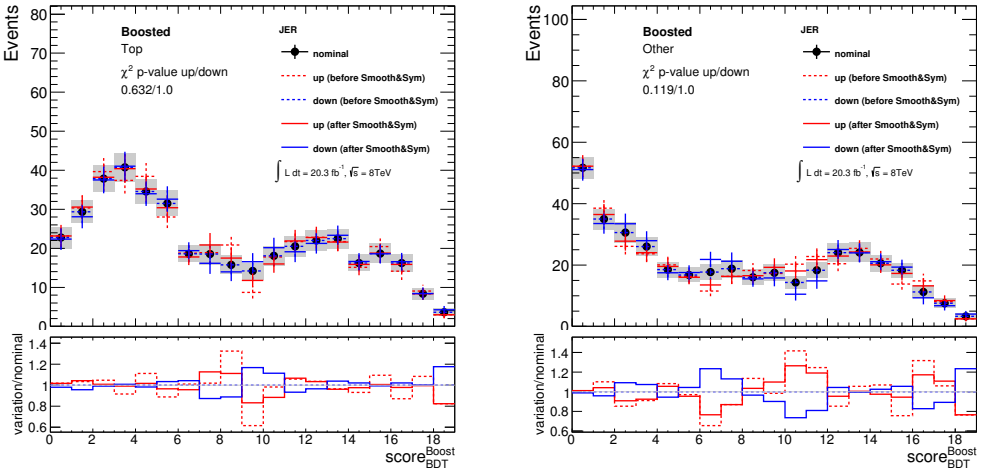

(a)

(b)

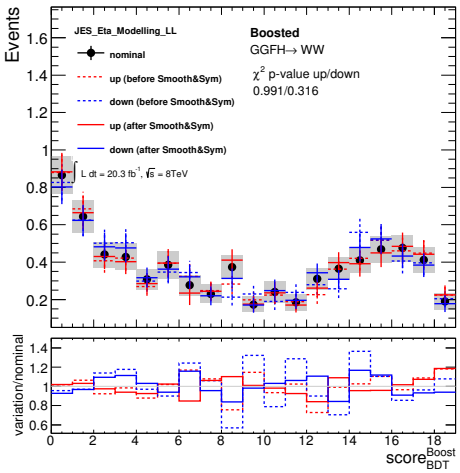

(c)

Figure 8.8. *Most significant shape uncertainties on signal and background samples in the Boosted category. Comparison of the nominal distribution with the variations before and after smoothing and symmetrization. The original binning has been re-mapped into equidistant bins from one to the maximal number of bins of the BDT classifier distribution used in the fit. A short description of the nuisance parameter acronyms can be found in appendix B.*

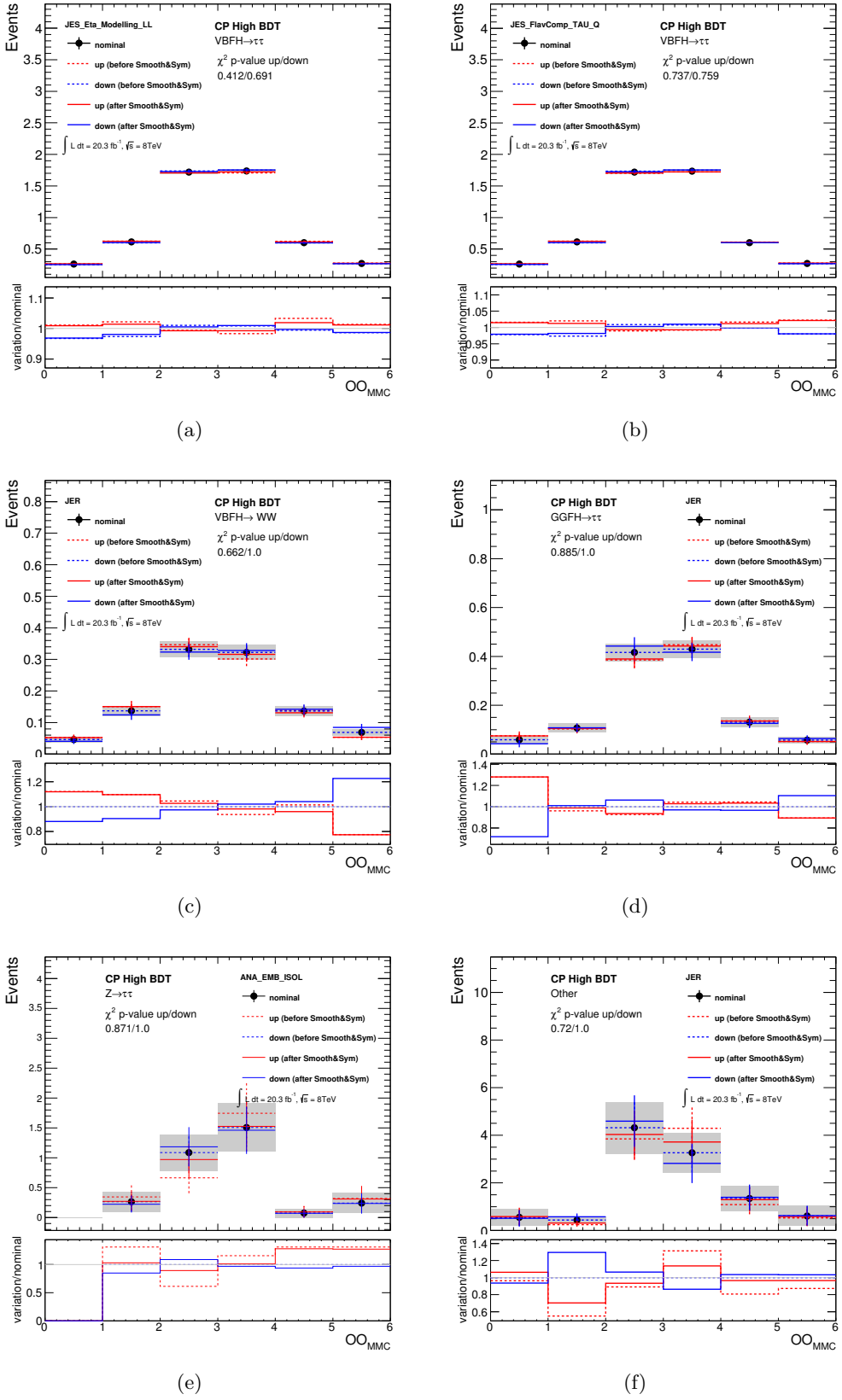

Figure 8.9. *Most significant shape uncertainties on signal and background samples in the signal region of the CP analysis. Comparison of the nominal distribution with the variations before and after smoothing and symmetrization. The original binning has been re-mapped into equidistant bins from one to the maximal number of bins of the Optimal Observable and signed $\Delta\phi(j_1, j_2)$ distribution used in the fit. A short description of the nuisance parameter acronyms can be found in appendix B.*

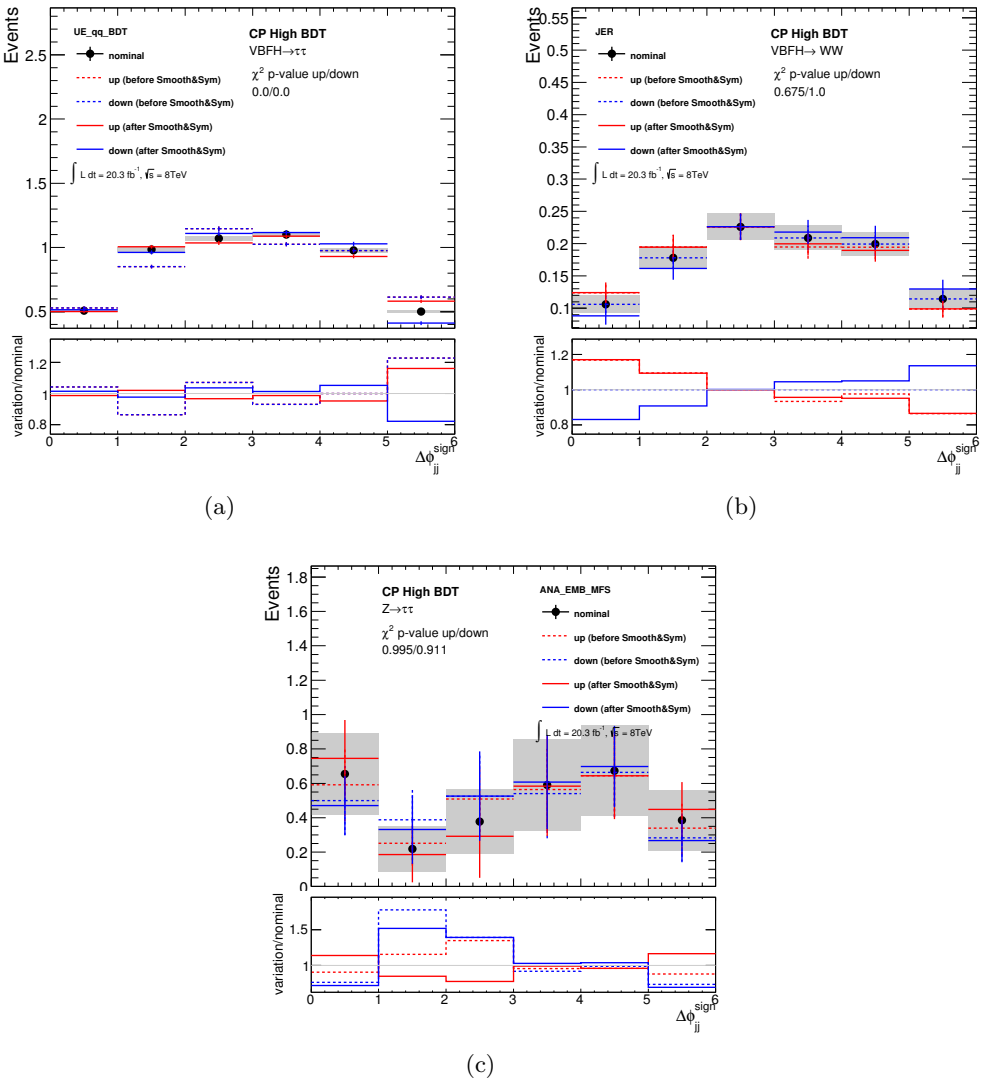

Figure 8.10. *Most significant shape uncertainties on signal and background samples in the signal region of the CP analysis. Comparison of the nominal distribution with the variations before and after smoothing and symmetrization. The original binning has been re-mapped into equidistant bins from one to the maximal number of bins of the Optimal Observable and signed $\Delta\phi(j_1, j_2)$ distribution used in the fit. A short description of the nuisance parameter acronyms can be found in appendix B.*

9 Statistical Data Analysis

The chapter provides an overview of the statistical methods, that are used in the analyses to extract the signal. They are based on a frequentistic maximum likelihood method. The first section 9.1 addresses basic principles of hypothesis testing. Second (9.2), the test statistic is explained, that is used in the search for $H \to \tau^+\tau^-$ to calculate the probability of agreement of a specific hypothesis with the measurement. In the third and fourth sections 9.3 and 9.4, the calculation of discovery significances and exclusion limits is described. The fifth section 9.5 presents the determination of confidence intervals in the CP analysis. In the last section 9.6, the likelihood function of the present analyses is specified.

9.1. Hypothesis Testing

The aim of hypothesis testing is to make a statement about the compatibility of the observed data with the outcome of a prediction model, called a hypothesis $\mathcal{H}$. Hypotheses can be realized in terms of probability densities $f(x)$ of a random variable x. If a hypothesis includes additional parameters $\boldsymbol{\theta} = \theta_1, ..., \theta_m$, the probability density $f(x|\boldsymbol{\theta})$ is called composite hypothesis. Each composite hypothesis $\mathcal{H}$ is defined by specific parameter values $\boldsymbol{\theta}$. The hypothesis under consideration is usually termed as *null hypothesis* $\mathcal{H}_0$ and tested against an *alternative hypothesis* $\mathcal{H}_1$. When testing hypotheses, an appropriate *test statistic* t needs to be defined, which provides a good separation between $\mathcal{H}_0$ and $\mathcal{H}_1$. The test statistic $t = t(\mathbf{x})$ is a single measure that depends on the actual observed dataset $\mathbf{x} = x_1, ..., x_n$.

Before introducing different test statistics, the *Likelihood function* $\mathcal{L}$ is defined

$$\mathcal{L}(\boldsymbol{\theta}) = f(\mathbf{x}|\boldsymbol{\theta}) = f(x_1|\boldsymbol{\theta}) \cdot ... \cdot f(x_n|\boldsymbol{\theta}), \tag{9.1}$$

where the measured random variables $\mathbf{x}$ are assumed to be statistically independent. Larger values of the likelihood function indicate a higher compatibility of the hypothesis with the measured data.

The likelihood function can be used to estimate parameters. The best-fit parameters $\hat{\boldsymbol{\theta}}$, which maximize the likelihood function based on solving the equations $\partial\mathcal{L}/\partial\theta_i = 0$, are denoted as maximum likelihood estimators.

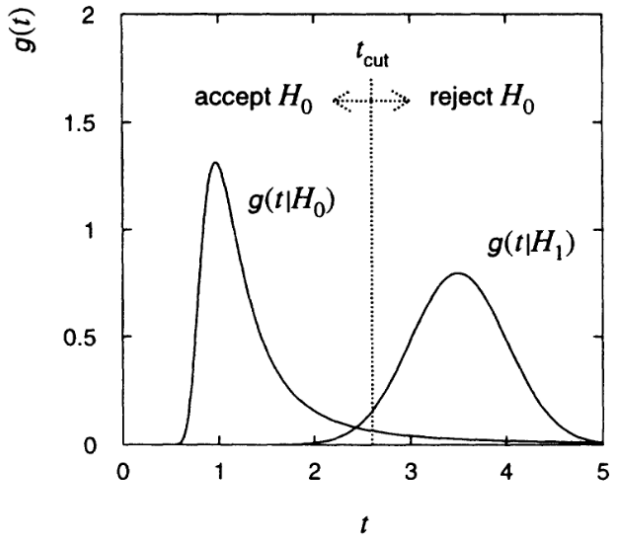

Figure 9.1. *Probability densities for the test statistic t assuming the hypothesis $\mathcal{H}_0$ or $\mathcal{H}_1$. The null hypothesis is rejected if the test statistic is observed in the critical region $t > t_{cut}$ [199].*

The optimal test statistic t with the highest statistical power[1] is defined by the ratio of likelihood functions (Neyman-Pearson-Lemma [199])

$$t = \frac{f(\mathbf{x}|\mathcal{H}_0)}{f(\mathbf{x}|\mathcal{H}_1)} = \frac{\mathcal{L}(\mathcal{H}_0)}{\mathcal{L}(\mathcal{H}_1)}. \tag{9.2}$$

The test statistic t is distributed according to the probability density $g(t|\mathcal{H}_0)$, where small values of t are preferred, or $g(t|\mathcal{H}_1)$ assuming hypothesis $\mathcal{H}_0$ or $\mathcal{H}_1$ to be true. $\mathcal{H}_0$ is accepted or rejected if the observed value t_{obs} of the test statistic is below or above a predefined critical value t_{cut} as shown in figure 9.1. The critical value corresponds to a specific choice of confidence level CL with

$$1 - CL = \alpha = \int_{t_{\text{cut}}}^{\infty} g(t|\mathcal{H}_0)dt. \tag{9.3}$$

The significance level α represents the probability of rejecting $\mathcal{H}_0$ even if it is true.

9.2. Test Statistics

One of the aims of the analysis of the search for $H \to \tau^+\tau^-$ is to select and estimate the signal yield. The parameter of interest of the present analysis is therefore chosen

[1] The statistical power of a test statistic is the probability to reject the null hypothesis if it is wrong [199].

to be the *signal strength* μ, which specifies the number of observed signal events normalised to the signal prediction from SM. That is, $\mu = 1$ characterizes the pure SM signal hypothesis and $\mu = 0$ the background only hypothesis, where the signal contribution is absent.

As an example, the hypotheses to test can be chosen such that $\mathcal{H}_0$ corresponds to the signal hypothesis with the parameter set $(\mu = 1, \boldsymbol{\theta})$ while $\mathcal{H}_1$ is defined by $(\mu = 0, \boldsymbol{\theta})$. The parameters $\boldsymbol{\theta}$ are called *nuisance parameters*, which typically reflect statistical or systematic uncertainties. The likelihood functions from equation 9.1 can then be rewritten as

$$\mathcal{L}(\mu, \boldsymbol{\theta}) = f(\mathbf{x}|\mu, \boldsymbol{\theta}) \tag{9.4}$$

to highlight the exceptional meaning of the parameter of interest μ.

The combination of equations 9.1, 9.2 and 9.4 yields the test statistic used at LEP [59]

$$t_{\text{LEP}} = \frac{\mathcal{L}(1, \boldsymbol{\theta})}{\mathcal{L}(0, \boldsymbol{\theta})} \tag{9.5}$$

with the nuisance parameters being fixed to predefined values. This test statistic can be modified to the one commonly used at Tevatron [60] by profiling the nuisance parameters based on the information from data. That is, maximum likelihood estimators are used instead of predefined fixed nuisance parameter values. The parameters are estimated in a constrained maximum likelihood fit $\mathcal{L}(\mu, \hat{\hat{\boldsymbol{\theta}}})$ under the assumption of the specific signal strength, where the profiled estimators are denoted as $\hat{\hat{\boldsymbol{\theta}}}$. The corresponding test statistic is the ratio of profiled likelihoods

$$t_{\text{Tevatron}} = \frac{\mathcal{L}(1, \hat{\hat{\boldsymbol{\theta}}})}{\mathcal{L}(0, \hat{\hat{\boldsymbol{\theta}}}')}. \tag{9.6}$$

The test statistic, which is used in the present analysis and also in many other analyses at the LHC, includes further modifications. The denominator of the likelihood ratio is exchanged by the best-fit maximum likelihood function $\mathcal{L}(\hat{\mu}, \hat{\boldsymbol{\theta}})$ with respect to all nuisance parameters and the parameter of interest. In this case, the best-fit nuisance parameters are denoted as $\hat{\mu}$ and $\hat{\boldsymbol{\theta}}$. In the numerator, the parameter of interest μ is fixed according to the null hypothesis with the corresponding profiled nuisance parameters $\hat{\hat{\boldsymbol{\theta}}}$. The test statistic is then generally defined as the *profile likelihood ratio*

$$t_\mu = \begin{cases} \frac{\mathcal{L}(\mu, \hat{\hat{\boldsymbol{\theta}}})}{\mathcal{L}(\hat{\mu}, \hat{\boldsymbol{\theta}})} & \hat{\mu} \geq 0 \\ \frac{\mathcal{L}(\mu, \hat{\hat{\boldsymbol{\theta}}})}{\mathcal{L}(0, \hat{\hat{\boldsymbol{\theta}}}')} & \hat{\mu} < 0. \end{cases} \tag{9.7}$$

The maximum likelihood estimator $\hat{\mu}$ is forced to be positive since the present analyses deals with positive signal rates. In case of downwards fluctuations ($\hat{\mu} < 0$), the best level of agreement between the prediction and the observed data is assumed to be at $\mu = 0$.

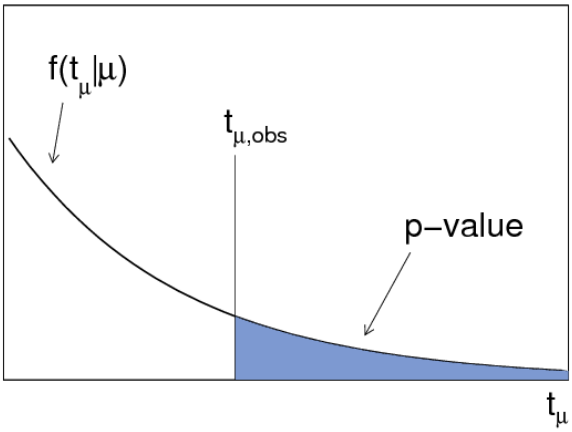

Figure 9.2. *p_μ-value of a hypothesis μ with respect to the observed test statistic $t_{\mu,obs}$ [202].*

The probability densities $g(t_\mu|\mu', \boldsymbol{\theta}')$ for a given tested signal strength μ under the assumption of a hypothesis with μ' can be determined by generating toy experiments. However, this procedure is very time consuming. Alternatively, the definition of the test statistic t_μ allows the approximation of the probability density by using analytic functions in the asymptotic limit of large samples. This approximation is based upon results from Wilks and Wald [200, 201]. For deriving the approximate asymptotic sampling distributions, it is convenient to write the likelihood ratio equivalently in terms of its logarithm

$$q_\mu = -2 \ln t_\mu. \tag{9.8}$$

Under the assumption of the large sample limit, $g(q_\mu|\mu', \boldsymbol{\theta}')$ is described by a χ^2 distribution with one degree of freedom. Its derivation is detailed in Ref. [202].

The compatibility of the null hypothesis $\mathcal{H}_0 = (\mu, \theta)$ with the observed test statistic $q_{\mu,\text{obs}}$ can be calculated in terms of the p_μ-value

$$p_\mu = \int_{q_{\mu,\text{obs}}}^{\infty} g(q_\mu|\mu, \boldsymbol{\theta}) dq_\mu, \tag{9.9}$$

which is the probability of the test statistic q_μ to be equal or less compatible than $q_{\mu,\text{obs}}$ under the null hypothesis μ. Figure 9.2 visualizes this relation. The p_μ-value is typically transformed into the *significance* Z_μ in terms of Gaussian standard deviations

$$\mathcal{Z}_\mu = \Phi^{-1}(1 - p_\mu) \tag{9.10}$$

with Φ being the Standard Gaussian Cumulative Distribution function.

9.3. Discovery Significance

In case of a potential discovery of new physics, one is interested in the compatibility of the observed data with the background only hypothesis. That is, $\mathcal{H}_0$ corresponds to the hypothesis $(\mu = 0, \boldsymbol{\theta})$. Equations 9.7 and 9.8 lead to the test statistic for discovery

$$q_0 = \begin{cases} -2 \ln t_0 & \hat{\mu} \geq 0 \\ 0 & \hat{\mu} < 0, \end{cases} \tag{9.11}$$

where the best-fit signal strength $\hat{\mu}$ is forced to be positive since positive signal rates are expected in the present analysis of the search for $H \to \tau^+\tau^-$. The null hypothesis, which is equivalent to the absence of signal, is typically rejected if

$$p_0 = \int_{q_{0,\mathrm{obs}}}^{\infty} g(q_0|0, \hat{\hat{\boldsymbol{\theta}}}) dq_0 \leq \alpha = 5,7 \cdot 10^{-7} \tag{9.12}$$

for the observed test statistic $q_{0,\mathrm{obs}}$ using equation 9.9 and 9.11. The confidence level $CL = 1 - p_0$ corresponds to a 5σ deviation based on equation 9.10. The nuisance parameters $\hat{\hat{\boldsymbol{\theta}}}$ are profiled in the corresponding fits to the observed data. In case of an expected p_0-value, the observed test statistic is replaced by the median $q_{0,\mathrm{exp}}$ of the probability density $g(q_0|1, \hat{\hat{\boldsymbol{\theta}}})$.

In the asymptotic approximation, the formula for calculating significances is simplified to

$$\mathcal{Z}_0 = \Phi^{-1}(1 - p_0) \simeq \sqrt{q_0}. \tag{9.13}$$

The observed significance $\mathcal{Z}_{0,\mathrm{obs}}$ can therefore be calculated using $q_{0,\mathrm{obs}}$. Concerning the expected significance $\mathcal{Z}_{0,\mathrm{exp}}$, the test statistic $q_{0,\mathrm{exp}}$ includes pseudo data with background and SM signal instead of data, which is often referred to as *Asimov* data.

9.4. Exclusion Limits

If no excess is observed in data, exclusion limits on the signal strength μ are calculated. The null hypothesis is chosen to be $\mathcal{H}_0 = (\mu > 0, \boldsymbol{\theta})$. The test statistic is then defined by

$$q_\mu = \begin{cases} -2 \ln t_\mu & \hat{\mu} \leq \mu \\ 0 & \hat{\mu} > \mu \ , \end{cases} \tag{9.14}$$

where t_μ is defined by equation 9.7. The case $\hat{\mu} > \mu$ is less compatible with the observed data and therefore the test statistic is set to $q_\mu = 0$. The observed upper limit $\mu_{\mathrm{up,obs}}$ on the signal strength corresponds then to the hypothesis, for which

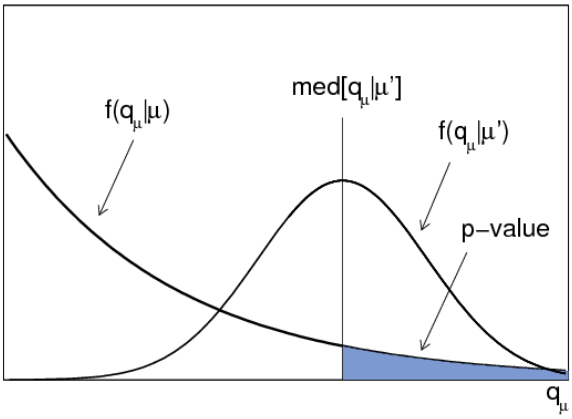

Figure 9.3. *The probability density $f(q_\mu|\mu)$ compared to $f(q_\mu|\mu')$ assuming an alternative hypothesis μ', where the median of the alternative hypothesis provides the test statistic value to calculate the expected p_μ-value [202].*

the observed test statistic is equal to the critical value of a predefined confidence level CL. It is calculated by solving

$$\begin{aligned} p_\mu &= \int_{q_{\mu,\text{obs}}}^{\infty} g(q_\mu|\mu, \hat{\hat{\boldsymbol{\theta}}}) dq_\mu \\ &= 1 - CL = \alpha, \end{aligned} \tag{9.15}$$

with $\mu = \mu_{\text{up,obs}}$, based on equation 9.9 and 9.14. The nuisance parameters are again set to the corresponding profiled maximum likelihood estimators with respect to data. The confidence level for exclusion limits is usually chosen to be $CL = 95\%$ and equation 9.15 can for example be solved in an iterative way.

In case of expected exclusion limits, the value of the test statistic q_μ of the upper limit $\mu_{\text{up,exp}}$ is equal to the median of the probability density $g(q_{\mu_{\text{up}}}|0, \hat{\hat{\boldsymbol{\theta}}})$ under the assumption of a true background only hypothesis as illustrated in figure 9.3. The constrained nuisance parameters are profiled to the observed data with μ set to zero. The $\pm 1/2\sigma$ bands on the expected upper limits are defined by the 68% and 95% confidence intervals of $g(q_{\mu_{\text{up}}}|0, \hat{\hat{\boldsymbol{\theta}}})$.

Problems arise when the experiment has little sensitivity, where $g(q_\mu|\mathcal{H}_0)$ and $g(q_\mu|\mathcal{H}_1)$ almost fully overlap. In this case, calculating the upper limit according to equation 9.15 would lead to an exclusion of $\mathcal{H}_0$ with a probability close to α in case of a significant downwards fluctuation. To avoid this scenario, the confidence level CL_s [203] is used

$$\begin{aligned} p'_\mu &= \frac{p_\mu}{1 - p_b} \\ &= \frac{1 - CL}{CL_b} = 1 - CL_s \end{aligned} \tag{9.16}$$

where p_b is defined by $p_b = \int_{-\infty}^{q_{\mu,\mathrm{obs}}} g(q_\mu|0,\hat{\hat{\boldsymbol{\theta}}})dq_\mu$.

In the asymptotic approximation, the observed upper limit $\mu_{\mathrm{up,obs}}$ is given by solving

$$p_{\mu_{\mathrm{up}}} = 1 - \Phi(\sqrt{q_\mu}), \tag{9.17}$$

resulting in $q_{\mu_{\mathrm{up}}} = 1.64^2$ corresponding to the confidence level of 95%. As for the expected CL_s exclusion limits, the median upper limit $\mu_{\mathrm{up,exp}}$ and the corresponding error bands ($N = \pm 1/2$) are calculated using

$$\mu_{\mathrm{up,exp}+N} = \sigma(\Phi^{-1}(1 - \alpha\Phi(N)) + N) \tag{9.18}$$

with $\sigma^2 = \mu_{\mathrm{up,exp}}/q_{\mu_{\mathrm{up,exp}}}$. The test statistic $q_{\mu_{\mathrm{up,exp}}}$ is evaluated based on background only pseudo data.

9.5. Central Confidence Interval

The parameter of interest in the CP analysis is the $\tilde{d}$ parameter (see section 2.3), which determines the contribution of the CP odd admixture to the CP even coupling predicted by the SM of the Higgs boson to vector bosons. The aim of the CP analysis is to quote the observed central confidence interval for $\tilde{d}$ based on the method of maximum likelihood as introduced in section 9.1. The best-fit value of the parameter of interest is given by its maximum likelihood estimator $\hat{\tilde{d}}$. The confidence interval is then defined by the variance of the estimator, which is determined by the approximative method of maximum likelihood as explained below.

The logarithm of the likelihood function of a generic parameter of interest θ can be approximated by a Taylor series about the maximum likelihood estimator $\hat{\theta}$

$$\begin{aligned} \ln\mathcal{L}(\theta) &= \ln\mathcal{L}(\hat{\theta}) + \left[\frac{\partial \ln\mathcal{L}}{\partial\theta}\right]_{\theta=\hat{\theta}}(\theta-\hat{\theta}) \\ &\quad + \frac{1}{2!}\left[\frac{\partial^2 \ln\mathcal{L}}{\partial\theta^2}\right]_{\theta=\hat{\theta}}(\theta-\hat{\theta})^2 + \ldots \end{aligned} \tag{9.19}$$

Since by definition $\ln\mathcal{L}(\hat{\theta}) = \ln\mathcal{L}_{\max}$ and $\partial\ln\mathcal{L}/\partial\theta = 0$, this Taylor series simplifies to

$$\ln\mathcal{L}(\theta) = \ln\mathcal{L}_{\max} - \frac{(\theta-\hat{\theta})^2}{2\widehat{\sigma^2}_{\hat{\theta}}}, \tag{9.20}$$

neglecting higher order terms. The variance of the maximum likelihood estimator in equation 9.20 is approximated by

$$\widehat{\sigma^2}_{\hat{\theta}} = -\left[\frac{\partial^2 \ln\mathcal{L}}{\partial\theta^2}\right]^{-1}_{\theta=\hat{\theta}}, \tag{9.21}$$

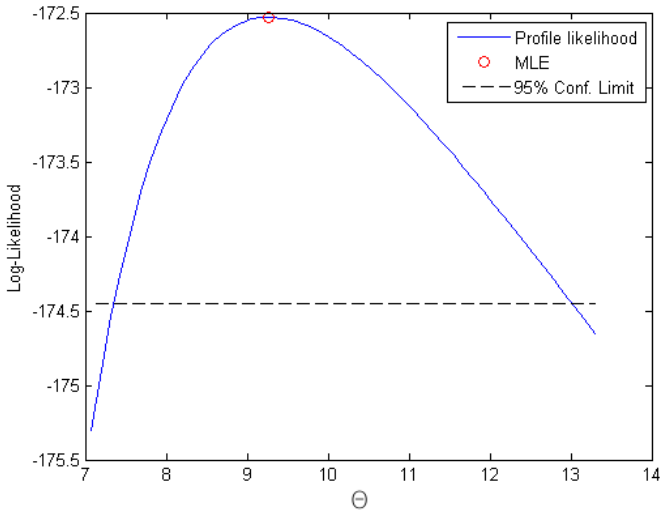

Figure 9.4. *Construction of approximative maximum likelihood confidence interval, where the decrease of the likelihood curve of about $\Delta \ln \mathcal{L} \approx 2$ with respect to the maximum likelihood estimator $\hat{\theta}$ corresponds to the central confidence interval 95%.*

based on the Rao-Cramér-Frechet bound in the large sample limit [199]. Equations 9.20 and 9.21 evaluated at $\hat{\theta} \pm N\hat{\sigma}_{\hat{\theta}}$ lead then to

$$\ln \mathcal{L}(\hat{\theta} \pm N\hat{\sigma}_{\hat{\theta}}) = \ln \mathcal{L}_{\max} - \frac{N^2}{2}. \tag{9.22}$$

Equation 9.22 is finally used to determine the frequentistic 68.3% or 95% ($N = \pm 1$ or $N = \pm 2$) central confidence interval $[\hat{\theta} - N\hat{\sigma}_{\hat{\theta}}, \hat{\theta} + N\hat{\sigma}_{\hat{\theta}},]$ by determining the θ value, at which the log-likelihood function decreases by 0.5 or 2 with respect to $\ln \mathcal{L}_{\max}$ at $\hat{\theta}$. The method is illustrated in figure 9.4. The log-likelihood curve might deviate from a parabola if the large sample limit is not guaranteed, leading to asymmetric boundary values of the confidence interval.

Due to technical reasons, the negative log-likelihood has been chosen as measure in the present CP analysis. Therefore, a minimum $\mathcal{L}_{\min}$ is expected at $\hat{\theta}$ and the approximative central confidence interval at 68% (95%) CL can be read off at an increase of 0.5 (2.0) in this negative log-likelihood. Furthermore, the likelihood curve is built by performing fits at various scan points representing different $\tilde{d}$ hypotheses. This results in discrete values for $-\ln \mathcal{L}(\tilde{d})$ with an additional linear interpolation.

9.6. Likelihood Function

In this section, the likelihood function is described, which is the basis for the test statistic q_μ in the search for $H \to \tau^+\tau^-$ and for deriving the central confidence

interval in the CP analysis. As explained in section 9.1, the likelihood function is a product of probability densities, which depend on certain nuisance parameters. The full likelihood function of the present analyses is defined by

$$\mathcal{L}(\boldsymbol{\phi}, \boldsymbol{\alpha}, \boldsymbol{\gamma}) = \prod_{r \in \text{Region}} \prod_{b_r \in \text{Bin}_r} \mathcal{P}(x_{rb_r}|\nu_{rb_r})\mathcal{P}(y_{rb_r}|y_{rb_r}\gamma_{rb_r}) \prod_{s \in \text{Syst}} \mathcal{G}(0|\alpha_s, 1) \quad (9.23)$$

The nomenclature and the components of likelihood function are explained below.

- *Indices*

  $r \in \text{Region}$
  Index for the various signal and control regions. The analysis of the search for $H \to \tau^+\tau^- \to \ell^+\ell^- 4\nu$ contains in total two signal region and four control regions for the VBF and Boosted category. The CP analysis is based on the VBF category and contains one signal region and three control regions.

  $b_r \in \text{Bin}_r$
  Index for single bins of the distributions within the different regions, which are used in the fitting procedure. Each BDT score distribution in the signal region of the VBF and Boosted category is composed of 19 bins. The Optimal Observable distribution in the signal region of the CP analysis is composed of 6 bins. The BDT score distribution of the $Z \to \tau^+\tau^-$ control region in the CP analysis contains 5 bins. All other control regions of both analyses are counting experiments only with one single bin.

  $s \in \text{Syst}$
  Index for the sources of systematic uncertainties. The individual sources are discussed in detail in chapter 8.

  $p \in \text{Process}$
  Index for the different physics processes. Beside the processes of interest for the different Higgs boson production modes and decays (see section 5.1 for the $H \to \tau^+\tau^- \to \ell^+\ell^- 4\nu$ and 6.1 for the CP analysis), there are $Z/\gamma* \to \tau\tau/ee/\mu\mu$, di-boson, top-quark and fake lepton background processes (see chapter 7).

  $n_{rp} \in \text{Norm}_{rp}$
  Index for unconstrained normalisation parameters. The index depends on the region and the process, whose normalisation is constrained by the fit.

  The signal and control regions and the number of bins of each corresponding distribution are summarized in table 9.1.

- *Nuisance parameters*

  $\boldsymbol{\phi} = (\phi_{rpn_{rp}})$
  These nuisance parameters represent unconstrained region and process specific normalisation factors. The samples of a specific process in the signal and control regions are typically correlated by these factors. E.g. the various Higgs boson signal samples in all regions of the present analyses are correlated

by the parameter of interest μ, which is treated as general unconstrained normalisation parameter of the Higgs boson production.

$\boldsymbol{\alpha} = (\alpha_s)$
Theses nuisance parameters represent systematic uncertainties. The normalisation of the individual processes depend on these parameters, which typically correlate a large set of samples in the analysis. E.g. the correct treatment of the jet energy scale uncertainty requires the correlation of all simulated samples within all regions, so that changes in the calorimeter response affect all corresponding background predictions simultaneously. The parameters are constrained by additional Gaussian probability density terms in the likelihood function, as explained below.

$\boldsymbol{\gamma} = (\gamma_{rb_r})$
Theses nuisance parameters represent statistical uncertainties. The parameters are bin-by-bin scale factors. An additional Poisson constraint term is added to the likelihood function for each of the scale factors, as explained below.

In total, the fit model of the search for $H \to \tau^+\tau^- \to \ell^+\ell^- 4\nu$ analysis contains 83 parameters for systematic uncertainties, 6 normalisation parameters and additional nuisance parameters for statistical uncertainties according to the number of bins in each region (19 parameters for each of both signal regions and one parameter for each of the control regions in each category, i.e. in total 42 nuisance parameters reflecting statistical uncertainties). The CP analysis uses 79 systematic uncertainty parameters, 4 normalisation parameters and additional statistical uncertainty parameters (6 parameters in the signal region, 5 parameters in the BDT control region and 2 for the top and the $Z/\gamma^* \to e^+e^-/\mu^+\mu^-$ control region). A summary of the nuisance parameters can be found in appendix B.

- *Probabilities*

$\mathcal{P}(x_{rb_r}|\nu_{rb_r}) = \frac{(\nu_{rb_r})^{x_{rb_r}} e^{-\nu_{rb_r}}}{x_{rb_r}!}$

The product of Poisson probabilities form the central component of the likelihood function. The actual measurement is denoted by $\mathbf{x} = (x_{rb_r})$, the number of observed events in each bin of the distribution in a specific region. The total number of expected events in the corresponding bin is given by

$$\nu_{rb_r} = \sum_{p \in \text{Process}} \nu_{rb_rp}(\alpha)\eta_{rp}(\alpha)\phi_{rp}\gamma_{rb_r}. \tag{9.24}$$

The number of expected events of a single process is defined by

$$\nu_{rb_rp}(\alpha) = \nu^0_{rb_rp} + \sum_{s \in \text{Syst}} \mathcal{I}_{\text{lin}}(\alpha_s|\nu^0_{rb_rp}, \nu^+_{rb_rps}, \nu^-_{rb_rps}) \tag{9.25}$$

with $\nu^0_{rb_rp}$ being the nominal value of the prediction in each bin. In addition, $\nu_{rb_rp}(\alpha)$ depends on the nuisance parameters $\boldsymbol{\alpha}$, which represent systematic

shape uncertainties. The size of the variation of the nominal value is controlled by the predefined $\pm 1\sigma$ values $\nu^{\pm}_{rb_rps}$ and the corresponding interpolation scheme $\mathcal{I}$, which is discussed below. In case of systematic shape variations, the most straightforward approach of piecewise linear interpolation $\mathcal{I}_{\text{lin}}$ is chosen. The predefined shape variations of the different samples are discussed in section 8.
Furthermore, there are also systematic uncertainties on the absolute normalisation of a specific process. They are represented by the factors

$$\eta_{rp}(\alpha) = \prod_{s \in \text{Syst}} \mathcal{I}_{\text{exp}}(\alpha_s | 1, \eta^{+}_{rps}, \eta^{-}_{rps}). \tag{9.26}$$

In this case, a piecewise exponential scheme $\mathcal{I}_{\text{exp}}$ is chosen to interpolate between the nominal value of unity and the $\pm 1\sigma$ variations $\eta^{\pm}_{rps}$ to avoid negative normalisation factors. The predefined variations on the normalisation of the individual samples are discussed in section 8. Interpolation schemes are explained in detail below.
The unconstrained normalisation factors

$$\phi_{rp} = \prod_{n_{rp} \in \text{Norm}_{rp}} \phi_{rpn_{rp}} \tag{9.27}$$

are defined by the product of all normalisation factors $\phi_{rpn_{rp}}$ of the process in a specific region.
The bin-by-bin normalisation factors γ_{rb_r} represent statistical uncertainties. All normalisation factors are initially set to nominal values of unity.

$\mathcal{P}(y_{rb_r} | y_{rb_r}\gamma_{rb_r}) = \frac{(y_{rb_r}\gamma_{rb_r})^{y_{rb_r}} e^{-y_{rb_r}\gamma_{rb_r}}}{y_{rb_r}!}$

These Poisson constraints approximate frequentistic auxiliary measurements, which account for statistical uncertainties. The bin-by-bin normalisation factors γ_{rb_r} allow to adjust the the true value $y_{rb_r}\gamma_{rb_r}$ with respect to the öbservedv̈alue y_{rb_r}, which is defined by

$$y_{rb_r} = \left[\sigma^{\text{rel}}_{rb_r}\right]^{-2}. \tag{9.28}$$

$\sigma^{\text{rel}}_{rb_r}$ denotes the relative statistical uncertainty of the total expected event yield in each bin. That is, y_{rb_r} is equivalent to the total number of bare events in the corresponding bin[2]. The γ_{rb_r} factors affect the prediction ν_{rb_r}.

$\mathcal{G}(0|\alpha_s, 1) = \frac{1}{\sqrt{2\pi}} \exp -\frac{\alpha^2}{2}$

These Gaussian constraints approximate frequentistic auxiliary measurement of global observables, which account for the sources of systematic uncertainties. The unknown true value α of the corresponding Gaussian distributions are

[2]Each bare event has an average event weight in this case, where the sum of these event weights results in the total expected event yield per bin

Search for $H \to \tau^+\tau^- \to \ell^+\ell^- 4\nu$		
Region	Variable	N_{bins}
VBF signal region	BDT score	19
VBF top quark region	Counting	1
VBF $Z \to e^+e^-/\mu^+\mu^-$ region	Counting	1
Boosted signal region	BDT score	19
Boosted top quark region	Counting	1
Boosted $Z \to e^+e^-/\mu^+\mu^-$ region	Counting	1
CP analysis		
Region	Variable	N_{bins}
CP signal region	Optimal Observable or	6
	Signed $\Delta\phi(j_1, j_2)$	6
CP $Z \to \tau^+\tau^-$ region	BDT score	5
CP Top region	Counting	1
CP $Z \to e^+e^-/\mu^+\mu^-$ region	Counting	1

Table 9.1. *Ingredients of the fitmodel (signal and control regions, discriminating variables and number of bins of the corresponding distributions) of the analysis of the search for $H \to \tau^+\tau^- \to \ell^+\ell^- 4\nu$ and the CP analysis.*

finally the nuisance parameters in the likelihood function. If α is shifted to a value ± 1 of the Standard Gaussian distribution, this translates into $\nu^{\pm}_{rb_rps}$ for shape uncertainties and $\eta^{\pm}_{rps}$ for normalisation uncertainties, as explained above.

- *Interpolation Schemes*

  Two different interpolation schemes are used in the present analyses. The piecewise linear approach

$$\mathcal{I}_{\text{lin}}(\alpha|A^0, A^+, A^-) = \begin{cases} \alpha(A^+ - A^0) & \alpha \geq 0 \\ \alpha(A^0 - A^-) & \alpha < 0 \end{cases} \tag{9.29}$$

  is used in the case of systematic shape uncertainties. It is is the most straightforward approach. A^0 is the nominal value of the prediction, while the values $A^{\pm}, A^-$ denote the $\pm 1\sigma$ variation of the prediction. On the other hand, there is the piecewise exponential approach

$$\mathcal{I}_{\text{exp}}(\alpha|A^0, A^+, A^-) = \begin{cases} (A^+/A^0)^{\alpha} & \alpha \geq 0 \\ (A^-/A^0)^{-\alpha} & \alpha < 0. \end{cases} \tag{9.30}$$

  It is used for systematic normalisation uncertainties with the advantage, that negative yields of the model predictions are excluded.

The likelihood function of the present analyses is parametrized and built with the HistFactory [204] software package, which is based on RooFit[205] and RooStats [206]. It provides a full collection of tools to perform the statistical data

analysis. Minimization routines for estimating the best-fit values of the nuisance parameters are based on Minuit2 and Minos [207].

Further information about the fit model of the search for $H \to \tau^+\tau^- \to \ell^+\ell^- 4\nu$ and the CP analysis can be found in appendix B. This includes an overview of all systematic uncertainties and the corresponding nuisance parameters, nuisance parameter rankings, which show the size of the impact of each nuisance parameter on the the parameter of interest μ and a summary of the correlations of the shape and normalisation uncertainties across the various regions in the analyses.

10 Results

10.1. Search for the Higgs Boson in $H \to \tau^+\tau^- \to \ell^+\ell^- 4\nu$ Decays

The signal extraction in this analysis is based on a fit to data, performed simultaneously in the VBF and the Boosted category on the final BDT classifier distributions, which are shown in figure 5.19. Additional single bin control regions are included in the fit in order to constrain the corresponding background normalisation. The fit strategy is summarized in figure 10.1.

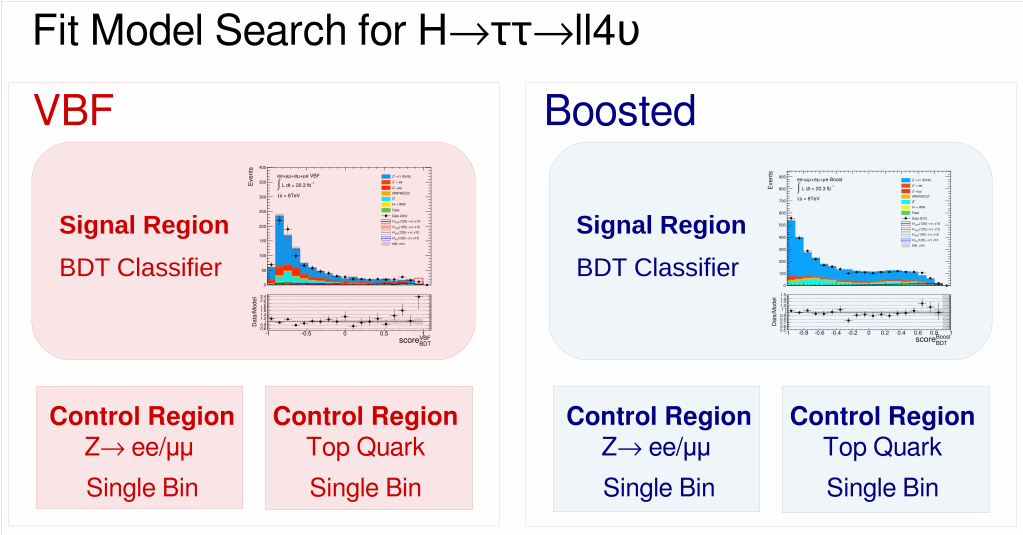

Figure 10.1. *Scheme of the fit model in the search for $H \to \tau^+\tau^- \to \ell^+\ell^- 4\nu$. Two categories, VBF and Boosted, with one signal and two control regions each are used in the fit. In the signal region, the fit is performed on the BDT classifier distribution. Control regions exploit event yields only.*

There are two such single bin control region types in each category, which are orthogonal to the signal region: one dedicated background-enriched control region for the $Z \to e^+e^-/\mu^+\mu^-$ processes, selecting events with an invariant di-lepton mass close to the Z boson mass, and one for top quark pair production processes, defined by an inversion of the b-Veto selection criterion. Therefore, the normalisations of the $Z/\gamma^* \to e^+e^-/\mu^+\mu^-$ and top quark background samples are unconstrained

in the fit and treated as uncorrelated between the VBF and Boosted category but correlated between signal and control regions in one category. The control region definitions and information about their purity are summarized in table 10.1. Since the sample of the minor di-boson background holds relatively low statistics in the signal region of both categories and since the BDT classifier distributions for di-boson and $Z/\gamma^* \to e^+e^-/\mu^+\mu^-$ events are similar, both processes are merged into one common sample in the fit to reduce the impact of statistical fluctuations in the background model.

The normalisation of the $Z/\gamma^* \to \tau^+\tau^-$ sample, which is the dominant background source in the analysis, is free floating in the fit and is mainly constrained in the very background-like region of the BDT classifier distributions. It is treated as correlated across both categories. No dedicated signal-free control region for $Z/\gamma^* \to \tau^+\tau^-$ events in the phase space of the VBF and Boosted category can be defined since the background component is irreducible.

Concerning the prediction for the fake lepton and $H \to W^+W^-$ background processes, the normalisation is fixed to the Standard Model. That is, no unconstrained normalisation factors besides systematic and statistical uncertainties based on Gaussian and Poisson constraints are included in the fit for these background components. The estimation of the various background processes is discussed in detail in chapter 7.

The parameter of interest is chosen to be the signal strength μ, which is defined as the ratio of the measured Higgs boson signal yield to the Standard Model expectation. It is unconstrained in the fit and correlated across the signal and control regions of the VBF and Boosted category. Thus, it reflects the overall normalisation of the combination of all Higgs boson production modes in the analysis. A value of $\mu = 1$

Category	Control region	Selection	Purity/Events
VBF	$Z \to e^+e^-/\mu^+\mu^-$ -enriched	VBF selection with $80 < m^{\text{vis}}_{ee/\mu\mu} < 100$ GeV same-flavour only	97% 1594 data 1545 $Z \to e^+e^-/\mu^+\mu^-$
	Top quark-enriched	VBF selection with b-jet tag	85%, 665 data, 567 top quark
Boosted	$Z \to e^+e^-/\mu^+\mu^-$ -enriched	Boosted selection with $80 < m^{\text{vis}}_{ee/\mu\mu} < 100$ GeV same-flavour only	96% 4053 data 3891 $Z \to e^+e^-/\mu^+\mu^-$
	Top quark-enriched	Boosted selection with b-jet tag	85%, 2384 data, 2021 top quark

Table 10.1. *Definitions of $Z \to e^+e^-/\mu^+\mu^-$- and top quark-enriched control regions in the VBF and Boosted category. The purity is defined as the ratio of expected events of the corresponding process divided by the observed data in the control region. The quoted event numbers are the observed number of data events and the expected event yields for $Z \to e^+e^-/\mu^+\mu^-$ or top quark processes in the corresponding control region.*

corresponds to the presence of a purely Standard Model Higgs boson signal and $\mu = 0$ to the absence of any signal.

Various sources of systematic uncertainties on the normalisation and the shape of the BDT classifier for all signal and background samples are considered in the fit. The relevant experimental, theory and background estimation uncertainties are explained in detail in chapter 8.

The fitting procedure is based on a maximum-likelihood approach, which considers statistical and systematic uncertainties in terms of nuisance parameters $\theta = (\theta_1, \theta_2, ...)$. Such nuisance parameters add further flexibility to the fit. The full likelihood function $\mathcal{L}(\mu, \theta)$ is explained in section 9.6. The minimization of $-\ln \mathcal{L}$ for estimating the best-fit $\hat{\mu}$ is performed with Minuit2 and the error on $\hat{\mu}$ is estimated with Minos [207]. More information about the fit model can be found in appendix B.

The combined measurement of the signal strength in the search for $H \to \tau^+\tau^- \to \ell^+\ell^- 4\nu$ in the VBF and Boosted category is based on 8 TeV data with an integrated luminosity of $\int \mathcal{L}dt = 20.3$ fb^{-1}. It results in the observed signal strength

$$\hat{\mu} = 2.10^{+0.95}_{-0.84} = 2.10^{+0.81}_{-0.74}\ (\text{stat.})\ ^{+0.41}_{-0.41}\ (\text{exp. syst.})\ ^{+0.18}_{-0.18}\ (\text{theo. syst.}) \quad (10.1)$$

assuming the Higgs boson mass $m_H = 125$ GeV. The best-fit signal strength $\hat{\mu}$ shows an upwards fluctuation of signal-like events in data, which is however in reasonable agreement with Standard Model prediction given the uncertainty. The measurement is mainly limited by statistics and detector related uncertainties as can be seen in the breakdown of the uncertainty into its statistical component and the systematic components due to experimental and theory uncertainties.

Figure 10.2 shows the postfit BDT classifier distributions of the background and signal prediction compared to data in the VBF and Boosted category. The excess in data with respect to SM background prediction ($\mu = 0$) is observed in the very signal-like bins of the BDT classifiers. The potential Higgs boson event candidates are highlighted in figure 10.3, showing the number of events as function of the signal S over background B ratio with respect to the binned BDT classifier distributions of both categories. Signal event candidates appear at larger values of $\log_{10}(S/B)$. In addition, the signal contribution for the best-fit signal strength $\hat{\mu} = 2.10$ is compared to SM signal ($\mu = 1$). A background only ($\mu = 0$) fit shows a marginally larger postfit background prediction, since the fit tries to compensate the excess found in data within the uncertainties of the prediction.

The normalisation factors of the $Z/\gamma^* \to \tau^+\tau^-$, $Z/\gamma^* \to e^+e^-/\mu^+\mu^-$ (+di-boson) and top quark background samples are unconstrained parameters in the fit. The postfit value of each normalisation factor is listed in table 10.2. Overall, the normalisation factors for the specific background components are close to unity, which indicates a good background modeling already at prefit level.

The postfit signal and background yields including systematic uncertainties are quoted in table 10.3. In the most signal-like bin of the BDT classifier distribution in

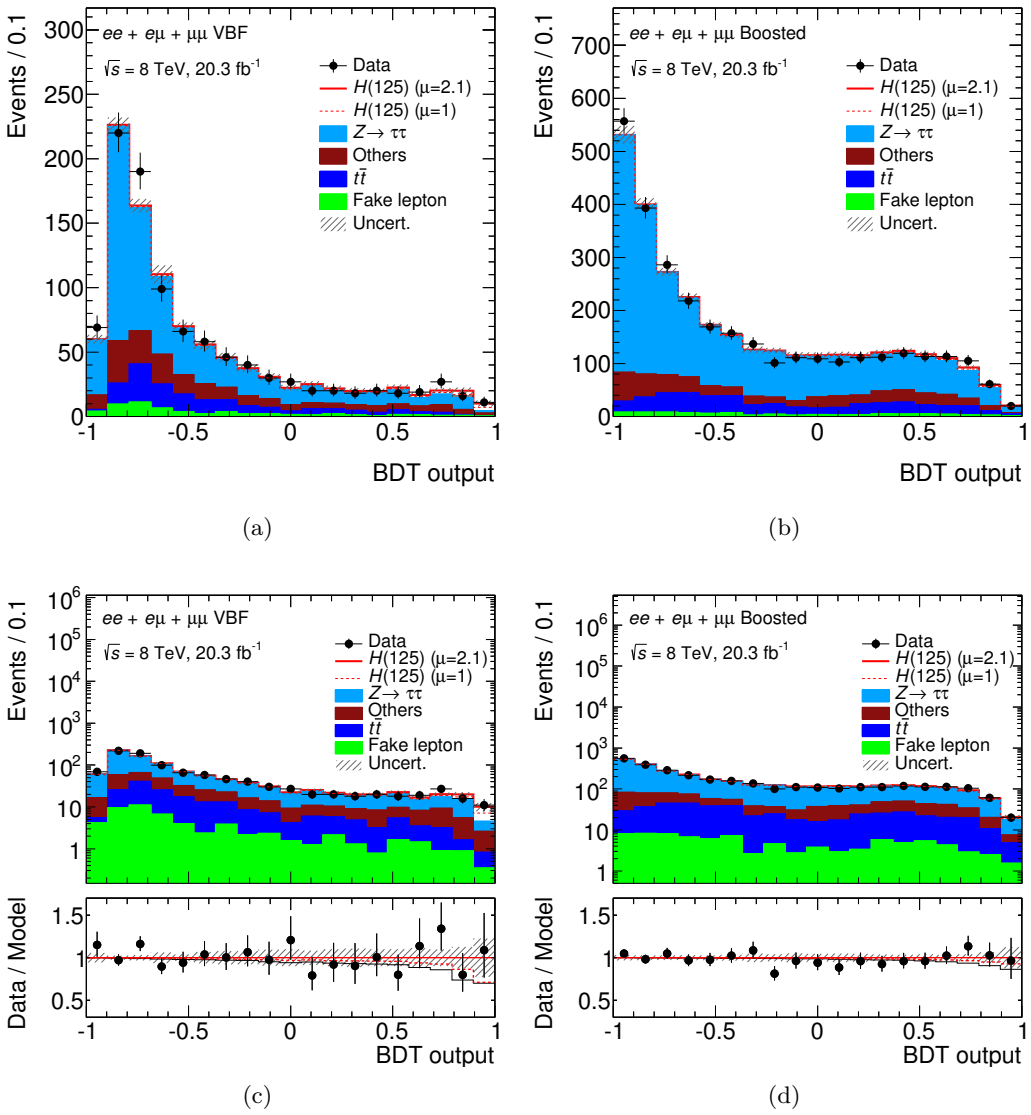

Figure 10.2. *Postfit BDT classifier distribution of the model and the observed data in the VBF (left) and Boosted (right) category. All nuisance parameters and normalisation factors have been adjusted in the fit to data. The upper row shows the distribution on linear and the lower row on logarithmic scale to visualize signal events in the region of high BDT classifier bins. The bottom panel shows the data over prediction ratio, where the solid red line at a value of one reflects the best-fit signal ($\mu = 2.10$) plus background prediction. The red dashed line contains SM signal ($\mu = 1$) and the black solid line background only prediction. Individual background components of $Z/\gamma^* \to e^+e^-/\mu^+\mu^-$, di-bosons and $H \to W^+W^-$ are summarized in Others. The error band contains statistical and systematic uncertainties.*

the VBF category, 11 events are observed: 5.3 ± 2.2 Higgs boson event candidates and 4.5 ± 2.3 background events are predicted after fitting, which demonstrates the good performance of the BDT in separating signal events.

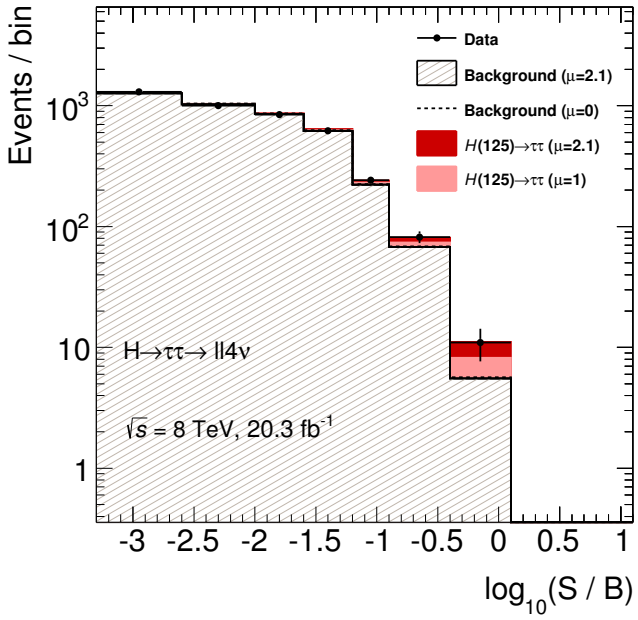

Figure 10.3. *Event yields as a function of* $\log_{10}(S/B)$*, where* S *(signal yield) and* B *(background yield) are taken from the BDT classifier bin of each event, assuming a signal strength* $\mu = 2.1$*. Events from the* $H \to \tau^+\tau^- \to \ell^+\ell^- 4\nu$ *analysis are included. The predicted background is obtained from the global fit* ($\hat{\mu} = 2.1$) *and signal yields are shown for* $m_H = 125$ *GeV at* $\mu = 1$ *and* $\mu = 2.1$*. The background-only distribution (dashed line) is obtained from the global fit, with* μ *fixed at zero [8].*

A detailed description of the statistical data analysis has been introduced in chapter 9. The LHC test statistic is defined as $q_\mu = -2\ln[\mathcal{L}(\mu, \hat{\hat{\theta}})/\mathcal{L}(\hat{\mu}, \hat{\theta})]$ with $\hat{\mu}$ and $\hat{\theta}$ being the best-fit signal strength and the set of nuisance parameters, which maximize the likelihood function. $\hat{\hat{\theta}}$ denotes the nuisance parameters, that maximize the likelihood function assuming a specific signal strength value μ.

The discovery significance of the observation is defined as the probability to obtain a result, which corresponds to at least the signal strength measured in data under

Category	Process	Postfit normalisation
VBF	$Z/\gamma^* \to e^+e^-/\mu^+\mu^-$	0.986 ± 0.307
	Top quark	1.008 ± 0.128
Boosted	$Z/\gamma^* \to e^+e^-/\mu^+\mu^-$	1.082 ± 0.278
	Top quark	1.038 ± 0.114
VBF+Boosted	$Z/\gamma^* \to \tau^+\tau^-$	1.058 ± 0.121

Table 10.2. *Postfit normalisation factors of the* $Z/\gamma^* \to \tau^+\tau^-$*,* $Z/\gamma^* \to e^+e^-/\mu^+\mu^-$*(+di-boson) and top quark samples in the VBF and Boosted category of the* $H \to \tau^+\tau^- \to \ell^+\ell^- 4\nu$ *channel.*

the assumption of a background-only hypotheses (p_0-value). The test statistic for calculating the p_0-value is q_0. Figure 10.4 shows the p_0-value for the combination of both categories and each category respectively with respect to different Higgs boson mass hypothesis. The observed significance for a Higgs boson signal with a mass of $m_H = 125$ GeV is 2.69 in terms of Gaussian standard deviations. It is larger than the expected significance of 1.34 due to the excess in data, which exceeds SM Higgs boson signal for $m_H = 125$ GeV. The expected significance is determined by using pseudo-data, which consists of the Standard Model background and signal for a given Higgs boson mass. The observed and expected significances are summarized in table 10.4 for the combination of both categories and for each category respectively, assuming a Higgs boson mass of $m_H = 125$ GeV. The combined sensitivity is mainly driven by the VBF category. The corresponding best-fit signal strength of each mass hypothesis is listed in table 10.5. For small mass hypotheses, the production cross section increases whereas the signal selection efficiency is decreasing due to softer spectra of the lepton momenta. High mass hypotheses result in a smaller cross sections but an increased selection efficiency. The interplay of both properties leads to an increase in the best-fit signal strength for very small or high Higgs boson mass hypothesis and therefore a decreased compatibility with the Standard Model compared to the intermediate mass range.

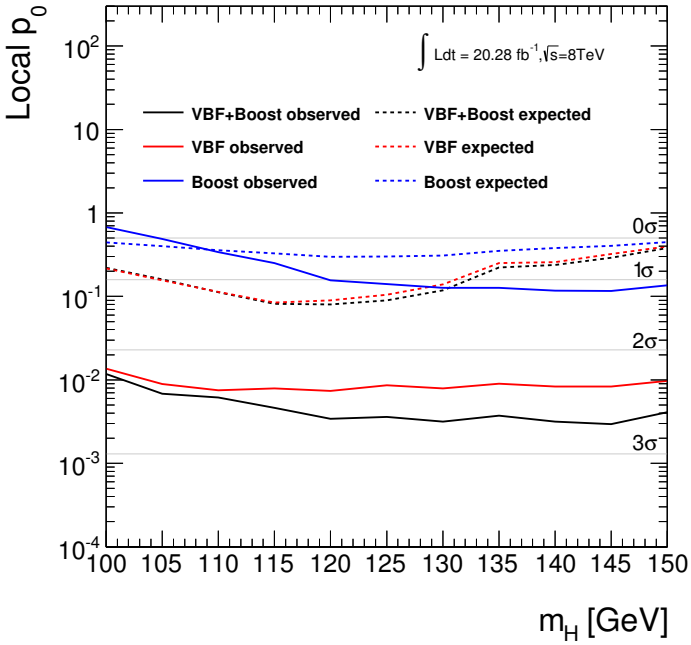

Figure 10.4. *Observed and expected significance in terms of the p_0-value as function of the mass of the Higgs boson for the VBF, Boosted and combined analysis of the $H \to \tau^+\tau^- \to \ell^+\ell^- 4\nu$ channel.*

The probability density functions $f(q_0|B)$ and $f(q_0|S+B)$, assuming background-only (B) or background including signal ($S+B$, $m_H = 125$ GeV) hypotheses, are

shown in figure 10.5 to visualize the discovery significances of the measurement. The observed q_0 is more compatible with the $S+B$ hypothesis equivalent to a higher p_0-value compared to the B hypothesis. The expected q_0 has been determined using pseudo-data including signal with $m_H = 125$ GeV.

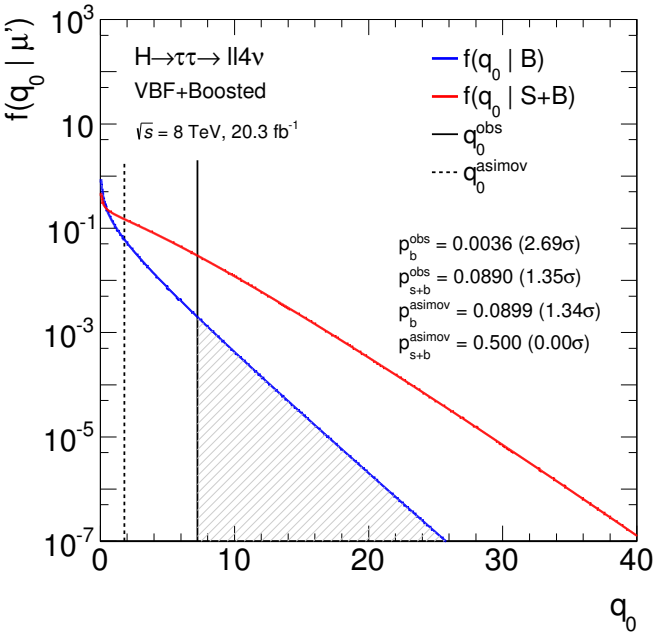

Figure 10.5. *Probability density function of the test statistic q_0 of the $H \to \tau^+\tau^- \to \ell^+\ell^- 4\nu$ channel under the assumption of background-only B (blue) and Standard Model signal $S+B$ (red). p_0 values are quoted for measured data (obs) and pseudo data (Asimov data, see section 9.3), assuming Standard Model signal with $\mu = 1$. The probability density function is based on asymptotic approximations [202].*

Furthermore, an upper limit on the signal strength μ has been calculated, using the test statistic q_μ. A specific μ_{up} is excluded at 95% confidence level, if the $p_{\mu_{\text{up}}}$-value of the corresponding observed test statistic is at most 5%, based on the probability density function $f(q_{\mu_{\text{up}}}|S(\mu_{\text{up}})+B)$. In case of the expected upper limit, the evaluation uses background-only pseudo-data. The excluded signal strength corresponds to the median of $f(q_{\mu_{\text{up}}}|B)$. Figure 10.6 shows the observed and expected exclusion limit as function of m_H. The observed (expected) upper limit at 95% confidence level is 3.7 ($1.6^{+0.7}_{-0.4}$) for the Higgs boson mass of $m_H = 125$ GeV. The deviation of the observed from the expected limit reflects the excess in data compared to the background only prediction.

To illustrate the compatibility of the observed signal with a Higgs boson mass of $m_H = 125$ GeV, figure 10.7 shows the invariant m_{MMC} distribution for the VBF and Boosted category and the combination of both at postfit level. An excess is observed in the region of intermediate m_{MMC} values in the VBF category. In case of the combined distribution, the events are weighted by $ln(1+S/B)$ with S being the signal and B the background prediction in bins of the corresponding BDT

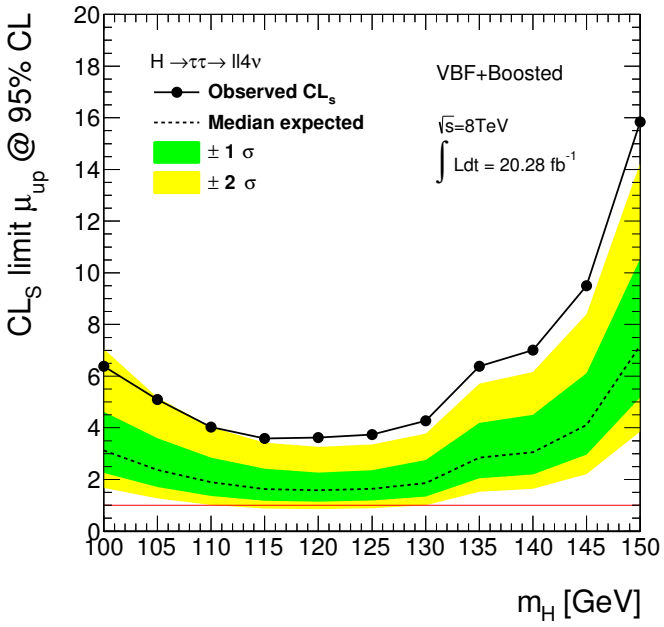

Figure 10.6. *Observed (solid line) and expected (dashed line) exclusion limit of the $H \to \tau^+\tau^- \to \ell^+\ell^- 4\nu$ channel at 95% CL_s confidence level based on the test statistic q_μ as function of the mass of the Higgs boson.*

classifier. Signal-like events are therefore enhanced while background-like events are suppressed. The weighted combined m_{MMC} distribution displays the excess in data, which is fully compatible with a Higgs boson mass of $m_H = 125$ GeV.

The measurement of the overall signal strength does not provide information about the single Higgs boson production modes. However due to the categorization into the VBF category, which is dominated by VBF signal events, and the Boosted category, enriched with events from GGH, the analysis is sensitive to both production modes individually. For this purpose, the signal strength is split up into two unconstrained parameters of interest in the fit: μ_{GGF} is the couplings strength for the GGH production mode and $\mu_{\mathrm{VBF+VH}}$ the combined couplings strength for the VBF and VH production modes. The best-fit values for the individual signal strengths assuming $m_H = 125$ GeV are

$$\begin{aligned} \hat{\mu}_{\mathrm{GGF}} &= 1.72^{+3.14}_{-2.92} \\ &= 1.72^{+2.45}_{-2.42}\ (\mathrm{stat.})\ ^{+1.62}_{-1.62}\ (\mathrm{exp.\ syst.})\ ^{+0.95}_{-0.95}\ (\mathrm{theo.\ syst.}) \quad (10.2) \\ \hat{\mu}_{\mathrm{VBF+VH}} &= 2.03^{+1.38}_{-1.22} \\ &= 2.03^{+1.21}_{-1.07}\ (\mathrm{stat.})\ ^{+0.58}_{-0.58}\ (\mathrm{exp.\ syst.})\ ^{+0.32}_{-0.27}\ (\mathrm{theo.\ syst.}). \quad (10.3) \end{aligned}$$

A scan in the parameter space of both signal strength parameters, including a full fit in each scan point, provides the 68% and 95% confidence level contours in the ($\mu_{\mathrm{VBF+VH}}$,μ_{GGF}) plane as shown in figure 10.8. The measurement of the individual signal strength parameters is consistent with Standard Model expectation within

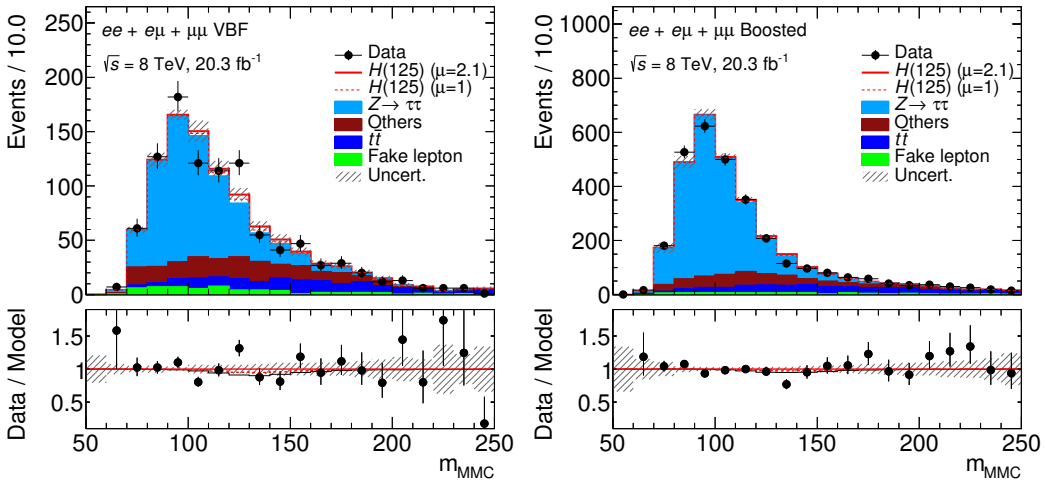

(a) (b)

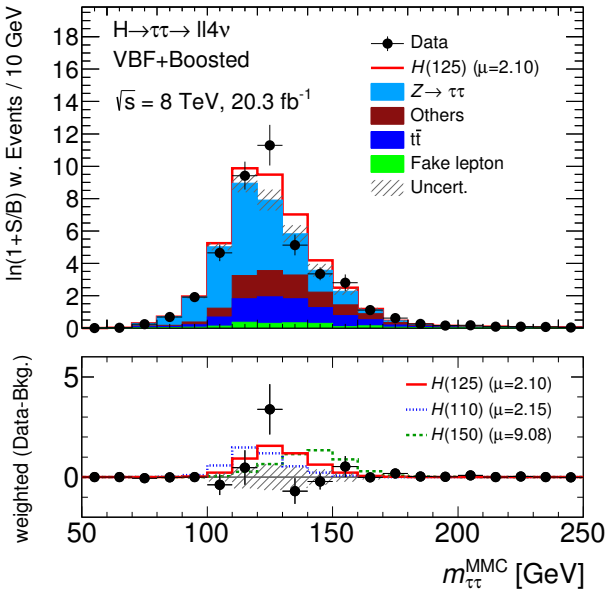

(c)

Figure 10.7. *Postfit distribution of m_{MMC} compared to data in VBF (a) and Boosted (b) category of the $H \to \tau^+\tau^- \to \ell^+\ell^- 4\nu$ channel. The bottom panel shows the data over prediction ratio, where the solid red line at a value of one reflects the best-fit signal ($\mu = 2.1$) plus background prediction. The red dashed line contains SM signal ($\mu = 1$) and the black solid line background only prediction. The combined m_{MMC} distribution (c) with weighted events according to $ln(1 + S/B)$, where S is the expected prefit signal and B the background prediction in bins of the corresponding BDT classifiers of the $H \to \tau^+\tau^- \to \ell^+\ell^- 4\nu$ channel. The bottom panel shows the weighted data over prediction ratio for various signal hypotheses normalized to their best-fit signal strength.*

one standard deviation while the background-only hypothesis is outside the 95% contour.

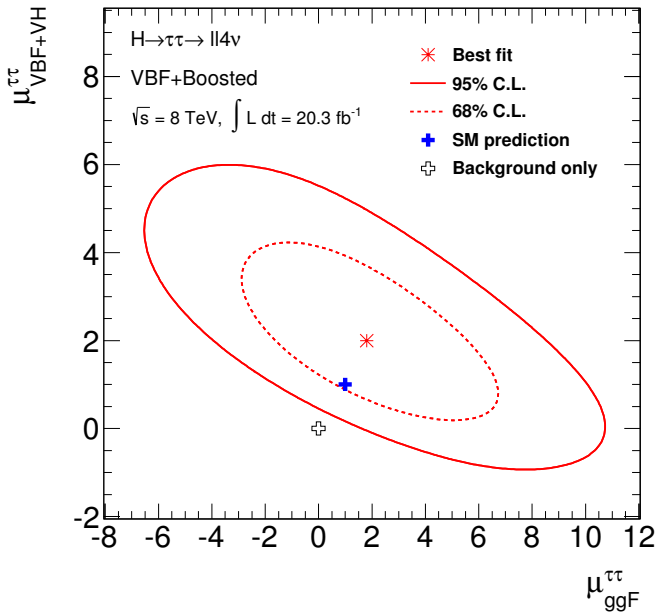

Figure 10.8. *68% and 95% confidence level contours in the plane of the two signal strength parameters μ_{GGF} and μ_{VBF+VH} of the $H \to \tau^+\tau^- \to \ell^+\ell^- 4\nu$ channel.*

Figure 10.9 summarizes the sources of uncertainties, which affects the overall postfit signal strength $\hat{\mu}$ substantially. The top-ranked nuisance parameters show the largest impact on $\hat{\mu}$, which is defined by the deviation of the fitted signal strength after fixing a specific nuisance parameter to its $\pm 1\sigma$ value from the nominal $\hat{\mu}$ value determined in a global fit. In addition, the postfit *pull* of each nuisance parameter and the *constraint* of its uncertainty is shown as explained below. Each nuisance parameter adds flexibility to the fit and allows the prediction model to compensate deviations with respect to the observed data. Nominal values of the nuisance parameters in the likelihood ($\boldsymbol{\phi}$, $\boldsymbol{\alpha}$, $\boldsymbol{\gamma}$, see section 9.6) are set to one, while the parameter values after performing a global fit usually deviate from one (pull) resulting in an increase or decrease of the expected event yields. In the figure, pulls are normalised to the standard deviation of the corresponding nuisance parameter. The estimated prefit standard deviation of each nuisance parameter might also change after fitting (constraint) according to the postfit log likelihood curve of the parameter (see section 9.5). No extreme pulls and constraints compared to the prefit values are observed, which indicates a reasonable behaviour of the underlying signal and background model. The statistical uncertainties of the most signal-like bins of the BDT classifier distributions are ranked high, which is expected because the analysis is statistically limited as shown above in terms of the uncertainty breakdown of the best-fit signal strength. Moreover, detector related uncertainties due to the jet energy scale and resolution measurements contribute significantly

to the total uncertainty, as well as uncertainties of the luminosity measurement, the electron energy scale and the modeling of the $Z/\gamma^* \to \tau^+\tau^-$ and fake lepton background samples. The normalisation of the dominant $Z/\gamma^* \to \tau^+\tau^-$ background is unconstrained in the fit and affects the final sensitivity too. Concerning theory related uncertainties, QCD scale variations of the simulated signal samples and the uncertainty on the $H \to \tau^+\tau^-$ branching ratio have the biggest impact on the signal strength.

The negative log likelihood scans of some of the most important systematic uncertainties are shown in figure 10.10: a jet energy scale uncertainty parameter, which is pulled to higher values, the jet energy resolution parameter, which is over-constrained, and a Embedding modeling parameter, which shows asymmetric behaviour. The likelihood scans are based on global fits where the single nuisance parameter of interest is fixed to specific parameter values in the range of $[-2\sigma, +2\sigma]$. These scans allow to determine the best-fit nuisance parameter value and its postfit uncertainty (see section 9.5). No double minima or other noticeable problems are observed and the behaviour is considered to be reasonable. The correlation of the most important systematic uncertainties are shown in figure 10.11. Overall, the correlations of the parameters shown are rather small except for the normalisation of the $Z/\gamma^* \to \tau^+\tau^-$ background model and the Embedding related muon isolation uncertainty as expected.

The analysis of the fully leptonic final state $H \to \tau^+\tau^- \to \ell^+\ell^- 4\nu$ makes an important contribution (signal strength $\hat{\mu} = 2.10^{+0.95}_{-0.84}$ with a significance of 2.69 for $m_H = 125$ GeV) to the combined analysis, which considers all τ lepton decay channels $\tau_{\text{lep}}\tau_{\text{had}}$, $\tau_{\text{had}}\tau_{\text{had}}$ and $\tau_{\text{lep}}\tau_{\text{lep}}$as discussed in Ref [8]. The present analysis provides further improvement to the overall sensitivity, which manifests the evidence for Higgs boson Yukawa couplings to τ leptons. The combined search for the Standard Model Higgs boson in the decay $H \to \tau^+\tau^-$ is described in chapter 11.

Process/Category	VBF			Boost		
	Total	2nd last bin	Last bin	Total	2nd last bin	Last bin
$(GGF)H \to \tau^+\tau^-$ ($m_H = 125$ GeV)	15 ± 7	1.1 ± 0.5	0.57 ± 0.27	28 ± 14	3.2 ± 1.6	1.6 ± 0.8
$(VBF)H \to \tau^+\tau^-$ ($m_H = 125$ GeV)	20 ± 8	4.1 ± 1.7	5.0 ± 2.1	8.2 ± 3.5	1.4 ± 0.6	0.73 ± 0.31
$(W)H \to \tau^+\tau^-$ ($m_H = 125$ GeV)	0.38 ± 0.16	< 0.1	< 0.1	5.6 ± 2.4	0.64 ± 0.27	0.32 ± 0.14
$(Z)H \to \tau^+\tau^-$ ($m_H = 125$ GeV)	0.21 ± 0.09	< 0.1	< 0.1	2.9 ± 1.2	0.30 ± 0.13	0.17 ± 0.07
$Z/\gamma^* \to \tau^+\tau^-$	579 ± 22	9.3 ± 1.1	1.9 ± 0.5	2170 ± 80	33.5 ± 2.6	10.4 ± 1.7
$Z/\gamma^* \to e^+e^-/\mu^+\mu^-$+ di-boson	183 ± 15	3.3 ± 0.4	1.2 ± 0.4	410 ± 40	9.1 ± 1.6	2.4 ± 1.4
Top quark	136 ± 18	0.73 ± 0.33	0.48 ± 0.25	390 ± 50	8.1 ± 1.3	3.3 ± 1.2
Fake	58 ± 12	0.9 ± 0.5	0.35 ± 0.24	92 ± 31	2.5 ± 0.9	1.5 ± 0.5
$(GG)H \to WW$ ($m_H = 125$ GeV)	3.1 ± 0.8	0.11 ± 0.05	0.14 ± 0.05	6.9 ± 2.1	0.42 ± 0.17	0.19 ± 0.12
$(VBF)H \to WW$ ($m_H = 125$ GeV)	3.46 ± 0.35	0.41 ± 0.05	0.39 ± 0.08	1.63 ± 0.17	0.112 ± 0.029	< 0.1
$(W)H \to WW$ ($m_H = 125$ GeV)	0.19 ± 0.07	< 0.1	< 0.1	0.99 ± 0.10	< 0.1	< 0.1
$(Z)H \to WW$ ($m_H = 125$ GeV)	< 0.1	< 0.1	< 0.1	0.67 ± 0.09	< 0.1	< 0.1
Total Background.	964 ± 22	14.8 ± 2.5	4.5 ± 2.3	3070 ± 60	54 ± 4	17.9 ± 2.6
Total Signal ($m_H = 125$ GeV)	36 ± 15	5.3 ± 2.2	5.6 ± 2.3	45 ± 20	5.6 ± 2.4	2.8 ± 1.2
Data	1014	16	11	3095	61	20

Table 10.3. *Postfit event yields (total, 2nd last and last bin of the BDT classifier) for the individual signal and background components in the VBF and the Boosted category of the $H \to \tau^+\tau^- \to \ell^+\ell^- 4\nu$ channel. The errors for the individual signal and background components contain systematic uncertainties only while systematic and statistical uncertainties are included in the total background.*

Signal	expected [σ]	observed [σ]
$H(125\text{ GeV}) \to \tau\tau$ VBF	1.25	2.38
$H(125\text{ GeV}) \to \tau\tau$ Boosted	0.52	1.08
$H(125\text{ GeV}) \to \tau\tau$ Combination	1.34	2.69

Table 10.4. *Observed and expected discovery significance in terms of Gaussian standard deviations assuming a Higgs boson mass of $m_H = 125$ GeV. Significances are quoted for each category standalone and the combination of both categories of the $H \to \tau^+\tau^- \to \ell^+\ell^- 4\nu$ channel.*

Signal	$\hat{\mu}_{\text{best}}$	$+\sigma_{\text{up}}$	$-\sigma_{\text{down}}$
$H(100\text{ GeV}) \to \tau\tau$	3.13	+1.8	−1.46
$H(105\text{ GeV}) \to \tau\tau$	2.65	+1.37	−1.15
$H(110\text{ GeV}) \to \tau\tau$	2.15	+1.07	−0.91
$H(115\text{ GeV}) \to \tau\tau$	1.96	+0.94	−0.81
$H(120\text{ GeV}) \to \tau\tau$	2.02	+0.92	−0.8
$H(125\text{ GeV}) \to \tau\tau$	2.10	+0.95	−0.84
$H(130\text{ GeV}) \to \tau\tau$	2.42	+1.08	−0.95
$H(135\text{ GeV}) \to \tau\tau$	3.63	+1.61	−1.44
$H(140\text{ GeV}) \to \tau\tau$	3.99	+1.76	−1.56
$H(145\text{ GeV}) \to \tau\tau$	5.33	+2.45	−2.11
$H(150\text{ GeV}) \to \tau\tau$	9.08	+3.97	−3.63

Table 10.5. *Best-fit signal strength values of the $H \to \tau^+\tau^- \to \ell^+\ell^- 4\nu$ channel with respect to data assuming various Higgs boson mass hypothesis.*

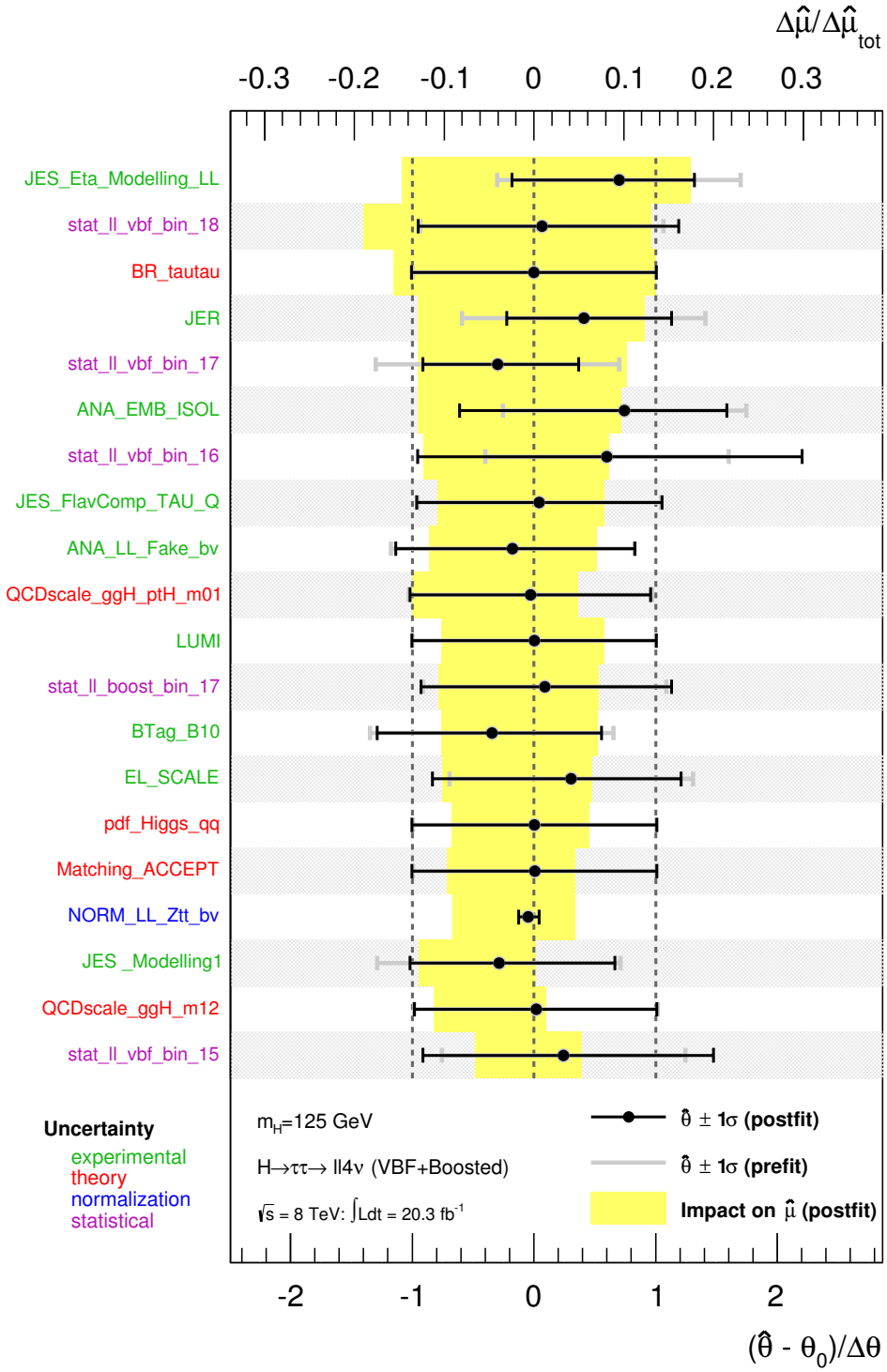

Figure 10.9. *Postfit pulls and constraints of nuisance parameters from the combined fit of the VBF and Boosted category of the $H \to \tau^+\tau^- \to \ell^+\ell^- 4\nu$ channel (lower x-axis). Impact of nuisance parameters on best fit signal strength (upper x-axis). Nuisance parameter importance ranking with respect to the impact on the signal strength (y-axis top-down). The first 20 nuisance parameters are shown with the largest impact. Normalisation factors are unconstrained in the fit and the error bars reflect absolute uncertainties.*

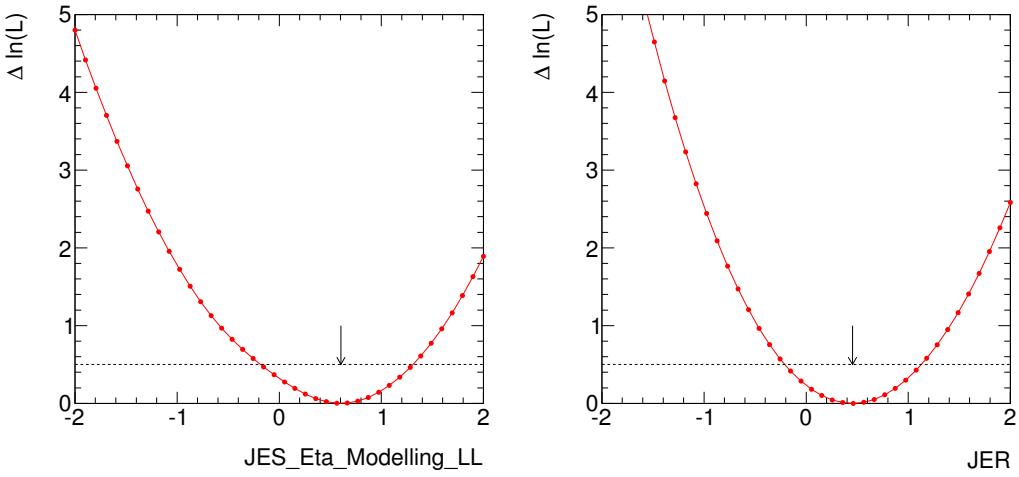

(a) (b)

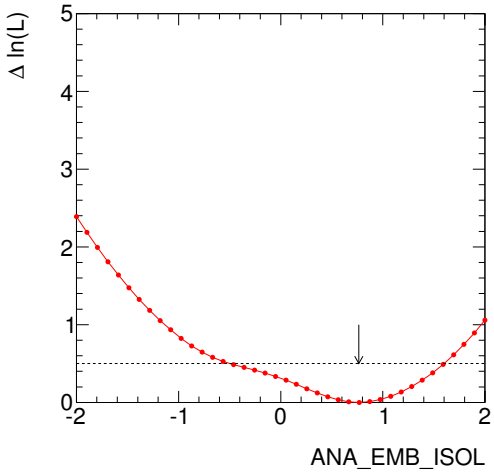

(c)

Figure 10.10. *Negative log likelihood scans for the most significant nuisance parameters in the combined fit model of the VBF and Boosted category of the $H \to \tau^+\tau^- \to \ell^+\ell^- 4\nu$ channel: a jet energy scale (left), jet energy resolution (middle) and Embedding modeling (right) nuisance parameter. Negative log likelihood as function of a nuisance parameter value, where the nominal default parameter value corresponds to zero and its deviation is normalised to the prefit standard deviation. The solid horizontal line indicates the $\pm 1\sigma$ uncertainty of the best-fit value at the minimum of the negative log likelihood curve. The acronyms of the nuisance parameters are explained in appendix B.*

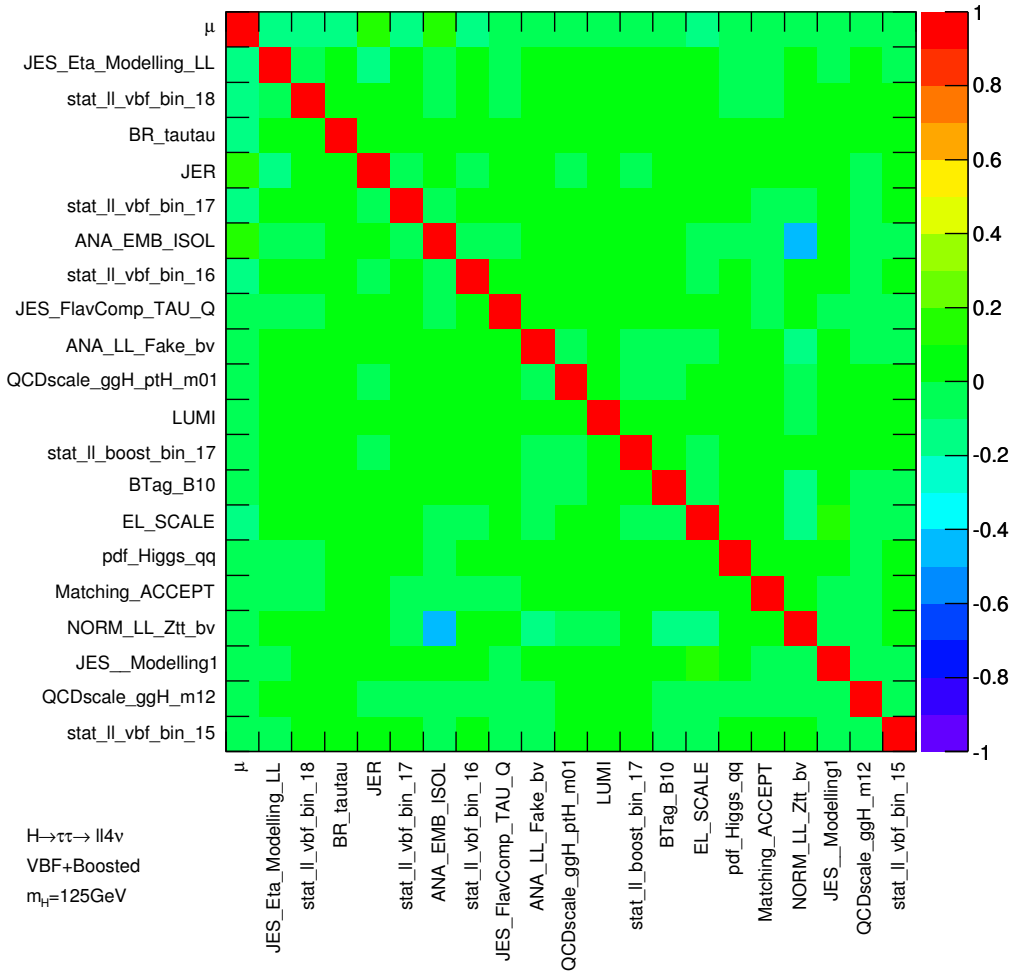

Figure 10.11. *Correlation matrix of the most important systematic uncertainties shown in figure B.1 for the combined fit model of the VBF and Boosted category of the $H \to \tau^+\tau^- \to \ell^+\ell^- 4\nu$ channel. The acronyms of the nuisance parameters are explained in appendix B.*

10.2. Test of CP Invariance in VBF Higgs Boson Production in $H \to \tau^+\tau^- \to \ell^+\ell^- 4\nu$ Decays

The CP analysis (see chapter 6) aims to test CP invariance in VBF Higgs boson production and to determine confidence intervals for the parameter $\tilde{d}$, which governs CP-violating effects. Specific CP-odd observables, which are sensitive to CP-violation in the HVV vertex called the Optimal Observable and signed $\Delta\phi(j_1, j_2)$, have been exploited. The analysis is based on the VBF category of the $H \to \tau^+\tau^- \to \ell^+\ell^- 4\nu$ analysis and the signal region is defined as the signal-like part of the BDT classifier distribution.

Deviations of the observed CP-odd observables mean value from zero would inevitably hint to physics beyond the Standard Model including CP-violation. The measured mean values in data for the Optimal Observable and the signed $\Delta\phi(j_1, j_2)$ distribution are

$$< OO > \;=\; +0.29 \pm 0.46 \quad \text{and} \tag{10.4}$$

$$< \text{signed}\Delta\phi(j_1, j_2) > \;=\; -0.14 \pm 0.24 \tag{10.5}$$

in the signal region of the CP analysis. This is consistent with the Standard Model, which predicts vanishing mean values, and no indications for CP-violation are observed.

Furthermore central confidence intervals on the $\tilde{d}$ parameter are determined, which describes CP-odd admixtures to the SM HVV couplings. The 68% confidence interval corresponding to $\pm 1\sigma$ can be read off from the corresponding negative log likelihood (NLL) profile as explained in section 9.5[1]. The negative log likelihood values as function of $\tilde{d}$ have been determined by performing global maximum likelihood fits to data for various CP-mixing scenarios. The signal normalisation μ of the VBF Higgs boson signal is treated as unconstrained, i.e. only the shape information is used. Non-VBF Higgs boson production processes are normalised to SM prediction and treated as background. The fit model consists of a signal region, defined by the signal-like BDT classifier region in the VBF category. The full distribution of the CP-odd variable, the Optimal Observable or signed $\Delta\phi(j_1, j_2)$, is used in the fit. Furthermore, three control regions are taken into account: a background-like BDT classifier region, exploiting the BDT classifier distribution itself, a dedicated top quark and a $Z/\gamma^* \to e^+e^-/\mu^+\mu^-$ enriched single bin region according to the control regions of the VBF category. The fit is performed simultaneously in all regions and bins of the corresponding distributions. Figure 10.12 illustrates the fit model of the CP analysis. More information about the fit model can be found in section 9.6 and appendix B. The modeling of the CP-odd observables and sources of systematic uncertainties are discussed in detail in the chapters 7 and 8.

[1] The minimum of the NLL profile indicates the best-fit maximum likelihood estimator of the $\tilde{d}$ parameter and the $\pm 1\sigma$ interval corresponds to the intersection of the NLL profile with the horizontal line at ΔNLL$= 0.5$.

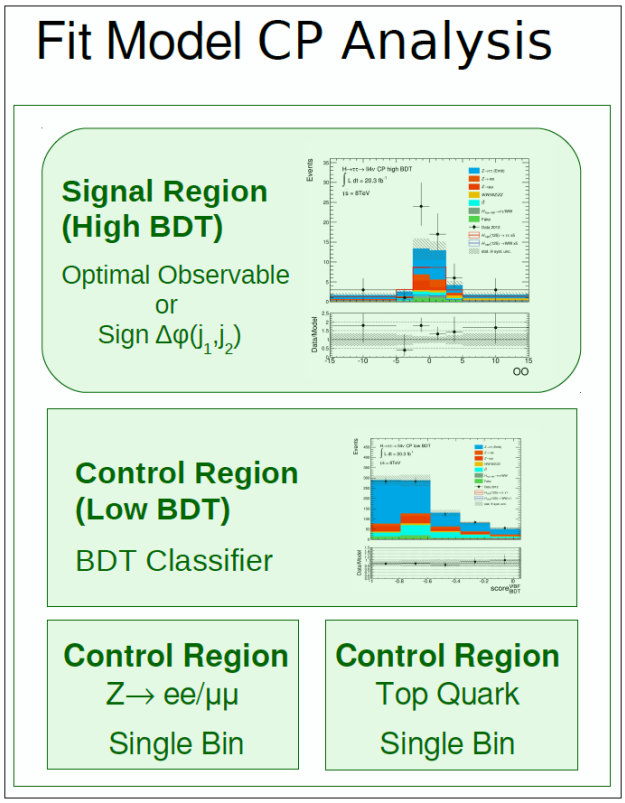

Figure 10.12. *Scheme of the fit model in the CP analysis. The signal region is defined by the region of high signal-like BDT classifier values in the VBF category. The full distributions of CP-odd variables are used in the fit. Three control regions are included in the fit: two single bin regions for top quark and $Z/\gamma^* \to e^+e^-/\mu^+\mu^-$ background components and the region of the low background-like values of the BDT classifier, where the BDT classifier distribution is exploited.*

The observed and expected NLL profiles as function of $\tilde{d}$ as well as the corresponding best-fit signal strength values are shown in figure 10.13 for fitting the distribution of the Optimal Observable. Each of the black points in the figure represents a fit including the determination of the corresponding NLL value for a certain $\tilde{d}$ hypothesis. The NLL profiles yield to an observed central confidence interval on the $\tilde{d}$ parameter of $[-0.03, 0.17]$ with an expected interval of $[-0.12, 0.11]$ at 68% confidence level. The asymmetric behaviour of the observed confidence interval might mainly stem from statistical fluctuations assuming SM Higgs boson signal. The intervals have been extracted using a linear interpolation between the $\tilde{d}$ scan points. Differences between linear and polynomial interpolation schemes are found to be small. For determining the expected profiles, pure SM VBF Higgs boson signal normalised to the best-fit signal strength $\hat{\mu} = 2.35^{+1.50}_{-1.35}$, taken from the fit to data at $\tilde{d}$=0, has been assumed. To compare the sensitivity of both fit model approaches using either the Optimal Observable or signed $\Delta\phi(j_1, j_2)$ in the signal region, the expected NLL profile for fitting signed $\Delta\phi(j_1, j_2)$ is included in addition, assuming pure SM signal with the same best-fit signal strength. The larger distance

ΔNLL from minimum to maximum indicates an increased sensitivity of the Optimal Observable compared to signed $\Delta\phi(j_1, j_2)$. Overall, an excess with respect to background only prediction is observed in data as expected from the analysis of the search for $H \to \tau^+\tau^- \to \ell^+\ell^- 4\nu$. This excess is found to be slightly larger compared to the result of the search analysis. However, it is still compatible with the SM Higgs boson signal prediction within statistical and systematic uncertainties. The best-fit signal strength values shrink for larger $\tilde{d}$ CP-mixing scenarios, since the compatibility with data is decreasing.

Alternative fits to signed $\Delta\phi(j_1, j_2)$ instead of the Optimal Observable results in an observed (expected) central confidence interval of $[-0.09, 0.09]$ ($[-0.11, 0.12]$) at 68% confidence level. The NLL profile and the best-fit signal strength as function of $\tilde{d}$ are shown in figure 10.14. A SM VBF Higgs boson signal normalised to $\hat{\mu} = 2.88^{+1.48}_{-1.30}$, which has been taken from the fit to data at $\tilde{d}$=0, is assumed in the derivation of the expected confidence interval. The best-fit signal strength using signed $\Delta\phi(j_1, j_2)$ is found to be larger than fitting the Optimal Observable. This is mainly due to the fact that both leading jets in the event are required to emerge in different hemispheres in case of signed $\Delta\phi(j_1, j_2)$, which results in a larger background rejection compared to the Optimal Observable. However it is still in reasonable agreement with SM within the uncertainties. The observed and expected confidence intervals for both CP-odd observables are summarized in table 10.6. Differences between the observed and expected NLL profile (larger ΔNLL values in case of the observed NLL profile) might stem mainly from downwards fluctuations in data, that increase the exclusion power of non-SM signal hypothesis.

Observable	observed	expected	$\hat{\mu}$ ($\tilde{d} = 0$, $m_H = 125$ GeV)
OO	$[-0.03, 0.17]$	$[-0.12, 0.11]$	$2.35^{+1.50}_{-1.35}$
signed $\Delta\phi(j_1, j_2)$	$[-0.09, 0.09]$	$[-0.11, 0.12]$	$2.88^{+1.48}_{-1.30}$

Table 10.6. *Observed and expected 68% confidence interval for CP-odd observables in the CP analysis and the best-fit signal strength including systematic and statistical uncertainties for SM VBF Higgs boson signal ($\tilde{d} = 0$, $m_H = 125$ GeV).*

No hints to CP-violation are observed and the measured central confidence intervals indicate a $\tilde{d}$ parameter value, which is compatible with pure SM Higgs boson signal at 68% confidence level.

The postfit event yields for the individual signal and background samples, which are used in the global fit of the Optimal Observable assuming a SM signal hypothesis ($\tilde{d}$=0), are quoted in table 10.7. The postfit normalisation factors of the $Z/\gamma^* \to \tau^+\tau^-$, $Z/\gamma^* \to e^+e^-/\mu^+\mu^-$ and top quark background samples are summarized in table 10.8 and agree with one. Figure 10.15 shows the corresponding postfit Optimal Observable distribution compared to data. The postfit distribution of the BDT classifier in the low BDT control region is also shown. Furthermore, postfit distributions for the fit of a CP-mixing signal hypothesis assuming $\tilde{d}$=0.1 are presented. In this case, the best-fit signal strength is found to be $\hat{\mu} = 2.05^{+1.33}_{-1.17}$

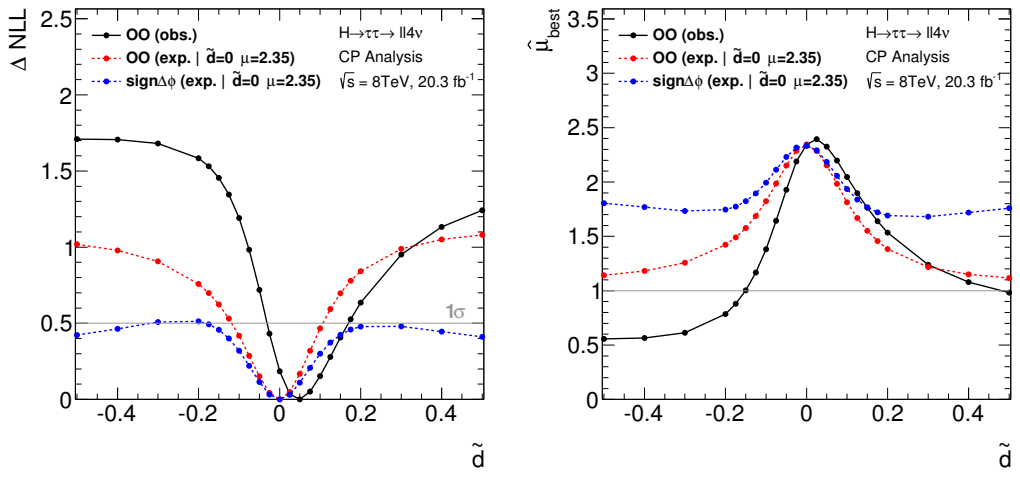

(a) (b)

Figure 10.13. *The negative log likelihood profile ΔNLL (a) and the corresponding best-fit signal strength values $\hat{\mu}_{best}$ (b) as function of $\tilde{d}$ for fitting the Optimal Observable. A global fit including an unconstrained signal normalisation is performed in all regions of the CP analysis at any $\tilde{d}$ scan point. The expected profiles assume pure SM VBF Higgs boson signal ($\tilde{d}$=0.0) using the observed best-fit signal strength $\hat{\mu}$ from the fit to data. The horizontal line at ΔNLL= 0.5 indicates the 68% confidence interval (a) and the line at $\hat{\mu}_{best} = 1$ a SM signal normalisation (b).*

and an asymmetric behaviour can be observed in the predicted Optimal Observable distribution for the signal. An equivalent set of distributions for a fit of the alternative CP-odd observable signed $\Delta\phi(j_1, j_2)$ is shown in figure 10.16. The SM signal and background predictions are in good agreement with the observed data for both CP-odd observables.

Several binning choices of the CP-odd observable distributions were tested and the one was chosen, which maximizes the ΔNLL distance from minimum to maximum while avoiding vanishing bin contents for the individual background samples. A number of six bins per distribution with the bin edges $[-15, -5, -2.5, 0, 5, 10, 15]$ in case of the Optimal Observable and equidistant bin widths from -3.15 to 3.15 in case of signed $\Delta\phi(j_1, j_2)$ was found to be a good working point providing sufficient amount of stats per bin. The signed $\Delta\phi(j_1, j_2)$ values for background events are distributed relatively flat for which reason an equidistant binning was found to be reasonable in contrast to the peak structure of the Optimal Observable, where a non-equidistant binning provides an improvement.

A consistency check of the fitting procedure with respect to central confidence intervals on the $\tilde{d}$ parameter is illustrated in figure 10.17 (a). It shows a comparison of the expected NLL profiles for fitting the Optimal Observable assuming SM VBF Higgs boson signal and a CP-mixing scenario of $\tilde{d}$=0.3. The signal samples are normalised to the best-fit signal strength respectively, which is observed in the fit to data. As expected, the minimum of the NLL profile is indeed found at a $\tilde{d}$ value

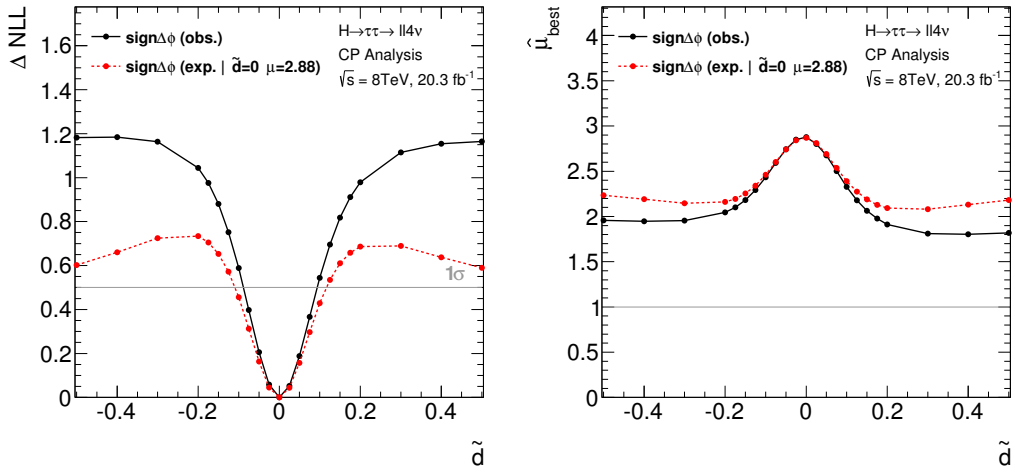

(a) (b)

Figure 10.14. *The negative log likelihood profile ΔNLL (a) and the corresponding best-fit signal strength values $\hat{\mu}_{best}$ (b) as function of $\tilde{d}$ for fitting signed $\Delta\phi(j_1, j_2)$. A global fit including an unconstrained signal normalisation is performed in all regions of the CP analysis at any $\tilde{d}$ scan point. The expected NLL profiles assume pure SM VBF Higgs boson signal ($\tilde{d}$=0.0) using the observed best-fit signal strength $\hat{\mu}$ from the fit to data. The horizontal line at ΔNLL= 0.5 indicates the 68% confidence interval (a) and the line at $\hat{\mu}_{best} = 1$ a SM signal normalisation (b).*

Process	Expected Number of Events
$(VBF)H \to \tau^+\tau^-$ (SM)	12.3 ± 3.6
$(VBF)H \to W^+W^-$ (SM)	2.5 ± 0.7
$Z/\gamma^* \to \tau^+\tau^-$	19.3 ± 1.0
Top quark	3.4 ± 0.9
$Z/\gamma^* \to e^+e^-/\mu^+\mu^-$+ di-boson	10.9 ± 1.7
Fake leptons	2.3 ± 0.3
(non-VBF)$H \to \tau^+\tau^-/W^+W^-$	1.6 ± 0.2
Total Signal (SM)	14.8 ± 3.7
Total Background	37.5 ± 2.5
Data	54

Table 10.7. *Postfit event yields for the individual signal and background components used in the fit model of the CP analysis. The fit was performed using the Optimal Observable for pure SM signal hypothesis with $\tilde{d}$=0, which yields to the best-fit signal strength of $\hat{\mu} = 2.35^{+1.50}_{-1.35}$. The errors for the individual signal and background components contain systematic uncertainties only while systematic and statistical uncertainties are included in the total background prediction.*

of 0.3, when using pseudo-data including SM background and the same CP-mixing signal hypothesis.

Figure 10.17 (b) shows the observed NLL profile for fitting the Optimal Observable as function of $\tilde{d}$ in an extended range of more extreme CP-mixing scenarios. These larger $\tilde{d}$ values already approximates a HVV coupling structure with dominant CP-odd part. The NLL profile converge on constant values close to the maxima in negative and positive directions. That is, despite the recovery of the symmetry of the Optimal Observable due to such extreme scenarios, as generally shown for CP-odd observables in figure 6.1 and 6.2, the analysis still keeps its exclusion power. This behaviour is due to an increase of the variance of the CP-odd observable distributions for more extreme $\tilde{d}$ scenarios and illustrates the good performance and sensitivity especially with respect to signal hypothesis of small CP-odd admixtures in the HVV vertex, which holds also for much more extreme scenarios.

The impact of nuisance parameters on the best-fit signal strength in the fit of the pure SM VBF Higgs boson signal at $\tilde{d}$=0 is shown in figure 10.18. Statistical uncertainties of the central bins are dominating in this case as well as the normalisation of the $Z/\gamma^* \to \tau^+\tau^-$ background sample and the jet energy resolution. No significant pulls and constraints of the nuisance parameters are observed. Figure 10.19 shows the correlations matrix of these nuisance parameters. Also here, no significant correlations occur. Figure 10.20 and 10.21 show similar nuisance parameter rankings and correlations for the signal hypothesis of $\tilde{d}$=0.1. Again, statistical uncertainties have the dominant impact on the signal strength followed by the jet energy resolution and the normalisation of the $Z/\gamma^* \to \tau^+\tau^-$ and $Z/\gamma^* \to e^+e^-/\mu^+\mu^-$ background samples. There is a larger correlation between the $Z/\gamma^* \to e^+e^-/\mu^+\mu^-$ normalisation and the jet energy resolution. This is however expected since the uncertainty on this specific systematic uncertainty component is relatively large and a small pull of the nuisance parameter might impact the normalisation therefore significantly (see section 7.2).

The CP analysis presented in this thesis is based on the $H \to \tau^+\tau^- \to \ell^+\ell^- 4\nu$ final state channel. It provides a test of the CP-invariance in HVV couplings. The observed 68% confidence intervals are determined to be $[-0.03, 0.17]$ for the Optimal Observable and $[-0.09, 0.09]$ for signed $\Delta\phi(j_1, j_2)$. Thus, no hints to CP-violation are observed and the results are consistent with the SM expectation. The combined CP analysis including also the semi-leptonic channel $H \to \tau_{\text{lep}}\tau_{\text{had}}$ is discussed in Ref. [9]. A summary of this combination is presented in chapter 11.

Process	Postfit normalisation
$Z/\gamma^* \to \tau^+\tau^-$	0.972 ± 0.098
$Z/\gamma^* \to e^+e^-/\mu^+\mu^-$	0.978 ± 0.459
Top quark	0.990 ± 0.105

Table 10.8. *Postfit normalisation factors of unconstrained background samples in the CP analysis. The fit was performed using the Optimal Observable for pure SM signal hypothesis with $\tilde{d}$=0. The errors include systematic and statistical uncertainties.*

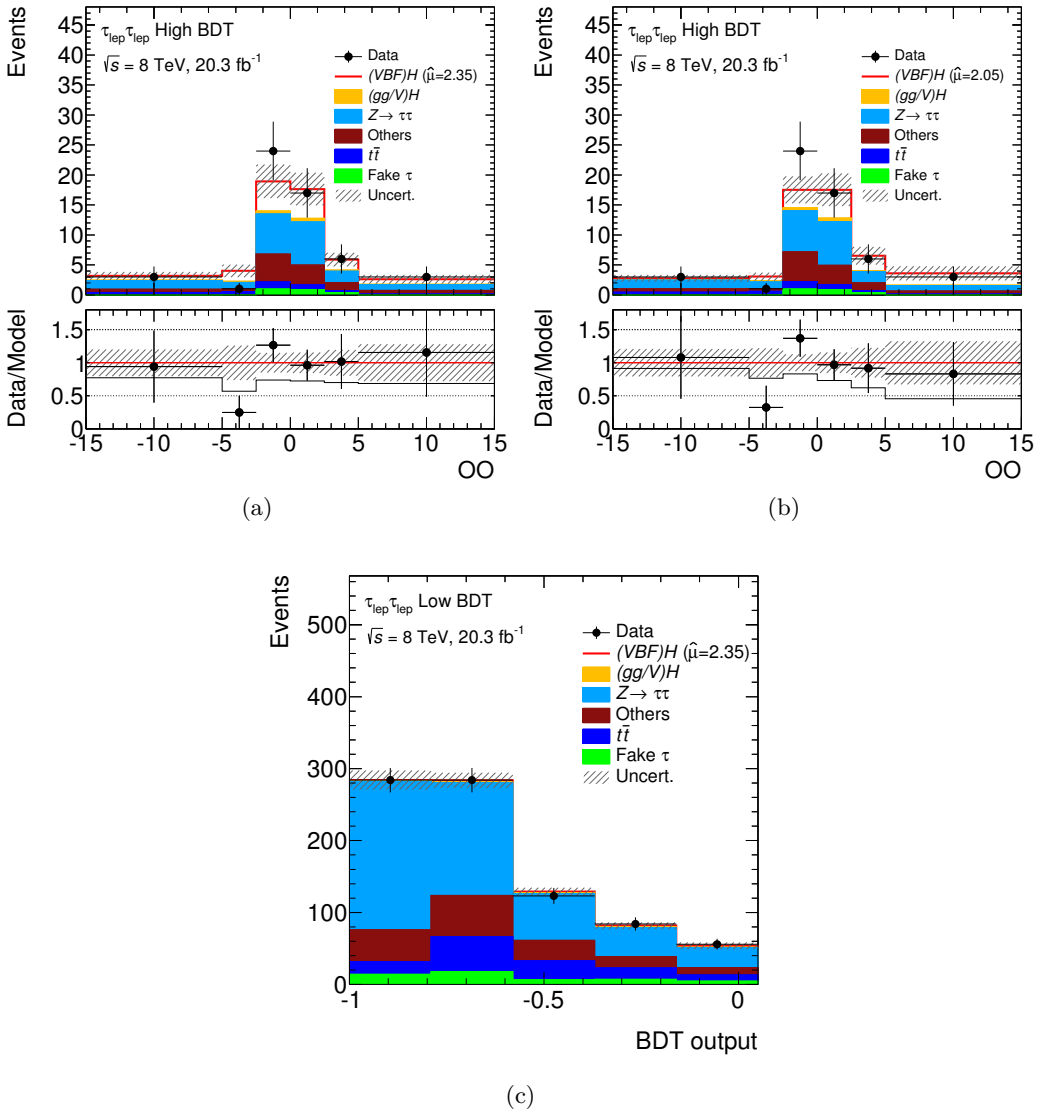

Figure 10.15. *Distributions of the Optimal Observable after performing a global fit in the CP analysis: postfit Optimal Observable distribution in the signal region for $\tilde{d}$=0 SM signal with $\hat{\mu} = 2.35^{+1.50}_{-1.35}$ (a) and $\tilde{d}$=0.1 CP-mixing signal with $\hat{\mu} = 2.05^{+1.33}_{-1.17}$ (b). The bottom panel show the data over prediction ratio, where the solid red line at a value of one reflects the best-fit signal plus background prediction and the black solid line the background only prediction. The postfit BDT classifier distribution in the low BDT control region after a global fit to pure SM signal (c). The error band includes statistical and systematic normalisation uncertainties.*

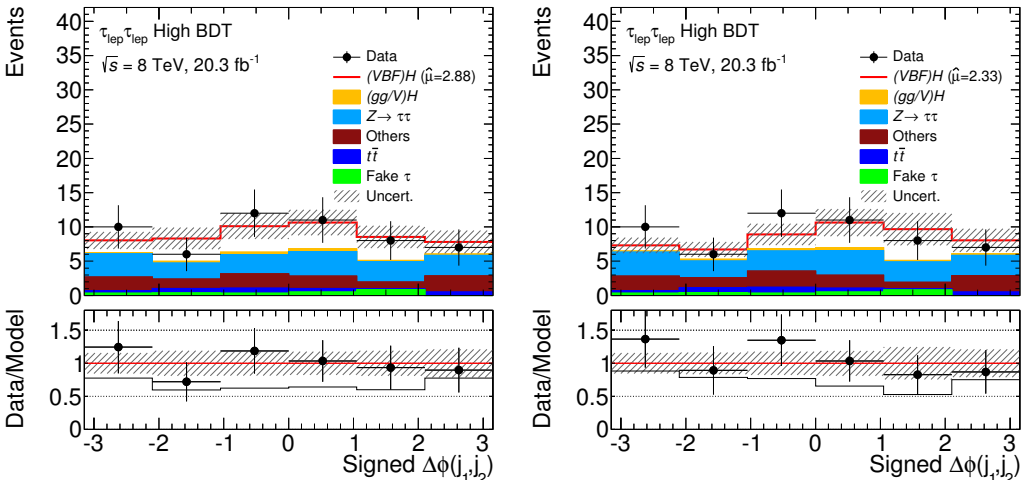

Figure 10.16. *Distributions of the Optimal Observable and signed $\Delta\phi(j_1, j_2)$ after performing a global fit in the CP analysis: postfit signed $\Delta\phi(j_1, j_2)$ distribution in the signal region for $\tilde{d}$=0 SM signal with $\hat{\mu} = 2.88^{+1.48}_{-1.30}$ (a) and $\tilde{d}$=0.1 CP-mixing signal with $\hat{\mu} = 2.33^{+1.36}_{-1.19}$ (b). The bottom panel show the data over prediction ratio, where the solid red line at a value of one reflects the best-fit signal plus background prediction and the black solid line the background only prediction. The error band includes statistical and systematic normalisation uncertainties.*

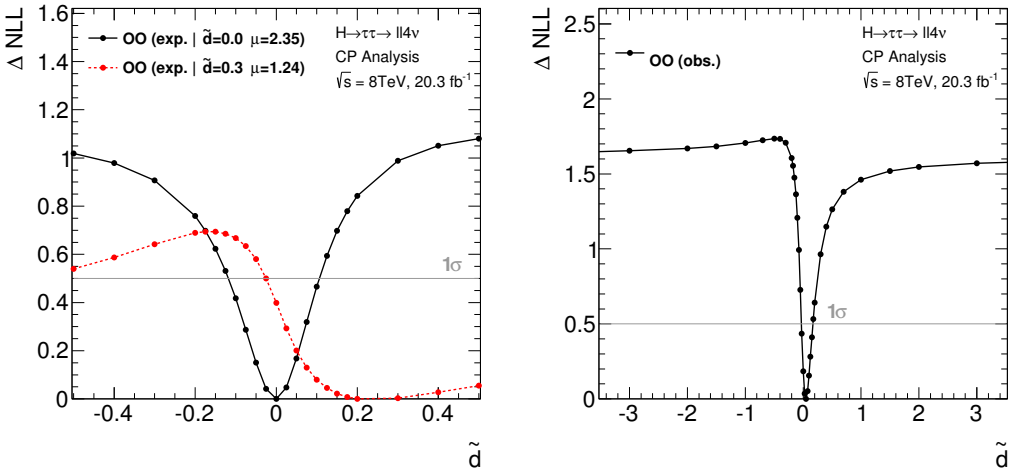

(a) (b)

Figure 10.17. *Expected NLL profile assuming SM signal (black) and CP-mixing signal with $\tilde{d}$=0.3 (red) in the fit of the Optimal Observable (a). The horizontal line at ΔNLL= 0.5 indicates the 68% confidence interval. The signal samples are normalised to the observed best-fit signal strength values of $\hat{\mu} = 2.35^{+1.50}_{-1.35}$ and $\hat{\mu} = 1.24^{+1.12}_{-0.94}$ for SM $\tilde{d}$=0.0 and $\tilde{d}$=0.3, respectively. The observed NLL profile for the Optimal Observable in an extended $\tilde{d}$ range (b) already approximates a HVV coupling structure with dominant CP-odd part.*

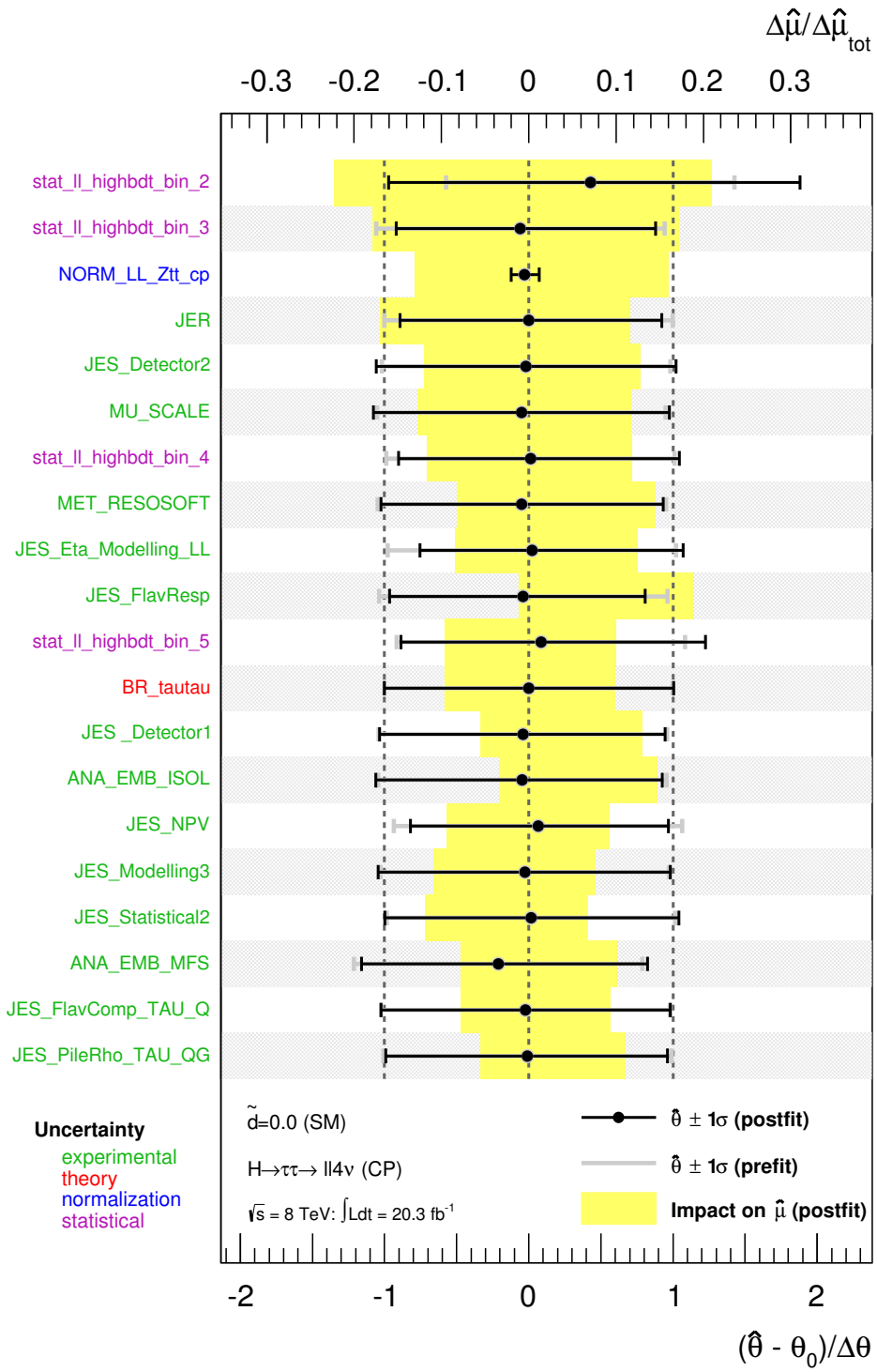

Figure 10.18. *Postfit pulls and constraints of nuisance parameters from the fit of the Optimal Observable assuming SM signal in the CP analysis (lower x-axis). Impact of nuisance parameters on best fit signal strength (upper x-axis). Nuisance parameter importance ranking with respect to the impact on the signal strength (y-axis top-down). The first 20 nuisance parameters are shown with the largest impact on $\hat{\mu}$. Normalisation factors are unconstrained in the fit and the error bars reflect absolute uncertainties.*

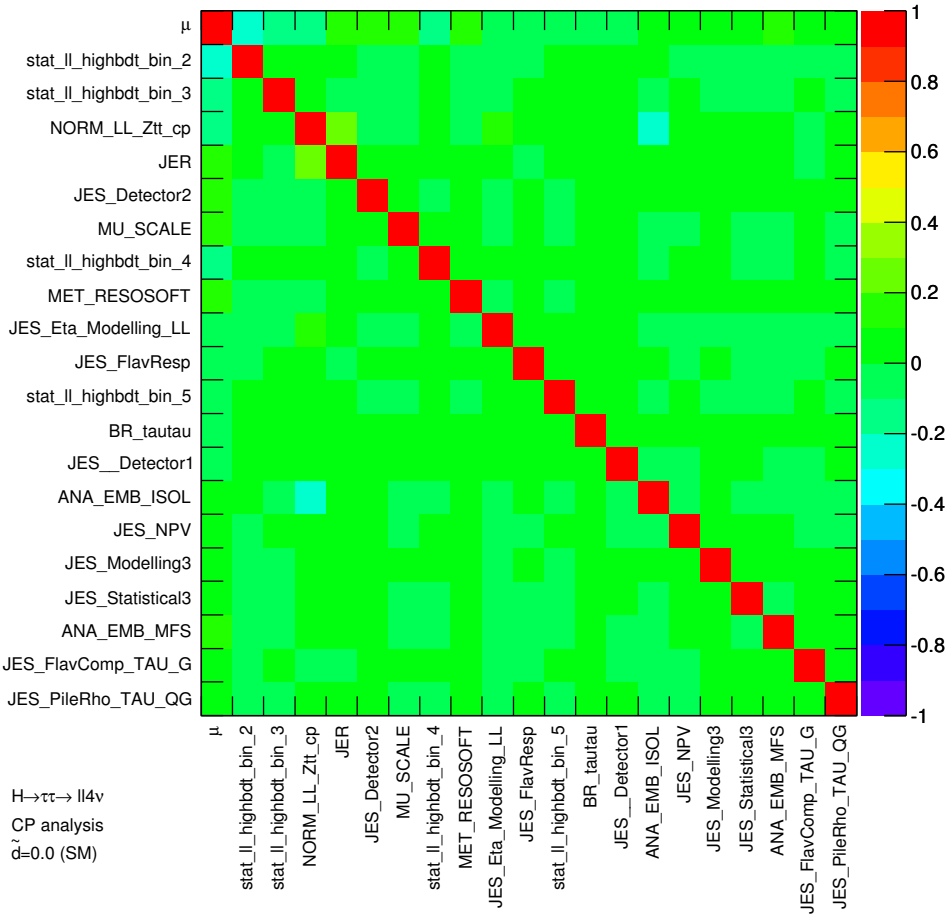

Figure 10.19. *Correlations of the first 20 nuisance parameters with the largest impact on $\hat{\mu}$ in the fit of pure SM VBF Higgs boson signal.*

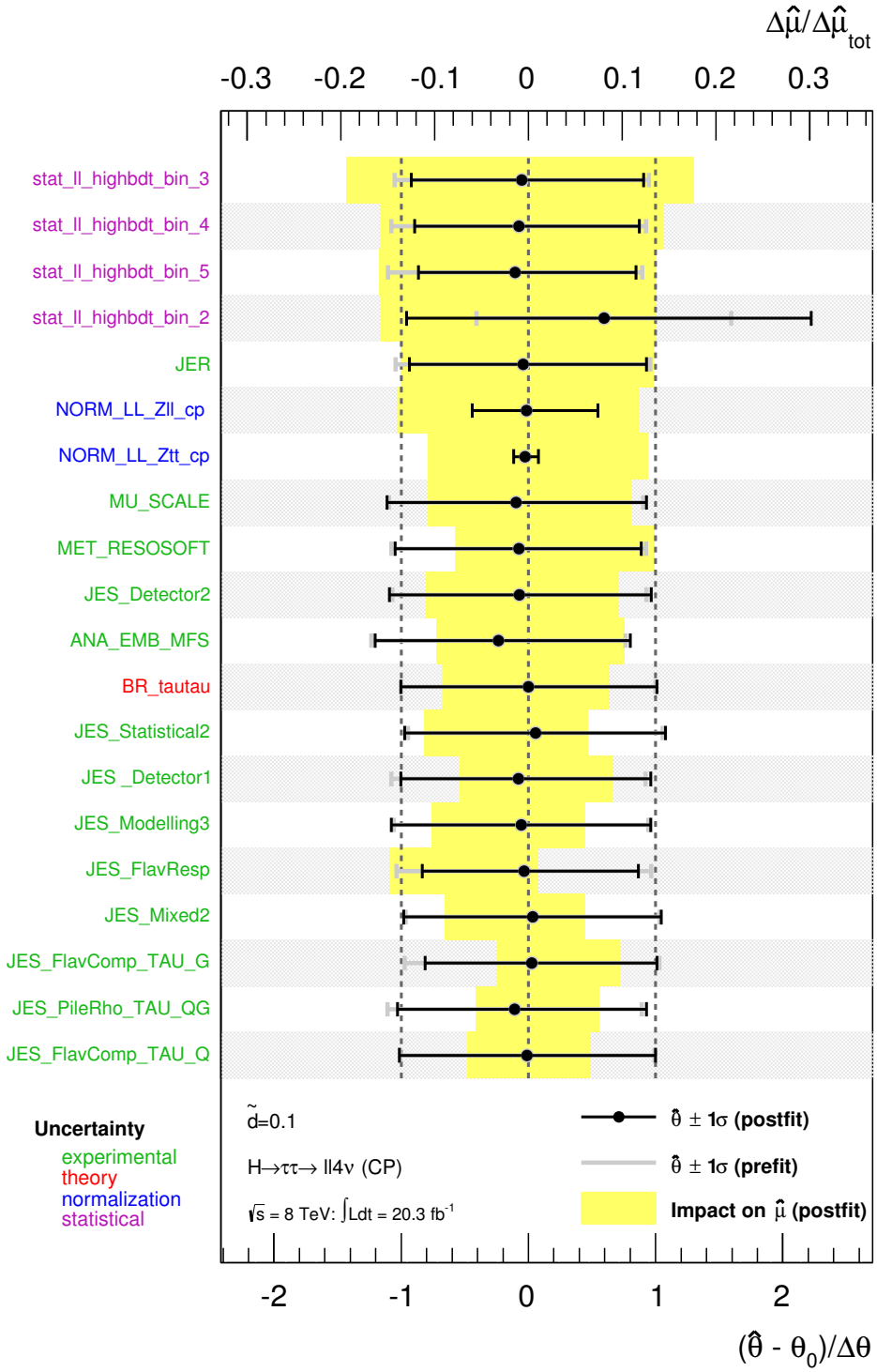

Figure 10.20. *Postfit pulls and constraints of nuisance parameters from the fit of the Optimal Observable assuming CP-mixing signal with $\tilde{d}$=0.1 in the CP analysis (lower x-axis). Impact of nuisance parameters on best fit signal strength (upper x-axis). Nuisance parameter importance ranking with respect to the impact on the signal strength (y-axis top-down). The first 20 nuisance parameters are shown with the largest impact on $\hat{\mu}$. Normalisation factors are unconstrained in the fit and the error bars reflect absolute uncertainties.*

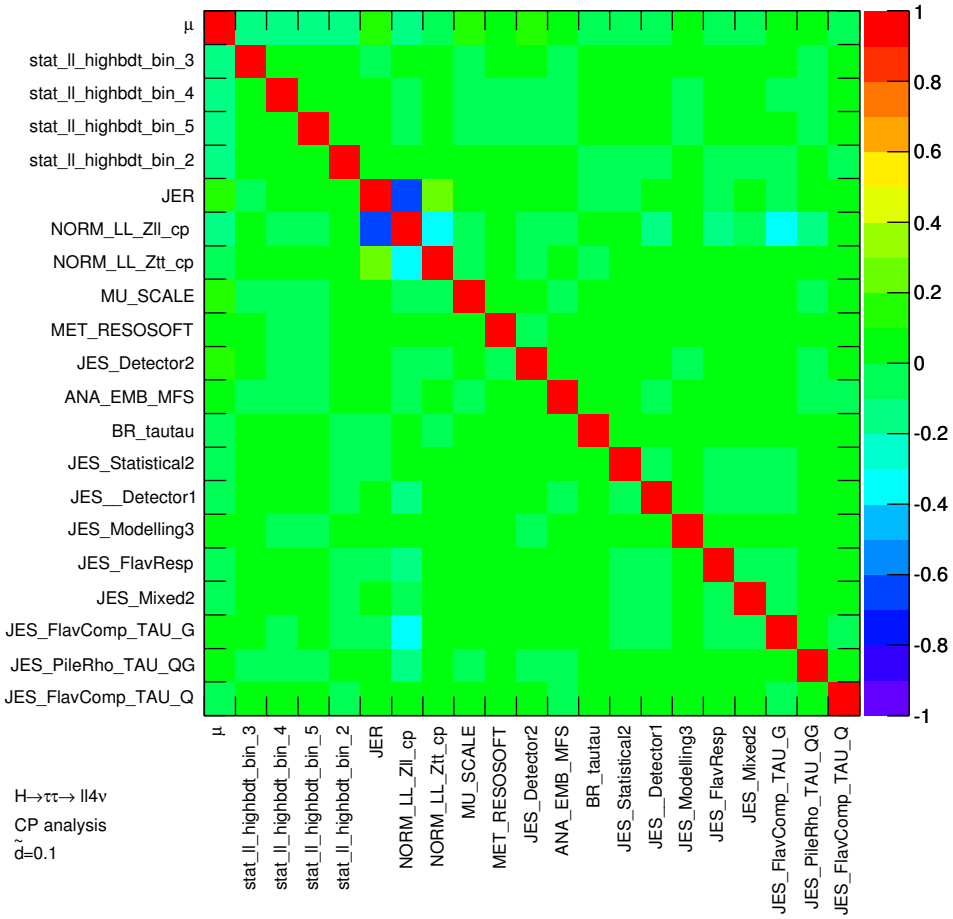

Figure 10.21. *Correlations of the first 20 nuisance parameters with the largest impact on $\hat{\mu}$ in the fit of CP-mixing VBF Higgs boson signal assuming $\tilde{d}$=0.1.*

11 Combination of $H \to \tau^+\tau^-$ Decay Channels

The chapter presents the results of the search for $H \to \tau^+\tau^-$ [8] for the combination of the different final states $\tau_{\text{lep}}\tau_{\text{lep}}$, $\tau_{\text{lep}}\tau_{\text{had}}$ and $\tau_{\text{had}}\tau_{\text{had}}$. It also summarizes the combined analysis of the test of CP invariance of the VBF Higgs boson production [9] in the decay channels $\tau_{\text{lep}}\tau_{\text{lep}}$ and $\tau_{\text{lep}}\tau_{\text{had}}$.

11.1. Search for the Higgs Boson in $H \to \tau^+\tau^-$ Decays

The combined search analysis aims the evidence of Higgs boson decays into τ leptons including signal strength measurements of the different Higgs boson production modes. The VBF and Boosted category of each of the $\tau_{\text{lep}}\tau_{\text{lep}}$, $\tau_{\text{lep}}\tau_{\text{had}}$ and $\tau_{\text{had}}\tau_{\text{had}}$ final state channels are combined, using the full 8 TeV dataset with an integrated luminosity of $\int \mathcal{L}dt = 20.3$ fb^{-1}and the full 7 TeV dataset with $\int \mathcal{L}dt = 4.5$ fb^{-1}. Each sub-channel and category exploits multivariate analysis techniques (MVA) in terms of boosted decision trees (BDTs). A global fit of the BDT classifier distributions to data is performed, assuming a Higgs boson mass of approximately 125 GeV according to the ATLAS measurement [208]. The postfit distributions of the BDT classifiers, using 8 TeV data, are shown in figure 11.1. A good separation between background and signal contributions of the BDTs is visible in all of the sub-channels and categories. The observed and expected number of events ordered in terms of $\log_{10}(S/B)$[1] of the BDT bin for the signal regions of all sub-channels and categories are shown in figure 11.2. The figure highlights the observed excess in the bins of signal-like BDT classifier values.

The observed excess in data with respect to prediction is consistent with a SM Higgs boson signal ($\mu = 1$) with $m_H = 125$ GeV within the uncertainties and the observed (expected) significance is 4.54 σ (3.43 σ). Thus, this observation provides strong evidence for Higgs boson Yukawa couplings to τ leptons. The observed and expected significances are summarized in table 11.3.

The combined best-fit signal strength is

$$\hat{\mu} = 1.43^{+0.27}_{-0.26}(\text{stat.})^{+0.32}_{-0.25}(\text{exp. syst.})^{+0.09}_{0.09}(\text{theo. syst.}). \tag{11.1}$$

[1] S/B is the number of expected signal divided by expected background events for each BDT bin in the various signal regions assuming $\mu = 1.4$

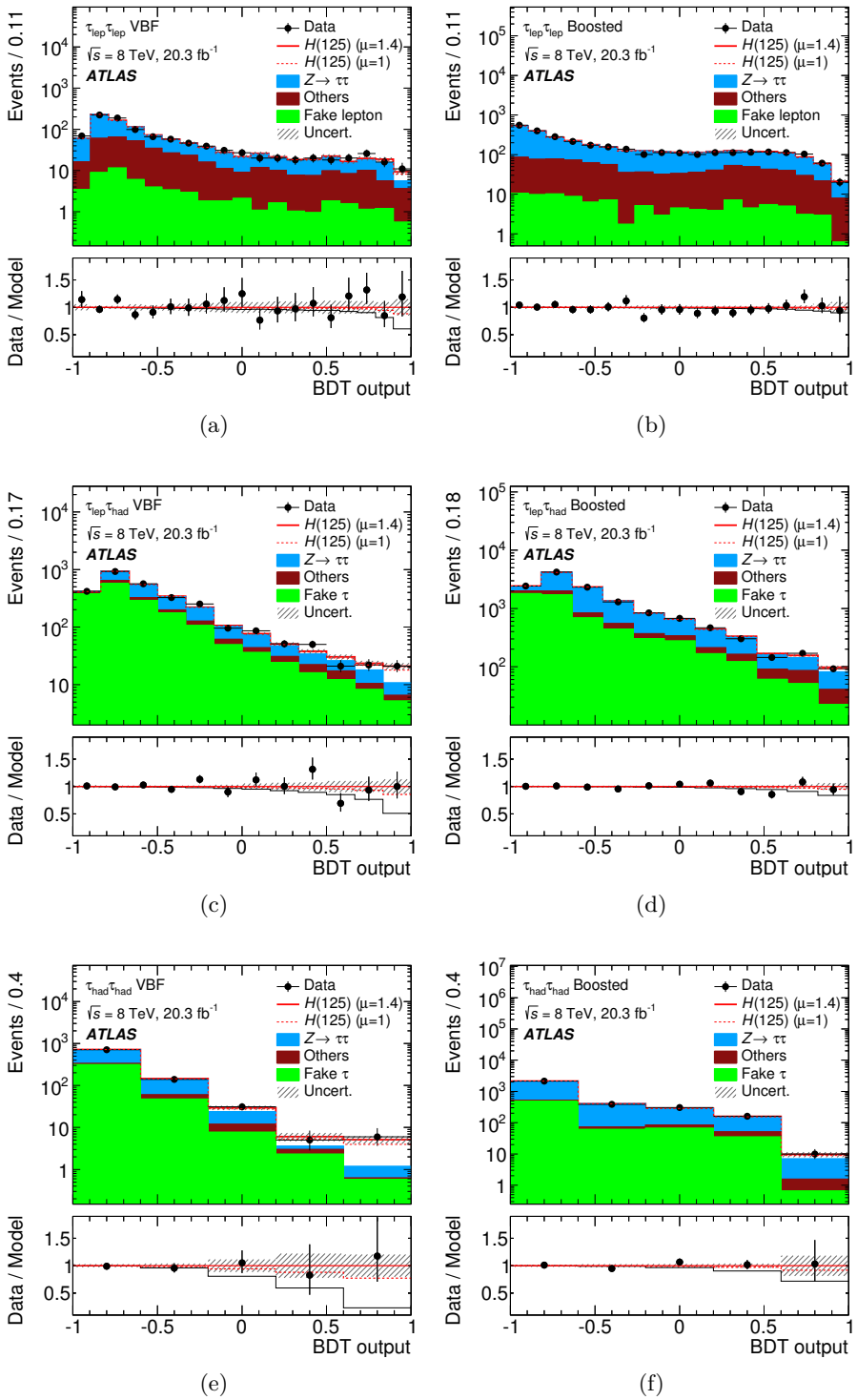

Figure 11.1. *Distributions of the BDT classifier for = 8 TeV data in the signal regions of the VBF (left) and Boosted (right) categories for the $\tau_{\text{lep}}\tau_{\text{lep}}$ (top), $\tau_{\text{lep}}\tau_{\text{had}}$ (middle) and $\tau_{\text{had}}\tau_{\text{had}}$ (bottom) channels. The Higgs boson signal ($m_H = 125$ GeV) is shown stacked with a signal strength of $\mu = 1$ (dashed line) and the best-fit signal strength $\hat{\mu} = 1.4$ (solid line) obtained in a global fit. The background predictions are also determined in the global fit. The size of the statistical and systematic normalisation uncertainties is indicated by the hashed band. The lower panel provides the number of data divided by predicted events (background contributions plus Higgs boson signal normalised to its best-fit signal strength). The dashed red and solid black lines represent the changes in the model when μ=1.0 or μ=0 are assumed [8].*

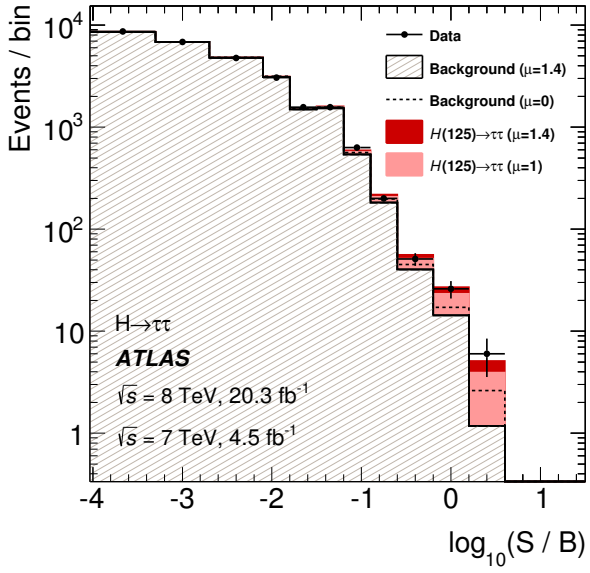

Figure 11.2. *Event yields as a function of* $\log_{10}(S/B)$*, where* S *(signal yield) and* B *(background yield) are taken from the BDT classifier bin of each event, assuming a signal strength* $\mu = 1.4$*. Events from all sub-channels and categories are included. The predicted background is obtained from the global fit* ($\hat{\mu} = 1.4$) *and signal yields are shown for* $m_H = 125$ GeV *at* $\mu = 1$ *and* $\mu = 1.4$*. The background-only distribution (dashed line) is obtained from the global fit, with* μ *fixed at zero [8].*

Channel and Category	Expected Significance (σ)	Observed Significance (σ)
$\tau_{\text{lep}}\tau_{\text{lep}}$ VBF	1.15	1.88
$\tau_{\text{lep}}\tau_{\text{lep}}$ Boosted	0.57	1.72
$\tau_{\text{lep}}\tau_{\text{lep}}$ Total	1.25	2.40
$\tau_{\text{lep}}\tau_{\text{had}}$ VBF	2.11	2.23
$\tau_{\text{lep}}\tau_{\text{had}}$ Boosted	1.11	1.01
$\tau_{\text{lep}}\tau_{\text{had}}$ Total	2.33	2.33
$\tau_{\text{had}}\tau_{\text{had}}$ VBF	1.70	2.23
$\tau_{\text{had}}\tau_{\text{had}}$ Boosted	0.82	2.56
$\tau_{\text{had}}\tau_{\text{had}}$ Total	1.99	3.25
Combined	3.43	4.54

Figure 11.3. *The expected and observed significances of the signal in each channel and category for the combined 7 and 8 TeV datasets [8].*

Figure 11.4 summarizes the signal strength values for fitting the sub-channels and categories individually. The semi-leptonic $\tau_{\text{lep}}\tau_{\text{had}}$ final state provides the largest contribution to the overall sensitivity. This is due to the increased branching ratio of the di-τ decay compared to the fully leptonic final state. Furthermore, the VBF category is found to be more sensitive than the Boosted category. 68% and 95% confidence level likelihood contours in the two dimensional plane ($\mu_{\text{VBF+VH}}$,μ_{GGF}) of the individual signal strength parameters are shown in figure 11.5. Both signal strength parameters were decoupled in the global fit in this case and the best-fit maximum likelihood estimator is fully consistent with SM expectation within one standard deviation σ.

Figure 11.6 shows the distribution of the reconstructed di-τ mass based on the MMC algorithm. It illustrates the consistency of the observed excess with a Higgs boson signal at $m_H = 125$ GeV. Events from all sub-channels and categories for the both center-of-mass energies are included, weighted by $\ln(1 + S/B)$[2] depending on the signal-to-background ratio in the corresponding BDT classifier bin. The measured signal strength is furthermore used to determine the cross section times branching ratio for the $H \to \tau^+\tau^-$ decay with $m_H = 125$ GeV, which is summarized in table 11.1. The predicted SM $\sigma \times BR$ is also included in the table. A cut-based analysis approach was used to cross-check the MVA analysis, which also confirms the evidence of a SM Higgs boson with $m_H = 125$ GeV, that couples to τ leptons.

Dataset	observed $\sigma \times BR$	expected $\sigma \times BR$
7 TeV	$1.0^{+0.9}_{-0.8}(\text{stat.})^{+0.9}_{-0.8}(\text{syst.})$ pb	1.09 ± 0.11 pb
8 TeV	$2.1^{+0.4}_{-0.4}(\text{stat.})^{+0.5}_{-0.4}(\text{syst.})$ pb	1.39 ± 0.14 pb

Table 11.1. *Measured and expected cross section times branching ratio $\sigma \times BR$ for the SM $H \to \tau^+\tau^-$ decay with $m_H = 125$ GeV.*

[2]The specific weighting includes information from the BDT classifier and therefore emphasizes signal-like events to visualize their corresponding reconstructed invariant mass.

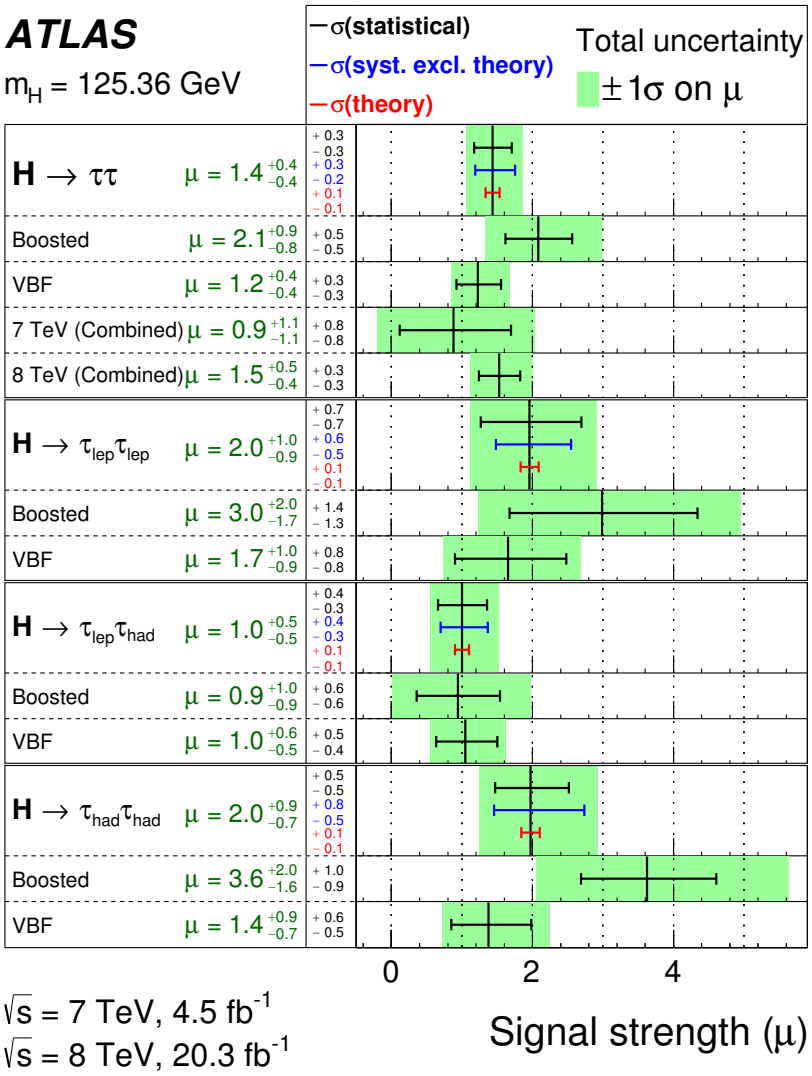

Figure 11.4. *The best-fit value $\hat{\mu}$ of the signal strength for the individual final state channels and their combination, using the full 7 TeV and 8 TeV datasets. The total $\pm 1\sigma$ uncertainty is indicated by the shaded green band, with the individual contributions from the statistical (black), experimental (blue) and the theory uncertainty (red) [8].*

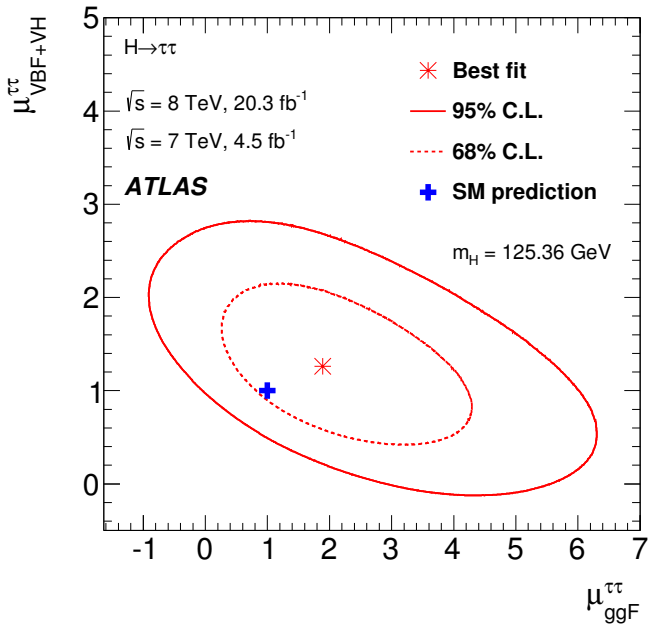

Figure 11.5. *Likelihood contours at 68% and 95% confidence level for the combination of all final state channels and categories in the ($\mu_{textGGF}$,μ_{VBF+VH}) plane of the individual signal strength parameters. A Higgs boson mass of $m_H = 125.36$ GeV is assumed according to the ATLAS Higgs boson mass measurement. The SM expectation is denoted as a plus symbol and the best-fit point to the data as a star symbol [8].*

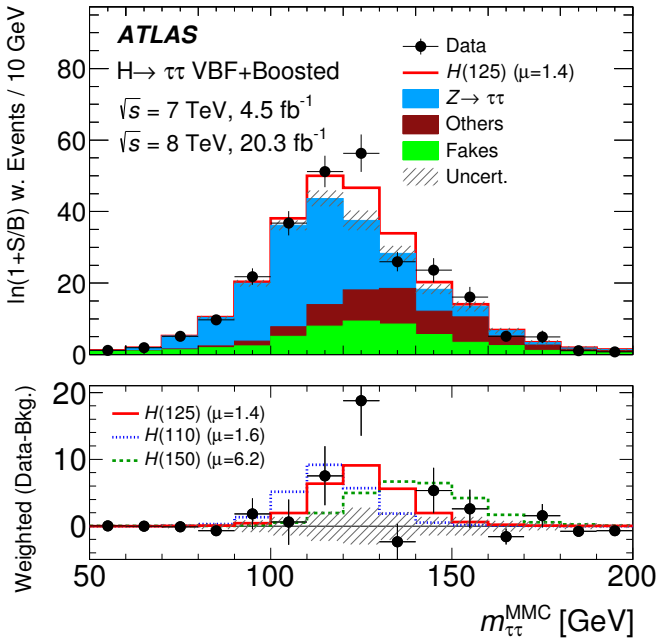

Figure 11.6. *Distributions of the reconstructed invariant di-τ mass using the MMC algorithm. Events are weighted by $\ln(1 + S/B)$ for all channels, depending on the number of signal (S) and background (B) events in the corresponding bin of the BDT classifier distribution. The background predictions are obtained from the global fit, using the m_H=125 GeV Higgs boson signal (best-fit $\hat{\mu}$=1.4). SM signal with m_H=125 GeV(red), m_H=110 GeV (blue) and m_H=150 GeV(green) are also shown in the bottom panel, where a signal strength (best-fit) of μ =1.4, 1.6 and 6.2 are used to normalise each of the signal samples respectively [8].*

11.2. Test of CP Invariance in VBF Higgs Boson Production in $H \to \tau^+\tau^-$ Decays

The combined CP analysis [9] includes the $\tau_{\text{lep}}\tau_{\text{lep}}$ final state, which has been discussed in detail in this thesis, and the $\tau_{\text{lep}}\tau_{\text{had}}$ final state, where one τ lepton decays leptonically and the other hadronically. The inclusion of the fully hadronic $\tau_{\text{had}}\tau_{\text{had}}$ final state has not been feasible on the timescale of this thesis. The full 8 TeV dataset with an amount of $\int \mathcal{L}dt = 20.3$ fb^{-1}was used in the combined analysis.

Figure 11.7 shows the postfit distributions of the Optimal Observable for the prediction compared to data in the $\tau_{\text{lep}}\tau_{\text{lep}}$ and the $\tau_{\text{lep}}\tau_{\text{had}}$ channel after performing a global combined fit under the assumption of pure SM VBF Higgs boson signal. The best-fit signal strength in this case is found to be $\hat{\mu} = 1.55^{+0.86}_{-0.77}$. The observed mean values of the Optimal Observable distributions in data are

$$< OO >_{\tau_{\text{lep}}\tau_{\text{lep}}} = +0.3 \pm 0.5 \tag{11.2}$$

$$< OO >_{\tau_{\text{lep}}\tau_{\text{had}}} = -0.3 \pm 0.4 \tag{11.3}$$

for the $\tau_{\text{lep}}\tau_{\text{lep}}$ and $\tau_{\text{lep}}\tau_{\text{had}}$ channel respectively. Therefore, no indications of CP-violation are observed in both channels and the VBF Higgs boson signal is consistent with SM prediction within the uncertainties.

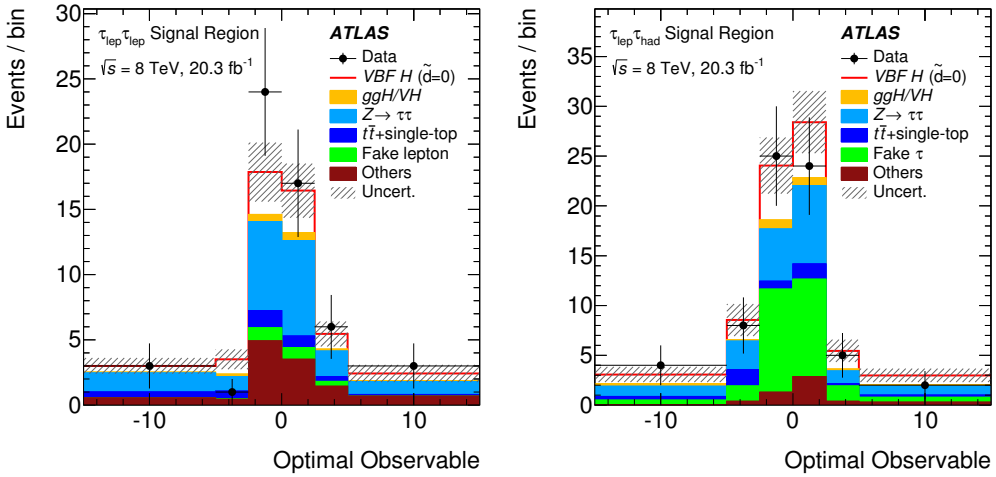

(a) (b)

Figure 11.7. *Distributions of the Optimal Observable in the signal region for the $\tau_{\text{lep}}\tau_{\text{lep}}$ (left) and $\tau_{\text{lep}}\tau_{\text{had}}$ (right) channel, after the global fit performed for the $\tilde{d} = 0$ hypothesis. The best-fit signal strength is $\hat{\mu} = 1.55^{+0.86}_{-0.77}$. The "Other" backgrounds include di-boson and $Z \to \ell\ell$. The error bands include all uncertainties [9].*

The observed and expected NLL profiles for the combined fit of the Optimal Observable and for each channel individually are shown in figure 11.8. The best-fit

signal strength and nuisance parameter values from the combined fit to data at each $\tilde{d}$ scan point have been used to determine the individual NLL profiles. A SM VBF Higgs boson signal hypothesis normalised to the corresponding best-fit $\hat{\mu}$ from data was assumed to determine the combined expected NLL profile. Using linear interpolation between the $\tilde{d}$ scan points results in the observed (expected) central confidence interval of $[-0.11, 0.05]$ ($[-0.08, 0.08]$) on the $\tilde{d}$ parameter at 68% confidence level, which is fully consistent with the SM HVV coupling structure. Concerning the expected NLL profile, SM signal ($\tilde{d}$=0.0) with $\mu = 1.55$ is assumed. Differences in the observed compared to the expected NLL profiles stem mainly from fluctuations in data.

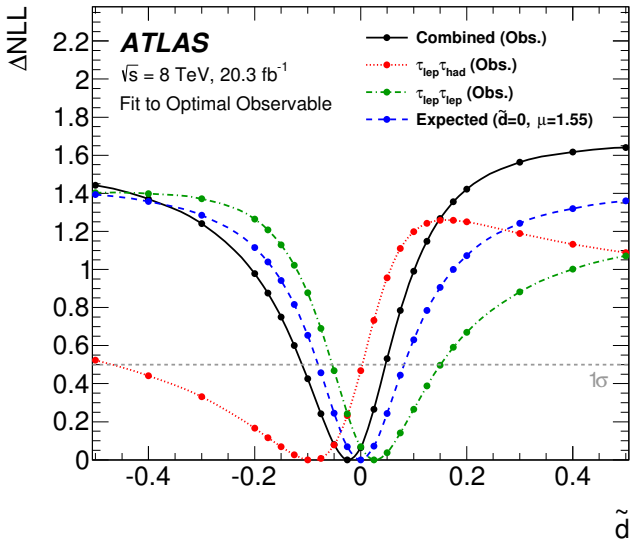

Figure 11.8. *Observed and expected ΔNLL as function of the $\tilde{d}$ values defining the underlying signal hypothesis, for $\tau_{\text{lep}}\tau_{\text{lep}}$ (green), $\tau_{\text{lep}}\tau_{\text{had}}$ (red) and their combination (black) using the Optimal Observable. The best-fit values of all nuisance parameters from the combined fit at each $\tilde{d}$ point have been used in all cases. Pseudo-data with SM backgrounds plus pure CP-even SM VBF signal ($\tilde{d}$=0), normalised to the best-fit signal-strength value $\hat{\mu} = 1.55^{+0.86}_{-0.77}$, has been used to calculate the expected NLL profile (blue). The markers indicate the points where an evaluation has been done. The lines correspond to linear interpolation between these points [9].*

Figure 11.9 shows the alternative CP-odd observable signed $\Delta\phi(j_1, j_2)$ distribution in both final state channel. The NLL profiles for the combined fit of the signed $\Delta\phi(j_1, j_2)$ observable is shown in 11.10. The observed maximum likelihood estimator is also in good agreement with the SM VBF Higgs boson signal prediction. Due to fluctuations in data, there are some differences in the observed compared to the expected NLL profile for signed $\Delta\phi(j_1, j_2)$. A direct comparison of the expected NLL profile for fitting the Optimal Observable and signed $\Delta\phi(j_1, j_2)$ assuming SM signal with $\mu = 1$ is shown in figure 11.11. The method of the Optimal Observable yields significant improvements in sensitivity compared to the simple signed $\Delta\phi(j_1, j_2)$ observable approach, which would not reach the 68% confidence

level for a SM signal $\mu = 1$.

In summary, the measurement of the central 68% confidence interval results in $[-0.11, 0.05]$ based on the method of the Optimal Observable. Thus, no evidence of CP-violation in the Higgs boson couplings to vector bosons is observed in the combined $H \to \tau^+\tau^-$ CP analysis.

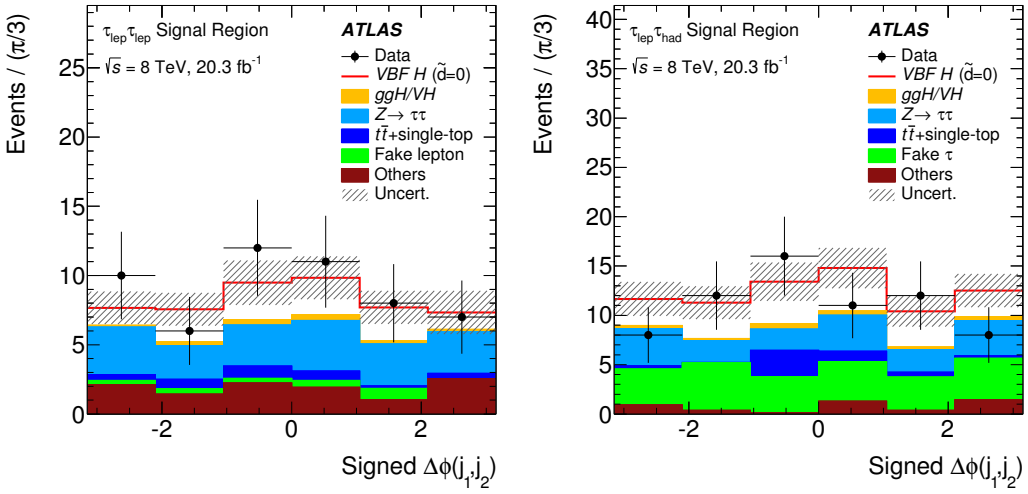

(a) (b)

Figure 11.9. *Distributions of the signed $\Delta\phi(j_1, j_2)$ variable in the signal region for the $\tau_{\text{lep}}\tau_{\text{lep}}$ (left) and $\tau_{\text{lep}}\tau_{\text{had}}$ (right) channel, after the global fit performed for the $\tilde{d}$=0.0 hypothesis. The best-fit signal strength is $\hat{\mu} = 2.02^{+0.87}_{-0.77}$. The "Other" backgrounds include di-boson and $Z \to \ell\ell$. The error bands include all uncertainties [9].*

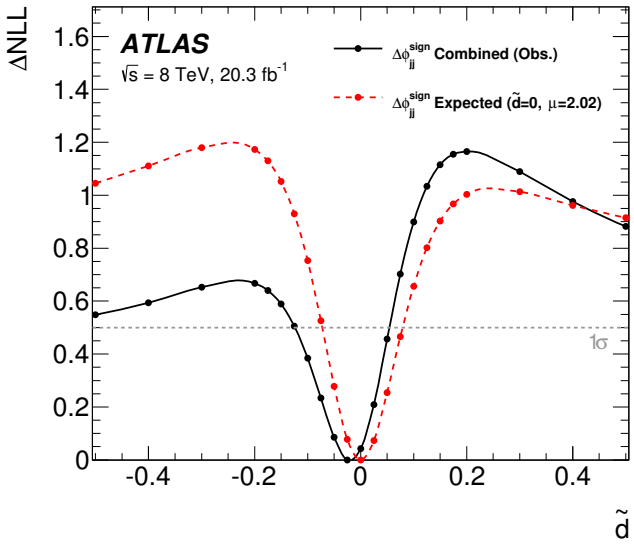

Figure 11.10. *Observed (black) and expected (red) ΔNLL for the combination of $\tau_{\text{lep}}\tau_{\text{lep}}$ and $\tau_{\text{lep}}\tau_{\text{had}}$ channels as function of the $\tilde{d}$ values defining the underlying signal hypothesis using signed $\Delta\phi(j_1, j_2)$. Pseudo-data with SM backgrounds plus pure CP-even VBF signal ($\tilde{d}$=0), normalised to the best-fit signal strength value $\hat{\mu} = 2.02^{+0.87}_{-0.77}$ of the combined fit using signed $\Delta\phi(j_1, j_2)$, have been used to calculate the expected values. The markers indicate the points where an evaluation has been done. The lines correspond to linear interpolation between these points [9].*

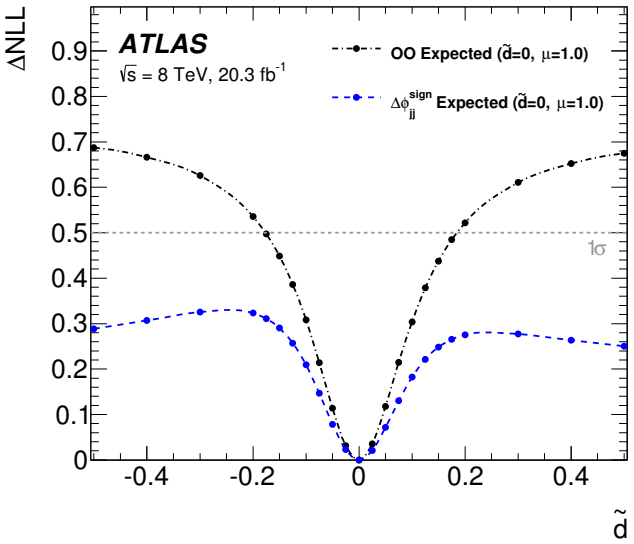

Figure 11.11. *Expected ΔNLL for the combination of the $\tau_{\text{lep}}\tau_{\text{lep}}$ and $\tau_{\text{lep}}\tau_{\text{had}}$ channels as function of the $\tilde{d}$ values defining the underlying signal hypothesis using the Optimal Observable (black) or signed $\Delta\phi(j_1, j_2)$(blue) as the final discriminating variable. Pseudo-data with SM backgrounds plus pure CP-even VBF signal ($\tilde{d}$=0) normalised to the SM expectation ($\mu = 1$) have been used to calculate the expected values in both cases. The markers indicate the points where an evaluation has been done. The lines correspond to linear interpolation between these points [9].*

12 Summary

The Higgs boson of the Standard Model is a consequence of spontaneous electroweak symmetry breaking, which is accomplished by the Englert-Brout-Higgs-Guralnik-Hagen-Kibble mechanism published in 1964 [3–5, 22, 23]. The mechanism introduces mass terms into the Standard Model Lagrangian for the W and Z gauge bosons, as it is observed in data. Without electroweak symmetry breaking, the Standard Model would predict only massless gauge bosons. The discovery of a Higgs boson consistent with the Standard Model thus solved one of the key questions in particle physics and confirmed that electroweak symmetry breaking is realized in nature [1, 2].

The scientific program at the LHC started in 2009. CMS and ATLAS declared the discovery of a Standard Model like Higgs boson with the mass of approximately 125 GeV in 2012 based on the combination of various analyses, which examine different Higgs boson production modes and decay channels [1, 2, 6]. The analyses involved in the discovery mainly consider the dominant Higgs boson production modes gluon fusion and vector-boson fusion and the decay into two photons, W or Z bosons. Meanwhile, further measurements delivered insight into the properties of the Higgs boson. Spin and parity quantum numbers and the tensor structure of Higgs boson interactions were found to be in good agreement with the Standard Model.

Couplings of the Standard Model Higgs boson to fermions, so-called Yukawa couplings, generate mass terms also for the fermions. The strength of the Yukawa coupling is predicted to be proportional to the corresponding fermion mass. The combination of the analyses, which led to the discovery of the Higgs boson, does include bosonic but not fermionic decay channels. For the channels with bosonic final states, Yukawa couplings play a role only indirectly through the heavy top quark loop in the gluon fusion Higgs boson production vertex. A direct access to Yukawa couplings at the LHC, which would explain the generation of fermion masses, is mainly based on the Higgs boson decay channels $H \to b\bar{b}$ and $H \to \tau^+\tau^-$. While final states with bottom quarks have a relatively large branching ratio of approximately 57%, it is challenging to increase the signal event selection efficiency in this case due to QCD multi-jet background processes, which is rather dominant at the LHC. Final states with two τ leptons have a much smaller branching ratio of 6%, however the suppression of QCD multi-jet processes and therefore the signal event selection efficiency is improved. The search for the Higgs boson in the $H \to \tau^+\tau^-$ decay is subject of this thesis.

There are three different $H \to \tau^+\tau^-$ decay channels that are accessed in the experiment depending on the subsequent τ lepton decay into hadrons or leptons:

$\tau_{\text{had}}\tau_{\text{had}}$, $\tau_{\text{lep}}\tau_{\text{had}}$ and $\tau_{\text{lep}}\tau_{\text{lep}}$. The branching ratios of these τ lepton decay modes are 42%, 45% and 12% respectively. This thesis presents detailed studies of the fully leptonic $\tau_{\text{lep}}\tau_{\text{lep}}$ decay channel $H \to \tau^+\tau^- \to \ell^+\ell^- 4\nu$, which provides a very clean final state topology including two electrons or muons or one electron and one muon along with four neutrinos. The search for the Higgs boson in this decay channel suffers only from a very low QCD multi-jet background contribution. The dominant irreducible background stems from $Z/\gamma^* \to \tau^+\tau^-$ processes, whose topology is nearly identical to the signal process. Results for the combination of all three final state channels are also presented.

The search for $H \to \tau^+\tau^- \to \ell^+\ell^- 4\nu$ presented in the thesis is based on the full 8 TeV dataset with an amount of $\int \mathcal{L}dt = 20.3$ fb^{-1} recorded with the ATLAS experiment. Two analysis categories are defined called the VBF and Boosted category. The VBF category targets signal events with Higgs bosons produced via vector-boson fusion mode. Such events are characterized by two tagging jets with high momentum and a large pseudo-rapidity gap between both jets. The Boosted category enriches signal events, where the Higgs boson is produced via gluon fusion. The selection is based on requiring at least one hard jet and high transverse momentum of the Higgs boson. $Z/\gamma^* \to \tau^+\tau^-$ processes are the dominant source of background events in the analysis and are therefore estimated in a data-driven way using the Embedding method. Further sources of background events stem from top quark, $Z/\gamma^* \to e^+e^-/\mu^+\mu^-$ and di-boson processes. Events with fake leptons, where jets are mis-identified as leptons, mainly originate from QCD multi-jet processes and play a minor role here. The multivariate technique of boosted decision trees is used in each of the categories to further separate signal from background events. A maximum likelihood fit of the boosted decision tree classifier distributions is then performed simultaneously in both categories to extract the normalisation, also called signal strength μ, of the Higgs boson signal samples. Additional top quark and $Z/\gamma^* \to e^+e^-/\mu^+\mu^-$ enriched data control regions are included in the fit to constrain the corresponding background normalisation. The best-fit Higgs boson signal strength value $\hat{\mu}$ is measured to be

$$\hat{\mu} \;=\; 2.10^{+0.81}_{-0.74}\ (\text{stat.})\ ^{+0.41}_{-0.41}\ (\text{exp. syst.})\ ^{+0.18}_{-0.18}\ (\text{theo. syst.}), \tag{12.1}$$

normalised to the Standard Model prediction using the full 8 TeV dataset. The observed excess is consistent with the Standard Model expectation ($\mu = 1$) corresponding to an observed (expected) discovery significance of 2.69 (1.34) standard deviations. The total uncertainty is dominated by the statistical uncertainty. In case of the $H \to \tau^+\tau^-$ combination of the $\tau_{\text{had}}\tau_{\text{had}}$, $\tau_{\text{lep}}\tau_{\text{had}}$ and $\tau_{\text{lep}}\tau_{\text{lep}}$ final state channels [8], the observed best-fit signal strength is

$$\hat{\mu}_{\text{comb}} = 1.43^{+0.27}_{-0.26}(\text{stat.})^{+0.32}_{-0.25}(\text{exp. syst.})^{+0.09}_{0.09}(\text{theo. syst.}) \tag{12.2}$$

with the observed (expected) significance of 4.54 (3.43) standard deviations based on 4.5 fb^{-1} at $\sqrt{s} = 7$ TeV and 20.3 fb^{-1} at $\sqrt{s} = 8$ TeV. The combined analysis provides thus clear evidence for a Standard Model-like Higgs boson and its Yukawa couplings to τ leptons. Furthermore, the reconstructed invariant di-τ mass of the

observed Higgs boson is consistent with the Higgs boson mass value of 125.09 ± 0.24 GeV GeV measured at CMS and ATLAS [6].

Besides the evidence for Yukawa couplings to τ leptons, a test of CP invariance in vector-boson fusion production of the Higgs boson is presented, based on the VBF category of the search for $H \to \tau^+\tau^-$. Indications of new sources of CP-violation potentially helps in understanding the baryon asymmetry in the universe. CP-violating contributions to the Standard Model CP-even HVV interactions (CP-mixing) can be parametrized by a single parameter $\tilde{d}$ within the framework of an effective field theory. The pure Standard Model coupling corresponds to $\tilde{d}$=0, while CP-mixing scenarios are defined by $\tilde{d} \neq 0$. CP-odd observables are utilized in the analysis, which are sensitive to CP-violation. Such observables result in a non-vanishing mean value in case of a CP-mixing Higgs boson signal. One such CP-odd observable that provides the highest sensitivity compared to others is called Optimal Observable. It is based on the full information of the high-dimensional phase space of the Higgs boson VBF production topology. The thesis focuses on testing the CP invariance in the fully leptonic decay channel $H \to \tau^+\tau^- \to \ell^+\ell^- 4\nu$. Results for the combination of the $\tau_{\text{lep}}\tau_{\text{had}}$ and $\tau_{\text{lep}}\tau_{\text{lep}}$ are also presented.

The test of CP invariance discussed in this thesis follows closely the analysis of the search for $H \to \tau^+\tau^- \to \ell^+\ell^- 4\nu$ using $\sqrt{s} = 8$ TeVdata with an amount of 20.3 fb^{-1}. A signal region is defined by selecting the signal-like bins of the boosted decision tree classifier in the VBF category. The full distribution of the Optimal Observable in this signal region is used in a maximum likelihood fit including further data control regions according to the VBF category of the search analysis to provide limits on the $\tilde{d}$ CP-mixing parameter. The fit is performed multiple times for different $\tilde{d}$ CP-mixing scenarios, where the outcome of this is a negative log likelihood profile, which allows to determine central confidence intervals for $\tilde{d}$.

The observed (Standard Model expected) central confidence interval for $\tilde{d}$ is found to be $[-0.03, 0.17]$ ($[-0.12, 0.11]$) at 68% confidence level. The combination of the $\tau_{\text{lep}}\tau_{\text{lep}}$ and $\tau_{\text{lep}}\tau_{\text{had}}$ final state channels is also based on the full $\sqrt{s} = 8$ TeV dataset and results in an observed (Standard Model expected) central confidence interval for $\tilde{d}$ of $[-0.11, 0.05]$ ($[-0.08, 0.08]$) at 68% confidence level [9]. The observed mean values $< OO >$ of the Optimal Observable distributions in the signal region are 0.3 ± 0.5 for the $\tau_{\text{lep}}\tau_{\text{lep}}$ and -0.3 ± 0.4 for the $\tau_{\text{lep}}\tau_{\text{had}}$ final state channel. The results are in good agreement with the Standard Model HVV interaction, which corresponds to $\tilde{d}$=0 and $< OO >= 0$, and no hints for CP-violation are observed. Besides the Optimal Observable, an alternative CP-odd observable called signed $\Delta\phi(j_1, j_2)$ has been tested and provides consistent results.

In summary, the results of the analysis of the search for $H \to \tau^+\tau^- \to \ell^+\ell^- 4\nu$ and the test of CP invariance in vector-boson fusion Higgs boson production, which are presented in the context of this thesis, further confirm the theory of the Standard Model of particle physics since no deviations from Standard Model were observed. Analyzing $H \to \tau^+\tau^-$ decays play an important role in fully characterizing the Standard Model Higgs boson, its Yukawa interactions and the mechanism of electroweak symmetry breaking. Upcoming data taking periods at the LHC will

increase the amount of data significantly. This will improve the ability to measure Higgs boson couplings especially to fermions, which is currently limited to a large extend by the statistical power of the dataset. More data and improved experimental analysis methods will also allow to investigate further Higgs boson production modes besides of the gluon fusion and vector-boson fusion modes, which are the dominant modes at the LHC, such as vector boson and top quark associated production modes in more detail. Increasing precision of the measurements of Higgs boson properties might be a key to search for physics beyond the Standard Model such as anomalous Higgs boson couplings, which could explain remaining open questions that are currently not covered by the Standard Model. Future LHC studies at higher center of mass energies will show if there is a superior theory such as supersymmetry within that the Standard Model is an effective theory at lower energies.

A Kinematic Distributions

A.1. Preselection

This section contains auxiliary distributions with respect to the preselection of the search for the Standard Model Higgs boson in the fully leptonic decay $H \to \tau^+\tau^- \to \ell^+\ell^- 4\nu$. Each background component is compared to the individual signal production modes for all variables, which are used in the preselection. The comparisons highlight the discriminating power of the variables and the corresponding cut on each variable is included in the figures.

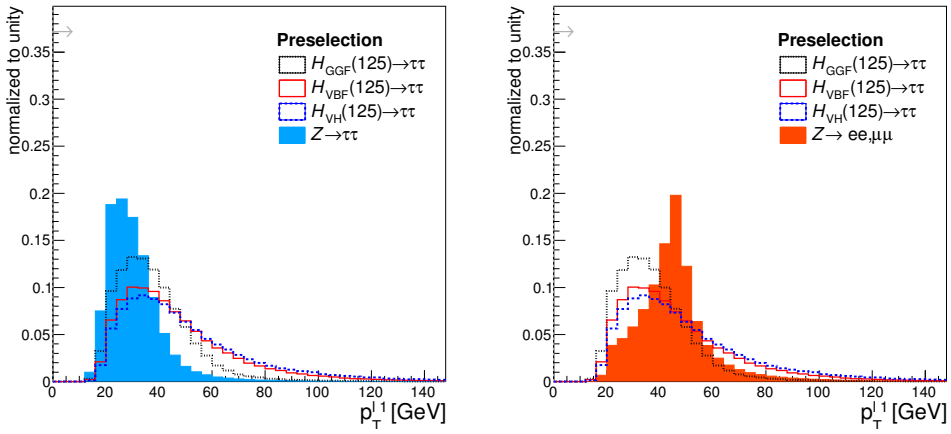

(a)

(b)

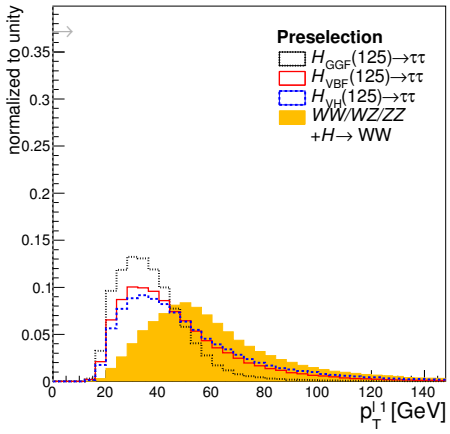

(c)

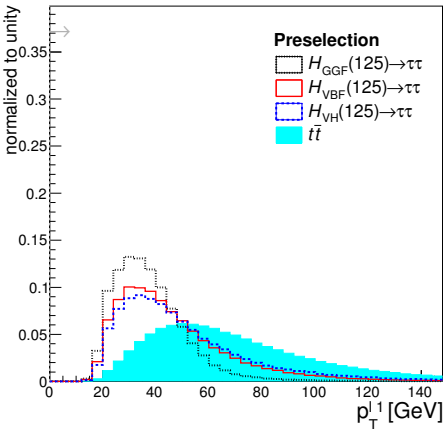

(d)

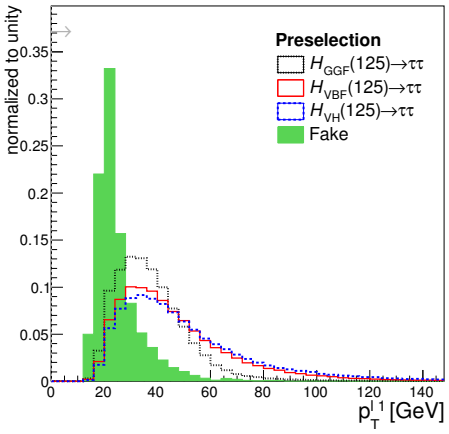

(e)

Figure A.1. *Distribution of the leading lepton momentum $p_T^{l_1}$ at preselection level, requiring data cleaning and basic selection cuts such as trigger, di-lepton and p_T^l thresholds. Comparison of different signal modes to each background source respectively.*

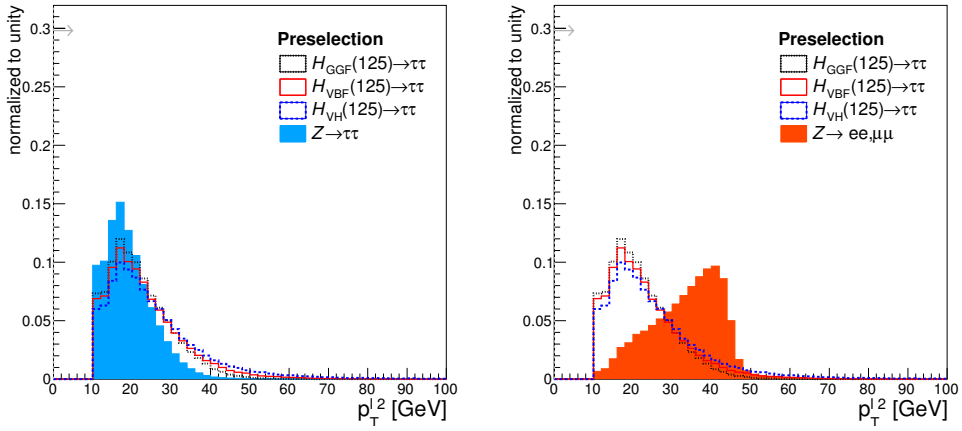

(a)

(b)

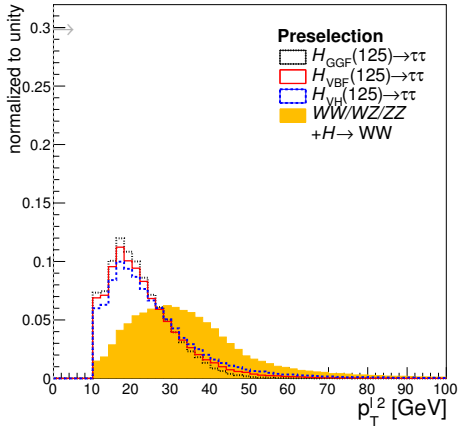

(c)

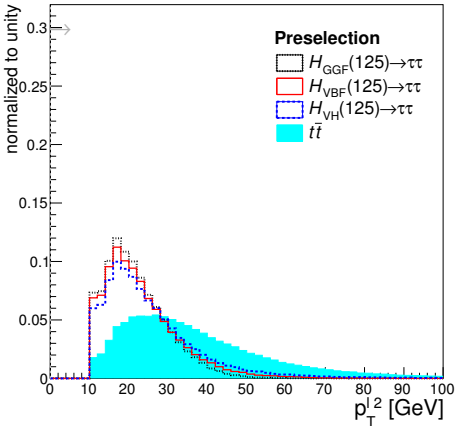

(d)

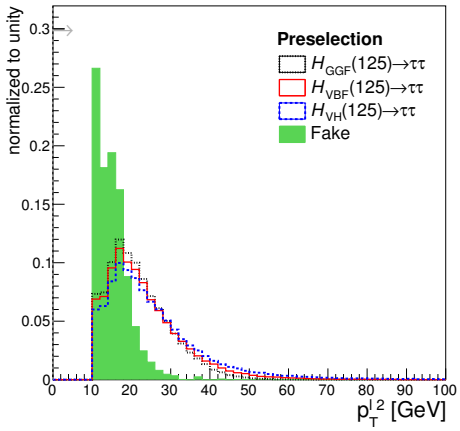

(e)

Figure A.2. *Distribution of the sub-leading lepton momentum $p_T^{l_2}$ at preselection level, requiring data cleaning and basic selection cuts such as trigger, di-lepton and p_T^l thresholds. Comparison of different signal modes to each background source respectively.*

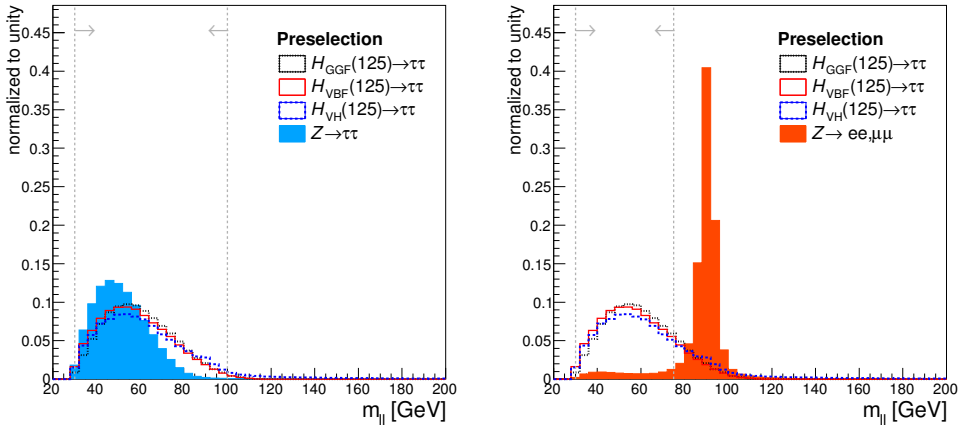

(a)

(b)

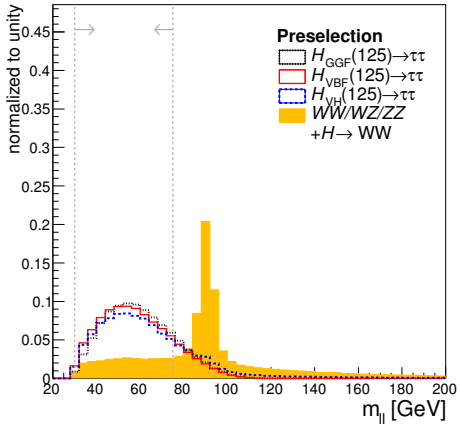

(c)

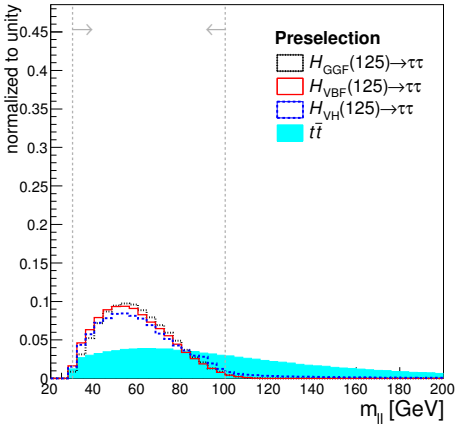

(d)

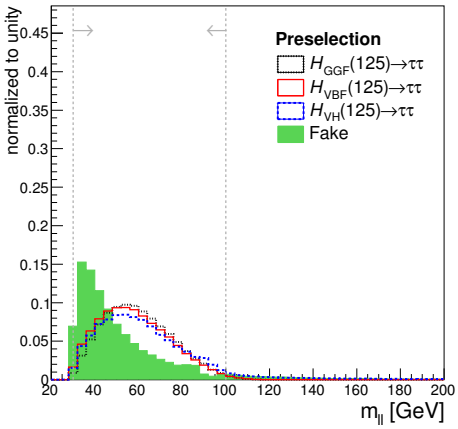

(e)

Figure A.3. *Distribution of the invariant di-lepton mass m_{ll} at preselection level, requiring data cleaning and basic selection cuts such as trigger, di-lepton and p_T^l thresholds. Comparison of different signal modes to each background source respectively.*

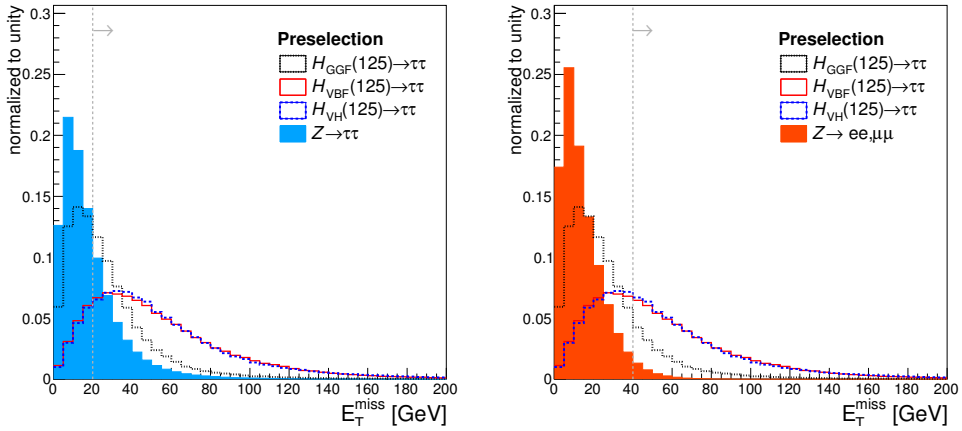

(a)

(b)

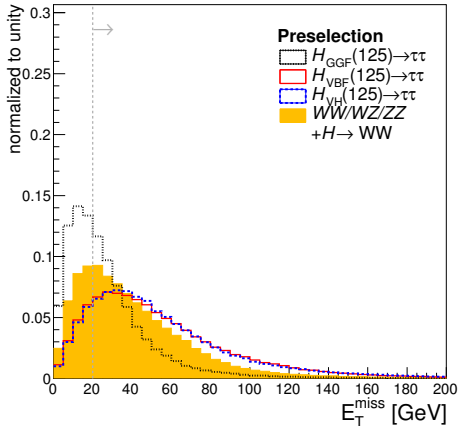

(c)

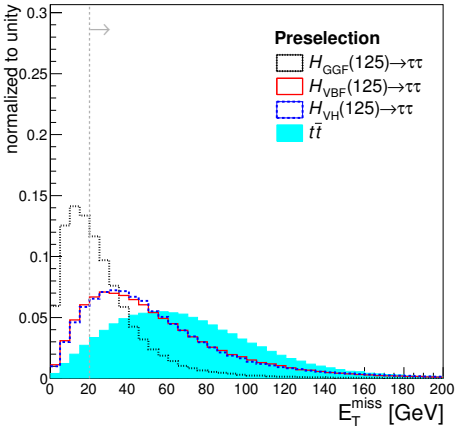

(d)

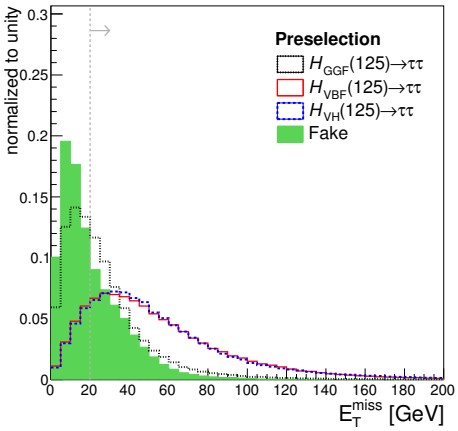

(e)

Figure A.4. *Distribution of missing transverse momentum $E_{\mathrm{T}}^{\mathrm{miss}}$ at preselection level, requiring data cleaning and basic selection cuts such as trigger, di-lepton and p_T^l thresholds. Comparison of different signal modes to each background source respectively.*

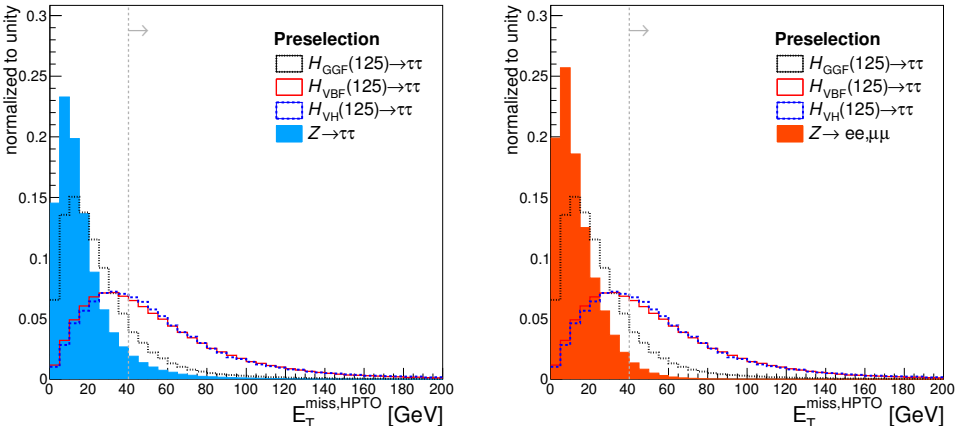

(a)

(b)

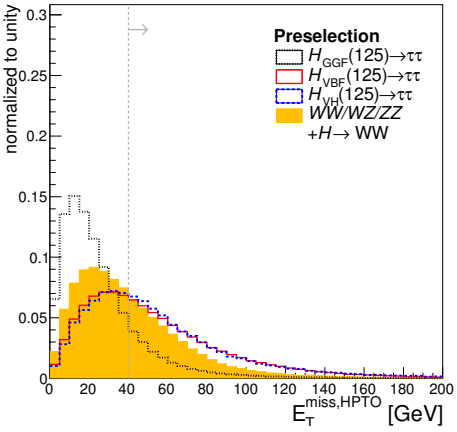

(c)

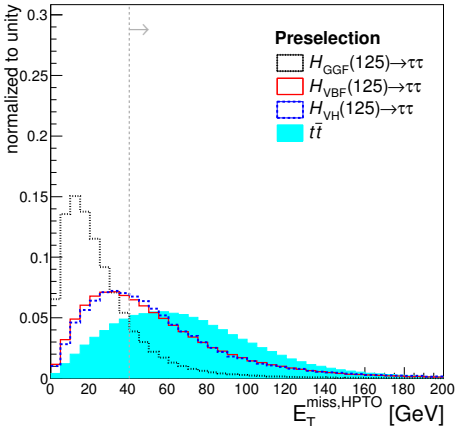

(d)

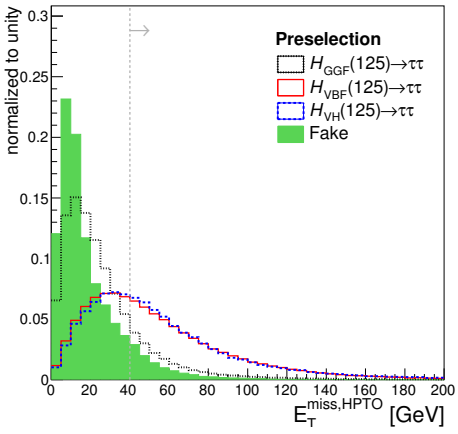

(e)

Figure A.5. *Distribution of the high-p_T object missing transverse momentum $E_{\mathrm{T}}^{\mathrm{miss,HPTO}}$ at preselection level, requiring data cleaning and basic selection cuts such as trigger, di-lepton and p_T^l thresholds. Comparison of different signal modes to each background source respectively.*

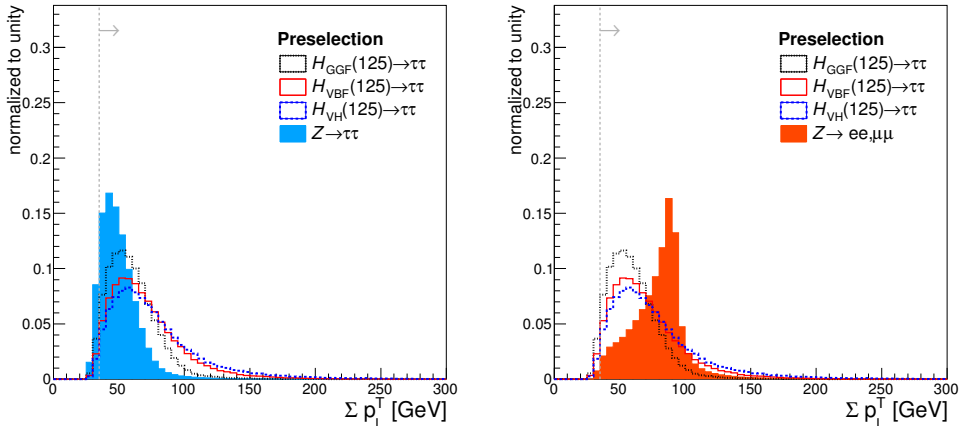

(a)

(b)

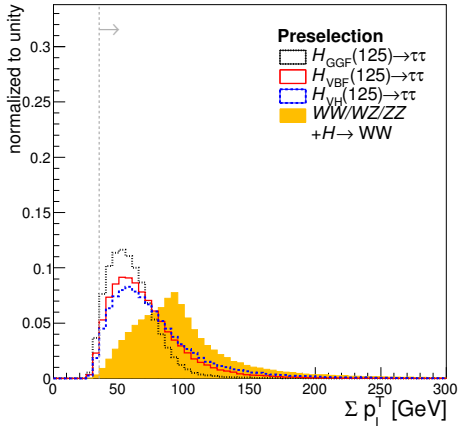

(c)

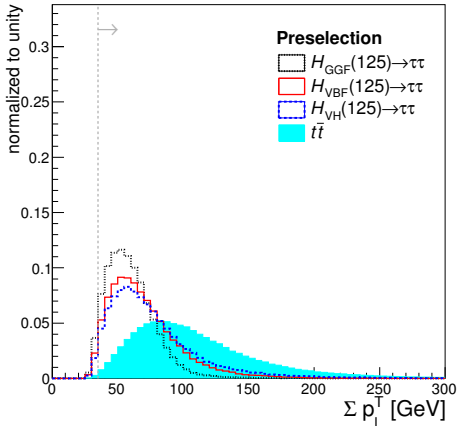

(d)

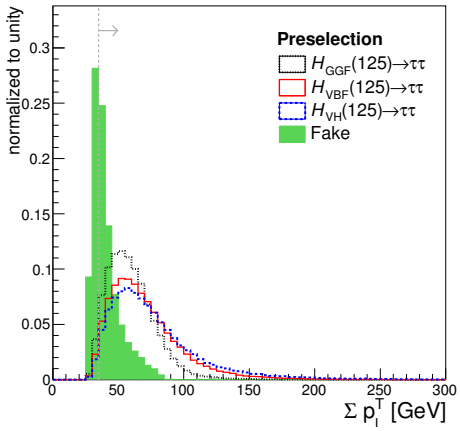

(e)

Figure A.6. *Distribution of the sum of lepton transverse momenta* $p_{\mathrm{T}}^{\ell_1} + p_{\mathrm{T}}^{\ell_2}$ *at preselection level, requiring data cleaning and basic selection cuts such as trigger, di-lepton and* p_T^l *thresholds. Comparison of different signal modes to each background source respectively.*

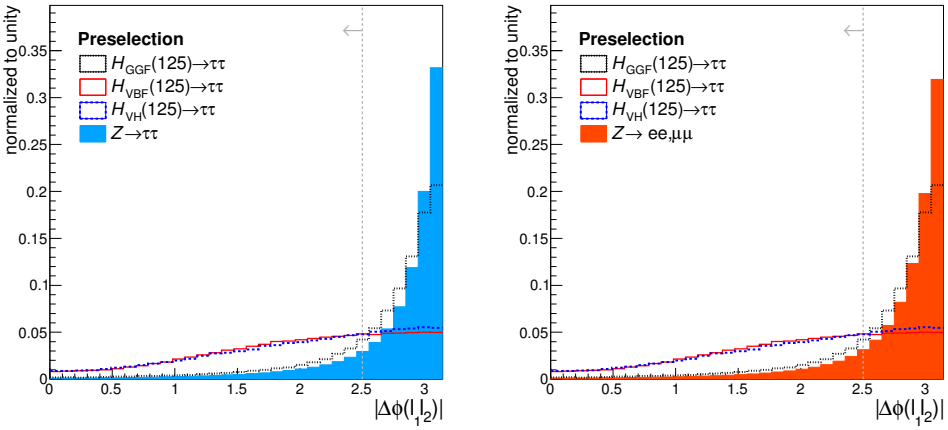

(a)

(b)

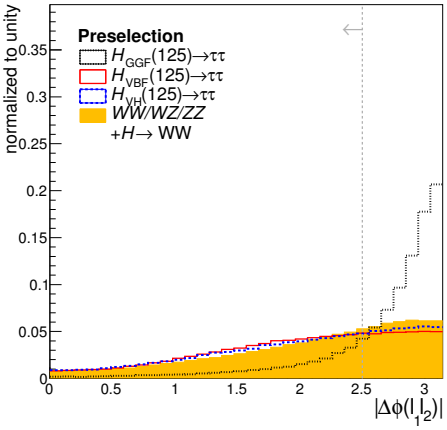

(c)

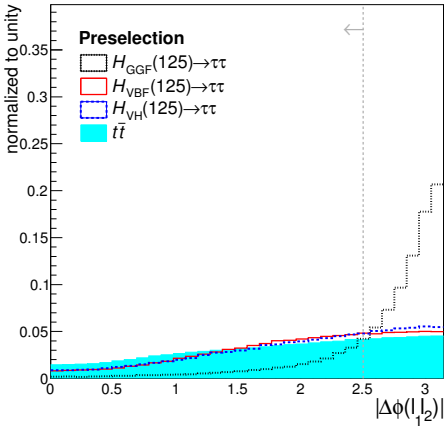

(d)

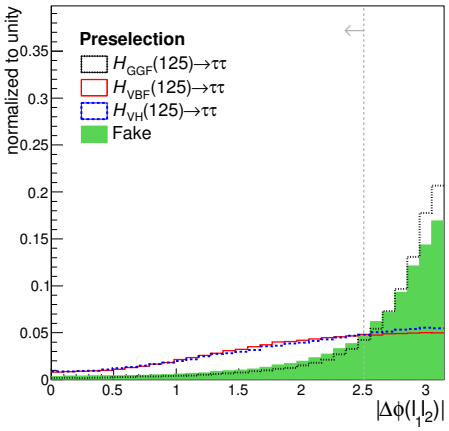

(e)

Figure A.7. *Distribution of $\Delta\phi(\ell_1, \ell_2)$ at preselection level, requiring data cleaning and basic selection cuts such as trigger, di-lepton and p_T^l thresholds. Comparison of different signal modes to each background source respectively.*

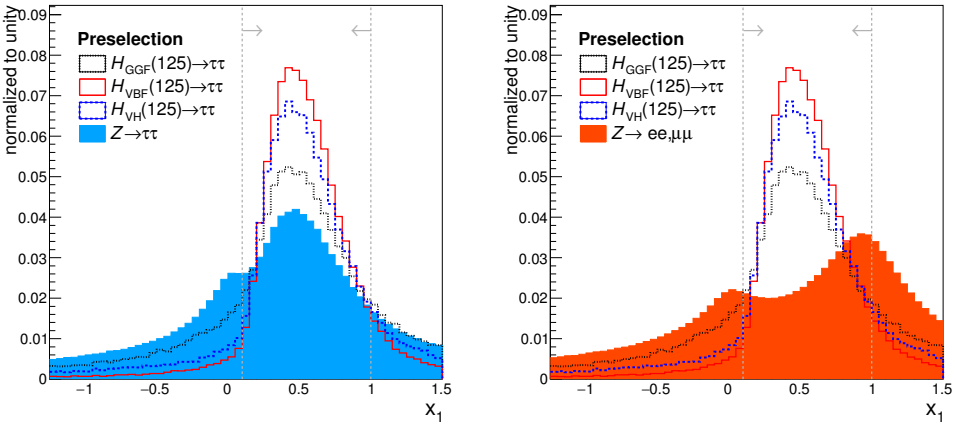

(a)

(b)

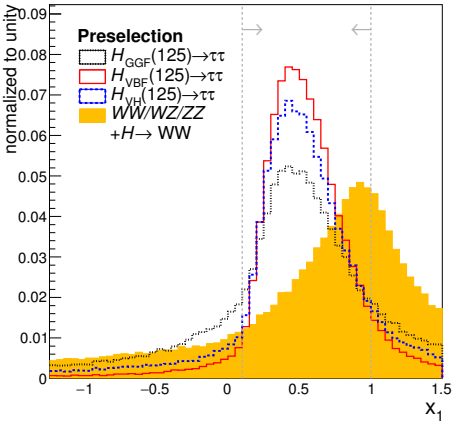

(c)

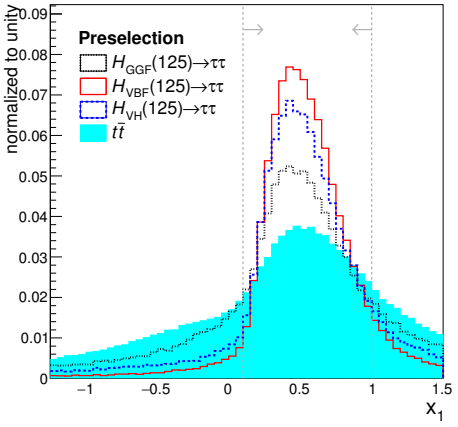

(d)

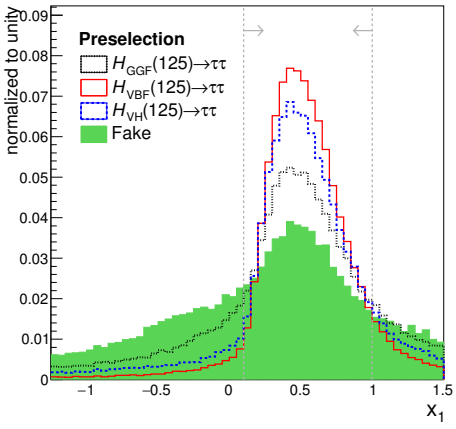

(e)

Figure A.8. *Distribution of x_1 at preselection level, requiring data cleaning and basic selection cuts such as trigger, di-lepton and p_T^l thresholds. Comparison of different signal modes to each background source respectively.*

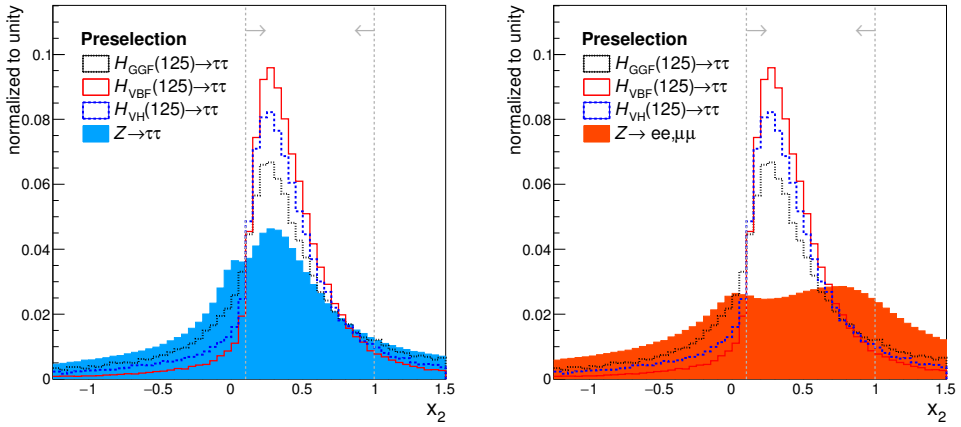

(a)

(b)

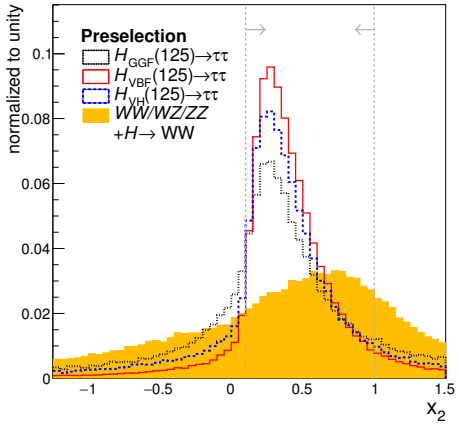

(c)

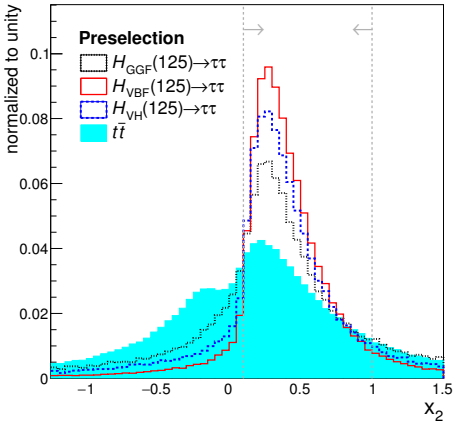

(d)

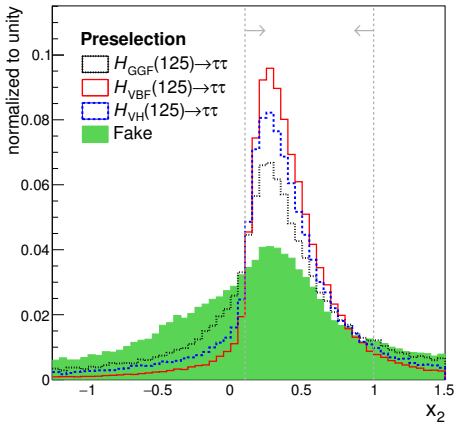

(e)

Figure A.9. *Distribution of x_2 at preselection level, requiring data cleaning and basic selection cuts such as trigger, di-lepton and p_T^l thresholds. Comparison of different signal modes to each background source respectively.*

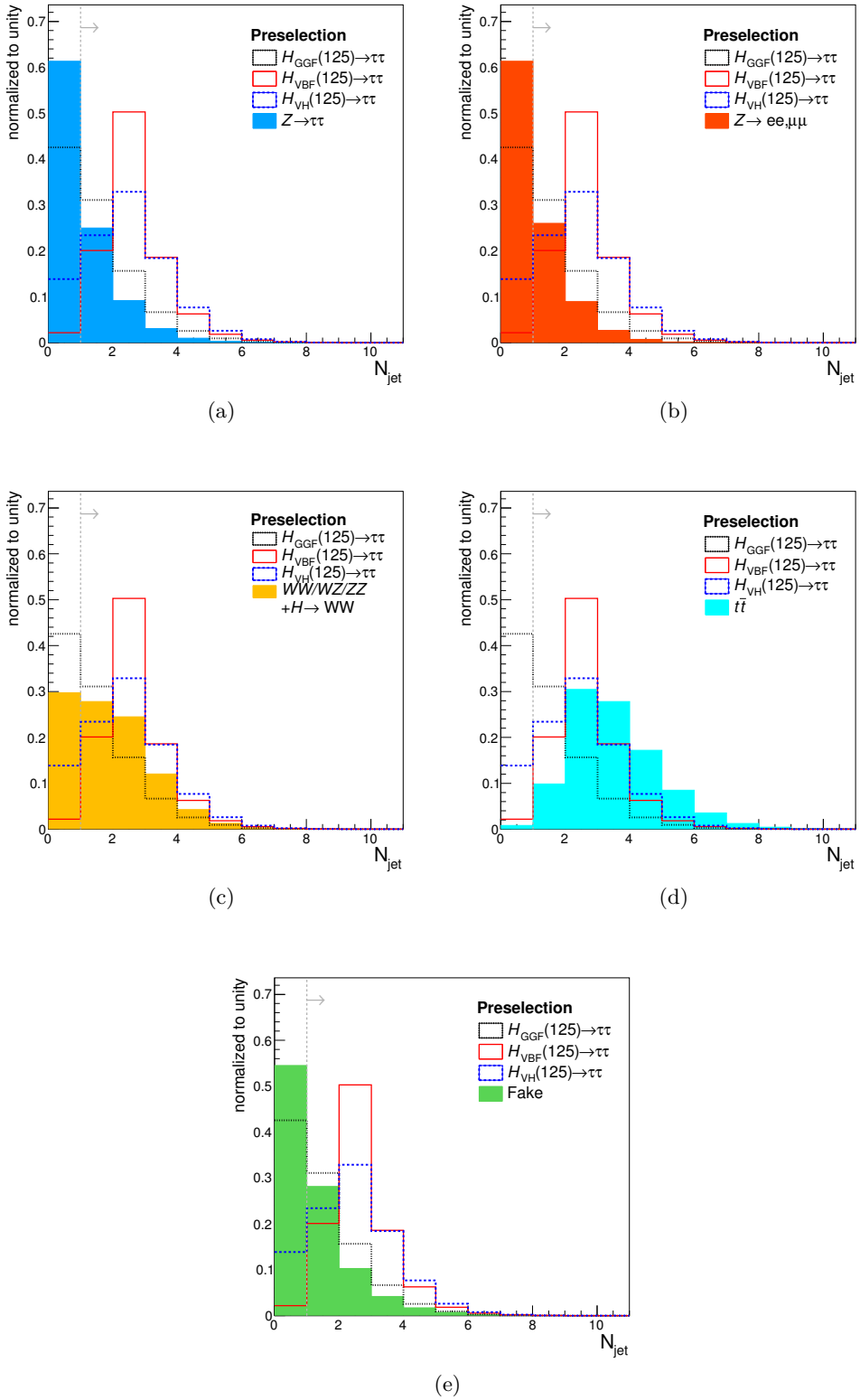

Figure A.10. *Distribution of the number of jets N_{jet} at preselection level, requiring data cleaning and basic selection cuts such as trigger, di-lepton and p_T^l thresholds. Comparison of different signal modes to each background source respectively.*

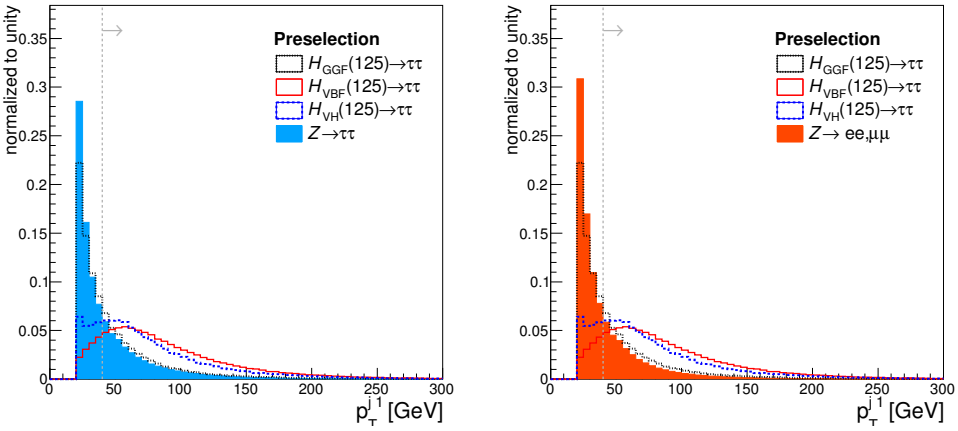

(a)

(b)

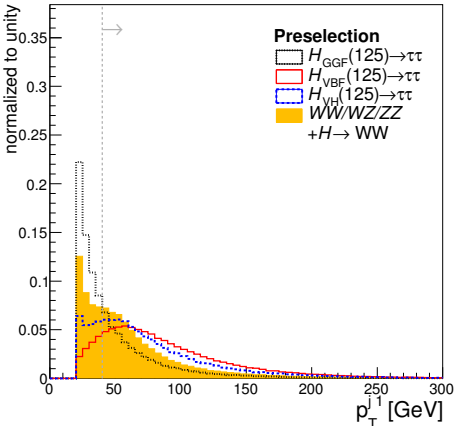

(c)

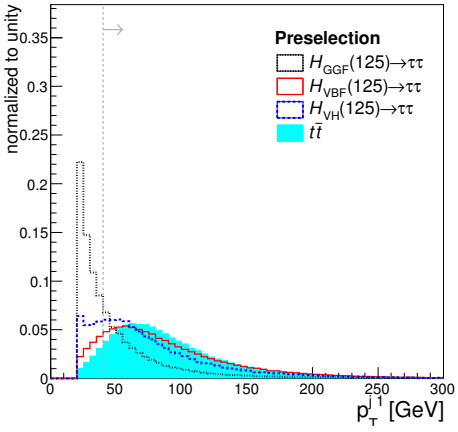

(d)

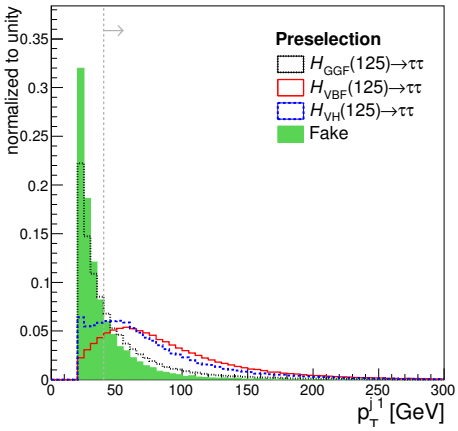

(e)

Figure A.11. *Distribution of the leading jet transverse momentum p_T^{j1} at preselection level, requiring data cleaning and basic selection cuts such as trigger, di-lepton and p_T^l thresholds. Comparison of different signal modes to each background source respectively.*

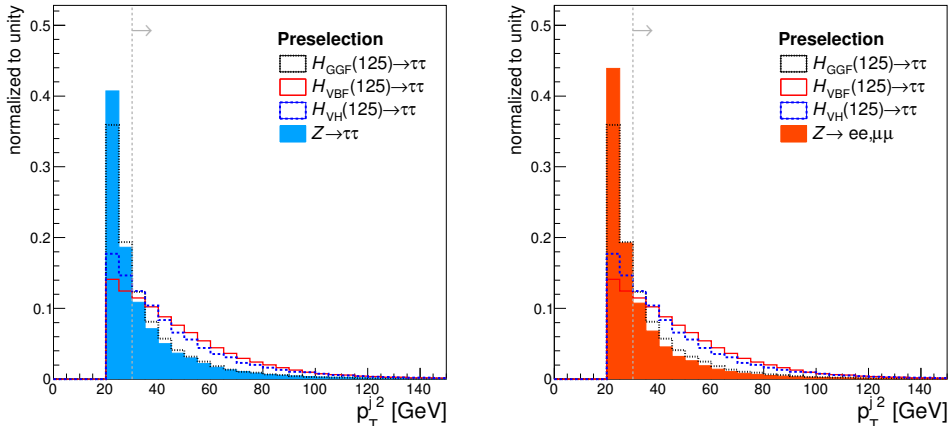

(a)

(b)

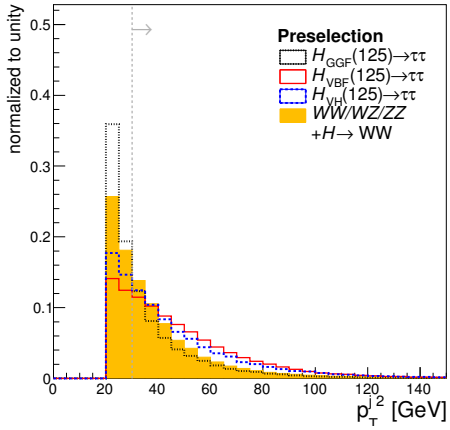

(c)

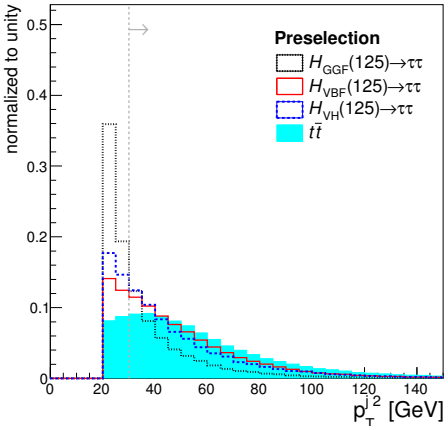

(d)

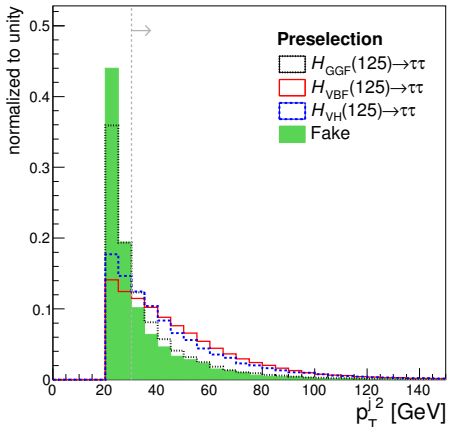

(e)

Figure A.12. *Distribution of the sub-leading jet transverse momentum $p_T^{l_2}$ at preselection level, requiring data cleaning and basic selection cuts such as trigger, di-lepton and p_T^l thresholds. Comparison of different signal modes to each background source respectively.*

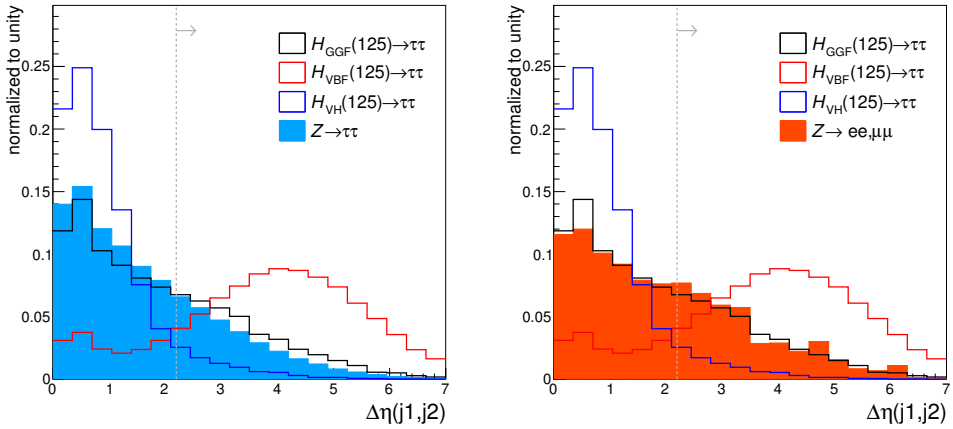

(a)

(b)

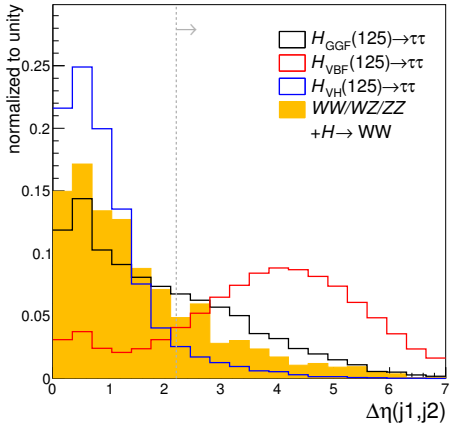

(c)

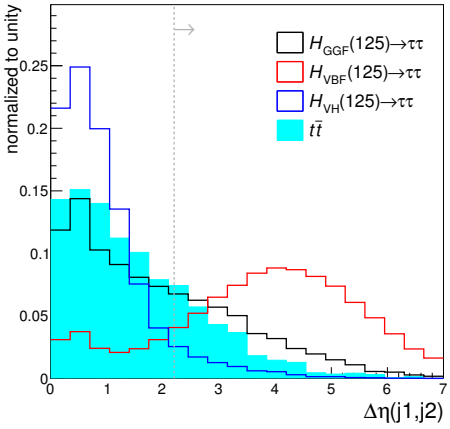

(d)

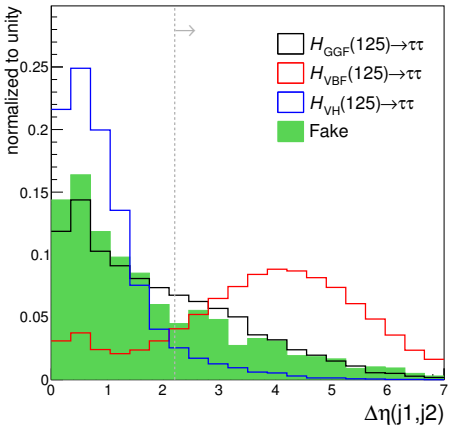

(e)

Figure A.13. *Distribution of $\Delta\eta(j_1, j_2)$ at preselection level, requiring data cleaning and basic selection cuts such as trigger, di-lepton and p_T^l thresholds. Comparison of different signal modes to each background source respectively.*

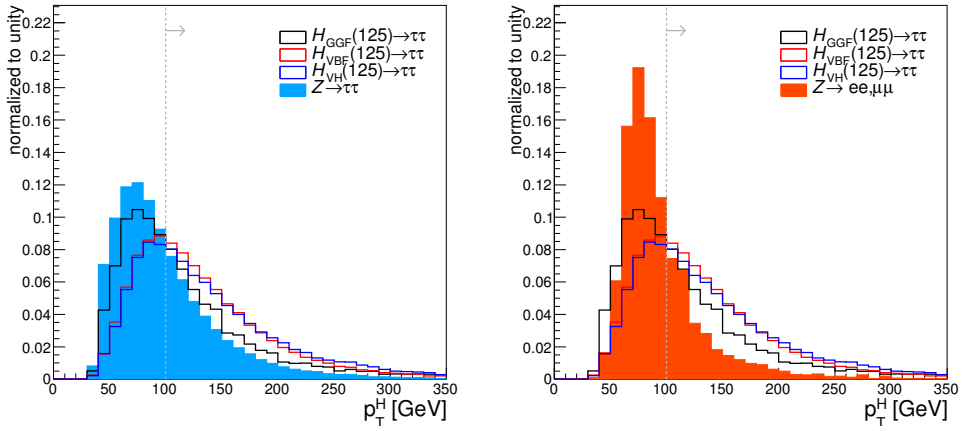

(a)

(b)

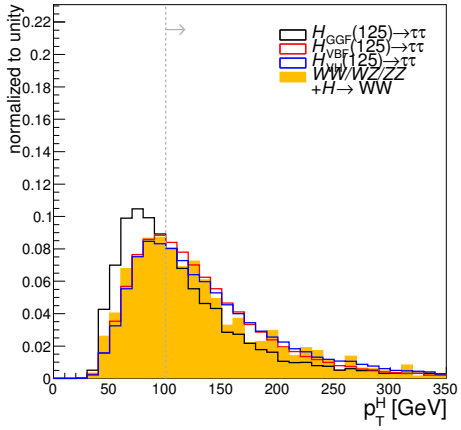

(c)

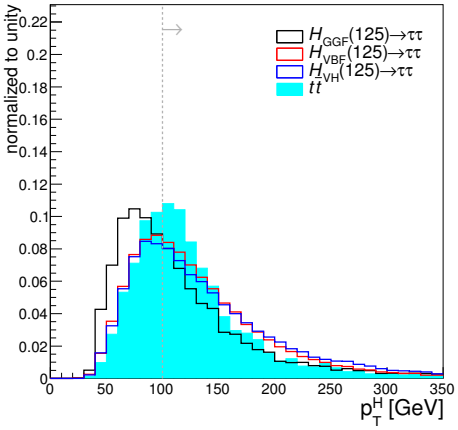

(d)

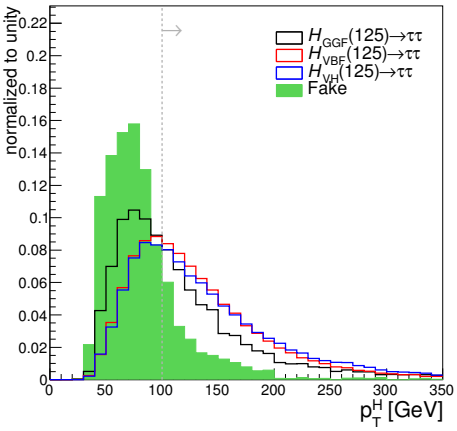

(e)

Figure A.14. *Distribution of the di-τ system transverse momentum p_T^H at preselection level, requiring data cleaning and basic selection cuts such as trigger, di-lepton and p_T^l thresholds. Comparison of different signal modes to each background source respectively.*

A.2. BDT input

This section contains auxiliary distributions of the BDT input variables in the VBF and the Boosted category of the search for the Standard Model Higgs boson in the fully leptonic decay $H \to \tau^+\tau^- \to \ell^+\ell^- 4\nu$. Each background component is compared to the individual signal production modes for all BDT input variables with respect to both categories. The comparisons highlight the discriminating power of the variables, which are combined in the BDTs to achieve optimal separation between signal and background.

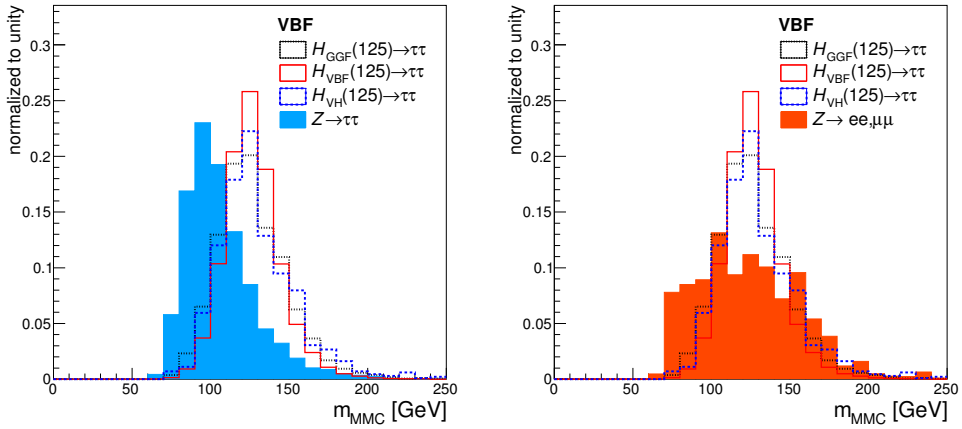

(a)

(b)

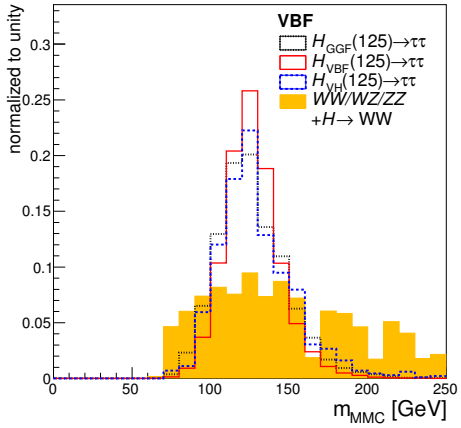

(c)

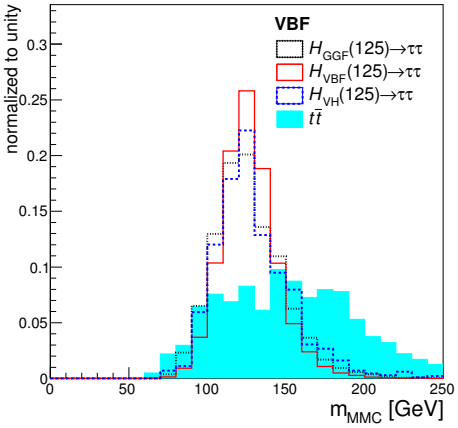

(d)

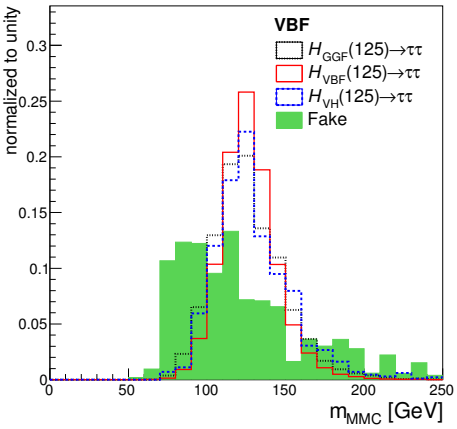

(e)

Figure A.15. *Distribution of m_{MMC} in the VBF category. Comparison of different signal modes to each background source respectively.*

Figure A.16. *Distribution of the Missing Mass Calculator invariant mass m_{MMC} in the VBF category. Comparison of different signal modes to each background source respectively.*

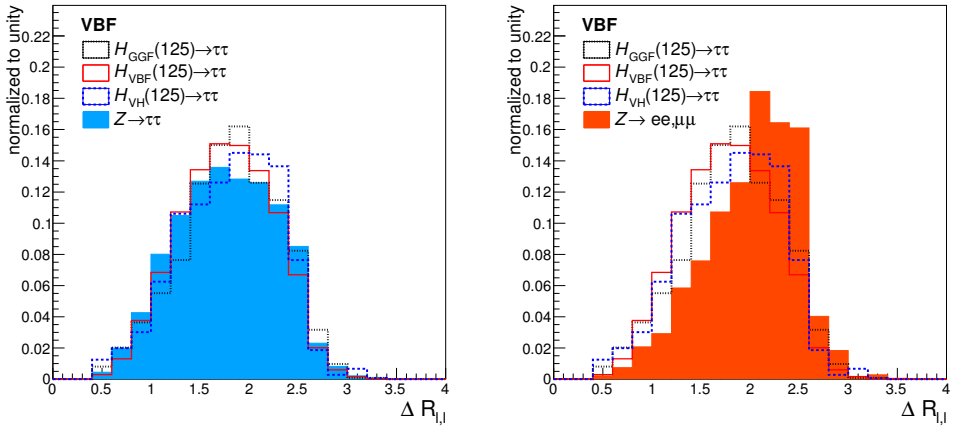

(a)

(b)

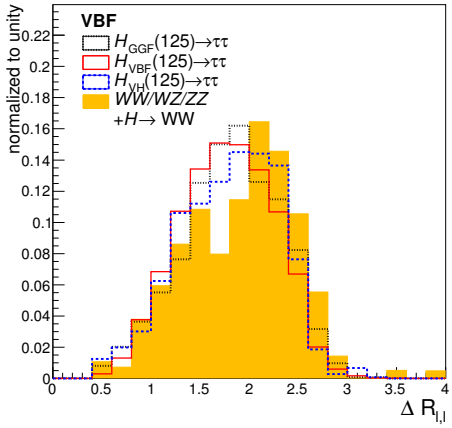

(c)

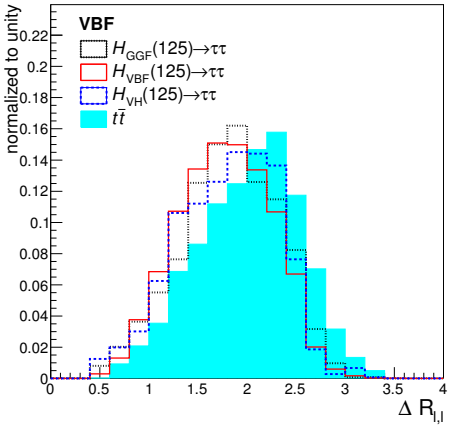

(d)

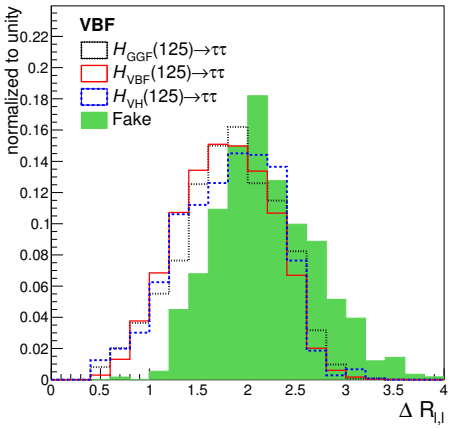

(e)

Figure A.17. *Distribution of $\Delta R(\ell_1, \ell_2)$ in the VBF category. Comparison of different signal modes to each background source respectively.*

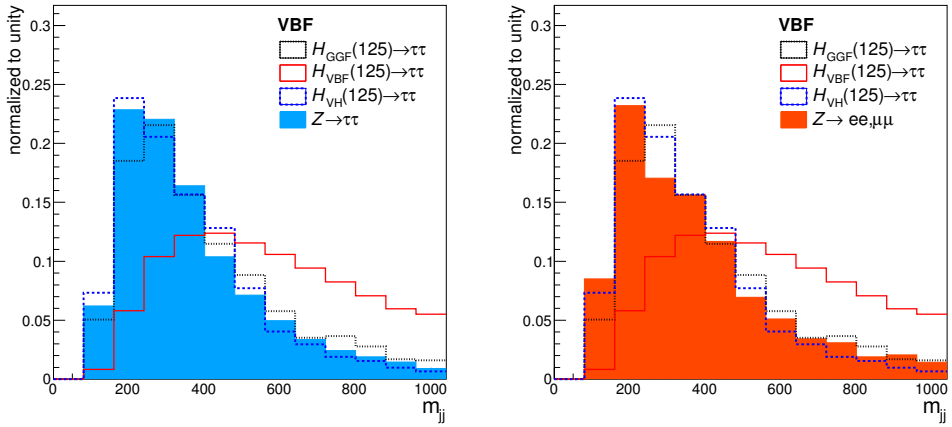

(a)

(b)

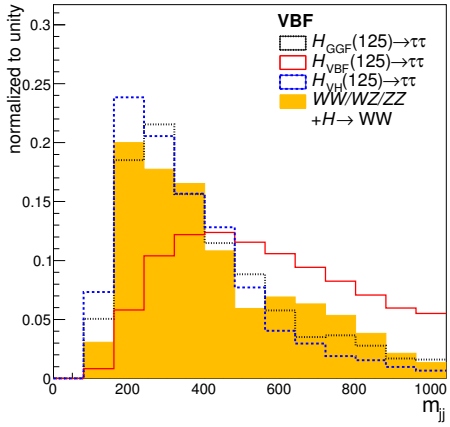

(c)

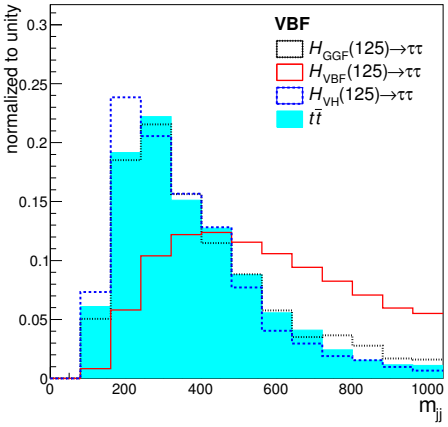

(d)

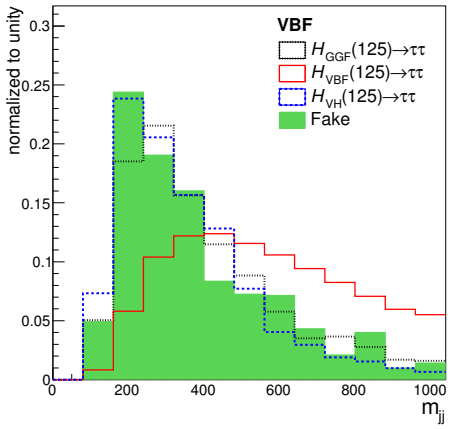

(e)

Figure A.18. *Distribution of $m_{j_1 j_2}$ in the VBF category. Comparison of different signal modes to each background source respectively.*

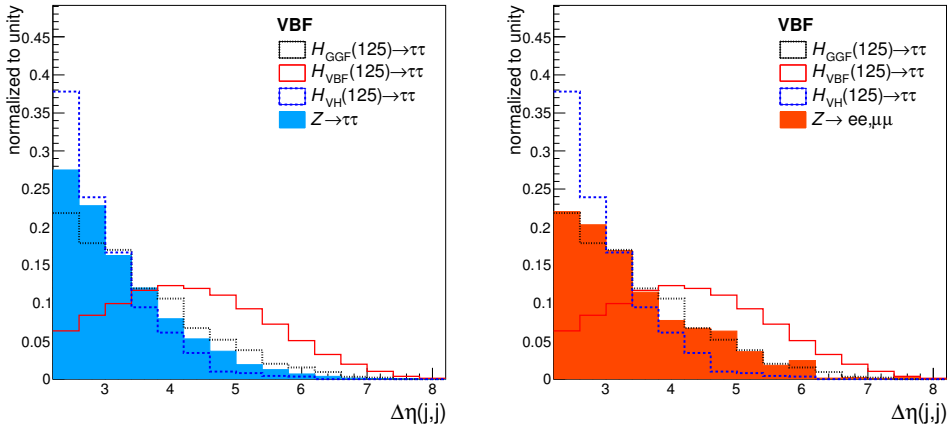

(a)

(b)

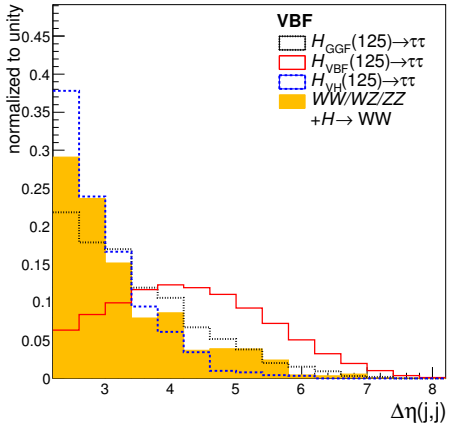

(c)

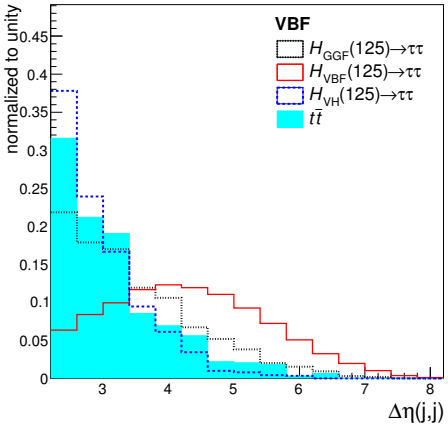

(d)

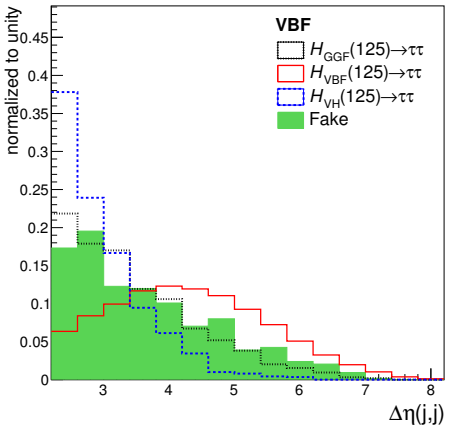

(e)

Figure A.19. *Distribution of $\Delta\eta(j_1, j_2)$ in the VBF category. Comparison of different signal modes to each background source respectively.*

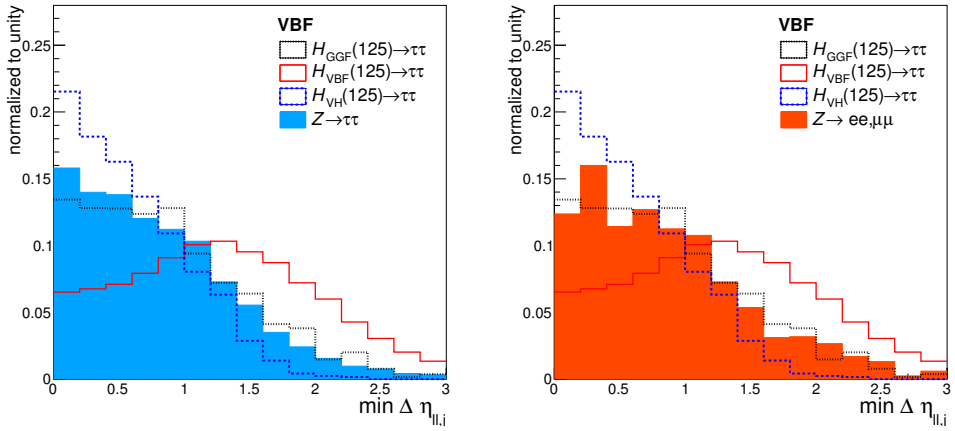

(a)

(b)

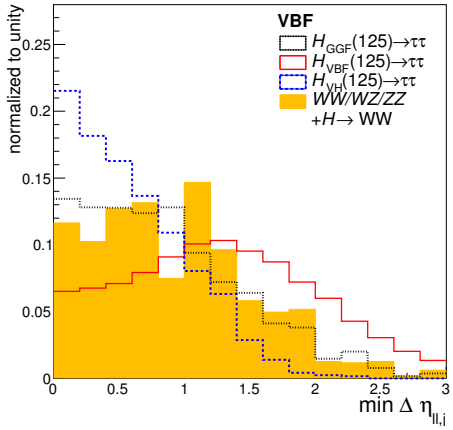

(c)

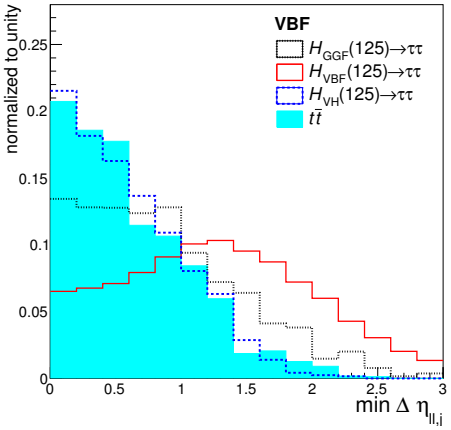

(d)

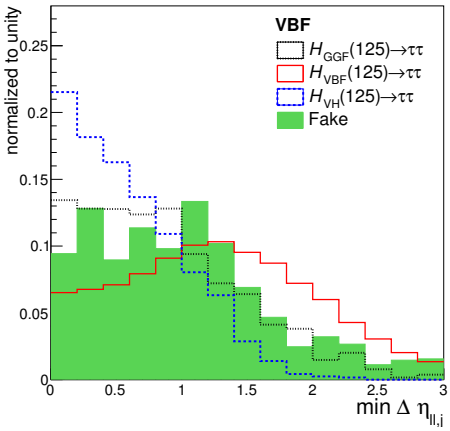

(e)

Figure A.20. *Distribution of min*$[\Delta\eta(\ell\ell, j)]$ *in the VBF category. Comparison of different signal modes to each background source respectively.*

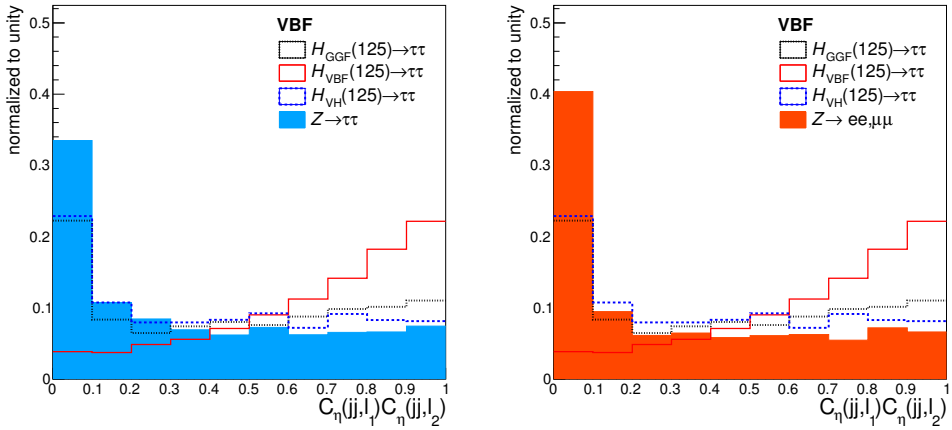

(a)

(b)

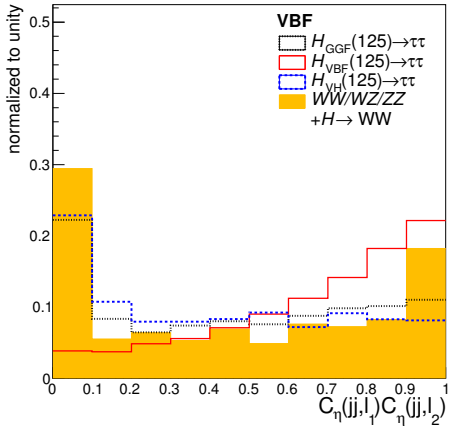

(c)

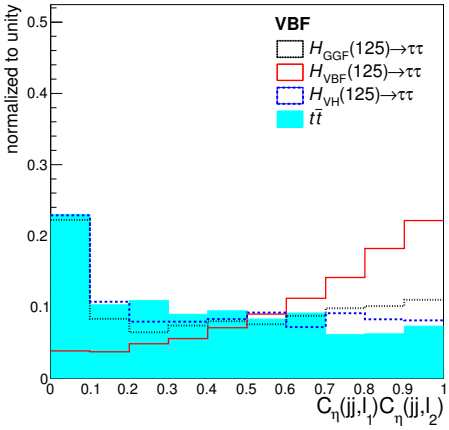

(d)

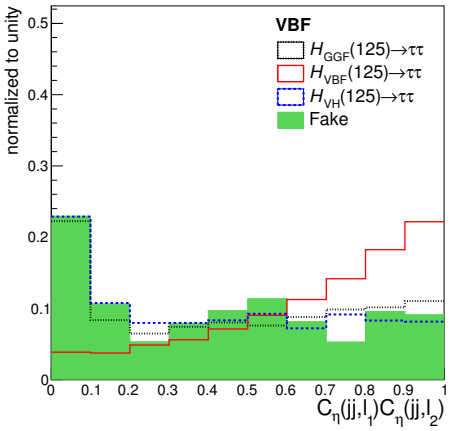

(e)

Figure A.21. *Distribution of $C_\eta(jj,\ell_1)\cdot C_\eta(jj,\ell_2)$ in the VBF category. Comparison of different signal modes to each background source respectively.*

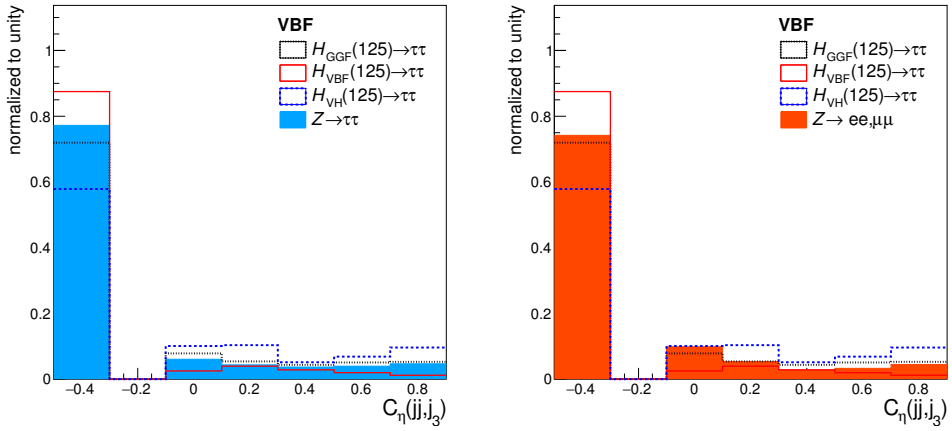

(a)

(b)

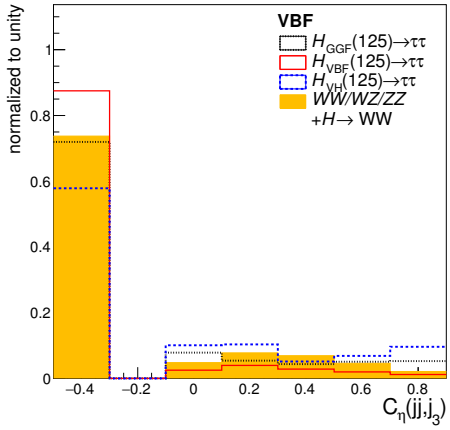

(c)

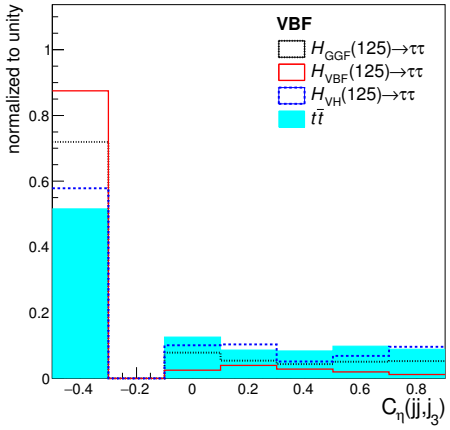

(d)

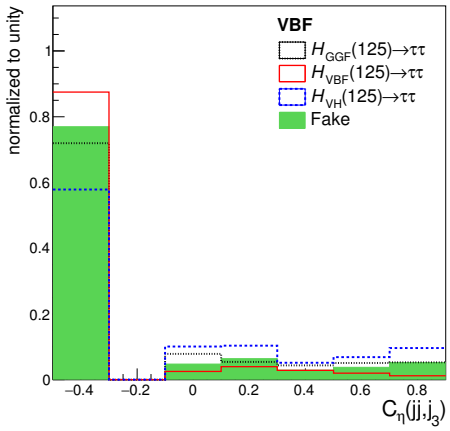

(e)

Figure A.22. *Distribution of $C_\eta(jj, j_3)$ in the VBF category. Comparison of different signal modes to each background source respectively.*

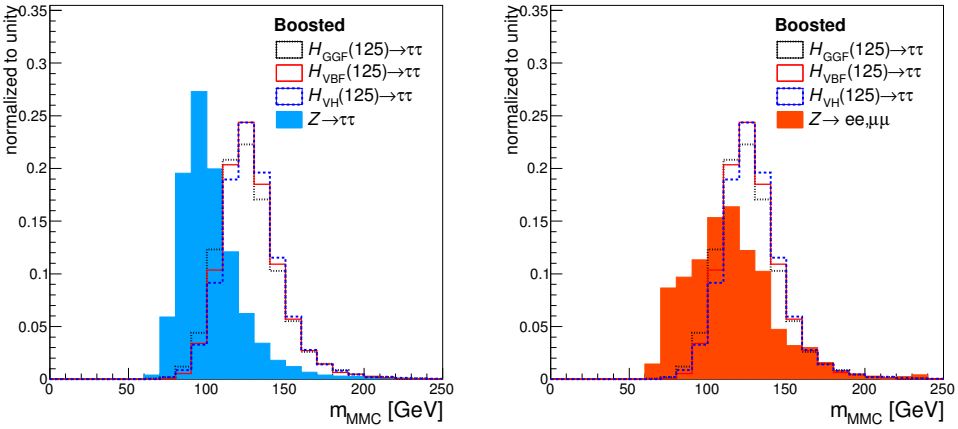

(a)

(b)

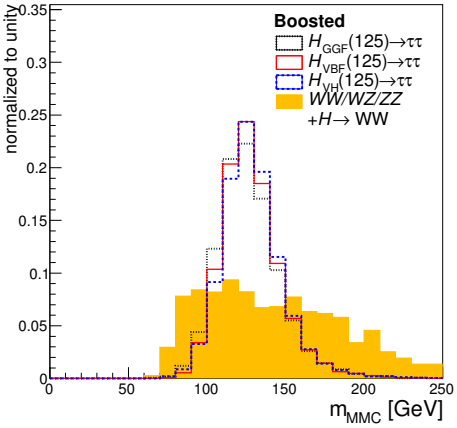

(c)

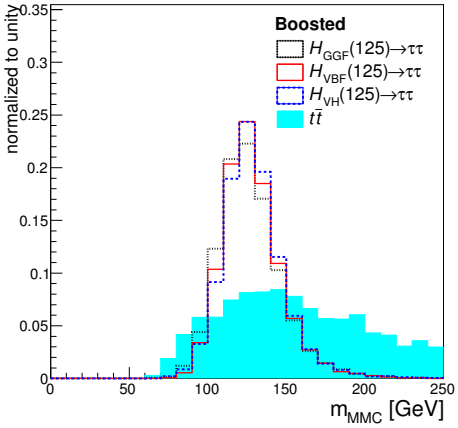

(d)

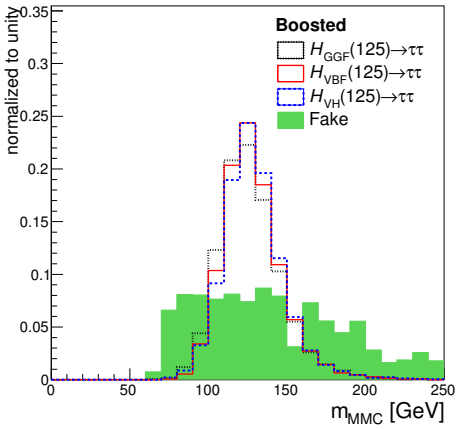

(e)

Figure A.23. *Distribution of m_{MMC} in the Boosted category. Comparison of different signal modes to each background source respectively.*

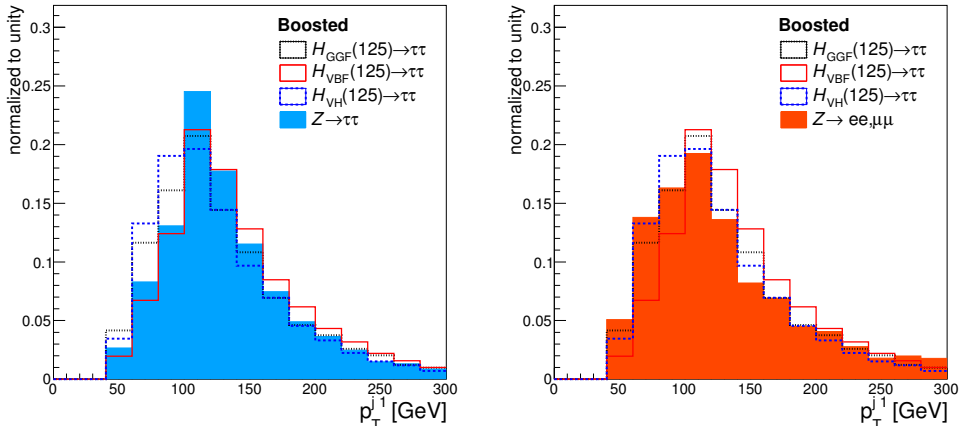

(a)

(b)

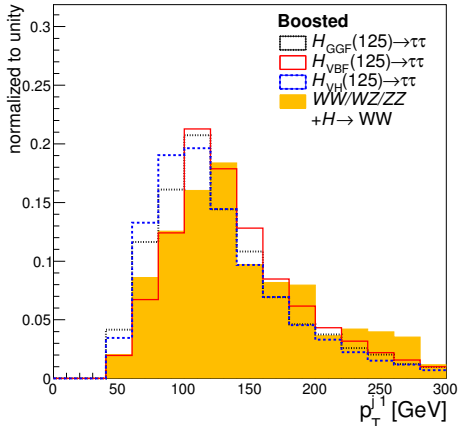

(c)

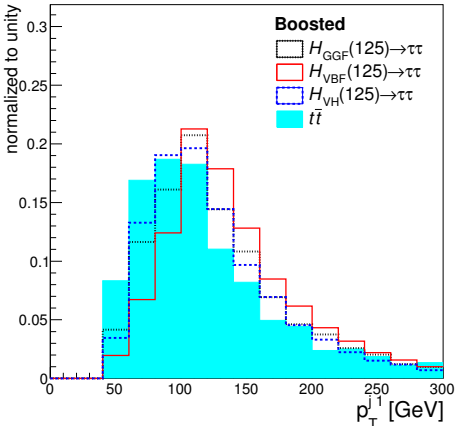

(d)

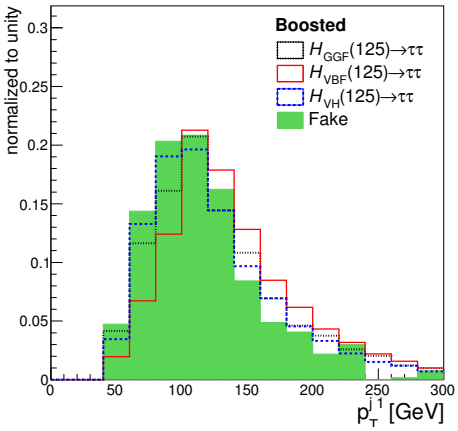

(e)

Figure A.24. *Distribution of $p_T^{j_1}$ in the Boosted category. Comparison of different signal modes to each background source respectively.*

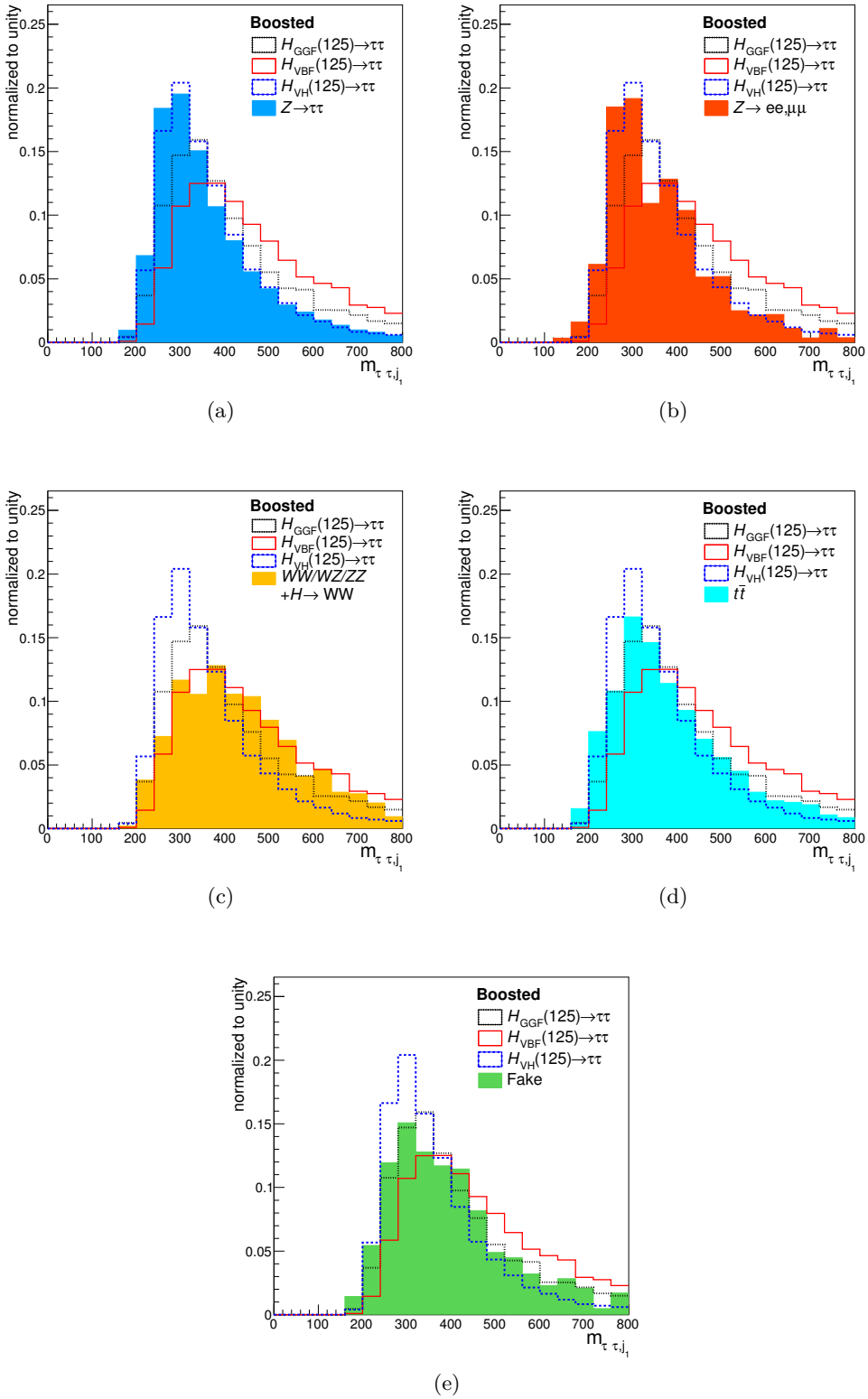

Figure A.25. *Distribution of $m_{\tau\tau j_1}$ in the Boosted category. Comparison of different signal modes to each background source respectively.*

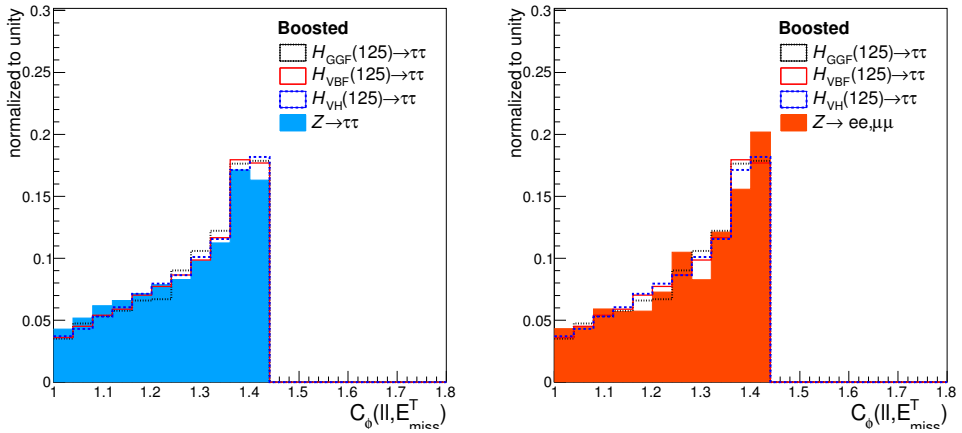

(a)

(b)

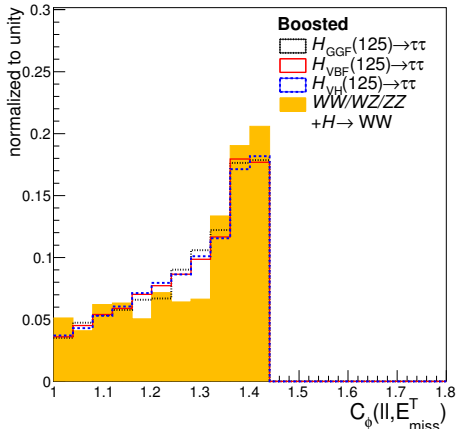

(c)

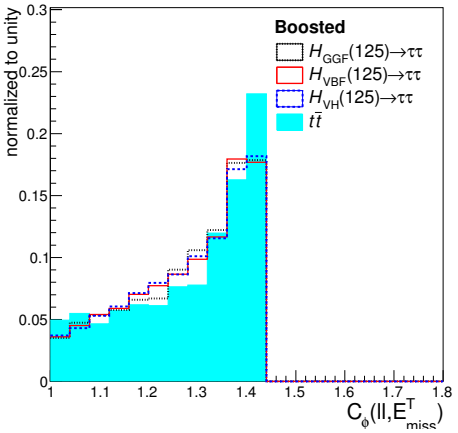

(d)

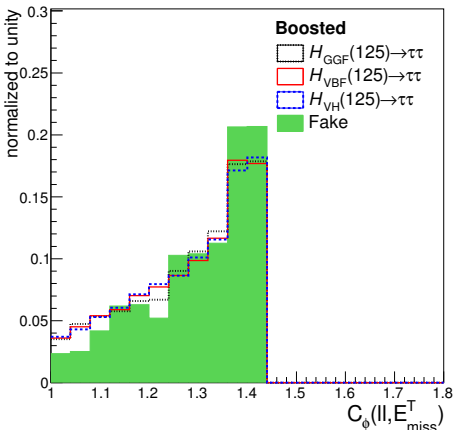

(e)

Figure A.26. *Distribution of $C_\phi(\ell\ell, E_{\mathrm{T}}^{\mathrm{miss}})$ in the Boosted category. Comparison of different signal modes to each background source respectively.*

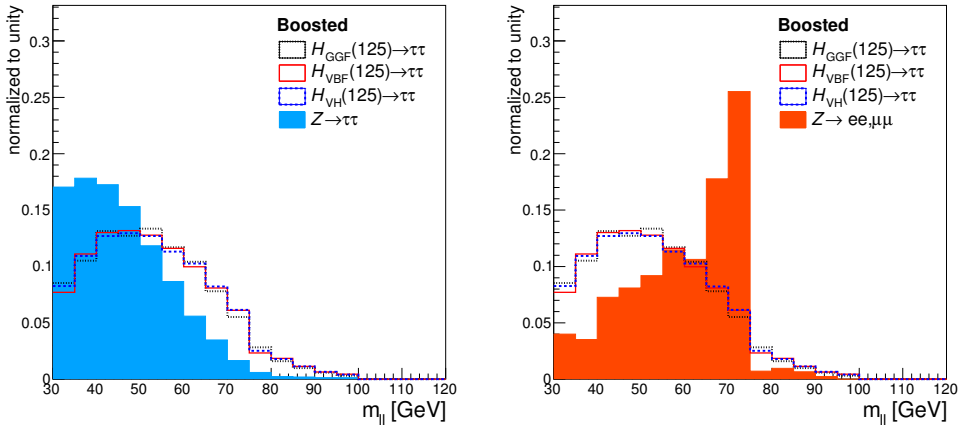

(a)

(b)

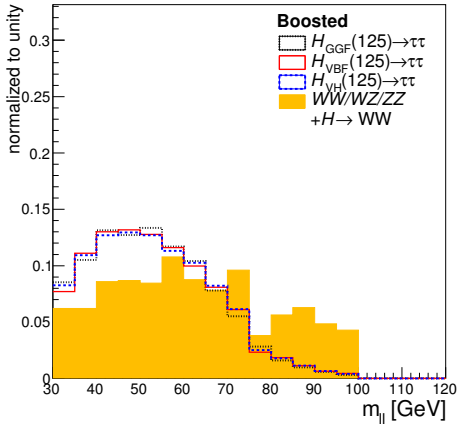

(c)

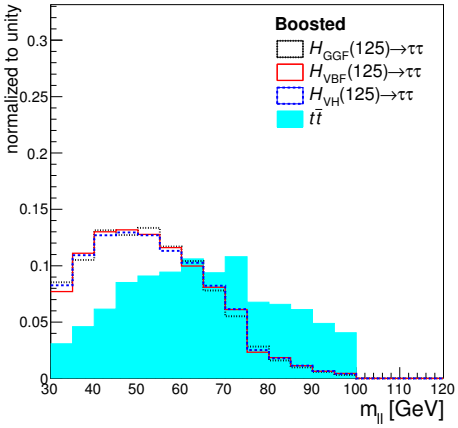

(d)

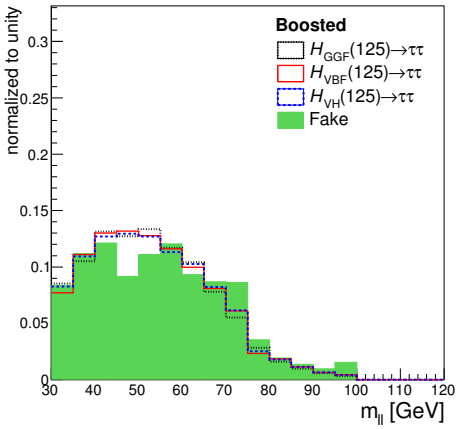

(e)

Figure A.27. *Distribution of $m_{\ell\ell}$ in the Boosted category. Comparison of different signal modes to each background source respectively.*

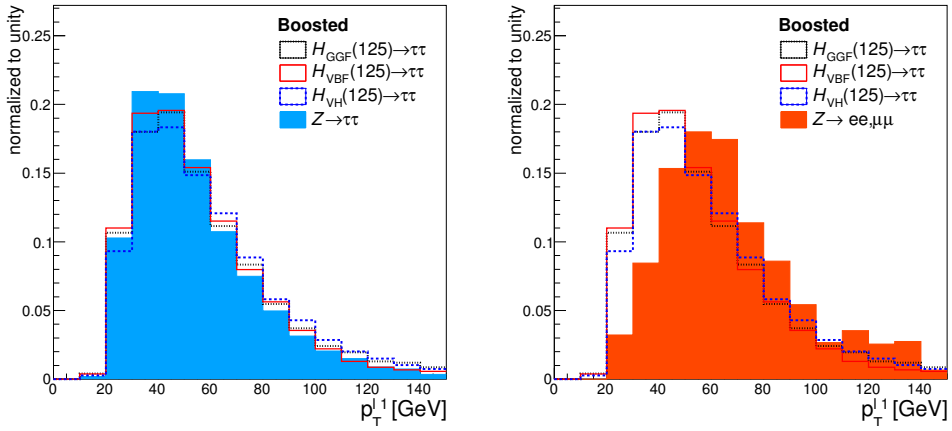

(a)

(b)

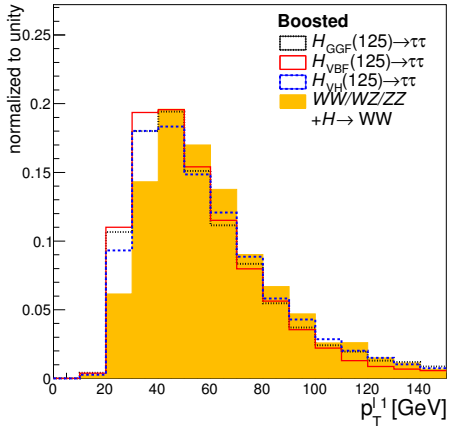

(c)

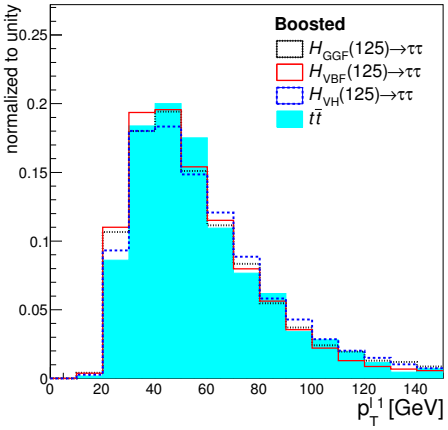

(d)

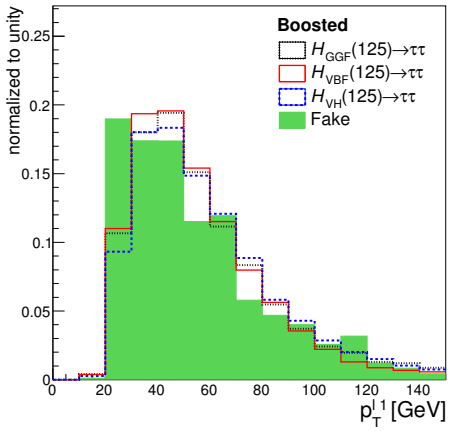

(e)

Figure A.28. *Distribution of $p_T^{\ell_1}$ in the Boosted category. Comparison of different signal modes to each background source respectively.*

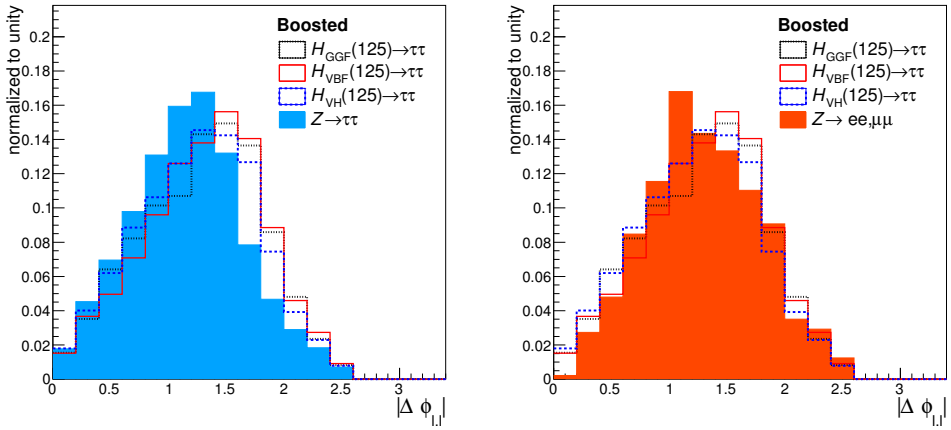

(a)

(b)

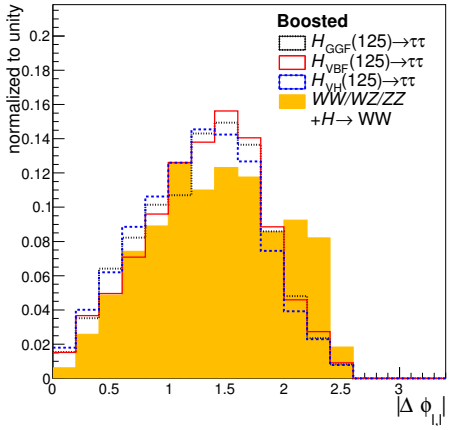

(c)

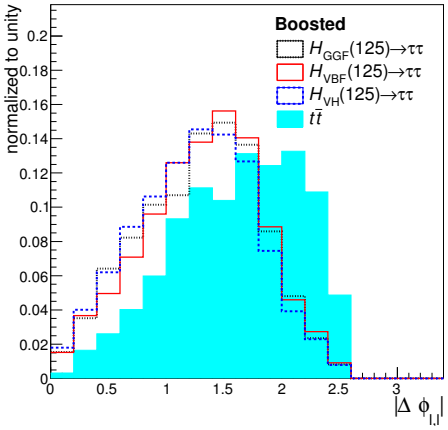

(d)

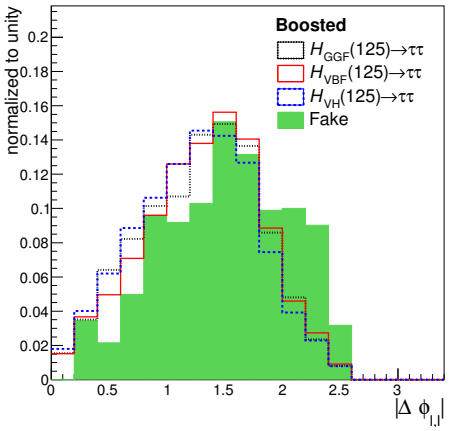

(e)

Figure A.29. *Distribution of $\Delta\phi(\ell_1, \ell_2)$ in the Boosted category. Comparison of different signal modes to each background source respectively.*

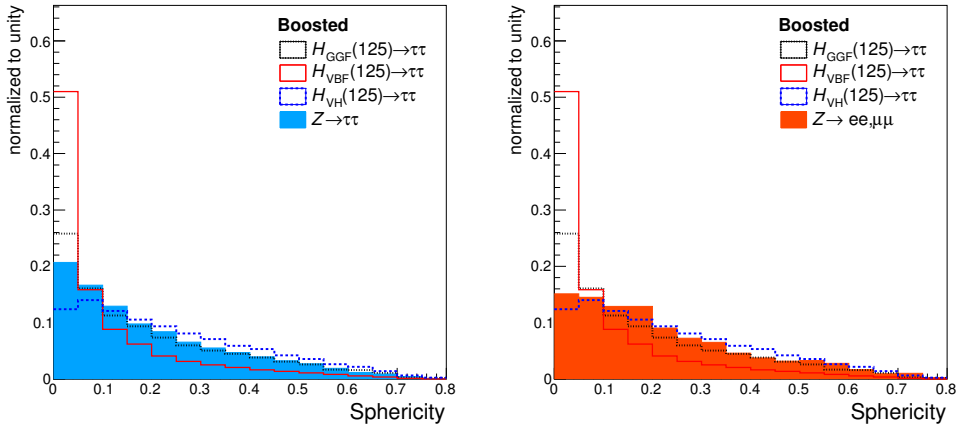

(a)

(b)

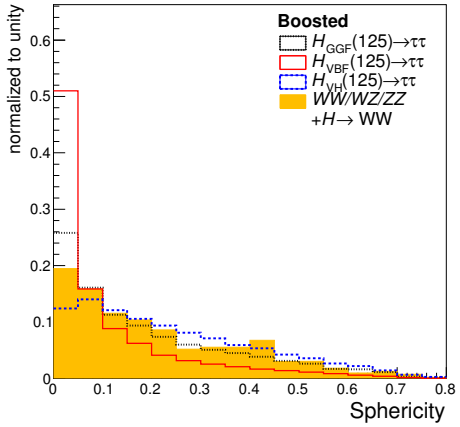

(c)

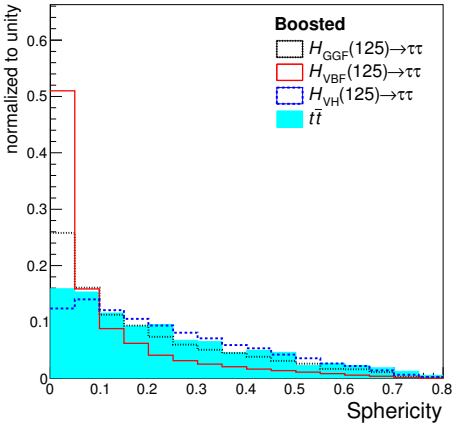

(d)

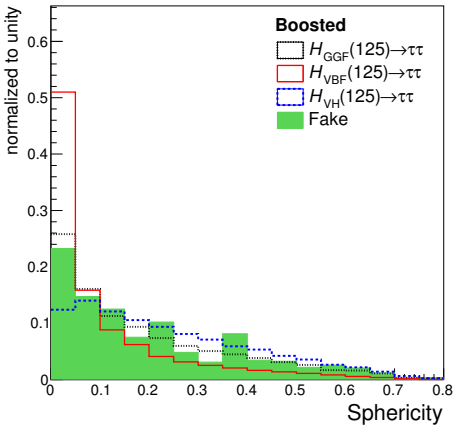

(e)

Figure A.30. *Distribution of the Sphericity in the Boosted category. Comparison of different signal modes to each background source respectively.*

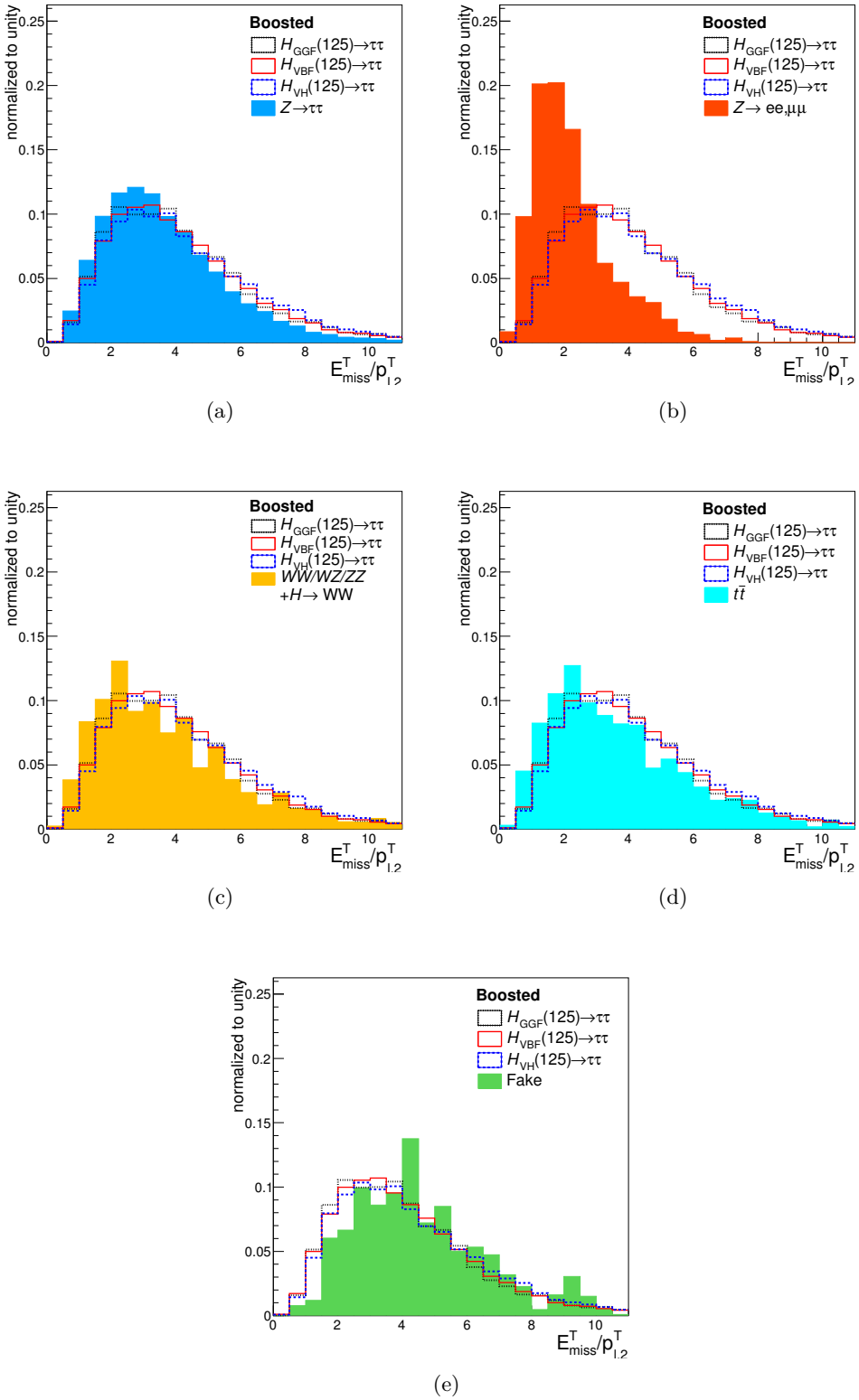

Figure A.31. *Distribution of $E_{\mathrm{T}}^{\mathrm{miss}}/p_{\mathrm{T}}^{\ell_2}$ in the Boosted category. Comparison of different signal modes to each background source respectively.*

A.3. BDT classifier

This section contains auxiliary distributions of the BDT classifiers in the VBF and the Boosted category of the search for the Standard Model Higgs boson in the fully leptonic decay $H \to \tau^+\tau^- \to \ell^+\ell^- 4\nu$. Each background component is compared to the individual signal production modes for both BDT classifiers. The comparisons highlight the separating power of the BDTs between signal and background. Signal-like events are accumulated at high values of the BDT classifier and background-like at low values.

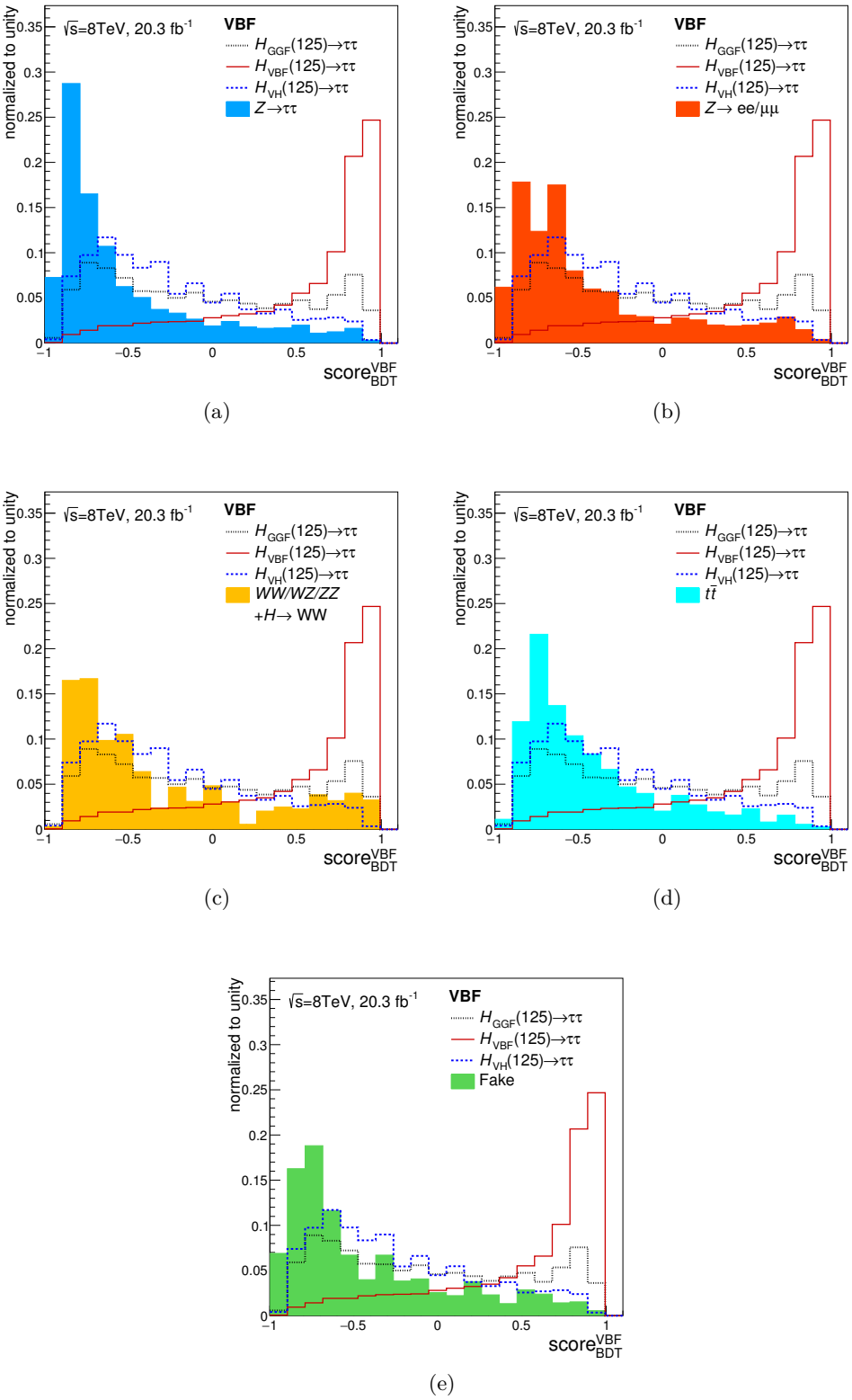

Figure A.32. *Distribution of the BDT classifier in the VBF category. Comparison of different signal modes to each background source respectively.*

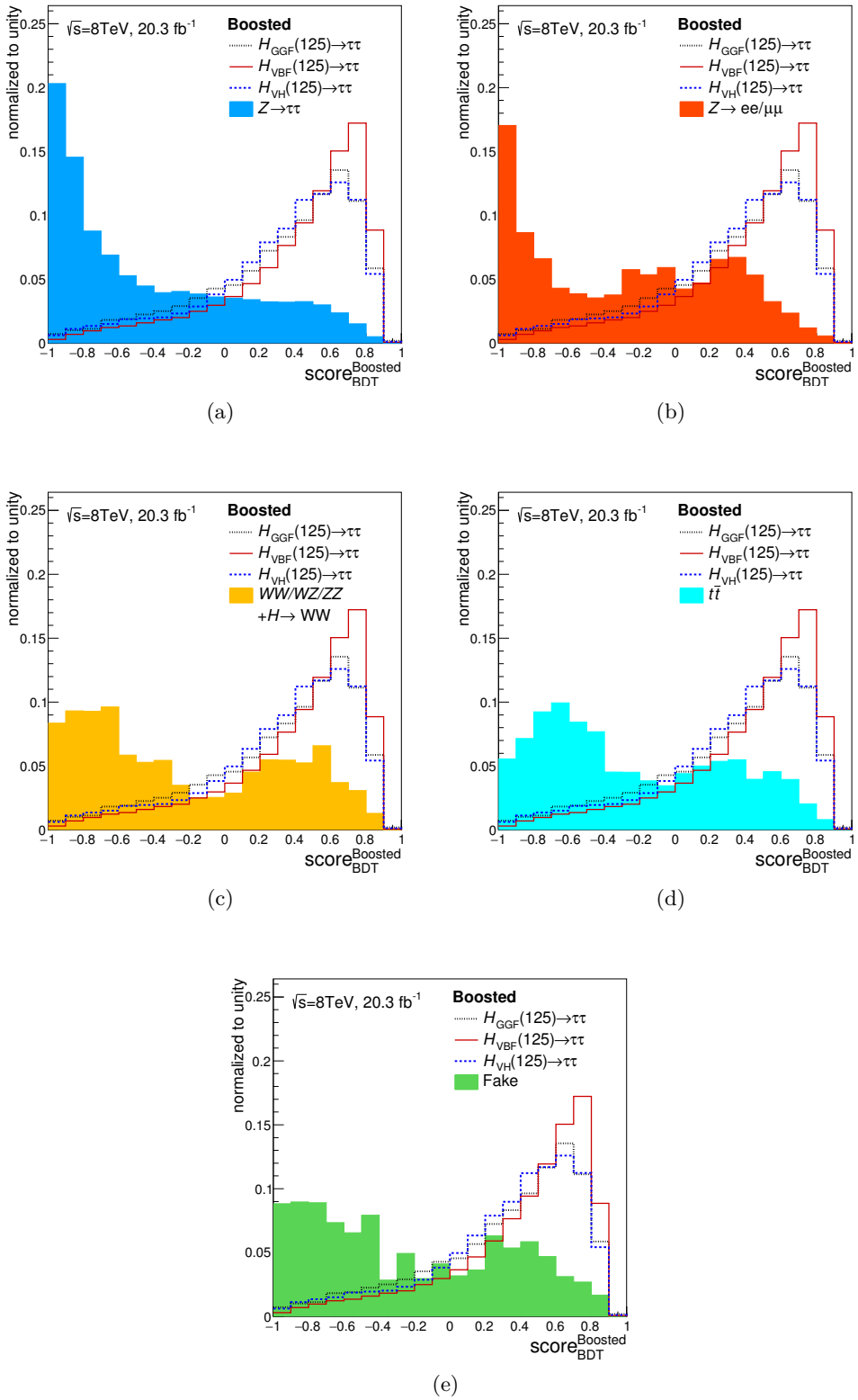

Figure A.33. *Distribution of the BDT classifier in the Boosted category. Comparison of different signal modes to each background source respectively.*

A.4. Optimal Observable

This section contains auxiliary distributions of the Optimal Observable in the signal region and the low BDT control region of the CP analysis in the decay $H \to \tau^+\tau^- \to \ell^+\ell^- 4\nu$. Each background component is compared to the pure Standard Model signal and a CP-mixing signal with a $\tilde{d}$ parameter of $+0.5$. The comparisons highlight the separating power of the Optimal Observable between Standard Model processes and CP-mixing signal. Standard Model processes have a mean value centered at an optimal Observable value of zero, while signal-like events are accumulated at higher values. The signal consists of (VBF)$H \to \tau^+\tau^-/W^+W^-$.

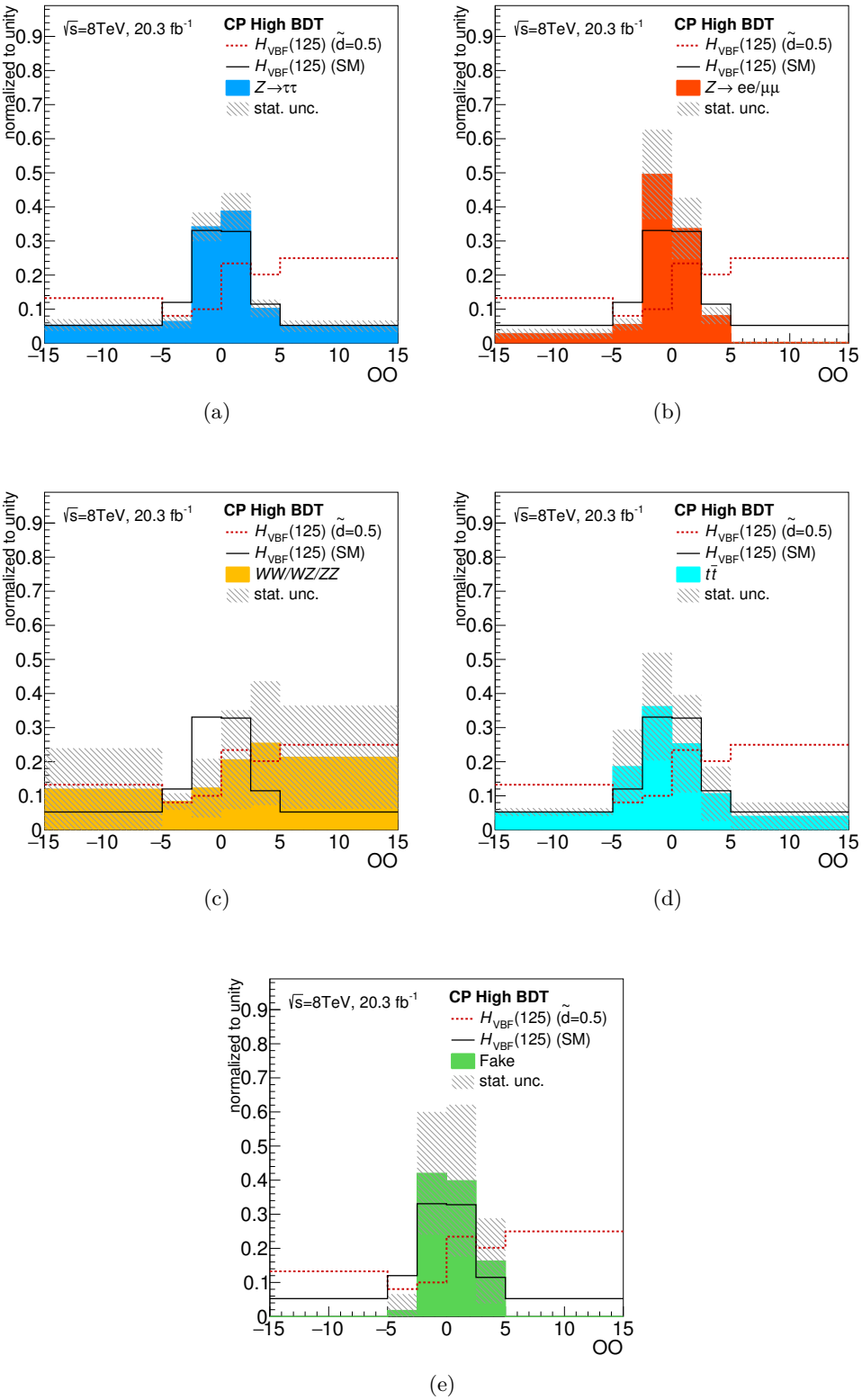

Figure A.34. *Distribution of the Optimal Observable in the high BDT signal region of the CP analysis. Comparison of different signal modes to each background source respectively.*

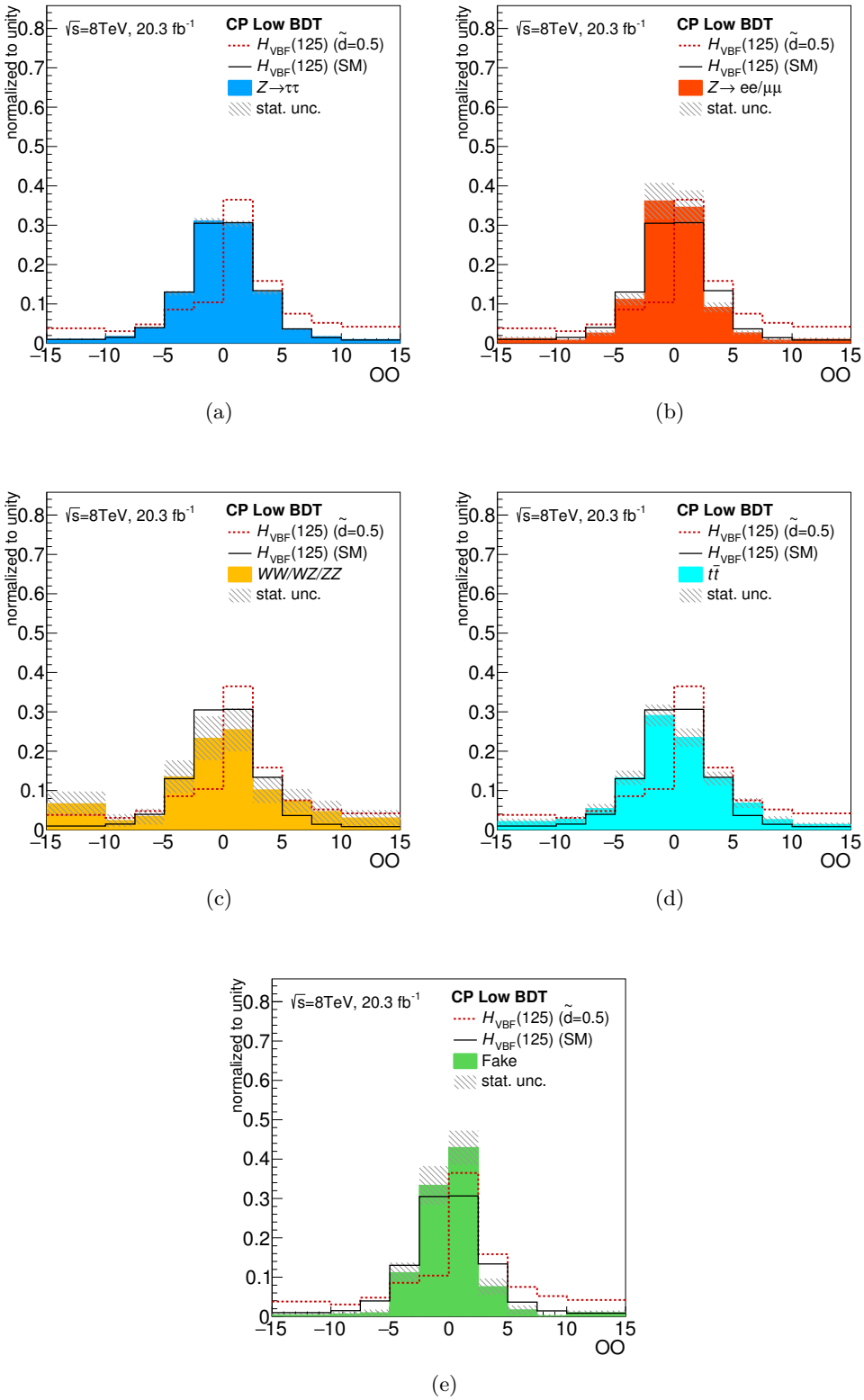

Figure A.35. *Distribution of the Optimal Observable in the low BDT control region of the CP analysis. Comparison of different signal modes to each background source respectively.*

B Fit Model

This section presents additional information about the fitmodel of the analysis of the search for $H \to \tau^+\tau^- \to \ell^+\ell^- 4\nu$ (see chapter 5) and the corresponding CP analysis (see chapter 6). Details about the statistical analysis can be found in chapter 9.

The full list of nuisance parameters, that are used in the fit models of both analyses, are summarized in table B.1 and B.2 including short parameter explanations. The impact of each nuisance parameter on the best-fit signal strength is shown in figure B.1 for the search for $H \to \tau^+\tau^- \to \ell^+\ell^- 4\nu$ and in figure B.2 and B.3 for the CP analysis fitting $\tilde{d}$=0.0 and $\tilde{d}$=0.1 signal. The upper x-axis shows the relative impact of postfit $\pm 1\sigma$ variations of single nuisance parameters on the best-fit signal strength $\hat{\mu}$ with respect to its total uncertainty. The nuisance parameters are ranked in decreasing order depending on the size if the variation of $\hat{\mu}$. The lower x-axis shows relative postfit shifts of the single nuisance parameters with respect to its initial value and the postfit uncertainty on the parameter. The complete information about the correlations of the nuisance parameters across the regions of the analyses are listed in the tables starting from B.3 for the search analysis and from B.15 for the CP analysis. Only the normalization and shape uncertainties are used in the fit that survive the pruning criteria.

NP	Description
Experimental	
LUMI	Luminosity
TRIG_LL_SF	Trigger efficiency
EL_EFF	Electron reconstruction and identification efficiency
JVF	Jet-Vertex-Fraction selection efficiency
MU_EFF_2012	Muon reconstruction and identification efficiency
BTag_B1-10	b-tagging efficiency b jets
BTag_C1-4	b-tagging efficiency c jets
BTag_L1-12	b-tagging efficiency light quark jets
BTag_T1-4	b-tagging efficiency hadronic τ jets
BCH_LL_bv	Masked modules in tile calorimeter
MUID_RES	Muon momentum resolution inner detector
MUMS_RES	Muon momentum resolution muon spectrometer
MU_SCALE	Muon momentum scale
EL_RES	Electron energy resolution
EL_SCALE	Electron energy scale
JER	Jet energy resolutiion
JES_Detector1-3	Jet energy scale, detector components
JES_Modelling1-4	Jet energy scale, modeling components
JES_Mixed1-2	Jet energy scale, mixed components
JES_Statistical1-3	Jet energy scale, statistical components
JES_Eta_Modelling_LL	Jet energy scale, intercalibration η dependence, modeling component
JES_2012_Eta_StatMethod	Jet energy scale, intercalibration η dependence, statistical component
JES_FlavResp	Jet energy scale, calorimeter response jet flavor dependence
JES_FlavComp_TAU_G/Q	Jet energy scale, jet flavor composition
JES_Flavb	Jet energy scale, b jet specific dependence
JES_PilePt	Jet energy scale, pile-up dependence, p_T^j component
JES_PileRho_TAU_GG/QG/QQ	Jet energy scale, pile-up dependence, jet topology component
JES_Mu	Jet energy scale, pile-up dependent, no. of average int. per bunch-crossing
JES_NPV	Pile-up dependent jet energy scale, no. of primary vertices
MET_RESOSOFT	Soft term $E_{\mathrm{T}}^{\mathrm{miss}}$ resolution
MET_SCALESOFT	Soft term $E_{\mathrm{T}}^{\mathrm{miss}}$ energy scale

Table B.1. *Summary and short explanation of the nuisance parameters representing systematic uncertainties and normalization factors in the present analyses. Details about the sources of uncertainties can be found in chapter 8. Q or G denotes quark or gluon initiated processes.*

NP	Description
Theory	
QCDscale_qqH	Missing higher orders, QCD scale of VBF Higgs boson processes
QCDscale_VH	Missing higher orders, QCD scale of VH Higgs boson processes
QCDscale_ggH_m12/BDT	Missing higher orders, QCD scale of ggH Higgs boson processes in VBF+Boosted category / CP analysis
QCDscale_ggH_ptH_m01	Missing higher orders, QCD scale of ggH Higgs boson processes, Boosted category
QCDscale_ggH_m23	Missing higher orders, QCD scale of ggH Higgs boson processes, third jet veto
NLO_EW_Higg	Missing higher orders, NLO electroweak correction of VBF Higgs boson processes
BR_tautau	Branching ratio $H \to \tau^+\tau^-$
BR_WW	Branching ratio $H \to W^+W^-$
pdf_Higgs_gg/qq	PDF parametrization, cross-section, VBF+VH/GGF Higgs boson processes
pdf_Higgs_gg/qq_ACCEPT	PDF parametrization, acceptance, VBF+VH/GGF Higgs boson processes
Matching_ACCEPT	Event generator choice, VBF+GGF Higgs boson processes
UE_gg/qq(_BDT)	Underlying event, VBF+VH/GGF Higgs boson processes in VBF+Boosted category (CP analysis)
Signal & Background Estimation	
ANA_EMB_ISOL	Embedding method, muon isolation
ANA_EMB_MFS	Embedding method, calorimeter cell subtraction
ANA_LL_Ztt_bv	Embedding method, trigger emulation
ANA_LL_Top_vbf/boost	Top quark background, control to signal region extrapolation, VBF/Boosted category
ANA_LL_Zll_vbf/boost	$Z/\gamma^* \to e^+e^-/\mu^+\mu^-$ background, control to signal region extrapolation, VBF/Boosted category
ANA_LL_Zll_vbf_DETAJJ	$Z/\gamma^* \to e^+e^-/\mu^+\mu^-$ background, $\Delta\eta(j_1, j_2)$ dependent re-weighting
ANA_LL_Fake_bv	Fake lepton background, template normalization
ANA_LL_Fake_bv_SH	Fake lepton background, template shape
REWEIGHT	CP analysis specific signal re-weighting of SM VBF Higgs boson samples
Normalization	
μ	Signal strentgh
norm_LL_Ztt_bv/cp	$Z/\gamma^* \to \tau^+\tau^-$ sample norm. parameter for the VBF+Boosted/CP analysis
norm_LL_Top_vbf/boost/cp	Top quark sample norm parameter for VBF/Boosted/CP
norm_LL_Zll_vbf/boost/cp	$Z/\gamma^* \to e^+e^-/\mu^+\mu^-$ sample norm parameter for VBF/Boosted/CP

Table B.2. *Summary and short explanation of the nuisance parameters representing systematic uncertainties and normalization factors in the present analyses. Details about the sources of uncertainties can be found in chapter 8. Q or G denotes quark or gluon initiated processes.*

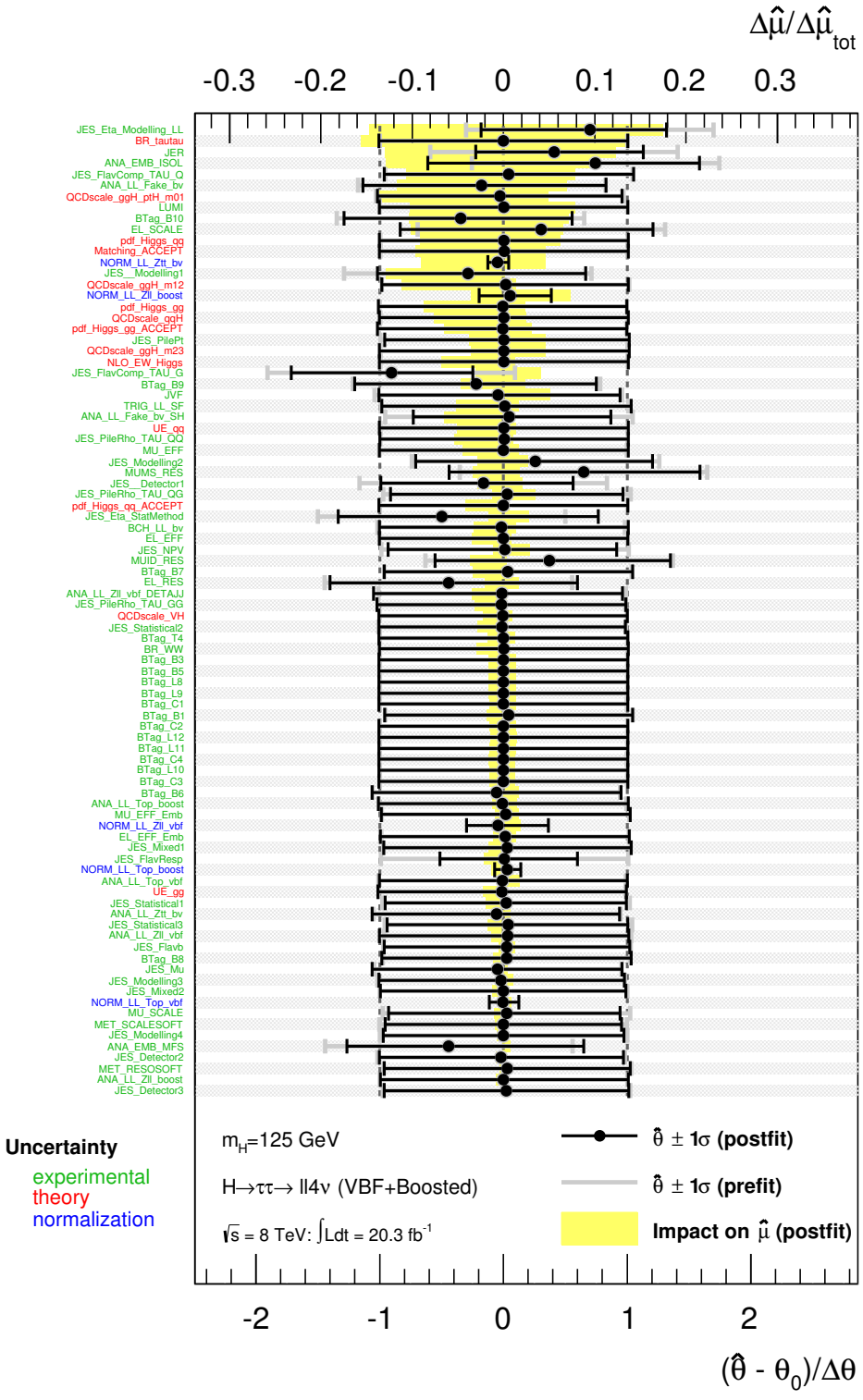

Figure B.1. *Postfit pulls and constraints of nuisance parameters from the combined fit of the VBF and Boosted category (lower x-axis). Impact of nuisance parameters on best fit signal strength (upper x-axis). Nuisance parameter importance ranking with respect to the impact on the signal strength (y-axis top-down). Normalization factors are unconstrained in the fit and the error bars reflect absolute uncertainties.*

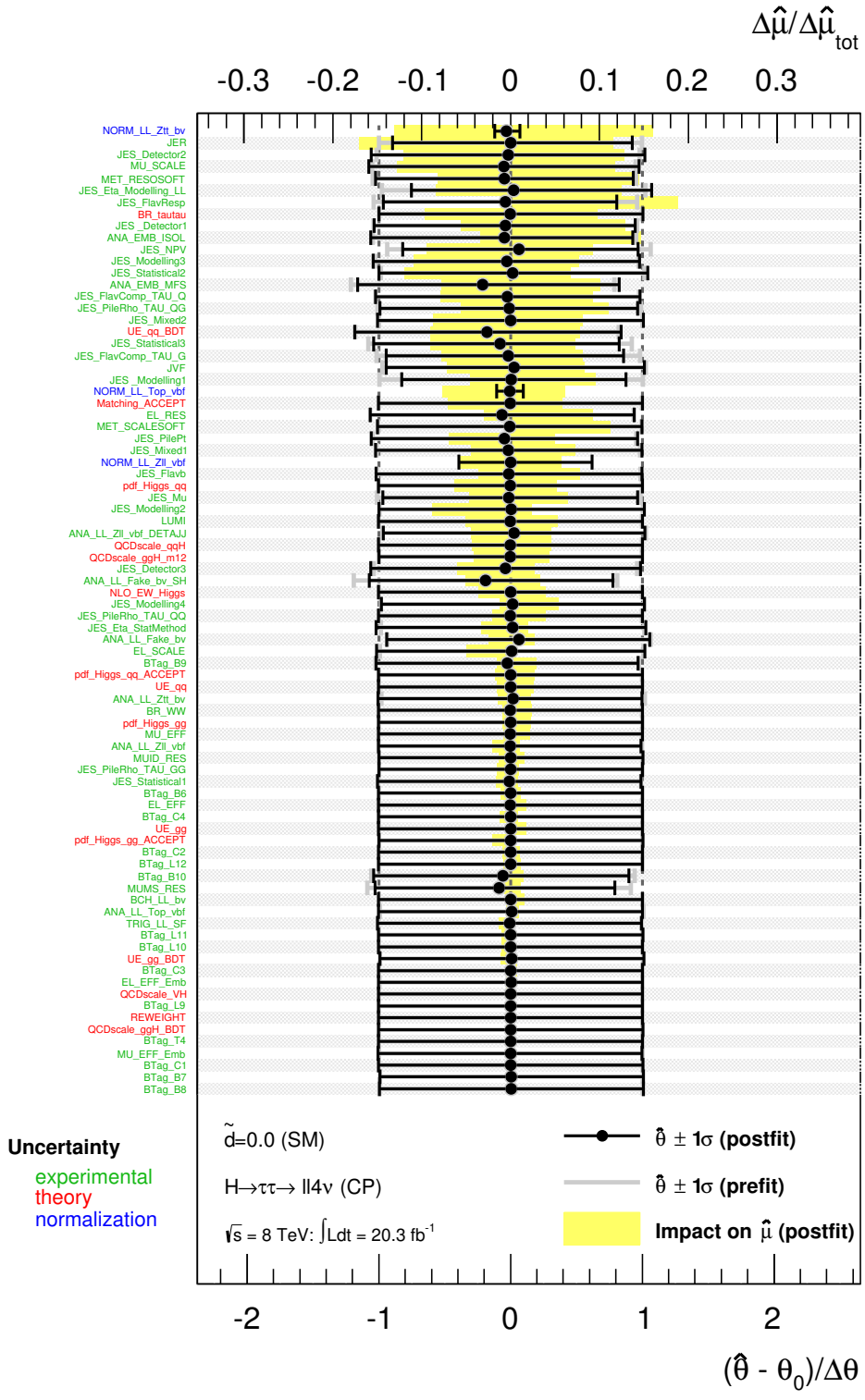

Figure B.2. *Postfit pulls and constraints of nuisance parameters from the fit of $\tilde{d}$=0.0 signal in the CP analysis (lower x-axis). Impact of nuisance parameters on best fit signal strength (upper x-axis). Nuisance parameter importance ranking with respect to the impact on the signal strength (y-axis top-down). Normalization factors are unconstrained in the fit and the error bars reflect absolute uncertainties.*

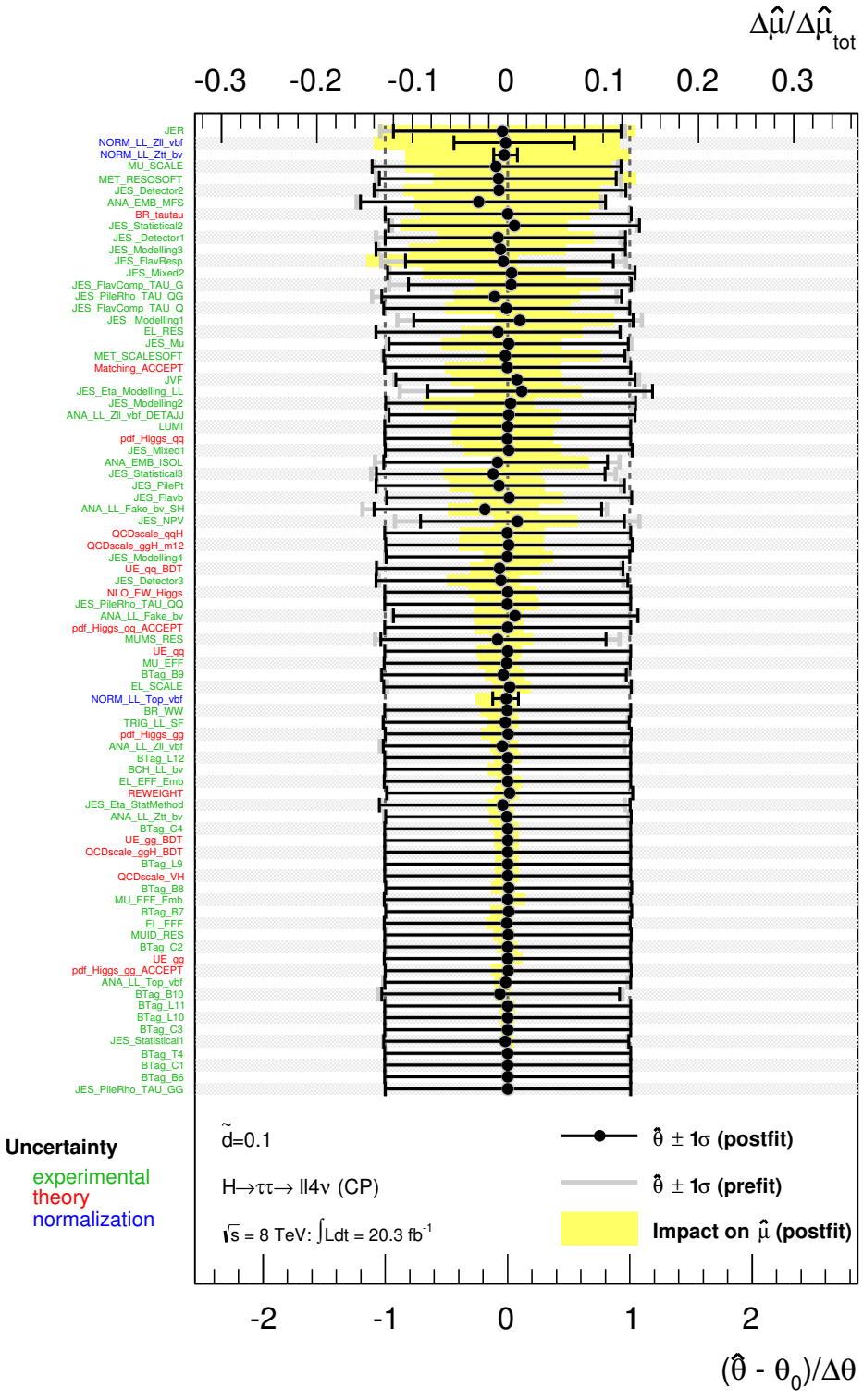

Figure B.3. *Postfit pulls and constraints of nuisance parameters from the fit of $\tilde{d}$=0.1 signal in the CP analysis (lower x-axis). Impact of nuisance parameters on best fit signal strength (upper x-axis). Nuisance parameter importance ranking with respect to the impact on the signal strength (y-axis top-down). Normalization factors are unconstrained in the fit and the error bars reflect absolute uncertainties.*

No	NP	VBF$H \to \tau^+\tau^-$	GGF$H \to \tau^+\tau^-$	W$H \to \tau^+\tau^-$	Z$H \to \tau^+\tau^-$
1	ANA_EMB_ISOL				
2	ANA_EMB_MFS				
3	ANA_LL_Fake_bv				
4	ANA_LL_Fake_bv_SH				
5	ANA_LL_Top_boost				
6	ANA_LL_Top_vbf				
7	ANA_LL_Zll_boost				
8	ANA_LL_Zll_vbf				
9	ANA_LL_Zll_vbf_DETAJJ				
10	ANA_LL_Ztt_bv				
11	BCH_LL_bv	$\mathrm{v}^n\mathrm{v}_t^n\mathrm{v}_z^n\ \mathrm{b}^n\mathrm{b}_t^n\mathrm{b}_z^n$	$\mathrm{v}^n\mathrm{v}_t^n\mathrm{v}_z^n\ \mathrm{b}^n\mathrm{b}_t^n\mathrm{b}_z^n$	$\mathrm{v}^n\mathrm{v}_t^n\mathrm{v}_z^n\ \mathrm{b}^n\mathrm{b}_t^n\mathrm{b}_z^n$	$\mathrm{v}^n\mathrm{v}_t^n\mathrm{v}_z^n\ \mathrm{b}^n\mathrm{b}_t^n\mathrm{b}_z^n$
12	BR_WW				
13	BR_tautau	$\mathrm{v}^n\mathrm{v}_t^n\mathrm{v}_z^n\ \mathrm{b}^n\mathrm{b}_t^n\mathrm{b}_z^n$	$\mathrm{v}^n\mathrm{v}_t^n\mathrm{v}_z^n\ \mathrm{b}^n\mathrm{b}_t^n\mathrm{b}_z^n$	$\mathrm{v}^n\mathrm{v}_t^n\mathrm{v}_z^n\ \mathrm{b}^n\mathrm{b}_t^n\mathrm{b}_z^n$	$\mathrm{v}^n\mathrm{v}_t^n\mathrm{v}_z^n\ \mathrm{b}^n\mathrm{b}_t^n\mathrm{b}_z^n$
14	BTag_B10	$\mathrm{v}_t^n\ \mathrm{b}_t^n$	$\mathrm{v}_t^n\ \mathrm{b}_t^n$		$\mathrm{v}^n\mathrm{v}_t^n\ \mathrm{b}_t^n$
15	BTag_B1		$\mathrm{v}_t^n\ \mathrm{b}_t^n$		b_t^n
16	BTag_B3				
17	BTag_B5				
18	BTag_B6				
19	BTag_B7				v_t^n
20	BTag_B8				
21	BTag_B9		b_t^n		$\mathrm{v}_t^n\ \mathrm{b}_t^n$
22	BTag_C1	$\mathrm{v}_t^n\ \mathrm{b}_t^n$	$\mathrm{v}_t^n\ \mathrm{b}_t^n$	$\mathrm{v}_t^n\ \mathrm{b}_t^n$	b_t^n
23	BTag_C2	$\mathrm{v}_t^n\ \mathrm{b}_t^n$	$\mathrm{v}_t^n\ \mathrm{b}_t^n$	$\mathrm{v}_t^n\ \mathrm{b}_t^n$	$\mathrm{v}_t^n\ \mathrm{b}_t^n$
24	BTag_C3	$\mathrm{v}_t^n\ \mathrm{b}_t^n$	$\mathrm{v}_t^n\ \mathrm{b}_t^n$	$\mathrm{v}_t^n\ \mathrm{b}_t^n$	b_t^n
25	BTag_C4	$\mathrm{v}_t^n\ \mathrm{b}_t^n$	$\mathrm{v}_t^n\ \mathrm{b}_t^n$	$\mathrm{v}_t^n\ \mathrm{b}^n\mathrm{b}_t^n\mathrm{b}_z^n$	$\mathrm{v}_t^n\ \mathrm{b}_t^n\mathrm{b}_z^n$
26	BTag_L10	$\mathrm{v}_t^n\ \mathrm{b}_t^n$	$\mathrm{v}_t^n\ \mathrm{b}_t^n$	b_t^n	
27	BTag_L11	$\mathrm{v}_t^n\ \mathrm{b}_t^n$	$\mathrm{v}_t^n\ \mathrm{b}_t^n$	$\mathrm{v}_t^n\ \mathrm{b}_t^n$	
28	BTag_L12	$\mathrm{v}_t^n\ \mathrm{b}_t^n$	$\mathrm{v}_t^n\ \mathrm{b}_t^n$	$\mathrm{v}_t^n\mathrm{v}_z^n\ \mathrm{b}_t^n$	$\mathrm{v}_t^n\ \mathrm{b}_t^n$
29	BTag_L8				
30	BTag_L9			v_t^n	
31	BTag_T4				

Table B.3. *Nuisance parameter (NP) correlations in the analysis of the search for $H \to \tau^+\tau^- \to \ell^+\ell^- 4\nu$ across the categories VBF/Boosted signal regions (v/b) using the BDT classifier distribution and the single bin top quark enriched (v_t/b_t) and $Z \to ee/\mu\mu$ enriched control regions (v_z/b_z). The superscript denotes if the NP is included as normalization (n) and/or shape uncertainty (s) in the specific region.*

No	NP	VBF$H \to \tau^+\tau^-$	GGF$H \to \tau^+\tau^-$	W$H \to \tau^+\tau^-$	Z$H \to \tau^+\tau^-$
32	EL_EFF	$v^n v_t^n v_z^n$ $b^n b_t^n b_z^n$	$v^n v_t^n v_z^n$ $b^n b_t^n b_z^n$	$v^n v_t^n v_z^n$ $b^n b_t^n b_z^n$	$v^n v_t^n$ $b^n b_t^n b_z^n$
33	EL_EFF_Emb				
34	EL_RES	v_z^n	$v_t^n v_z^n$ b_z^n	v_t^n b_z^n	b_z^n
35	EL_SCALE	v_z^n b^s b_z^n	$v_t^n v_z^n$ $b^s b_t^n b_z^n$	$v^n v_t^n v_z^n$ $b_t^n b_z^n$	$v^n v_t^n$ $b^s b_t^n b_z^n$
36	JER	$v^{sn} v_t^n v_z^n$ $b^s b_t^n b_z^n$	$v^n v_t^n v_z^n$ $b^{sn} b_t^n b_z^n$	$v^{sn} v_t^n v_z^n$ b^{sn} b_z^n	$v^{sn} v_t^n v_z^n$ b^s b_z^n
37	JES_Detector1	$v^{sn} v_t^n v_z^n$ $b^{sn} b_t^n b_z^n$	$v^{sn} v_t^n v_z^n$ $b^{sn} b_t^n b_z^n$	$v^{sn} v_t^n$ $b^{sn} b_t^n b_z^n$	$v^{sn} v_t^n v_z^n$ $b^{sn} b_t^n b_z^n$
38	JES_Modelling1	$v^{sn} v_t^n v_z^n$ $b^{sn} b_t^n b_z^n$	$v^{sn} v_t^n v_z^n$ $b^{sn} b_t^n b_z^n$	$v^{sn} v_t^n v_z^n$ $b^{sn} b_t^n b_z^n$	$v^{sn} v_t^n v_z^n$ $b^{sn} b_t^n b_z^n$
39	JES_Detector2	v_z^n b_z^n	b_z^n	v_t^n b_z^n	b^s
40	JES_Detector3	v^s v_z^n b_z^n	b_z^n	$v^n v_t^n$ b_z^n	v^n b^s b_z^n
41	JES_Eta_StatMethod	$v^{sn} v_t^n v_z^n$ $b_t^n b_z^n$	$v^n v_t^n$ b^n b_z^n	$v^{sn} v_t^n$ $b^n b_t^n b_z^n$	$v^n v_t^n$ $b^n b_t^n b_z^n$
42	JES_Mixed1	v_z^n	b_z^n	b_z^n	v^n b^s
43	JES_Mixed2	b_z^n	b^s	$v^n v_t^n$ b_z^n	v_t^n b_z^n
44	JES_Modelling2	v_z^n b_z^n	b_z^n	$v^n v_t^n$ b^s	$v_t^n v_z^n$
45	JES_Modelling3	v_z^n		v_t^n b_z^n	$b^s b_t^n b_z^n$
46	JES_Modelling4	v_z^n	b_z^n	$v^n v_t^n$ b_z^n	
47	JES_PilePt	v^s v_z^n b_z^n	v_t^n $b_t^n b_z^n$	v_t^n b_z^n	b^s b_z^n
48	JES_PileRho_TAU_GG		$v^n v_t^n v_z^n$ $b^{sn} b_t^n b_z^n$		
49	JES_PileRho_TAU_QG				
50	JES_PileRho_TAU_QQ	$v^n v_t^n v_z^n$ $b^s b_t^n b_z^n$		$v^{sn} v_t^n$ $b^{sn} b_t^n b_z^n$	v^n v_z^n $b^{sn} b_t^n b_z^n$
51	JES_Statistical1	$v_t^n v_z^n$ b_t^n	$v^n v_t^n$ b^s b_z^n	$v^n v_t^n$ $b_t^n b_z^n$	$v^n v_t^n$ $b^s b_t^n b_z^n$
52	JES_Statistical2	v^s		v_t^n b_z^n	b^s b_z^n
53	JES_Statistical3	v_z^n $b_t^n b_z^n$	v_t^n b_z^n	$v^n v_t^n$ b_z^n	v_t^n $b^n b_t^n b_z^n$
54	JES_Eta_Modelling_LL	$v^{sn} v_t^n v_z^n$ $b^s b_t^n b_z^n$	$v^{sn} v_t^n v_z^n$ $b^{sn} b_t^n b_z^n$	$v^{sn} v_t^n v_z^n$ $b^{sn} b_t^n b_z^n$	$v^{sn} v_t^n v_z^n$ $b^{sn} b_t^n b_z^n$
55	JES_FlavComp_TAU_G		$v^{sn} v_t^n v_z^n$ $b^{sn} b_t^n b_z^n$		
56	JES_FlavComp_TAU_Q	$v^{sn} v_t^n v_z^n$ $b^{sn} b_t^n b_z^n$		$v^{sn} v_t^n v_z^n$ $b^{sn} b_t^n b_z^n$	$v^{sn} v_t^n v_z^n$ $b^{sn} b_t^n b_z^n$
57	JES_FlavResp	$v^{sn} v_t^n v_z^n$ $b^{sn} b_t^n b_z^n$	$v^n v_t^n v_z^n$ $b^{sn} b_t^n b_z^n$	$v^{sn} v_t^n v_z^n$ $b^{sn} b_t^n b_z^n$	$v^{sn} v_t^n v_z^n$ $b^{sn} b_t^n b_z^n$
58	JES_Flavb		v_t^n b_t^n	v_t^n	v_t^n $b_t^n b_z^n$
59	JES_Mu	$v^s v_t^n v_z^n$ b_t^n	$v^n v_t^n v_z^n$ b_z^n	$v^n v_t^n$ b_z^n	v^n v_z^n b_z^n
60	JES_NPV	$v^{sn} v_t^n v_z^n$ $b_t^n b_z^n$	$v^n v_t^n v_z^n$ $b^s b_t^n b_z^n$	$v^{sn} v_t^n$ b^{sn} b_z^n	$v^{sn} v_t^n v_z^n$ $b^{sn} b_t^n b_z^n$
61	JVF	$v_t^n v_z^n$ b_t^n	$v^n v_t^n$ b_z^n	$v^n v_t^n$ $b_t^n b_z^n$	$v^n v_t^n v_z^n$

Table B.4. *Nuisance parameter (NP) correlations in the analysis of the search for $H \to \tau^+\tau^- \to \ell^+\ell^- 4\nu$ across the categories VBF/Boosted signal regions (v/b) using the BDT classifier distribution and the single bin top quark enriched (v_t/b_t) and $Z \to ee/\mu\mu$ enriched control regions (v_z/b_z). The superscript denotes if the NP is included as normalization (n) and/or shape uncertainty (s) in the specific region.*

No	NP	VBF$H \to \tau^+\tau^-$	GGF$H \to \tau^+\tau^-$	W$H \to \tau^+\tau^-$	Z$H \to \tau^+\tau^-$
62	LUMI	$\mathrm{v}^n\mathrm{v}_t^n\mathrm{v}_z^n$ $\mathrm{b}^n\mathrm{b}_t^n\mathrm{b}_z^n$	$\mathrm{v}^n\mathrm{v}_t^n\mathrm{v}_z^n$ $\mathrm{b}^n\mathrm{b}_t^n\mathrm{b}_z^n$	$\mathrm{v}^n\mathrm{v}_t^n\mathrm{v}_z^n$ $\mathrm{b}^n\mathrm{b}_t^n\mathrm{b}_z^n$	$\mathrm{v}^n\mathrm{v}_t^n\mathrm{v}_z^n$ $\mathrm{b}^n\mathrm{b}_t^n\mathrm{b}_z^n$
63	MET_RESOSOFT	v_z^n b_z^n	v_t^n b^s b_z^n	v_t^n b^s	$\mathrm{v}^n\mathrm{v}_t^n$ b^s b_z^n
64	MET_SCALESOFT	v_z^n b^s b_z^n	v^n	b^s b_z^n	$\mathrm{v}^n\mathrm{v}_t^n$ b^s b_z^n
65	MUID_RES	b_z^n	v_z^n	b_z^n	b_z^n
66	MUMS_RES	v_z^n	v_z^n b_z^n	v_z^n b_z^n	v_z^n b^s
67	MU_EFF	$\mathrm{v}^n\mathrm{v}_t^n\mathrm{v}_z^n$ $\mathrm{b}^n\mathrm{b}_t^n\mathrm{b}_z^n$	$\mathrm{v}^n\mathrm{v}_t^n\mathrm{v}_z^n$ $\mathrm{b}^n\mathrm{b}_t^n\mathrm{b}_z^n$	$\mathrm{v}^n\mathrm{v}_t^n\mathrm{v}_z^n$ $\mathrm{b}^n\mathrm{b}_t^n\mathrm{b}_z^n$	$\mathrm{v}^n\mathrm{v}_t^n\mathrm{v}_z^n$ $\mathrm{b}^n\mathrm{b}_t^n\mathrm{b}_z^n$
68	MU_EFF_Emb				
69	MU_SCALE	b^s b_z^n	v_z^n b^s b_z^n	v_z^n	b^s b_z^n
70	Matching_ACCEPT	$\mathrm{v}^n\mathrm{v}_t^n\mathrm{v}_z^n$			
71	TRIG_LL_SF	$\mathrm{v}^n\mathrm{v}_t^n\mathrm{v}_z^n$ $\mathrm{b}^n\mathrm{b}_t^n\mathrm{b}_z^n$	$\mathrm{v}^n\mathrm{v}_t^n\mathrm{v}_z^n$ $\mathrm{b}^n\mathrm{b}_t^n\mathrm{b}_z^n$	$\mathrm{v}^n\mathrm{v}_t^n\mathrm{v}_z^n$ $\mathrm{b}^n\mathrm{b}_t^n\mathrm{b}_z^n$	$\mathrm{v}^n\mathrm{v}_t^n\mathrm{v}_z^n$ $\mathrm{b}^n\mathrm{b}_t^n\mathrm{b}_z^n$
72	UE_gg		$\mathrm{v}^n\mathrm{v}_t^n\mathrm{v}_z^n$ $\mathrm{b}^n\mathrm{b}_t^n\mathrm{b}_z^n$		
73	UE_qq	$\mathrm{v}^n\mathrm{v}_t^n\mathrm{v}_z^n$ $\mathrm{b}^n\mathrm{b}_t^n\mathrm{b}_z^n$			
74	NLO_EW_Higgs	$\mathrm{v}^n\mathrm{v}_t^n\mathrm{v}_z^n$ $\mathrm{b}^n\mathrm{b}_t^n\mathrm{b}_z^n$			
75	QCDscale_VH			$\mathrm{v}^n\mathrm{v}_t^n\mathrm{v}_z^n$ $\mathrm{b}^n\mathrm{b}_t^n\mathrm{b}_z^n$	$\mathrm{v}^n\mathrm{v}_t^n\mathrm{v}_z^n$ $\mathrm{b}^n\mathrm{b}_t^n\mathrm{b}_z^n$
76	QCDscale_ggH_m12		$\mathrm{v}^n\mathrm{v}_t^n\mathrm{v}_z^n$ $\mathrm{b}^n\mathrm{b}_t^n\mathrm{b}_z^n$		
77	QCDscale_ggH_m23		v^s		
78	QCDscale_ggH_ptH_m01		$\mathrm{b}^n\mathrm{b}_t^n\mathrm{b}_z^n$		
79	QCDscale_qqH	$\mathrm{v}^n\mathrm{v}_t^n\mathrm{v}_z^n$ $\mathrm{b}^n\mathrm{b}_t^n\mathrm{b}_z^n$			
80	pdf_Higgs_gg		$\mathrm{v}^n\mathrm{v}_t^n\mathrm{v}_z^n$ $\mathrm{b}^n\mathrm{b}_t^n\mathrm{b}_z^n$		
81	pdf_Higgs_gg_ACCEPT		$\mathrm{v}^n\mathrm{v}_t^n\mathrm{v}_z^n$ $\mathrm{b}^n\mathrm{b}_t^n\mathrm{b}_z^n$		
82	pdf_Higgs_qq	$\mathrm{v}^n\mathrm{v}_t^n\mathrm{v}_z^n$ $\mathrm{b}^n\mathrm{b}_t^n\mathrm{b}_z^n$		$\mathrm{v}^n\mathrm{v}_t^n\mathrm{v}_z^n$ $\mathrm{b}^n\mathrm{b}_t^n\mathrm{b}_z^n$	$\mathrm{v}^n\mathrm{v}_t^n\mathrm{v}_z^n$ $\mathrm{b}^n\mathrm{b}_t^n\mathrm{b}_z^n$
83	pdf_Higgs_qq_ACCEPT	$\mathrm{v}^n\mathrm{v}_t^n\mathrm{v}_z^n$ $\mathrm{b}^n\mathrm{b}_t^n\mathrm{b}_z^n$		$\mathrm{v}^n\mathrm{v}_t^n\mathrm{v}_z^n$ $\mathrm{b}^n\mathrm{b}_t^n\mathrm{b}_z^n$	$\mathrm{v}^n\mathrm{v}_t^n\mathrm{v}_z^n$ $\mathrm{b}^n\mathrm{b}_t^n\mathrm{b}_z^n$

Table B.5. *Nuisance parameter (NP) correlations in the analysis of the search for* $H \to \tau^+\tau^- \to \ell^+\ell^- 4\nu$ *across the categories VBF/Boosted signal regions (v/b) using the BDT classifier distribution and the single bin top quark enriched* ($\mathrm{v}_t/\mathrm{b}_t$) *and* $Z \to ee/\mu\mu$ *enriched control regions* ($\mathrm{v}_z/\mathrm{b}_z$)*. The superscript denotes if the NP is included as normalization (n) and/or shape uncertainty (s) in the specific region.*

No	NP	VBF$H \to W^+W^-$	GGF$H \to W^+W^-$	W$H \to W^+W^-$	Z$H \to W^+W^-$
1	ANA_EMB_ISOL				
2	ANA_EMB_MFS				
3	ANA_LL_Fake_bv				
4	ANA_LL_Fake_bv_SH				
5	ANA_LL_Top_boost				
6	ANA_LL_Top_vbf				
7	ANA_LL_Zll_boost				
8	ANA_LL_Zll_vbf				
9	ANA_LL_Zll_vbf_DETAJJ				
10	ANA_LL_Ztt_bv				
11	BCH_LL_bv	$\mathrm{v}_t^n \mathrm{v}_z^n$ $\mathrm{b}_t^n \mathrm{b}_z^n$	$\mathrm{v}_t^n \mathrm{v}_z^n$ $\mathrm{b}_t^n \mathrm{b}_z^n$	$\mathrm{v}_t^n \mathrm{v}_z^n$ $\mathrm{b}_t^n \mathrm{b}_z^n$	$\mathrm{v}_t^n \mathrm{v}_z^n$ $\mathrm{b}_t^n \mathrm{b}_z^n$
12	BR_WW	$\mathrm{v}_t^n \mathrm{v}_z^n$ $\mathrm{b}_t^n \mathrm{b}_z^n$	$\mathrm{v}_t^n \mathrm{v}_z^n$ $\mathrm{b}_t^n \mathrm{b}_z^n$	$\mathrm{v}_t^n \mathrm{v}_z^n$ $\mathrm{b}_t^n \mathrm{b}_z^n$	$\mathrm{v}_t^n \mathrm{v}_z^n$ $\mathrm{b}_t^n \mathrm{b}_z^n$
13	BR_tautau				
14	BTag_B10	v_t^n b_t^n	v_t^n b_t^n		
15	BTag_B1		b_t^n		b_t^n
16	BTag_B3				b_t^n
17	BTag_B5				b_t^n
18	BTag_B6				b_t^n
19	BTag_B7				b_t^n
20	BTag_B8		v_t^n		
21	BTag_B9		v_t^n b_t^n		b_t^n
22	BTag_C1	v_t^n b_t^n	b_t^n	b_t^n	b_t^n
23	BTag_C2	v_t^n b_t^n	v_t^n b_t^n	b_t^n	b_t^n
24	BTag_C3	v_t^n b_t^n	b_t^n	b_t^n	
25	BTag_C4	v_t^n b_t^n	v_t^n b_t^n	$\mathrm{b}^n \mathrm{b}_t^n$	$\mathrm{b}^n \mathrm{b}_t^n$
26	BTag_L10	v_t^n b_t^n	b_t^n		b_t^n
27	BTag_L11	v_t^n b_t^n	v_t^n b_t^n		b_t^n
28	BTag_L12	v_t^n b_t^n	v_t^n b_t^n		$\mathrm{b}_t^n \mathrm{b}_z^n$
29	BTag_L8	b_t^n	b_t^n		
30	BTag_L9				
31	BTag_T4				

Table B.6. *Nuisance parameter (NP) correlations in the analysis of the search for $H \to \tau^+\tau^- \to \ell^+\ell^- 4\nu$ across the categories VBF/Boosted signal regions (v/b) using the BDT classifier distribution and the single bin top quark enriched (v_t/b_t) and $Z \to ee/\mu\mu$ enriched control regions (v_z/b_z). The superscript denotes if the NP is included as normalization (n) and/or shape uncertainty (s) in the specific region.*

No	NP	VBF$H \to W^+W^-$	GGF$H \to W^+W^-$	W$H \to W^+W^-$	Z$H \to W^+W^-$
32	EL_EFF	$\mathrm{v}^n\mathrm{v}_t^n\mathrm{v}_z^n$ $\mathrm{b}^n\mathrm{b}_t^n\mathrm{b}_z^n$	$\mathrm{v}^n\mathrm{v}_t^n$ $\mathrm{b}^n\mathrm{b}_t^n\mathrm{b}_z^n$	v^n $\mathrm{b}^n\mathrm{b}_t^n\mathrm{b}_z^n$	b^n b_z^n
33	EL_EFF_Emb				
34	EL_RES	$\mathrm{v}_t^n\mathrm{v}_z^n$ $\mathrm{b}^n\mathrm{b}_t^n$	v^n $\mathrm{b}_t^n\mathrm{b}_z^n$	v^n b^n	b^n
35	EL_SCALE	$\mathrm{v}_t^n\mathrm{v}_z^n$ $\mathrm{b}^{sn}\mathrm{b}_t^n\mathrm{b}_z^n$	v^n $\mathrm{b}^n\mathrm{b}_t^n\mathrm{b}_z^n$	v^n b^n	b^n
36	JER	$\mathrm{v}^{sn}\mathrm{v}_t^n\mathrm{v}_z^n$ $\mathrm{b}^{sn}\mathrm{b}_t^n\mathrm{b}_z^n$	$\mathrm{v}^{sn}\mathrm{v}_t^n\mathrm{v}_z^n$ $\mathrm{b}^{sn}\mathrm{b}_t^n\mathrm{b}_z^n$	v^n $\mathrm{b}^n\mathrm{b}_t^n$	$\mathrm{b}^n\mathrm{b}_t^n$
37	JES_Detector1	$\mathrm{v}^n\mathrm{v}_t^n\mathrm{v}_z^n$ $\mathrm{b}^{sn}\mathrm{b}_t^n\mathrm{b}_z^n$	$\mathrm{v}^n\mathrm{v}_t^n\mathrm{v}_z^n$ $\mathrm{b}^{sn}\mathrm{b}_t^n\mathrm{b}_z^n$	$\mathrm{b}^n\mathrm{b}_t^n$	b^n
38	JES_Modelling1	$\mathrm{v}^{sn}\mathrm{v}_t^n\mathrm{v}_z^n$ $\mathrm{b}^{sn}\mathrm{b}_t^n\mathrm{b}_z^n$	$\mathrm{v}^{sn}\mathrm{v}_t^n\mathrm{v}_z^n$ $\mathrm{b}^{sn}\mathrm{b}_t^n\mathrm{b}_z^n$	$\mathrm{b}^n\mathrm{b}_t^n$	$\mathrm{b}^n\mathrm{b}_t^n$
39	JES_Detector2	$\mathrm{v}_t^n\mathrm{v}_z^n$ b^s	v_t^n $\mathrm{b}^{sn}\mathrm{b}_t^n$	b^n	$\mathrm{b}^n\mathrm{b}_t^n$
40	JES_Detector3	$\mathrm{v}_t^n\mathrm{v}_z^n$ b^{sn}	$\mathrm{v}^n\mathrm{v}_t^n$ b^{sn}		$\mathrm{b}^n\mathrm{b}_t^n$
41	JES_Eta_StatMethod	$\mathrm{v}^{sn}\mathrm{v}_t^n\mathrm{v}_z^n$ $\mathrm{b}^{sn}\mathrm{b}_t^n\mathrm{b}_z^n$	$\mathrm{v}^n\mathrm{v}_t^n$ $\mathrm{b}^{sn}\mathrm{b}_t^n\mathrm{b}_z^n$	b^n	$\mathrm{b}^n\mathrm{b}_t^n$
42	JES_Mixed1		b_t^n	b^n	
43	JES_Mixed2	v_t^n	$\mathrm{v}^n\mathrm{v}_t^n$ $\mathrm{b}^n\mathrm{b}_t^n$	b^n	b^n
44	JES_Modelling2	$\mathrm{v}_t^n\mathrm{v}_z^n$ $\mathrm{b}^{sn}\mathrm{b}_t^n$	v_t^n $\mathrm{b}^{sn}\mathrm{b}_t^n\mathrm{b}_z^n$	b^n	$\mathrm{b}^n\mathrm{b}_t^n$
45	JES_Modelling3	$\mathrm{v}_t^n\mathrm{v}_z^n$ b^{sn}	$\mathrm{b}^{sn}\mathrm{b}_t^n$	b^n	$\mathrm{b}^n\mathrm{b}_t^n$
46	JES_Modelling4	$\mathrm{v}_t^n\mathrm{v}_z^n$	v^n $\mathrm{b}^{sn}\mathrm{b}_t^n$	b^n	$\mathrm{b}^n\mathrm{b}_t^n$
47	JES_PilePt	$\mathrm{v}^s\mathrm{v}_t^n\mathrm{v}_z^n$ b^{sn}	$\mathrm{v}^n\mathrm{v}_t^n$ $\mathrm{b}^{sn}\mathrm{b}_t^n$		b^n
48	JES_PileRho_TAU_GG		$\mathrm{v}^n\mathrm{v}_t^n$ $\mathrm{b}^{sn}\mathrm{b}_t^n$		
49	JES_PileRho_TAU_QG				
50	JES_PileRho_TAU_QQ	$\mathrm{v}^n\mathrm{v}_t^n\mathrm{v}_z^n$ $\mathrm{b}^s\mathrm{b}_t^n$		b^n	$\mathrm{b}^n\mathrm{b}_t^n$
51	JES_Statistical1	$\mathrm{v}^n\mathrm{v}_t^n\mathrm{v}_z^n$ $\mathrm{b}^s\mathrm{b}_t^n$	$\mathrm{v}^{sn}\mathrm{v}_t^n$ $\mathrm{b}^{sn}\mathrm{b}_t^n$	b^n	b^n
52	JES_Statistical2	v_t^n	$\mathrm{v}^n\mathrm{v}_t^n$ $\mathrm{b}^n\mathrm{b}_t^n$		b^n
53	JES_Statistical3	$\mathrm{v}_t^n\mathrm{v}_z^n$ b^{sn}	$\mathrm{v}^n\mathrm{v}_t^n$ $\mathrm{b}^{sn}\mathrm{b}_t^n$	b^n	$\mathrm{b}^n\mathrm{b}_t^n$
54	JES_Eta_Modelling_LL	$\mathrm{v}^{sn}\mathrm{v}_t^n\mathrm{v}_z^n$ $\mathrm{b}^{sn}\mathrm{b}_t^n\mathrm{b}_z^n$	$\mathrm{v}^{sn}\mathrm{v}_t^n\mathrm{v}_z^n$ $\mathrm{b}^{sn}\mathrm{b}_t^n\mathrm{b}_z^n$	v^n $\mathrm{b}^n\mathrm{b}_t^n$	$\mathrm{b}^n\mathrm{b}_t^n$
55	JES_FlavComp_TAU_G		$\mathrm{v}^{sn}\mathrm{v}_t^n\mathrm{v}_z^n$ $\mathrm{b}^{sn}\mathrm{b}_t^n\mathrm{b}_z^n$		
56	JES_FlavComp_TAU_Q	$\mathrm{v}^{sn}\mathrm{v}_t^n\mathrm{v}_z^n$ $\mathrm{b}^{sn}\mathrm{b}_t^n\mathrm{b}_z^n$		$\mathrm{b}^n\mathrm{b}_t^n$	b^n
57	JES_FlavResp	$\mathrm{v}^n\mathrm{v}_t^n\mathrm{v}_z^n$ $\mathrm{b}^{sn}\mathrm{b}_t^n$	$\mathrm{v}^n\mathrm{v}_t^n\mathrm{v}_z^n$ $\mathrm{b}^{sn}\mathrm{b}_t^n\mathrm{b}_z^n$	$\mathrm{b}^n\mathrm{b}_t^n$	b^n
58	JES_Flavb	v_t^n b_t^n	v_t^n b_t^n		$\mathrm{b}^n\mathrm{b}_t^n$
59	JES_Mu	$\mathrm{v}_t^n\mathrm{v}_z^n$ b^{sn} b_z^n	$\mathrm{v}^n\mathrm{v}_t^n$ $\mathrm{b}^{sn}\mathrm{b}_t^n$	b^n	b^n
60	JES_NPV	$\mathrm{v}^n\mathrm{v}_t^n\mathrm{v}_z^n$ $\mathrm{b}^{sn}\mathrm{b}_t^n$	$\mathrm{v}^{sn}\mathrm{v}_t^n\mathrm{v}_z^n$ $\mathrm{b}^{sn}\mathrm{b}_t^n$	$\mathrm{b}^n\mathrm{b}_t^n$	b^n
61	JVF	v_t^n b_t^n	$\mathrm{v}^n\mathrm{v}_t^n$	v^n b^n	

Table B.7. *Nuisance parameter (NP) correlations in the analysis of the search for $H \to \tau^+\tau^- \to \ell^+\ell^- 4\nu$ across the categories VBF/Boosted signal regions (v/b) using the BDT classifier distribution and the single bin top quark enriched (v_t/b_t) and $Z \to ee/\mu\mu$ enriched control regions (v_z/b_z). The superscript denotes if the NP is included as normalization (n) and/or shape uncertainty (s) in the specific region.*

No	NP	VBF$H \to W^+W^-$	GGF$H \to W^+W^-$	W$H \to W^+W^-$	Z$H \to W^+W^-$
62	LUMI	$v^n v_t^n v_z^n$ $b^n b_t^n b_z^n$	$v^n v_t^n v_z^n$ $b^n b_t^n b_z^n$	$v^n v_t^n v_z^n$ $b^n b_t^n b_z^n$	$v^n v_t^n v_z^n$ $b^n b_t^n b_z^n$
63	MET_RESOSOFT	v_t^n $b^{sn} b_t^n$	v^n $b^{sn} b_t^n$	b^n	b^n
64	MET_SCALESOFT	v_t^n b^s	b^s		$b^n b_t^n$
65	MUID_RES	v_t^n			
66	MUMS_RES	v_t^n	b_t^n	b^n	b^n
67	MU_EFF	$v^n v_t^n v_z^n$ $b^n b_t^n b_z^n$	$v^n v_t^n v_z^n$ $b^n b_t^n$	v^n $b^n b_t^n b_z^n$	$b^n b_t^n$
68	MU_EFF_Emb				
69	MU_SCALE	v_t^n	b^s		b_t^n
70	Matching_ACCEPT				
71	TRIG_LL_SF	$v^n v_t^n v_z^n$ $b^n b_t^n b_z^n$	$v^n v_t^n v_z^n$ $b^n b_t^n b_z^n$	v^n $b^n b_t^n b_z^n$	v^n $b^n b_t^n$
72	UE_gg		$v^n v_t^n v_z^n$ $b^n b_t^n b_z^n$		
73	UE_qq	$v^n v_t^n v_z^n$ $b^n b_t^n b_z^n$			
74	NLO_EW_Higgs	$v^n v_t^n v_z^n$ $b^n b_t^n b_z^n$			
75	QCDscale_VH			$v^n v_t^n v_z^n$ $b^n b_t^n b_z^n$	$v^n v_t^n v_z^n$ $b^n b_t^n b_z^n$
76	QCDscale_ggH_m12		$v^n v_t^n v_z^n$ $b^n b_t^n b_z^n$		
77	QCDscale_ggH_m23				
78	QCDscale_ggH_ptH_m01		$b^n b_t^n b_z^n$		
79	QCDscale_qqH	$v^n v_t^n v_z^n$ $b^n b_t^n b_z^n$			
80	pdf_Higgs_gg		$v^n v_t^n v_z^n$ $b^n b_t^n b_z^n$		
81	pdf_Higgs_gg_ACCEPT				
82	pdf_Higgs_qq	$v^n v_t^n v_z^n$ $b^n b_t^n b_z^n$			
83	pdf_Higgs_qq_ACCEPT				

Table B.8. *Nuisance parameter (NP) correlations in the analysis of the search for $H \to \tau^+\tau^- \to \ell^+\ell^- 4\nu$ across the categories VBF/Boosted signal regions (v/b) using the BDT classifier distribution and the single bin top quark enriched (v_t/b_t) and $Z \to ee/\mu\mu$ enriched control regions (v_z/b_z). The superscript denotes if the NP is included as normalization (n) and/or shape uncertainty (s) in the specific region.*

No	NP	$Z \to \tau_e\tau_e$	$Z \to \tau_\mu\tau_\mu$	$Z \to \tau_e\tau_\mu$	$Z \to \tau_\mu\tau_e$
1	ANA_EMB_ISOL	$\mathrm{v}^n\mathrm{v}_t^n\mathrm{v}_z^n$ $\mathrm{b}^n\mathrm{b}_t^n\mathrm{b}_z^n$	$\mathrm{v}^n\mathrm{v}_t^n\mathrm{v}_z^n$ $\mathrm{b}^n\mathrm{b}_t^n\mathrm{b}_z^n$	$\mathrm{v}^n\mathrm{v}_t^n\mathrm{v}_z^n$ $\mathrm{b}^{sn}\mathrm{b}_t^n\mathrm{b}_z^n$	$\mathrm{v}^n\mathrm{v}_t^n\mathrm{v}_z^n$ $\mathrm{b}^n\mathrm{b}_t^n\mathrm{b}_z^n$
2	ANA_EMB_MFS	$\mathrm{v}^{sn}\mathrm{v}_t^n\mathrm{v}_z^n$ $\mathrm{b}^{sn}\mathrm{b}_t^n\mathrm{b}_z^n$	$\mathrm{v}^{sn}\mathrm{v}_t^n\mathrm{v}_z^n$ $\mathrm{b}^n\mathrm{b}_t^n\mathrm{b}_z^n$	$\mathrm{v}^{sn}\mathrm{v}_t^n\mathrm{v}_z^n$ $\mathrm{b}^{sn}\mathrm{b}_t^n\mathrm{b}_z^n$	$\mathrm{v}^{sn}\mathrm{v}_t^n\mathrm{v}_z^n$ $\mathrm{b}^{sn}\mathrm{b}_t^n\mathrm{b}_z^n$
3	ANA_LL_Fake_bv				
4	ANA_LL_Fake_bv_SH				
5	ANA_LL_Top_boost				
6	ANA_LL_Top_vbf				
7	ANA_LL_Zll_boost				
8	ANA_LL_Zll_vbf				
9	ANA_LL_Zll_vbf_DETAJJ				
10	ANA_LL_Ztt_bv	$\mathrm{v}^n\mathrm{v}_t^n\mathrm{v}_z^n$ $\mathrm{b}^n\mathrm{b}_t^n\mathrm{b}_z^n$	$\mathrm{v}^n\mathrm{v}_t^n\mathrm{v}_z^n$ $\mathrm{b}^n\mathrm{b}_t^n\mathrm{b}_z^n$		
11	BCH_LL_bv				
12	BR_WW				
13	BR_tautau				
14	BTag_B10				
15	BTag_B1				
16	BTag_B3				
17	BTag_B5				
18	BTag_B6				
19	BTag_B7				
20	BTag_B8				
21	BTag_B9				
22	BTag_C1				
23	BTag_C2				
24	BTag_C3				
25	BTag_C4				
26	BTag_L10				
27	BTag_L11				
28	BTag_L12				
29	BTag_L8				
30	BTag_L9				
31	BTag_T4				

Table B.9. *Nuisance parameter (NP) correlations in the analysis of the search for $H \to \tau^+\tau^- \to \ell^+\ell^- 4\nu$ across the categories VBF/Boosted signal regions (v/b) using the BDT classifier distribution and the single bin top quark enriched (v_t/b_t) and $Z \to ee/\mu\mu$ enriched control regions (v_z/b_z). The superscript denotes if the NP is included as normalization (n) and/or shape uncertainty (s) in the specific region.*

No	NP	$Z \to \tau_e\tau_e$	$Z \to \tau_\mu\tau_\mu$	$Z \to \tau_e\tau_\mu$	$Z \to \tau_\mu\tau_e$
32	EL_EFF				
33	EL_EFF_Emb	$\mathrm{v}^n\mathrm{v}_t^n\mathrm{v}_z^n$ $\mathrm{b}^n\mathrm{b}_t^n\mathrm{b}_z^n$		$\mathrm{v}^n\mathrm{v}_t^n$ $\mathrm{b}^n\mathrm{b}_t^n$	$\mathrm{v}^n\mathrm{v}_t^n$ $\mathrm{b}^n\mathrm{b}_t^n$
34	EL_RES	$\mathrm{v}^n\mathrm{v}_t^n\mathrm{v}_z^n$ $\mathrm{b}^s\mathrm{b}_t^n\mathrm{b}_z^n$		v_t^n $\mathrm{b}^s\mathrm{b}_t^n$	v_t^n $\mathrm{b}^s\mathrm{b}_t^n$
35	EL_SCALE	$\mathrm{v}^{sn}\mathrm{v}_t^n\mathrm{v}_z^n$ $\mathrm{b}^{sn}\mathrm{b}_t^n\mathrm{b}_z^n$		$\mathrm{v}^{sn}\mathrm{v}_t^n$ $\mathrm{b}^{sn}\mathrm{b}_t^n$	$\mathrm{v}^n\mathrm{v}_t^n$ $\mathrm{b}^{sn}\mathrm{b}_t^n$
36	JER				
37	JES_Detector1				
38	JES_Modelling1				
39	JES_Detector2				
40	JES_Detector3				
41	JES_Eta_StatMethod				
42	JES_Mixed1				
43	JES_Mixed2				
44	JES_Modelling2				
45	JES_Modelling3				
46	JES_Modelling4				
47	JES_PilePt				
48	JES_PileRho_TAU_GG				
49	JES_PileRho_TAU_QG				
50	JES_PileRho_TAU_QQ				
51	JES_Statistical1				
52	JES_Statistical2				
53	JES_Statistical3				
54	JES_Eta_Modelling_LL				
55	JES_FlavComp_TAU_G				
56	JES_FlavComp_TAU_Q				
57	JES_FlavResp				
58	JES_Flavb				
59	JES_Mu				
60	JES_NPV				
61	JVF				

Table B.10. *Nuisance parameter (NP) correlations in the analysis of the search for $H \to \tau^+\tau^- \to \ell^+\ell^- 4\nu$ across the categories VBF/Boosted signal regions (v/b) using the BDT classifier distribution and the single bin top quark enriched (v_t/b_t) and $Z \to ee/\mu\mu$ enriched control regions (v_z/b_z). The superscript denotes if the NP is included as normalization (n) and/or shape uncertainty (s) in the specific region.*

No	NP	$Z \to \tau_e\tau_e$	$Z \to \tau_\mu\tau_\mu$	$Z \to \tau_e\tau_\mu$	$Z \to \tau_\mu\tau_e$
62	LUMI				
63	MET_RESOSOFT				
64	MET_SCALESOFT				
65	MUID_RES		$\mathrm{v}_t^n\ \mathrm{b}^s$	v_t^n	v_t^n
66	MUMS_RES		$\mathrm{v}_z^n\ \mathrm{b}^s\ \mathrm{b}_z^n$	v_t^n	v_t^n
67	MU_EFF				
68	MU_EFF_Emb		$\mathrm{v}^n\mathrm{v}_t^n\mathrm{v}_z^n\ \mathrm{b}^n\mathrm{b}_t^n\mathrm{b}_z^n$	$\mathrm{v}^n\mathrm{v}_t^n\ \mathrm{b}^n\mathrm{b}_t^n$	$\mathrm{v}^n\mathrm{v}_t^n\ \mathrm{b}^n\mathrm{b}_t^n$
69	MU_SCALE		b^s	v_t^n	$\mathrm{v}_t^n\ \mathrm{b}^s$
70	Matching_ACCEPT				
71	TRIG_LL_SF				
72	UE_gg				
73	UE_qq				
74	NLO_EW_Higgs				
75	QCDscale_VH				
76	QCDscale_ggH_m12				
77	QCDscale_ggH_m23				
78	QCDscale_ggH_ptH_m01				
79	QCDscale_qqH				
80	pdf_Higgs_gg				
81	pdf_Higgs_gg_ACCEPT				
82	pdf_Higgs_qq				
83	pdf_Higgs_qq_ACCEPT				

Table B.11. *Nuisance parameter (NP) correlations in the analysis of the search for $H \to \tau^+\tau^- \to \ell^+\ell^- 4\nu$ across the categories VBF/Boosted signal regions (v/b) using the BDT classifier distribution and the single bin top quark enriched (v_t/b_t) and $Z \to ee/\mu\mu$ enriched control regions (v_z/b_z). The superscript denotes if the NP is included as normalization (n) and/or shape uncertainty (s) in the specific region.*

No	NP	top quark	$Z \to ee/\mu\mu$ & di-boson	fake leptons
1	ANA_EMB_ISOL			
2	ANA_EMB_MFS			
3	ANA_LL_Fake_bv			$\mathrm{v}^n\mathrm{v}_t^n\mathrm{v}_z^n$ $\mathrm{b}^n\mathrm{b}_t^n\mathrm{b}_z^n$
4	ANA_LL_Fake_bv_SH			$\mathrm{v}^s\mathrm{v}_t^n\mathrm{v}_z^n$ $\mathrm{b}^n\mathrm{b}_t^n\mathrm{b}_z^n$
5	ANA_LL_Top_boost	$\mathrm{b}^n\mathrm{b}_t^n\mathrm{b}_z^n$		
6	ANA_LL_Top_vbf	$\mathrm{v}^n\mathrm{v}_t^n\mathrm{v}_z^n$		
7	ANA_LL_Zll_boost		$\mathrm{b}^n\mathrm{b}_t^n\mathrm{b}_z^n$	
8	ANA_LL_Zll_vbf		$\mathrm{v}^n\mathrm{v}_t^n\mathrm{v}_z^n$	
9	ANA_LL_Zll_vbf_DETAJJ		$\mathrm{v}^n\mathrm{v}_t^n\mathrm{v}_z^n$ $\mathrm{b}^n\mathrm{b}_t^n\mathrm{b}_z^n$	
10	ANA_LL_Ztt_bv			
11	BCH_LL_bv	$\mathrm{v}^n\mathrm{v}_t^n\mathrm{v}_z^n$ $\mathrm{b}^n\mathrm{b}_t^n\mathrm{b}_z^n$	$\mathrm{v}^n\mathrm{v}_t^n\mathrm{v}_z^n$ $\mathrm{b}^n\mathrm{b}_t^n\mathrm{b}_z^n$	
12	BR_WW			
13	BR_tautau			
14	BTag_B10	$\mathrm{v}^n\mathrm{v}_t^n\mathrm{v}_z^n$ $\mathrm{b}^n\mathrm{b}_t^n\mathrm{b}_z^n$	v_t^n b_t^n	
15	BTag_B1	b^n	b_t^n	
16	BTag_B3			
17	BTag_B5			
18	BTag_B6	v_z^n b^n b_z^n		
19	BTag_B7	v^n v_z^n b^n b_z^n		
20	BTag_B8	v^n v_z^n b^n b_z^n		
21	BTag_B9	$\mathrm{v}^n\mathrm{v}_t^n\mathrm{v}_z^n$ $\mathrm{b}^n\mathrm{b}_t^n\mathrm{b}_z^n$	b_t^n	
22	BTag_C1		v_t^n b_t^n	
23	BTag_C2		v_t^n b_t^n	
24	BTag_C3		v_t^n b_t^n	
25	BTag_C4		v_t^n b_t^n	
26	BTag_L10		v_t^n b_t^n	
27	BTag_L11		v_t^n b_t^n	
28	BTag_L12		v_t^n b_t^n	
29	BTag_L8			
30	BTag_L9			
31	BTag_T4		v_t^n	

Table B.12. *Nuisance parameter (NP) correlations in the analysis of the search for $H \to \tau^+\tau^- \to \ell^+\ell^- 4\nu$ across the categories VBF/Boosted signal regions (v/b) using the BDT classifier distribution and the single bin top quark enriched (v_t/b_t) and $Z \to ee/\mu\mu$ enriched control regions (v_z/b_z). The superscript denotes if the NP is included as normalization (n) and/or shape uncertainty (s) in the specific region.*

No	NP	top quark	$Z \to ee/\mu\mu$ & di-boson	fake leptons
32	EL_EFF	$\mathrm{v}^n \mathrm{v}_t^n\ \mathrm{b}^n \mathrm{b}_t^n$	$\mathrm{v}^n\ \mathrm{v}_z^n\ \mathrm{b}^n \mathrm{b}_t^n \mathrm{b}_z^n$	
33	EL_EFF_Emb			
34	EL_RES	$\mathrm{v}_z^n\ \mathrm{b}_z^n$	b_t^n	
35	EL_SCALE	$\mathrm{v}^n \mathrm{v}_t^n \mathrm{v}_z^n\ \mathrm{b}^n \mathrm{b}_t^n \mathrm{b}_z^n$	$\mathrm{v}^n \mathrm{v}_t^n \mathrm{v}_z^n\ \mathrm{b}^n \mathrm{b}_t^n \mathrm{b}_z^n$	
36	JER	$\mathrm{v}^{sn}\ \mathrm{v}_z^n\ \mathrm{b}^s\ \mathrm{b}_z^n$	$\mathrm{v}^{sn} \mathrm{v}_t^n \mathrm{v}_z^n\ \mathrm{b}^{sn} \mathrm{b}_t^n \mathrm{b}_z^n$	
37	JES_Detector1	$\mathrm{v}^n \mathrm{v}_t^n \mathrm{v}_z^n\ \mathrm{b}^n \mathrm{b}_t^n \mathrm{b}_z^n$	$\mathrm{v}^n \mathrm{v}_t^n \mathrm{v}_z^n\ \mathrm{b}^{sn} \mathrm{b}_t^n \mathrm{b}_z^n$	
38	JES_Modelling1	$\mathrm{v}^{sn} \mathrm{v}_t^n \mathrm{v}_z^n\ \mathrm{b}^{sn} \mathrm{b}_t^n \mathrm{b}_z^n$	$\mathrm{v}^{sn} \mathrm{v}_t^n \mathrm{v}_z^n\ \mathrm{b}^{sn} \mathrm{b}_t^n \mathrm{b}_z^n$	
39	JES_Detector2	b_z^n	$\mathrm{v}^n \mathrm{v}_t^n\ \mathrm{b}^n \mathrm{b}_t^n \mathrm{b}_z^n$	
40	JES_Detector3	b_z^n	$\mathrm{v}^n \mathrm{v}_t^n \mathrm{v}_z^n\ \mathrm{b}^n \mathrm{b}_t^n \mathrm{b}_z^n$	
41	JES_Eta_StatMethod	$\mathrm{v}^n \mathrm{v}_t^n \mathrm{v}_z^n\ \mathrm{b}^{sn} \mathrm{b}_t^n \mathrm{b}_z^n$	$\mathrm{v}^n \mathrm{v}_t^n \mathrm{v}_z^n\ \mathrm{b}^{sn} \mathrm{b}_t^n \mathrm{b}_z^n$	
42	JES_Mixed1	b_z^n	$\mathrm{v}^n\ \mathrm{b}_z^n$	
43	JES_Mixed2	b_z^n	$\mathrm{v}^n\ \mathrm{v}_z^n$	
44	JES_Modelling2	$\mathrm{b}^n\ \mathrm{b}_z^n$	$\mathrm{v}^n \mathrm{v}_t^n \mathrm{v}_z^n\ \mathrm{b}^{sn} \mathrm{b}_t^n \mathrm{b}_z^n$	
45	JES_Modelling3	v^n	$\mathrm{v}^n \mathrm{v}_t^n \mathrm{v}_z^n\ \mathrm{b}^n \mathrm{b}_t^n \mathrm{b}_z^n$	
46	JES_Modelling4	b_z^n	$\mathrm{v}^n \mathrm{v}_t^n \mathrm{v}_z^n\ \mathrm{b}^n \mathrm{b}_t^n \mathrm{b}_z^n$	
47	JES_PilePt	$\mathrm{v}_z^n\ \mathrm{b}_z^n$	$\mathrm{v}^n \mathrm{v}_t^n \mathrm{v}_z^n\ \mathrm{b}^{sn} \mathrm{b}_t^n \mathrm{b}_z^n$	
48	JES_PileRho_TAU_GG			
49	JES_PileRho_TAU_QG	$\mathrm{v}^n \mathrm{v}_t^n \mathrm{v}_z^n\ \mathrm{b}^n \mathrm{b}_t^n \mathrm{b}_z^n$	$\mathrm{v}^n \mathrm{v}_t^n \mathrm{v}_z^n\ \mathrm{b}^n \mathrm{b}_t^n \mathrm{b}_z^n$	
50	JES_PileRho_TAU_QQ			
51	JES_Statistical1	$\mathrm{v}_t^n \mathrm{v}_z^n\ \mathrm{b}_t^n \mathrm{b}_z^n$	$\mathrm{v}^n \mathrm{v}_t^n \mathrm{v}_z^n\ \mathrm{b}^n \mathrm{b}_t^n \mathrm{b}_z^n$	
52	JES_Statistical2	b_z^n	v^n	
53	JES_Statistical3	$\mathrm{v}_t^n \mathrm{v}_z^n\ \mathrm{b}_t^n \mathrm{b}_z^n$	$\mathrm{v}^n \mathrm{v}_t^n \mathrm{v}_z^n\ \mathrm{b}^n \mathrm{b}_t^n \mathrm{b}_z^n$	
54	JES_Eta_Modelling_LL	$\mathrm{v}^{sn} \mathrm{v}_t^n \mathrm{v}_z^n\ \mathrm{b}^{sn} \mathrm{b}_t^n \mathrm{b}_z^n$	$\mathrm{v}^{sn} \mathrm{v}_t^n \mathrm{v}_z^n\ \mathrm{b}^{sn} \mathrm{b}_t^n \mathrm{b}_z^n$	
55	JES_FlavComp_TAU_G	$\mathrm{v}^{sn} \mathrm{v}_t^n \mathrm{v}_z^n\ \mathrm{b}^{sn} \mathrm{b}_t^n \mathrm{b}_z^n$	$\mathrm{v}^{sn} \mathrm{v}_t^n \mathrm{v}_z^n\ \mathrm{b}^{sn} \mathrm{b}_t^n \mathrm{b}_z^n$	
56	JES_FlavComp_TAU_Q			
57	JES_FlavResp	$\mathrm{v}^{sn} \mathrm{v}_t^n \mathrm{v}_z^n\ \mathrm{b}^n \mathrm{b}_t^n$	$\mathrm{v}^n \mathrm{v}_t^n \mathrm{v}_z^n\ \mathrm{b}^{sn} \mathrm{b}_t^n \mathrm{b}_z^n$	
58	JES_Flavb	$\mathrm{v}_t^n \mathrm{v}_z^n\ \mathrm{b}^n \mathrm{b}_t^n \mathrm{b}_z^n$	b_t^n	
59	JES_Mu	$\mathrm{v}^n \mathrm{v}_t^n \mathrm{v}_z^n\ \mathrm{b}_z^n$	$\mathrm{v}^n \mathrm{v}_t^n \mathrm{v}_z^n\ \mathrm{b}^n \mathrm{b}_t^n \mathrm{b}_z^n$	
60	JES_NPV	$\mathrm{v}_t^n \mathrm{v}_z^n\ \mathrm{b}^n \mathrm{b}_t^n \mathrm{b}_z^n$	$\mathrm{v}^n \mathrm{v}_t^n \mathrm{v}_z^n\ \mathrm{b}^n \mathrm{b}_t^n \mathrm{b}_z^n$	
61	JVF	$\mathrm{v}_z^n\ \mathrm{b}_z^n$	$\mathrm{v}^n \mathrm{v}_t^n \mathrm{v}_z^n\ \mathrm{b}^n \mathrm{b}_t^n \mathrm{b}_z^n$	

Table B.13. *Nuisance parameter (NP) correlations in the analysis of the search for $H \to \tau^+\tau^- \to \ell^+\ell^- 4\nu$ across the categories VBF/Boosted signal regions (v/b) using the BDT classifier distribution and the single bin top quark enriched (v_t/b_t) and $Z \to ee/\mu\mu$ enriched control regions (v_z/b_z). The superscript denotes if the NP is included as normalization (n) and/or shape uncertainty (s) in the specific region.*

No	NP	top quark	$Z \to ee/\mu\mu$ & di-boson	fake leptons
62	LUMI			
63	MET_RESOSOFT	$\mathrm{v}_z^n\ \mathrm{b}^n\ \mathrm{b}_z^n$	$\mathrm{v}^n\ \mathrm{b}^n\mathrm{b}_t^n$	
64	MET_SCALESOFT	$\mathrm{v}_z^n\ \mathrm{b}_z^n$	$\mathrm{v}^n\mathrm{v}_t^n\mathrm{v}_z^n\ \mathrm{b}^n\mathrm{b}_t^n\mathrm{b}_z^n$	
65	MUID_RES	v_z^n	v_t^n	
66	MUMS_RES	v_z^n	$\mathrm{v}_t^n\ \mathrm{b}_t^n$	
67	MU_EFF	$\mathrm{v}^n\mathrm{v}_t^n\mathrm{v}_z^n\ \mathrm{b}^n\mathrm{b}_t^n\mathrm{b}_z^n$	$\mathrm{v}^n\mathrm{v}_t^n\mathrm{v}_z^n\ \mathrm{b}^n\mathrm{b}_t^n\mathrm{b}_z^n$	
68	MU_EFF_Emb			
69	MU_SCALE	$\mathrm{v}^n\ \mathrm{v}_z^n\ \mathrm{b}_z^n$	$\mathrm{v}_t^n\ \mathrm{b}^n\mathrm{b}_t^n\mathrm{b}_z^n$	
70	Matching_ACCEPT			
71	TRIG_LL_SF	$\mathrm{v}^n\mathrm{v}_t^n\mathrm{v}_z^n\ \mathrm{b}^n\mathrm{b}_t^n\mathrm{b}_z^n$	$\mathrm{v}^n\mathrm{v}_t^n\mathrm{v}_z^n\ \mathrm{b}^n\mathrm{b}_t^n\mathrm{b}_z^n$	
72	UE_gg			
73	UE_qq			
74	NLO_EW_Higgs			
75	QCDscale_VH			
76	QCDscale_ggH_m12			
77	QCDscale_ggH_m23			
78	QCDscale_ggH_ptH_m01			
79	QCDscale_qqH			
80	pdf_Higgs_gg			
81	pdf_Higgs_gg_ACCEPT			
82	pdf_Higgs_qq			
83	pdf_Higgs_qq_ACCEPT			

Table B.14. *Nuisance parameter (NP) correlations in the analysis of the search for $H \to \tau^+\tau^- \to \ell^+\ell^- 4\nu$ across the categories VBF/Boosted signal regions (v/b) using the BDT classifier distribution and the single bin top quark enriched (v_t/b_t) and $Z \to ee/\mu\mu$ enriched control regions (v_z/b_z). The superscript denotes if the NP is included as normalization (n) and/or shape uncertainty (s) in the specific region.*

No	NP	VBF$H \to \tau^+\tau^-$	GGF$H \to \tau^+\tau^-$	W$H \to \tau^+\tau^-$	Z$H \to \tau^+\tau^-$
1	ANA_EMB_ISOL				
2	ANA_EMB_MFS				
3	ANA_LL_Fake_bv				
4	ANA_LL_Fake_bv_SH				
5	ANA_LL_Top_vbf				
6	ANA_LL_Zll_vbf				
7	ANA_LL_Zll_vbf_DETAJJ				
8	ANA_LL_Ztt_bv				
9	BCH_LL_bv	h^n $l^n t^n z^n$	h^n $l^n t^n z^n$	h^n $l^n t^n z^n$	h^n $l^n t^n z^n$
10	BR_WW				
11	BR_tautau	h^n $l^n t^n z^n$	h^n $l^n t^n z^n$	h^n $l^n t^n z^n$	h^n $l^n t^n z^n$
12	BTag_B10	t^n	t^n		h^n $l^n t^n$
13	BTag_B6				
14	BTag_B7				t^n
15	BTag_B8				
16	BTag_B9		t^n		t^n
17	BTag_C1	t^n		h^n t^n	h^n
18	BTag_C2	t^n	t^n	t^n	t^n
19	BTag_C3	t^n	t^n	t^n	
20	BTag_C4	t^n	t^n	$t^n z^n$	t^n
21	BTag_L10	t^n	t^n		
22	BTag_L11	t^n		t^n	h^n
23	BTag_L12	t^n	t^n	$t^n z^n$	h^n t^n
24	BTag_L9			t^n	
25	BTag_T4				

Table B.15. *Nuisance parameter (NP) correlations in the CP analysis for $\tilde{d}$=0.0 across the high BDT signal region (h) using the Optimal Observable distribution, the low BDT control region (l) using the BDT classifier distribution and the single bin top quark enriched (t) and $Z \to ee/\mu\mu$ enriched control region (z). The superscript denotes if the NP is included as normalization (n) and/or shape uncertainty (s) in the specific region.*

No	NP	VBF$H \to \tau^+\tau^-$	GGF$H \to \tau^+\tau^-$	W$H \to \tau^+\tau^-$	Z$H \to \tau^+\tau^-$
26	EL_EFF	h^n $l^n t^n z^n$	h^n $l^n t^n z^n$	h^n $l^n t^n z^n$	h^n $l^n t^n$
27	EL_EFF_Emb				
28	EL_RES	l^n z^n	h^n z^n	h^n $l^n t^n$	h^n
29	EL_SCALE	h^n z^n	h^n $l^n t^n z^n$	h^n $l^n t^n z^n$	h^n $l^n t^n$
30	JER	h^{sn} $l^n t^n z^n$	h^s $l^n t^n z^n$	h^{sn} $l^n t^n z^n$	h^{sn} $l^n t^n z^n$
31	JES_Detector1	h^{sn} $l^n t^n z^n$	h^n $t^n z^n$	h^n $l^n t^n$	h^n $l^n t^n z^n$
32	JES_Modelling1	h^n $l^n t^n z^n$	h^n $l^n t^n z^n$	h^n $l^n t^n z^n$	h^n $l^n t^n z^n$
33	JES_Detector2	z^n		h^n $l^n t^n$	h^n l^n
34	JES_Detector3	z^n	h^n	h^n $l^n t^n$	h^n
35	JES_Eta_StatMethod	h^n $t^n z^n$	h^n $l^n t^n z^n$	h^n $l^n t^n$	h^n $l^n t^n$
36	JES_Mixed1	z^n	z^n	h^n l^n	h^n
37	JES_Mixed2		l^n	h^n $l^n t^n$	h^n $l^n t^n$
38	JES_Modelling2	l^n z^n	h^n $l^n t^n z^n$	h^n $l^n t^n$	h^n $l^n t^n z^n$
39	JES_Modelling3	z^n	h^n	h^n $l^n t^n$	h^n l^n
40	JES_Modelling4	z^n		h^n $l^n t^n$	h^n
41	JES_PilePt	z^n	h^n $l^n t^n z^n$	h^n t^n	h^n
42	JES_PileRho_TAU_GG		h^n $l^n t^n z^n$		
43	JES_PileRho_TAU_QG				
44	JES_PileRho_TAU_QQ	h^n $l^n t^n z^n$		h^n $l^n t^n$	h^n l^n z^n
45	JES_Statistical1	h^n l^n z^n	h^n z^n	h^n $l^n t^n$	h^n $l^n t^n$
46	JES_Statistical2		h^n	h^n t^n	h^n
47	JES_Statistical3	h^n z^n	h^n	h^n $l^n t^n$	h^n $l^n t^n$
48	JES_Eta_Modelling_LL	h^{sn} $l^n t^n z^n$	h^{sn} $l^n t^n z^n$	h^{sn} $l^n t^n z^n$	h^{sn} $l^n t^n z^n$
49	JES_FlavComp_TAU_G		h^n $l^n t^n z^n$		
50	JES_FlavComp_TAU_Q	h^{sn} $l^n t^n z^n$		h^n $l^n t^n z^n$	h^n $l^n t^n z^n$
51	JES_FlavResp	h^{sn} $l^n t^n z^n$	h^n $l^n t^n z^n$	h^n $l^n t^n z^n$	h^n $l^n t^n z^n$
52	JES_Flavb		t^n	t^n	h^n $l^n t^n$
53	JES_Mu	h^n $l^n t^n z^n$	h^n t^n	h^n $l^n t^n$	h^n $l^n t^n z^n$
54	JES_NPV	h^n $l^n t^n z^n$	h^n $l^n t^n z^n$	h^n $l^n t^n$	h^n $l^n t^n z^n$
55	JVF	$l^n t^n z^n$	$l^n t^n z^n$	h^n $l^n t^n$	h^n $l^n t^n z^n$

Table B.16. *Nuisance parameter (NP) correlations in the CP analysis for $\tilde{d}$=0.0 across the high BDT signal region (h) using the Optimal Observable distribution, the low BDT control region (l) using the BDT classifier distribution and the single bin top quark enriched (t) and $Z \to ee/\mu\mu$ enriched control region (z). The superscript denotes if the NP is included as normalization (n) and/or shape uncertainty (s) in the specific region.*

No	NP	VBF$H \to \tau^+\tau^-$	GGF$H \to \tau^+\tau^-$	W$H \to \tau^+\tau^-$	Z$H \to \tau^+\tau^-$
56	LUMI	h^n $l^n t^n z^n$	h^n $l^n t^n z^n$	h^n $l^n t^n z^n$	h^n $l^n t^n z^n$
57	MET_RESOSOFT	l^n z^n	h^n $l^n t^n z^n$	h^n $l^n t^n$	h^n $l^n t^n$
58	MET_SCALESOFT	l^n z^n	h^n $l^n t^n$	h^n l^n	h^n $l^n t^n$
59	MUID_RES		h^n z^n	h^n l^n	h^n
60	MUMS_RES	l^n z^n	z^n	h^n z^n	h^n l^n z^n
61	MU_EFF	h^n $l^n t^n z^n$	h^n $l^n t^n z^n$	h^n $l^n t^n z^n$	h^n $l^n t^n z^n$
62	MU_EFF_Emb				
63	MU_SCALE		h^n z^n	h^n l^n z^n	h^n
64	Matching_ACCEPT	h^n $l^n t^n z^n$			
65	TRIG_LL_SF	h^n $l^n t^n z^n$	h^n $l^n t^n z^n$	h^n $l^n t^n z^n$	h^n $l^n t^n z^n$
66	UE_gg		h^n $l^n t^n z^n$		
67	UE_gg_BDT		h^s		
68	UE_qq	h^n $l^n t^n z^n$			
69	UE_qq_BDT	h^s			
70	NLO_EW_Higgs	h^n $l^n t^n z^n$			
71	QCDscale_VH			h^n $l^n t^n z^n$	h^n $l^n t^n z^n$
72	QCDscale_ggH_BDT		h^s		
73	QCDscale_ggH_m12		h^n $l^n t^n z^n$		
74	QCDscale_qqH	h^n $l^n t^n z^n$			
75	REWEIGHT	h^s			
76	pdf_Higgs_gg		h^n $l^n t^n z^n$		
77	pdf_Higgs_gg_ACCEPT		h^n $l^n t^n z^n$		
78	pdf_Higgs_qq	h^n $l^n t^n z^n$		h^n $l^n t^n z^n$	h^n $l^n t^n z^n$
79	pdf_Higgs_qq_ACCEPT	h^n $l^n t^n z^n$		h^n $l^n t^n z^n$	h^n $l^n t^n z^n$

Table B.17. *Nuisance parameter (NP) correlations in the CP analysis for $\tilde{d}$=0.0 across the high BDT signal region (h) using the Optimal Observable distribution, the low BDT control region (l) using the BDT classifier distribution and the single bin top quark enriched (t) and $Z \to ee/\mu\mu$ enriched control region (z). The superscript denotes if the NP is included as normalization (n) and/or shape uncertainty (s) in the specific region.*

No	NP	VBF$H \to W^+W^-$	GGF$H \to W^+W^-$	W$H \to W^+W^-$	Z$H \to W^+W^-$
1	ANA_EMB_ISOL				
2	ANA_EMB_MFS				
3	ANA_LL_Fake_bv				
4	ANA_LL_Fake_bv_SH				
5	ANA_LL_Top_vbf				
6	ANA_LL_Zll_vbf				
7	ANA_LL_Zll_vbf_DETAJJ				
8	ANA_LL_Ztt_bv				
9	BCH_LL_bv	$\mathrm{h}^n\ \mathrm{l}^n\mathrm{t}^n\mathrm{z}^n$	$\mathrm{h}^n\ \mathrm{l}^n\mathrm{t}^n\mathrm{z}^n$	$\mathrm{h}^n\ \mathrm{l}^n\mathrm{t}^n\mathrm{z}^n$	$\mathrm{h}^n\ \mathrm{l}^n\mathrm{t}^n\mathrm{z}^n$
10	BR_WW	$\mathrm{h}^n\ \mathrm{l}^n\mathrm{t}^n\mathrm{z}^n$	$\mathrm{h}^n\ \mathrm{l}^n\mathrm{t}^n\mathrm{z}^n$	$\mathrm{h}^n\ \mathrm{l}^n\mathrm{t}^n\mathrm{z}^n$	$\mathrm{h}^n\ \mathrm{l}^n\mathrm{t}^n\mathrm{z}^n$
11	BR_tautau				
12	BTag_B10	t^n	t^n		
13	BTag_B6				
14	BTag_B7				
15	BTag_B8		t^n		
16	BTag_B9	t^n	t^n		
17	BTag_C1	t^n			
18	BTag_C2	t^n	t^n		
19	BTag_C3	t^n			
20	BTag_C4	t^n	t^n		
21	BTag_L10	t^n			
22	BTag_L11	t^n	t^n		
23	BTag_L12	t^n	t^n		
24	BTag_L9				
25	BTag_T4				

Table B.18. *Nuisance parameter (NP) correlations in the CP analysis for $\tilde{d}$=0.0 across the high BDT signal region (h) using the Optimal Observable distribution, the low BDT control region (l) using the BDT classifier distribution and the single bin top quark enriched (t) and $Z \to ee/\mu\mu$ enriched control region (z). The superscript denotes if the NP is included as normalization (n) and/or shape uncertainty (s) in the specific region.*

No	NP	VBF$H \to W^+W^-$	GGF$H \to W^+W^-$	W$H \to W^+W^-$	Z$H \to W^+W^-$
26	EL_EFF	h^n $l^n t^n z^n$	h^n $l^n t^n$	l^n	
27	EL_EFF_Emb				
28	EL_RES	h^n l^n	h^n	l^n	
29	EL_SCALE	h^n $l^n t^n z^n$	h^n l^n	l^n	
30	JER	h^{sn} $l^n t^n z^n$	h^n $l^n t^n z^n$	l^n	
31	JES_Detector1	h^n $l^n t^n z^n$	h^n $l^n t^n z^n$	l^n	
32	JES_Modelling1	h^{sn} $l^n t^n z^n$	h^n $l^n t^n z^n$	l^n	
33	JES_Detector2	h^n l^n	h^n $l^n t^n$	l^n	
34	JES_Detector3	h^n l^n	h^n $l^n t^n$	l^n	
35	JES_Eta_StatMethod	h^n $l^n t^n z^n$	$l^n t^n$		
36	JES_Mixed1	h^n l^n	l^n	l^n	
37	JES_Mixed2	h^n l^n	h^n $l^n t^n$	l^n	
38	JES_Modelling2	h^n $l^n t^n$	h^n $l^n t^n$	l^n	
39	JES_Modelling3	h^n l^n	h^n l^n	l^n	
40	JES_Modelling4	h^n l^n	h^n	l^n	
41	JES_PilePt	h^n l^n	h^n $l^n t^n$	l^n	
42	JES_PileRho_TAU_GG		h^n $l^n t^n$		
43	JES_PileRho_TAU_QG				
44	JES_PileRho_TAU_QQ	h^n $l^n t^n$		l^n	
45	JES_Statistical1	h^n l^n	h^n $l^n t^n$	l^n	
46	JES_Statistical2	h^n l^n	h^n $l^n t^n$	l^n	
47	JES_Statistical3	h^n l^n	h^n $l^n t^n$	l^n	
48	JES_Eta_Modelling_LL	h^n $l^n t^n z^n$	h^n $l^n t^n z^n$	l^n	
49	JES_FlavComp_TAU_G		h^n $l^n t^n z^n$		
50	JES_FlavComp_TAU_Q	h^n $l^n t^n z^n$		l^n	
51	JES_FlavResp	h^n $l^n t^n z^n$	h^n $l^n t^n z^n$	l^n	
52	JES_Flavb	t^n	t^n		
53	JES_Mu	h^n $l^n t^n$	h^n $l^n t^n$		
54	JES_NPV	h^n $l^n t^n$	h^n $l^n t^n z^n$	l^n	
55	JVF	h^n l^n	h^n $l^n t^n$	l^n	

Table B.19. *Nuisance parameter (NP) correlations in the CP analysis for $\tilde{d}$=0.0 across the high BDT signal region (h) using the Optimal Observable distribution, the low BDT control region (l) using the BDT classifier distribution and the single bin top quark enriched (t) and $Z \to ee/\mu\mu$ enriched control region (z). The superscript denotes if the NP is included as normalization (n) and/or shape uncertainty (s) in the specific region.*

No	NP	VBF$H \to W^+W^-$	GGF$H \to W^+W^-$	W$H \to W^+W^-$	Z$H \to W^+W^-$
56	LUMI	h^n $l^n t^n z^n$	h^n $l^n t^n z^n$	h^n $l^n t^n z^n$	h^n $l^n t^n z^n$
57	MET_RESOSOFT	h^n $l^n t^n$	h^n l^n		
58	MET_SCALESOFT	$l^n t^n$	h^n l^n	l^n	
59	MUID_RES	h^n	h^n	l^n	
60	MUMS_RES	h^n	h^n	l^n	
61	MU_EFF	h^n $l^n t^n z^n$	h^n $l^n t^n z^n$	l^n	
62	MU_EFF_Emb				
63	MU_SCALE	h^n t^n	h^n	l^n	
64	Matching_ACCEPT				
65	TRIG_LL_SF	h^n $l^n t^n z^n$	h^n $l^n t^n z^n$	l^n	l^n
66	UE_gg		h^n $l^n t^n z^n$		
67	UE_gg_BDT		h^s		
68	UE_qq	h^n $l^n t^n z^n$			
69	UE_qq_BDT	h^s			
70	NLO_EW_Higgs	h^n $l^n t^n z^n$			
71	QCDscale_VH			h^n $l^n t^n z^n$	h^n $l^n t^n z^n$
72	QCDscale_ggH_BDT				
73	QCDscale_ggH_m12		h^n $l^n t^n z^n$		
74	QCDscale_qqH	h^n $l^n t^n z^n$			
75	REWEIGHT	h^s			
76	pdf_Higgs_gg		h^n $l^n t^n z^n$		
77	pdf_Higgs_gg_ACCEPT				
78	pdf_Higgs_qq	h^n $l^n t^n z^n$			
79	pdf_Higgs_qq_ACCEPT				

Table B.20. *Nuisance parameter (NP) correlations in the CP analysis for $\tilde{d}$=0.0 across the high BDT signal region (h) using the Optimal Observable distribution, the low BDT control region (l) using the BDT classifier distribution and the single bin top quark enriched (t) and $Z \to ee/\mu\mu$ enriched control region (z). The superscript denotes if the NP is included as normalization (n) and/or shape uncertainty (s) in the specific region.*

No	NP	$Z \to \tau_e\tau_e$	$Z \to \tau_\mu\tau_\mu$	$Z \to \tau_e\tau_\mu$	$Z \to \tau_\mu\tau_e$
1	ANA_EMB_ISOL	$h^n\ l^n t^n z^n$	$h^n\ l^{sn} t^n z^n$	$h^n\ l^{sn} t^n$	$h^{sn}\ l^n t^n$
2	ANA_EMB_MFS	$h^n\ l^{sn} t^n z^n$	$h^n\ t^n z^n$	$h^n\ l^{sn} t^n$	$h^n\ l^{sn} t^n$
3	ANA_LL_Fake_bv				
4	ANA_LL_Fake_bv_SH				
5	ANA_LL_Top_vbf				
6	ANA_LL_Zll_vbf				
7	ANA_LL_Zll_vbf_DETAJJ				
8	ANA_LL_Ztt_bv	$h^n\ l^n t^n z^n$	$h^n\ l^n t^n z^n$		
9	BCH_LL_bv				
10	BR_WW				
11	BR_tautau				
12	BTag_B10				
13	BTag_B6				
14	BTag_B7				
15	BTag_B8				
16	BTag_B9				
17	BTag_C1				
18	BTag_C2				
19	BTag_C3				
20	BTag_C4				
21	BTag_L10				
22	BTag_L11				
23	BTag_L12				
24	BTag_L9				
25	BTag_T4				

Table B.21. *Nuisance parameter (NP) correlations in the CP analysis for $\tilde{d}$=0.0 across the high BDT signal region (h) using the Optimal Observable distribution, the low BDT control region (l) using the BDT classifier distribution and the single bin top quark enriched (t) and $Z \to ee/\mu\mu$ enriched control region (z). The superscript denotes if the NP is included as normalization (n) and/or shape uncertainty (s) in the specific region.*

No	NP	$Z \to \tau_e\tau_e$	$Z \to \tau_\mu\tau_\mu$	$Z \to \tau_e\tau_\mu$	$Z \to \tau_\mu\tau_e$
26	EL_EFF				
27	EL_EFF_Emb	$\mathrm{h}^n\ \mathrm{l}^n\mathrm{t}^n\mathrm{z}^n$		$\mathrm{h}^n\ \mathrm{l}^n\mathrm{t}^n$	$\mathrm{h}^n\ \mathrm{l}^n\mathrm{t}^n$
28	EL_RES	$\mathrm{h}^n\ \mathrm{l}^s\mathrm{t}^n\mathrm{z}^n$		$\mathrm{h}^n\ \mathrm{l}^{sn}\mathrm{t}^n$	$\mathrm{h}^n\ \mathrm{l}^s\mathrm{t}^n$
29	EL_SCALE	$\mathrm{h}^n\ \mathrm{l}^{sn}\mathrm{t}^n\mathrm{z}^n$		$\mathrm{h}^n\ \mathrm{l}^{sn}\mathrm{t}^n$	$\mathrm{h}^n\ \mathrm{l}^{sn}\mathrm{t}^n$
30	JER				
31	JES_Detector1				
32	JES_Modelling1				
33	JES_Detector2				
34	JES_Detector3				
35	JES_Eta_StatMethod				
36	JES_Mixed1				
37	JES_Mixed2				
38	JES_Modelling2				
39	JES_Modelling3				
40	JES_Modelling4				
41	JES_PilePt				
42	JES_PileRho_TAU_GG				
43	JES_PileRho_TAU_QG				
44	JES_PileRho_TAU_QQ				
45	JES_Statistical1				
46	JES_Statistical2				
47	JES_Statistical3				
48	JES_Eta_Modelling_LL				
49	JES_FlavComp_TAU_G				
50	JES_FlavComp_TAU_Q				
51	JES_FlavResp				
52	JES_Flavb				
53	JES_Mu				
54	JES_NPV				
55	JVF				

Table B.22. *Nuisance parameter (NP) correlations in the CP analysis for $\tilde{d}$=0.0 across the high BDT signal region (h) using the Optimal Observable distribution, the low BDT control region (l) using the BDT classifier distribution and the single bin top quark enriched (t) and $Z \to ee/\mu\mu$ enriched control region (z). The superscript denotes if the NP is included as normalization (n) and/or shape uncertainty (s) in the specific region.*

No	NP	$Z \to \tau_e\tau_e$	$Z \to \tau_\mu\tau_\mu$	$Z \to \tau_e\tau_\mu$	$Z \to \tau_\mu\tau_e$
56	LUMI				
57	MET_RESOSOFT				
58	MET_SCALESOFT				
59	MUID_RES		h^n t^n	h^n	h^n $l^s t^n$
60	MUMS_RES		h^n z^n	h^n	h^n $l^{sn} t^n$
61	MU_EFF				
62	MU_EFF_Emb		h^n $l^n t^n z^n$	h^n $l^n t^n$	h^n $l^n t^n$
63	MU_SCALE		h^n	h^n	h^n $l^{sn} t^n$
64	Matching_ACCEPT				
65	TRIG_LL_SF				
66	UE_gg				
67	UE_gg_BDT				
68	UE_qq				
69	UE_qq_BDT				
70	NLO_EW_Higgs				
71	QCDscale_VH				
72	QCDscale_ggH_BDT				
73	QCDscale_ggH_m12				
74	QCDscale_qqH				
75	REWEIGHT				
76	pdf_Higgs_gg				
77	pdf_Higgs_gg_ACCEPT				
78	pdf_Higgs_qq				
79	pdf_Higgs_qq_ACCEPT				

Table B.23. *Nuisance parameter (NP) correlations in the CP analysis for $\tilde{d}$=0.0 across the high BDT signal region (h) using the Optimal Observable distribution, the low BDT control region (l) using the BDT classifier distribution and the single bin top quark enriched (t) and $Z \to ee/\mu\mu$ enriched control region (z). The superscript denotes if the NP is included as normalization (n) and/or shape uncertainty (s) in the specific region.*

No	NP	top quark	$Z \to ee/\mu\mu$ & di-boson	fake leptons
1	ANA_EMB_ISOL			
2	ANA_EMB_MFS			
3	ANA_LL_Fake_bv			h^n $l^n t^n z^n$
4	ANA_LL_Fake_bv_SH			l^{sn}
5	ANA_LL_Top_vbf	h^n $l^n t^n z^n$		
6	ANA_LL_Zll_vbf		h^n $l^n t^n z^n$	
7	ANA_LL_Zll_vbf_DETAJJ		h^n $l^n t^n z^n$	
8	ANA_LL_Ztt_bv			
9	BCH_LL_bv	h^n $l^n t^n z^n$	h^n $l^n t^n z^n$	
10	BR_WW			
11	BR_tautau			
12	BTag_B10	h^n $l^n t^n z^n$	t^n	
13	BTag_B6	z^n		
14	BTag_B7	l^n z^n		
15	BTag_B8	l^n z^n		
16	BTag_B9	h^n $l^n t^n z^n$		
17	BTag_C1		t^n	
18	BTag_C2		t^n	
19	BTag_C3		t^n	
20	BTag_C4		t^n	
21	BTag_L10		t^n	
22	BTag_L11		t^n	
23	BTag_L12		t^n	
24	BTag_L9			
25	BTag_T4		t^n	

Table B.24. *Nuisance parameter (NP) correlations in the CP analysis for $\tilde{d}$=0.0 across the high BDT signal region (h) using the Optimal Observable distribution, the low BDT control region (l) using the BDT classifier distribution and the single bin top quark enriched (t) and $Z \to ee/\mu\mu$ enriched control region (z). The superscript denotes if the NP is included as normalization (n) and/or shape uncertainty (s) in the specific region.*

No	NP	top quark	$Z \to ee/\mu\mu$ & di-boson	fake leptons
26	EL_EFF	$h^n\ l^n t^n$	z^n	
27	EL_EFF_Emb			
28	EL_RES	$h^n\ l^n\ z^n$	h^n	
29	EL_SCALE	$h^n\ l^n t^n z^n$	$h^n\ l^n t^n z^n$	
30	JER	$h^n\ l^{sn}\ z^n$	$h^{sn}\ l^{sn} t^n z^n$	
31	JES_Detector1	$h^n\ l^n t^n z^n$	$h^n\ l^n t^n z^n$	
32	JES_Modelling1	$h^n\ l^n t^n z^n$	$h^{sn}\ l^{sn} t^n z^n$	
33	JES_Detector2	$h^n\ l^n$	$h^n\ l^n t^n$	
34	JES_Detector3	h^n	$h^n\ l^n t^n z^n$	
35	JES_Eta_StatMethod	$h^n\ l^n t^n z^n$	$h^n\ l^n t^n z^n$	
36	JES_Mixed1	h^n	$h^n\ l^n$	
37	JES_Mixed2	$h^n\ l^n$	$h^n\ l^n\ z^n$	
38	JES_Modelling2	$h^n\ l^n$	$h^n\ l^n t^n z^n$	
39	JES_Modelling3	h^n	$h^n\ l^n t^n z^n$	
40	JES_Modelling4	h^n	$h^n\ l^n t^n z^n$	
41	JES_PilePt	$h^n\ l^n\ z^n$	$h^n\ l^n t^n z^n$	
42	JES_PileRho_TAU_GG			
43	JES_PileRho_TAU_QG	$h^n\ l^n t^n z^n$	$h^n\ l^n t^n z^n$	
44	JES_PileRho_TAU_QQ			
45	JES_Statistical1	$h^n\ t^n z^n$	$h^n\ l^n t^n z^n$	
46	JES_Statistical2	$h^n\ l^n$	$h^n\ l^n\ z^n$	
47	JES_Statistical3	$h^n\ l^{sn}\ z^n$	$h^n\ l^n t^n z^n$	
48	JES_Eta_Modelling_LL	$h^n\ l^{sn} t^n z^n$	$h^{sn}\ l^{sn} t^n z^n$	
49	JES_FlavComp_TAU_G	$h^n\ l^{sn} t^n z^n$	$h^{sn}\ l^{sn} t^n z^n$	
50	JES_FlavComp_TAU_Q			
51	JES_FlavResp	$h^n\ l^{sn} t^n z^n$	$h^{sn}\ l^{sn} t^n z^n$	
52	JES_Flavb	$h^n\ l^n t^n z^n$	h^n	
53	JES_Mu	$h^n\ l^n t^n z^n$	$h^n\ l^n t^n z^n$	
54	JES_NPV	$h^n\ l^n t^n z^n$	$h^{sn}\ l^n t^n z^n$	
55	JVF	$h^n\ z^n$	$h^n\ l^n t^n z^n$	

Table B.25. *Nuisance parameter (NP) correlations in the CP analysis for $\tilde{d}$=0.0 across the high BDT signal region (h) using the Optimal Observable distribution, the low BDT control region (l) using the BDT classifier distribution and the single bin top quark enriched (t) and $Z \to ee/\mu\mu$ enriched control region (z). The superscript denotes if the NP is included as normalization (n) and/or shape uncertainty (s) in the specific region.*

No	NP	top quark	$Z \to ee/\mu\mu$ & di-boson	fake leptons
56	LUMI			
57	MET_RESOSOFT	h^n z^n	h^n $l^n t^n z^n$	
58	MET_SCALESOFT	h^n l^n z^n	h^n $l^n t^n z^n$	
59	MUID_RES	h^n l^n z^n	h^n t^n	
60	MUMS_RES	h^n l^{sn} z^n	h^n $l^n t^n$	
61	MU_EFF	h^n $l^n t^n z^n$	h^n $l^n t^n z^n$	
62	MU_EFF_Emb			
63	MU_SCALE	h^n l^n z^n	h^n t^n	
64	Matching_ACCEPT			
65	TRIG_LL_SF	h^n $l^n t^n z^n$	h^n $l^n t^n z^n$	
66	UE_gg			
67	UE_gg_BDT			
68	UE_qq			
69	UE_qq_BDT			
70	NLO_EW_Higgs			
71	QCDscale_VH			
72	QCDscale_ggH_BDT			
73	QCDscale_ggH_m12			
74	QCDscale_qqH			
75	REWEIGHT			
76	pdf_Higgs_gg			
77	pdf_Higgs_gg_ACCEPT			
78	pdf_Higgs_qq			
79	pdf_Higgs_qq_ACCEPT			

Table B.26. *Nuisance parameter (NP) correlations in the CP analysis for $\tilde{d}$=0.0 across the high BDT signal region (h) using the Optimal Observable distribution, the low BDT control region (l) using the BDT classifier distribution and the single bin top quark enriched (t) and $Z \to ee/\mu\mu$ enriched control region (z). The superscript denotes if the NP is included as normalization (n) and/or shape uncertainty (s) in the specific region.*

Bibliography

[1] CMS Collaboration, C. Collaboration, *Observation of a new boson at a mass of 125 GeV with the CMS experiment at the LHC*, *Phys. Lett. B* **716** (2012) no. arXiv:1207.7235. CMS-HIG-12-028. CERN-PH-EP-2012-220 30–61. 59 p. http://cds.cern.ch/record/1471016.

[2] G. A. et al., *Observation of a new particle in the search for the standard model higgs boson with the {ATLAS} detector at the {LHC}*, *Physics Letters B* **716** (2012) no. 1 1 – 29. http://www.sciencedirect.com/science/article/pii/S037026931200857X.

[3] P. W. Higgs, *Broken Symmetries and the Masses of Gauge Bosons*, *Phys. Rev. Lett.* **13** (1964) 508–509.

[4] P. W. Higgs, *Spontaneous Symmetry Breakdown without Massless Bosons*, *Phys. Rev.* **145** (1966) 1156–1163.

[5] F. Englert and R. Brout, *Broken Symmetry and the Mass of Gauge Vector Mesons*, *Phys. Rev. Lett.* **13** (1964) 321–323.

[6] ATLAS, CMS, G. Aad et al., *Combined Measurement of the Higgs Boson Mass in pp Collisions at $\sqrt{s} = 7$ and 8 TeV with the ATLAS and CMS Experiments*, *Phys. Rev. Lett.* **114** (2015) 191803, [arXiv:1503.0758].

[7] ATLAS, G. Aad et al., *Modelling $Z \to \tau\tau$ processes in ATLAS with τ-embedded $Z \to \mu\mu$ data*, *JINST* **10** (2015) no. 09 P09018, [arXiv:1506.0562].

[8] T. A. collaboration et al, *Evidence for the higgs-boson yukawa coupling to tau leptons with the atlas detector*, *JHEP* **1504** (2015) 117, [arXiv:1501.0494]. http://link.springer.com/article/10.1007%2FJHEP04%282015%29117.

[9] ATLAS, G. Aad et al., *Test of CP Invariance in vector-boson fusion production of the Higgs boson using the Optimal Observable method in the ditau decay channel with the ATLAS detector*, arXiv:1602.0451.

[10] Super-Kamiokande Collaboration, Y. e. a. Fukuda, *Evidence for oscillation of atmospheric neutrinos*, *Phys. Rev. Lett.* **81** (1998) 1562–1567. http://link.aps.org/doi/10.1103/PhysRevLett.81.1562.

[11] SNO Collaboration, Q. R. e. a. Ahmad, *Measurement of the rate of $\nu_e + d \to p + p + e^-$ interactions produced by ^8b solar neutrinos at the sudbury neutrino observatory*, *Phys. Rev. Lett.* **87** (2001) 071301. http://link.aps.org/doi/10.1103/PhysRevLett.87.071301.

[12] SNO Collaboration, Q. R. e. a. Ahmad, *Direct evidence for neutrino flavor transformation from neutral-current interactions in the sudbury neutrino observatory*, *Phys. Rev. Lett.* **89** (2002) 011301. http://link.aps.org/doi/10.1103/PhysRevLett.89.011301.

[13] Particle Data Group, K. A. Olive et al., *Review of Particle Physics*, *Chin. Phys.* **C38** (2014) 090001.

[14] P. Schmüser, *Feynman-Graphen und Eichtheorien für Experimentalphysiker*, Springer, zweite, neubearbeitete auflage 1995 ed.

[15] D. Griffiths, *Introduction to Elementary Particles*, Wiley-VCH, 2nd revised edition ed.

[16] G. 't Hooft and M. J. G. Veltman, *Regularization and Renormalization of Gauge Fields*, *Nucl. Phys.* **B44** (1972) 189–213.

[17] S. L. Glashow, *Partial Symmetries of Weak Interactions*, *Nucl. Phys.* **22** (1961) 579–588.

[18] S. Weinberg, *A Model of Leptons*, *Phys. Rev. Lett.* **19** (1967) 1264–1266.

[19] A. Salam, *Weak and Electromagnetic Interactions*, *Conf. Proc.* **C680519** (1968) 367–377.

[20] N. Cabibbo, *Unitary Symmetry and Leptonic Decays*, *Phys. Rev. Lett.* **10** (1963) 531–533.

[21] M. Kobayashi and T. Maskawa, *CP Violation in the Renormalizable Theory of Weak Interaction*, *Prog. Theor. Phys.* **49** (1973) 652–657.

[22] G. S. Guralnik, C. R. Hagen, and T. W. B. Kibble, *Global Conservation Laws and Massless Particles*, *Phys. Rev. Lett.* **13** (1964) 585–587.

[23] T. W. B. Kibble, *Symmetry breaking in nonAbelian gauge theories*, *Phys. Rev.* **155** (1967) 1554–1561.

[24] A. Djouadi, *The Anatomy of electro-weak symmetry breaking. I: The Higgs boson in the standard model*, *Phys. Rept.* **457** (2008) 1–216, [hep-ph/0503172].

[25] CMS, W. de Boer, *The Discovery of the Higgs Boson with the CMS Detector and its Implications for Supersymmetry and Cosmology*, arXiv:1309.0721. https://inspirehep.net/record/1252561/files/arXiv:1309.0721.pdf.

[26] D. J. Gross and F. Wilczek, *Ultraviolet Behavior of Nonabelian Gauge Theories*, *Phys. Rev. Lett.* **30** (1973) 1343–1346.

[27] H. D. Politzer, *Reliable Perturbative Results for Strong Interactions?*, *Phys. Rev. Lett.* **30** (1973) 1346–1349.

[28] z.B.: N.R. Mohapatra, *Unification and Supersymmetry: The Frontiers of Quark-Lepton Physics*, Springer, New York [u.a.], 2. ed. (1992).

[29] z.B.: E. W. Kolb and M. S. Turner, *The Early Universe*, Addison-Wesley, New York (1990).

[30] S. Weinberg, *Gauge Hierarchies*, *Phys. Lett.* **B82** (1979) 387.

[31] M. J. G. Veltman, *The Infrared - Ultraviolet Connection*, *Acta Phys. Polon.* **B12** (1981) 437.

[32] C. H. Llewellyn Smith and G. G. Ross, *The Real Gauge Hierarchy Problem*, *Phys. Lett.* **B105** (1981) 38.

[33] z.B.: I.J. Aitchison, *Supersymmetry In Particle Physics: An Elementary Introduction*, Cambridge, University Press (2007).

[34] J. Wess and B. Zumino, *Supergauge Transformations in Four-Dimensions*, *Nucl. Phys.* **B70** (1974) 39–50.

[35] LHC Higgs Cross Section Working Group, S. Dittmaier et al., *Handbook of LHC Higgs Cross Sections: 1. Inclusive Observables*, arXiv:1101.0593. http://arxiv.org/abs/1101.0593.

[36] K. Riesselmann, *Limitations of a standard model Higgs boson*, hep-ph/9711456.
http://alice.cern.ch/format/showfull?sysnb=0263144.

[37] G. Degrassi, S. Di Vita, J. Elias-Miro, J. R. Espinosa, G. F. Giudice, G. Isidori, and A. Strumia, *Higgs mass and vacuum stability in the Standard Model at NNLO*, *JHEP* **08** (2012) 098, [arXiv:1205.6497].

[38] Tevatron Electroweak Working Group, CDF, DELPHI, Heavy Flavour Group, ALEPH, SLD Electroweak Working Group, LEP Electroweak Working Group, SLD, OPAL, D0, L3, *Precision Electroweak Measurements and Constraints on the Standard Model*, arXiv:0811.4682.

[39] CDF, D0, T. Aaltonen et al., *Combined CDF and D0 Upper Limits on Standard Model Higgs Boson Production with up to 8.2 fb^{-1} of Data*, in *Proceedings, 46th Rencontres de Moriond on Electroweak Interactions and Unified Theories*, 2011. arXiv:1103.3233.

[40] DELPHI, OPAL, LEP Electroweak, ALEPH, L3, S. Schael et al., *Electroweak Measurements in Electron-Positron Collisions at W-Boson-Pair Energies at LEP*, *Phys. Rept.* **532** (2013) 119–244, [arXiv:1302.3415].

[41] ATLAS, G. Aad et al., *Measurements of the Higgs boson production and decay rates and coupling strengths using pp collision data at $\sqrt{s} = 7$ and 8 TeV in the ATLAS experiment*, *Eur. Phys. J.* **C76** (2016) no. 1 6, [arXiv:1507.0454].

[42] ATLAS Collaboration, *Study of the spin and parity of the Higgs boson in diboson decays with the ATLAS detector*, *Eur. Phys. J.* **C75** (2015) 476, [arXiv:1506.0566].

[43] CMS Collaboration, *Constraints on the spin-parity and anomalous HVV couplings of the Higgs boson in proton collisions at 7 and 8 TeV*, *Phys. Rev.* **D92** (2015) 012004, [arXiv:1411.3441].

[44] A. D. Sakharov, *Baryon asymmetry of the universe*, *Sov. Phys. Usp.* **34** (1991) 417–421.

[45] A. D. Sakharov, *Baryonic Asymmetry of the Universe*, [Zh. Eksp. Teor. Fiz.76,1172(1979)], *Sov. Phys. JETP* **49** (1979) 594–599.

[46] A. D. Sakharov, *Violation of CP Invariance, c Asymmetry, and Baryon Asymmetry of the Universe*, [Usp. Fiz. Nauk161,61(1991)], *Pisma Zh. Eksp. Teor. Fiz.* **5** (1967) 32–35.

[47] P. Huet and E. Sather, *Electroweak baryogenesis and standard model CP violation*, *Phys. Rev.* **D51** (1995) 379–394, [hep-ph/9404302].

[48] M. B. Gavela, P. Hernandez, J. Orloff, and O. Pene, *Standard model CP violation and baryon asymmetry*, *Mod. Phys. Lett.* **A9** (1994) 795–810, [hep-ph/9312215].

[49] Planck, P. A. R. Ade et al., *Planck 2015 results. XIII. Cosmological parameters*, arXiv:1502.0158.

[50] ATLAS, ATLAS Collaboration, *Constraints on non-Standard Model Higgs boson interactions in an effective Lagrangian using differential cross sections measured in the $H \to \gamma\gamma$ decay channel at $\sqrt{s} = 8$ TeV with the ATLAS detector*, *Phys. Lett.* **B753** (2016) 69–85, [arXiv:1508.0250].

[51] W. Buchmuller and D. Wyler, *Effective Lagrangian Analysis of New Interactions and Flavor Conservation*, *Nucl. Phys.* **B268** (1986) 621–653.

[52] B. Grzadkowski, M. Iskrzynski, M. Misiak, and J. Rosiek, *Dimension-Six Terms in the Standard Model Lagrangian*, *JHEP* **10** (2010) 085, [arXiv:1008.4884].

[53] V. Hankele, G. Klamke, D. Zeppenfeld, and T. Figy, *Anomalous Higgs boson couplings in vector boson fusion at the CERN LHC*, *Phys. Rev.* **D74** (2006) 095001, [hep-ph/0609075].

[54] OPAL, OPAL Collaboration, G. Abbiendi et al., *Measurement of W boson polarizations and CP violating triple gauge couplings from W^+W^- production at LEP*, *Eur. Phys. J.* **C19** (2001) 229–240, [hep-ex/0009021].

[55] ALEPH, ALEPH Collaboration, S. Schael et al., *Improved measurement of the triple gauge-boson couplings gamma WW and ZWW in e^+e^- collisions*, *Phys. Lett.* **B614** (2005) 7–26.

[56] DELPHI, DELPHI Collaboration, J. Abdallah et al., *Study of W boson polarisations and Triple Gauge boson Couplings in the reaction $e^+e^- \to W^+W^-$ at LEP 2*, *Eur. Phys. J.* **C54** (2008) 345–364, [arXiv:0801.1235].

[57] L3 Collaboration, P. Achard et al., *Search for anomalous couplings in the Higgs sector at LEP*, *Phys. Lett.* **B589** (2004) 89–102, [hep-ex/0403037].

[58] Lyndon Evans and Philip Bryant, *LHC Machine*, *JINST* **3** (2008) no. S08001 . http://iopscience.iop.org/1748-0221/3/08/S08001.

[59] CERN. Geneva, *LEP design report*, CERN-LEP-84-01. https://cds.cern.ch/record/102083.

[60] *Design report Tevatron 1 Project*, FERMILAB-DESIGN-1982-01. http://lss.fnal.gov/archive/design/.

[61] CERN, *LHC Design Report*, . http://ab-div.web.cern.ch/ab-div/Publications/LHC-DesignReport.html.

[62] M. Benedikt et al, *The PS Complex as Proton Pre-Injector for the LHC - Design and Implementation Report*, CERN 2000-03. http://blas.web.cern.ch/blas/Publications/2000-03.pdf.

[63] F. Blas et al, *Conversion of the PS complex as LHC proton pre-injector*, CERN-PS-97-048-DI. https://cdsweb.cern.ch/record/328735.

[64] D.J. Warner et al, *CERN heavy-ion facility design report*, CERN-93-01. https://cds.cern.ch/record/249000/.

[65] M. Chanel, *LEIR: The Low Energy Ion Ring at CERN*, CERN/PS 2002-015 (AE). http://epaper.kek.jp/e02/PAPERS/THPLE074.pdf.

[66] Collier P. et al, *The SPS as injector for LHC: Conceptual design*, CERN-SL-97-007-DI. http://cds.cern.ch/record/322782.

[67] *Exhibition: BIG SCIENCE The LHC in pictures*, . http://bigscience.web.cern.ch/bigscience/Welcome.html.

[68] The ATLAS Collaboration et al, *The ATLAS Experiment at the CERN Large Hadron Collider*, *JINST* **3** (2008) no. S08003 . http://iopscience.iop.org/1748-0221/3/08/S08003/pdf/1748-0221_3_08_S08003.pdf.

[69] CMS Collaboration et al, *The CMS experiment at the CERN LHC*, *JINST* **3** (2008) no. S08004 . http://iopscience.iop.org/1748-0221/3/08/S08004/.

[70] The ALICE Collaboration et al , *The ALICE experiment at the CERN LHC*, *JINST* **3** (2008) no. S08002 . http://iopscience.iop.org/1748-0221/3/08/S08002.

[71] The LHCb Collaboration et al, *The LHCb Detector at the LHC*, *JINST* **3** (2008) no. S08005 . http://iopscience.iop.org/1748-0221/3/08/S08005/.

[72] MoEDAL Collaboration et al, *Technical Design Report of the MoEDAL Experiment*, CERN-LHCC-2009-006, MoEDAL-TDR-001. http://moedal.web.cern.ch/sites/moedal.web.cern.ch/files/publications/tdr-v7.pdf.

[73] LHCf Collaboration et al, *Technical design report of the LHCf experiment: Measurement of photons and neutral pions in the very forward region of LHC*, LHCF-TDR-001, CERN-LHCC-2006-004. http://cds.cern.ch/record/926196.

[74] TOTEM Collaboration et al, *TOTEM: Technical design report. Total cross section, elastic scattering and diffraction dissociation at the Large Hadron Collider at CERN*, CERN-LHCC-2004-002, TOTEM-TDR-001. http://cds.cern.ch/record/704349.

[75] The ATLAS Collaboration et al, *Luminosity Determination in pp Collisions at $\sqrt{s} = 7$ TeV Using the ATLAS Detector at the LHC*, CERN-PH-EP-2010-069, *Eur. Phys. J.* **C71** (2011) no. 1630 . http://arxiv.org/abs/1101.2185.

[76] The ATLAS Collaboration et al, *Improved luminosity determination in pp collisions at $\sqrt{s} = 7$ TeV using the ATLAS detector at the LHC* , CERN-PH-EP-2013-026, *Eur. Phys. J.* **C73** (2011) no. 2518 . http://link.springer.com/article/10.1140/epjc/s10052-013-2518-3.

[77] The ATLAS Collaboration et al, *Integrated luminosity summary plots for 2011-2012 data taking*, . https://twiki.cern.ch/twiki/bin/view/AtlasPublic/LuminosityPublicResults.

[78] The ATLAS collaboration et al, *The ATLAS Data Acquisition and High Level Trigger Systems: Experience and Upgrade Plans*, ATL-DAQ-PROC-2012-073. http://cds.cern.ch/record/1459209.

[79] W. S. J.M. Campbell, J.W. Huston, *Hard interactions of quarks and gluons: a primer for lhc physics*, *Rep. Prog. Phys.* **70** (2007) no. 89 . http://arxiv.org/abs/hep-ph/0611148.

[80] The ATLAS Collaboration et al, *The ATLAS Simulation Infrastructure*, *Eur. Phys. J.* **C70** (2010) no. 3 823–874. http://inspirehep.net/record/856179.

[81] S. M. Torbjörn Sjöstrand and P. Skands, *Pythia 6.4 physics and manual*, *JHEP* **05** (2006) no. 026 . http://iopscience.iop.org/1126-6708/2006/05/026.

[82] T. Gleisberg et al, *Event generation with SHERPA 1.1*, SLAC-PUB-13420, *JHEP* **02** (2009) no. 007 . http://iopscience.iop.org/1126-6708/2009/02/007/.

[83] Siegert, Frank, *Monte-Carlo event generation for the LHC*, *Durham theses* (2010) . http://etheses.dur.ac.uk/484/.

[84] G. Altarelli and G. Parisi, *Asymptotic freedom in parton language*, *Nucl. Phys.* **B** (1977) no. 126 298. http://www.sciencedirect.com/science/article/pii/0550321377903844.

[85] Yu.L. Dokshitzer, *Calculation of the Structure Functions for Deep Inelastic Scattering and e+ e- Annihilation by Perturbation Theory in Quantum Chromodynamics*, *Sov. Phys. JETP* (1977) no. 46 641. inspirehep.net/record/126153.

[86] V.N. Gribov, L.N. Lipatov, *Deep inelastic e p scattering in perturbation theory*, *Sov. J. Nucl. Phys.* (1972) no. 15 438. http://www.slac.stanford.edu/spires/topcites/1996/eprints/by_hep-ex_annual.shtml.

[87] Richard D. Ball et al, *Parton distributions with LHC data*, CERN-PH-TH/2012-03, arXiv:1207.1303. http://arxiv.org/abs/1207.1303.

[88] New parton distributions for collider physics, *Hung-Liang Lai et al*, MSUHEP-100707, *Phys. Rev.* **D** (2010) no. 82:07402 . http://hep.pa.msu.edu/cteq/public/cteq6.html.

[89] A.D. Martin et al, *Parton distributions for the LHC*, Cavendish-HEP-08/16, *Eur. Phys. J.* **C** (2009) no. 63 189. http://arxiv.org/abs/0901.0002.

[90] B. R. W. R. K. Ellis, W. J. Stirling, *QCD and Collider Physics*, Cambridge University Press, 2003.

[91] Peter Zeiler Skands, *Tuning Monte Carlo Generators: The Perugia Tune*, CERN-PH-TH/2010-113, *Phys. Rev.* **D** (2010) no. 82:074018 . http://arxiv.org/pdf/1005.3457v5.pdf.

[92] Stefano Catani et al, *QCD Matrix Elements + Parton Showers*, *JHEP* **11** (2001) no. 063 . http://iopscience.iop.org/1126-6708/2001/11/063/.

[93] Stephen Mrenna and Peter Richardson, *Matching matrix elements and parton showers with HERWIG and PYTHIA*, *JHEP* **05** (2004) no. 040 . http://iopscience.iop.org/1126-6708/2004/05/040/.

[94] Gennaro Corcella et al, *HERWIG 6: an event generator for hadron emission reactions with interfering gluons (including supersymmetric processes)* , *JHEP* **01** (2001) no. 010 . http://iopscience.iop.org/1126-6708/2001/01/010/.

[95] Michelangelo L. Mangano et al, *ALPGEN, a generator for hard multiparton processes in hadronic collisions*, *JHEP* **07** (2003) no. 001 . http://iopscience.iop.org/1126-6708/2003/07/001/.

[96] Borut Paul Kersevan, Elzbieta Richter-Was, *The Monte Carlo Event Generator AcerMC 2.0 with Interfaces to PYTHIA 6.2 and HERWIG 6.5*, TPJU-6/2004. http://arxiv.org/abs/hep-ph/0405247.

[97] Paolo Nason, *A New Method for Combining NLO QCD with Shower Monte Carlo Algorithms*, Bicocca-FT-04-11, *JHEP* **11** (2004) no. 040 . http://iopscience.iop.org/1126-6708/2004/11/040/.

[98] Stefano Frixione and Bryan R. Webber, *Matching NLO QCD computations and parton shower simulations*, Cavendish-HEP-02/01, *JHEP* **06** (2002) no. 029 . http://iopscience.iop.org/1126-6708/2002/06/029/.

[99] Piotr Golonka, Zbigniew Was, *PHOTOS Monte Carlo: a precision tool for QED correctionsin Z and W decays*, CERN-PH-TH/2005-091, *Eur. Phys. J.* **C** (2006) no. 45 97. http://arxiv.org/abs/hep-ph/0506026.

[100] Stanislaw Jadach, Johann H. KÃ¼hn, Zbigniew Was, *TAUOLA - a library of Monte Carlo programs to simulate decays of polarized τ leptons*, *Comp. Phys. Commun.* **64** (1991) no. 2 275. http://www.sciencedirect.com/science/article/pii/001046559190038M.

[101] S. Agostinelli et al, *Geant4 - a simulation toolkit*, *Nucl. Instrum. Methods Phys. Res.* **A** (2003) no. 506 250–303. http://www.sciencedirect.com/science/article/pii/S0168900203013688.

[102] The ATLAS Collaboration et al, *ATLAS computing technical design report*, ATLAS-TDR-017. https://cdsweb.cern.ch/record/837738/files/lhcc-2005-022.pdf.

[103] T. Cornelissen et al., *Concepts, Design and Implementation of the ATLAS New Tracking (NEWT)*, ATL-SOFT-PUB-2007-007. https://cdsweb.cern.ch/record/1020106.

[104] The ATLAS Collaboration et al, *Performance of the ATLAS Inner Detector Track and Vertex Reconstruction in the High Pile-Up LHC Environment*, ATLAS-CONF-2012-042. http://cds.cern.ch/record/1435196.

[105] ATLAS Collaboration, *Performance of the ATLAS Inner Detector Track and Vertex Reconstruction in the High Pile-Up LHC Environment*, Tech. Rep. ATLAS-CONF-2012-042, CERN, Geneva, 2012.

[106] The ATLAS Collaboration et al, *Performance of primary vertex reconstruction in proton-proton collisions at $\sqrt{s} = 7$ TeV in the ATLAS experiment*, ATLAS-CONF-2010-069. https://cdsweb.cern.ch/record/1281344.

[107] The ATLAS Collaboration et al, *Electron reconstruction and identification efficiency measurements with the ATLAS detector using the 2011 LHC proton-proton collision data*, CERN-PH-EP-2014-040, arXiv:1404.2240. https://atlas.web.cern.ch/Atlas/GROUPS/PHYSICS/PAPERS/PERF-2013-03/.

[108] The ATLAS Collaboration et al, *Electron efficiency measurements with the ATLAS detector using the 2012 LHC proton-proton collision data*, ATLAS-CONF-2014-032. https://atlas.web.cern.ch/Atlas/GROUPS/PHYSICS/CONFNOTES/ATLAS-CONF-2014-032/.

[109] The ATLAS Collaboration et al, *Public Egamma Trigger Plots for Collision Data*, ATL-COM-DAQ-2014-058. https://twiki.cern.ch/twiki/bin/view/AtlasPublic/EgammaTriggerPublicResults.

[110] The ATLAS Collaboration et al, *Improved electron reconstruction in ATLAS using the Gaussian Sum Filter-based model for bremsstrahlung*, ATLAS-CONF-2012-047. https://atlas.web.cern.ch/Atlas/GROUPS/PHYSICS/CONFNOTES/ATLAS-CONF-2012-047/.

[111] The ATLAS Collaboration et al, *Electron performance measurements with the ATLAS detector using the 2010 LHC proton-proton collision data*, CERN-PH-EP-2011-117, *Eur. Phys. J.* **C72** (2012) 1909, [arXiv:1110.3174]. http://link.springer.com/article/10.1140%2Fepjc%2Fs10052-012-1909-1.

[112] The ATLAS Collaboration, *Performance of the ATLAS muon trigger in pp collisions at $\sqrt{s} = 8$ TeV*, CERN-PH-EP-2014-154, *Eur. Phys. J.* **C75** (2015) no. 120 , [arXiv:1408.3179]. http://link.springer.com/article/10.1140/epjc/s10052-015-3325-9.

[113] The ATLAS Collaboration, *Measurement of the muon reconstruction performance of the ATLAS detector using 2011 and 2012 LHC proton-proton collision dat*, CERN-PH-EP-2014-151, *Eur. Phys. J.* **C74** (2014) no. 3130 , [arXiv:1408.3179]. http://arxiv.org/abs/1407.3935.

[114] The ATLAS Collaboration, *Expected performance of the ATLAS experiment - detector, trigger and physics*, CERN-OPEN-2008-020, arXiv:0901.0512. http://arxiv.org/abs/0901.0512.

[115] W. Lampl et al., *Calorimeter Clustering Algorithms: Description and Performance*, ATL-LARG-PUB-2008-002. http://cdsweb.cern.ch/record/1099735.

[116] The ATLAS Collaboration et al, *Jet energy measurement and its systematic uncertainties in proton-proton collisions at $\sqrt{s} = 7$ TeV with the ATLAS detector*, CERN-PH-EP-2013-222, *Eur. Phys. J.* **C** (2015) no. 75:17 , [arXiv:1406.0076]. http://link.springer.com/article/10.1140%2Fepjc%2Fs10052-014-3190-y.

[117] C. Cojocaru et al., *Hadronic calibration of the ATLAS liquid argon end-cap calorimeter in the pseudorapidity region $1.6 < |\eta| < 1.8$ in beam tests*, MPP-2004-81, *Nucl. Instrum. Meth.* **A** (2004) no. 531 481–514, [physics/0407009]. http://www.sciencedirect.com/science/article/pii/S0168900204012884.

[118] E. Abat et al., *Combined performance studies for electrons atthe 2004 ATLAS combined test-beam*, *JINST* **5** (2010) no. P11006 . http://iopscience.iop.org/1748-0221/5/11.

[119] M. Aharrouche et al., *Measurement of the response of theATLAS liquid argon barrel calorimeter to electrons at the 2004 combined test-beam*, *Nucl. Instrum. Meth.* **A** (2010) no. 614 400–432. http://www.sciencedirect.com/science/article/pii/S0168900209023924.

[120] J. Colas et al., *Response uniformity of the ATLAS liquid argonelectromagnetic calorimeter*, *Nucl. Instrum. Meth.* **A** (2007) no. 582 429–455, [arXiv:0709.1094]. http://www.sciencedirect.com/science/article/pii/S0168900207018591.

[121] M. Aharrouche et al., *Energy linearity and resolution of theATLAS electromagnetic barrel calorimeter in an electrontest-beam*, *Nucl. Instrum. Meth.* **A** (2006) no. 568 601–623, [physics/0608012]. http://www.sciencedirect.com/science/article/pii/S0168900206013222.

[122] P. Adragna et al., *Testbeam studies of production modules of theATLAS Tile calorimeter*, ATL-TILECAL-PUB-2009-002, *Nucl. Instrum. Meth.* **A** (2009) no. 606 362–394. http://www.sciencedirect.com/science/article/pii/S016890020900792X.

[123] J. Pinfold et al., *Performance of the ATLAS liquid argon endcapcalorimeter in the pseudorapidity region $2.5 < |\eta| < 4.0$ in beam tests*, *JINST* **8** (2013) no. P05006 . http://iopscience.iop.org/1748-0221/8/05/P05006/.

[124] M. Aharrouche et al, *Study of the response of ATLASelectromagnetic liquid argon calorimeters to muons*, *Nucl. Instrum. Meth.* **A** (2009) no. 606 419–431. http://www.sciencedirect.com/science/article/pii/S0168900209009462.

[125] The ATLAS Collaboration, *Electron performance measurement swith the ATLAS detector using the 2010 LHC proton-protoncollision data*, CERN-PH-EP-2011-117, *Eur. Phys. J.* **C** (2012) no. 72:1909 , [arXiv:1110.3174]. http://link.springer.com/article/10.1140%2Fepjc%2Fs10052-012-1909-1.

[126] The ATLAS Collaboration, *Jet energy measurement with the ATLAS detector in proton-proton collisions at* $\sqrt{s} = 7$ *TeV*, CERN-PH-EP-2011-191, *Eur. Phys. J.* **C** (2013) no. 73:2304 , [arXiv:1112.6426]. http://link.springer.com/article/10.1140%2Fepjc%2Fs10052-013-2304-2.

[127] M. Cacciari et al, *The anti-k_t jet clustering algorithm*, LPTHE-07-03, *JHEP* **04** (2008) no. 063 , [arXiv:0802.1189]. http://iopscience.iop.org/1126-6708/2008/04/063/.

[128] M. Cacciari and G. P. Salam, *Dispelling the N^3 myth for the kt jet-finder*, *Phys. Lett. B* **641** (2006) no. 1 57–61. http://www.sciencedirect.com/science/article/pii/S0370269306010094.

[129] M. Cacciari, G. P. Salam and G. Soyez, *FastJet*, . http://fastjet.fr/, Website.

[130] D. W. Miller et al, *Jet-Vertex Association Algorithm*, ATL-COM-PHYS-2008-008. https://cds.cern.ch/record/1082880.

[131] The ATLAS Collaboration, *Characterisation and mitigation of beam-induced backgrounds observed in the ATLAS detector during the 2011 proton-proton run*, CERN-PH-EP-2012-313, *JINST* **8** (2013) no. P07004 , [arXiv:1303.0223]. http://iopscience.iop.org/1748-0221/8/07/P07004/.

[132] The ATLAS Collaboration et al, *Calibration of the performance of b-tagging for c and light-flavour jets in the 2012 ATLAS data*, ATLAS-CONF-2014-046. https://cds.cern.ch/record/1741020.

[133] The ATLAS Collaboration et al, *Commissioning of the ATLAS high-performance b-tagging algorithms in the 7 TeV collision data*, ATLAS-CONF-2011-102. https://cds.cern.ch/record/1369219.

[134] The ATLAS Collaboration et al, *Calibration of b-tagging using dileptonic top pair events in a combinatorial likelihood approach with the ATLAS experiment*, ATLAS-CONF-2014-004. https://cds.cern.ch/record/1664335.

[135] The ATLAS Collaboration et al, *Identification and energy calibration of hadronically decaying tau leptons with the ATLAS experiment in pp collisions at* $\sqrt{s} = 8$ *TeV*, CERN-PH-EP-2014-227, arXiv:1412.7086. http://arxiv.org/abs/1412.7086.

[136] The ATLAS Collaboration et al, *Performance of Missing Transverse Momentum Reconstruction in ATLAS studied in Proton-Proton Collisions recorded in 2012 at* $\sqrt{s} = 8$ *TeV*, ATLAS-CONF-2013-082. https://cds.cern.ch/record/1570993.

[137] The ATLAS Collaboration et al, *Pile-up Correction in Missing Transverse Momentum Reconstruction in the ATLAS Experiment in Proton-Proton Collisions at* $\sqrt{s} = 8$ *TeV*, ATLAS-CONF-2014-019. https://cds.cern.ch/record/1702055.

[138] LHC Higgs Cross Section Working Group, S. Heinemeyer et al., *Handbook of LHC Higgs Cross Sections: 3. Higgs Properties*, arXiv:1307.1347. http://arxiv.org/abs/1307.1347.

[139] A. Djouadi, M. Spira, and P. Zerwas, *Production of higgs bosons in proton colliders.* $\{QCD\}$ *corrections*, *Physics Letters B* **264** (1991) no. 3-4 440–446. http://www.sciencedirect.com/science/article/pii/037026939190375Z.

[140] S. Dawson, *Radiative corrections to higgs boson production*, *Nuclear Physics B* **359** (1991) no. 2-3 283–300. http://www.sciencedirect.com/science/article/pii/0550321391900612.

[141] M. Spira, A. Djouadi, D. Graudenz, and R. Zerwas, *Higgs boson production at the* $\{LHC\}$, *Nuclear Physics B* **453** (1995) no. 1-2 17–82. http://www.sciencedirect.com/science/article/pii/0550321395003797.

[142] R. V. Harlander and W. B. Kilgore, *Next-to-next-to-leading order higgs production at hadron colliders*, . http://link.aps.org/doi/10.1103/PhysRevLett.88.201801.

[143] C. Anastasiou and K. Melnikov, *Higgs boson production at hadron colliders in* $\{NNLO\}$ $\{QCD\}$, *Nuclear Physics B* **646** (2002) no. 1-2 220–256. http://www.sciencedirect.com/science/article/pii/S0550321302008374.

[144] V. Ravindran, J. Smith, and W. van Neerven, $\{NNLO\}$ *corrections to the total cross section for higgs boson production in hadron-hadron collisions*, *Nuclear Physics B* **665** (2003) no. 0 325–366. http://www.sciencedirect.com/science/article/pii/S0550321303004577.

[145] S. C. et al, *Soft-gluon resummation for higgs boson production at hadron colliders*, *JHEP* **07** (2003) no. 028 CERN-TH/2003-117, [hep-ph/0306211]. http://iopscience.iop.org/1126-6708/2003/07/028/.

[146] U. Aglietti, R. Bonciani, G. Degrassi, and A. Vicini, *Two-loop light fermion contribution to higgs production and decays*, *Physics Letters B* **595** (2004) no. 1-4 432 – 441. http://www.sciencedirect.com/science/article/pii/S0370269304009268.

[147] S. Actis, G. Passarino, C. Sturm, and S. Uccirati, {*NLO*} *electroweak corrections to higgs boson production at hadron colliders*, *Physics Letters B* **670** (2008) no. 1 12–17. http://www.sciencedirect.com/science/article/pii/S0370269308012689.

[148] T. Sjostrand, S. Mrenna, and P. Z. Skands, *A Brief Introduction to PYTHIA 8.1*, *Comput.Phys.Commun.* **178** (2008) 852–867, [arXiv:0710.3820]. http://xxx.lanl.gov/abs/0710.3820.

[149] M. Ciccolini, A. Denner, and S. Dittmaier, *Strong and electroweak corrections to the production of a higgs boson + 2 jets via weak interactions at the large hadron collider*, . http://link.aps.org/doi/10.1103/PhysRevLett.99.161803.

[150] M. Ciccolini, D. A., and D. S., *Electroweak and qcd corrections to higgs production via vector-boson fusion at the cern lhc*, . http://link.aps.org/doi/10.1103/PhysRevD.77.013002.

[151] K. A. et al, *Vbfnlo: A parton level monte carlo for processes with electroweak bosons*, *Computer Physics Communications* **180** (2009) no. 9 1661–1670. http://www.sciencedirect.com/science/article/pii/S0010465509001027.

[152] O. Brein, A. Djouadi, and R. Harlander, {*NNLO*} {*QCD*} *corrections to the higgs-strahlung processes at hadron colliders*, *Physics Letters B* **579** (2004) no. 1-2 149–156. http://www.sciencedirect.com/science/article/pii/S0370269303017234.

[153] M. L. Ciccolini, S. Dittmaier, and M. Krämer, *Electroweak radiative corrections to associated WH and ZH production at hadron colliders*, . http://link.aps.org/doi/10.1103/PhysRevD.68.073003.

[154] S. Catani, L. Cieri, G. Ferrera, D. de Florian, and M. Grazzini, *Vector boson production at hadron colliders: A fully exclusive qcd calculation at next-to-next-to-leading order*, . http://link.aps.org/doi/10.1103/PhysRevLett.103.082001.

[155] S. Catani and M. Grazzini, *Next-to-next-to-leading-order subtraction formalism in hadron collisions and its application to higgs-boson production at the large hadron collider*, . http://link.aps.org/doi/10.1103/PhysRevLett.98.222002.

[156] J. M. Campbell, R. K. Ellis, and C. Williams, *Vector boson pair production at the LHC*, *JHEP* **1107** (2011) 018, [arXiv:1105.0020].

[157] T. Binoth, M. Ciccolini, N. Kauer, and M. Kramer, *Gluon-induced W-boson pair production at the LHC*, *JHEP* **0612** (2006) 046, [hep-ph/0611170].

[158] M. Cacciari, M. Czakon, M. Mangano, A. Mitov, and P. Nason, *Top-pair production at hadron colliders with next-to-next-to-leading logarithmic*

soft-gluon resummation, *Phys.Lett.* **B710** (2012) 612–622, [arXiv:1111.5869].

[159] P. BÃ¤rnreuther, M. Czakon, and A. Mitov, *Percent Level Precision Physics at the Tevatron: First Genuine NNLO QCD Corrections to $q\bar{q} \to t\bar{t} + X$*, *Phys.Rev.Lett.* **109** (2012) 132001, [arXiv:1204.5201].

[160] M. Czakon and A. Mitov, *NNLO corrections to top-pair production at hadron colliders: the all-fermionic scattering channels*, *JHEP* **1212** (2012) 054, [arXiv:1207.0236].

[161] M. Czakon and A. Mitov, *NNLO corrections to top pair production at hadron colliders: the quark-gluon reaction*, *JHEP* **1301** (2013) 080, [arXiv:1210.6832].

[162] M. Czakon, P. Fiedler, and A. Mitov, *Total Top-Quark Pair-Production Cross Section at Hadron Colliders Through $O(\alpha_S^4)$*, *Phys.Rev.Lett.* **110** (2013) 252004, [arXiv:1303.6254].

[163] M. Czakon and A. Mitov, *Top++: A Program for the Calculation of the Top-Pair Cross-Section at Hadron Colliders*, *Comput.Phys.Commun.* **185** (2014) 2930, [arXiv:1112.5675].

[164] N. Kidonakis, *NNLL resummation for s-channel single top quark production*, *Phys.Rev.* **D81** (2010) 054028, [arXiv:1001.5034].

[165] N. Kidonakis, *Next-to-next-to-leading-order collinear and soft gluon corrections for t-channel single top quark production*, *Phys.Rev.* **D83** (2011) 091503, [arXiv:1103.2792].

[166] N. Kidonakis, *Two-loop soft anomalous dimensions for single top quark associated production with a W- or H-*, *Phys.Rev.* **D82** (2010) 054018, [arXiv:1005.4451].

[167] ATLAS, G. Aad et al., *Measurement of the inclusive jet cross-section in proton-proton collisions at $\sqrt{s} = 7$ TeV using 4.5 fb^{-1} of data with the ATLAS detector*, *JHEP* **1502** (2015) 153, [arXiv:1410.8857].

[168] ATLAS, G. Aad et al., *Measurement of dijet cross sections in pp collisions at 7 TeV centre-of-mass energy using the ATLAS detector*, *JHEP* **1405** (2014) 059, [arXiv:1312.3524].

[169] M. Grazzini and H. Sargsyan, *Heavy-quark mass effects in higgs boson production at the lhc*, *Journal of High Energy Physics* **2013** (2013) no. 9 . http://dx.doi.org/10.1007/JHEP09%282013%29129.

[170] P. Bolzoni, F. Maltoni, S.-O. Moch, and M. Zaro, *Higgs boson production via vector-boson fusion at next-to-next-to-leading order in qcd*, . http://link.aps.org/doi/10.1103/PhysRevLett.105.011801.

[171] M. Ciccolini, A. Denner, and S. Dittmaier, *Strong and electroweak corrections to the production of a higgs boson + 2 jets via weak interactions at the large hadron collider*, . http://link.aps.org/doi/10.1103/PhysRevLett.99.161803.

[172] M. Ciccolini, D. A., and D. S., *Electroweak and qcd corrections to higgs production via vector-boson fusion at the cern lhc*, . http://link.aps.org/doi/10.1103/PhysRevD.77.013002.

[173] Jonathan Pumplin et al, *New Generation of Parton Distributions with Uncertainties from Global QCD Analysis* , *JHEP* **07** (2002) no. 012 . http://iopscience.iop.org/1126-6708/2002/07/012/.

[174] ATLAS, *Combined Standard Model Higgs boson searches with up to 2.3 fb-1 of pp collisions at sqrts=7 TeV at the LHC*, .

[175] ATLAS, *Summary of ATLAS Pythia 8 tunes*, .

[176] ATLAS, G. Aad et al., *Observation and measurement of Higgs boson decays to WW^* with the ATLAS detector*, arXiv:1412.2641.

[177] R. Ellis, I. Hinchliffe, M. Soldate, and J. V. D. Bij, *Higgs decay to $\tau^+\tau^-$ a possible signature of intermediate mass higgs bosons at high energy hadron colliders*, *Nuclear Physics B* **297** (1988) no. 2 221 – 243. http://www.sciencedirect.com/science/article/pii/0550321388900193.

[178] N. Moeser, *A Sensitivity Study for Higgs Boson Production in Vector Boson Fusion in the $H \to \tau\tau \to lh + 3\nu$ Final State with ATLAS*. PhD thesis, Bonn U., 2011-09-15.

[179] A. Elagin, P. Murat, A. Pranko, and A. Safonov, *A New Mass Reconstruction Technique for Resonances Decaying to di-tau*, *Nucl.Instrum.Meth.* **A654** (2011) 481–489, [arXiv:1012.4686].

[180] Hoecker, A. et al, *TMVA 4 - Toolkit for Multivariate Data Analysis with ROOT*, physics/0703039. http://tmva.sourceforge.net.

[181] J. R. Quinlan, *Bagging, boosting, and c4.s*, in *Proceedings of the Thirteenth National Conference on Artificial Intelligence - Volume 1*, AAAI'96, pp. 725–730, AAAI Press, 1996.

[182] G. Hanson et al., *Evidence for Jet Structure in Hadron Production by e^+e^- Annihilation*, *Phys. Rev. Lett.* **35** (1975) 1609.

[183] D. Atwood and A. Soni, *Analysis for magnetic moment and electric dipole moment form factors of the top quark via $e^+e^- \to t$ anti-t*, *Phys. Rev. D* **45** (1992) 2405–2413. http://link.aps.org/doi/10.1103/PhysRevD.45.2405.

[184] M. Davier, L. Duflot, F. L. Diberder, and A. RougÃ©, *The optimal method for the measurement of tau polarization*, *Physics Letters B* **306** (1993) no. 3

411 – 417. http://www.sciencedirect.com/science/article/pii/037026939390101M.

[185] M. Diehl and O. Nachtmann, *Optimal observables for the measurement of three gauge boson couplings in $e^+e^- \to w^+w^-$*, *Zeitschrift fÃ¼r Physik C Particles and Fields* **62** (1994) no. 3 397–411. http://dx.doi.org/10.1007/BF01555899.

[186] M. Diehl, O. Nachtmann, and F. Nagel, *Triple gauge couplings in polarized e- e+ —¿ W- W+ and their measurement using optimal observables*, *Eur. Phys. J.* **C27** (2003) 375–397, [hep-ph/0209229].

[187] M. Diehl and O. Nachtmann, *Anomalous three gauge couplings in e+ e- —¿ W+ W- and 'optimal' strategies for their measurement*, *Eur. Phys. J.* **C1** (1998) 177–190, [hep-ph/9702208].

[188] J. Alwall, R. Frederix, S. Frixione, V. Hirschi, F. Maltoni, O. Mattelaer, H. S. Shao, T. Stelzer, P. Torrielli, and M. Zaro, *The automated computation of tree-level and next-to-leading order differential cross sections, and their matching to parton shower simulations*, *JHEP* **07** (2014) 079, [arXiv:1405.0301].

[189] V. Hankele, G. Klamke, D. Zeppenfeld, and T. Figy, *Anomalous Higgs boson couplings in vector boson fusion at the CERN LHC*, *Phys. Rev.* **D74** (2006) 095001, [hep-ph/0609075].

[190] J. Alwall, M. Herquet, F. Maltoni, O. Mattelaer, and T. Stelzer, *MadGraph 5 : Going Beyond*, *JHEP* **06** (2011) 128, [arXiv:1106.0522].

[191] J. M. Campbell, R. K. Ellis, R. Frederix, P. Nason, C. Oleari, and C. Williams, *NLO Higgs Boson Production Plus One and Two Jets Using the POWHEG BOX, MadGraph4 and MCFM*, *JHEP* **07** (2012) 092, [arXiv:1202.5475].

[192] K. Hamilton, P. Nason, and G. Zanderighi, *MINLO: Multi-Scale Improved NLO*, *JHEP* **10** (2012) 155, [arXiv:1206.3572].

[193] Z. Czyczula, T. Przedzinski, and Z. Was, *TauSpinner Program for Studies on Spin Effect in tau Production at the LHC*, *Eur. Phys. J.* **C72** (2012) 1988, [arXiv:1201.0117].

[194] A. Kaczmarska, J. Piatlicki, T. Przedzinski, E. Richter-Was, and Z. Was, *Application of TauSpinner for Studies on τ-Lepton Polarization and Spin Correlations in Z, W and H Decays at the LHC*, *Acta Phys. Polon.* **B45** (2014) no. 10 1921–1946, [arXiv:1402.2068].

[195] I. W. Stewart and F. J. Tackmann, *Theory Uncertainties for Higgs and Other Searches Using Jet Bins*, *Phys. Rev.* **D85** (2012) 034011, [arXiv:1107.2117].

[196] ATLAS, *Procedure for the LHC Higgs boson search combination in summer 2011*, .

[197] ATLAS Collaboration, *Combined Standard Model Higgs boson searches with up to 2.3 fb-1 of pp collisions at sqrts=7 TeV at the LHC*, Tech. Rep. ATLAS-CONF-2011-157, CERN, Geneva, 2011.

[198] R. Brun and F. Rademakers, *ROOT: An object oriented data analysis framework*, *Nucl. Instrum. Meth.* **A389** (1997) 81–86.

[199] G. Cowan, *Statistical data analysis*, Oxford, Oxford University Press (1997) p 216.

[200] S. S. Wilks, *The Large-Sample Distribution of the Likelihood Ratio for Testing Composite Hypotheses*, *Ann. Math. Statist.* **9** (1938) no. 1 60–62. http://dx.doi.org/10.1214/aoms/1177732360.

[201] A. Wald, *Tests of statistical hypotheses concerning several parameters when the number of observations is large*, *Transactions of the American Mathematical Society* **54** (1943) no. 3 426–482. http://www.jstor.org/stable/1990256.

[202] G. Cowan, K. Cranmer, E. Gross, and O. Vitells, *Asymptotic formulae for likelihood-based tests of new physics*, [Erratum: Eur. Phys. J.C73,2501(2013)], *Eur. Phys. J.* **C71** (2011) 1554, [arXiv:1007.1727].

[203] A. L. Read, *Presentation of search results: the cl s technique*, *Journal of Physics G: Nuclear and Particle Physics* **28** (2002) no. 10 2693. http://stacks.iop.org/0954-3899/28/i=10/a=313.

[204] ROOT Collaboration, K. Cranmer, G. Lewis, L. Moneta, A. Shibata, and W. Verkerke, *HistFactory: A tool for creating statistical models for use with RooFit and RooStats*, Tech. Rep. CERN-OPEN-2012-016, New York U., New York, Jan, 2012.

[205] W. Verkerke and D. Kirkby, *The RooFit toolkit for data modeling*, *ArXiv Physics e-prints* (2003) , [physics/0306116].

[206] L. Moneta, K. Cranmer, G. Schott, and W. Verkerke, *The RooStats project*, in *Proceedings of the 13th International Workshop on Advanced Computing and Analysis Techniques in Physics Research. February 22-27, 2010, Jaipur, India. http://acat2010.cern.ch/. Published online at ¡A href="http://pos.sissa.it/cgi-bin/reader/conf.cgi?confid=93"¿http://pos.sissa.it/cgi-bin/reader/conf.cgi?confid=93¡/A¿, p.57*, p. 57, 2010. arXiv:1009.1003.

[207] F. James and M. Roos, *Minuit: a system for function minimization and analysis of the parameter errors and corrections*, *Comput. Phys. Commun.* **10** (1975) no. CERN-DD-75-20 343–367. 38 p. http://lcgapp.cern.ch/project/cls/work-packages/mathlibs/minuit/index.html.

[208] ATLAS, G. Aad et al., *Measurement of the Higgs boson mass from the $H \to \gamma\gamma$ and $H \to ZZ^* \to 4\ell$ channels with the ATLAS detector using 25 fb^{-1} of pp collision data*, *Phys. Rev.* **D90** (2014) no. 5 052004, [arXiv:1406.3827].

Acknowledgement

I want to take the opportunity on the last page of this thesis to thank everybody, who has been involved in my every day work throughout the last years.

Ich möchte all denen danken, die zum Gelingen dieser Arbeit in beträchtlicher Art und Weise beigetragen haben. Lieber Markus, ich möchte an erster Stelle dir für die Möglichkeit danken, in deiner Arbeitsgruppe in einem der in dieser Zeit spannendsten Themen zu promovieren. Die Entscheidung, den Weg in die Teilchenphysik mit dir als Mentor einzuschlagen, war eine gute Entscheidung. Vom stets freundlichen und hilfsbereiten Umgang sowie deiner fachlichen Kompetenz habe ich sehr profitiert. Ich bin glücklich über die lehrreiche Zeit am Physkalischen Institut, die Reisen ans CERN und darüber, meinen Teil zur Suche nach dem Higgs Boson bei ATLAS beigetragen zu haben. Stan, ein nicht minder großes Dankeschön an dich. Deine Unterstützung sowie die positive Energie, die jeden Tag in unser Büro schwappte, waren und bleiben großartig. Solch einen Kollegen kann man sich nur wünschen. Bedanken möchte ich mich auch bei all meinen Mitstreitern: Florian, Felix, Dirk, Claudia, Vakhtang, Julian, Elias, Philip, Michel, Holger, Anton, Alena und Uli. Ihr habt es mir wirklich leicht gemacht, jeden Tag gerne ins Institut zu kommen. Ein explizites Dankeschön an meinen Kollegen Michael; ohne dich wäre der erfolgreiche Umgang mit der IT wohl kaum möglich gewesen. Liebe Chris, herzlichen Dank für deine große Hilfe bei den alltäglichen bürokratischen Hürden. Besonderen Dank auch an meine Büro-Mitbewohnerin und Leidensgenossin Anna; den fachlichen und kollegialen Austausch mit dir habe ich zu jeder Zeit sehr genossen.

So wichtig mein Freiburger Physik-Mikrokosmos für diese Arbeit auch war, so wichtig war und ist für mich die Welt außerhalb der Teilchenphysik. Max, Johannes, Jacki, Matthias, Marcel und Michi, bei Euch möchte ich mich für das Zuhören bei Bier und Wein und für all die tollen Stunden bedanken, in der ich mir meinen Doktoranden-Kummer von der Seele reden durfte. Liebe Jule und Yannis sowie Bernhard, Pia, Birgit mit Familie, Waltraud und Jürgen, meine Basis und ständige Motivation; ihr seid einfach die Besten, vielen Dank fürs da sein. Ganz besonders dein Interesse an meiner Arbeit, Jule, sowie die große Geduld, die du mir in den anstrengenden Phasen meiner Doktorandenzeit entgegengebracht hast, imponieren mir sehr. Du bist schlichtweg toll! Freiburg und meine Jahre am Physikalischen Institut werden mir immer in schöner Erinnerung bleiben.